

JUNE 2021

AJNR

VOLUME 42 • PP 995-1181

AJNR

AMERICAN JOURNAL OF NEURORADIOLOGY

JUNE 2021
VOLUME 42
NUMBER 6
WWW.AJNR.ORG

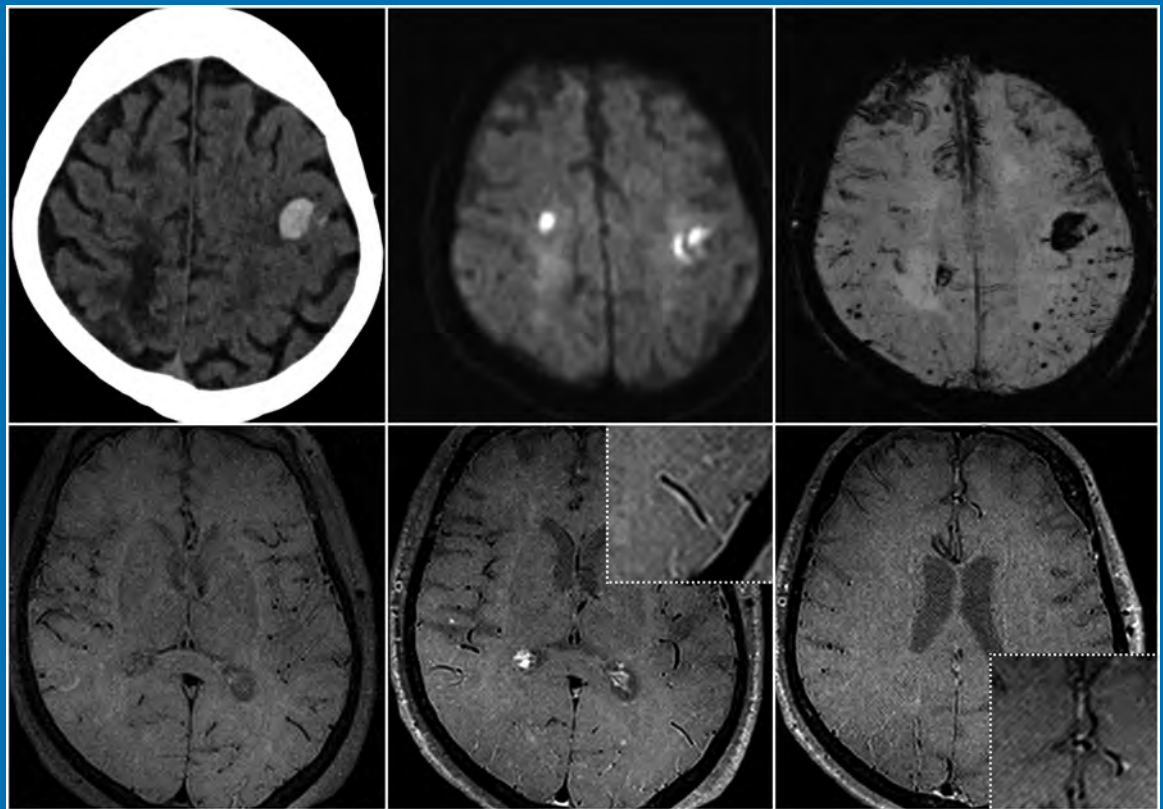
THE JOURNAL OF DIAGNOSTIC AND
INTERVENTIONAL NEURORADIOLOGY

Prediction of future stroke in amyloid angiopathy

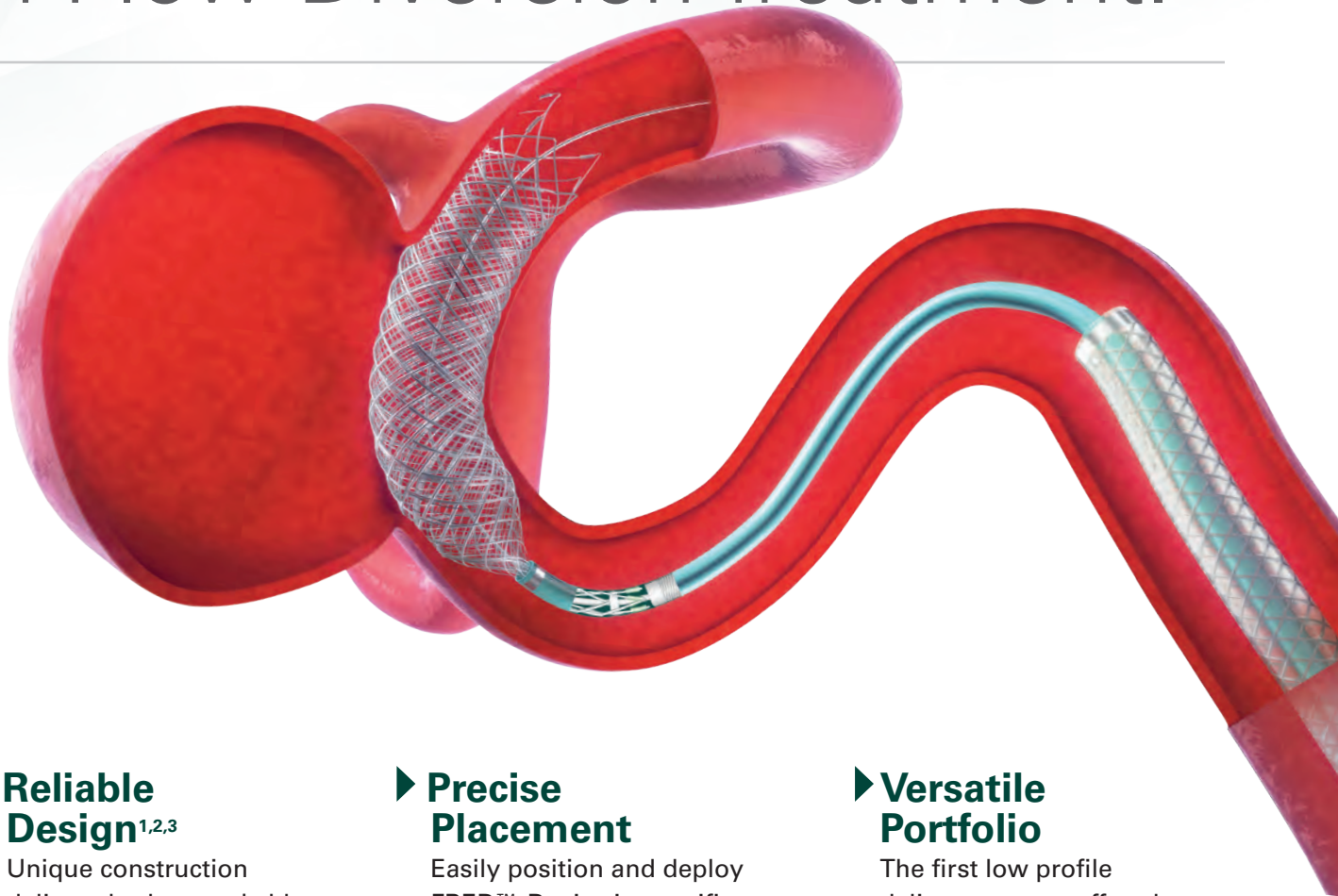
Improving demyelinating lesion detection of the anterior visual pathways

Flow diversion for unruptured ICA bifurcation aneurysms

Official Journal ASNR • ASFNR • ASHNR • ASPNR • ASSR



The New Standard of **Ease and Simplicity** in Flow Diversion Treatment.



► **Reliable Design**^{1,2,3}

Unique construction delivers both remarkable ease of use and excellent flow diversion^{1,2,3}

► **Precise Placement**

Easily position and deploy FRED™ Device in specific, targeted locations^{4,5,6}

► **Versatile Portfolio**

The first low profile delivery system offered in combination with large diameter and long length options

References:

1. TR11-211 2. TR13-171 3. TR15-055 4. TR13-192 5. TR15-072 6. TR19-145

The Flow Re-Direction Endoluminal Device (FRED™) System is indicated for use in the internal carotid artery from the petrous segment to the terminus for the endovascular treatment of adult patients (22 years of age or older) with wide-necked (neck width ≥ 4 mm or dome-to-neck ratio < 2) saccular or fusiform intracranial aneurysms arising from a parent vessel with a diameter ≥ 2.0 mm and ≤ 5.0 mm.

Use of the FRED™ System is contraindicated under these circumstances: Patients in whom anticoagulant, anti-platelet therapy, or thrombolytic drugs are contraindicated. Patients with known hypersensitivity to metal such as nickel-titanium and metal jewelry. Patients with anatomy that does not permit passage or deployment of the FRED™ System. Patients with an active bacterial infection. Patients with a pre-existing stent in place at the target aneurysm. Patients in whom the parent vessel size does not fall within the indicated range. Patients who have not received dual anti-platelet agents prior to the procedure. For complete indications, contraindications, potential complications, warnings, precautions, and instructions, see instructions for use (IFU provided in the device).

RX Only: Federal (United States) law restricts this device to sale by or on the order of a physician.

MICROVENTION™ and FRED™ are registered trademarks of MicroVention, Inc. in the United States and other jurisdictions. © 2020 MicroVention, Inc. 04/2020.



MIDRC

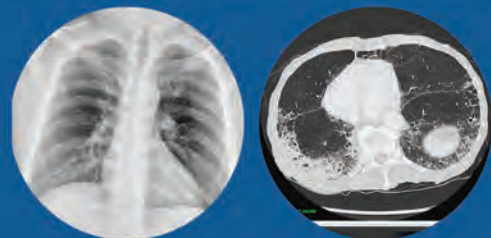
MEDICAL IMAGING AND DATA RESOURCE CENTER.

Medical Imaging in the Fight against COVID-19 Call for Contributions

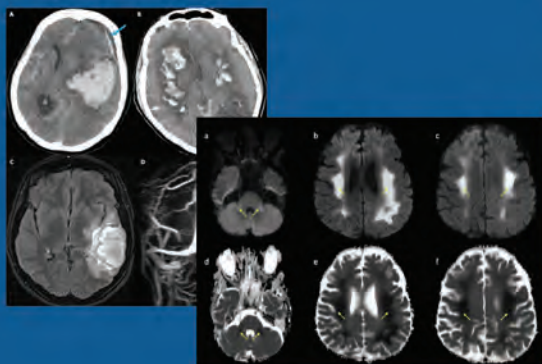
The Medical Imaging and Data Resource Center (MIDRC) is a multi-organizational initiative in the fight against the ongoing worldwide pandemic co-led by the ACR®, the RSNA, and the AAPM and is hosted at the University of Chicago.



The primary goal is to accelerate machine learning research by creating a high quality COVID-19 image commons linked to relevant clinical data made available as a public resource.



ASNR has teamed up with MIDRC to advance the understanding of the neuroimaging manifestations of COVID-19 and to enhance the MIDRC image commons.



- To ensure success, MIDRC encourages all institutions and hospitals, both small and large, to donate their COVID-19 medical images and data to the cause.
- MIDRC provides a HIPAA-compliant mechanism to securely submit medical images and clinical metadata, and is committed to helping institutions throughout the submission process.

Visit midrc.org for more information



National Institute of Biomedical Imaging and Bioengineering
Creating Biomedical Technologies to Improve Health



Simplify the MOC Process



Manage your CME Credits Online

CMEgateway.org

Available to Members of Participating Societies

American Board of Radiology (ABR)
American College of Radiology (ACR)
American Roentgen Ray Society (ARRS)
American Society of Neuroradiology (ASNR)
Commission on Accreditation of Medical
Physics Educational Programs, Inc. (CAMPEP)
Radiological Society of North America (RSNA)
Society of Interventional Radiology (SIR)
SNM
The Society for Pediatric Radiology (SPR)

It's Easy and Free!

Log on to CME Gateway to:

- View or print reports of your CME credits from multiple societies from a single access point.
- Print an aggregated report or certificate from each participating organization.
- Link to SAMs and other tools to help with maintenance of certification.

American Board of Radiology (ABR) participation!

By activating ABR in your organizational profile, your MOC-fulfilling CME and SAM credits can be transferred to your own personalized database on the ABR Web site.

Sign Up Today!

go to CMEgateway.org

We're Inside Every Great Neuroradiologist!

ASNR MEMBERS RECEIVE

American Journal of Neuroradiology (AJNR)

The leading neuroradiology research journal, published monthly

Neurographics

Bimonthly educational journal with CME for members

ASNR Annual Meeting

Discounts for members on the field's premier conference

eCME

Online collection of lectures and articles with SA-CME and Category 1 credit

Advocacy

Coding/reimbursement, quality standards and practice guidelines; demonstrating neuroradiology's value!

Networking

Access to 5,000 peers

... And More!

Join the leaders in neuroradiology today!

Learn more at www.asnr.org/join

ASNR

American Society of Neuroradiology

800 Enterprise Dr., Suite 205, Oak Brook, IL 60523 • (630)574-0220 • membership@asnr.org • www.asnr.org

AJNR *go green*

***AJNR* urges American Society of Neuroradiology members to reduce their environmental footprint by voluntarily suspending their print subscription.**

The savings in paper, printing, transportation, and postage directly fund new electronic enhancements and expanded content.

The digital edition of *AJNR* presents the print version in its entirety, along with extra features including:

- Publication Preview
- Case Collection
- Podcasts
- The *AJNR* News Digest
- The *AJNR* Blog

It also reaches subscribers much faster than print. An electronic table of contents will be sent directly to your mailbox to notify you as soon as it publishes.

Readers can search, reference, and bookmark current and archived content 24 hours a day on www.ajnr.org.

ASNR members who wish to opt out of print can do so by using the *AJNR* Go Green link on the *AJNR* Website (<http://www.ajnr.org/content/subscriber-help-and-services>). Just type your name in the email form to stop print and spare our ecosystem.

FRED™

Flow Re-Direction
Endoluminal Device

FLOW DIVERSION.



SIMPLIFIED.



MicroVention Worldwide
Innovation Center
35 Enterprise
Aliso Viejo, CA 92656 USA
MicroVention UK Limited
MicroVention Europe S.A.R.L.
MicroVention Deutschland GmbH
Web

PH +1 714.247.8000

PH +1 44 (0) 191 258 6777

PH +33 (1) 39 21 77 46

PH +49 211 210 798-0

microvention.com

Explore the New ASNR Career Center



Your Premier Resource for Professional Development

- Access to jobs in the National Healthcare Career Network
- Confidential resume posting
- One-time free resume review
- Professional online profile
- Saved jobs capability

Start here: careers.asnr.org

ASNR
American Society of Neuroradiology

TAKE A NEW **APPROACH** TO RADIAL

Rist™ Radial Access System

The Rist™ Radial Access System features the first guide catheter designed for the unique demands of accessing the neurovasculature through the radial pathway.^{1,2}



See Rist™ in action.

Scan code with your smart phone or visit
[medtronic.com/TakeANewApproach](https://www.medtronic.com/TakeANewApproach)

1. INCTR-12549 2. INCTR-12736

CAUTION: Federal (USA) law restricts this device to sale by or on the order of a physician. Indications, contraindications, warnings and instructions for use can be found on the product labeling supplied with each device. The Rist™ 079 Radial Access Guide Catheter is indicated for the introduction of interventional devices into the peripheral, coronary, and neuro vasculature. The Rist™ Radial Access Selective Catheter is indicated for the introduction of interventional devices into the peripheral, coronary and neuro vasculature. It can be used to facilitate introduction of diagnostic agents in the neuro vasculature. It is not intended to facilitate introduction of diagnostic agents in coronary or peripheral arteries.

© 2021 Medtronic. All rights reserved. Medtronic, Medtronic logo and Further, Together are trademarks of Medtronic. All other brands are trademarks of a Medtronic company. UC202119233 EN

Medtronic

AJNR

AMERICAN JOURNAL OF NEURORADIOLOGY

JUNE 2021
VOLUME 42
NUMBER 6
WWW.AJNR.ORG

Publication Preview at www.ajnr.org features articles released in advance of print. Visit www.ajnrblog.org to comment on AJNR content and chat with colleagues and AJNR's News Digest at <http://ajnrdigest.org> to read the stories behind the latest research in neuroimaging.

995 **PERSPECTIVES** *H. Pendharkar*

EDITORIAL

996 **Insights into the AJNR Review Process** *M.D. Alvin, et al.*

REVIEW ARTICLE

  998 **Complete Evaluation of Dementia: PET and MRI Correlation and Diagnosis for the Neuroradiologist** *J.D. Oldan, et al.* **ADULT BRAIN**

GENERAL CONTENTS

  1008 **Brain and Lung Imaging Correlation in Patients with COVID-19: Could the Severity of Lung Disease Reflect the Prevalence of Acute Abnormalities on Neuroimaging? A Global Multicenter Observational Study** *A. Mahammedi, et al.* **ADULT BRAIN**

 1017 **Impact of SARS-CoV-2 Pandemic on “Stroke Code” Imaging Utilization and Yield** *D.R. Shatzkes, et al.* **ADULT BRAIN**

 1023 **Absent Cortical Venous Filling Is Associated with Aggravated Brain Edema in Acute Ischemic Stroke** *H. Xia, et al.* **ADULT BRAIN**

   1030 **Tissue at Risk and Ischemic Core Estimation Using Deep Learning in Acute Stroke** *Y. Yu, et al.* **ADULT BRAIN FUNCTIONAL**

   1038 **Vessel Wall Enhancement on Black-Blood MRI Predicts Acute and Future Stroke in Cerebral Amyloid Angiopathy** *J.S. McNally, et al.* **ADULT BRAIN FUNCTIONAL**

 1046 **Clinical Features of Cytotoxic Lesions of the Corpus Callosum Associated with Aneurysmal Subarachnoid Hemorrhage** *H. Toi, et al.* **ADULT BRAIN**

 1052 **Diagnostic Accuracy of Arterial Spin-Labeling MR Imaging in Detecting the Epileptogenic Zone: Systematic Review and Meta-analysis** *J.Y. Zeng, et al.* **ADULT BRAIN FUNCTIONAL**

  1061 **Dedicated 3D-T2-STIR-ZOOMit Imaging Improves Demyelinating Lesion Detection in the Anterior Visual Pathways of Patients with Multiple Sclerosis** *E. Pravatà, et al.* **ADULT BRAIN**

 1069 **A Novel Method to Measure Venular Perivascular Spaces in Patients with MS on 7T MRI** *I.C. George, et al.* **ADULT BRAIN FUNCTIONAL**

AJNR (Am J Neuroradiol ISSN 0195–6108) is a journal published monthly, owned and published by the American Society of Neuroradiology (ASNR), 800 Enterprise Drive, Suite 205, Oak Brook, IL 60523. Annual dues for the ASNR include approximately 21% for a journal subscription. The journal is printed by Intellicor Communications, 330 Eden Road, Lancaster, PA 17601; Periodicals postage paid at Oak Brook, IL and additional mailing offices. Printed in the U.S.A. POSTMASTER: Please send address changes to American Journal of Neuroradiology, P.O. Box 3000, Denville, NJ 07834, U.S.A. Subscription rates: nonmember \$410 (\$480 foreign) print and online, \$320 online only; institutions \$470 (\$540 foreign) print and basic online, \$935 (\$1000 foreign) print and extended online, \$380 online only (basic), \$825 online only (extended); single copies are \$35 each (\$40 foreign). Indexed by PubMed/MEDLINE, BIOSIS Previews, Current Contents (Clinical Medicine and Life Sciences), EMBASE, Google Scholar, HighWire Press, Q-Sensei, RefSeek, Science Citation Index, SCI Expanded, Meta/CZI, ReadCube, and Semantic Scholar. Copyright © American Society of Neuroradiology.

	1073	MRI Shrimp Sign in Cerebellar Progressive Multifocal Leukoencephalopathy: Description and Validation of a Novel Observation <i>N. Adra, et al.</i>	ADULT BRAIN
☰	1080	Repeatability of Automated Image Segmentation with BraTumIA in Patients with Recurrent Glioblastoma <i>N. Abu Khalaf, et al.</i>	ADULT BRAIN FUNCTIONAL
★ ☰	1087	Flow-Diversion Treatment for Unruptured ICA Bifurcation Aneurysms with Unfavorable Morphology for Coiling <i>F. Cagnazzo, et al.</i>	INTERVENTIONAL
☰	1093	Propensity Score Analysis of Flow Diverters Placed in Scaffolding Stents <i>A. Poker, et al.</i>	INTERVENTIONAL
☰	1099	Predictors of the Effects of Flow Diversion in Very Large and Giant Aneurysms <i>H.J. Bae, et al.</i>	INTERVENTIONAL
☰	1104	Differential Contribution of ASPECTS Regions to Clinical Outcome after Thrombectomy for Acute Ischemic Stroke <i>S.M. Seyedsaadat, et al.</i>	INTERVENTIONAL
🖋️	1109	Teleproctoring for Neurovascular Procedures: Demonstration of Concept Using Optical See-Through Head-Mounted Display, Interactive Mixed Reality, and Virtual Space Sharing—A Critical Need Highlighted by the COVID-19 Pandemic <i>A.T. Rai, et al.</i>	INTERVENTIONAL
☰	1116	Delayed Contrast-Enhanced MR Angiography for the Assessment of Internal Carotid Bulb Patency in the Context of Acute Ischemic Stroke: An Accuracy, Interrater, and Intrarater Agreement Study <i>W. Boisseau, et al.</i>	EXTRACRANIAL VASCULAR
	1123	MRI Posttreatment Surveillance for Head and Neck Squamous Cell Carcinoma: Proposed MR NI-RADS Criteria <i>M.M. Ashour, et al.</i>	HEAD & NECK
	1130	Detection of Optic Neuritis on Routine Brain MRI without and with the Assistance of an Image Postprocessing Algorithm <i>A. Schroeder, et al.</i>	HEAD & NECK
	1136	Susceptibility-Weighted Imaging of the Pediatric Brain after Repeat Doses of Gadolinium-Based Contrast Agent <i>K. Ozturk, et al.</i>	PEDIATRICS
🔑 ☰	1144	Accumulation of Brain Hypointense Foci on Susceptibility-Weighted Imaging in Childhood Ataxia Telangiectasia <i>R.A. Dineen, et al.</i>	PEDIATRICS
☰	1151	Ganglionic Eminence Anomalies and Coexisting Cerebral Developmental Anomalies on Fetal MR Imaging: Multicenter-Based Review of 60 Cases <i>M. Scarabello, et al.</i>	PEDIATRICS
☰	1157	Anatomic Variation of the Superficial Temporal Artery and Posterior Auricular Artery in a Pediatric Moyamoya Disease Population <i>S. Lee, et al.</i>	PEDIATRICS
	1163	Congenital Nasal Pyriform Aperture Stenosis: Evidence of Premature Fusion of the Midline Palatal Suture <i>T.M. Wine, et al.</i>	PEDIATRICS
☰	1167	Neuroimaging Features of Ectopic Cerebellar Tissue: A Case Series Study of a Rare Entity <i>G. Orman, et al.</i>	PEDIATRICS
☰	1174	Comparison of Radiologists and Other Specialists in the Performance of Lumbar Puncture Procedures Over Time <i>D.R. Johnson, et al.</i>	SPINE

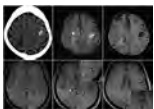
ONLINE FEATURES

LETTERS

- E33 Acute Stroke Imaging in Transfer Patients Who Received Recent Intravenous Iodinated Contrast at an Outside Facility: An Unrecognized Problem That Deserves More Attention** *E. Gulko, et al.*
- E34 Notification of a Voluntary Product Recall for Software Used in a Prior Published Article** *J.M. Mettenburg*
- E35 Improving Access to Fast MRI for Emergent Shunt Evaluation**
C.M. Pfeifer, et al.

BOOK REVIEWS *R.M. Quencer, Section Editor*

Please visit www.ajnrblog.org to read and comment on Book Reviews.



Vessel wall enhancement in McNally JS, et al.



Indicates Editor's Choices selection



Indicates Fellows' Journal Club selection



Indicates open access to non-subscribers at www.ajnr.org



Indicates article with supplemental online data



Indicates article with supplemental online video



Evidence-Based Medicine Level 1



Evidence-Based Medicine Level 2

EDITOR-IN-CHIEF

Jeffrey S. Ross, MD

Professor of Radiology, Department of Radiology,
Mayo Clinic College of Medicine, Phoenix, AZ

SENIOR EDITORS

Harry J. Cloft, MD, PhD

Professor of Radiology and Neurosurgery,
Department of Radiology, Mayo Clinic College of
Medicine, Rochester, MN

Christopher G. Filippi, MD

Professor and Alice Ettinger-Jack R. Dreyfuss
Chair of Radiology,
Tufts University School of Medicine,
Radiologist-in-Chief
Tufts University Medical Center, Boston, MA

Thierry A.G.M. Huisman, MD

Radiologist-in-Chief, Texas Children's Hospital,
Houston, TX

Yvonne W. Lui, MD

Associate Professor of Radiology,
Chief of Neuroradiology,
New York University School of Medicine,
New York, NY

C.D. Phillips, MD, FACR

Professor of Radiology, Weill Cornell Medical
College, Director of Head and Neck Imaging,
New York-Presbyterian Hospital, New York, NY

Lubdhra M. Shah, MD, MS

Professor of Radiology and Director of Spine
Imaging, University of Utah Department of
Radiology and Imaging Sciences, Salt Lake City, UT

STATISTICAL SENIOR EDITOR

Bryan A. Comstock, MS

Senior Biostatistician,
Department of Biostatistics,
University of Washington, Seattle, WA

ARTIFICIAL INTELLIGENCE DEPUTY EDITOR

Peter D. Chang, MD

Assistant Professor-in-Residence,
Departments of Radiological Sciences,
Computer Sciences, and Pathology,
Director, Center for Artificial Intelligence in
Diagnostic Medicine (CAIDM),
University of California, Irvine, Irvine, CA

EDITORIAL BOARD

Ashley H. Aiken, Atlanta, GA

Lea M. Alhilali, Phoenix, AZ

Mohammed A. Almekhlafi, Calgary, Alberta,
Canada

Joachim Berkefeld, Frankfurt, Germany

Aashim Bhatia, Pittsburgh, PA

Waleed Brinjikji, Rochester, MN

Judah Burns, New York, NY

Danielle Byrne, Dublin, Ireland

Federico Cagnazzo, Montpellier, France

J. Levi Chazen, New York, NY

James Y. Chen, San Diego, CA

Gloria C. Chiang, New York, NY

Daniel Chow, Irvine, CA

Kars C.J. Compagne, Rotterdam, The Netherlands

Arturo Consoli, Suresnes, France

Seena Dehkharghani, New York, NY

Nilesh K. Desai, Houston, TX

Yonghong Ding, Rochester, MN

Birgit Ertl-Wagner, Toronto, Ontario, Canada

Clifford J. Eskey, Hanover, NH

Massimo Filippi, Milan, Italy

Nils D. Forkert, Calgary, Alberta, Canada

Ana M. Franceschi, New York, NY

Frank Gaillard, Melbourne, Australia

Joseph J. Gemmete, Ann Arbor, Michigan

Wende N. Gibbs, Phoenix, AZ

Philipp Götz, Erlangen, Germany

Brent Griffith, Detroit, MI

Joseph M. Hoxworth, Phoenix, Arizona

Raymond Y. Huang, Boston, MA

Gábor Janiga, Magdeburg, Germany

Christof Karmonik, Houston, TX

Timothy J. Kaufmann, Rochester, MN

Hillary R. Kelly, Boston, MA

Toshibumi Kinoshita, Akita, Japan

Alexander W. Korutz, Chicago, IL

Stephen F. Kralik, Houston, TX

Alexander Lerner, Los Angeles, CA

Yinsheng Li, Madison, WI

Franklin A. Marden, Chicago, IL

Markus A. Möhlenbruch, Heidelberg, Germany

Kambiz Nael, Los Angeles, CA

Renato Hoffmann Nunes, Sao Paulo, Brazil

Sasan Partovi, Cleveland, OH

Johannes A.R. Pfaff, Salzburg, Austria

Laurent Pierot, Reims, France

Alireza Radmanesh, New York, NY

Prashant Raghavan, Baltimore, MD

Eytan Raz, New York, NY

Paul M. Ruggieri, Cleveland, OH

Sebastian Schafer, Madison, WI

Maksim Shapiro, New York, NY

Timothy Shepherd, New York, NY

James Shin, New York, NY

Mark S. Shiroishi, Los Angeles, CA

Bruno P. Soares, Baltimore, MD

Jason F. Talbott, San Francisco, CA

Ruth Thiex, Everett, Washington

Vincent Thijs, Melbourne, Victoria, Australia

Anderanik Tomasian, Los Angeles, CA

Fabio Triulzi, Milan, Italy

Anja G. van der Kolk, Utrecht, the Netherlands

Arastoo Vossough, Philadelphia, PA

Elysa Widjaja, Toronto, Ontario, Canada

Leonard Yeo, Singapore

Woong Yoon, Gwangju, South Korea

David M. Yousem, Evergreen, CO

Carlos Zamora, Chapel Hill, NC

Chengcheng Zhu, Seattle, WA

EDITORIAL FELLOW

Matthew D. Alvin, Baltimore, MD

SPECIAL CONSULTANTS TO THE EDITOR

AJNR Blog Editor

Neil Lal, Denver, CO

Case of the Month Editor

Nicholas Stence, Aurora, CO

Case of the Week Editors

Matylda Machnowska, Toronto, Ontario, Canada

Anvita Pauranik, Calgary, Alberta, Canada

Vinil Shah, San Francisco, CA

Classic Case Editor

Sandy Cheng-Yu Chen, Taipei, Taiwan

Health Care and Socioeconomics Editor

Pina C. Sanelli, New York, NY

Physics Editor

Greg Zaharchuk, Stanford, CA

Podcast Editor

Courtney Tomblinson, Nashville, TN

Deputy Podcast Editor

Kevin Hiatt, Winston-Salem, NC

Twitter Editor

Roger Jordan, Houston, TX

Official Journal:

American Society of Neuroradiology

American Society of Functional Neuroradiology

American Society of Head and Neck Radiology

American Society of Pediatric Neuroradiology

American Society of Spine Radiology

Founding Editor

Juan M. Taveras

Editors Emeriti

Mauricio Castillo, Robert I. Grossman,

Michael S. Huckman, Robert M. Quencer

Managing Editor

Karen Halm

Assistant Managing Editor

Laura Wilhelm

Editorial Assistant

Margaret B. Sabato

Executive Director, ASNR

Mary Beth Hepp



Title: Freccia Tricolori. The Festa della Repubblica, celebrated annually on June 2nd, is looked forward to by locals and tourists alike. Flying high for more than two centuries, the IL Tricolori is a testimony to the fact that the clouds cannot dampen the human spirit. Hope, faith, and love are what stand by mankind forever. This moment of Freccia Tricolori was captured at the Colosseum, Rome on one such occasion.

Hima Pendharkar, PDMRD, DNB, DM, Additional Professor, Department of Neuro Imaging & Interventional Radiology, National Institute of Mental Health & Neuro Sciences, Bangalore, Karnataka, India

Insights into the *AJNR* Review Process

M.D. Alvin,
C. Toote, and J.S. Ross

Manuscript peer review is a critical process to ensure that published manuscripts are scientifically and methodologically sound. While the general process is straightforward, the specifics can be complicated and, from the outside, very opaque. The type of peer review is not standardized across journals, and the number of reviewers and the impact of reviewers' recommendations on an editor's decision vary across the industry. This variability can be frustrating to both authors and reviewers, particularly when reviewers disagree on recommendations. At times it may leave authors wondering how a decision is rendered and how influential reviewers' opinions are on the final decision to accept or reject the manuscript.

Given this variability, we sought to assess manuscript reviews and outcomes for the *AJNR*. Manuscript data were acquired for both the past year and past 5 years. We tallied the total number of manuscripts submitted, the initial decision, and the number of revisions as well as outcomes of those revisions. The number of reviews and impact on accept/reject rates were assessed. Reviewer recommendation concordance and discordance were assessed relative to manuscript decision outcome.

During 5 years, 7328 manuscripts were submitted with initial manuscript decisions as follows: reject (74.8%), major revision (14.5%), minor revision (7%), and accept (3.6%), with similar rates during the past year. In addition to the rejection rate of 74.8% during the past 5 years, we found a 73.1% rejection rate during the past year, with nearly all (99%) manuscripts receiving initial decisions of minor or major revisions eventually being accepted. Previously, Rosenkrantz and Harisinghani¹ retrospectively reviewed 696 Original Research manuscripts submitted to the *American Journal of Roentgenology* in 2012 with the goal of providing authors with useful metrics from first submission to eventual publication. They found that >90% of articles needing minor revision and about 50% of those needing major revision were eventually accepted. The latter clearly differs from our findings here, where 99% of manuscripts needing major revision were accepted. It is important to note that the "Major Revision" decision is entitled "Provisional Acceptance Pending Major Revision" for *AJNR*, suggesting that reviewer recommendations and Senior Editor decisions with this designation imply acceptance at the outset, in contrast to other journals. Rosenkrantz and Harisinghani also found that the more revisions, the more likely that acceptance would be obtained. Nearly 100% of revisions were performed by authors when requested. The overall *AJR* acceptance rate was 25.3%, and the authors proposed reducing this rate to cut down the length of time from acceptance to

publication. This acceptance rate is nearly identical to that found in our study for *AJNR* (ie, 25.2% for the past 5 years, 26.9% for the past year).

We devoted a large part of our analysis to the reviews and reviewers. First, we found that most manuscripts were reviewed either by 2 reviewers or the Editor-in-Chief or Senior Editor alone. This finding was expected as the Senior Editor is tasked with sorting through a portion of all submitted manuscripts and selecting only a subset to be sent to reviewers while rejecting the rest. The Editor-in-Chief will also accept some manuscripts without review, generally limited to Editorials, Brief Reports, or Perspectives rather than Original Research articles. We also found that the more reviews a manuscript underwent, the less likely that it would be accepted. This may be related to the complexity of the topic, a niche topic, or the greater likelihood of reviewer recommendation discordance influencing the Senior Editor. The trend during the past year to fewer 2-reviewer reviews and more Senior Editor-only and 3+-reviewer reviews likely relates to variability in types and subtypes of manuscripts submitted with slightly fewer Original Research articles when comparing the past year with the past 5 years.

We also looked at how reviewer recommendation discordance impacted the editor's decision for the manuscript. Approximately half of all manuscripts with ≥ 2 reviews demonstrated reviewer discordance and approximately half demonstrated concordance. As anticipated, discordance was higher among 3+ reviewers compared with 2 reviewers. Discordance led to about a 5% higher rate of rejection relative to all manuscripts during the 5-year period for both 2-reviewer and 3+-reviewer cases. For the past year, the rejection rate in 2-reviewer discordant cases has been nearly identical to that of all manuscripts, while it has been about 13% higher for 3+-reviewer discordant cases (ie, a final acceptance rate of only 13.6%). Additionally, when we broke down the data by manuscript type and subtype, Brief/Technical Reports had a much lower likelihood of acceptance for 3+-reviewer discordance (15.4%) versus 2 reviewers (35.7%), with a similar discrepancy seen for Review Articles (26.1% versus 38.8%). The lower acceptance for Brief/Technical Report discordant reviews likely relates to the relatively higher bar for acceptance overall for this the type of submission versus the primary focus of the *AJNR* on Original Research articles.

Finally, we found that if reviewers agreed on a recommendation, the likelihood of rejection was lower than if they disagreed on a recommendation, suggesting a certain degree of influence on the editor's final decision, especially with regard to rejection. The impact of the reviewer's recommendation on the editor's decision has been previously studied. Vintzileos et al² retrospectively assessed the influence of a reviewer's recommendation on the final editorial decision to accept or reject an obstetric manuscript for publication. Five reviewers' 635 reviews were analyzed, with the highest correlation found for a reject recommendation with a reject final decision (93%). Accept with minor revisions had a 67% acceptance rate, whereas accept with major revisions had a 40% acceptance rate. No variations among the reviewers (including the quality of the reviews) were found to influence the

Matthew D. Alvin is the 2020 *AJNR* Editorial Fellow.
<http://dx.doi.org/10.3174/ajnr.A7090>

final decision—that is, it did not matter if the reviewer was more senior or had performed more reviews in the past. This is similar to our findings on reviewer experience.

Similar to Vintzileos et al², Kravitz et al³ explored the relationship between reviewers' recommendations and the final manuscript decision for the *Journal of General Internal Medicine* between 2004 and 2008. Assessing 2264 manuscripts and 5881 associated reviews, the authors found that reviewers' recommendations agreed or disagreed with one another just barely beyond chance. When all reviewers agreed on rejection (6.9% of the time), 88% of those manuscripts received a final decision of rejection. In contrast, when all reviewers argued against rejection (47.7% of the time), only 20% of those manuscripts received a final decision of rejection. The overall rejection rate was 48%, arguing that the reviewers' recommendations significantly influenced the editor's decision to accept or reject the manuscript. When any level of disagreement was present among reviewers' recommendations (45.4% of the time), the rejection rate was 70.6%. This is similar, though slightly less, to our findings on reviewer discordance and rejection rate.

In summary, *AJNR* acceptance/rejection rates have been stable during the past 5 years. Manuscripts with initial decisions of major revision are almost always eventually accepted. The more

reviews, the less likely a manuscript will be accepted. Manuscripts with discordant reviewer recommendations had about a 5% higher rejection rate during the past 5 years and 13% higher during the past year if there were 3+ reviewers. Manuscripts with concordant reviewer recommendations were less likely to be rejected, suggesting that reviewers have an influence on the final decision. We hope that these observations help provide more transparency to prospective authors about the *AJNR* peer review process and provide valuable insight to the *AJNR* editors and reviewers.

REFERENCES

1. Rosenkrantz AB, Harisinghani M. **Metrics for original research articles in the AJR: from first submission to final publication.** *AJR Am J Roentgenol* 2015;204:1152–56 CrossRef Medline
2. Vintzileos AM, Ananth CV, Odibo AO, et al. **The relationship between a reviewer's recommendation and editorial decision of manuscripts submitted for publication in obstetrics.** *Am J Obstet Gynecol* 2014;211:703.e1–e5 CrossRef Medline
3. Kravitz RL, Franks P, Feldman MD, et al. **Editorial peer reviewers' recommendations at a general medical journal: are they reliable and do editors care?** *PLoS One* 2010;5:e10072 CrossRef Medline

Complete Evaluation of Dementia: PET and MRI Correlation and Diagnosis for the Neuroradiologist

J.D. Oldan, V.L. Jewells, B. Pieper, and T.Z. Wong



ABSTRACT

SUMMARY: This article will familiarize neuroradiologists with the pathophysiology, clinical findings, and standard MR imaging and PET imaging features of multiple forms of dementia as well as new emerging techniques. Cases were compiled from multiple institutions with the goal of improved diagnostic accuracy and improved patient care as well as information about biomarkers on the horizon. Dementia topics addressed include the following: Alzheimer disease, frontotemporal dementia, cerebral amyloid angiopathy, Lewy body dementia, Parkinson disease and Parkinson disease variants, amyotrophic lateral sclerosis, multisystem atrophy, Huntington disease vascular dementia, and Creutzfeldt-Jakob disease.

ABBREVIATIONS: AD = Alzheimer disease; CAA = cerebral amyloid angiopathy; CBD = corticobasilar degeneration; FTD = frontotemporal dementia; LBD = Lewy body dementia; MCI = mild cognitive impairment; MH = microhemorrhages; MSA = multisystem atrophy; PD = Parkinson disease; PSP = progressive supranuclear palsy; rsfMRI = resting-state fMRI

In patients who present with cognitive impairment, obtaining MR imaging is standard practice, but PET strengthens interpretation. Neurodegenerative syndromes are diagnosed by clinical findings/Lumbar Puncture markers and not pathology, and they may overlap. This overview of neurodegenerative syndromes and their MR imaging/PET appearances includes Alzheimer disease (AD), frontotemporal dementia (FTD), cerebral amyloid angiopathy (CAA), Lewy body dementia (LBD), Parkinson disease (PD), amyotrophic lateral sclerosis, multisystem atrophy (MSA), progressive supranuclear palsy (PSP), corticobasilar degeneration (CBD), Huntington disease, vascular dementia, and Creutzfeldt-Jakob disease. The discussion includes newer MR imaging techniques (resting-state fMRI [rsfMRI]/task-based MR imaging), DTI, and iron deposition as well as novel nuclear medicine agents. Our goal was familiarization of neuroradiologists with nuclear medicine and molecular imaging diagnoses and novel imaging techniques.

Institutional review board (University of North Carolina) approval and a waiver of patient consent was obtained (study No. 20–2089).

Alzheimer Disease

AD, the second most common neurodegenerative disorder after stroke, affects 10% of the population older than 65 years of age, and it is the sixth leading cause of death with US annual costs of \$236 billion. Clinical symptom similarities hamper diagnosis, leading to a low 71%–87% sensitivity and 44%–71% specificity.¹ Despite no cure, diagnosis is helpful because cholinesterase inhibitors delay cognitive decline, and there is the need for institutionalization and improved end-of-life planning.¹

Molecular imaging modalities demonstrate elevated amyloid- β and τ proteins. Amyloid- β impacts synaptic function, while age-accumulating τ neurofibrillary tangles cause neuroinflammation and neurodegeneration and finally dementia.^{2,3} Additional causations include inflammatory microglial (M2) and poor amyloid- β clearance by astrocytes.³ Drugs targeting amyloid fail because of a long prodromal and asymptomatic inflammatory phase and other processes of AD, suggesting an urgent need for earlier diagnosis and better surrogate markers.²⁻⁵ Preventative measures include exercise and appropriate sleep (impact glymphatic system amyloid and τ removal)^{3,6} and diabetes and stress control (preventing inflammation and BBB disruption).³⁻⁷ Tau formation and neuronal damage cascade also occur in Parkinson, amyotrophic lateral sclerosis, multiple sclerosis, and Huntington disease (Online Supplemental Data).⁸

Received April 4, 2020; accepted after revision November 14.

From the Department of Radiology (J.D.O., V.L.J.), University of North Carolina, Chapel Hill, North Carolina; Department of Radiology (B.P.), Richard L. Roudebush VA Medical Center, Indianapolis, Indiana; and Department of Radiology (T.Z.W.), Duke University Hospital, Durham, North Carolina.

Paper previously presented, in part, at: Annual AOCR Convention 2019, Merging Mind and Muscle, April 8–12, 2019, San Antonio, Texas.

Please address correspondence to Valerie L. Jewells, MD, University of North Carolina, 100 Manning Dr, 3324 Old Infirmary Building, Campus Box 7510, Chapel Hill, NC 27599-7510; e-mail: jewells@med.unc.edu

Indicates open access to non-subscribers at www.ajnr.org

Indicates article with online supplemental data.

<http://dx.doi.org/10.3174/ajnr.A7079>

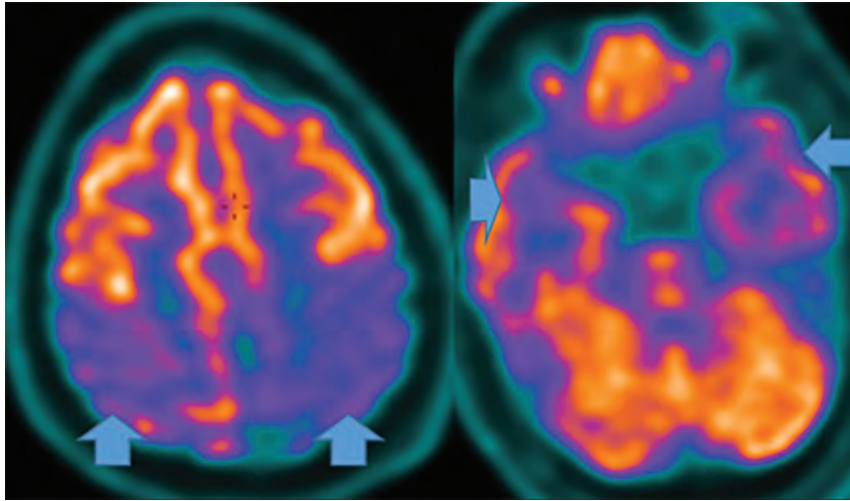


FIG 1. FDG-PET in a patient with AD demonstrates decreased bilateral parietal and temporal uptake (arrows). FDG uptake in the occipital lobe is preserved (not shown). The degree of abnormalities correlates with symptoms.

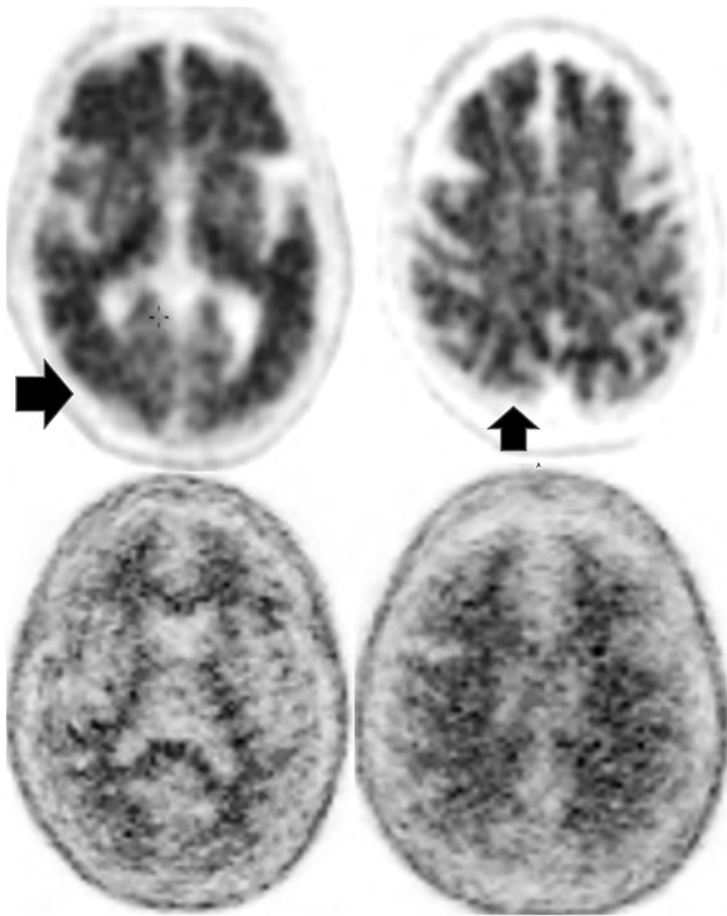


FIG 2. Upper row: Abnormal florbetapir PET (arrows) shows diffuse cortical uptake with loss of GM-WM differentiation, indicating a high amyloid plaque burden. Lower row: A 65-year-old woman with MCI. Florbetapir scan demonstrates normal WM uptake without accumulation in the cortical gray matter, indicating no amyloid plaque. This finding effectively rules out AD (lower images courtesy of Dr Olga James, Duke University).

Two AD forms exist, early (younger than 65 years of age, which is less common and associated with autosomal dominant *Presenilin* genes 1 and 2) and late-onset (older than 65 years of age). Predisposing factors for late-onset are female sex (related to metabolic differences and medium fatty acid chains), the *APOE4* variant (a fat metabolism protein associated with increased amyloid deposition 1 decade before diagnosis; heterozygotes [$3\times$ risk]; homozygotes [$15\times$ risk]), and FDG-PET uptake reductions when asymptomatic.^{4,8} Trauma is also associated with increased τ and amyloid deposition and microhemorrhages (MHs).^{3,4,9} Tau formation spreads confluent via neurons and glia and neural networks in a prionlike manner, correlating with atrophy.^{4,6,7,10,11}

MR imaging demonstrates precuneus, parietal, hippocampal, entorhinal cortex, and temporal atrophy, with frontal lobe involvement in advanced cases. FDG-PET demonstrates decreased temporoparietal uptake (sensitivity = 80%–93% and specificity = 60%–76%),^{3,11} with possible decreased inferior parietal, frontal, lateral temporal, and precuneus uptake mirroring atrophy on MR imaging.^{12,13} Particularly specific PET findings include posterior cingulate involvement with occipital sparing (Fig 1).¹³ However, similar hypometabolism is seen in PD, bilateral parietal subdural hematomas, radiation, or vascular disease.⁸ Opinions vary with regard to FDG-PET use for conversion of mild cognitive impairment (MCI) to AD (sensitivity = 97% and specificity = 50%–76%),^{3,13–15} while scans with negative findings indicating progression to AD are unlikely for 3 years.³

Amyloid deposition is associated with FDG-PET decline and precedes τ changes, which, in turn, precede abnormal glucose metabolism, all of which precede clinical symptomatology.^{3,4} Several tracers help visualize amyloid. Pittsburgh compound B (¹¹C-P, 20-minute half-life) is logistically difficult and, hence, never reached commercial use.¹⁶ Longer half-life commercially available ¹⁸F tracers are the following: florbetapir (Amyvid), florbetaben

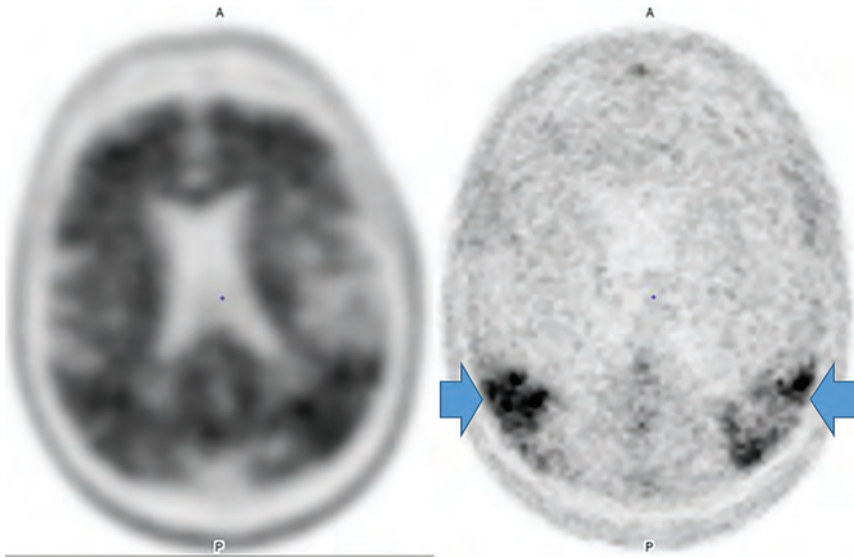


FIG 3. Increased amyloid plaque burden in the posterior parietal and frontal lobes on florbetaPET (left) with corresponding tracer uptake in the parietal lobes on tau PET images (right, arrows). Note that the τ tracer more clearly localizes to sites of neuronal damage. The pattern is most consistent with AD (images courtesy of Dr James Burke, Duke University).

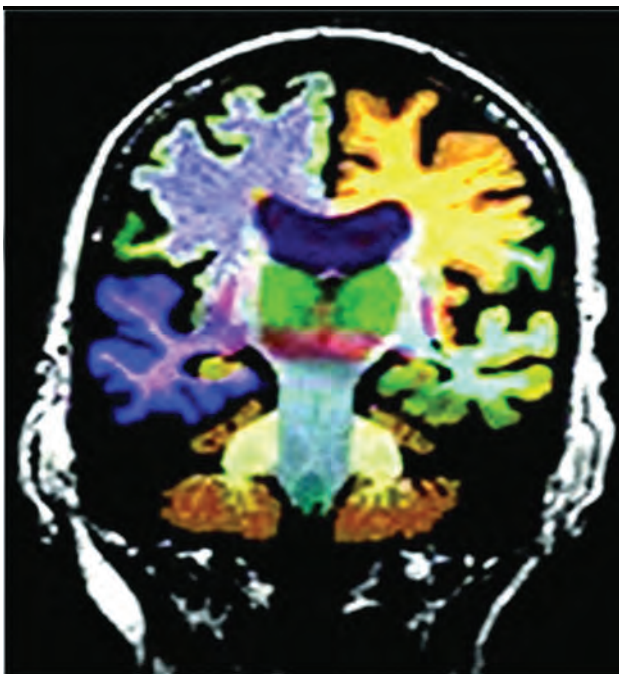


FIG 4. Commercial volumetric assessment shows lobar and deep, superficial GM differentiation by color for comparative analysis. For instance, the right frontal lobe GM is green, while the underlying WM is blue. This image was previously published in the *American Journal of Neuroradiology*. (Tanpitukpongse et al²⁴).

(Vizamyl), and flutemetamol (Neuraceq). Recently, flortaucipir (Tavid) received FDA approval. A meta-analysis of florbetaPET and florbetaben (89%–90% sensitivity and 87%–88% specificity) demonstrated no difference between agents.¹⁷ Data distinguishing AD and MCI, however, are mixed,¹⁷ with rates of PET positive for

MCI intermediate between patients with AD and controls.¹⁴ Pooled (sensitivity and specificity) values of multiple methods of AD diagnosis versus controls are the following: MR imaging (visual inspection, 83/89), SPECT (80/85), FDG-PET (90–94/73–89), CSF amyloid- β (80/82), CSF T- τ (82/90) and p- τ (80/83), and ¹⁸F amyloid- β (90–92/84–100).^{3,17} This finding explains the poor diagnostic capability with 1 test and the need for improved methods of AD diagnosis.

Amyloid- β demonstrates higher negative-than-positive predictive values because 25% of postmortem examinations of cognitively healthy individuals and 21% of cognitively healthy patients have deposition; however, lack of accumulation usually excludes AD and 50% of patients with AD can have other pathologies.^{8,17,18} Therefore, amyloid is a good exclusionary test but limited for severity

stratification or progression depiction. Amyloid tracers in AD accumulate in the gray matter, while controls have primarily white matter uptake,¹⁹ producing GM-WM differentiation loss, particularly in the precuneus, posterior cingulate gyrus, and lateral-frontal and temporal lobes (Fig 2).^{20,21}

Unlike amyloid, which does not correlate with severity,^{3,22} τ uptake correlates strongly with cognitive impairment and dementia severity.^{3,22} Tau, particularly outside the medial temporal lobe is suspicious for AD, even in cases negative for amyloid (Fig 3).²³ However, FTD, PD, PSP, CBD, traumatic encephalopathy, and Down syndrome also accumulate τ .^{3,22} Tau, unfortunately, has concentrations 5–20 times lower than amyloid, with amygdala and striatum off-target binding.²²

AD MR imaging structural assessment reveals hippocampal (26%–27%), entorhinal (38%–40%), and thalamic and caudate volume loss (due to multiregion connections), which is asymptomatic and precedes hippocampal loss and cortical atrophy.^{3,20,24} This feature is accompanied by increased DTI diffusivity.^{3,20,24} Volume loss of hippocampal regions with both NeuroQuant (<https://www.cortechs.ai/products/neuroquant>) and Neuroreader (<https://brainreader.net/>) is the single best prediction of AD from MCI at 3-year follow-up compared with other regions (Fig 4).²⁴ T2 WM hyperintensity burden and the Fazekas score (particularly perivascular) show promise, correlating with Montreal Cognitive Assessment scores and amyloid burden, while negatively correlating with FDG-PET uptake.^{25–27} T2 abnormalities occur 20 years before disease expression, particularly in late-myelinating regions secondary to neurodegeneration and poor oligodendrocyte repair.²⁸ Additionally, iron SWI measurement, rsfMRI/task-based fMRI, arterial spin-labeling, MR spectroscopy (lower NAA and higher mIns), and DTI (reduced hippocampal, thalamic, and caudate anisotropy) are under investigation.^{4,20,25,27} In summary, WM burden predicts AD and cognitive decline and correlates with amyloid and τ CSF levels and

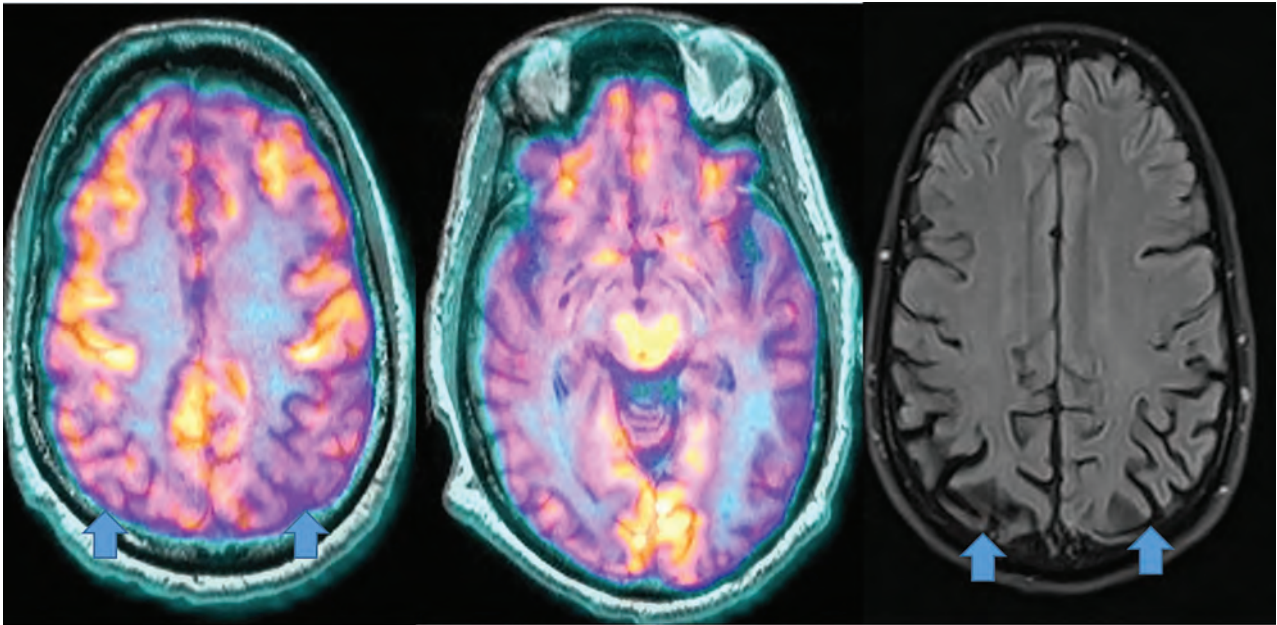


FIG 5. Posterior cortical atrophy (AD variant) demonstrates preserved frontal and caudate but decreased lateral occipital and parietotemporal uptake (*left*, 2 color images), while an axial FLAIR (black and white), right MRI image demonstrates focal posterior parietal (*arrows*) and parieto-occipital atrophy (*arrows*). This patient demonstrated temporal sparing (not shown).

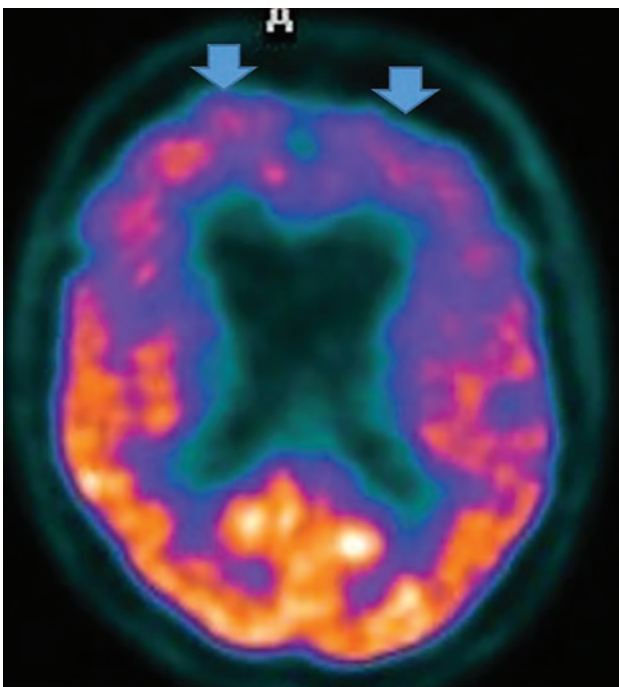


FIG 6. FTD. Frontal and behavioral variant demonstrates reduced bifrontal FDG-PET uptake (*arrows*). Also note the enlargement of the frontal horns of the lateral ventricles, a common finding.

decreased perfusion and abnormal DTI networks before atrophy or abnormal findings on FDG-PET.²⁸

A new possible surrogate marker is iron (Fe), because amyloid- β causes oligodendrocyte toxicity, preventing myelin repair.^{28,29} Subsequently, Fe released during myelin breakdown creates phosphorylated- τ/τ .^{29,30} Additionally, rsfMRI and task-

based MR imaging show potential, demonstrating impaired default mode network connectivity correlating with amyloid- β deposition,^{4,27,31,32} and frontoparietal and visual network hypoactivation in MCI relative to controls as well as visual, default, limbic, and dorsal and ventral attention network hypoactivation in AD relative to controls.³² Dynamic susceptibility contrast-enhanced and arterial spin-labeling MR imaging assessment is another focus of MR imaging research.^{3,27} New nuclear medicine tracers targeting dopamine and serotonin/cholinergic/GABAergic systems and microglial neuroinflammation (translocator protein agents correlate with amyloid) and astrocyte agents are under investigation.^{3,8,27,33} Unfortunately, translocator protein agents exhibit 3 genetic-related nucleotide polymorphisms affecting uptake, poor resolution, and more activity later rather than earlier in the disease process.^{3,8,27,33} [¹¹C]-deuterium-L-deprenyl [¹¹C]-DED and [¹¹C]-deprenyl-D2 are less well-studied.^{3,8,25,27,33} Hopefully, the ongoing Alzheimer's Disease Neuroimaging Initiative 3 trial will yield answers with regard to these new methods.

Posterior Cortical Atrophy. Posterior cortical atrophy (an AD variant) presents with declining visual association skills affecting the lateral occipital lobes (unlike classic AD), while preserving the frontal lobes and caudate (unlike LBD), often with subtle MR imaging findings (Fig 5).³⁴

Frontotemporal Dementia

FTD demonstrates 3 variants: behavioral, semantic, and nonfluent agrammatic aphasia. Related syndromes include FTD motor neuron disease, PSP, and CBD, discussed separately. FTD neuropathology is variable, with τ , TAR DNA-binding protein 43/FET proteins, and sometimes amyloid (Online Supplemental Data).^{8,31,35}

Behavioral variant FTD (the most common variant) shows progressive behavior and cognition deterioration; perseverative,

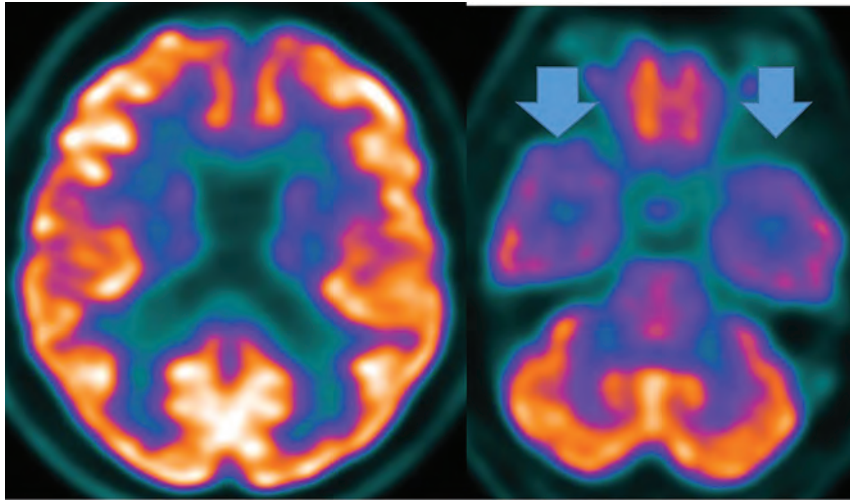


FIG 7. FTD. Semantic and temporal variant demonstrates significant reduced bitemporal uptake (arrows) without reduced frontal FDG-PET uptake as seen in Fig 6.

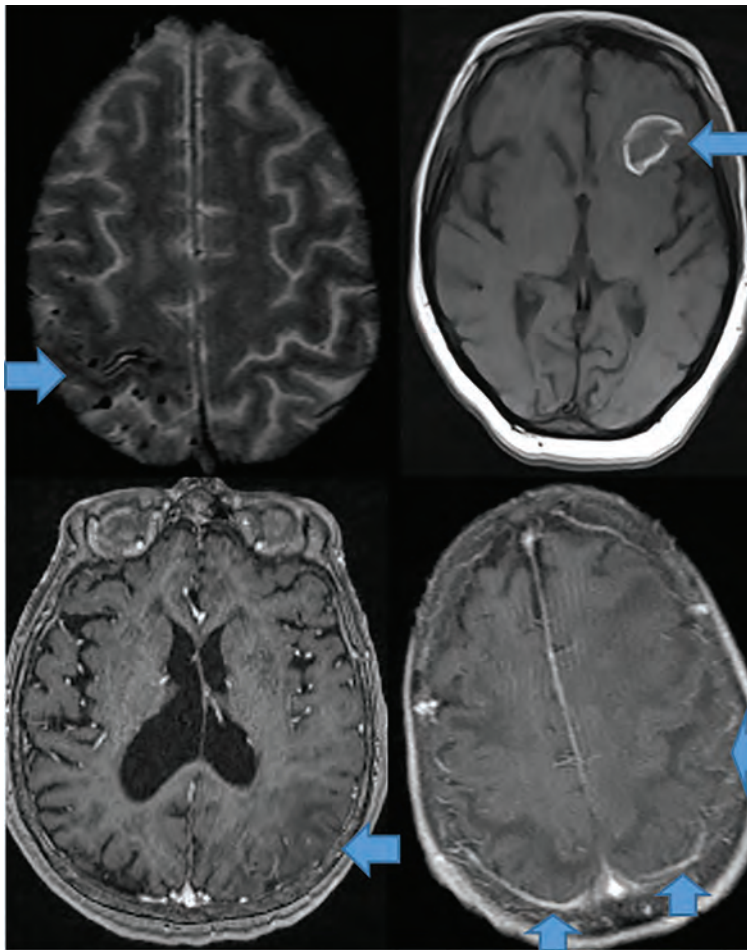


FIG 8. CAA presents as multiple forms. In the classic CAA form (top left, axial T2), subarachnoid hemorrhage is common as seen at the arrow, on susceptibility weighted imaging with clustered right fronto-parietal MHs in the adjacent brain parenchyma. Large frontal parenchymal hemorrhages can also be seen in classic CAA (top right image, axial T1). The inflammatory cerebral amyloidosis type will demonstrate edema as seen in this case with left parietal edema/mass effect (bottom left, axial +C T1 at arrow). While the Amyloid- β related angitis variant commonly demonstrates dural/leptomeningeal enhancement seen posteriorly (arrows), (bottom right image, axial +C T1 at arrow). Note the lack of mass effect in the Amyloid- β angitis variant.

stereotyped, compulsive and ritualistic behavior; and hyperorality and dietary changes, but it spares memory and visuospatial functions. MR imaging demonstrates frontal and anterior-temporal atrophy, while FDG-PET reveals decreased cortical medial-frontal, orbital-frontal, anterior cingulate, and fronto-insular uptake,³⁵ with expected differences between frontal, behavioral (Fig 6), temporal, and semantic (Fig 7) variants.³⁶ Anterior cingulate, temporal, caudate, and thalamic involvement is a key difference from AD and correlates with disease progression.^{33,37,38} FTD typically does not show amyloid uptake, but τ uptake has been seen.³³

Patients with the semantic variant demonstrate impaired confrontation naming, single-word comprehension, object knowledge, and surface dyslexia and dysgraphia, sparing speech production. MR imaging reveals anterior-temporal atrophy, correlating with FDG-PET and SPECT hypoperfusion and hypometabolism.³⁵ Finally, patients with the nonfluent and agrammatic variant lack grammar and speech apraxia but have impaired complex-sentence comprehension, sparing single-word comprehension/object knowledge. MR imaging demonstrates left posterior, fronto-insular atrophy, while FDG-PET and SPECT depict hypoperfusion and hypometabolism in the same region.³⁵

Newer MR imaging techniques demonstrate thalamic atrophy³⁹ and DTI tract differences between the behavioral variant (uncinate fasciculus, genu, and cingulum) and Primary Progressive Aphasia, while AD shows increased fractional isotropy and mean diffusivity.⁴⁰ Behavioral variant subtypes demonstrate regional prefrontal-cortical, anterior-temporal, insular, anterior cingulate, and striatum volume loss.⁴⁰ Meanwhile, rsfMRI reveals reduced salience network connectivity in the behavioral variant, abnormal executive dorsal attention-control and auditory networks, and increased default mode network connectivity, positively correlating with symptom severity.³¹ Additionally, Fe deposition assessment differentiates those with the behavioral variant from controls and those with the Primary Progressive Aphasia variant from those with the behavioral variant.⁴¹

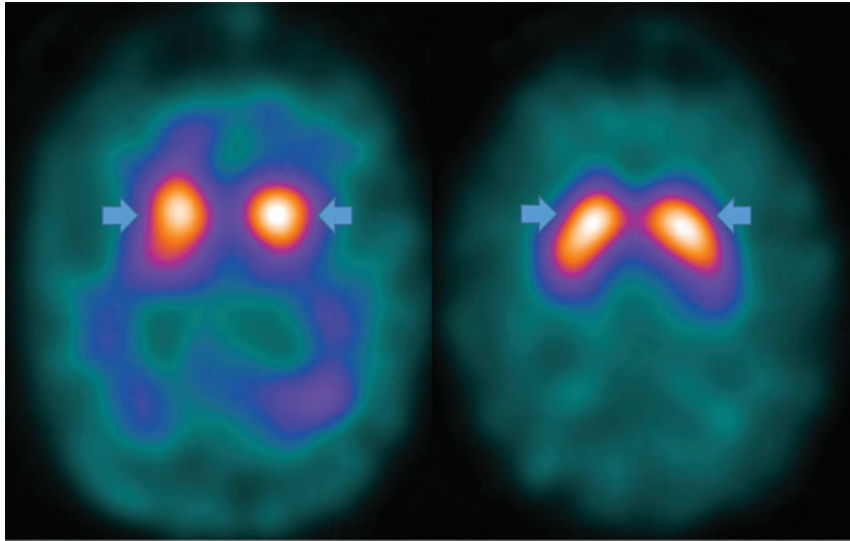


FIG 9. PD decreased putamen > caudate head uptake results in the classic change from a “comma” (right image arrows) to a “period” (left image arrows) appearance. Note abnormal (left) and normal (right) findings on DaTSCANS.

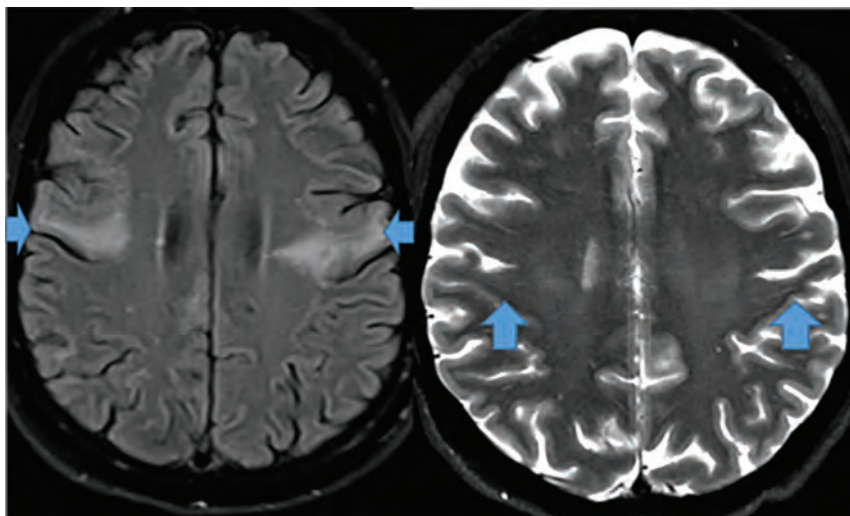


FIG 10. Amyotrophic lateral sclerosis demonstrates significant bilateral precentral sulcus increased corticospinal tract FLAIR signal (arrows, axial image, left) and decreased axial T2 precentral sulcus signal, “motor band sign” (right, arrows) on MR imaging.

Cerebral Amyloid Angiopathy

CAA dementia occurs in elderly normotensive individuals. Pathophysiologically, amyloid deposits in cortical and meningeal arterioles and capillary walls.⁴² Patients present with basal ganglia-sparing subcortical lobar MHs. There are 3 forms: classic, inflammatory, and amyloid-related angiitis.^{42,43} Patients with classic amyloid can demonstrate superficial siderosis, subarachnoid hemorrhage, and multiple MHs with posterior-predisposition T2 FLAIR changes (Fig 8) due to higher lipoprotein concentration.⁴⁴ Inflammatory amyloid (poorest prognosis) exhibits clustered MHs, minimal enhancement, and significant mass effect (Fig 8). Amyloid- β -related angiitis, however, lacks mass effect but often has meningeal enhancement (Fig 8). Cerebral MHs correlate with neurologic deficits.^{45,46}

Given the presence of amyloid, amyloid PET findings are often positive, but being negative excludes CAA^{42,45} (sensitivity = 77%–92% and specificity = 66%–88% versus controls);⁴⁶ however, the more common AD may coexist.⁴² Hence, some authors propose an occipital-to-global amyloid ratio to differentiate CAA with regard to AD (AD spares the occipital lobes).⁴⁶ Definitive FDG-PET CAA diagnosis awaits future research.

Parkinson Disease and Related Syndromes

PD presents with resting tremor and cognitive decline secondary to decreased pigmented, substantia nigra/pars compacta dopaminergic neurons, and α -synuclein protein intraneuronal Lewy body inclusions.⁴⁷ T2 MR imaging shows an absent substantia nigra swallowtail sign, indistinctness, and Fe deposition.⁴⁸

FDG-PET differentiates Parkinson disease from related dementias via decreased basal ganglia uptake,⁴⁹ while ¹⁸F fluorodopa demonstrates decreased striatal uptake.⁵⁰ Parkinson disease appears similar to AD on FDG-PET, but with greater visual cortex involvement and relative medial-temporal cortex preservation.⁵⁰ Amyloid and (less frequently) τ imaging is positive.⁵¹ The principal nuclear medicine study used to evaluate PD is ¹²³I-ioflupane/DaTSCAN (GE Healthcare) SPECT (Fig 9) showing decreased putamen and caudate uptake.⁵¹

There are 3 PD variants: PSP, amyotrophic lateral sclerosis, and MSA. PSP (possibly an FTD variant) demonstrates anterior-midbrain convexity loss on sagittal views (hummingbird sign) with interpeduncular cistern widening, and patients demonstrate upward gaze paralysis.⁵² Amyotrophic lateral sclerosis demonstrates motor strip and corticospinal tract hyperintense T2 FLAIR signal secondary to Fe deposition (Fig 10). MSA presents with autonomic failure and a T2 brain stem “hot cross buns” configuration (Fig 11).⁵²

Parkinsonian syndromes reveal decreased FDG-PET uptake; PSP in the medial frontal, premotor, prefrontal, brain stem, and thalamic regions; and MSA in the putamen, cerebellum, and brain stem regions (Fig 12).^{33,47,49} Finally, CBD demonstrates asymmetric decreased parietal and primary sensorimotor cortex, medial and lateral premotor, striatum, and thalamic uptake contralateral to clinical findings.³³ PD may show cortical and striatal amyloid uptake.³³ Tau tracers may accumulate in the inferior-temporal cortex in PD, while they are in the frontal-temporal, posterior-cingulate, subthalamic,

midbrain, and cerebellar WM in PSP. In CBD, Tau uptake is seen in the frontal, and parietal cortex (not seen in MSA).^{33,52}

With MR imaging, increased substantia nigra quantitative SWI suggests biomarker potential, as does prefrontal cortex and putamen Fe, which correlates with lower cognitive function.^{30,52,53} Likewise, rsfMRI default mode network assessment reveals altered striatum, motor, cerebellar, and basal ganglia connectivity, though disease heterogeneity inhibits biomarker progress.^{31,32}

Lewy Body Dementia (DLB)

DLB α -synuclein pathology represents 15% of neurodegenerative disease, and like Parkinson disease, it sometimes exhibits amyloid and τ pathology.⁵⁴ Indicative criteria (diagnostic if present) include radiologic biomarkers for DLB-reduced dopamine transport on DaTSCAN SPECT or fluorodopa PET, or low

Metaiodobenzylguanidine (MIBG) cardiac uptake. Supportive criteria are relative CT/MR imaging medial temporal lobe preservation and low uptake on SPECT/PET perfusion and metabolism (FDG) imaging, with reduced generalized uptake, reduced occipital uptake, and cingulate preservation.⁵⁵

Regardless, FDG-PET demonstrates temporoparietal involvement. Unlike AD, the occipital lobes are not spared.⁵⁶ The most sensitive PET finding is lateral-occipital cortex involvement (88%), while the most specific finding is posterior cingulate preservation (Fig 13).³³ DaTSCAN SPECT (80% accurate for AD differentiation) shows decreased putamen > caudate uptake.⁵⁴ ¹²³I Metaiodobenzylguanidine (MIBG) (catecholamine-receptor tracer) assessment shows decreased cardiac activity secondary to postganglionic-sympathetic cardiac innervation degeneration.⁵⁴ Tau tracers show posterior-temporoparietal, occipital-cortical, and precuneus uptake.²⁹ On MR imaging, medial-temporal preservation (regarding AD) is supportive but nonspecific, as is occipital hypometabolism and preserved posterior and midcingulate metabolism on FDG-PET (decreased posterior cingulate uptake is AD-specific).

Novel rsfMRI demonstrates widespread connectivity alterations without a current extent and disease localization consensus.³¹ Recently, the swallow tail sign was described in DLB.⁴⁸

Huntington Disease

Huntington disease is a rare autosomal dominant disease demonstrating increased chromosome 4pCAG-trinucleotide repeats, increased gamma-aminobutyric acid, and neuronal loss. The more common adult form presents

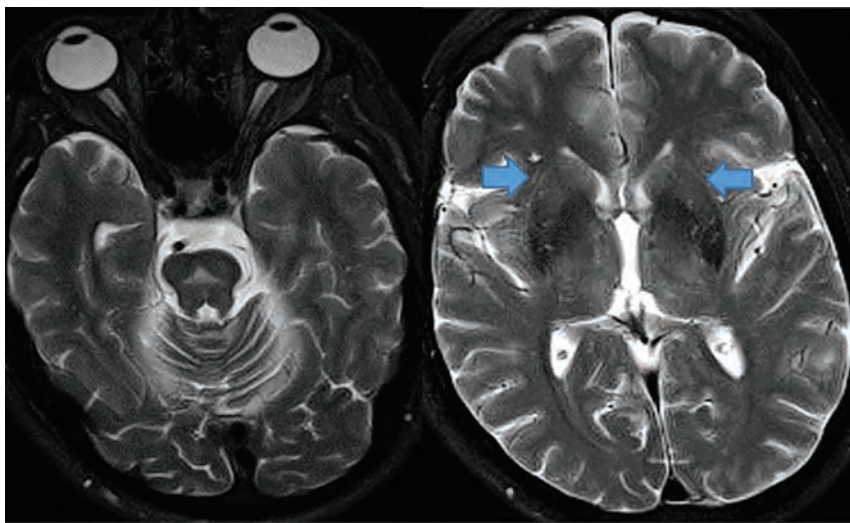


FIG 11. MSA demonstrates a pontine hot cross bun sign (left, axial T2 hyperintensity) with putamen atrophy (right, arrows, axial T2).

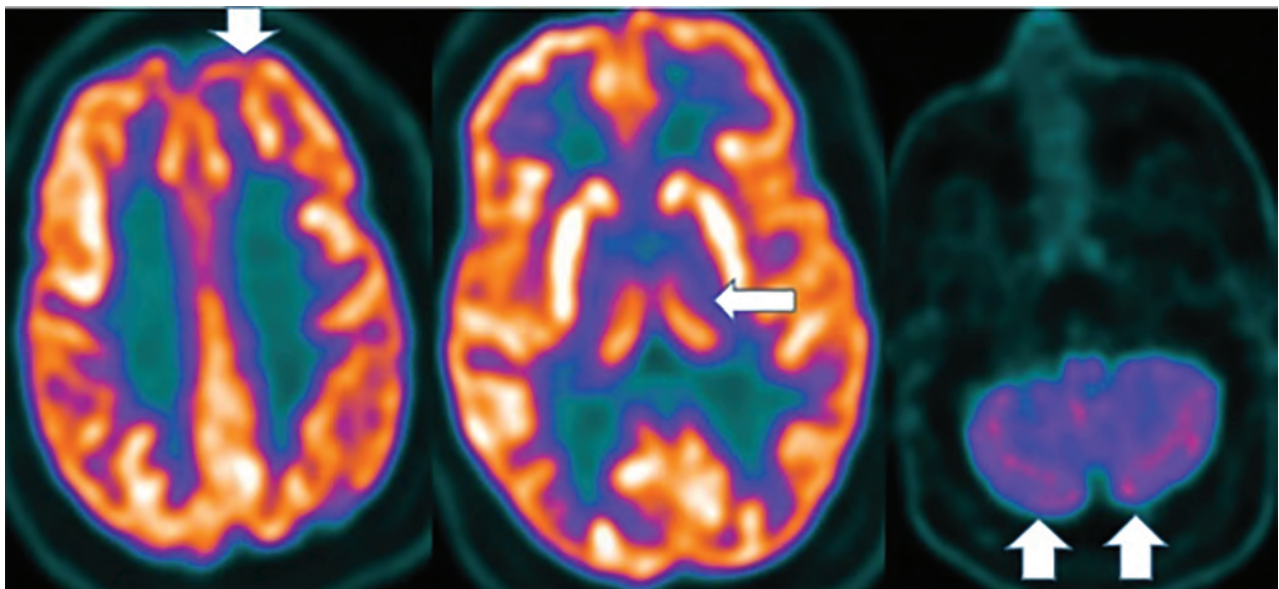


FIG 12. MSA- Cerebellar FDG-PET reveals decreased medial frontal (left), thalamic (middle), and cerebellar (right) uptake (arrows).

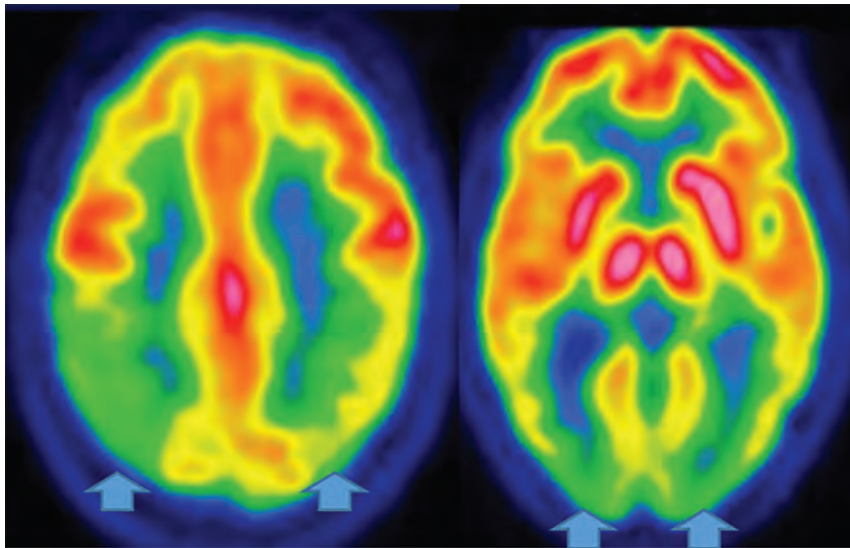


FIG 13. DLB. FDG-PET reveals reduced posterior parietal and occipital activity (*arrows*), but preserved posterior cingulate uptake (images courtesy Dr. Daniel Silverman, University of California, Los Angeles).

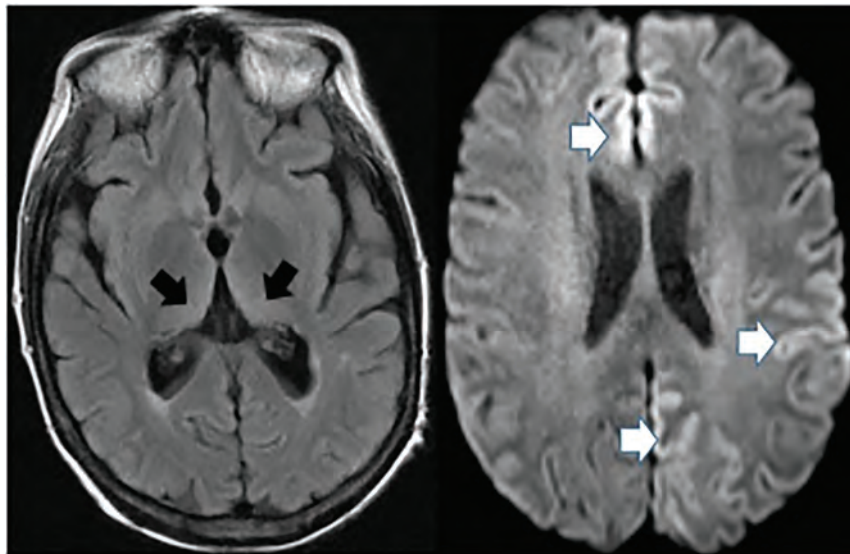


FIG 14. Creutzfeldt-Jakob disease demonstrates hockey stick configuration (*black arrows*), medial thalamic increased FLAIR (*left axial image*) as well as medial frontal, left parietal and occipital cortical increased signal (*white arrows*) (cortical ribbon sign, *right axial image*).

with chorea and dystonia, swallowing difficulty, abnormal and slow eye movements, and impaired gait and posture and balance. By the fourth-to-fifth decades, cognitive decline and word-finding difficulty and emotional lability are seen. Patients presenting at younger than 20 years of age have the rarer juvenile form.⁵⁷

MR imaging demonstrates frontal horn box-shaped dilation and caudate atrophy. There are no nuclear medicine diagnostic findings, though FDG-PET demonstrates striatal and cortical hypometabolism with increased thalamus and occipital and cerebellar uptake.⁵⁷⁻⁶⁰ rsfMRI exhibits visual, motor, and basal ganglia network abnormalities.^{32,40}

Vascular Dementia

While strokes are more common than any other neurodegenerative disease, they rarely present in FDG-PET. MR imaging and PET reveal a sharp demarcation of involved arterial territories. If the frontal or internal capsule is affected, there may be loss of uptake and atrophy in the contralateral cerebellum (crossed-cerebellar diaschisis).³⁴

Creutzfeldt-Jakob Disease

Creutzfeldt-Jakob disease causes rapid cognitive decline from altered prion protein accumulation, producing neurotoxicity and cortical/subcortical spongiform necrosis. On MR imaging, striatum and neocortex increased T2 FLAIR (medial-thalamic hockey-stick configuration) is noted, often also affecting the cortex (Fig 14). SPECT reveals widely inconsistent perfusion variations, and FDG-PET shows cortical and basal ganglia involvement in later stages.⁶¹

CONCLUSIONS

This article addresses clinical, pathologic, MR imaging, and PET findings, including new techniques, to educate the readership. Major differentiating MR imaging and PET and pathologic facts are summarized (Online Supplemental Data) to assist with greater understanding. Complicating imaging diagnosis are concomitant pathologies with similar abnormal metabolites.^{3,5} Hence, MR imaging techniques like atrophy analysis; MR spectroscopy; DTI;^{4,20,24} quantitative SWI Fe analysis in AD, FTD, PD, and LBD;^{2,9,30,41,48,53,54} and task-based/rsfMRI in AD, LBD, FTD, and PD^{4,24,27,31,32,37,40} are under investigation. Currently, direct comparisons of SWI and fMRI techniques with molecu-

lar imaging and clinical markers are lacking, possibly slowing diagnosis and understanding of disease progression. Also lacking are multitracer comparative studies, possibly cost-related and due to poor reimbursement by payors. However, newer techniques and radiotracers (τ [PI-2620], a cholinergic, dopaminergic, translocator protein) show needed great promise. Additionally, quantitative atrophy and WM burden analysis as a standard part of examinations with multifactorial analysis of molecular imaging (PET and MR imaging)^{3,24} and Lumbar Puncture findings like the "DuBois criteria" promise better accuracy and treatment development, both urgently needed in our aging society.⁴

ACKNOWLEDGMENTS

We thank Olga James, James Burkek, and Daniel Silverman for contribution of images.

Disclosures: Valerie L Jewells—UNRELATED: Payment for Development of Educational Presentations: American Osteopathic College of Radiology. Comments: I gave a lecture on this topic and received a \$250 stipend. Terence Z. Wong—RELATED: Consulting Fee or Honorarium: Lilly USA, LLC. Comments: In 2012, I served as a consultant to develop educational training materials for the interpretation of florbetapir scans (amyloid imaging for dementia).

REFERENCES

1. Beach TG, Monsell SE, Phillips LE, et al. Accuracy of the clinical diagnosis of Alzheimer disease at National Institute on Aging Alzheimer Disease Centers, 2005–2010. *J Neuropathol Exp Neurol* 2012;71:266–73 CrossRef Medline
2. Sala Frigerio C, De Strooper B. Alzheimer's disease mechanisms and emerging roads to novel therapeutics. *Annu Rev Neurosci* 2016;39:57–79 CrossRef Medline
3. Femminella GD, Thayanandan T, Calsolaro V, et al. Imaging and molecular mechanisms of Alzheimer's disease: a review. *Int J Mol Sci* 2018;19:3702 CrossRef Medline
4. Reiman EM, Jagust WJ. Brain imaging in the study of Alzheimer's disease. *Neuroimage* 2012;61:505–16 CrossRef Medline
5. Arnold M, Nho K, Kueider-Paisley A, et al. Sex and APOE4 genotype modify the Alzheimer's disease serum metabolome. *Nat Commun* 2020;11:1148 CrossRef Medline
6. Rasmussen MK, Mestre H, Nedergaard M. The glymphatic pathway in neurological disorders. *Lancet Neurol* 2018;17:1016–24 CrossRef Medline
7. Hay J, Johnson VE, Smith DH, et al. Chronic traumatic encephalopathy: the neuropathological legacy of traumatic brain injury. *Annu Rev Pathol* 2016;11:21–45 CrossRef Medline
8. Tiepolt S, Patt M, Aghakhanyan G, et al. Current radiotracers to image neurodegenerative disease. *EJNMMI Radiopharm Chem* 2019;4:17 CrossRef Medline
9. Yates PA, Desmond PM, Phal PM, et al. AIBL Research Group. Incidence of cerebral microbleeds in preclinical Alzheimer disease. *Neurology* 2014;82:1266–73 CrossRef Medline
10. Barthélemy NR, Li Y, Joseph-Mathurin N, et al. Dominantly Inherited Alzheimer Network. A soluble phosphorylated tau signature links tau, amyloid and the evolution of stages of dominantly inherited Alzheimer's disease. *Nat Med* 2020;26:398–407 CrossRef Medline
11. Khosravi M, Newberg A, Alavi A. Cognitive impairment and dementias. *Semin Nucl Med* 2018;48:498–512 CrossRef Medline
12. Ibanez V, Pietrini P, Alexander GE, et al. Regional glucose metabolic abnormalities are not the result of atrophy in Alzheimer's disease. *Neurology* 1998;50:1585–93 CrossRef Medline
13. Ma HR, Sheng LQ, Pan PL, et al. Cerebral glucose metabolic prediction from amnesic mild cognitive impairment to Alzheimer's dementia: a meta-analysis. *Transl Neurodegener* 2018;7:9 CrossRef Medline
14. Smailagic N, Lafortune L, Kelly S, et al. 18F-FDG PET for prediction of conversion to Alzheimer's disease dementia in people with mild cognitive impairment: an updated systematic review of test accuracy. *J Alzheimers Dis* 2018;64:1175–94 CrossRef Medline
15. Martinez G, Vernooij RW, Fuentes PP, et al. 18F-PET with florbetapir for the early diagnosis of Alzheimer's disease dementia and other dementias in people with mild cognitive impairment (MCI). *Cochrane Database Syst Rev* 2017;11:CD012216 CrossRef Medline
16. Morris E, Chalkidou A, Hammers A, et al. Diagnostic accuracy of (18)F amyloid PET tracers for the diagnosis of Alzheimer's disease: a systematic review and meta-analysis. *Eur J Nucl Med Mol Imaging* 2016;43:374–85 CrossRef Medline
17. Johnson KA, Sperling RA, Gidicsin CM, et al. AV45-A11 study group. Florbetapir (F18-AV-45) PET to assess amyloid burden in Alzheimer's disease dementia, mild cognitive impairment, and normal aging. *Alzheimers Dement* 2013;9:S72–83 CrossRef Medline
18. Aizenstein HJ, Nebes RD, Saxton JA, et al. Frequent amyloid deposition without significant cognitive impairment among the elderly. *Arch Neurol* 2008;65:1509–17 CrossRef Medline
19. Zukotynski K, Kuo PH, Mikulis D, et al. PET/CT of dementia. *AJR Am J Roentgenol* 2018;211:246–59 CrossRef Medline
20. Ryan NS, Keihaninejad S, Shakespeare TJ, et al. Magnetic resonance imaging evidence for presymptomatic change in thalamus and caudate in familial Alzheimer's disease. *Brain* 2013;136:1399–414 CrossRef Medline
21. Laforce R Jr, Soucy JP, Sellami L, et al. Molecular imaging in dementia: past, present, and future. *Alzheimers Dement* 2018;14:1522–52 CrossRef Medline
22. Villemagne VL, Okamura N. In vivo tau imaging: obstacles and progress. *Alzheimers Dement* 2014;10:S254–64 CrossRef Medline
23. Hyman BT, Phelps CH, Beach TG, et al. National Institute on Aging-Alzheimer's Association guidelines for the neuropathologic assessment of Alzheimer's disease. *Alzheimers Dement* 2012;8:1–13 CrossRef Medline
24. Tanpitukpongse TP, Mazurowski MA, Ikkena J, et al. Predictive utility of marketed volumetric software tools in subjects at risk for Alzheimer disease: do regions outside the hippocampus matter? *AJNR Am J Neuroradiol* 2017;38:546–52 CrossRef Medline
25. Yueniwati Y, Wangsadajaja C, Yulidani IG, et al. The role of brain MRI as an early detector of cognitive impairment. *J Neurosci Rural Pract* 2018;9:350–53 CrossRef Medline
26. No HJ, Yi HA, Won KS, et al. Association between white matter lesions and cerebral glucose metabolism in patient with cognitive impairment. *Rev Esp Med Nucl Imagen Mol* 2019;38:160–66 CrossRef Medline
27. Chandra A, Dervenoulas G, Politis M; Alzheimer's Disease Neuroimaging Initiative. Magnetic resonance imaging in Alzheimer's disease and mild cognitive impairment. *J Neurol* 2019;266:1293–1302 CrossRef Medline
28. Nasrabad SE, Rizvi B, Goldman JE, et al. White matter changes in Alzheimer's disease: a focus on myelin and oligodendrocytes. *Acta Neuropathol Commun* 2018;6:22 CrossRef Medline
29. Belaidi AA, Bush AI. Iron neurochemistry in Alzheimer's disease and Parkinson's disease: targets for therapeutics. *J Neurochem* 2016;139(Suppl 1):179–97 CrossRef Medline
30. Gao L, Jiang J, Cai Z, et al. Brain iron deposition analysis using susceptibility-weighted imaging and its association with body iron levels in patients with mild cognitive impairment. *Mol Med Rep* 2017;16:8209–15 CrossRef Medline
31. Hohenfeld C, Werner CJ, Reetz K. Resting-state connectivity in neurodegenerative disorders: Is there potential for an imaging biomarker. *Neuroimage Clin* 2018;18:849–70 CrossRef Medline
32. Li HJ, Hou XH, Liu HH, et al. Towards systems neuroscience in mild cognitive impairment and Alzheimer's disease: a meta-analysis of 75 fMRI studies. *Hum Brain Mapp* 2015;36:1217–32 CrossRef Medline
33. Wilson H, Pagano G, Politis M. Dementia spectrum disorders: lessons learnt from decades with PET research. *J Neural Transm (Vienna)* 2019;126:233–51 CrossRef Medline
34. Brown RK, Bohnen NI, Wong KK, et al. Brain PET in suspected dementia: patterns of altered FDG metabolism. *Radiographics* 2014;34:684–701 CrossRef Medline
35. Olney NT, Spina S, Miller BL. Frontotemporal dementia. *Neurol Clin* 2017;35:339–74 CrossRef Medline
36. Diehl J, Grimmer T, Drzezga A, et al. Cerebral metabolic patterns at early stages of frontotemporal dementia and semantic dementia: a PET study. *Neurobiol Aging* 2004;25:1051–56 CrossRef Medline
37. Grimmer T, Diehl J, Drzezga A, et al. Region-specific decline of cerebral glucose metabolism in patients with frontotemporal

- dementia: a prospective 18F-FDG-PET study. *Dement Geriatr Cogn Disord* 2004;18:32–36 CrossRef Medline
38. Diehl-Schmid J, Grimmer T, Drzezga A, et al. **Decline of cerebral glucose metabolism in frontotemporal dementia: a longitudinal 18F-FDG-PET-study.** *Neurobiol Aging* 2007;28:42–50 CrossRef Medline
 39. Bocchetta M, Gordon E, Cardoso MJ, et al. **Thalamic atrophy in frontotemporal dementia: not just a C9orf72 problem.** *Neuroimage Clin* 2018;18:675–81 CrossRef Medline
 40. Jakabek D, Power BD, MacFarlane MD, et al. **Regional structural hypo- and hyper-connectivity of frontal-striatal and frontal-thalamic pathways in behavioral variant frontotemporal dementia.** *Hum Brain Mapp* 2018;39:4083–93 CrossRef Medline
 41. Sheela KR, Kesavadas C, Varghese T, et al. **Assessment of iron deposition in brain in frontotemporal dementia and its correlation with behavioral traits.** *AJNR Am J Neuroradiol* 2017;38:1953–58 CrossRef Medline
 42. Farid K, Charidimou A, Baron JC. **Amyloid positron emission tomography in sporadic cerebral amyloid angiopathy: a systematic critical update.** *Neuroimage Clin* 2017;15:247–63 CrossRef Medline
 43. Miller-Thomas MM, Sipe AD, Benzinger TL, et al. **Multimodality review of amyloid-related disease of the central nervous system.** *Radiographics* 2016;36:1147–63 CrossRef Medline
 44. Werring DJ, Gregoire SM, Cipolotti L. **Cerebral microbleeds and vascular cognitive impairment.** *J Neurol Sci* 2010;299:131–35 CrossRef Medline
 45. Jang H, Jang YK, Kim HJ, et al. **Clinical significance of amyloid beta positivity in patients with probable cerebral amyloid angiopathy markers.** *Eur J Nucl Med Mol Imaging* 2019;46:1287–98 CrossRef Medline
 46. Charidimou A, Farid K, Tsai HH, et al. **Amyloid-PET burden and regional distribution in cerebral amyloid angiopathy: a systematic review and meta-analysis of biomarker performance.** *J Neurol Neurosurg Psychiatry* 2018;89:410–17 CrossRef Medline
 47. Sarikaya I. **PET imaging in neurology: Alzheimer's and Parkinson's diseases.** *Nucl Med Commun* 2015;36:775–81 CrossRef Medline
 48. Shams S, Fallmar S, Schwarz S, et al. **MRI of the swallow tail sign: a useful marker in the diagnosis of Lewy body disease?** *AJNR Am J Neuroradiol* 2017;38:1737–41 CrossRef
 49. Eidelberg D, Moeller JR, Dhawan V, et al. **The metabolic anatomy of Parkinson's disease: complementary [18F]fluorodeoxyglucose and [18F]fluorodopa positron emission tomographic studies.** *Mov Disord* 1990;5:203–13 CrossRef Medline
 50. Webb J, Willette AA. **Aging modifies the effect of GCH1 RS11158026 on DAT uptake and Parkinson's disease clinical severity.** *Neurobiol Aging* 2017;50:39–46 CrossRef Medline
 51. Patro SN, Glikstein R, Hanagandi P, et al. **Role of neuroimaging in multidisciplinary approach towards non-Alzheimer's dementia.** *Insights Imaging* 2015;6:531–44 CrossRef Medline
 52. Bhattacharya K, Saadia D, Eisenkraft B, et al. **Brain magnetic resonance imaging in multiple-system atrophy and Parkinson disease: a diagnostic algorithm.** *Arch Neurol* 2002;59:835–42 CrossRef Medline
 53. Belaidi AA, Bush AI. **Iron neurochemistry in Alzheimer's disease and Parkinson's disease: targets for therapeutics.** *J Neurochem* 2016;139(Suppl 1):179–97 CrossRef Medline
 54. Thomas GE, Leyland LA, Scahrag AE, et al. **Brain iron deposition is linked with cognitive severity in Parkinson's disease.** *J Neurol Neurosurg Psych* 2020;0:1–8 CrossRef Medline
 55. Surendranathan A, O'Brien JT. **Clinical imaging in dementia with Lewy bodies.** *Evid Based Ment Health* 2018;21:61–65 CrossRef Medline
 56. McKeith IG, Boeve BF, Dickson DW, et al. **Diagnosis and management of dementia with Lewy bodies: fourth consensus report of the DLB consortium.** *Neurology* 2017;89:88–100 CrossRef Medline
 57. McColgan P, Tabrizi SJ. **Huntington's disease: a clinical review.** *Eur J Neurol* 2018;25(1):24–23 CrossRef Medline
 58. Agosta F, Altomare D, Festari C, et al. EANM-EAN Task Force for the Prescription of FDG-PET for Dementing Neurodegenerative Disorders. **Clinical utility of FDG-PET in amyotrophic lateral sclerosis and Huntington's disease.** *Eur J Nucl Med Mol Imaging* 2018;45:1546–56 CrossRef Medline
 59. Gaura V, Lavisse S, Payoux P, et al. **Association between motor symptoms and brain metabolism in early Huntington disease.** *JAMA Neurol* 2017;74:1088–96 CrossRef Medline
 60. Pagano G, Niccolini F, Politis M. **Current status of PET imaging in Huntington's disease.** *Eur J Nucl Med Mol Imaging* 2016;43:1171–82 CrossRef Medline
 61. Caobelli F, Cobelli M, Pizzocaro C, et al. **The role of neuroimaging in evaluating patients affected by Creutzfeldt-Jakob disease: a systematic review of the literature.** *J Neuroimaging* 2015;25:2–13 CrossRef Medline

Brain and Lung Imaging Correlation in Patients with COVID-19: Could the Severity of Lung Disease Reflect the Prevalence of Acute Abnormalities on Neuroimaging? A Global Multicenter Observational Study

A. Mahammedi, A. Ramos, N. Bargalló, M. Gaskill, S. Kapur, L. Saba, H. Carrete Jr, S. Sengupta, E. Salvador, A. Hilario, Y. Revilla, M. Sanchez, M. Perez-Nuñez, S. Bachir, B. Zhang, L. Oleaga, J. Sergio, L. Koren, P. Martin-Medina, L. Wang, M. Benegas, F. Ostos, G. Gonzalez-Ortega, P. Calleja, G. Udstuen, B. Williamson, V. Khandwala, S. Chadalavada, D. Woo, and A. Vagal



ABSTRACT

PURPOSE: Our aim was to study the association between abnormal findings on chest and brain imaging in patients with coronavirus disease 2019 (COVID-19) and neurologic symptoms.

MATERIALS AND METHODS: In this retrospective, international multicenter study, we reviewed the electronic medical records and imaging of hospitalized patients with COVID-19 from March 3, 2020, to June 25, 2020. Our inclusion criteria were patients diagnosed with Severe Acute Respiratory Syndrome coronavirus 2 (SARS-CoV-2) infection with acute neurologic manifestations and available chest CT and brain imaging. The 5 lobes of the lungs were individually scored on a scale of 0–5 (0 corresponded to no involvement and 5 corresponded to >75% involvement). A CT lung severity score was determined as the sum of lung involvement, ranging from 0 (no involvement) to 25 (maximum involvement).

RESULTS: A total of 135 patients met the inclusion criteria with 132 brain CT, 36 brain MR imaging, 7 MRA of the head and neck, and 135 chest CT studies. Compared with 86 (64%) patients without acute abnormal findings on neuroimaging, 49 (36%) patients with these findings had a significantly higher mean CT lung severity score (9.9 versus 5.8, $P < .001$). These patients were more likely to present with ischemic stroke (40 [82%] versus 11 [13%], $P < .0001$) and were more likely to have either ground-glass opacities or consolidation (46 [94%] versus 73 [84%], $P = .01$) in the lungs. A threshold of the CT lung severity score of >8 was found to be 74% sensitive and 65% specific for acute abnormal findings on neuroimaging. The neuroimaging hallmarks of these patients were acute ischemic infarct (28%), intracranial hemorrhage (10%) including microhemorrhages (19%), and leukoencephalopathy with and/or without restricted diffusion (11%). The predominant CT chest findings were peripheral ground-glass opacities with or without consolidation.

CONCLUSIONS: The CT lung disease severity score may be predictive of acute abnormalities on neuroimaging in patients with COVID-19 with neurologic manifestations. This can be used as a predictive tool in patient management to improve clinical outcome.

ABBREVIATIONS: COVID-19 = coronavirus disease 2019; GGOs = ground-glass opacities; PRES = posterior reversible encephalopathy syndrome; SARS-CoV-2 = Severe Acute Respiratory Syndrome coronavirus 2; TIPIIC = Transient Perivascular Inflammation of the Carotid artery syndrome

Severe Acute Respiratory Syndrome coronavirus 2 (SARS-CoV-2) began in Wuhan, China, in December 2019 and has rapidly spread around the world to become a pandemic.¹

Extensive studies have described chest and brain imaging characteristics associated with coronavirus disease 2019 (COVID-19).^{2–13} The hallmarks of COVID-19 infection on chest imaging

Received October 26, 2020; accepted after revision January 4, 2021.

From the Departments of Neuroradiology, (A.M., A.V., M.G., L.W., G.U., B.W., V.K.), Cardiopulmonary Imaging, (S.K.), Neurology (S.S., D.W.), and Department of Informatics and Interventional Radiology, (S.C.), University of Cincinnati Medical Center, Cincinnati, Ohio; Departments of Epidemiology and Biostatistics (B.Z.) and Pediatrics, (S.B.), Cincinnati Children's Hospital Medical Center, Cincinnati, Ohio; Departments of Neuroradiology (A.R., E.S., A.H., L.K., P.M.-M.), Cardiopulmonary Imaging (Y.R., M.P.-N.) and Neurology (F.O., G.G.-O., P.C.), Hospital Universitario 12 de Octubre, Madrid, Spain; Departments of Neuroradiology (L.O., N.B.) and Cardiopulmonary Imaging (M.S., M.B., J.S.), Hospital Clinic de Barcelona, Sunyer Biomedical Research Institute, Barcelona, Spain; Department of Neuroradiology

(L.S.), Azienda Ospedaliero Universitaria di Cagliari, Monserrato (Cagliari), Italy; Department of Neuroradiology (H.C.), Escola Paulista de Medicina, Federal University of São Paulo, São Paulo, Brazil.

Please address correspondence to Abdelkader Mahammedi, MD, Department of Radiology, University of Cincinnati Medical Center, 234 Goodman St, Cincinnati, OH 45267-0525; e-mail: abdelkader.mahammedi@uc.edu

Indicates open access to non-subscribers at www.ajnr.org

Indicates article with online supplemental data.

<http://dx.doi.org/10.3174/ajnr.A7072>

are now well-established, including bilateral and peripheral ground-glass and consolidative pulmonary opacities.²⁻⁵ COVID-19-related brain imaging findings such as ischemic infarcts, hemorrhages, and multiple patterns of leukoencephalopathy⁶⁻¹³ are also well-known. The clinical symptomatology has been linked to the imaging findings with up to 47% of patients with COVID-19 with neurologic symptoms demonstrating acute neuroimaging findings⁶ and patients with high lung severity scores being admitted to the intensive care unit.³ The incidence of neurologic symptoms is higher in patients with more severe respiratory disease.^{10,13} There is increasing evidence that patients with acute lung injury are at risk of brain injury through hypoxemia and/or proinflammatory mediators that connect both the brain and the lungs.¹⁴⁻¹⁷ However, little information is available on the potential association between the prevalence of neuroimaging abnormalities and the severity of CT lung findings in patients with COVID-19. The objective of this study was to examine the association between chest and brain imaging abnormalities in patients with COVID-19. We hypothesized that the severity of lung disease may predict acute abnormalities on neuroimaging in patients with COVID-19 with neurologic symptoms.

MATERIALS AND METHODS

Study Design and Patient Population

We used a retrospective, multicenter study design from 5 academic institutions in 4 countries: Spain, Italy, Brazil, and the United States (University of Cincinnati Medical Center, Cincinnati, Ohio; University Hospital 12 de Octubre, Madrid, Spain; Hospital Clínic de Barcelona, Barcelona, Spain; University of Cagliari, Cagliari, Italy; and Federal University of Sao Paulo, Sao Paulo, Brazil). Institutional review board approval and waivers were obtained at all institutions. Our inclusion criteria were the following: 1) hospitalized patients who were positive for COVID-19 via real-time polymerase chain reaction of respiratory secretions obtained by bronchoalveolar lavage, endotracheal aspirate, nasopharyngeal swab, or oropharyngeal swab from March 3 to June 25, 2020; 2) the presence of acute neurologic symptoms during the hospital stay; 3) available chest CT and brain CT and/or MR imaging. We reviewed the electronic medical records to extract clinical, laboratory, and demographic data.

Image Acquisition

All noncontrast brain and chest CT scans were obtained as per standard-of-care protocols. The MR imaging of the brain and MRA of the head and neck were performed on 1.5T scanners with standardized protocols. Gd-DTPA (0.1 mmol/kg of gadobutrol, Gadovist; Bayer Schering Pharma) was used for contrast studies.

Image Interpretation

For each patient, all neuroimaging was evaluated for the following characteristics: 1) T2/FLAIR white matter signal abnormality: nonconfluent punctate and/or confluent white matter lesions with and/or without restricted diffusion and/or microhemorrhage; 2) enhancement: leptomeningeal, parenchymal, and cranial nerves; 3) acute ischemic infarcts: vascular territory, small/watershed zone, and cardioembolic; 4) intracranial hemorrhages:

parenchymal, subarachnoid, and microhemorrhage; 5) acute leukoencephalopathy; 6) posterior reversible encephalopathy syndrome (PRES); and 7) hypoxic-ischemic encephalopathy. All neuroimaging was divided into 2 groups: acute-versus-nonacute neuroimaging findings. Patients with chronic microvascular ischemic disease, remote infarcts, or chronic demyelinating disease but without acute neuroimaging findings were counted in the group of nonacute neuroimaging. Scans were compared with prior examinations if available. Imaging findings without prior neuroimaging were considered acute if compatible with acute patient symptoms. The mean timeframe difference between the scans of patients with acute-versus-nonacute neuroimaging was 2 days.

Chest CT scans were evaluated for the following characteristics: 1) the presence and/or absence of ground-glass opacities (GGOs) and/or consolidation; 2) crazy paving pattern; 3) cavitation, pleural effusions, or lymphadenopathy; 4) CT lung severity score; 5) predominant zonal distribution; and 6) lobar involvement. A semiquantitative CT-based severity score of pulmonary disease burden was measured by counting the involvement of lung lobes similar to that in Pan et al.⁴ Each of the 5 lung lobes was scored from 0 to 5 as the following: 0, no involvement; one, <5% involvement; two, 25% involvement; three, 26%–49% involvement; four, 50%–75% involvement; and five, >75% involvement. The CT lung severity score was the sum of the individual lobar scores and ranged from 0 (no involvement) to 25 (maximum involvement). In patients with multiple chest CT scans, only scans with the greatest severity were selected, and all were performed approximately 7–12 days after the initial onset of respiratory symptoms. All scans were reviewed by 6 neuroradiologists and 5 chest radiologists in consensus.

Statistical Analysis

Analyses were performed to describe the distribution of the variables of interest. Continuous variables were presented as mean [SD] or median and range. The normality of continuous variables was assessed by the Kolmogorov-Smirnov test. Categorical variables were presented as frequencies and percentages. Continuous variables were compared using the 2-sample *t* test or Wilcoxon rank sum test. Proportions for categorical variables were compared using the χ^2 test or Fisher exact test. The logistic regression model was used to assess the association between abnormalities on acute neuroimaging and the CT lung severity score. Prediction ability was evaluated using a receiver operating characteristic curve. The optimal threshold and the sensitivity and specificity at the threshold were reported. All statistical analyses were performed using STATA software (Version 15; StataCorp). The significance threshold was set at a 2-sided *P* value < .05.

RESULTS

A total of 172 consecutive hospitalized patients with COVID-19 with acute neurologic symptoms were reviewed. Of these, 135 patients fit our inclusion criteria (Fig 1, flow chart). The demographic and neurologic clinical characteristics are shown in the Online Supplemental Data. The mean age was 68.2 [SD, 15.1] years (age range, 17–94 years), and 86 (64%) were men.

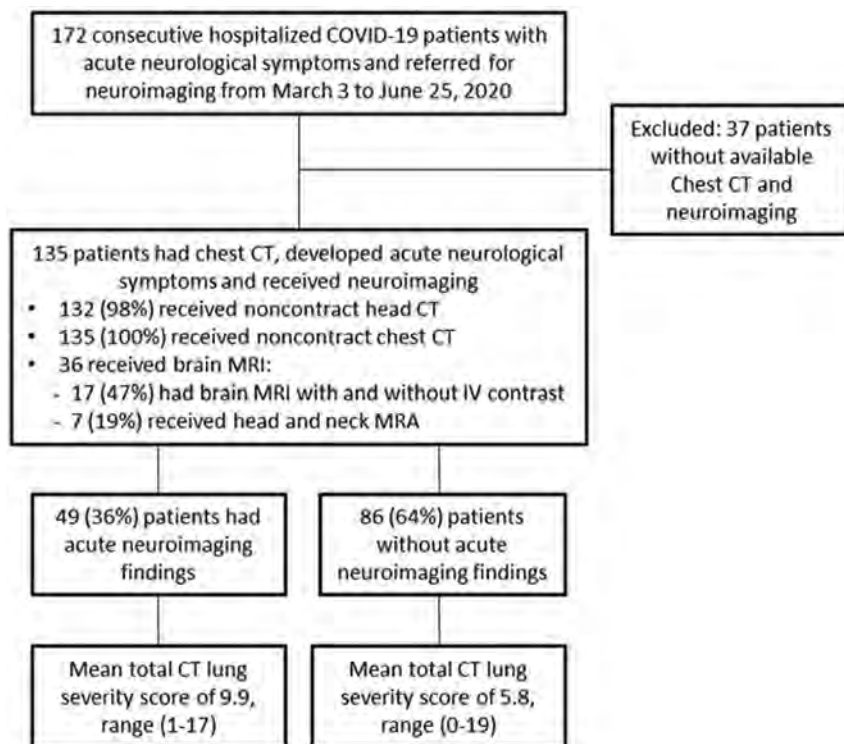


FIG 1. Flow chart of the study.

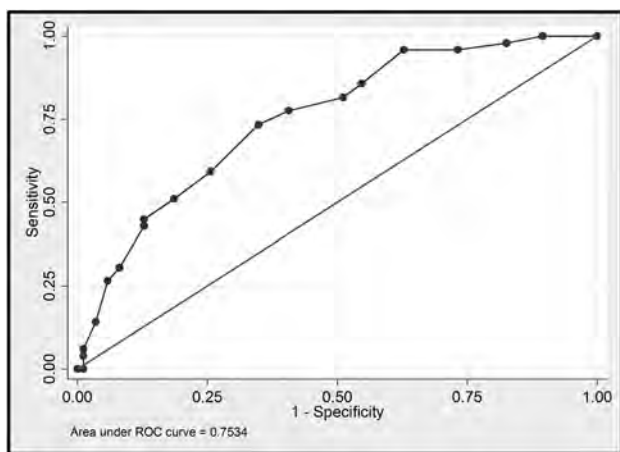


FIG 2. Receiver operating characteristic curve showing the sensitivity and specificity of the CT lung severity score as a predictor of acute neuroimaging abnormalities in patients with COVID-19 with neurologic symptoms. The area under the curve corresponds to the accuracy. ROC indicates receiver operating characteristic.

Demographics, medical history, and neurologic clinical characteristics are shown in the Online Supplemental Data.

Association between Neuroimaging and CT Chest Findings

A total of 132 noncontrast brain CT scans, 36 brain MR images, and 135 noncontrast chest CT scans were reviewed. Of these, 7 (19%) patients underwent head and neck MRA, while 17 (47%) patients had brain MR imaging with and without IV contrast, of

which only 6 scans included both 3D-FLAIR and 3D T1-weighted postcontrast images. Of the 135 patients, 49 (36%) had acute abnormalities on neuroimaging and 86 (64%) patients had nonacute neuroimaging findings. The patients with acute abnormalities on neuroimaging had a significantly higher mean CT lung severity score versus those without acute neuroimaging abnormalities (9.9 [SD, 4.2] versus 5.8 [SD, 4.3], $P < .001$). Compared with patients without acute abnormalities on neuroimaging, patients with acute abnormalities on neuroimaging were more likely to present with ischemic stroke (40 [82%] versus 11 [13%], $P < .0001$) and were more likely to have either GGOs or consolidation (46 [94%] versus 73 [84%], $P = .01$). A threshold CT lung severity score of >8 was found to be 74% sensitive and 65% specific for acute abnormalities on neuroimaging (Fig 2).

None of the remaining neurologic symptoms and patient characteristics, including age and medical history, demonstrated a significant statistical difference. The average time interval between the lung CT and brain imaging was 6 days.

Neuroimaging Characteristics

The neuroimaging hallmark of these patients was acute ischemic infarcts in 38 (28%), intracranial hemorrhage in 14 (10%), and white matter disease in 22 (36%). Of the ischemic infarcts, 21 (15%) were large, 10 (7%) were small/watershed infarcts, 5 (4%) were cardioembolic, and 2 (1%) were hypoxic-ischemic encephalopathy. Microhemorrhage in 7 (19%) was the most common intracranial hemorrhage followed by subarachnoid hemorrhage in 4 (3%). The most frequent MR imaging findings of white matter disease were nonconfluent punctate multifocal T2/FLAIR hyperintense lesions with associated microbleeds in 7 (19%) (4 [11%] with and 3 [8%] without associated restricted diffusion) and confluent symmetric T2/FLAIR hyperintensity involving the deep and subcortical white matter in 4 (11%) (2 [5%] with and 2 [5%] without associated restricted diffusion) (Fig 3). Neuroimaging characteristics are shown in Table. Patients with nonacute neuroimaging findings had normal scan findings; varying degrees of chronic microvascular ischemic disease, remote infarcts, or chronic demyelinating disease, but no acute abnormalities on neuroimaging. The median time from hospital admission to brain imaging was 9 days. Of the 49 (36%) patients with acute abnormalities on neuroimaging, 13 were in the intensive care unit and on mechanical ventilation at the time of neuroimaging, with a mean duration of 12 days.

CT Chest Characteristics

Of the 135 patients, the predominant CT chest patterns were peripheral, either GGOs or consolidation (Online Supplemental

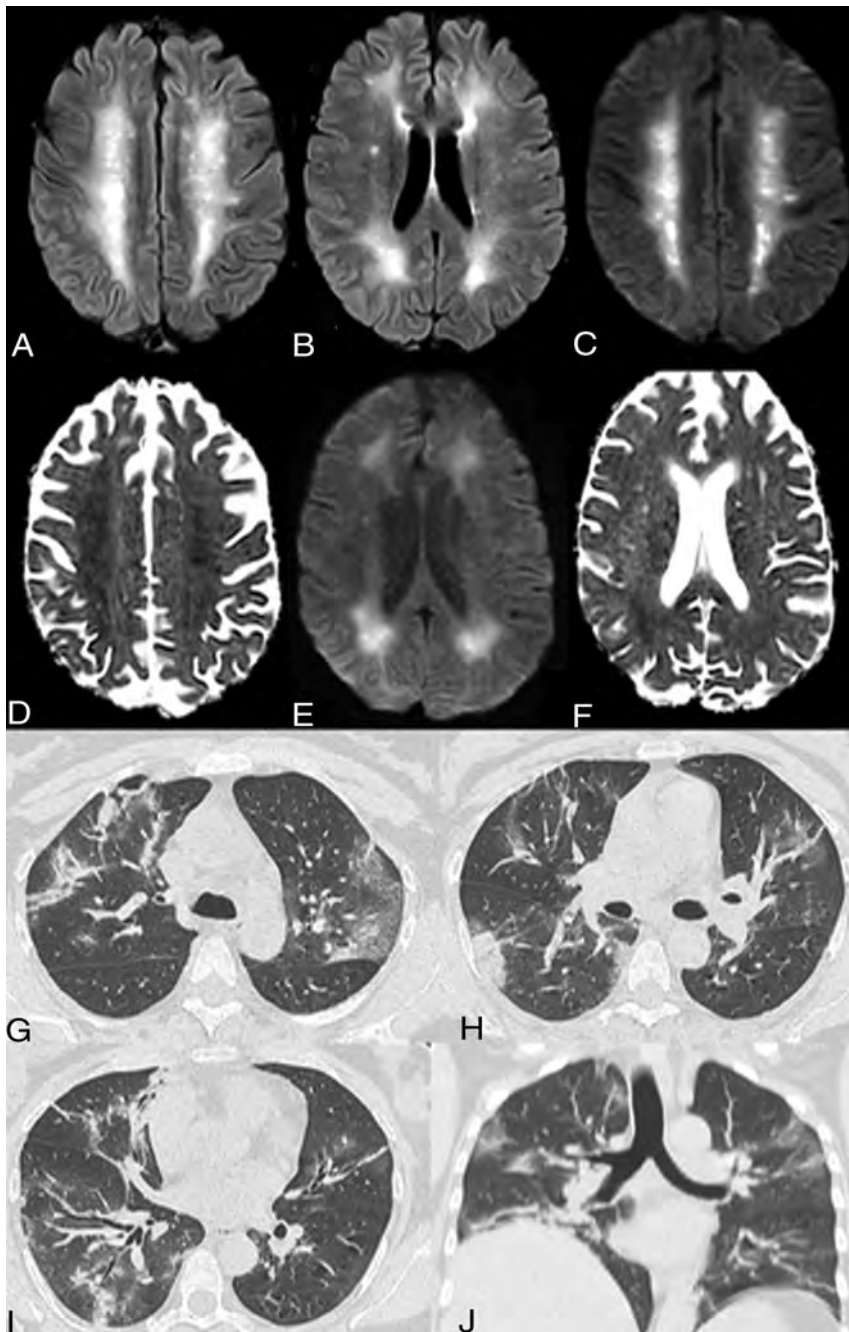


FIG 3. Acute leukoencephalopathy. A 48-year-old man without a history of seizures presented with convulsions and altered mental status. Extensive and confluent symmetric deep and subcortical white matter FLAIR hyperintensities in the bilateral centra semiovale (A) and periventricular frontal and parietal regions (B) with associated mild restricted diffusion on DWI/ADC images, most prominent in the centra semiovale (C and D) and peritrigonal regions (E and F). No associated enhancement or microbleed was seen on the T1 postcontrast and SWI (not shown). Coronal MPR and axial noncontrast images in lung windows demonstrate mixed ground-glass and consolidative opacities in all lobes with a lower lung and peripheral predominance (G–J). The CT lung severity score was 16 (right upper lobe, right lower lobe, left upper lobe, left lower lobe, 25%–49% and right middle lobe 50%–75%). The chest CT scan was obtained 8 days after the initial onset of respiratory symptoms.

Data). Sixteen (12%) patients had neither GGOs nor consolidation. Of the 119 (88%) patients with either GGOs, consolidation, or both, 46 had only GGOs without consolidation, and 7 patients

had consolidation without GGOs. The most involved was the left lower lobe in 102 (75%), followed by the right lower lobe in 97 (72%). One hundred patients (81%) had peripheral predominant distribution, and 61 (45%) had lower zone involvement. The mean CT lung severity score was 7.3 [SD, 4.1] (range, 0–19).

DISCUSSION

In this global, multi-institutional study, we found that patients with COVID-19 with neurologic symptoms and acute abnormalities on neuroimaging had, on average, a significantly higher CT lung severity score compared with those without acute neuroimaging findings. A threshold CT lung severity score of >8 was found to be 74% sensitive and 65% specific for acute abnormalities on neuroimaging. To the best of our knowledge, this is the first study describing the brain and lung imaging correlation in patients with COVID-19. Our findings show that compared with patients without acute abnormalities on neuroimaging, patients with acute abnormalities on neuroimaging were more likely to present with ischemic stroke and were more likely to have either GGOs or consolidation. The neuroimaging features of these patients were variable without a specific pattern but were dominated by acute ischemic infarct, intracranial hemorrhage, and leukoencephalopathy. The predominant CT chest pattern was peripheral GGOs with or without consolidation. We also reported 2 cases of probable COVID-19-associated carotidynia or the new term, Transient Perivascular Inflammation of the Carotid artery (TIPIC) syndrome.¹⁸

Although accumulating evidence suggests that patients with severe COVID-19 might have a cytokine storm syndrome, resulting in a multiorgan inflammatory response, the underlying pathophysiology of brain and lung association in COVID-19 remains unclear.^{9,19,20} The multisystemic manifestations in COVID-19 infection, including central neurologic symptoms, can be potentially

explained by the presence of angiotensin-converting enzyme 2 receptors in multiple human organs, including the brain and lungs.^{10,21} Currently, however, we have a poor mechanistic

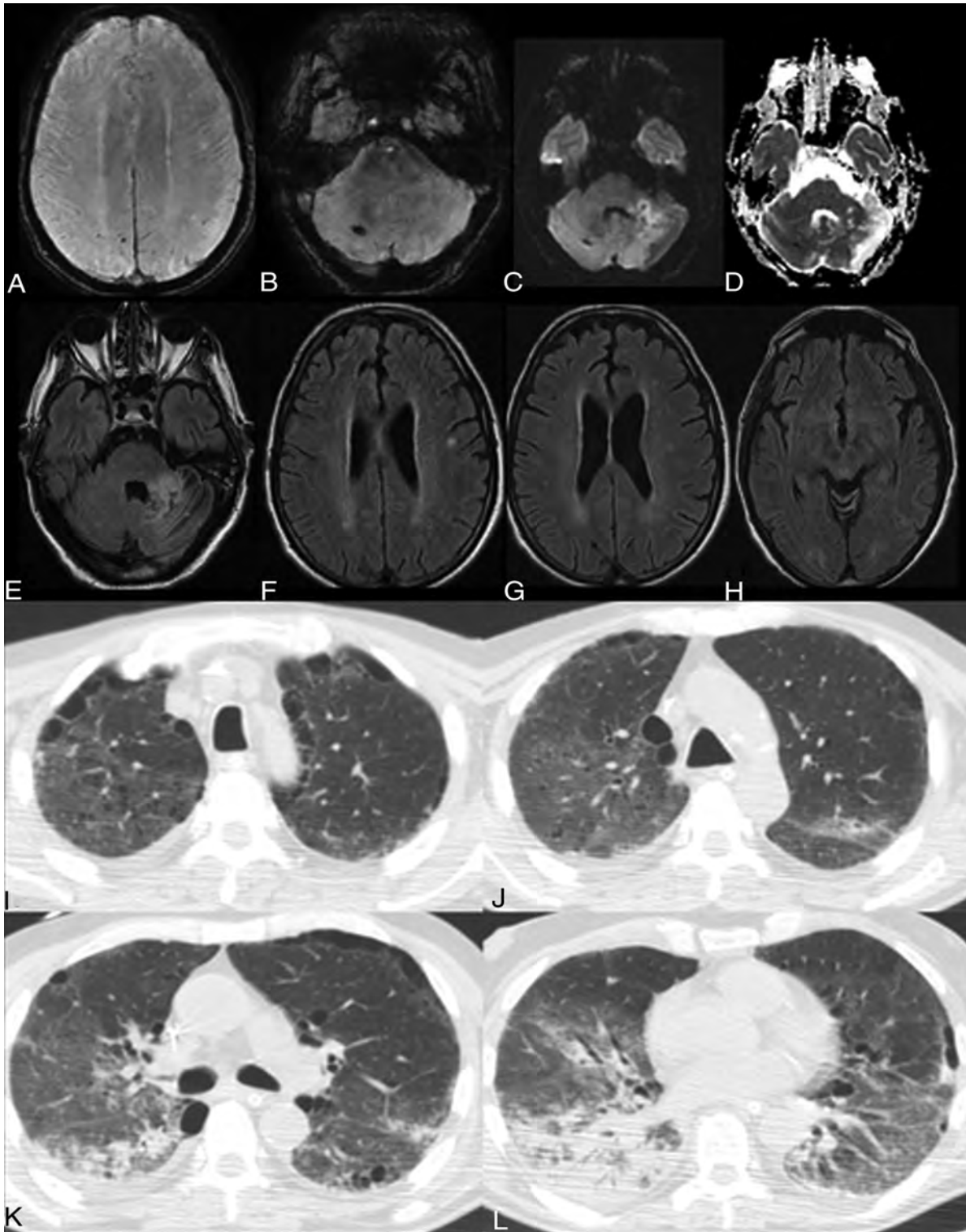


FIG 4. Acute infarct, multifocal microbleeds, and subcortical white matter FLAIR hyperintensity. A 65-year-old man presented with altered mental status and ischemic stroke. Available prior brain MR imaging findings from 1 month ago were normal. *A* and *B*, New punctate microbleeds on gradient-echo sequences in the right superior parietal lobule, left inferior parietal lobule, and right cerebellum. Note a small area of restricted diffusion in the anterior left cerebellum on DWI/ADC images (*C–D*) with FLAIR hyperintensities (*E*), consistent with acute infarct. New punctate deep and subcortical white matter FLAIR hyperintensities without associated hemorrhage or restricted diffusion in the left-greater-than-right frontal (*F*), parietal (*G*), and occipital lobes (*H*). Axial chest CT images show right apical GGOs and biapical paraseptal emphysema (*I*). Bilateral GGOs are right greater than left (*J*). Patchy consolidations in the apical segment of the lower lobe of the right lung (*K*). Extensive consolidation with an air bronchogram in the right lower lobe (*L*). The CT lung severity score was 14. The chest CT scan was obtained 10 days after initial onset of respiratory symptoms.

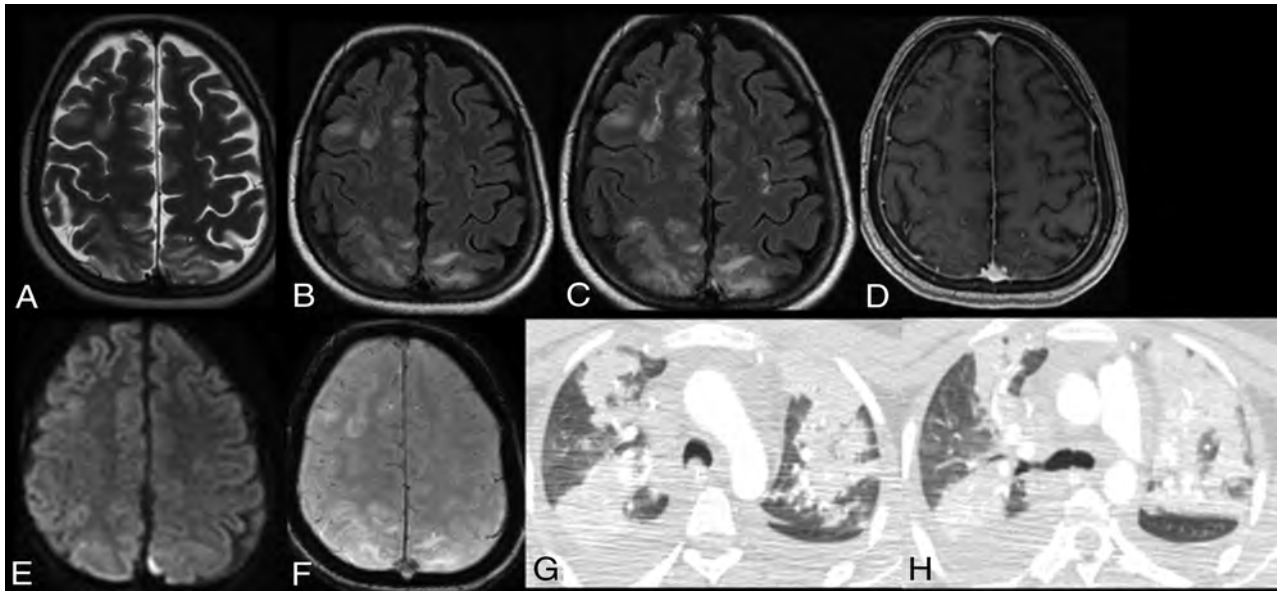


FIG 5. PRES. A 25-year-old woman presented with altered mental status and ischemic stroke. *A* and *B*, Extensive cortical and subcortical areas of T2/FLAIR hyperintensity in the right frontal and bilateral parietal lobes. Associated patchy and confluent leptomeningeal enhancement is seen only on FLAIR postcontrast image (*C*) but not on T1 postcontrast image (*D*). Note no restriction diffusion or hemosiderin on DWI and gradient-echo sequences (*E* and *F*). Axial chest CT scans show new extensive bilateral patchy consolidations in the upper lobes with bilateral right-more-than-left pleural effusions (*G* and *H*). The CT lung severity score was 12. The chest CT scan was obtained 7 days after the initial onset of respiratory symptoms.

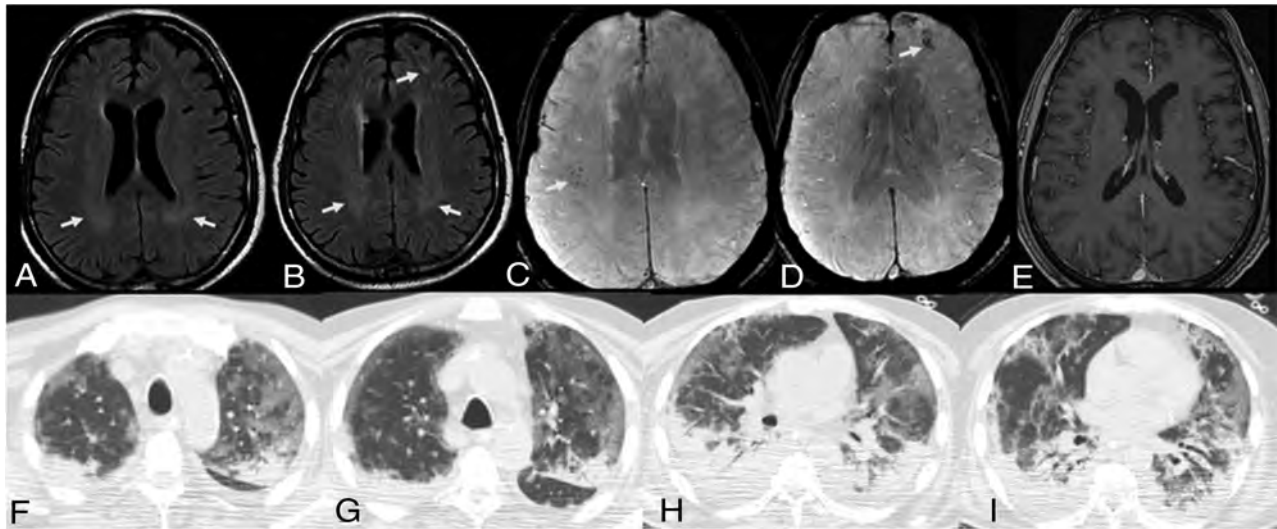


FIG 6. Multifocal microbleeds and deep white matter FLAIR hyperintensities. A 63-year-old man presented with altered mental status. Available prior brain MR imaging findings from 3 months ago were normal. Note confluent periventricular white matter T2/FLAIR hyperintensities, most prominent in the peritrigonal regions (*A* and *B*), with new punctate microbleeds on gradient-echo sequences in the right frontoparietal regions (*C*) and left frontal lobe (*D*). No associated enhancement is seen on the T1 postcontrast image. Axial chest CT images in lung windows show bilateral, peripheral, predominant ground-glass opacities and dependent consolidations in the upper and lower lobes (*F*–*I*). Note air bronchograms in both lower lobes (*H* and *I*). The CT lung severity score was 18. The chest CT scan was obtained 11 days after the initial onset of respiratory symptoms.

understanding of the neurologic manifestations, whether these arise from critical illness or from direct CNS invasion of SARS-CoV-2 or represent treatment-related complications from current COVID-19 therapies including intensive care unit–related complications.^{9,22} PRES and multifocal cerebral thrombotic microangiopathy were reported to be complications of the new COVID-19

antiviral and immunosuppressive drugs such as tocilizumab, which was used in 12 patients in our series.^{22,23}

Postmortem neuropathologic examinations in 18 patients with COVID-19 showed only hypoxic changes without signs of encephalitis.^{24,25} Furthermore, it has been suggested that recruitment of immune cells by either direct viral infection or immune-

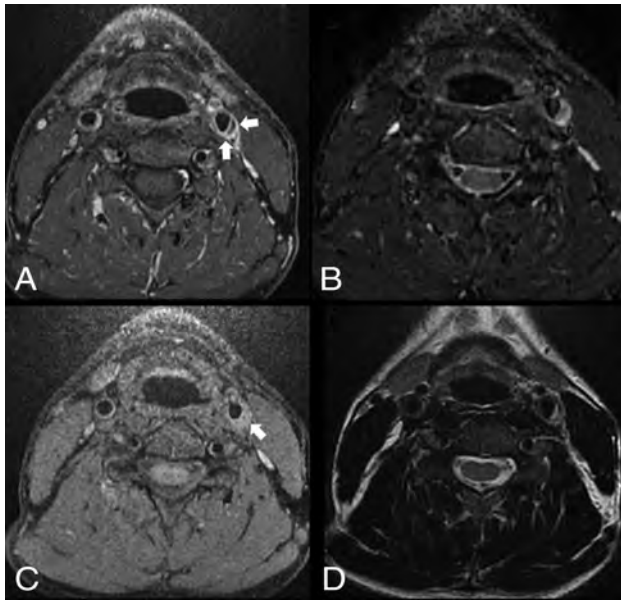


FIG 7. Left TIPIC (carotidynia). A 40-year-old man without significant medical history or known trauma presented with myoclonus and acute tenderness overlying the left carotid artery with increased pulsation. Axial T1 fat-saturated postcontrast image shows asymmetric enhancement and nonstenotic thickening of the left common carotid wall (A, arrows), with T1 precontrast hyperintensity of a crescent-shaped subintimal focus (C, arrow), which is also hyperintense on T2 fat-saturated and T2-weighted (B and D) images. Differential considerations include carotidynia or dissection. However, given the significantly improved symptoms after anti-inflammatory treatment, the lack of luminal stenosis, and the patient's neck pain characteristics, findings are most consistent with carotidynia. No follow-up imaging was available.

mediated damage across different organ vascular beds may lead to endothelial damage, which results in stroke, hemorrhage, and thrombosis.^{9,26} Additionally, it is thought that this latter triggers extensive pulmonary intravascular immunothrombosis and potentially also promotes intraplaque inflammation and destabilization.²⁷ This could be the underlying mechanism in our 2 patients with COVID-19-associated TIPIC. Although the differential diagnosis may include dissection, the combination of clinical and imaging criteria was most consistent with carotidynia. These criteria include the presence of acute pain overlying the carotid artery with increased pulsation, significantly improved symptoms after anti-inflammatory treatment, no significant medical history or known trauma, eccentric perivascular wall thickening, and enhancement without significant luminal stenosis.¹⁸

Our findings concur with additional published literature including Mao et al¹⁰ from Wuhan, China, who reported that 27 (51%) of the patients with CNS symptoms had severe respiratory disease, but there was no description of brain and lung imaging features. Similar to other investigators who described neuroimaging features in severe COVID-19,^{7,8,13} our findings showed multiple patterns of white matter disease and hemorrhage; however, none of these studies have demonstrated an association of neuroimaging with the CT lung severity score or with a specific CT lung pattern. Consistent with previous studies,^{7,8,13} confluent white matter T2

hyperintensities with or without restricted diffusion reported in 2 of our patients (Fig 3) are nonspecific but can be related to delayed posthypoxic leukoencephalopathy; however, the main differential diagnoses include hypoxic-ischemic injury, infectious or autoimmune encephalitis, hypoglycemia, and seizure. Our chest CT findings largely concur with previous investigations insofar as the chest CT hallmark of COVID-19 infection is ground-glass and consolidative pulmonary opacities, with bilateral and peripheral lung distribution.²⁻⁵

Indeed, there is minimal research in the area where acute lung injury and severe brain injury coincide. Acute lung injury occurs in 20% of patients with brain injury and is associated with a poor outcome.¹⁴ Patients with acute respiratory distress syndrome are at risk of brain injury through hypoxemia and/or proinflammatory mediators that connect both the brain and the lungs.¹⁵⁻¹⁷ It is hypothesized that sensory neurons in the airways may provide a sensing mechanism to detect the inflammatory intensity in the lung, creating a feedback mechanism to the brain, thus illustrating lung-brain communication.¹⁵ Hippocampal neuronal cell damage was demonstrated in a porcine acute lung injury model with increased serum proinflammatory mediators.¹⁷ Nevertheless, the underlying pathophysiology of brain-lung association in patients with COVID-19 remains unclear. The identification of the correlation between lung and brain findings could be important for targeting optimized therapies, particularly in stroke prevention. Our findings could be explored in future studies to potentially develop preventive and therapeutic strategies that can improve outcomes in patients with COVID-19.

There are several important limitations to our study including a retrospective design. Second, the known temporal variation of chest CT findings may affect the uniformity of the CT lung severity score;^{4,28} however, only scans with the greatest severity were selected, and all were performed approximately 7–12 days after the initial onset of respiratory symptoms, to minimize this limitation. Third, the impaired consciousness of the patients limited the ability to perform clinicoradiologic correlations, particularly in assessing disease severity and clinical outcomes. Fourth, patients with unstable conditions with critical illness may have delayed or no imaging, which may affect accurate capture of imaging characteristics and therefore underestimate their prevalence. Fifth, compared with MR imaging, CT has a low sensitivity for white matter disease, which may also underestimate the results in patients who only underwent CT neuroimaging. Finally, it is difficult to establish the coincidence of imaging findings versus causality in critically ill patients and to differentiate the imaging findings from those of current COVID-19 therapy-related complications.

CONCLUSIONS

Our study demonstrates that patients with COVID-19 with neurologic symptoms and acute abnormalities on neuroimaging had a higher CT lung severity score compared with patients with COVID-19 with neurologic symptoms and nonacute neuroimaging findings. Future larger datasets with imaging-pathologic correlation may help in understanding the common mechanisms of brain and lung injury.

Neuroimaging characteristics of hospitalized patients with COVID-19 with new onset of neurologic symptoms^a

Neuroimaging Characteristics	All Patients (n = 135), CT (n = 132) or MR imaging (n = 36)
T2/FLAIR white matter signal abnormality	
Nonconfluent punctate deep and subcortical white matter disease	22/36 (61)
Isolated, nonspecific	9/36 (25)
Associated restricted diffusion only ^b	6/36 (17)
Associated microhemorrhage only ^b	3/36 (8)
Associated microhemorrhage and restricted diffusion ^b	4/36 (11)
Confluent symmetric T2 hyperintensity without restricted diffusion or hemorrhage	2/36 (5)
Confluent symmetric T2 hyperintensity with mild restricted diffusion ^c	2/36 (5)
Enhancement (MR imaging with and without IV contrast)	2/17 (12)
Leptomeningeal ^d	2/17 (12)
Parenchymal ^e	0/17 (0)
Cranial nerves	
Acute ischemic infarcts	36/135 (27)
Vascular territory	21/135 (15)
Small/watershed infarcts	10/135 (7)
Cardioembolic	5/135 (4)
Intracranial hemorrhages	14/135 (10)
Parenchymal	3/135 (2)
Subarachnoid	4/135 (3)
Microhemorrhage	7/36 (19)
Acute leukoencephalopathy ^c	4/36 (11)
PRES	3/36 (8)
Hypoxic-ischemic encephalopathy	2/36 (5)
TIPIC ^f	2/7 (28)

^aNumbers in parentheses are percentages.

^bThought to be most consistent with acute lacunar infarcts with a few associated microhemorrhages (Figs 4 and 6).

^cAcute leukoencephalopathy. A 48-year-old man without a history of seizures presented with convulsion and altered mental status (Fig 3).

^dSeen on FLAIR postcontrast only and likely related to PRES (Fig 5).

^eSeptic emboli with atypical left parietal abscess. A 70-year-old woman with high blood pressure, chronic kidney disease, and type 2 diabetes mellitus. Long admission in the intensive care unit with intubation for COVID-19 and bilateral pneumonia. She presented with alteration of mental state and difficulty to progress in the weaning process. No history of malignancy (Online Supplemental Data).

^fLeft TIPIC (carotidynia). A 40-year-old man without significant medical history or known trauma presented with myoclonus and acute tenderness overlying the left carotid artery with increased pulsation. His symptoms significantly improved after steroid therapy (Fig 7).

ACKNOWLEDGMENTS

We thank all patients and their families involved in the study.

Disclosures: Ana Ramos—UNRELATED: Employment: Hospital 12 de Octubre. Nuria Bargallo—UNRELATED: Employment: Domicilio. Soma Sengupta—UNRELATED: Consultancy: NovoCure; Grants/Grants Pending: R01, R21; Payment for Lectures Including Service on Speakers Bureaus: University of Kentucky, Neurology Grand Rounds; Patents (Planned, Pending or Issued): patents but no money involved; Other: equity in a start-up, currently no finances in the start-up. Achala Vagal—RELATED: Grant: National Institutes of Health, Comments: R01 NIH/NINDS NS103824, R01 NIH/NINDS/NIA NS117643, R01 NIH/NINDS/N100417, NIH/NINDS U01NS100699, NIH/NINDS U01NS10772.* *Money paid to the institution.

REFERENCES

- Novel coronavirus (2019-nCoV) situation reports. <https://www.who.int/emergencies/diseases/novel-coronavirus-2019/situation-reports>. Accessed April 4, 2020
- Bernheim A, Mei X, Huang M, et al. Chest CT findings in coronavirus disease-19 (COVID-19): relationship to duration of infection. *Radiology* 2020;295:200463 CrossRef Medline
- Chung M, Bernheim A, Mei X, et al. CT imaging features of 2019 novel coronavirus (2019-nCoV). *Radiology* 2020;295:202–07 CrossRef Medline
- Pan F, Ye T, Sun P, et al. Time course of lung changes at chest CT during recovery from coronavirus disease 2019 (COVID-19). *Radiology* 2020;295:715–21 CrossRef Medline
- Ng MY, Lee EY, Yang J, et al. Imaging profile of the COVID-19 infection: radiologic findings and literature review. *Radiology: Cardiothoracic Imaging* 2020;2:e200034 CrossRef
- Mahammed A, Saba L, Vagal A, et al. Imaging in neurological disease of hospitalized patients with COVID-19: an Italian multicenter retrospective observational study. *Radiology* 2020;297:E270–73 CrossRef Medline
- Radmanesh A, Derman A, Lui YW, et al. COVID-19-associated diffuse leukoencephalopathy and microhemorrhages. *Radiology* 2020;297:E223–27 CrossRef Medline
- Kremer S, Lersy F, de Sèze J, et al. Brain MRI findings in severe COVID-19: a retrospective observational study. *Radiology* 2020;297:E242–51 CrossRef Medline
- Chougar L, Shor N, Weiss N, et al. CoCo Neurosciences Study Group. Retrospective observational study of brain magnetic resonance imaging findings in patients with acute SARS-CoV-2 infection and neurological manifestations. *Radiology* 2020;297:E313–23 CrossRef Medline
- Mao L, Jin H, Wang M, et al. Neurologic manifestations of hospitalized patients with coronavirus disease 2019 in Wuhan, China. *JAMA Neurol* 2020;77:683–90 CrossRef Medline
- Li Y, Li M, Wang M, et al. Acute cerebrovascular disease following COVID-19: a single center, retrospective, observational study. *Stroke Vasc Neurol* 2020;5:279–84 CrossRef Medline
- Klironomos S, Tzortzakakis A, Kits A, et al. Nervous system involvement in COVID-19: results from a retrospective consecutive neuroimaging cohort. *Radiology* 2020;297:E324–34 CrossRef Medline
- Kandemirli SG, Dogan L, Sarikaya ZT, et al. Brain MRI findings in patients in the intensive care unit with COVID-19 infection. *Radiology* 2020;297:E232–35 CrossRef Medline
- Mascia L. Acute lung injury in patients with severe brain injury: a double hit model. *Neurocrit Care* 2009;11:417–26 CrossRef Medline

15. Moldoveanu B, Otmishi P, Jani P, et al. **Inflammatory mechanisms in the lung.** *J Inflamm Res* 2009;2:1–11 Medline
16. Tracey KJ. **The inflammatory reflex.** *Nature* 2002;420:853–59 CrossRef Medline
17. Raabe A, Wissing H, Zwissler B. **Brain cell damage and S-100B increase after acute lung injury.** *Anesthesiology* 2005;102:713–14 CrossRef Medline
18. Lecler A, Obadia M, Savatovsky J, et al. **TIPIC syndrome: beyond the myth of carotidynia, a new distinct unclassified entity.** *AJNR Am J Neuroradiol* 2017;38:1391–98 CrossRef Medline
19. Mehta P, McAuley DF, Brown M, et al. **COVID-19: consider cytokine storm syndromes and immunosuppression.** *Lancet* 2020;395:1033–34 CrossRef Medline
20. Grau AJ, Bugge F, Becher H, et al. **Recent bacterial and viral infection is a risk factor for cerebrovascular ischemia: clinical and biochemical studies.** *Neurology* 1998;50:196–203 CrossRef Medline
21. Hamming I, Timens W, Bulthuis MLC, et al. **Tissue distribution of ACE2 protein, the functional receptor for SARS coronavirus: a first step in understanding SARS pathogenesis.** *J Pathol* 2004;203:631–37 CrossRef Medline
22. Zubair AS, McAlpine LS, Gardin T, et al. **Neuropathogenesis and neurologic manifestations of the coronaviruses in the age of coronavirus disease 2019: a review.** *JAMA Neurol* 2020;77:1018–27 CrossRef Medline
23. **Tocilizumab-associated multifocal cerebral thrombotic microangiopathy.** *Neurology Clinical Practice.* January 29, 2016. <https://cp.neurology.org/content/6/3/e24.short>. Accessed September 7, 2020
24. Solomon IH, Normandin E, Bhattacharyya S, et al. **Neuropathological features of Covid-19.** *N Engl J Med* 2020;383:989–92 CrossRef Medline
25. Matschke J, Lütgehetmann M, Hagel C, et al. **Neuropathology of patients with COVID-19 in Germany: a post-mortem case series.** *Lancet Neurol* 2020;19:919–29 CrossRef Medline
26. Varga Z, Flammer AJ, Steiger P, et al. **Endothelial cell infection and endotheliitis in COVID-19.** *Lancet* 2020;395:1417–18 CrossRef Medline
27. McGonagle D, O'Donnell JS, Sharif K, et al. **Immune mechanisms of pulmonary intravascular coagulopathy in COVID-19 pneumonia.** *Lancet Rheumatol* 2020;2:e437–45 CrossRef Medline
28. Wang Y, Dong C, Hu Y, et al. **Temporal changes of CT findings in 90 patients with COVID-19 pneumonia: a longitudinal study.** *Radiology* 2020;296:E55–64 CrossRef Medline

Impact of SARS-CoV-2 Pandemic on “Stroke Code” Imaging Utilization and Yield

 D.R. Shatzkes,  A.B. Zlochower,  J.M. Steinklein,  B.K. Pramanik,  C.G. Filippi,  S. Azhar,  J.J. Wang, and  P.C. Sanelli



ABSTRACT

BACKGROUND AND PURPOSE: Indirect consequences of the Severe Acute Respiratory Syndrome coronavirus 2 (SARS-CoV-2) pandemic include those related to failure of patients to seek or receive timely medical attention for seemingly unrelated disease. We report our experience with stroke code imaging during the early pandemic months of 2020.

MATERIALS AND METHODS: Retrospective review of stroke codes during the 2020 pandemic and both 2020 and matched 2019 prepandemic months was performed. Patient variables were age, sex, hospital location, and severity of symptoms based on the NIHSS. We reviewed the results of CT of the head, CTA, CTP, and MR imaging examinations and classified a case as imaging-positive if any of the imaging studies yielded a result that related to the clinical indication for the study. Both year-to-year and sequential comparisons were performed between pandemic and prepandemic months.

RESULTS: A statistically significant decrease was observed in monthly stroke code volumes accompanied by a statistically significant increased proportion of positive imaging findings during the pandemic compared with the same months in the prior year ($P < .001$) and prepandemic months in the same year ($P < .001$). We also observed statistically significant increases in average NIHSS scores ($P = .045$ and $P = .03$) and the proportion of inpatient stroke codes ($P = .003$ and $P = .03$).

CONCLUSIONS: During our pandemic period, there was a significantly decreased number of stroke codes but simultaneous increases in positivity rates, symptom severity, and inpatient codes. We postulate that this finding reflects the documented reluctance of patients to seek medical care during the pandemic, with the shift toward a greater proportion of inpatient stroke codes potentially reflecting the neurologic complications of the virus itself.

ABBREVIATIONS: COVID-19 = coronavirus disease 2019; RT-PCR = real-time polymerase chain reaction; SARS-CoV-2 = Severe Acute Respiratory Syndrome coronavirus 2

The impact of the Severe Acute Respiratory Syndrome coronavirus 2 (SARS-CoV-2) coronavirus disease 2019 (COVID-19) pandemic has reverberated throughout virtually all facets of daily life, with implications beyond those associated with the viral infection itself. Within radiology, overall imaging use initially dropped sharply, largely due to suspension of elective clinical practice.¹ In addition, shifts in specific technique and

subspecialty use have paralleled evolving recommendations regarding diagnosis, understanding of disease manifestations, and increasing recognition of delayed and chronic disease complications. For example, the role of chest CT during the pandemic underwent shifts from initial use for diagnosis, particularly when real-time polymerase chain reaction (RT-PCR) testing availability was limited, to later use primarily for assessment of patients with worsening or chronic respiratory failure.² At the time of this writing, at least partial recovery of imaging volumes has occurred in many centers.³

In New York City, one of the early epicenters of COVID-19 in the world, this disease initially overtook all others in health care use, with concerns regarding the availability of hospital beds and supportive technology to accommodate the rapidly growing number of severely ill patients. Nevertheless, it was intuitively expected during the early stages of the pandemic that the frequency of other illnesses in the population would be unchanged by the presence of the virus. If anything, the multisystem strain of

Received November 2, 2020; accepted after revision December 18.

From the Departments of Radiology and Otolaryngology (D.R.S.), Radiology (A.B.Z., J.M.S., B.K.P., C.G.F., P.C.S.), Neurology (S.A.), and Institute for Health Innovations and Outcomes Research (J.J.W.), Feinstein Institutes for Medical Research, Zucker School of Medicine at Hofstra/Northwell, Northwell Health, Manhasset, New York.

Please address correspondence to Deborah R. Shatzkes, MD, Departments of Radiology and Otolaryngology, Zucker School of Medicine at Hofstra/Northwell, Lenox Hill Hospital, Northwell Health, 100 E. 77th St, NY, New York 10075; e-mail: shatzkes@hotmail.com; @DShatzkes

 Indicates open access to non-subscribers at www.ajnr.org

<http://dx.doi.org/10.3174/ajnr.A7038>

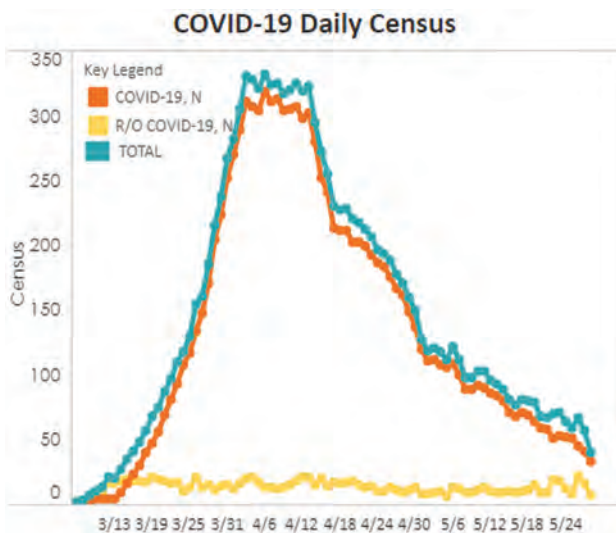


FIG 1. Hospital census March 13, 2020, through May 24, 2020, shows the timing of the COVID-19 surge. The turquoise line indicates total hospital census; the orange line, patients positive for COVID-19; and the yellow line, patients under investigation for COVID-19. N indicates the number of patients in each category.

the disease seemed likely to exacerbate pre-existing morbidities, so that underlying neurologic, cardiovascular, metabolic, and other chronic conditions might worsen during viral infections, resulting in an increased incidence of acute events. In February, first reports of prothrombotic complications of SARS-CoV-2 were published, further supporting the likelihood of an increase in emergency presentation of vascular-related diseases such as pulmonary embolism, myocardial infarction, and stroke.⁴

Paradoxically, however, reports in the cardiovascular literature showed a decrease in the incidence of diagnosed myocardial infarction during the initial weeks of the pandemic.⁵ At about the same time, reports in the media confirmed a growing suspicion that patients were choosing to stay home with cardiac and other acute symptoms that would have otherwise brought them to the emergency department due to fears of contracting the disease at health care facilities.⁶ Statistics compiled from the New York City Fire Department, which manages the city’s 911 emergency response system, showed a striking increase of emergency calls that resulted in “refusals of medical aid” during March (118%) and early April (235%).⁷ Furthermore, emergency departments noted early drops in census followed by progressive increases, the latter composed primarily of patients with COVID-19-related illness.⁸

The first confirmed case of COVID-19 infection was diagnosed on RT-PCR testing at our 450-bed New York City hospital in early March 2020, with our peak occurring in early April (Fig 1). As both the emergency department and hospital censuses became dominated by patients positive for COVID-19, we noticed a trend toward a reduced frequency of stroke code-related imaging. This observed trend was later confirmed in a correspondence to the *New England Journal of Medicine* describing a concurrent 39% decrease in the use of the RAPid processing of PerfusIon and Diffusion (RAPID; iSchemaView) software

platform used at ours and many other US institutions to identify patients who might benefit from endovascular thrombectomy in the setting of acute stroke.⁹ Simultaneously, we began to note trends toward increased positivity rates of stroke code imaging, as well as shifts in patient demographics, including a greater proportion of stroke codes initiated in the inpatient setting. The purpose of this study was to retrospectively review our institution’s stroke codes during the early COVID-19 pandemic (March 1 to April 30, 2020) to quantify imaging use and further analyze the positive imaging findings.

MATERIALS AND METHODS

In this retrospective Health Insurance Portability and Accountability Act-compliant, institutional review board-approved study, an initial query was performed at our academic teaching hospital’s Radiology Information System for all “CT Head Stroke Protocol” studies performed between January 1, 2019, and April 30, 2019, and January 1, 2020, and April 30, 2020, to perform year-to-year comparisons. Typically, a stroke code is called when there is acute onset (<24 hours) of a neurologic deficit, though it may also be initiated if the duration is uncertain. A speaker announces “stroke code” and location to alert the stroke team; this is followed by emergent CT of the brain, typically followed by CTA of the neck and circle of Willis and CT perfusion studies when appropriate, for which results are dictated and communicated directly to the stroke team within 20 minutes of the patient being placed on the CT scanner. Patients were included if there was performance of, at minimum, the CT brain portion of the stroke code imaging evaluation. Exclusion criteria were cancellation of the code by the stroke team (typically because presentation was thought atypical for stroke) as well as stroke codes called in patients with known strokes (generally in patients transferred for treatment in whom changes in neurologic status were suspected).

Five board-certified radiologists, 4 with Certificates of Added Qualification in neuroradiology and with years of experience ranging from 2 to 26, reviewed the reports of each stroke code imaging study as well as the reports of any follow-up CT or brain MR imaging. We additionally reviewed the medical record and compiled relevant clinical information, including age, sex, patient service location (emergency department or inpatient setting), and NIHSS score at presentation.¹⁰ We included the COVID-19 RT-PCR-positivity status for March and April 2020, when these data were available.

Because our primary goal was to assess the yield of the stroke code for any acute neurologic event, we classified a case as imaging-positive if any of the stroke code CT or follow-up imaging studies yielded a result that related to the acute clinical indication for the study, whether or not it represented an ischemic stroke based on Trial of Org 10172 in Acute Stroke Treatment (TOAST) stroke classification.¹¹ Examples of imaging-positive nonischemic diagnoses were hypertensive and traumatic intracranial hemorrhages as well as tumors and abscesses. However, chronic imaging findings such as encephalomalacia and vascular calcifications were not included as imaging-positive cases. In cases in which the initial reviewer was uncertain regarding positivity, this determination was made by consensus review.

Table 1: Comparison of the monthly stroke code volume in 2020 and 2019

Month	2020 No. (%)	2019 No. (%)	P Value
January	121 (34)	84 (21)	<.001
February	113 (32)	96 (24)	
March	67 (19)	105 (27)	
April	56 (16)	108 (28)	
January/February	234 (66)	180 (46)	<.001
March/April	123 (34)	213 (54)	

Statistical Analysis

The dataset was split for statistical analyses into the following time periods: 1) 2020 COVID 3/4, representing the COVID-19 pandemic period from March 1 to April 30, 2020; 2) 2020 pre-COVID 1/2, representing the time period before the COVID-19 pandemic from January 1 to February 29, 2020; 3) 2019 pre-COVID 3/4, representing the same months during the COVID-19 pandemic in the prior year from March 1 to April 30, 2019; and 4) 2019 pre-COVID 1/2, representing the same months during the pre-COVID-19 time period in the prior year from January 1 to February 28, 2019. Multiple comparisons of the study groups were performed. Comparison of the 2020 COVID 3/4 and 2019 pre-COVID 3/4 was performed to assess differences during the COVID-19 pandemic compared with the same months in the prior year, 2019, to account for any monthly or seasonal variation in the data. Comparison of 2020 COVID 3/4 and 2020 pre-COVID 1/2 was performed to assess differences during the COVID-19 pandemic compared with the prior months in the same year to account for yearly variations in the data. Comparison of 2020 pre-COVID 1/2 and 2019 pre-COVID 1/2 was performed to assess whether differences existed in 2020 in the months before the pandemic, to assess other possible variations unknown in the data.

The χ^2 and *t* tests were used to compare the demographic and clinical factors and imaging positivity rates among the study groups. *P* values < .05 were considered statistically significant. SAS, Version 9.4 (SAS Institute) was used for all statistical analyses.

RESULTS

There were 750 consecutive patients for whom a stroke code was called and who underwent, at minimum, a CT scan of the brain. Twenty-nine patients who were transferred with a known diagnosis of stroke and 8 patients for whom the stroke code was cancelled were excluded.

From January 1 to April 30, 2019, a total of 393 CT stroke codes were performed; and from January 1 to April 30, 2020, a total of 357 CT stroke codes were performed. A statistically significant difference was observed in both the monthly and bimonthly proportions of the stroke code volumes in 2020 compared with 2019 (*P* < .001, Table 1).

Study Population Characteristics

The demographic and clinical characteristics of the study cohort are presented in Table 2. There were 45% (337/750) men and 55% (413/750) women, with an average age of 65.4 years (range, 18–98 years). No statistically significant differences were

identified among the 3 comparisons with regard to patient age and sex. Furthermore, there were no statistically significant differences in the demographic and clinical characteristics and in the imaging-positive rates when comparing the 2020 COVID 1/2 and 2019 pre-COVID 1/2 periods.

Eighty-three percent (620/750) of stroke codes were called in the emergency department, and 17% (130/750), on inpatient floors. Statistically significant differences were identified in the incidence of inpatient-versus-emergency department location in comparisons of 2020 COVID 3/4 with either 2019 pre-COVID 3/4 or 2020 pre-COVID 1/2 periods (*P* = .0034 and *P* = .0335, respectively).

With regard to the NIHSS, statistically significant differences in symptom severity were identified in the comparison of 2020 COVID 3/4 and both 2020 pre-COVID 1/2 (*P* = .014) and 2019 pre-COVID 3/4 (*P* = .045) periods, with a higher proportion of patients presenting with worse NIHSS scores during the COVID-19 pandemic.

Of 123 stroke codes performed during the COVID-19 months of March and April 2020, twenty-seven percent (33/123) of patients were diagnosed as COVID-19-positive based on RT-PCR testing, 28% (35/123) were negative, and 45% (55/123) were not tested. Fourteen of the 33 (42%) stroke codes in the COVID-19-positive population were performed on inpatients. This represented the only statistically significant (*P* = .0380) frequency change in our measured variables between COVID-19-positive and -negative patients during this period.

Stroke Code Imaging Yield

Table 2 reveal a statistically significantly increased proportion of imaging-positive cases during the 2020 COVID 3/4 period compared with the 2019 pre-COVID 3/4 (*P* < .001) and 2020 pre-COVID 1/2 (*P* < .001) periods. Figure 2 illustrates the total number of stroke codes and imaging-positive cases by month.

Neurologic diagnoses designated as imaging-positive that did not fall into the TOAST classification of ischemic stroke were the following: intraparenchymal hematoma (*n* = 6), subdural hematoma (*n* = 5), subarachnoid hemorrhage (*n* = 5), primary brain tumor (*n* = 4), metastatic disease (*n* = 3), Guillain-Barré syndrome (*n* = 1), encephalitis (*n* = 1), and posterior reversible encephalopathy syndrome (*n* = 1). No statistically significant differences were identified in the proportion of nonischemic diagnoses during the 2020 COVID-19 pandemic compared with the same months in the prior year and pre-COVID-19 months in the same year.

DISCUSSION

Our data confirm previous reports of diminished numbers of stroke presentations during the early phases of the COVID-19 pandemic. Kansagra et al⁹ reported a 39% drop in RAPID software use from their defined prepandemic period of February 1 through February 29, 2020, compared with the pandemic period from March 26 through April 8, 2020, and de Havenon et al¹² showed an approximately 18% drop in hospitalizations with a discharge diagnosis of stroke. In an analysis of data from a national repository of electronic health records from visits to Veterans Affairs facilities, Baum et al¹³ found a 41.9% reduction

Table 2: Comparison of the demographic and clinical characteristics of the study cohort stratified by time periods

	2020 Pre- COVID 1/2	2019 Pre- COVID 1/2	P Value	2020 COVID 3/4	2019 Pre- COVID 3/4	P Value	2020 COVID 3/4	2020 Pre- COVID 1/2	P Value
No.	234	180		123	213		123	234	
Mean age (range) (yr)	66.1 (18–98)	65.7 (22–98)	.81	66.4 (25–97)	63.8 (20–101)	.18	66.4	66.1	.87
Sex (No.) (%)									
Male	102 (44)	73 (41)	.54	67 (54)	95 (45)	.08	67 (54)	102 (44)	.05
Female	132 (56)	107 (59)		56 (46)	118 (55)		56 (46)	132 (56)	
Location (No.) (%)									
ED	192 (82)	157 (87)	.15	89 (72)	182 (85)	.003	89 (72)	192 (82)	.03
Inpatient	42 (18)	23 (13)		34 (28)	31 (15)		34 (28)	42 (18)	
Mean NIHSS	4.7	4.4	.65	7.3	5.2	.045	7.3	4.8	.01
Positive imaging findings (No.) (%)	42 (18)	32 (18)	.96	42 (34)	37 (17)	<.001	42 (34)	42 (18)	<.001

Note:—ED indicates emergency department; NA, not available.

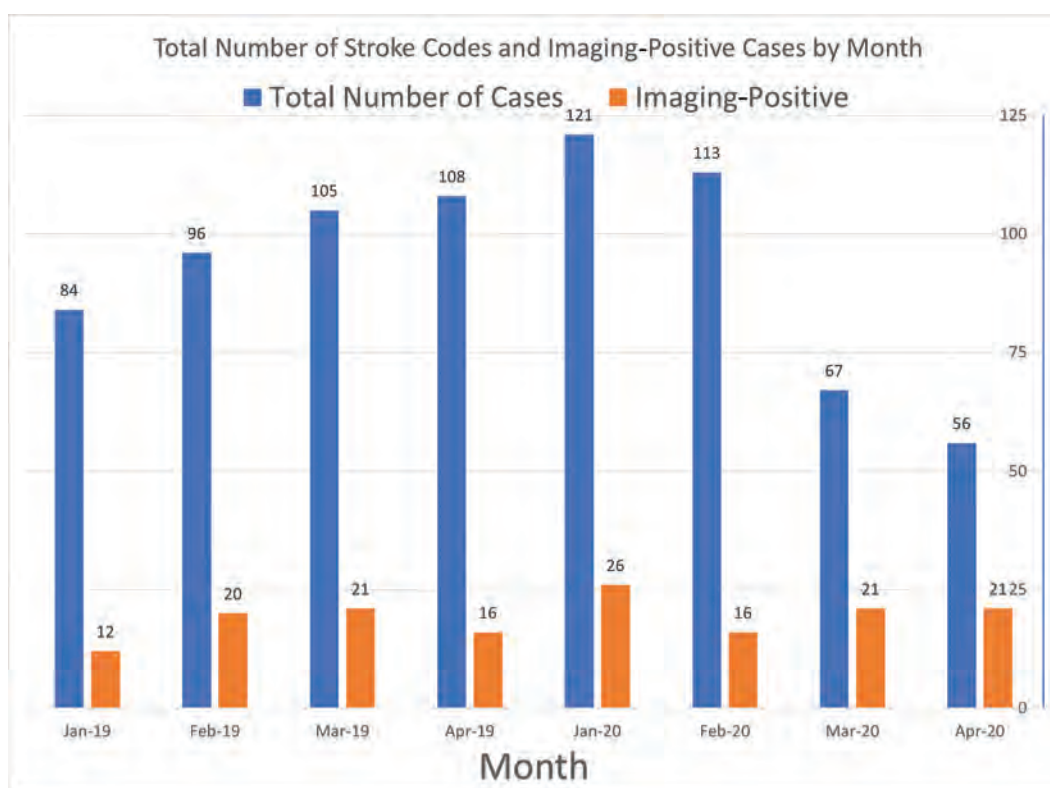


FIG 2. Total number of stroke codes and imaging-positive cases by month.

in overall admissions, with a 51.9% decrease in patients admitted with a principal diagnosis of stroke. It is likely that this drop is multifactorial in origin, though it seems probable that the reluctance of patients to seek medical aid was a primary contributor. A nationwide examination of emergency department visits performed by the Centers for Disease Control and Prevention showed a 42% drop during the pandemic period.¹⁴ In a nationwide survey with >1000 responders by the Society for Cardiovascular Angiography and Interventions, 61% of responders thought they were likely to acquire COVID-19 in a hospital, and half were more afraid of contracting the disease than experiencing a heart attack or stroke.¹⁵ Reduced availability of health care resources, including ambulances, likely contributed to reduced emergency department

presentations, as well. Additionally, it is possible that in the early phase of the pandemic, many providers in emergency departments overwhelmed with patients with COVID-19 were less likely to activate a stroke code for less compelling clinical presentations. Recommendations regarding “protected” hyperacute stroke management using personal protective equipment and other safety measures did not emerge until later in the pandemic, and fear of nosocomial infection may have similarly impacted the provider threshold for initiating a stroke code for perceived lesser-yield presentations.¹⁶

We observed a statistically significant increase in the rate of imaging-positive stroke codes during the 2020 COVID-19 months compared with 2019 and the 2020 pre-COVID-19 months,

accompanied by a simultaneous statistically significant increase in the proportion of patients presenting with severe stroke symptoms (based on the NIHSS). These findings suggest that patients who presented to the hospital with stroke-like symptoms during the pandemic period were more likely to have more severe symptomatology and to have an attributable acute neurologic event. Of note, a report by Paliwal et al¹⁷ of patients presenting with acute stroke symptoms before and during the pandemic showed that while there was a significant decline in acute stroke activations during the pandemic, the median NIHSS score was unchanged.

Any evaluation of stroke during the pandemic era must consider the now well-documented increased incidence of acute cerebrovascular disease in these patients. Early reports of an increased incidence of acute ischemic stroke, venous sinus thrombosis, and cerebral hemorrhage in SARS-CoV-2-infected patients emerged from China in early April 2020,¹⁸ with a pooled analysis of the literature published in late April demonstrating an approximately 2.5-fold increased incidence of stroke in patients with severe COVID-19.¹⁹ Postulated etiologies include sepsis-induced coagulopathy associated with high D-dimer and fibrinogen levels as well as endothelial damage related to binding of the spike protein of the virus to angiotensin-converting enzyme 2 receptors on the vascular endothelium.²⁰ While 33 of 123 stroke codes during the 2020 COVID-19 months were performed on patients who tested positive for SARS-CoV-2, an even greater number ($n = 55$) were not tested during this period, reflecting the limited availability of testing during the early pandemic months and precluding precise quantification of the contribution of SARS-CoV-2-related stroke to our observed increased yield. Fourteen of the 33 stroke codes in the COVID-19-positive population (44%) were performed on inpatients, contributing to the statistically significant increase in overall frequency of inpatient codes performed during the COVID-19 months. We postulate that this increase in the relative frequency of inpatient stroke codes may reflect a shift toward sicker inpatients, as the hospital census shifted toward mostly COVID-19-positive patients and specifically those sick enough to require admission and away from those undergoing elective procedures and other less serious causes of hospitalization.

The implications of our findings with regard to these first and subsequent waves of the COVID-19 pandemic, as well as to future pandemics, are numerous. At the time of this report, excess mortality during the pandemic related to both COVID-19-related illness and unrelated disease has only begun to be quantified. On May 11, 2020, the New York City Department of Health and Mental Hygiene COVID-19 response team published a preliminary estimate of excess mortality during the COVID-19 outbreak and found that 22% (5293) of excess deaths between March 11 and May 2 were not identified as either laboratory-confirmed or probable COVID-19-associated deaths.²¹ Numerous factors make precise attribution of these deaths impossible, including-but-not-limited-to the vast array of potential etiologies and testing being limited and inaccurate in early stages of the pandemic. However, the authors stated, "Social distancing practices, the demand on hospitals and health care providers, and public fear related to COVID-19 might lead to delays in seeking or obtaining

lifesaving care."²¹ Certainly, our findings of decreased numbers of stroke codes with increased positivity rates suggest that many patients with transient or mild neurologic events may have not obtained appropriate early or comprehensive testing and intervention and are at high risk of subsequent morbidity and mortality. It is hoped that with the knowledge gained during the initial experience with this disease, practice will be modified to prepare for any future waves, and, specifically, for a larger proportion of more serious neurologic presentations in both emergency and inpatient departments.

Limitations of this study include limited and sometimes inaccurate testing for SARS-CoV-2 during the pandemic months as well as an inability to establish direct causality of the SARS-CoV-2 virus to those strokes occurring in COVID-19-positive patients. However, the main purpose of the analyses was not to compare COVID-19-positive and -negative groups in this study. Given that this is a retrospective study, the statistical analysis included patients with missing data variables. Additionally, all associations between our observed changes in stroke code use and reported reluctance of patients to present to the hospital and other potential causes represent conjecture and are unlikely to be proved with certainty. There are competing pressures between these effects and the expected increase in the frequency of stroke and other neurologic manifestations related to SARS-CoV-2 infection, and the contributions of each to overall change cannot be accurately quantified.

CONCLUSIONS

During the March and April 2020 COVID-19 surge in New York City, we observed a decrease in the number of stroke codes and an increase in imaging-positivity rates and the severity of presenting symptoms. While the etiologies of these shifts cannot be determined with certainty, we postulate that our findings reflect an observed reluctance of patients to seek medical care due to fears of contracting SARS-CoV-2, potentially coupled with other factors such as the overwhelming demand on health care workers during this period. A simultaneous shift toward a greater proportion of inpatient stroke codes may reflect the documented thromboembolic and other neurologic complications of the virus itself, a competing pressure on stroke code volumes that suggests an even greater reduction in new presentations to the emergency department. It seems likely that our findings represent a contributing factor toward the observed excess mortality beyond that directly associated with SARS-CoV-2 infection and may portend additional excess mortality from cerebrovascular causes during the recovery period and beyond.

Disclosures: Christopher G. Filippi—UNRELATED: Consultancy: Syntactx, Comments: interpretation of clinical trials of brain MR imaging examinations; Grants/Grants Pending: Foundation of the American Society of Neuroradiology grant and National MS Society Grant; Payment for Manuscript Preparation: article in the journal *Topics in Magnetic Resonance Imaging* (April 2020)*; Stock/Stock Options: minority stakeholder in start-up Avicenna.ai. Pina C. Sanelli—UNRELATED: Grants/Grants Pending: Siemens, Comments: research partnership.* *Money paid to the institution.

REFERENCES

1. Naidich JJ, Boltyenkov A, Wang JJ, et al. **Impact of the COVID-19 pandemic on imaging case volumes.** *J Am Coll Radiol* 2020;17:865–72 CrossRef Medline

2. Rubin GD, Ryerson CJ, Haramati LB, et al. **The role of chest imaging in patient management during the COVID-19 from the Fleischner Society.** *Chest* 2020;158:106–16 CrossRef Medline
3. Lang M, Yeung T, Mendoza DP, et al. **Imaging volume trends and recovery during the COVID-19 pandemic: a comparative analysis between a large urban academic hospital and its affiliated imaging centers.** *Acad Radiol* 2020;27:1353–62 CrossRef Medline
4. Huang C, Wang Y, Li X, et al. **Clinical features of patients infected with 2019 novel coronavirus in Wuhan, China.** *Lancet* 2020;395:497–506 CrossRef Medline
5. Garcia S, Albaghdadi MS, Meraj PM, et al. **Reduction in ST-segment elevation cardiac catheterization laboratory activations in the United States during COVID-19 pandemic.** *J Am Coll Cardiol* 2020;75:2871–72 CrossRef Medline
6. Revive Health. **COVID-19 consumer survey findings report: Part 3.** <https://www.thinkrevivehealth.com/covid-19/survey-findings-part-3>. Accessed April 30, 2020
7. **New Yorkers are refusing to be hospitalized over fear of getting coronavirus.** *New York Post* April 12, 2020. https://nypost.com/2020/04/12/coronavirus-fears-have-new-yorkers-avoiding-hospitals-in-nyc/?utm_source=email_sitebuttons&utm_medium=site%20buttons&utm_campaign=site%20button. Accessed April 30, 2020
8. Comelli I, Scioscioli F, Cervellin G. **Impact of the COVID-19 epidemic on census, organization and activity of a large urban emergency department.** *Acta Biomed* 2020;91:45–49 CrossRef Medline
9. Kansagra AP, Goyal MS, Hamilton S, et al. **Collateral effect of Covid-19 on stroke evaluation in the United States.** *N Engl J Med* 2020;383:400–01 CrossRef Medline
10. Powers WJ, Rabinstein AA, Ackerson T, et al. **Guidelines for the Early Management of Patients with Acute Ischemic Stroke: 2019 Update to the 2018 Guidelines for the Early Management of Acute Ischemic Stroke—A Guideline for Healthcare Professionals from the American Heart Association/American Stroke Association.** *Stroke* 2019;50:10–31 CrossRef Medline
11. Adams HP Jr, Biller J. **Classification of subtypes of ischemic stroke; history of the Trial of Org 10172 in acute stroke treatment classification.** *Stroke* 2015;46:e114–17 CrossRef Medline
12. de Havenon A, Ney J, Callaghan B, et al. **A rapid decrease in stroke, acute coronary syndrome, and corresponding interventions at 65 United States hospitals following emergence of COVID-19.** *medRxiv* 2020 May 11. [Epub ahead of print] CrossRef Medline
13. Baum A, Schwartz MD. **Admissions to Veterans Affairs Hospitals for emergency conditions during the COVID-19 pandemic.** *JAMA* 2020;324:96–99 CrossRef Medline
14. Hartnett KP, Kite-Powell A, DeVies J, et al; National Syndromic Surveillance Program Community of Practice. **Impact of the COVID-19 pandemic on emergency department visits: United States, January 1, 2019–May 30, 2020.** *MMWR Morb Mortal Wkly Rep* 2020;69:699–704 CrossRef Medline
15. Grines CL. **Consumer Survey Comparing Fear of COVID-19 Versus Heart Attack or Stroke.** September 4, 2020. <https://scai.org/consumer-survey-comparing-fear-covid-19-versus-heart-attack-or-stroke>. Accessed October 1, 2020
16. Khosravani H, Rajendram P, Notario L, et al. **Protected code stroke: hyperacute stroke management during the coronavirus disease 2019 (COVID-19) pandemic.** *Stroke* 2020;51:1891–95 CrossRef Medline
17. Paliwal PR, Tan BY, Leow AS, et al. **Impact of the COVID-19 pandemic on hyperacute stroke treatment: experience from a comprehensive stroke centre in Singapore.** *J Thromb Thrombolysis* 2020;50:596–603 CrossRef Medline
18. Mao L, Jin H, Wang M, et al. **Neurologic manifestations of hospitalized patients with coronavirus disease 2019 in Wuhan, China.** *JAMA Neurol* 2020;77:683–90 CrossRef Medline
19. Aggarwal G, Lippi G, Henry BM. **Cerebrovascular disease is associated with an increased disease severity in patients with coronavirus disease 2019 (COVID-19): a pooled analysis of published literature.** *Int J Stroke* 2020;15:385–89 CrossRef Medline
20. Hess DC, Eldahshan W, Rutkowski E. **COVID-19-related stroke.** *Transl Stroke Res* 2020;11:322–25 CrossRef Medline
21. New York City Department of Health and Mental Hygiene (DOHMH) COVID-19 Response Team. **Preliminary estimate of excess mortality during the COVID-19 outbreak: New York City, March 11–May 2, 2020.** *MMWR Morb Mortal Wkly Rep* 2020;69:603–05 CrossRef Medline

Absent Cortical Venous Filling Is Associated with Aggravated Brain Edema in Acute Ischemic Stroke

H. Xia, H. Sun, S. He, M. Zhao, W. Huang, Z. Zhang, Y. Xue, P. Fu, and W. Chen



ABSTRACT

BACKGROUND AND PURPOSE: Predicting malignant cerebral edema can help identify patients who may benefit from appropriate evidence-based interventions. We investigated whether absent cortical venous filling is associated with more pronounced early brain edema, which leads to malignant cerebral edema.

MATERIALS AND METHODS: Patients with acute ischemic stroke caused by large-vessel occlusion in the MCA territory who presented between July 2017 and September 2019 to our hospital were included. Collateral filling was rated using the modified Tan scale on CTA, and good collaterals were defined as a score of 2–3. The Cortical Vein Opacification Score (COVES) was calculated, and absent cortical venous filling was defined as a score of 0. Early brain edema was determined using net water uptake on baseline CT images. Malignant cerebral edema was defined as a midline shift of ≥ 5 mm on follow-up imaging or a massive cerebral swelling leading to decompressive hemicraniectomy or death. Multivariate linear and logistic regression models were performed to analyze data.

RESULTS: A total of 163 patients were included. Net water uptake was significantly higher in patients with absent than in those with favorable cortical venous filling (8.1% versus 4.2%; $P < .001$). In the multivariable regression analysis, absent cortical venous filling ($\beta = 2.04$; 95% CI, 0.75–3.32; $P = .002$) was significantly and independently associated with higher net water uptake. Absent cortical venous filling (OR, 14.68; 95% CI, 4.03–53.45; $P < .001$) and higher net water uptake (OR, 1.29; 95% CI, 1.05–1.58; $P = .016$) were significantly associated with increased likelihood of malignant cerebral edema.

CONCLUSIONS: Patients with absent cortical venous filling were associated with an increased early brain edema and a higher risk of malignant cerebral edema. These patients may be targeted for optimized adjuvant antiedematous treatment.

ABBREVIATIONS: COVES = Cortical Vein Opacification Score; MCE = malignant cerebral edema; NWU = net water uptake; AIS = acute ischemic stroke; OIT = onset to imaging time; ICAS = intracranial atherosclerosis

Malignant cerebral edema (MCE) is a lethal complication mainly of large infarctions in the MCA territory.¹ It usually occurs within the first 3 days after the onset of stroke and is characterized by an abrupt neurologic decline associated with massive swelling of the infarcted brain tissues.² The subsequent cerebral herniation due to intracranial pressure increase is the main cause

of death, with a mortality rate approaching 80% with conservative treatment.³ Three randomized controlled trials provided evidence that early decompressive surgery is an efficient way to increase the likelihood of favorable functional outcomes and reduce the mortality rate.⁴ Therefore, early identification of patients at risk of MCE would facilitate timely selection of appropriate evidence-based interventions.

Net water uptake (NWU), a quantitative imaging biomarker used to estimate water uptake in ischemic stroke lesions, was first applied to distinguish stroke onset within and beyond 4.5 hours.⁵ Mounting evidence suggests the importance of NWU because it has been reported as a surrogate marker for developing MCE.⁶ Recently, the arterial collateral status has been observed as it relates to the early edema progression rate.⁷ However, the absence of cortical venous filling could potentially be a better indicator of aggravating brain edema than the arterial collateral status because the venous system is responsible for approximately 70% of the cerebral blood volume.⁸ In a case series including 14

Received July 17, 2020; accepted after revision December 01.

From the Department of Radiology (H.X.), Shaoxing People's Hospital (Shaoxing Hospital, Zhejiang University School of Medicine), Shaoxing, Zhejiang, China; and Department of Radiology (H.S., S.H., M.Z., W.H., Z.Z., Y.X., P.F., W.C.), The First Affiliated Hospital of Wenzhou Medical University, Wenzhou, Zhejiang, China.

This study was funded by the Zhejiang Provincial Key Laboratory of Aging and Neurological Disorder Research (LH-001), and the Scientific Technology Planning Projects of Wenzhou, China (Y20170216).

Please address correspondence to Weijian Chen, MD, Department of Radiology, The First Affiliated Hospital of Wenzhou Medical University, Nanbai Xiang St, Ouhai District, Wenzhou, Zhejiang, 325000, China; e-mail: wyyycwj@163.com

Indicates open access to non-subscribers at www.ajnr.org

<http://dx.doi.org/10.3174/ajnr.A7039>

patients, cranial venous outflow abnormalities increased the rate of early fatal edema after MCA infarction.⁹ Nonetheless, studies on the role of the cortical veins in the development of MCE are limited, and it remains unclear whether absent cortical venous filling is an independent risk factor affecting NWU in patients with stroke.

Recently, the Cortical Vein Opacification Score (COVES) was introduced as a simple method to assess the cortical venous filling status on CTA. It well reflects the intracranial microcirculation function and can predict whether patients will benefit from endovascular treatment.¹⁰ Thus, the aim of our study was to investigate the relationship between absent cortical venous filling, as assessed using the COVES, and early brain edema, as assessed using NWU, and whether they can predict the occurrence of MCE. We hypothesized that absent cortical venous filling would lead to an increase in early brain edema, which in turn leads to MCE.

MATERIALS AND METHODS

Data supporting the findings of this study are available from the corresponding author on reasonable request.

Patients

We retrospectively reviewed the data of patients diagnosed with acute ischemic stroke (AIS) caused by large-vessel occlusion in the MCA territory in our institution from July 2017 to September 2019. All procedures performed in studies involving human participants were in accordance with the ethical standards of the institutional and national research committee and with the 1964 Helsinki declaration and its later amendments or comparable ethical standards. Written informed consent was obtained from each patient or an appropriate family member. The inclusion criteria were as follows: 1) known time window from symptom onset to admission imaging of <8 hours; 2) multimodal CT performed on admission, which included NCCT, CTP, and CTA; 3) AIS with complete occlusion of the distal internal carotid artery, MCA, or both, confirmed by conventional and dynamic CTA constructed from CTP; 4) follow-up CT acquired 24–72 hours after symptom onset; and 5) absence of intracranial hemorrhage, or pre-existing infarction. Baseline clinical characteristics and demographic information were recorded including age, sex, NIHSS score, onset to imaging time (OIT), IV administration of tPA, and endovascular treatment.

Image Acquisition

All patients underwent multimodal CT at admission with NCCT, CTP, and CTA performed on a 64-section CT scanner (Lightspeed VCT; GE Healthcare). First, NCCT was performed (120 kV; 300 mA; section thickness, 5 mm) from the foramen magnum to the vertex to detect early ischemic changes and exclude intracranial hemorrhage. If appropriate, CTP (8 cm in the z-axis using the shuttle mode technique, 80 kV, 375 mA, 0.4 s/rotation, 6-s prescan delay after injection of contrast medium, 60-s total imaging duration) with a total of 352 images by 22 consecutive spiral acquisitions was performed immediately after NCCT. A total of 50 mL of iodinated contrast agent was administered at a flow rate of 5 mL/s followed by a saline flush of 50 mL at a rate of 5 mL/s. Subsequently, helical

CTA (100 kV; 500 mA; section thickness, 0.625 mm) was performed with acquisition from the aortic arch to the vertex after administration of 40 mL of an iodinated contrast agent injected at a rate of 4.0 mL/s followed by a 30-mL saline flush.

Image Analysis

Imaging data were independently assessed by 2 radiologists with more than 3 years of experience in stroke imaging, who were blinded to the clinical status and outcome data. The observers were informed about the laterality of symptoms just before evaluation. Any disagreements between the 2 observers were resolved by a senior medical chief neuroradiologist.

The ASPECTS was used to detect early ischemic burden on NCCT images.¹¹ Early ischemic burden was defined as loss of gray–white differentiation and tissue hypoattenuation using a narrow window and level settings to maximize the contrast between the normal and infarcted brain.

Collateral filling was rated using the modified Tan scale on baseline CTA maximum intensity projection images as follows: 0 indicated absent collaterals of the occluded MCA territory, 1 indicated collaterals filling >0% but <50% of the occluded MCA territory, 2 indicated filling >50% but <100% of the occluded MCA territory, and 3 indicated 100% collateral filling of the occluded MCA territory. Poor collateral filling was defined as a score of 0–1 and good collateral filling as a score of 2–3.¹²

The COVES was used to assess the venous opacification on baseline CTA source images, as absent (0), moderate (1), or full (2) in the vein of Labbe, sphenoparietal sinus, and superficial middle cerebral vein. The sum for the hemisphere ipsilateral to the occlusion was calculated and ranged between 0 and 6. The absence of cortical vein opacification was defined as a score of 0, and a score >0 was considered favorable as mentioned in a previous study.¹⁰

The ischemic lesion NWU was measured by a commercial software, Mistar (Apollo Medical Imaging Technology), using the singular value deconvolution with delay and dispersion method. First, previous thresholds were applied to measure the entire ischemic lesion (delay time >3 s) and ischemic core (relative cerebral blood flow <30%).¹³ Next, the ROI was generated automatically in the ischemic lesion core. Then the core-based ROI was copied to the corresponding NCCT image using Mistar software. The ROI sampling of the ischemic core in NCCT was assessed by densitometric measurements and designated as D_{ischemic} . A mirrored ROI was placed in the contralateral hemisphere within the normal tissue designated as D_{normal} . To exclude the voxels of adjacent CSF and skull, a threshold value of 20–80 HU was chosen. D_{ischemic} and D_{normal} were then used to calculate the quantitative NWU based on the formula from Broocks et al¹⁴ as shown in Fig 1.

According to previous studies,^{15,16} MCE was defined as 1) a midline shift of ≥ 5 mm at the level of septum pellucidum or 2) a massive cerebral swelling requiring decompressive hemicraniectomy or leading to death.

Statistical Analysis

All statistical analyses were performed using SPSS 25.0 (IBM) and GraphPad Prism (GraphPad Software). Continuous variables were reported as means \pm SD or median (25th–75th percentile).

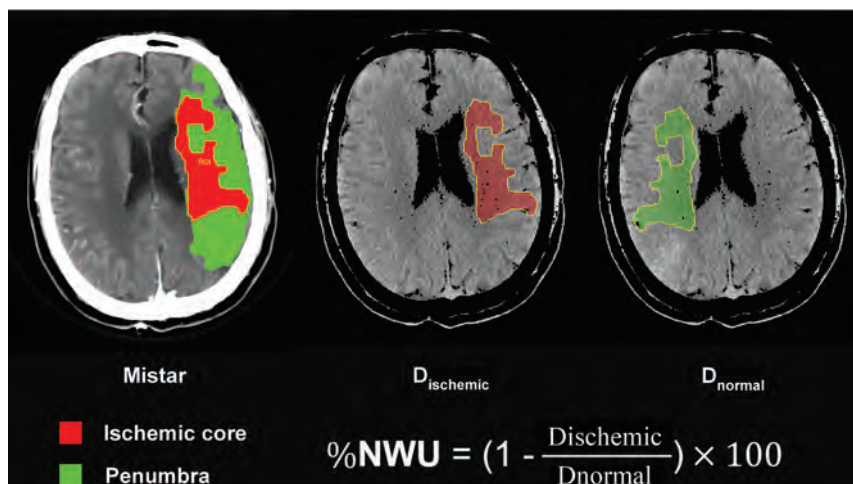


FIG 1. Quantification of NWU. NWU is determined in admission noncontrast CT. The ROI is generated automatically in the ischemic lesion core, which is measured with Mistar. The mean attenuation of D_{ischemic} and D_{normal} are used to calculate NWU based on the formula shown.

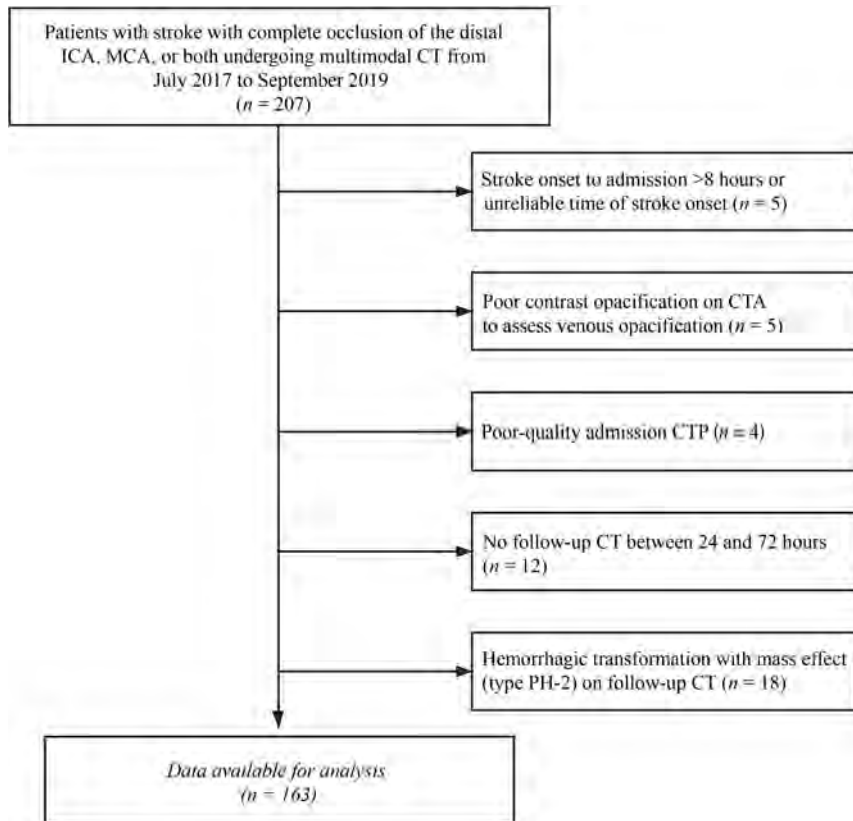


FIG 2. Flowchart of patient selection.

Categoric variables were reported as numbers (percentages). The differences among groups were evaluated using the Student *t* test for normally distributed continuous data, Mann-Whitney U test for non-normally distributed continuous data, and Pearson χ^2 test for categoric data. The correlation between collateral filling, cortical venous filling status, and NWU was described by Kendall

correlation analysis. The relationship between the cortical venous filling status (COVES was examined as a continuous variable and dichotomized into “absent” and “favorable” cortical venous filling) and early brain edema (NWU on NCCT images) was analyzed using linear regression. Variables with $P < .1$ in univariable linear regression were included in a multivariable linear regression analysis. Independent factors for MCE were evaluated using a binary logistic regression analysis. Factors with $P < .1$ from the univariate analysis were entered into the multivariable logistic regression analysis. Interrater reliability of the COVES score was tested by κ statistics. Results with P values of $< .05$ are considered significant for all statistical analyses.

RESULTS

During the study period, data on 207 consecutive patients with complete occlusion of the distal internal carotid artery, MCA, or both, undergoing multimodal CT were collected. A total of 163 patients met all inclusion criteria and were included in the analysis. The patient selection process is shown in Fig 2. The patient characteristics are listed in Table 1. The median age was 69 (IQR 58–78) years, and 103 (63%) patients were men. The baseline NIHSS score was 11.34 ± 5.43 , and the median OIT was 191 (IQR 116–259) minutes. Among all patients, 82 (50%) underwent endovascular treatment, and 68 (42%) received IV thrombolysis. There were 112 (69%) patients with good collateral filling. At baseline, NWU was 4.9% (IQR 2.98–7.33).

Comparing patients with absent (COVES = 0) versus favorable cortical venous filling (COVES > 0), the former had a significantly higher baseline NIHSS score (13.5 versus 11; $P = .001$), lower ASPECTS (4.5 versus 9; $P < .001$), and a lower rate of good collateral filling (22% versus

80%; $P < .001$). No significant differences were found in age, sex, OIT, endovascular treatment, or IV thrombolysis (Table 2).

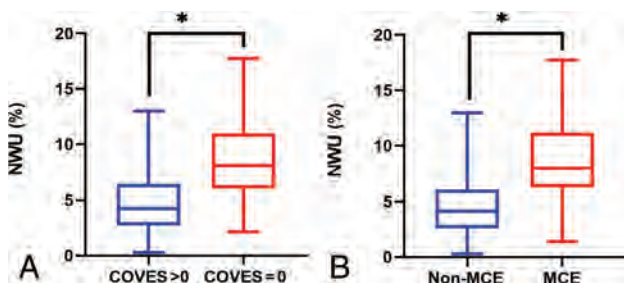
Absent cortical venous filling correlated positively with NWU (Kendall $\tau = 0.37$; 95% CI, 0.27–0.46; $P < .001$). The collateral filling and NWU also showed a significant correlation (Kendall $\tau = -0.30$; 95% CI, -0.41 to -0.19 ; $P < .001$). Moreover, cortical

Table 1: Patient characteristics according to the presence of MCE

Patient Characteristic	Overall (n = 163)	MCE (n = 39)		Non-MCE (n = 124)		P Value
		24%	76%			
Age in years, median (IQR)	69 (58–78)	74 (61–81)	69 (57.25–76)		.131	
Male sex, n (%)	103 (63%)	20 (51%)	83 (67%)		.077	
Admission NIHSS, mean ± SD	11.34 ± 5.43	14.03 ± 5.11	10.49 ± 5.27		<.001	
OIT in minutes, median (IQR)	191 (116–259)	201 (128–277)	189.5 (115.25–258.75)		.858	
IV thrombolysis, n (%)	68 (42%)	12 (31%)	56 (45%)		.112	
Endovascular treatment, n (%)	82 (50%)	19 (49%)	63 (51%)		.820	
Good collateral filling, n (%)	112 (69%)	12 (31%)	100 (81%)		<.001	
ASPECTS, median (IQR)	9 (7–10)	4 (2–7)	9 (8–10)		<.001	
COVES = 0, n (%)	32 (20%)	26 (67%)	6 (5%)		<.001	
NWU in %, median (IQR)	4.89 (2.98–7.33)	8.01 (6.29–11.19)	4.15 (2.59–6.11)		<.001	

Table 2: Patient characteristics according to the COVES

Patient Characteristic	COVES >0 (n = 131)		COVES =0 (n = 32)		P Value
	80%	20%			
Age in years, median (IQR)	70 (60–77)	68.5 (53.75–78.75)		.383	
Male sex, n (%)	84 (64%)	19 (60%)		.618	
Admission NIHSS, median (IQR)	11 (6–14)	13.5 (10–18)		.001	
OIT in minutes, median (IQR)	188 (118–261)	205 (110.5–252.75)		.910	
IV thrombolysis, n (%)	58 (44%)	10 (31%)		.180	
Endovascular treatment, n (%)	65 (50%)	17 (53%)		.722	
Good collateral filling, n (%)	105 (80%)	7 (22%)		<.001	
ASPECTS, median (IQR)	9 (7–10)	4.5 (2.25–7.75)		<.001	
NWU in %, median (IQR)	4.24 (2.73–6.46)	8.11 (6.08–11.00)		<.001	

**FIG 3.** Relationship of cortical venous filling, early brain edema, and MCE. A, Boxplot shows that NWU was significantly higher in patients with COVES = 0 than in those with COVES > 0. B, Boxplot shows that NWU was significantly higher in patients with MCE than in those without MCE. * indicates $P < .001$.

venous filling significantly correlated with collateral filling (Kendall $\tau = -0.50$; 95% CI, -0.64 to -0.34 ; $P < .001$).

Impact of Cortical Venous Filling on Early Brain Edema

NWU was significantly higher in patients with absent cortical venous filling than in those with favorable cortical venous filling (8.1% versus 4.2%; $P < .001$) (Fig 3). Furthermore, as seen in Table 2 and Table 3, in the multivariable linear regression analyses, the ASPECTS ($\beta = -0.50$; 95% CI, -0.70 to -0.30 ; $P < .001$) and absent cortical venous filling ($\beta = 2.04$; 95% CI, -0.75 to 3.32 ; $P = .002$) were 2 significant factors associated with NWU adjusted for baseline NIHSS score and collateral filling (Table 3 and Fig 4).

Factors Associated with MCE

A total of 39 (24%) patients developed MCE. As shown in Table 1, patients with MCE had higher baseline NIHSS score (14.03

versus 10.49; $P < .001$) and NWU (8.0% versus 4.2%; $P < .001$) (Fig 3), lower ASPECTS (4 versus 9; $P < .001$), higher rate of absent cortical venous filling (67% versus 4.8%; $P < .001$), and lower rate of good collateral filling (31% versus 81%, $P < .001$) compared with patients without MCE.

In the univariable logistic regression analysis, multiple factors were associated with MCE. The significant variables from the univariate analysis were entered into the multivariate logistic regression. Male sex (OR, 0.31; 95% CI, 0.096–0.987; $P = .047$), ASPECTS (OR, 0.77; 95% CI, 0.60–0.97; $P = .029$), absent cortical venous filling (OR, 14.68; 95% CI, 4.03–53.44; $P < .001$), and NWU (OR, 1.29; 95% CI, 1.05–1.58; $P = .016$) were significantly associated with increased likelihood of MCE after adjustment for confounding factors (Table 3).

Interobserver Analysis

Interrater reliability for COVES score on baseline CTA source images was substantial ($\kappa = 0.75$).

DISCUSSION

The aim of our study was to investigate the relationship between absent cortical venous filling and early brain edema assessed using NWU and its impact on the occurrence of MCE. Our study revealed that absent cortical venous filling was strongly associated with higher early brain edema, and both absent cortical venous filling and higher NWU were independent predictors of the risk for the development of MCE in patients with large-vessel occlusion in the MCA territory.

These results may support our original hypothesis that absent cortical venous filling is responsible for the onset of MCE by inducing early brain edema. The underlying pathophysiological mechanisms of MCE may be abnormal venous drainage; the

Table 3: Univariable and multivariable linear regression analyses to predict NWU and univariable and multivariable logistic regression analyses to predict MCE

Impact on NWU in multivariate regression			
Parameter	Coefficient	95% CI	P Value
Univariable analysis			
Age (1-year increase)	0.009	-0.03-0.05	.667
Male sex	-0.29	-1.38-0.79	.597
Admission NIHSS	0.17	0.07-0.26	.001
Onset to imaging time (1 minute)	0.004	-0.001-0.009	.147
Good collateral filling	-2.90	-3.93-1.86	<.001
ASPECTS	-0.70	-0.86-0.54	<.001
COVES = 0	3.99	2.83-5.15	<.001
Multivariable analysis			
Admission NIHSS	-0.01	-0.08-0.10	.811
Good collateral filling	-0.46	-1.59-0.67	.423
ASPECTS	-0.50	-0.70-0.30	<.001
COVES = 0	2.04	0.75-3.32	.002
Prediction of MCE			
Parameter			
Univariable analysis			
Age (1-year increase)	1.02	0.99-1.05	.300
Male sex	0.52	0.25-1.08	.079
Admission NIHSS	1.14	1.06-1.23	.001
OIT (1 minute)	1.001	0.997-1.004	.733
IV thrombolysis	0.54	0.25-1.16	.115
Endovascular treatment	0.92	0.45-1.89	.820
Good collateral filling	0.11	0.05-0.24	<.001
ASPECTS	0.59	0.50-0.70	<.001
COVES = 0	39.33	13.68-113.12	<.001
NWU	1.58	1.35-1.85	<.001
Multivariable analysis			
Male sex	0.31	0.10-0.99	.047
Admission NIHSS	1.02	0.91-1.35	.730
Good collateral filling	0.75	0.22-2.63	.657
ASPECTS	0.77	0.60-0.97	.029
COVES = 0	14.68	4.03-53.45	<.001
NWU	1.29	1.05-1.58	.016

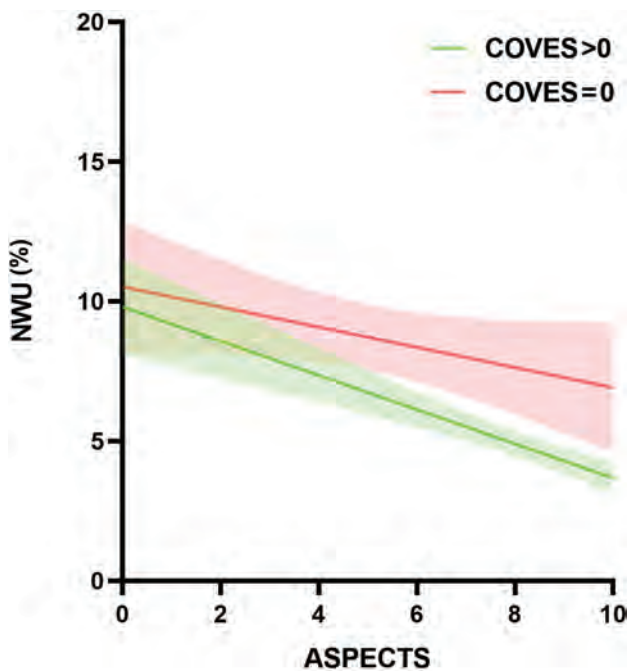


FIG 4. Impact of absent cortical venous filling on early brain edema according to baseline ASPECTS.

subsequent resistance to CSF absorption would lead to increased venous pressure, which would increase the leakage of fluid into the perivascular space, leading to brain edema.¹⁷ Our results are in accordance with those of a recent study that investigated the association between quantitative lesion water uptake and malignant infarction.⁶ The authors concluded that NWU is a significant predictor for developing MCE. We further found that absent cortical venous filling was significantly associated with higher early brain edema and could predict the occurrence of MCE. Thus, these findings can be of great clinical significance in patients without cortical venous filling and can indicate who should receive adjuvant treatment with neuroprotectants and edema prevention therapies such as IV glibenclamide.¹⁸ However, whether absent cortical venous filling plays any other role in the development of MCE needs to be further elucidated.

Previous studies showed that collateral filling is significantly associated with an early edema progression rate and plays a role in the development of MCE.^{7,19} Our univariate analysis showed that patients with MCE had a significantly lower rate of good collateral filling than those without MCE. However, in the multivariate analysis, this factor could not predict NWU or the occurrence of MCE. This may be due to the high correlation between cortical venous filling and collateral filling (Kendall $\tau = -0.499$; 95% CI, -0.638 to -0.342 ; $P < .001$); however, no collinearity was found

between them. A previous nonhuman primate model showed that absent cortical venous filling indicated a less extensive collateral circulation.²⁰ A recent clinical study that included 228 patients with AIS also demonstrated that venous outflow is affected by the reduction of arterial flow.²¹ Therefore, this suggests that cortical venous filling can provide additional information on both the occurrence of MCE and arterial collateral status. From our results, we can reasonably infer that cortical veins may play a more important role than arterial collateral in the development of MCE. These findings prompt us to combine arterial collateral and cortical vein to better evaluate patients with stroke, resulting in better treatment.

Some clinical factors may also predict MCE. Previous studies in Western countries showed that younger age significantly increased the risk of MCE.^{22,23} The possible reason for this is that the brain volume gradually decreases with increasing age; thus, younger patients are more likely to develop MCE because there is a lower intracranial volume to accommodate brain edema.¹ However, the results of our study did not show the same findings. This discrepancy may be attributed to the differences in the etiologic composition of patients with stroke between China and Western countries. Intracranial atherosclerosis (ICAS) is common in the Chinese population, accounting for 33%–50% of AIS cases.²⁴ In contrast, AIS is most commonly caused by cardioembolism in Western countries. Previous clinical research showed patients with cardioembolism tend to be older than those with ICAS²⁵ and are more likely to experience a large hemispheric infarction,²⁶ which is the main cause of MCE.²⁷ Our patients may have a higher proportion of ICAS, which makes the effect of age on MCE insignificant. However, our study did not measure the proportions of each etiology and the role of etiology in age and MCE because this was not the primary objective of this study. Another clinical factor, female sex, was shown to be an independent predictor of MCE, which is consistent with the results of previous studies^{28,29} indicating that a more efficacious stroke management may be needed in female patients. Although research efforts with a focus on sex differences in neuroinflammation, neuroprotection, and neuronal cell death signaling have recently received more attention,^{30–32} the reasons for this phenomenon remain obscure.

To the best of our knowledge, this is the first study to investigate the relationship between cortical venous filling, early brain edema, and MCE. One of the strengths of our study is that early brain edema was directly assessed by NWU, which calculates the water uptake based on the CT attenuation and has been proved as the criterion standard for histopathologic water uptake volume measurement.^{33,34} In addition, we selected the COVES to evaluate intracranial venous filling. This scoring method removes the deep cerebral venous system and more accurately reflects the status of the microcirculation.^{10,35} Although dynamic CTA may be a better way to assess cortical venous filling than conventional CTA,³⁶ this technique requires advanced imaging and complex postprocessing. Our method was simple and convenient to use and has achieved good interobserver agreement, as previously described.¹⁰

This study has several limitations. First, it was a retrospective single-center study, and the number of patients was relatively small; thus, selection bias inevitably existed. Another drawback of

this study can be attributed to the large variation in venous anatomy, though the 3 cortical veins chosen for the COVES had lesser anatomic variability than that of other veins. Third, NWU measurement may be imprecise in very small ischemic core volumes. However, we improved the precision using the Mistar software to measure the ischemic core assisting in determining the ROI. Furthermore, the recanalization status is a significant predictor of the occurrence of MCE. However, in this study, we did not include this factor mainly because many patients without endovascular treatment were unable to obtain recanalization data because of the absence of follow-up vascular imaging. Finally, we could not determine whether absent cortical venous filling leads to MCE because of early brain edema; we aim to perform a mediation analysis to explore this hypothesis more thoroughly in future studies.

CONCLUSIONS

We observed that absent cortical venous filling was significantly associated with early brain edema and the occurrence of MCE. Early brain edema may be the link between absent cortical venous filling and MCE. The clinical implication of these results is that absent cortical venous filling may assist in the selection of patients at risk for MCE in whom optimized adjuvant antiedematous treatment would be indicated.

Disclosures: Weijian Chen—RELATED: Grant: Zhenjiang Provincial Key Laboratory of Aging and Neurological Disorder Research (LH-001), the Scientific Technology Planning Projects of Wenzhou and China (Y20170216).

REFERENCES

1. Hacke W, Schwab S, Horn M, et al. **“Malignant” middle cerebral artery territory infarction: clinical course and prognostic signs.** *Arch Neurol* 1996;53:309–15 CrossRef Medline
2. Qureshi AI, Suarez JI, Yahia AM, et al. **Timing of neurologic deterioration in massive middle cerebral artery infarction: a multicenter review.** *Crit Care Med* 2003;31:272–77 CrossRef Medline
3. Berrouschot J, Sterker M, Bettin S, et al. **Mortality of space-occupying (“malignant”) middle cerebral artery infarction under conservative intensive care.** *Intensive Care Med* 1998;24:620–23 CrossRef Medline
4. Vahedi K, Hofmeijer J, Juettler E, et al. **Early decompressive surgery in malignant infarction of the middle cerebral artery: a pooled analysis of three randomised controlled trials.** *Lancet Neurol* 2007;6:215–22 CrossRef Medline
5. Minnerup J, Broocks G, Kalkoffen J, et al. **Computed tomography-based quantification of lesion water uptake identifies patients within 4.5 hours of stroke onset: a multicenter observational study.** *Ann Neurol* 2016;80:924–34 CrossRef Medline
6. Broocks G, Flottmann F, Scheibel A, et al. **Quantitative lesion water uptake in acute stroke computed tomography is a predictor of malignant infarction.** *Stroke* 2018;49:1906–12 CrossRef Medline
7. Broocks G, Kemmling A, Meyer L, et al. **Computed tomography angiography collateral profile is directly linked to early edema progression rate in acute ischemic stroke.** *Stroke* 2019;50:3424–30 CrossRef Medline
8. Ito H, Kanno I, Iida H, et al. **Arterial fraction of cerebral blood volume in humans measured by positron emission tomography.** *Ann Nucl Med* 2001;15:111–16 CrossRef Medline
9. Yu W, Rives J, Welch B, et al. **Hypoplasia or occlusion of the ipsilateral cranial venous drainage is associated with early fatal edema of middle cerebral artery infarction.** *Stroke* 2009;40:3736–39 CrossRef Medline

10. Jansen IGH, van Vuuren AB, van Zwam WH, et al. **Absence of cortical vein opacification is associated with lack of intra-arterial therapy benefit in stroke.** *Radiology* 2018;286:643–50 CrossRef Medline
11. Pexman JH, Barber PA, Hill MD, et al. **Use of the Alberta Stroke Program Early CT Score (ASPECTS) for assessing CT scans in patients with acute stroke.** *AJNR Am J Neuroradiol* 2001;22:1534–42 Medline
12. Tan IY, Demchuk AM, Hopyan J, et al. **CT angiography clot burden score and collateral score: correlation with clinical and radiologic outcomes in acute middle cerebral artery infarct.** *AJNR Am J Neuroradiol* 2009;30:525–31 CrossRef Medline
13. Lin L, Bivard A, Kleinig T, et al. **Correction for delay and dispersion results in more accurate cerebral blood flow ischemic core measurement in acute stroke.** *Stroke* 2018;49:924–30 CrossRef Medline
14. Brooks G, Flottmann F, Ernst M, et al. **Computed tomography-based imaging of voxel-wise lesion water uptake in ischemic brain: relationship between density and direct volumetry.** *Invest Radiol* 2018;53:207–13 CrossRef Medline
15. Cheng Y, Wu S, Wang Y, et al. **External validation and modification of the edema score for predicting malignant brain edema after acute ischemic stroke.** *Neurocrit Care* 2020;32:104–12 CrossRef Medline
16. Kauw F, Bennink E, de Jong H, et al. **Intracranial cerebrospinal fluid volume as a predictor of malignant middle cerebral artery infarction.** *Stroke* 2019; May 16 [Epub ahead of print] CrossRef Medline
17. Alperin N, Lee SH, Mazda M, et al. **Evidence for the importance of extracranial venous flow in patients with idiopathic intracranial hypertension (IIH).** *Acta Neurochir Suppl* 2005;95:129–32 CrossRef Medline
18. Vorasayan P, Bevers MB, Beslow LA, et al. **Intravenous glibenclamide reduces lesional water uptake in large hemispheric infarction.** *Stroke* 2019;50:3021–27 CrossRef Medline
19. Horsch AD, Dankbaar JW, Stemerding TA, et al. **Imaging findings associated with space-occupying edema in patients with large middle cerebral artery infarcts.** *AJNR Am J Neuroradiol* 2016;37:831–37 CrossRef Medline
20. Sasaki M, Honmou O, Radtke C, et al. **Development of a middle cerebral artery occlusion model in the nonhuman primate and a safety study of I.V. infusion of human mesenchymal stem cells.** *PLoS One* 2011;6:e26577 CrossRef Medline
21. Zhang S, Lai Y, Ding X, et al. **Absent filling of ipsilateral superficial middle cerebral vein is associated with poor outcome after reperfusion therapy.** *Stroke* 2017;48:907–14 CrossRef Medline
22. Miao J, Song X, Sun W, et al. **Predictors of malignant cerebral edema in cerebral artery infarction: a meta-analysis.** *J Neurol Sci* 2020;409:116607 CrossRef Medline
23. Wu S, Yuan R, Wang Y, et al. **Early prediction of malignant brain edema after ischemic stroke.** *Stroke* 2018;49:2918–27 CrossRef Medline
24. Wang Y, Zhao X, Liu L, et al. **Prevalence and outcomes of symptomatic intracranial large artery stenoses and occlusions in China: the Chinese Intracranial Atherosclerosis (CICAS) Study.** *Stroke* 2014;45:663–69 CrossRef Medline
25. Lee JS, Hong JM, Lee KS, et al. **Endovascular therapy of cerebral arterial occlusions: intracranial atherosclerosis versus embolism.** *J Stroke Cerebrovasc Dis* 2015;24:2074–80 CrossRef Medline
26. Rebello LC, Bouslama M, Haussen DC, et al. **Stroke etiology and laterals: atheroembolic strokes have greater collateral recruitment than cardioembolic strokes.** *Eur J Neurol* 2017;24:762–67 CrossRef Medline
27. Wartenberg KE. **Malignant middle cerebral artery infarction.** *Curr Opin Crit Care* 2012;18:152–63 CrossRef Medline
28. Kasner SE, Demchuk AM, Berrouschot J, et al. **Predictors of fatal brain edema in massive hemispheric ischemic stroke.** *Stroke* 2001;32:2117–23 CrossRef Medline
29. Jaramillo A, Góngora-Rivera F, Labreuche J, et al. **Predictors for malignant middle cerebral artery infarctions: a postmortem analysis.** *Neurology* 2006;66:815–20 CrossRef Medline
30. Klein SL, Marriott I, Fish EN. **Sex-based differences in immune function and responses to vaccination.** *Trans R Soc Trop Med Hyg* 2015;109:9–15 CrossRef Medline
31. Mirza MA, Ritzel R, Xu Y, et al. **Sexually dimorphic outcomes and inflammatory responses in hypoxic-ischemic encephalopathy.** *J Neuroinflammation* 2015;12:32 CrossRef Medline
32. Szychala MS, Honarpisheh P, McCullough LD. **Sex differences in neuroinflammation and neuroprotection in ischemic stroke.** *J Neurosci Res* 2017;95:462–71 CrossRef Medline
33. Brooks G, Flottmann F, Ernst M, et al. **Computed tomography-based imaging of voxel-wise lesion water uptake in ischemic brain: relationship between density and direct volumetry.** *Invest Radiol* 2018;53:207–13 CrossRef
34. Dzialowski I, Klotz E, Goericke S, et al. **Ischemic brain tissue water content: CT monitoring during middle cerebral artery occlusion and reperfusion in rats.** *Radiology* 2007;243:720–26 CrossRef Medline
35. Hoffman H, Ziechmann R, Swarnkar A, et al. **Cortical vein opacification for risk stratification in anterior circulation endovascular thrombectomy.** *J Stroke Cerebrovasc Dis* 2019;28:1710–17 CrossRef Medline
36. van den Wijngaard IR, Wermer MJ, Boiten J, et al. **Cortical venous filling on dynamic computed tomographic angiography: a novel predictor of clinical outcome in patients with acute middle cerebral artery.** *Stroke* 2016;47:762–67 CrossRef

Tissue at Risk and Ischemic Core Estimation Using Deep Learning in Acute Stroke

Y. Yu, Y. Xie, T. Thamm, E. Gong, J. Ouyang, S. Christensen, M.P. Marks, M.G. Lansberg, G.W. Albers, and G. Zaharchuk



ABSTRACT

BACKGROUND AND PURPOSE: In acute stroke patients with large vessel occlusions, it would be helpful to be able to predict the difference in the size and location of the final infarct based on the outcome of reperfusion therapy. Our aim was to demonstrate the value of deep learning–based tissue at risk and ischemic core estimation. We trained deep learning models using a baseline MR image in 3 multicenter trials.

MATERIALS AND METHODS: Patients with acute ischemic stroke from 3 multicenter trials were identified and grouped into minimal ($\leq 20\%$), partial (20%–80%), and major ($\geq 80\%$) reperfusion status based on 4- to 24-hour follow-up MR imaging if available or into unknown status if not. Attention-gated convolutional neural networks were trained with admission imaging as input and the final infarct as ground truth. We explored 3 approaches: 1) separate: train 2 independent models with patients with minimal and major reperfusion; 2) pretraining: develop a single model using patients with partial and unknown reperfusion, then fine-tune it to create 2 separate models for minimal and major reperfusion; and 3) thresholding: use the current clinical method relying on apparent diffusion coefficient and time-to-maximum of the residue function maps. Models were evaluated using area under the curve, the Dice score coefficient, and lesion volume difference.

RESULTS: Two hundred thirty-seven patients were included (minimal, major, partial, and unknown reperfusion: $n = 52, 80, 57,$ and $48,$ respectively). The pretraining approach achieved the highest median Dice score coefficient (tissue at risk = 0.60, interquartile range, 0.43–0.70; core = 0.57, interquartile range, 0.30–0.69). This was higher than the separate approach (tissue at risk = 0.55; interquartile range, 0.41–0.69; $P = .01$; core = 0.49; interquartile range, 0.35–0.66; $P = .04$) or thresholding (tissue at risk = 0.56; interquartile range, 0.42–0.65; $P = .008$; core = 0.46; interquartile range, 0.16–0.54; $P < .001$).

CONCLUSIONS: Deep learning models with fine-tuning lead to better performance for predicting tissue at risk and ischemic core, outperforming conventional thresholding methods.

ABBREVIATIONS: AUC = area under the curve; DSC = Dice score coefficient; iCAS = Imaging Collaterals in Acute Stroke; IQR = interquartile range; Tmax = time-to-maximum of the residue function

As demonstrated in recent Endovascular Therapy following Imaging Evaluation for Ischemic Stroke 3 (DEFUSE 3) and Extending the Time for Thrombolysis in Emergency Neurological Deficits (EXTEND) trials,^{1,2} perfusion imaging can be used to triage patients with acute ischemic stroke to reperfusion therapy in addition to the original “time window.” The DWI/PWI mismatch paradigm is the most common way of triaging patients,³ especially in those exceeding 6 hours of stroke onset.

The tissue at risk, sometimes called the penumbra, reflects the maximal extent of infarct if only minimal reperfusion is

achieved, defined by time-to-maximum of the residue function (Tmax) > 6 seconds region using standard clinical software. Likewise, the ischemic core reflects the minimal ischemic lesion if major reperfusion is achieved, which has been defined by an ADC value < $620 \times 10^{-6} \text{ mm}^2/\text{s}$.⁴ Despite the simplicity and ease of use of single-value thresholds to identify salvageable tissue, such approaches have difficulty distinguishing benign

Paper previously presented at: Annual Meeting of the American Society of Neuroradiology, May 19–23, 2019; Boston, Massachusetts; and International Stroke Conference, February 18–21, 2020; Los Angeles, California.

Please address correspondence to Greg Zaharchuk, MD, PhD, The Richard M. Lucas Center for Imaging, Department of Radiology, Stanford University, 1201 Welch Road, Stanford, CA 94305. e-mail: gregz@stanford.edu; @yannan_yu; @GregZ_MD

Indicates open access to non-subscribers at www.ajnr.org

Indicates article with online supplemental data.

<http://dx.doi.org/10.3174/ajnr.A7081>

Received July 30, 2020; accepted after revision December 28.

From the Departments of Radiology (Y.Y., Y.X., T.T., M.P.M., G.Z.), Electrical Engineering (E.G., J.O.), and Neurology (S.C., M.G.L., G.W.A.), Stanford University, Stanford, California. This study was funded by National Institutes of Health (R01-NS066506, R01-NS039325).

The funders had no role in study design; collection, analysis, and interpretation of data; the writing of the report; and in the decision to submit the paper for publication.

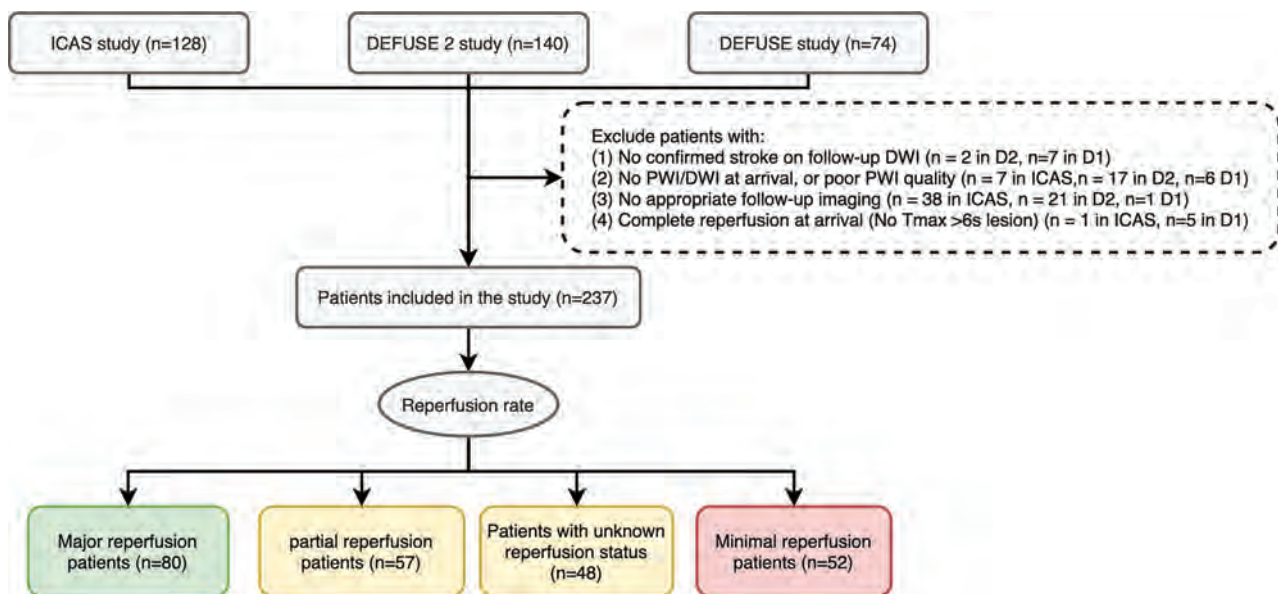


FIG 1. Flow diagram of the study. According to the reperfusion rate calculated from baseline and 4- to 24-hour perfusion-weighted imaging, patients are grouped into major reperfusion ($\geq 80\%$), partial reperfusion (20%–80%), minimal reperfusion ($\leq 20\%$), and unknown reperfusion status (if 4- to 24-hour perfusion imaging was not performed). D1 indicates DEFUSE study; D2, DEFUSE 2 study.

hypoperfusion from tissue at risk⁵ and may fail to capture the complexity of the disease evolution.

Machine learning is a class of algorithms that automatically learn from data and provide predictions. Studies have shown that machine learning can be used to predict final stroke lesions from acute imaging data.^{6–13} Convolutional neural networks are a subtype of machine learning that do not require humans to define relevant features, instead extracting features automatically from images using many hidden layers (giving rise to the term “deep learning”).^{14–16} One type of deep convolutional neural network known as a U-net has shown much promise for segmentation tasks in medical imaging.¹⁷

The most obvious approach to define the ischemic core and tissue at risk is to train 2 separate models using patients with complete or no reperfusion. However, such patients account only for a small subgroup of all patients who undergo reperfusion therapy, and the performance of deep learning models improves with increased sample size.¹⁸ Therefore, the aim of this study was to explore whether deep learning could provide a more accurate estimation of tissue at risk and ischemic core, and what is the most efficient and accurate approach with limited clinical data.

We evaluated 2 different approaches: training using targeted cases (patients with minimal and major reperfusion) only (separate training approach); or pretraining on a much wider cross-section of cases (including those with partial reperfusion) followed by fine-tuning on the targeted cases (pretraining approach). We hypothesized that the pretraining approach is superior to separate training and that both methods outperform the current clinical standard thresholding method based on the DWI/PWI mismatch.

MATERIALS AND METHODS

Patient Population

Patients with acute ischemic stroke were enrolled from 3 prospective, multicenter stroke trials: Imaging Collaterals in Acute Stroke

(iCAS) from April 2014 to August 2017 ($n = 128$), DEFUSE from April 2001 to April 2005 ($n = 74$), and DEFUSE 2 from July 2008 to October 2011 ($n = 140$). iCAS^{19,20} is a multicenter observational study that enrolled patients with clinical acute ischemic stroke symptoms attributable to the anterior circulation, an NIHSS score of ≥ 5 , and onset-to-imaging time of ≤ 24 hours. The DEFUSE and DEFUSE 2 protocols enrolled similar patients within a shorter time window (≤ 12 hours) and results have been reported.^{21,22}

We excluded patients on the basis of the following criteria: 1) no confirmed ischemic stroke on follow-up DWI; 2) no PWI or DWI at arrival, or poor PWI quality; 3) no follow-up T2 FLAIR images within 3–7 days after stroke onset for iCAS and DEFUSE 2, or within 30 days for DEFUSE; or 4) complete reperfusion on initial PWI (no Tmax > 6 seconds lesion) (Fig 1).

iCAS (NCT02225730) and DEFUSE (NCT01349946) were approved by the institutional review boards of the participating institutions, and written consent was obtained for each participant. This study has been approved for retrospective analysis by the institutional review boards.

Imaging Protocol

All images were acquired at either 1.5T or 3T. Patients underwent MR imaging, including DWI ($b=0$ and $b=1000$ s/mm²) and dynamic susceptibility contrast-enhanced PWI using gadolinium-based contrast agents according to the standard protocol of each site. Postprocessing software (RAPID; iSchemaView) was used to reconstruct perfusion parameter maps: Tmax, MTT, CBV, and CBF. This software also automatically generates ADC segmentation with a threshold of $< 620 \times 10^{-6}$ mm²/s and Tmax segmentation with a threshold of > 6 seconds. Most patients underwent a follow-up PWI study within 24 hours, which was used to classify patients into minimal, partial, and major reperfusion as described below.

Patients with T2 FLAIR obtained at 3–7 days after stroke onset were used to evaluate the model performance; DEFUSE

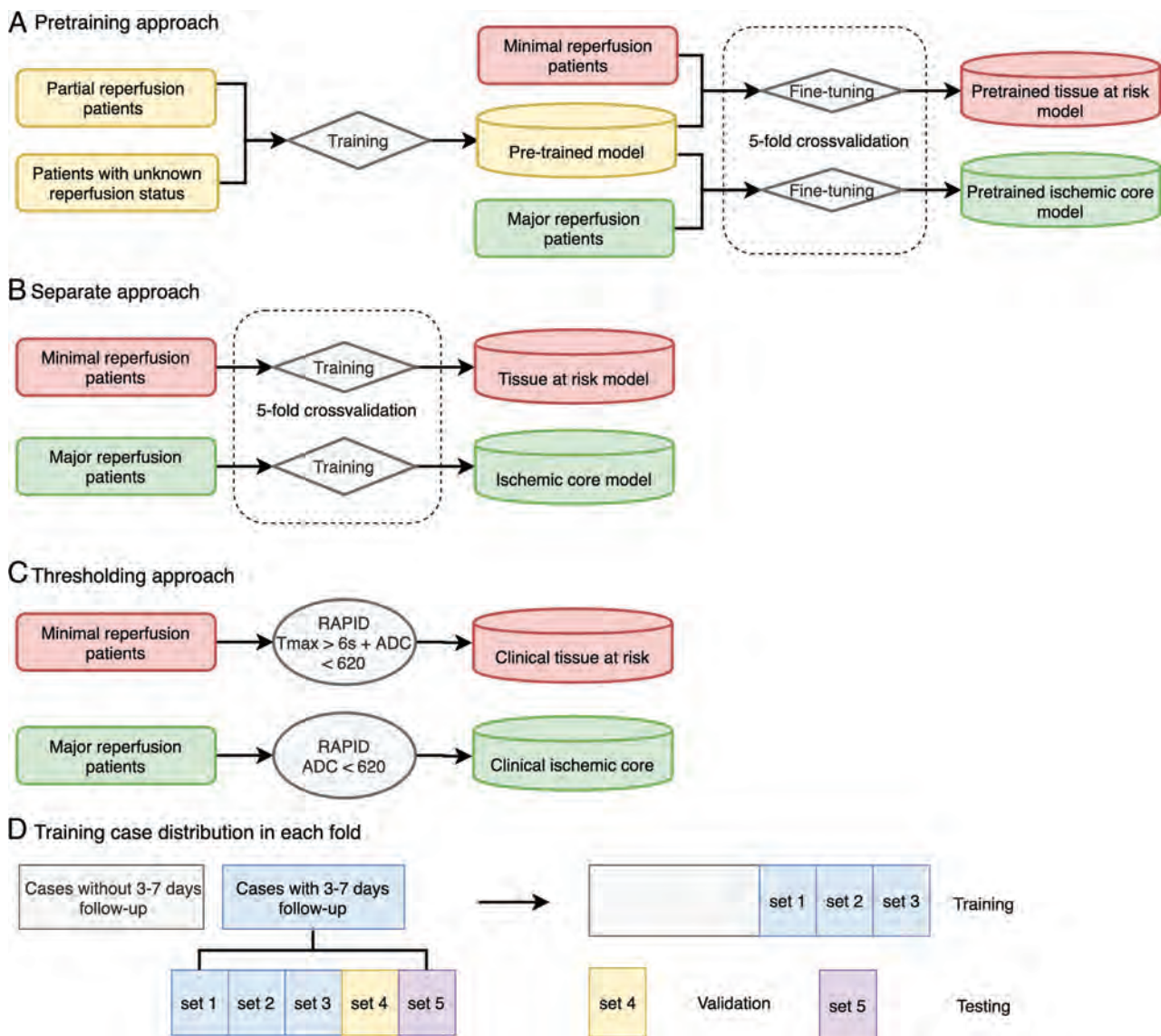


FIG 2. Illustration of 3 approaches to define tissue at risk and ischemic core and detailed case distribution during 5-fold cross-validation. The pretraining deep learning approach (A), the separate deep learning approach (B), and the thresholding approach (C). For the pretraining, 94 patients with partial/unknown reperfusion were used in the training set, and 11 patients with 3- to 7-day follow-up were used only in training (A and B), while patients with 3- to 7-day follow-up were used in training, validation, and testing. Patients with 3- to 7-day follow-up were divided randomly into 5 sets and used in training, validation, and testing with a ratio of 3:1:1. For each fold of the tissue-at-risk model, 37 cases were used for fine-tuning on the pretrained model, 6 for validation, and 6–7 for testing. For each fold of the ischemic core model, 48 cases were used for the fine-tuning; 13, for validation; and 13–14, for testing.

cases with DWI obtained at 4–8 hours and/or T2 FLAIR at 30 days after stroke treatment (because 24-hour and 3- to 7-day images were not part of the study protocol) were only used to train the deep learning algorithms but were not used for testing (Fig 2).

Imaging Analysis

Investigators at a core laboratory reviewed all studies. Neuroradiologists who were blinded to clinical information segmented the final infarct lesion on the follow-up studies. The segmented infarct lesions were used as ground truth for the deep learning model.

Patients were classified into 4 reperfusion categories based on the baseline and the 4- to 24-hour PWI study. We relied on the

reperfusion rate rather than the TICI recanalization score to classify patients because it reflects the tissue reperfusion and predicts outcome better than recanalization.^{23,24} Reperfusion status was calculated as

$$\text{Reperfusion Rate} = 100\% \times (1 - [\text{Tmax}_{24\text{hr}} > 6 \text{ seconds lesion} / \text{Tmax}_{\text{baseline}} > 6 \text{ seconds lesion}]).$$

Patients with reperfusion rates of $\leq 20\%$ and $\geq 80\%$ were classified as having minimal and major reperfusion, respectively.^{25,26} Otherwise, they were classified as having partial reperfusion (if 4- to 24-hour PWI was available) or with unknown reperfusion (if not). Patients with minimal reperfusion were used to define tissue at risk, while those with major reperfusion were used to define ischemic core.

Imaging Preprocessing

All images were coregistered and normalized to the Montreal Neurological Institute template space using Matlab 2016b (MathWorks) and SPM 12 (<http://www.fil.ion.ucl.ac.uk/spm/software/spm12>). Of note, the spatial coverage of perfusion imaging was usually smaller than that of diffusion imaging, and only voxels with both diffusion and perfusion information were included in the model.

For input to the deep learning model, DWI ($b=1000$ s/mm² images), ADC, Tmax, MTT, CBV, and CBF were normalized by the mean of their parenchymal tissue value. To preserve important information from the absolute value of Tmax and ADC, we created 2 masks separately for Tmax > 6 seconds and ADC < 620×10^{-6} mm²/s using simple thresholding.

Training Approaches

A neural network called attention-gated U-net was used in this study and was reported in previous literature¹² (Online Supplemental Data and Online Fig 1). In short, the model takes 5 consecutive slices of DWI, ADC, Tmax, MTT, CBF, CBV, and masks of Tmax and ADC as input and gives a probability map of infarct segmentation with voxel values that ranged from 0 to 1 as output. A value close to 1 indicates that the voxel is more likely to be infarcted, while a value close to 0 indicates that the voxel is likely to be spared. The consecutive slices provided the model with more context than a single section of an image.

We explored the pretraining, separate, and thresholding approaches to test which one performed best (Fig 2). In the pretraining approach, a single model was first trained using patients with partial and unknown reperfusion status. Then, starting from these weights, 2 separate models were generated by fixing the weights in the encoder layers but fine-tuning the decoding layers, one using patients with minimal reperfusion to create a tissue-at-risk model and the other using patients with major reperfusion to create an ischemic core model. In the separate approach, 2 separate models were trained from scratch with patients with either minimal or major reperfusion. Because there were relatively fewer subjects who fell into these extreme cases, there was less data for each of the separate models for training. In the thresholding approach, the clinically used Tmax and ADC segmentations from RAPID were used. The union of Tmax > 6 seconds and ADC < 620×10^{-6} mm²/s was used to define tissue at risk. Tissue with ADC < 620×10^{-6} mm²/s was used to define the ischemic core.²⁷

During the pretraining phase, 10% of the cases were used as a validation set and the rest were used for training. Five-fold cross-validation was performed for the separate approach and the fine-tuning part of the pretraining approach to reduce bias (Fig 2). Given the multicenter, multivendor nature of the dataset, this system represented the best test of the generalizability of the model.

Performance Evaluation

The area under the curve (AUC) was calculated for both the deep learning models and the Tmax and ADC thresholding method. The AUC was calculated for each case within the ipsilateral stroke hemisphere, except in 1 case for which there were bilateral strokes.

To calculate the Dice score coefficient (DSC) and lesion volume difference between prediction and ground truth, we set a threshold probability of .5 for all deep learning models. To calculate the mismatch ratio predicted by the models, we also applied the tissue-at-risk model to patients with major reperfusion, and the ischemic core model, to those with minimal reperfusion.

Statistical Analysis

Statistical analysis was performed using STATA (Version 15.0; StataCorp). The χ^2 or Fisher exact test and the Kruskal-Wallis equality-of-populations rank test were performed for demographic and clinical information. Paired-sample Wilcoxon tests were performed to compare AUC, DSC, lesion volume difference, and absolute lesion volume differences between the pretraining approach and separate approach, as well as the pretraining approach and the Tmax/ADC thresholding methods. The concordance correlation coefficient (ρ_c) was used to analyze the lesion volume predictions. Because infarct volumes were not normally distributed, cubic root transformation was performed for the ρ_c calculation. The correlation was considered excellent with $\rho_c > 0.70$, moderate when ρ_c was between 0.50 and 0.70, and low with $\rho_c < 0.50$.²⁸ All tests were 2-sided, and $P \leq .008$ was considered statistically significant after adjustment by the Benjamini-Hochberg method.

RESULTS

We reviewed 342 patients from DEFUSE 1, DEFUSE 2, and iCAS and eventually included 237 patients (Fig 1). Fifty-two patients were classified as having minimal reperfusion; 57, as partial reperfusion; 80, as major reperfusion; and 48, as unknown reperfusion. Clinical and imaging information is summarized in the Table. The time for training a model was 5 hours, and the time for generating prediction for each patient was 30 seconds with our current workstation. Figure 3 shows several examples of predictions using the 3 approaches. Online Supplemental Data show the effect of the attention map at each level in the U-net.

Prediction of Tissue at Risk

The evaluations were performed in 33 patients with minimal reperfusion with T2 FLAIR follow-up at 3–7 days. As shown in Online Supplemental Table 2, the pretraining approach achieved the highest AUC (0.92; interquartile range [IQR], 0.89–0.95) and DSC (0.60; IQR, 0.43–0.70) compared with the separate approach and thresholding method. There was no statistical difference in the volume difference or the absolute volume difference among the 3 approaches. However, the volume of tissue at risk predicted by the pretraining approach showed excellent concordance ($\rho_c = 0.822$; 95% CI, 0.725–0.919) with the true infarct volume compared with the separate ($\rho_c = 0.685$; 95% CI, 0.517–0.852) and thresholding ($\rho_c = 0.657$; 95% CI, 0.511–0.804) approaches. The volumetric agreement between the pretraining approach and the true lesion volume and the percentage volume difference are shown in the Online Supplemental Data and the Table.

Prediction of Ischemic Core

The evaluations were performed in 67 patients with major reperfusion with T2 FLAIR follow-up at 3–7 days. The pretraining

Clinical and imaging information of patients included^a

	All Patients (n = 237)	Minimal Reperfusion (n = 52)	Major Reperfusion (n = 80)	Partial Reperfusion (n = 57)	Unknown Reperfusion (n = 48)	P Value
Male	108 (46)	27 (52)	39 (49)	25 (44)	17 (35)	.3
Age (yr)	66 [SD, 16]	64 [SD, 16]	66 [SD, 16]	69 [SD, 14]	64 [SD, 17]	.4
Hypertension	159 (67)	39 (75)	50 (63)	39 (68)	31 (65)	.3
Diabetes	58 (25)	14 (27)	18 (23)	15 (26)	11 (23)	.8
Dyslipidemia	97 (41)	24 (46)	30 (38)	30 (53)	13 (28)	.6
Atrial fibrillation	73 (31)	12 (23)	27 (34)	21 (37)	13 (28)	.4
Treatment methods						.004
IV tPA only	79 (33)	25 (48)	18 (22)	21 (37)	15 (31)	
Direct thrombectomy	62 (26)	8 (15)	29 (36)	16 (28)	9 (19)	
Bridging therapy	77 (32)	13 (25)	31 (39)	16 (28)	17 (35)	
No treatment	19 (8)	6 (12)	2 (3)	4 (7)	7 (15)	
Onset-to-treatment time (hr)	5.7 (4.7–7.4)	5.8 (5.2–6.3)	5.8 (4.6–7.8)	5.4 (4.6–6.4)	5.8 (4.9–7.7)	.9
Baseline DWI lesion volume (mL)	22 (8–57)	20 (6–63)	17 (6–43)	31 (16–83)	31 (13–61)	.01
Baseline Tmax lesion volume (mL)	115 (68–173)	98 (48–158)	115 (71–160)	126 (66–188)	123 (80–171)	.3
PWI/DWI mismatch ratio ^b	3.8 (1.9–8.6)	2.9 (1.4–6.8)	5.4 (2.3–13.9)	3.3 (2.0–5.8)	3.2 (1.6–6.6)	.006
Baseline NIHSS	14 (10–19)	13 (8–19)	15 (9–19)	16 (10–19)	14 (11–19)	.3
Symptomatic hemorrhage	27 (11)	7 (13)	8 (10)	8 (14)	4 (8)	.1
Reperfusion rate (%)	69 (15–97)	0 (0–9)	100 (92–100)	55 (37–68)	NA	<.001
Final infarct volume (mL)	49 (14–108)	59 (28–204)	19 (8–62)	77 (33–149)	57 (22–112)	<.001
90-day mRS	3 (1–4)	3 (2–4)	2 (1–3)	4 (2–5)	3 (1–4)	<.001

Note:—NA indicates not applicable.

^aData are expressed as No. (%), median [IQR], or mean [SD].

^bThe upper limit of the mismatch ratio was set to 20 if a small or no ischemic core lesion presented at baseline.

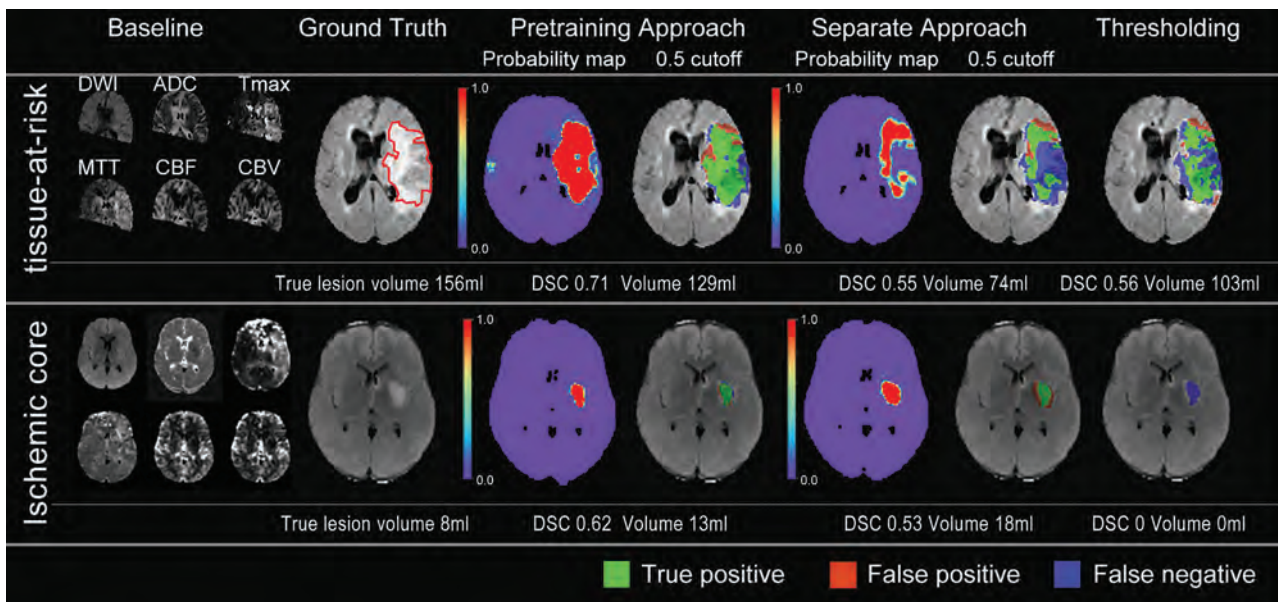


FIG 3. Two representative cases of predictions from the pretraining, separate, and thresholding approaches. *Upper row:* A 71-year-old man treated with IV tPA only, which achieved 0% reperfusion. Of note, only voxels with both diffusion and perfusion information are included in the model. His true lesion is used to define tissue at risk. *Lower row:* A 45-year-old man treated with IV tPA and thrombectomy, which achieved 100% reperfusion. His true lesion is used to define ischemic core. The pretraining approach had more accurate prediction than either the separate approach or the thresholding method, both visually, with DSC analysis, and volumetrically (Online Supplemental Data). Green areas overlaid on the FLAIR image represent true-positive, blue represents false-negative, and red represents false-positive.

approach again achieved the highest AUC (0.94; IQR, 0.89–0.97) and DSC (0.57; IQR, 0.30–0.69) compared with the separate approach and the thresholding method. The pretraining approach also showed less biased volume prediction compared with the thresholding approach and achieved excellent concordance ($\rho_c = 0.756$; 95% CI, 0.651–0.860) with the true infarct volume compared with the separate approach ($\rho_c = 0.657$; 95% CI, 0.519–0.795) and thresholding ($\rho_c = 0.625$; 95% CI, 0.489–0.762). The volumetric agreement between the pretraining approach and the true lesion volume and the percentage volume difference are shown in the Online Supplemental Data and the Table.

Mismatch Patterns Predicted from the Deep Learning Models

The median mismatch ratio yielded by the pretraining approach was 2.0 (IQR, 1.5–4.2) for patients with minimal reperfusion and 2.7 (IQR, 2.0–5.4) for patients with major reperfusion, compared with 2.9 (IQR, 1.4–6.8; $P = .07$) and 5.4 (IQR, 2.3–13.9; $P < .001$) given by the thresholding approach. Examples of mismatch predicted by the 2 different approaches are shown in Fig 4.

DISCUSSION

By analyzing data from 3 multicenter clinical trials, this study showed that a pretraining approach using deep learning in which a large heterogeneous population is used to first train a common model, which is then bifurcated into models for minimal and major reperfusion, performs better than using separate training in a smaller group of patients with extreme reperfusion. Furthermore, it outperformed current clinically available prediction methods based on a threshold of the DWI/PWI mismatch for identifying tissue at risk and ischemic core in acute ischemic stroke.

Currently, $T_{max} > 6$ seconds and $ADC < 620 \times 10^{-6} \text{ mm}^2/\text{s}$ are the state-of-the-art estimations for tissue fate with no reperfusion and complete reperfusion.^{1,22,27} However, these thresholds are derived from linear analysis and have not been validated in large cohorts.²⁹ Factors such as collateral status and gray/white matter content may result in different susceptibilities to ischemia.³⁰ This study suggested that the single-valued thresholding approach could be outperformed using a nonlinear analysis method such as deep learning. While we have shown the capabilities of deep learning using MR imaging as the initial imaging study, we recognize that CT is becoming increasingly used for stroke triage. Similar methods could likely be used with CT data, and this MR imaging–based approach using pretraining could act as a starting point for training a CT-based triaging system, given the wide availability of CT scanners and the ability to extract similar perfusion parameters.

Previous traditional and machine learning studies used only patients with minimal and major reperfusion to generate the criteria of tissue at risk and ischemic core.^{6,25,26} In patients with ischemic stroke who received reperfusion therapy using the latest devices, $>50\%$ of patients have partial reperfusion when the reperfusion rate at 24 hours is intermediate (20%–80%) or the TICI score is between 2a and 2b.^{1,31,32} Our results show that an approach that trained models separately in patients with minimal and major reperfusion had only moderate correlation with true lesion volume and had only a minor advantage compared with

conventional thresholding methods. This finding is likely because the separate approach “wastes” many cases that could potentially be used to improve the network prediction. If we wanted to use the separate approach to achieve the same level of predictive accuracy as the pretraining approach, it likely requires a much larger training set, which is challenging for clinical studies. For example, in the current study, the pretrained model ultimately had access to approximately 2–3 times more individual cases for training than the separate models. Therefore, the pretraining approach (fine-tuning on a pretrained model) is a promising approach to maximally use all available stroke data to improve the performance.

Fine-tuning techniques have been discussed in previous literature.³³ Fine-tuning on the last layer is preferred when the prediction task is within the pretrained model, while fine-tuning on the last several layers is preferred for a more specific task as in this study. Previous studies have shown that using models pretrained on nonmedical image data may also perform well in medical imaging data.³⁴ However, medical images such as MR imaging and CT are often quantitative or semiquantitative and in gray-scale, differing from nonmedical photos. Complicated network structure, filters, and pre-extracted features for regular photos may be resource-consuming and redundant for MR imaging and CT data and may not offer much performance benefit.³⁵ This study showed that pretraining using medical imaging data of the same category and same cohort achieved excellent performance. In the future, establishing pretrained models exclusively for medical imaging may help translate deep learning models into clinical workflow application most efficiently.

Compared with previous studies that used machine learning and deep learning to predict tissue fate,^{6,7,12} the accuracy and visual reliability of our model are promising. Some may argue that if more cases are used in the training set, they will always benefit the model performance. A previous study that trained prediction models in all patients with stroke regardless of reperfusion status¹² showed good accuracy but had biased prediction in patients with minimal and major reperfusion, with under- and overestimations in lesion size, respectively. The current study shows that refining the training strategy to specifically include patients with extreme reperfusion states as a fine-tuning step will provide less biased predictions. McKinley et al⁶ trained 2 random forest classifiers on 15 cases with TICI 3 (ischemic core classifier) and 10 cases with TICI 0 (penumbra classifier). They reported a mean DSC of 0.32 [SD, 0.23] in cases with TICI grades 1 and 2a and 0.34 [SD, 0.22] in cases with TICI grades 2b and 3. The models presented in this study appear to perform better, though it is difficult to compare metrics across studies that used different models and datasets. Therefore, validating our models in the same dataset is an important step for translation to clinical practice in the future.

After careful validation in a separate cohort and further improvement in predictive accuracy, the models can be applied to the triaging system in emergency departments. Similar to the current commercial software and workstations that apply 2 thresholds ($T_{max} > 6$ seconds and $ADC < 620 \times 10^{-6} \text{ seconds}/\text{mm}^2$), patients' images could be fed separately into the 2 models, which then generate predictions of tissue at risk and ischemic core. A larger mismatch ratio between tissue at risk and ischemic core indicates more benefit from reperfusion treatment, which

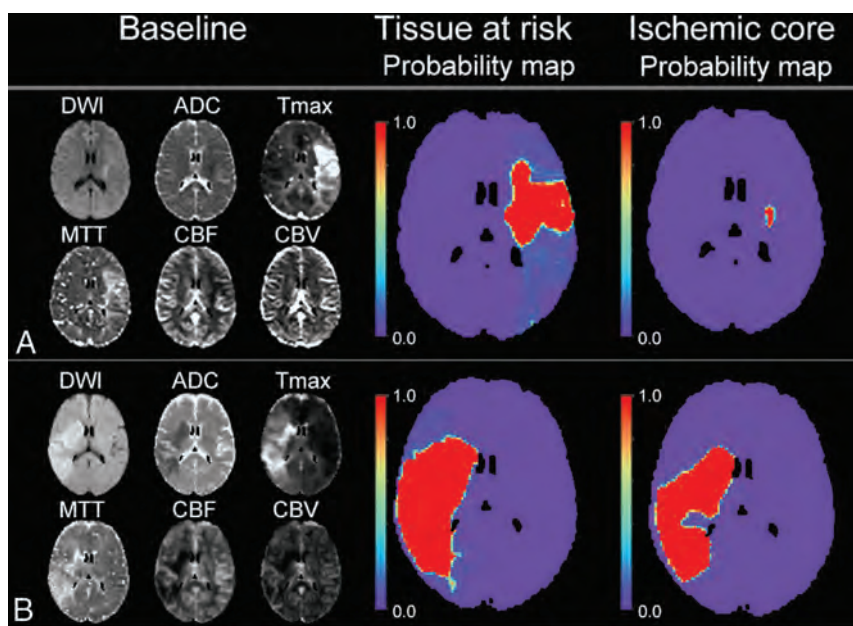


FIG 4. Example of how the deep learning models would be used for triage compared with the thresholding method. *A*, A 44-year-old woman with a large mismatch between tissue at risk and ischemic core prediction (mismatch ratio of 11.8), indicating a small stroke if the patient received successful treatment or a much larger stroke if the patient did not receive any treatment. *B*, 44-year-old woman with a small mismatch ratio of 1.4, indicating limited tissue salvage despite successful treatment. This illustrates how estimated tissue outcome (with and without reperfusion) can be obtained from the deep learning approach and can facilitate clinical decision-making on whether to treat the patient (see Online Supplemental Data for detailed image).

can facilitate the timely clinical decision-making for patient triaging (Fig 4). However, new criteria for the cutoff of the mismatch ratio would be required because the current target mismatch criteria^{4,21} were established solely with the thresholding approach.

There are several limitations to this study. Treatment varied with respect to the use of thrombectomy and thrombolysis. Although we considered the most important factor, reperfusion status, in this study, clinical factors such as age, onset time to imaging, or other risk factors were not included in the analysis. It is our future aim to incorporate such clinical factors into the deep learning models and test whether it can further improve performance. The patient cohort in this study mainly had onset-to-imaging time exceeding 4.5 hours, which may affect the association between baseline imaging and tissue fate. However, no consensus has been reached on whether the perfusion profile is time-dependent,^{36,37} and patients presenting with prolonged symptoms represent the most important cohort for a clinical imaging triaging system. The model may not be directly applicable to images in the original space because the training data were in the Montreal Neurological Institute template space. However, the template space may help reduce the model overfitting and provide important spatial information. The model may be further fine-tuned with data in the original space to reduce the processing time in real clinical settings.

We did not perform outcome analysis because the dataset was not ideal for this purpose. Further studies are required to investigate whether using the model prediction improves clinical outcome, but

it stands to reason that given the choice, a method that more accurately identifies dead and at-risk tissue would allow clinicians to make better decisions about thrombectomy. The data processing and model parameters were chosen on the basis of previous experience, and we did not extensively search all combinations of hyperparameters or fine-tuning techniques, given time and computational constraints. Although better combinations could provide improvement, our study demonstrated the feasibility of using pretraining for stroke imaging prediction and can be used as a jumping-off point for future studies seeking even better performance. Further studies are also warranted investigating whether prediction directly from source perfusion images will improve the performance.

CONCLUSIONS

This multicenter study showed that an attention-gated deep convolutional neural network can be used to identify tissue at risk and core in acute ischemic stroke at levels superior to the current clinical state of the art. Further

clinical validation is required for these methods to be incorporated as a deep learning acute stroke triaging system.

ACKNOWLEDGMENTS

We appreciate the statistical consultation provided by Jarrett Rosenberg, PhD, and Tie Liang, EdD, Radiologic Sciences Laboratory, Department of Radiology, Stanford University.

Disclosures: Yannan Yu—RELATED: Support for Travel to Meetings for the Study or Other Purposes: Stanford University; UNRELATED: Employment: Stanford University. Yuan Xie—UNRELATED: Employment: Subtle Medical Inc. Thoralf Thamm—RELATED: Grant: National Institutes of Health, Comments: Project No. 2R01NS066506-04A1.* Enhao Gong—UNRELATED: Board Membership: Subtle Medical; Employment: Subtle Medical; Stock/Stock Options: Subtle Medical. Søren Christensen—UNRELATED: Stock/Stock Options: iSchemaView, RAPID. Michael P. Marks—RELATED: Grant: National Institutes of Health*; UNRELATED: Board Membership: ThrombX Medical, Comments: no funds received but do have stock; Stock/Stock Options: ThrombX Medical. Maarten G. Lansberg—RELATED: Grant: National Institute of Neurological Disorders and Stroke.* Gregory W. Albers—UNRELATED: Consultancy: Genentech, iSchemaView; Stock/Stock Options: iSchemaView. Greg Zaharchuk—RELATED: Grant: National Institutes of Health*; UNRELATED: Board Membership: Subtle Medical; Expert Testimony: various Medico-legal consulting; Grants/Grants Pending: various National Institutes of Health projects, GE Healthcare, Bayer Healthcare*; Royalties: Cambridge University Press; Stock/Stock Options: equity, Subtle Medical. *Money paid to the institution.

REFERENCES

1. Albers GW, Marks MP, Kemp S, et al. DEFUSE 3 Investigators. **Thrombectomy for stroke at 6 to 16 hours with selection by perfusion imaging.** *N Engl J Med* 2018;378:708–18 CrossRef Medline

2. Ma H, Campbell BC, Parsons MW, et al. EXTEND Investigators. **Thrombolysis guided by perfusion imaging up to 9 hours after onset of stroke.** *N Engl J Med* 2019;380:1795–1803 CrossRef Medline
3. Campbell BC, Ma H, Ringleb PA, et al. EXTEND, ECASS-4, and EPITHET Investigators. **Extending thrombolysis to 4.5-9 h and wake-up stroke using perfusion imaging: a systematic review and meta-analysis of individual patient data.** *Lancet* 2019;394:139–47 CrossRef Medline
4. Albers GW, Lansberg MG, Kemp S, et al. **A multicenter randomized controlled trial of endovascular therapy following imaging evaluation for ischemic stroke (DEFUSE 3).** *Int J Stroke* 2017;12:896–905 CrossRef Medline
5. Nagakane Y, Christensen S, Ogata T, et al. EPITHET Investigators. **Moving beyond a single perfusion threshold to define penumbra: a novel probabilistic mismatch definition.** *Stroke* 2012;43:1548–55 CrossRef Medline
6. McKinley R, Hani L, Gralla J, et al. **Fully automated stroke tissue estimation using random forest classifiers (FASTER).** *J Cereb Blood Flow Metab* 2017;37:2728–41 CrossRef Medline
7. Nielsen A, Hansen MB, Tietze A, et al. **Prediction of tissue outcome and assessment of treatment effect in acute ischemic stroke using deep learning.** *Stroke* 2018;49:1394–1401 CrossRef Medline
8. Pinto A, McKinley R, Alves V, et al. **Stroke lesion outcome prediction based on MRI imaging combined with clinical information.** *Front Neurol* 2018;9:1060 CrossRef Medline
9. Stier N, Vincent N, Liebeskind D, et al. **Deep learning of tissue fate features in acute ischemic stroke.** *Proceedings (IEEE Int Conf Bioinformatics Biomed)* 2015;2015:1316–21 CrossRef Medline
10. Winder AJ, Siemonsen S, Flottmann F, et al. **Comparison of classification methods for voxel-based prediction of acute ischemic stroke outcome following intra-arterial intervention.** *Proceedings of the SPIE* 2017;10134:101344B CrossRef
11. Yu Y, Guo D, Lou M, et al. **Prediction of hemorrhagic transformation severity in acute stroke from source perfusion MRI.** *IEEE Trans Biomed Eng* 2018;65:2058–65 CrossRef Medline
12. Yu Y, Xie Y, Thamm T, et al. **Use of deep learning to predict final ischemic stroke lesions from initial magnetic resonance imaging.** *JAMA Netw Open* 2020;3:e200772 CrossRef Medline
13. McKinley R, Hung F, Wiest R, et al. **A machine learning approach to perfusion imaging with dynamic susceptibility contrast MR.** *Front Neurol* 2018;9:717 CrossRef Medline
14. Chilamkurthy S, Ghosh R, Tanamala S, et al. **Deep learning algorithms for detection of critical findings in head CT scans: a retrospective study.** *Lancet* 2018;392:2388–96 CrossRef Medline
15. Wang K, Shou Q, Ma SJ, et al. **Deep learning detection of penumbral tissue on arterial spin labeling in stroke.** *Stroke* 2020;51:489–97 CrossRef Medline
16. Robben D, Boers AM, Marquering HA, et al. **Prediction of final infarct volume from native CT perfusion and treatment parameters using deep learning.** *Med Image Anal* 2020;59:101589 CrossRef Medline
17. Ronneberger O, Fischer P, Brox T. U-Net: Convolutional Networks for Biomedical Image Segmentation. In: Navab N, Hornegger J, Well AN, et al, eds. *Medical Image Computing and Computer-Assisted Intervention*. Springer; 2015:9351
18. Howard AG. **Some Improvements on Deep Convolutional Neural Network Based Image Classification.** *arXiv e-prints* 2013. <https://arxiv.org/abs/1312.5402>. Accessed December 01, 2013
19. Zaharchuk G, Marks MP, Do HM, et al. **Introducing the Imaging the Collaterals in Acute Stroke (iCAS) multicenter MRI trial.** *Stroke* 2015;46 (Suppl 1):AWMP16
20. Thamm T, Guo J, Rosenberg J, et al. iCAS Study Investigators. **Contralateral hemispheric cerebral blood flow measured with arterial spin labeling can predict outcome in acute stroke.** *Stroke* 2019;50:3408–15 CrossRef Medline
21. Lansberg MG, Straka M, Kemp S, et al. DEFUSE 2 Study Investigators. **MRI profile and response to endovascular reperfusion after stroke (DEFUSE 2): a prospective cohort study.** *Lancet Neurol* 2012;11:860–67 CrossRef Medline
22. Albers GW, Thijs VN, Wechsler L, et al. DEFUSE Investigators. **Magnetic resonance imaging profiles predict clinical response to early reperfusion: the Diffusion and Perfusion Imaging Evaluation for Understanding Stroke Evolution (DEFUSE) study.** *Ann Neurol* 2006;60:508–17 CrossRef Medline
23. Eilaghi A, Brooks J, d'Este C, et al. **Reperfusion is a stronger predictor of good clinical outcome than recanalization in ischemic stroke.** *Radiology* 2013;269:240–48 CrossRef Medline
24. Cho TH, Nighoghossian N, Mikkelsen IK, et al. **Reperfusion within 6 hours outperforms recanalization in predicting penumbra salvage, lesion growth, final infarct, and clinical outcome.** *Stroke* 2015;46:1582–89 CrossRef Medline
25. Bivard A, Levi C, Spratt N, et al. **Perfusion CT in acute stroke: a comprehensive analysis of infarct and penumbra.** *Radiology* 2013;267:543–50 CrossRef Medline
26. Yu Y, Han Q, Ding X, et al. **Defining core and penumbra in ischemic stroke: a voxel- and volume-based analysis of whole brain CT perfusion.** *Sci Rep* 2016;6:20932 CrossRef Medline
27. Purushotham A, Campbell BC, Straka M, et al. **Apparent diffusion coefficient threshold for delineation of ischemic core.** *Int J Stroke* 2015;10:348–53 CrossRef Medline
28. Mukaka MM. **Statistics corner: a guide to appropriate use of correlation coefficient in medical research.** *Malawi Med J* 2012;24:69–71 Medline
29. Olivot JM, Mlynash M, Thijs VN, et al. **Optimal Tmax threshold for predicting penumbral tissue in acute stroke.** *Stroke* 2009;40:469–75 CrossRef Medline
30. Murphy BD, Fox AJ, Lee DH, et al. **White matter thresholds for ischemic penumbra and infarct core in patients with acute stroke: CT perfusion study.** *Radiology* 2008;247:818–25 CrossRef Medline
31. Campbell BC, Mitchell PJ, Kleinig TJ, et al. **Endovascular therapy for ischemic stroke with perfusion-imaging selection.** *N Engl J Med* 2015;372:1009–18 CrossRef Medline
32. Berkhemer OA, Fransen PS, Beumer D, et al. MR CLEAN Investigators. **A randomized trial of intraarterial treatment for acute ischemic stroke.** *N Engl J Med* 2015;372:11–20 CrossRef Medline
33. Yosinski J, Clune J, Bengio Y, et al. **How transferable are features in deep neural networks?** In: *Proceedings of the 27th International Conference on Neural Information Processing Systems*, ACM Digital Library 2014:3320–28
34. Tajbakhsh N, Shin JY, Gurudu SR, et al. **Convolutional neural networks for medical image analysis: full training or fine tuning?** *IEEE Trans Med Imaging* 2016;35:1299–1312 CrossRef Medline
35. Raghu M, Zhang C, Kleinberg J, et al. **Transfusion: Understanding Transfer Learning for Medical Imaging.** *arXiv.org* 2019. <https://arxiv.org/abs/1902.07208>. Accessed February 01, 2019
36. Qiao Y, Zhu G, Patrie J, et al. **Optimal perfusion computed tomographic thresholds for ischemic core and penumbra are not time dependent in the clinically relevant time window.** *Stroke* 2014;45:1355–62 CrossRef Medline
37. d'Este CD, Boesen ME, Ahn SH, et al. **Time-dependent computed tomographic perfusion thresholds for patients with acute ischemic stroke.** *Stroke* 2015;46:3390–97 CrossRef Medline

Vessel Wall Enhancement on Black-Blood MRI Predicts Acute and Future Stroke in Cerebral Amyloid Angiopathy

J.S. McNally, A. Sakata, M.D. Alexander, L.D. Dewitt, J.A. Sonnen, S.T. Menacho, G.J. Stoddard, S.-E. Kim, and A.H. de Havenon



ABSTRACT

BACKGROUND AND PURPOSE: Cerebral amyloid angiopathy (CAA) is a known risk factor for ischemic stroke though angiographic imaging is often negative. Our goal was to determine the relationship between vessel wall enhancement (VWE) in acute and future ischemic stroke in CAA patients.

MATERIALS AND METHODS: This was a retrospective study of patients with new-onset neurologic symptoms undergoing 3T vessel wall MR imaging from 2015 to 2019. Vessel wall enhancement was detected on pre- and postcontrast flow-suppressed 3D T1WI. Interrater agreement was evaluated in cerebral amyloid angiopathy–positive and age-matched negative participants using a prevalence- and bias-adjusted kappa analysis. In patients with cerebral amyloid angiopathy, multivariable Poisson and Cox regression were used to determine the association of vessel wall enhancement with acute and future ischemic stroke, respectively, using backward elimination of confounders to $P < .20$.

RESULTS: Fifty patients with cerebral amyloid angiopathy underwent vessel wall MR imaging, including 35/50 (70.0%) with ischemic stroke and 29/50 (58.0%) with vessel wall enhancement. Prevalence- and bias-corrected kappa was 0.82 (95% CI, 0.71–0.93). The final regression model for acute ischemic stroke included vessel wall enhancement (prevalence ratio = 1.5; 95% CI, 1.1–2.2; $P = .022$), age (prevalence ratio = 1.02; 95% CI, 1.0–1.05; $P = .036$), time between symptoms and MR imaging (prevalence ratio = 0.9; 95% CI, 0.8–0.9; $P < .001$), and smoking (prevalence ratio = 0.7; 95% CI, 0.5–1.0; $P = .042$) with c-statistic = 0.92 (95% CI, 0.84–0.99). Future ischemic stroke incidence with cerebral amyloid angiopathy was 49.7% (95% CI, 34.5%–67.2%) per year over a total time at risk of 37.5 person-years. Vessel wall enhancement–positive patients with cerebral amyloid angiopathy demonstrated significantly shorter stroke-free survival with 63.9% (95% CI, 43.2%–84.0%) versus 32.2% (95% CI, 14.4%–62.3%) ischemic strokes per year, chi-square = 4.9, $P = .027$. The final model for future ischemic stroke had a c-statistic of 0.70 and included initial ischemic stroke (hazard ratio = 3.4; 95% CI, 1.0–12.0; $P = .053$) and vessel wall enhancement (hazard ratio = 2.5; 95% CI, 0.9–7.0; $P = .080$).

CONCLUSIONS: Vessel wall enhancement is associated with both acute and future stroke in patients with cerebral amyloid angiopathy.

ABBREVIATIONS: CAA = cerebral amyloid angiopathy; HR = hazard ratio; PR = prevalence ratio; VWE = vessel wall enhancement; vwMRI = vessel wall MR imaging; AIS = acute ischemic stroke; SPACE = sampling perfection with application-optimized contrasts by using different flip angle evolutions

Vessel wall enhancement (VWE) can be detected using vessel wall MR imaging (vwMRI) using flow-suppressed, contrast-enhanced black-blood T1-weighted sequences.^{1,2} In the setting of

intracranial atherosclerosis, VWE is a known independent risk factor for acute ischemic stroke (AIS).^{3,4} Other pathologies also affect the vessel wall, including vasculitis, reversible cerebral vasoconstriction syndrome, and Moyamoya disease and their findings on vwMRI that have been previously described.^{1,5,6} Very recently, a case series found VWE in 2 of 5 patients (40%) with cerebral amyloid angiopathy (CAA).⁷ Although this small study showed

Received October 12, 2020; accepted after revision December 11.

From the Department of Radiology (J.S.M., A.S., M.D.A., S.-E.K.), Utah Center for Advanced Imaging Research; Utah, and Departments of Pathology (J.A.S.), Neurosurgery (S.T.M.), Internal Medicine (G.J.S.), and Neurology (L.D.D., A.H.d.H.), University of Utah, Salt Lake City, Utah

Gregory J. Stoddard performed statistical analyses.

This work was supported by the American Heart Association Scientist Development Grant 17SDG33460420 (McNally), NIH/NINDS K23NS105924 (A.H.H.), a grant from the National Institutes of Health R01 HL127582 (S.-E.K., J.S.M.). This investigation was supported by the University of Utah Population Health Research (PHR) Foundation, with funding in part from the National Center for Research Resources and the National Center for Advancing Translational Sciences, National Institutes of Health, through Grant UL1TR001067-05, 8UL1TR0010105 and UL1RR025764).

Please address correspondence to Scott McNally, MD, PhD, University of Utah, Department of Radiology, 30 North 1900 East #1A071, Salt Lake City, UT 84132-2140; e-mail: scott.mcnally@hsc.utah.edu

Indicates open access to non-subscribers at www.ajnr.org

Indicates article with online supplemental data.

<http://dx.doi.org/10.3174/ajnr.A7047>

that VWE can occur in patients with noninflammatory CAA, its neurologic impact is unknown.

In addition to lobar hemorrhage, CAA is an important cause of transient neurologic complaints (amyloid spells), cognitive impairment, and ischemic infarcts.⁸⁻¹⁰ The pathogenesis of CAA is complex and related to amyloid- β deposition in the small- to medium-sized vessel walls, resulting in necrosis, vessel rupture, or thrombosis.¹¹⁻¹³ Because of this, imaging techniques that highlight vessel wall pathology, such as vwMRI, may have diagnostic and prognostic impact in patients with CAA. Brain imaging currently plays a vital role in CAA diagnosis using the modified Boston criteria.¹⁴ The most common acute imaging finding in patients with CAA is hemorrhage from vessel rupture.¹⁵ Microinfarcts can be seen in animal models of CAA¹⁶ and are present in 30%–60% of patients with CAA,^{17,18} contributing to cortical thinning.¹⁹ CAA imaging criteria depend primarily on the presence of prior hemorrhage on susceptibility-weighted sequences,²⁰ including siderosis and microhemorrhages in lobar, cortical- or subcortical locations.¹⁴ CAA disproportionately affects older adults, with increasing prevalence after age 60 years.²¹ Because of this, the modified Boston criteria for CAA use a threshold of 55 years or older.

Patients with CAA often undergo work-up for acute neurologic deficits concerning for ischemic stroke, which can be detected on MR imaging.²² Evaluation of ischemic stroke risk in patients with CAA has important diagnostic and prognostic impact because it is a significant contributor to cognitive decline.²³ These patients have complex medical histories, and because vessel wall pathology may not easily be seen with lumen imaging, this necessitates further evaluation with vessel wall imaging techniques. Because of their complicated nature, neurology consultation and vwMRI are often performed in the work-up of patients with CAA at our institution. In light of this and given the importance of VWE in a variety of intracranial vasculopathies, our goal was to determine the association of VWE with AIS in patients with CAA undergoing vwMRI during stroke work-up. In this study, we evaluated both acute concurrent and future ischemic stroke risk while controlling for potential cerebrovascular confounders. Our hypothesis was that in patients with CAA, VWE would be associated with both concurrent and future ischemic stroke.

MATERIALS AND METHODS

The data in this manuscript are available upon reasonable request.

Study Design and Cohort

Institutional review board approval was obtained before this retrospective study at our academic center from 2015 to 2019 in patients undergoing vwMRI for acute neurologic deficits concerning for ischemic stroke. Because of the retrospective nature, informed consent was not required by the institutional review board. In this protocol, all patients with CAA included had probable or possible CAA (based on modified Boston criteria and microhemorrhages detected before vwMRI) and documented acute focal neurologic deficits warranting vwMRI during the stroke work-up. All patients with CAA admitted under the neurology team with suspected stroke during this time period underwent vwMRI work-up per protocol. Although a few scans exhibited mild motion artifacts, none was sufficient to exclude

any participants from interpretation. Chart review was used to determine age, sex, and other potential cerebrovascular confounders at the time of vwMRI.

CAA Diagnosis

Patients diagnosed with probable or possible CAA were included in this study. Modified Boston criteria were used by a vascular neurologist to diagnose CAA.¹⁴ Briefly, modified Boston criteria for probable CAA included age 55 years or older, appropriate clinical history, and MR imaging age findings demonstrating either 1) multiple hemorrhages restricted to lobar, cortical, or corticosubcortical regions of varying sizes or ages without another cause or 2) a single lobar, cortical, or corticosubcortical hemorrhage and focal (≤ 3 sulci) or disseminated (> 3 sulci) cortical superficial siderosis without another cause. Cases of possible CAA were also included based on the modified Boston criteria definition: single lobar, cortical, or corticosubcortical hemorrhage without other cause. Twelve of our CAA cases were also confirmed with biopsy.

vwMRI Protocol

All MR imaging was obtained at 3T on Verio, Trio, or Prisma platforms (Siemens) with standard head coils and a standard contrast dose of MultiHance (Bracco), 0.1 mmol/kg. Sequences included those in the Online Supplemental Data. The sampling perfection with application-optimized contrasts by using different flip angle evolutions (SPACE; Siemens) sequences were acquired with delay alternating with nutation for tailored excitation flow suppression.²⁴ Images were obtained in this order—precontrast: DWI, SWI, TOF, T2 SPACE, T1 SPACE and postcontrast: TOF and T1 SPACE.

Brain Parenchymal Findings

Both acute and future ischemic stroke were determined using the American Heart Association definition of CNS infarction as previously described.²⁵ Briefly, acute or future ischemic stroke was defined by brain cell death attributable to ischemia based on 1) imaging evidence of cerebral infarction or 2) clinical symptoms persisting ≥ 24 hours, with other causes excluded. We also reviewed neurovascular clinic or inpatient charts to determine presence of AIS occurring at the time of imaging for concurrent stroke and at follow-up visits or neuroimaging for future stroke. Although all patients with CAA in this study had the clinical suspicion of stroke, only DWI-positive and low-ADC value acute infarcts were included as positive for AIS. In addition, the DWI positive infarct did not have to necessarily explain the patient's presentation and could be included even if clinically silent. The variable time between symptom onset and MR imaging was included as a potential confounder in the statistical analysis. Acute infarct was defined using DWI derived from DTI trace images described previously with parameters in the Online Supplemental Data.²⁶ DTI trace outperforms conventional diffusion-weighted sequences in detecting acute infarcts.²⁷ Brain DWI was interpreted by a subspecialty-trained, Certificate of Added Qualification–certified neuroradiologist blinded to vascular imaging. Follow-up imaging was only performed if patients developed an additional new, acute neurologic deficit concerning for ischemic stroke. DWI was the primary imaging determinant for both acute and future ischemic infarct in all patients. Although we had access to both CT and

FLAIR imaging for all patients, these did not show additional interval infarcts not detected by DWI. Acute hemorrhage was also diagnosed on a CT scan by a neuroradiologist blinded to vascular imaging.

Vessel Wall Enhancement

Two separate board-certified radiologists evaluated VWE using T1 SPACE pre- and postcontrast sequences on vwMRI, blinded to additional imaging or clinical information. In cases of disagreement, a third radiologist was used as a tiebreaker. A signal threshold was used for VWE positivity using signal at or above the pituitary infundibulum as previously described.^{1,3} VWE was graded in a binary manner—either positive or negative for the entire set of brain images of each patient. This was done for the whole brain without regard to vascular segment, nor was it necessarily coupled with the area of DWI positivity. In addition to evaluating whole-brain VWE, we evaluated territorial VWE in patients with acute ischemic infarcts. VWE was evaluated in medium to small artery walls and only in vessels with confirmed arterial flow visible on TOF (including the first- through fourth-order branches of the circle of Willis). The TOF was only used to confirm the vessel was an artery and not a vein, and the VWE readers did not simultaneously grade the TOF for stenosis (see later discussion). Enhancement along a single vessel wall was considered positive, though in all positive patients, >1 vessel was involved.

Stenosis on vwMRI

Maximum percent diameter stenosis was determined per the Warfarin-Aspirin Symptomatic Intracranial Disease trial measurement of intracranial stenosis.²⁸ The subspecialty-trained, Certificate of Added Qualification–certified neuroradiologist determined stenosis blinded from DWI and VWE images at the time of TOF evaluation (and performed after a 2-month washout period). Of all intracranial arteries visible on TOF, the artery with maximum stenosis was selected using a combination of axial imaging, multiplanar reformats, maximum intensity projections, and 3D reformats. Then the diameter (b) at the level of maximal stenosis and diameter (a) of the downstream vessel distal to the stenosis were used to calculate percent diameter stenosis using the formula $[(a-b)/a] \times 100\%$. Stenosis was measured at the narrowest segment of the vessel (b) perpendicular to the long axis of the vessel on multiplanar reformats using a submillimeter measurement tool. From the Warfarin-Aspirin Symptomatic Intracranial Disease trial, in cases in which the downstream segment of the vessel was diseased, a proximal normal vessel segment was used for the comparison diameter (a). In cases in which the entire vessel was diseased, the contralateral vessel was used for the comparison diameter (a).

Interrater Reliability

For interrater reliability, we evaluated an equal number of negative control participants alongside the patients with CAA. This group of CAA-negative patients were age-matched (older than 55 years old) and had undergone vwMRI during the same time period, with the same protocol, and in the same scanners. These patients had no evidence of probable or possible CAA, vascular stenosis, aneurysm, or acute stroke or hemorrhage. Interrater reliability for the binary vwMRI measurement of positive or negative enhancement

was calculated in the combined group of CAA and negative control participants blinded to all other imaging and clinical covariates using prevalence- and bias-adjusted kappa statistics.

Statistical Analysis

Univariable binary Poisson regression, with robust standard errors, was used in the patients with CAA to determine the prevalence ratio (PR) of vwMRI factors, as well as clinical confounders for concurrent AIS as determined by retrospective chart review. These confounders included maximum percent stenosis, age, female sex, hypertension, hyperlipidemia, diabetes, smoking, antiplatelet use, anticoagulation use, antihypertension use, and statin use. Systemic inflammatory markers (erythrocyte sedimentation rate and C-reactive protein) were also recorded in 30 of the 50 patients with CAA. The time between symptom onset and MR imaging was also evaluated in relation to AIS. Next, all potential confounding variables with $P < .20$ from the univariable analysis were placed in an initial multivariable binary Poisson regression model with robust standard errors for the prediction of AIS; then variables were eliminated in a backward fashion until all remaining variables met the threshold $P < .20$.

Accuracy of the prediction of AIS was determined using the area under the receiver operating characteristic curve, also called the c-statistic. Lastly, we investigated whether the presence of VWE predicted future ischemic stroke using Kaplan-Meier survival analysis to estimate the ischemic event rate. Ischemic event rates per 100 person-years were calculated for each outcome, and the formula $\text{annual risk} = 1(\exp[-\text{event rate} \times \text{time}])$ was used to estimate the absolute annual risk. Time to event was further analyzed for stroke by use of univariable followed by multivariable Cox regression analysis. After univariable analysis, factors with $P < .20$ were placed in an initial multivariable model; then variables underwent backward elimination to a threshold $P < .20$. All patients were followed up by chart review for interval stroke symptoms to the end of the study in 2019. Cox regression was used to account for variable times to event.

In binary outcome models, 5 outcome events for every predictor are sufficient to avoid overfitting.²⁹ Our final model for future stroke met this. The final Poisson regression model, however, did not, and this is known to increase the likelihood of finding false-positive predictors.³⁰ To assess the stability of the final Poisson model, the bootstrap inclusion fraction was computed for each predictor, which is the percentage of times the variable remains in the final model in a large number of bootstrap resamples in which the variable selection is repeated.^{31,32} Predictors with bootstrap inclusion fractions <50% were dropped from the final model as unreliable because these would not likely remain as significant predictors in future datasets.

All statistical analyses were performed using Stata-15.1 statistical software (StataCorp).

RESULTS

CAA Study Population

Characteristics of the patients with CAA are listed in Table 1. A total of 50 patients met CAA study criteria, with vwMRI obtained within 7 days of stroke symptom onset. These patients included those with probable (43/50) and possible (7/50) CAA; 35/50

(70.0%) patients had AIS, 23/50 (46.0%) had acute hemorrhage, and 19/50 (38.0%) had both. Potential confounders included maximum percent stenosis (14.9 ± 20.8 , mean \pm SD), patient age (71.9 ± 7.7 years), female sex (27/50, 54.0%), hypertension (43/50, 86.0%), hyperlipidemia (32/50, 64.0%), diabetes (14/50, 28.0%), smoking (19/50, 38.0%), antiplatelet use (18/50, 36.0%), anticoagulant use (5/50, 10.0%), antihypertensive use (37/50, 74.0%), statin use (27/50, 54.0%), time between symptom onset and MR imaging (3.9 ± 2.6 days), and elevated inflammatory markers, which were recorded in 30 patients (10, 33.3%).

VWE Interrater Reliability

The 50 patients with CAA were combined with 50 negative control participants without CAA, acute hemorrhage, ischemic stroke, or vascular pathology. Patients with CAA demonstrated VWE (29/50, 58.0%), whereas negative control participants did not (0/50, 0.0%). Fig 1 illustrates 3 separate patients with CAA with variable degrees

of VWE including a VWE negative scan, a single VWE positive artery on a single image, and a VWE positive scan with multiple arteries involved on the same image. In the combined group of 50 CAA and 50 negative control patients, the radiology reviewers agreed 91/100 times with a third tie-breaker used 9 times. Interrater reliability for VWE was “substantial,” with a prevalence- and-bias-corrected kappa = 0.82 (95% CI, 0.71–0.93).

Factors Associated with Acute Ischemic Stroke in Patients with CAA

A representative patient with CAA presenting with AIS and VWE is shown in Fig 2. Leptomeningeal and brain biopsy was also performed in this particular patient as shown in the Online Supplemental Data. In this index case, pathology showed evidence of CAA coupled with vessel wall inflammation. Overall, 35/50 patients with CAA were positive for AIS, and 23 of these were VWE positive, with 22/23 matched to the vascular territory (95.7%). There were 5/50 patients with CAA with >50% stenosis and 0/50 with >70% stenosis. Of those with >50% stenosis, 1/5 had an acute ischemic infarct within the stenosis territory, though this patient did not have a future ischemic stroke. Univariable analysis with factors and potential confounders associated with AIS are depicted in Table 2.

Factors associated with concurrent AIS meeting the $P < .20$ threshold were entered into the initial multivariable model. These included: VWE (PR = 1.6; 95% CI, 1.0–2.5; $P = .044$), age (PR = 1.01; 95% CI, 0.99–1.05; $P = .146$), diabetes (PR = 1.3; 95% CI, 1.0–1.9; $P = .080$), time between symptom onset and MR imaging (PR = 0.9; 95% CI, 0.8–1.0; $P = .006$) and smoking (PR = 0.7; 95% CI, 0.4–1.1; $P = .095$). These did not include maximum percent stenosis (PR = 1.6; 95% CI, 0.7–3.6; $P = .297$) or other confounders. Also, in the 30 patients with recorded systemic inflammatory markers, these were not associated with AIS (PR = 1.2; 95% CI, 0.9–1.7; $P = .282$). After sequential backwards elimination to a threshold $P < .20$, 4 factors remained in the final model: VWE (PR = 1.5; 95% CI, 1.1–2.2; $P = .022$), age (PR = 1.02; 95% CI, 1.0–1.05; $P = .036$), time between symptoms and MR imaging (PR = 0.9; 95% CI, 0.8–0.9; $P < .001$), and smoking (PR = 0.7; 95% CI, 0.5–1.0; $P = .042$). The final model discriminatory value

Table 1: Characteristics of patients with CAA

Patient Characteristic	n = 50
Probable CAA, n (%)	43 (86.0)
Biopsy proved, n (%)	12 (24.0)
Possible CAA, n (%)	7 (14.0)
Neurologic outcomes	
Ischemic stroke, n (%)	35 (70.0)
Hemorrhage, n (%)	23 (46.0)
Both, n (%)	19 (38.0)
VWE	29 (58.0)
Clinical confounders	
Maximum percent stenosis, mean (SD)	14.9 (20.8)
Age, mean (SD), y	71.9 (7.7)
Female sex, n (%)	27 (54.0)
Hypertension, n (%)	43 (86.0)
Hyperlipidemia, n (%)	32 (64.0)
Diabetes, n (%)	14 (28.0)
Smoking, n (%)	19 (38.0)
Antiplatelet, n (%)	18 (36.0)
Anticoagulation, n (%)	5 (10.0)
Antihypertension, n (%)	37 (74.0)
Statin, n (%)	27 (54.0)
Time between symptom onset and MR imaging in days, mean (SD)	3.9 (2.6)
Inflammatory marker elevation, n (%), n = 30 available	10 (33.3)

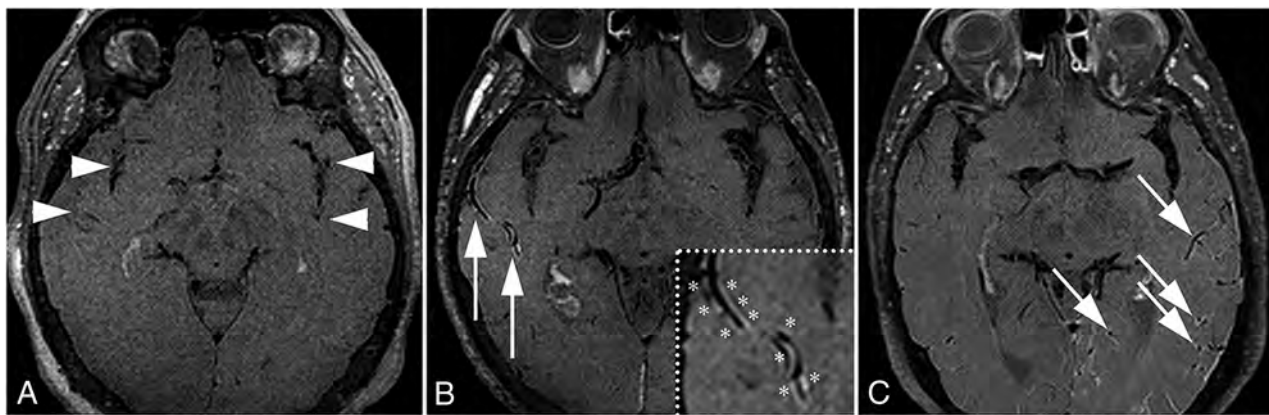


FIG 1. Variation of VWE findings in patients with CAA. A, This patient with CAA had no VWE along the intracranial arteries (arrowheads). B, There was VWE along a single right MCA branch in the representative image (arrows, inset with asterisks). C, There were multiple left MCA branches with VWE on the same image (arrows).

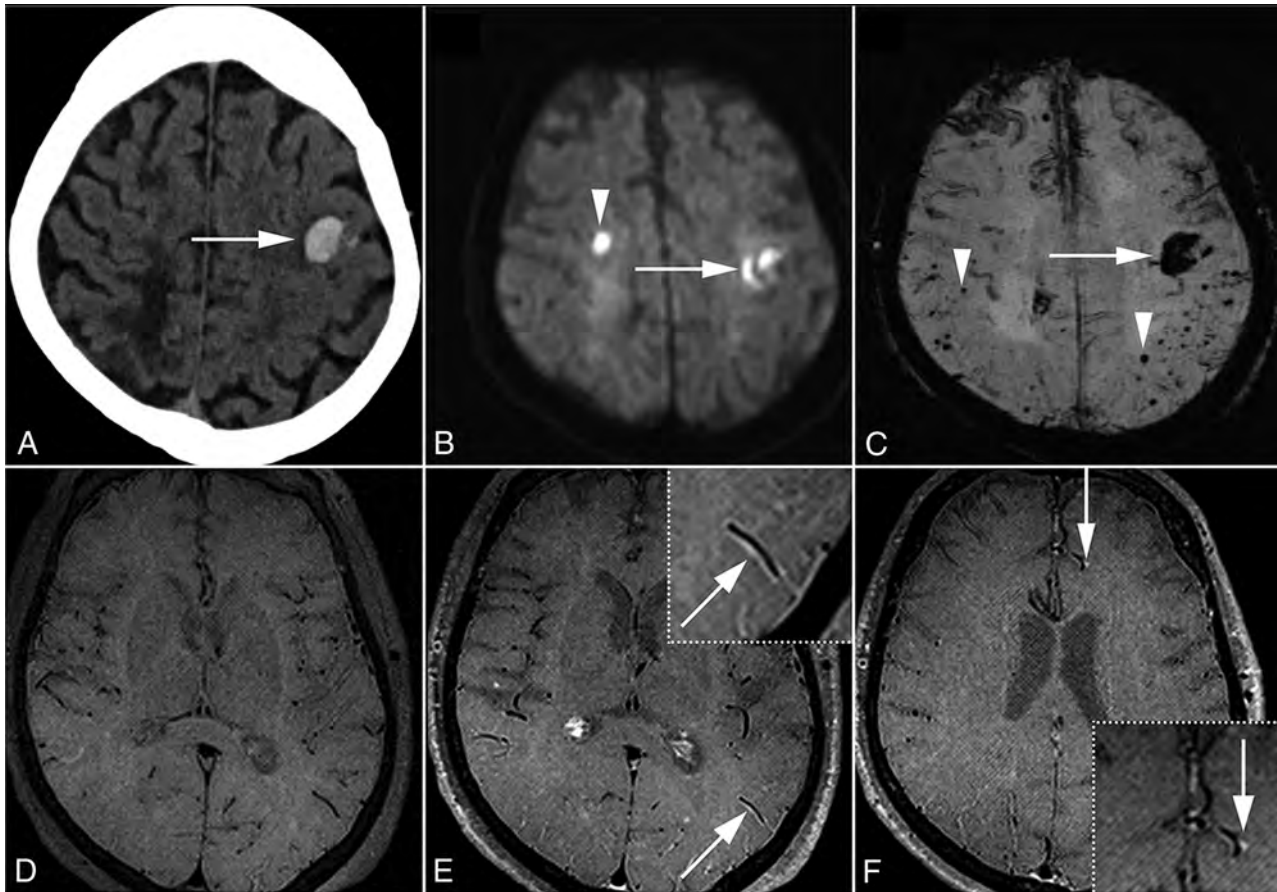


FIG 2. Representative patient with CAA with acute hemorrhage, AIS, and VWE. This 69-year-old woman with acute right hand incoordination and aphasia. Acute left frontal parenchymal hemorrhage was detected on CT (A, arrow). DWI showed a small acute right frontal infarct (B, arrowhead) in addition to the hemorrhage (arrow). SWI demonstrated multiple peripheral and subcortical microhemorrhages (C, arrowheads) in addition to the acute hemorrhage (arrow). Vessel wall imaging with pre- (D) and postcontrast T1 SPACE (E and F) revealed VWE along arterial branches (E, arrow, inset; F, arrow, inset).

Table 2: Univariable Poisson regression CAA vwMRI findings and AIS

Stroke Predictor	Stroke (-) (n = 15)	Stroke (+) (n = 35)	Univariable PR (95% CI)	P Value
VWE, n (%)	5 (33.3)	24 (68.6)	1.6 (1.0–2.5)	.044
Maximum percent stenosis, mean (SD)	10.3 (20.7)	16.9 (20.8)	1.6 (0.7–3.6)	.297
Age, mean (SD)	69.4 (8.5)	73.0 (7.2)	1.01 (0.99–1.05)	.146
Female, n (%)	7 (46.7)	20 (57.1)	1.1 (0.8–1.7)	.507
Hypertension, n (%)	13 (86.7)	30 (85.7)	1.0 (0.6–1.6)	.928
Hyperlipidemia, n (%)	10 (66.7)	22 (62.9)	1.0 (0.7–1.4)	.796
Diabetes, n (%)	2 (13.3)	12 (34.3)	1.3 (1.0–1.9)	.080
Smoking, n (%)	9 (60.0)	11 (31.4)	0.7 (0.4–1.1)	.095
Antiplatelet, n (%)	5 (33.3)	13 (37.1)	1.1 (0.7–1.5)	.796
Anticoagulation, n (%)	1 (6.7)	4 (11.4)	1.2 (0.7–1.9)	.546
Antihypertension, n (%)	12 (80.0)	25 (71.4)	0.9 (0.6–1.3)	.499
Statin, n (%)	8 (53.3)	19 (54.3)	1.0 (0.7–1.5)	.951
Time between symptom onset and MR imaging in days, mean (SD)	5.5 (2.4)	3.2 (2.3)	0.9 (0.8–1.0)	.006
Inflammatory marker elevation, n (%), n = 30 available	1 (16.7) n = 6	9 (37.5) n = 24	1.2 (0.9–1.7)	.282

Note:—Univariable Poisson regression was initially performed with PR values, with 95% CI and P values above. All potential confounding variables with $P < .20$ from the univariable analysis were placed in an initial multivariable Poisson regression model for AIS; then variables were eliminated in a backward fashion to the threshold $P < .20$. Four factors remained in the final multivariable regression model for AIS: VWE (PR = 1.5; 95% CI, 1.1–2.2; $P = .022$), age (PR = 1.02; 95% CI, 1.0–1.05; $P = .036$), time between symptoms and MR imaging (PR = 0.9; 95% CI, 0.8–0.9; $P < .001$), and smoking (PR = 0.7; 95% CI, 0.5–1.0; $P = .042$).

was c-statistic = 0.92 (95% CI, 0.84–0.99). The bootstrap inclusion fraction was computed for each predictor, and all variables in the final model were stable, meaning the results were not due to overfitting.

Future Stroke Prediction

In this study patients with CAA had an overall time at risk of 37.5 person-years and incident stroke event rate of 49.7% (95% CI, 34.5%–67.2%) per year. Kaplan-Meier survival analysis (Fig 3) demonstrated significantly shorter stroke-free survival with VWE. VWE-positive patients with CAA had a higher ischemic event rate of 63.9% (95% CI, 43.2%–84.0%) per year compared with VWE-negative patients with CAA with 32.2% (95% CI, 14.4%–62.3%) per year, with chi-square = 4.9 and $P = .027$. Univariable Cox regression analysis for

stroke showed that 3 factors significantly increased future stroke risk: initial stroke (hazard ratio [HR] = 4.2; 95% CI, 1.2–14.3; $P = .023$), VWE (HR = 3.1; 95% CI, 1.1–8.6; $P = .027$), and

smoking (HR = 0.5; 95% CI, 0.2–1.3; $P = .135$). These were the only variables with $P < .20$ from the univariable analysis and were placed in the initial multivariable Cox regression model. After multivariable regression, only 2 variables remained in the final model at the $P < .20$ threshold and predicted future ischemic stroke with a c-statistic of 0.70. The final model consisted of initial ischemic stroke (HR = 3.4; 95% CI, 1.0–12.0; $P = .053$) and VWE (HR = 2.5; 95% CI, 0.9–7.0; $P = .080$).

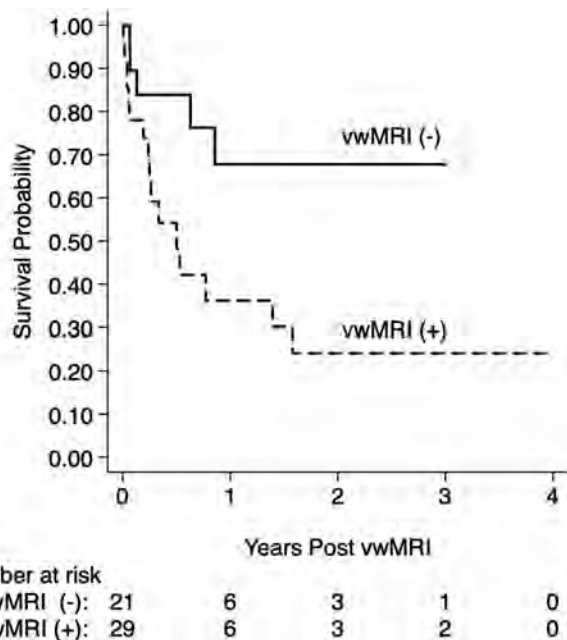


FIG 3. Future stroke risk analysis. Kaplan-Meier survival curves are shown for patients with CAA with versus without VWE, vwMRI (+) versus (-). In the 50 participants, the total time at risk was 37.5 person-years, and incidence event rate of ischemic stroke was 49.7% (95% CI, 34.5%–67.2%) per year. Patients with CAA with VWE demonstrated significantly shorter stroke-free survival with an event rate of 63.9% (95% CI, 43.2%–84.0%) per year compared with 32.2% (95% CI, 14.4%–62.3%), chi-square = 4.9, $P = .027$. As discussed in Table 3, multivariable Cox regression followed by backward elimination to a threshold P value of 0.20 showed that VWE was 1 of 2 factors remaining in the final future stroke prediction model (VWE HR = 2.5; 95% CI, 0.9–7.0; $P = .080$ and initial ischemic stroke HR = 3.4; 95% CI, 1.0–12.0; $P = .053$).

DISCUSSION

This study adds support to the growing literature on ischemic stroke risk in CAA by investigating the prognostic impact of vwMRI. Our data show that vwMRI can identify VWE in patients with CAA with high interrater reliability, paralleling previous studies in other vasculopathies.^{1,3} Furthermore, VWE was an essential predictor of both acute and future ischemic stroke in CAA, with VWE associated with significantly shorter stroke-free survival.

Ischemic stroke occurs often in patients with CAA despite negative angiographic imaging.^{33,34} Our study confirms the lack of association with lumen stenosis. This corresponds to prior work finding no association between vascular occlusion or stenosis with white matter hyperintensities in CAA.^{35,36} Although lumen imaging lacks the resolution of small-vessel pathology, this limitation does not appear to affect contrast leakage as detected by vwMRI. Our observed 70% prevalence for concurrent ischemic infarcts and 42% prevalence of future stroke is slightly higher than previously reported acute microinfarcts in 30%–60% of patients with CAA.^{17,18} This may reflect some degree of selection bias, given that only symptomatic patients with CAA underwent vwMRI. Because of this, these data should be applied to symptomatic patients with CAA presenting with acute neurologic deficits. Variable time between stroke symptom onset and vwMRI was a potential limitation, though this was accounted for in the final regression model and VWE remained associated with AIS. Other potential limitations include variable follow-up methods and time periods for stroke follow-up evaluation.

Table 3: Univariable Cox regression for future ischemic stroke

Stroke Predictor	Future Stroke (-) (n = 29)	Future Stroke (+) (n = 21)	Univariable HR (95% CI)	P Value
Initial stroke, n (%)	17 (58.6)	18 (85.7)	4.2 (1.2–14.3)	.023
VWE, n (%)	13 (44.8)	16 (76.2)	3.1 (1.1–8.6)	.027
Maximum percent stenosis, mean (SD)	17.1 (22.5)	11.9 (18.3)	0.7 (0.1–6.4)	.723
Age, mean (SD)	72.6 (8.2)	71.0 (7.1)	1.0 (0.9–1.0)	.651
Female, n (%)	13 (44.8)	14 (66.7)	1.5 (0.6–3.7)	.397
Hypertension, n (%)	24 (82.8)	18 (90.5)	1.7 (0.4–7.1)	.499
Hyperlipidemia, n (%)	17 (58.6)	15 (71.4)	1.3 (0.5–3.5)	.552
Diabetes, n (%)	7 (24.1)	7 (33.3)	1.3 (0.5–3.3)	.571
Smoking, n (%)	14 (48.3)	6 (28.6)	0.5 (0.2–1.3)	.135
(interval) Antiplatelet, n (%)	9 (31.0)	6 (28.6)	0.8 (0.3–2.1)	.649
(interval) Anticoagulation, n (%)	3 (10.3)	1 (4.8)	0.4 (0.05–2.8)	.336
(interval) Antihypertension, n (%)	23 (79.3)	17 (81.0)	1.3 (0.4–3.8)	.662
(interval) Statin, n (%)	22 (75.9)	14 (66.7)	0.7 (0.3–1.6)	.372
(interval) Immunosuppression, n (%)	7 (24.1)	10 (47.6)	1.5 (0.7–3.7)	.322
Elevated inflammatory markers, n (%), n = 30 available	5 (33.3) n = 15	5 (33.3) n = 15	1.1 (0.4–3.1)	.928

Note:—Interval indicates interval treatment with the listed medication as a potential confounder.

Univariable Cox regression was initially performed with HR values, with 95% CI and P values below. All potential confounding variables with $P < .20$ from the univariable analysis were placed in an initial multivariable Cox regression model for future ischemic stroke; then variables were eliminated in a backward fashion to the threshold $P < .20$. Two factors remained in the final multivariable regression model for future ischemic stroke: initial ischemic stroke (HR = 3.4; 95% CI, 1.0–12.0; $P = .053$) and VWE (HR = 2.5; 95% CI, 0.9–7.0; $P = .080$).

Another limitation was the single-center nature, though multiple different scanners and separate observers were used for internal validation. With the growing clinical use of vwMRI it should soon be possible to confirm these findings at additional centers, potentially with future multicenter studies. Additionally, our study was not designed to determine best treatment or preventative strategies against future ischemic stroke in CAA. Although some additional confounders were associated with initial ischemic stroke, future stroke prevention is the critical issue. Also, although our study did not include asymptomatic CAA control participants, the patients with CAA without acute or follow-up infarcts on DWI served as the comparator groups in our regression analyses. A future study on asymptomatic patients with CAA could determine silent stroke risk in this population.

Our dataset also had limited information on VWE linked with CAA-related inflammation, which is characterized by rapid cognitive decline, vascular inflammation, and lobar edema.^{37,38} Systemic inflammation did not contribute to stroke risk in our group of patients with CAA, though the role of local inflammation is not yet well defined. Although most patients did not undergo biopsy, 1 patient in the Online Supplemental Data showed CAA-related inflammation on pathology that corresponded with VWE. It is clear though that VWE does not always meet the threshold of pathology-defined CAA-related inflammation related to leukocyte infiltration.⁷ Local proinflammatory cascades may still be activated, resulting in endothelial dysfunction and contrast leakage before overt leukocyte infiltration on pathology. The traditional dichotomy of CAA with or without inflammation may instead represent a spectrum of proinflammatory cascades as with other neuroimmunologic diseases, including multiple sclerosis.³⁹ Without an overt link to inflammation on pathology, however, the use of novel immunotherapies in patients with CAA with VWE remains premature.

The strengths of this imaging study include a sizable number of patients with CAA undergoing unique evaluation with vwMRI. Although the retrospective design is a limitation, this applies to most imaging studies of patients with CAA. More important, our conclusions are relevant to symptomatic patients with CAA in whom diagnostic and treatment decisions are made on an urgent basis, and there was a high risk of future stroke correlated with VWE on initial vwMRI, which allows for prognostication in these patients. Also, despite the minority of patients undergoing confirmatory biopsy, the results remain generalizable to patients with suspected CAA by imaging. By evaluating all participants with CAA who underwent imaging, these results translate to clinical practice in the work-up of acute neurologic deficits or rapid neurologic decline. These patients with CAA tend to benefit the most from rapid diagnosis, stroke prevention strategies, and close follow-up. Future research is warranted to develop or identify treatment strategies against the CAA disease processes leading to VWE.

CONCLUSIONS

VWE can be reliably detected on black-blood vwMRI in patients with CAA presenting with new-onset focal neurologic symptoms, and this is associated with AIS. VWE was highly associated with concurrent AIS on multivariable regression analysis. Most important, initial stroke and VWE were essential factors predicting

future ischemic stroke risk in this cohort of patients with CAA. The use of vwMRI can have diagnostic and prognostic impact in this high-risk population and may serve as the target for future trials aimed at decreasing stroke risk.

Disclosures: J. Scott McNally—RELATED: Grant: AHA, NIH, Comments: This work was supported by the American Heart Association Scientist Development Grant 17SDG33460420 (McNally), NIH/NINDS K23NS105924 (A.H.H.), a grant from the National Institutes of Health R01 HL127582 (S.-E.K., J.S.M.), and a grant from the National Institutes of Health, UL1TR002538 (G.J.S.)*. Gregory Stoddard—UNRELATED: Grants/Grants Pending: NIH, Comments: A grant supports the statistical core I worked for, but it is not specific to this project. The NIH has requested we mention their grant numbers as an acknowledgment in the manuscript when I work on a project: This investigation was supported by the University of Utah Population Health Research (PHR) Foundation, with funding in part from the National Center for Research Resources and the National Center for Advancing Translational Sciences, National Institutes of Health, through Grant UL1TR002538 (formerly 5UL1TR001067-05, 8UL1TR000105 and UL1RR025764)*. Adam de Havenon—UNRELATED: Grants/Grants Pending: NIH/NINDS.* *Money paid to institution.

REFERENCES

- Mossa-Basha M, Hwang WD, De Havenon A, et al. **Multicontrast high-resolution vessel wall magnetic resonance imaging and its value in differentiating intracranial vasculopathic processes.** *Stroke* 2015;46:1567–73 CrossRef Medline
- Alexander MD, de Havenon A, Kim SE, et al. **Assessment of quantitative methods for enhancement measurement on vessel wall magnetic resonance imaging evaluation of intracranial atherosclerosis.** *Neuroradiology* 2019;61:643–50 CrossRef Medline
- de Havenon A, Mossa-Basha M, Shah L, et al. **High-resolution vessel wall MRI for the evaluation of intracranial atherosclerotic disease.** *Neuroradiology* 2017;59:1193–1202 CrossRef Medline
- Kim JM, Jung KH, Sohn CH, et al. **Intracranial plaque enhancement from high resolution vessel wall magnetic resonance imaging predicts stroke recurrence.** *Int J Stroke* 2016;11:171–79 CrossRef Medline
- Mossa-Basha M, de Havenon A, Becker KJ, et al. **Added value of vessel wall magnetic resonance imaging in the differentiation of Moyamoya vasculopathies in a non-Asian cohort.** *Stroke* 2016;47:1782–88 CrossRef Medline
- Mossa-Basha M, Alexander M, Gaddikeri S, et al. **Vessel wall imaging for intracranial vascular disease evaluation.** *J Neurointerv Surg* 2016;8:1154–59 CrossRef Medline
- Hao Q, Tsankova NM, Shoirah H, et al. **Vessel wall MRI enhancement in noninflammatory cerebral amyloid angiopathy.** *AJNR Am J Neuroradiol* 2020;41:446–48 CrossRef Medline
- Kimberly WT, Gilson A, Rost NS, et al. **Silent ischemic infarcts are associated with hemorrhage burden in cerebral amyloid angiopathy.** *Neurology* 2009;72:1230–35 CrossRef Medline
- Gregoire SM, Charidimou A, Gadapa N, et al. **Acute ischaemic brain lesions in intracerebral haemorrhage: multicentre cross-sectional magnetic resonance imaging study.** *Brain* 2011;134:2376–86 CrossRef Medline
- Vallat W, Maundrell A, Leyden J, et al. **Cerebral amyloid angiopathy causing cortical microinfarction.** *J Clin Neurosci* 2013;20:1802–04 CrossRef Medline
- Mandybur TI. **Cerebral amyloid angiopathy: the vascular pathology and complications.** *J Neuropathol Exp Neurol* 1986;45:79–90 Medline
- Vonsattel JP, Myers RH, Hedley-Whyte ET, et al. **Cerebral amyloid angiopathy without and with cerebral hemorrhages: a comparative histological study.** *Ann Neurol* 1991;30:637–49 CrossRef Medline
- Yamada M. **Cerebral amyloid angiopathy: emerging concepts.** *J Stroke* 2015;17:17–30 CrossRef Medline
- Linn J, Halpin A, Demaerel P, et al. **Prevalence of superficial siderosis in patients with cerebral amyloid angiopathy.** *Neurology* 2010;74:1346–50 CrossRef Medline

15. Smith EE, Eichler F. **Cerebral amyloid angiopathy and lobar intracerebral hemorrhage.** *Arch Neurol* 2006;63:148–51 CrossRef Medline
16. Milner E, Zhou ML, Johnson AW, et al. **Cerebral amyloid angiopathy increases susceptibility to infarction after focal cerebral ischemia in Tg2576 mice.** *Stroke* 2014;45:3064–69 CrossRef Medline
17. van Veluw SJ, Charidimou A, van der Kouwe AJ, et al. **Microbleed and microinfarct detection in amyloid angiopathy: a high-resolution MRI-histopathology study.** *Brain* 2016;139:3151–62 CrossRef Medline
18. Lauer A, van Veluw SJ, William CM, et al. **Microbleeds on MRI are associated with microinfarcts on autopsy in cerebral amyloid angiopathy.** *Neurology* 2016;87:1488–92 CrossRef Medline
19. Fotiadis P, van Rooden S, van der Grond J, et al. **Cortical atrophy in patients with cerebral amyloid angiopathy: a case-control study.** *Lancet Neurol* 2016;15:811–19 CrossRef Medline
20. Cheng AL, Batool S, McCreary CR, et al. **Susceptibility-weighted imaging is more reliable than T2*-weighted gradient-recalled echo MRI for detecting microbleeds.** *Stroke* 2013;44:2782–86 CrossRef Medline
21. Greenberg SM, Vonsattel JP. **Diagnosis of cerebral amyloid angiopathy. Sensitivity and specificity of cortical biopsy.** *Stroke* 1997;28:1418–22 CrossRef Medline
22. Ter Telgte A, Scherlek AA, Reijmer YD, et al. **Histopathology of diffusion-weighted imaging-positive lesions in cerebral amyloid angiopathy.** *Acta Neuropathol* 2020;139:799–812 CrossRef Medline
23. Hecht M, Kramer LM, von Arnim CAF, et al. **Capillary cerebral amyloid angiopathy in Alzheimer's disease: association with allocortical/hippocampal microinfarcts and cognitive decline.** *Acta Neuropathol* 2018;135:681–94 CrossRef Medline
24. Li L, Miller KL, Jezzard P. **DANTE-prepared pulse trains: a novel approach to motion-sensitized and motion-suppressed quantitative magnetic resonance imaging.** *Magn Reson Med* 2012;68:1423–38 CrossRef Medline
25. Sacco RL, Kasner SE, Broderick JP, et al. **An updated definition of stroke for the 21st century: a statement for healthcare professionals from the American Heart Association/American Stroke Association.** *Stroke* 2013;44:2064–89 CrossRef Medline
26. McNally JS, Kim SE, Yoon HC, et al. **Carotid magnetization-prepared rapid acquisition with gradient-echo signal is associated with acute territorial cerebral ischemic events detected by diffusion-weighted MRI.** *Circ Cardiovasc Imaging* 2012;5:376–82 CrossRef Medline
27. Chou MC, Tzeng WS, Chung HW, et al. **T2-enhanced tensor diffusion trace-weighted image in the detection of hyper-acute cerebral infarction: comparison with isotropic diffusion-weighted image.** *Eur J Radiol* 2010;74:e89–e94 CrossRef Medline
28. Samuels OB, Joseph GJ, Lynn MJ, et al. **A standardized method for measuring intracranial arterial stenosis.** *AJNR Am J Neuroradiol* 2000;21:643–46 Medline
29. Vittinghoff E, McCulloch CE. **Relaxing the rule of ten events per variable in logistic and Cox regression.** *Am J Epidemiol* 2007;165:710–18 CrossRef Medline
30. Vittinghoff EG, Shiboski SC, McCulloch CE. *Regression Methods in Biostatistics: Linear, Logistic, Survival, and Repeated Measures Models.* Springer-Verlag; 2005:134
31. Royston P, Sauerbrei W. **Bootstrap assessment of the stability of multivariate models.** *Stat Med* 2009;9:547–70 CrossRef Medline
32. Sauerbrei W, Schumacher M. **A bootstrap resampling procedure for model building: application to the Cox regression model.** *Stat Med* 1992;11:2093–09 CrossRef Medline
33. Menon RS, Kidwell CS. **Neuroimaging demonstration of evolving small vessel ischemic injury in cerebral amyloid angiopathy.** *Stroke* 2009;40:e675–677–e677 CrossRef Medline
34. van Veluw SJ, Lauer A, Charidimou A, et al. **Evolution of DWI lesions in cerebral amyloid angiopathy: evidence for ischemia.** *Neurology* 2017;89:2136–42 CrossRef Medline
35. Boulouis G, Charidimou A, Auriel E, et al. **Intracranial atherosclerosis and cerebral small vessel disease in intracerebral hemorrhage patients.** *J Neurol Sci* 2016;369:324–29 CrossRef Medline
36. Honda K. **Cerebral arterial occlusion did not promote the prevalence of cerebral amyloid angiopathy.** *J Alzheimers Dis* 2016;54:269–74 CrossRef Medline
37. Eng JA, Frosch MP, Choi K, et al. **Clinical manifestations of cerebral amyloid angiopathy-related inflammation.** *Ann Neurol* 2004;55:250–56 CrossRef Medline
38. Sperling R, Salloway S, Brooks DJ, et al. **Amyloid-related imaging abnormalities in patients with Alzheimer's disease treated with bapineuzumab: a retrospective analysis.** *Lancet Neurol* 2012;11:241–49 CrossRef Medline
39. Lassmann H. **Pathogenic mechanisms associated with different clinical courses of multiple sclerosis.** *Front Immunol* 2018;9:3116. CrossRef Medline

Clinical Features of Cytotoxic Lesions of the Corpus Callosum Associated with Aneurysmal Subarachnoid Hemorrhage

H. Toi, K. Yagi, S. Matsubara, K. Hara, and M. Uno



ABSTRACT

BACKGROUND AND PURPOSE: Patients with SAH due to a ruptured intracranial aneurysm occasionally show reversible high-signal lesions in the splenium of the corpus callosum on DWI. These lesions are called cytotoxic lesions of the corpus callosum. This study retrospectively reviewed cases of aneurysmal SAH and investigated clinical features of cytotoxic lesions of the corpus callosum associated with SAH.

MATERIALS AND METHODS: Participants comprised 259 patients with aneurysmal SAH who had undergone curative treatment at our hospital. We examined the following items related to cytotoxic lesions of the corpus callosum: occurrence rate, timing of appearance and disappearance of the lesions, lesion size, aneurysm location, severity of SAH, treatment method, clinical course, and outcome.

RESULTS: Among the 259 cases, DWI detected cytotoxic lesions of the corpus callosum in 33 patients (12.7%). The mean periods from the onset of SAH to detection and disappearance of cytotoxic lesions of the corpus callosum were 6.3 days (range, 0–25 days) and 35.7 days (range, 9–78 days), respectively. Cytotoxic lesions of the corpus callosum were classified into 2 types: a small type localized in the splenium in 26 cases (78.9%) and a large type spread along the ventricle in 7 cases (21.2%). The severity of SAH, coiling, hydrocephalus, and poor mRS score at discharge were significantly higher in the group with cytotoxic lesions of the corpus callosum. However, multivariate analysis did not identify cytotoxic lesions of the corpus callosum as a risk factor for poor outcome.

CONCLUSIONS: Cytotoxic lesions of the corpus callosum appear at a frequency of 12.7% in patients with aneurysmal SAH. Cytotoxic lesions of the corpus callosum associated with SAH take several days to appear and subsequently resolve within about a month. Cytotoxic lesions of the corpus callosum were likely to occur in patients with high-grade SAH but did not represent a predictor of poor outcome.

ABBREVIATIONS: CLOCC = cytotoxic lesions of the corpus callosum; DCI = delayed cerebral ischemia

MR imaging findings of cytotoxic lesions of the corpus callosum (CLOCC) are known to appear in association with various pathologic conditions such as encephalitis, encephalopathy, metabolic disorder (hypoglycemia and hypernatremia), antiepileptic drug withdrawal, alcoholism, infection, and seizure.^{1–14} A series of cases showing CLOCC associated with coronavirus disease 2019 was also recently reported.¹⁵ These lesions are clearly detectable, especially on DWI.¹³ In patients with SAH due to a ruptured intracranial aneurysm, reversible high-signal

lesions (ie, CLOCC) are sometimes observed on DWI in the splenium of the corpus callosum during the clinical course, but the frequency of appearance and associations with clinical findings remain unclear.^{14,16} The present study retrospectively reviewed cases of aneurysmal SAH and investigated the clinical features of CLOCC associated with SAH.

MATERIALS AND METHODS

Patient Data

This study included 286 patients with aneurysmal SAH who had been treated in the Department of Neurosurgery at Kawasaki Medical School between April 2009 and June 2016. Any patients who did not undergo serial MR imaging or who had SAH of unknown origin were excluded. The management, treatment, and clinical course of patients with SAH that does not require clipping or coiling, such as in perimesencephalic SAH, differ markedly in

Received August 9, 2020; accepted after revision December 1.

From the Department of Neurosurgery (H.T., K.Y., S.M., K.H., M.U.), Kawasaki Medical School, Kurashiki, Okayama, Japan; and Department of Neurosurgery (H.T.), Oita Oka Hospital, Oita, Japan.

Please address correspondence to Hiroyuki Toi, MD, PhD, Department of Neurosurgery, Kawasaki Medical School, 577 Matsushima, Kurashiki, Okayama 701-0192, Japan; e-mail: ht11251974@yahoo.co.jp

<http://dx.doi.org/10.3174/ajnr.A7055>

patients with SAH requiring treatment.¹⁷ To minimize variability in the investigated cohort, we, therefore, included only patients with an aneurysm that was identified and subsequently clipped or coiled. Patients with traumatic SAH were also excluded. The main confounder for callosal lesions in patients with SAH having experienced trauma is diffuse axonal injury. We retrospectively examined patients with aneurysmal SAH focusing on CLOCC. Clinical data were collected from the medical records of patients, and we examined the following items related to the lesion: timing of the appearance and disappearance of lesions; locations of aneurysms; history of hypertension and diabetes mellitus; severity of SAH according to both Hunt and Hess grade and Fisher group; treatment method; clinical course involving development of delayed cerebral ischemia (DCI) and/or hydrocephalus; and mRS score at discharge.

“Clinical deterioration caused by DCI” is a concept proposed by a multidisciplinary research group as an important outcome measure in patients with aneurysmal subarachnoid hemorrhage.¹⁸ Briefly, clinical deterioration caused by DCI is a secondary outcome measure in patients with aneurysmal subarachnoid hemorrhage defined as the following: “The occurrence of focal neurologic impairment (such as hemiparesis, aphasia, apraxia, hemianopia, or neglect), or a decrease of at least two points on the Glasgow Coma Scale (either on the total score or on one of its individual components [eye, motor on either side, verbal]). This should last for at least 1 hour, is not apparent immediately after aneurysm occlusion, and cannot be attributed to other causes by means of clinical assessment, CT or MR imaging scanning of the brain, and appropriate laboratory studies.”¹⁸

Imaging Methods

In all cases, DWI, FLAIR, T2WI, and MRA were performed before and after clipping or coiling with 3T scanners (Vantage Titan 3T MRT-3010, Canon Medical Systems; or Ingenia 3T CX, Philips Healthcare) or 1.5T scanners (Excelart Vantage MRT-2003, Canon Medical Systems; or Signa Excite, GE Healthcare). Acquisition parameters for DWI were the following: TR, 6000 ms; TE, 95 ms; matrix, 256 × 128 or 192 × 128; FOV, 24 cm; section thickness, 5 mm; interslice gap, 0.5; axial sections, 26; flip/flop angle, 90°/180; b-values, 0 and 1000 s/mm².

Patients underwent MR imaging at the time of admission, once in the first week, and once in the second week. In some cases, more images were obtained at the discretion of the attending physicians. We defined CLOCC as high-signal areas observable in the splenium of the corpus callosum on DWI that disappeared during follow-up. We chose DWI as the sequence to confirm the disappearance of CLOCC because of its clarity, though CLOCC can also be observed with FLAIR and T2WI. We also confirmed that CLOCC showed a reduced ADC corresponding with the DWI hyperintensity to exclude T2-shinethrough artifacts. CLOCC can be distinguished from ischemia because they also disappear on T2WI and FLAIR. We classified CLOCC into a small type localized to the splenium and a large type extending along the ventricle, in accordance with previous reports, and examined the ratio of types.^{9,16}

Treatment of Aneurysms and General Management

All patients underwent digital subtraction angiography on admission. Selection of treatment with clipping or endovascular coil

embolization resulted from a consensus reached between the treating neurosurgeon and the interventional neuroradiologist after analyzing the risks and chances of success of both therapeutic modalities for each case. All patients received 0.9% normal saline at a rate of 1 mL/kg/h, with an appropriate dosage of supplemental 5% albumin solution administered to maintain positive fluid balance. Oral statins and mineralocorticoids were not routinely administered. Persistent fever (temperature exceeding 38.5°C) was treated with acetaminophen and surface cooling devices. Angiography was routinely performed on patients in whom DCI developed, and endovascular treatment of vasospasm entailed either intra-arterial chemical vasodilation with fasudil hydrochloride hydrate (Eri; Asahi Kasei Pharma) or balloon angioplasty. We did not change the treatment protocol after detecting CLOCC. The protocol for this retrospective study was approved by the ethics committee at our institution, and the board waived the requirement to obtain patient consent (approval No. 2780).

Statistical Analysis

Numeric data are expressed as mean [SD] or median (interquartile range). Categorical variables are expressed as numbers (percentages). Statistical analyses were performed using SPSS statistical and computing software, Version 24 (IBM). For intergroup comparisons, we used the χ^2 test, Fisher exact test, Student *t* test, and the Mann-Whitney *U* test. To assess independent predictors of poor outcome, we first performed univariate logistic regression; then, those possible predictors showing values of $P < .10$ were included in the multivariate analysis. In all analyses, values of $P < .05$ were considered statistically significant.

RESULTS

Of the 286 cases of aneurysmal SAH, we excluded 12 cases that could not be evaluated due to early death, 10 cases that showed SAH of unknown origin, and 5 cases in which only external ventricular drainage was performed. The remaining 259 patients underwent curative treatment (clipping or coiling) and MR imaging multiple times, and we analyzed these cases. Of the 259 cases, DWI detected CLOCC in 33 patients (12.7%). These patients comprised 5 men and 28 women, with a mean age of 68.6 years (range, 40–94 years). In 33 cases with CLOCC, the mean period from the onset of SAH to detection of CLOCC was 6.3 days (range, 0–25 days). MR imaging showed CLOCC in 4 cases on day zero, 21 cases within days 1–7, five cases within days 8–14, and 3 cases on or after day 15. CLOCC were detected after clipping or coiling in 25 cases (75.8%) and before clipping or coiling in 8 cases (24.2%). CLOCC resolved in all cases, and the mean period from onset of SAH to the disappearance of CLOCC was 35.7 days (range, 9–78 days). On DWI, CLOCC were classified as the small type localized to the splenium (mean maximum diameter, 10.4 mm) or the large type extending along the ventricle (Fig 1). Among all 33 patients with CLOCC, 26 patients (78.9%) showed the small type and 7 cases (21.2%) showed the large type. CLOCC were identified as asymmetric in 16 of the 33 patients.

Clinical characteristics of patients with and without CLOCC are shown in Table 1. Regarding age, severity of the Hunt and Hess grade, severity of the Fisher score group, and treatment method, significant differences were seen between groups. The

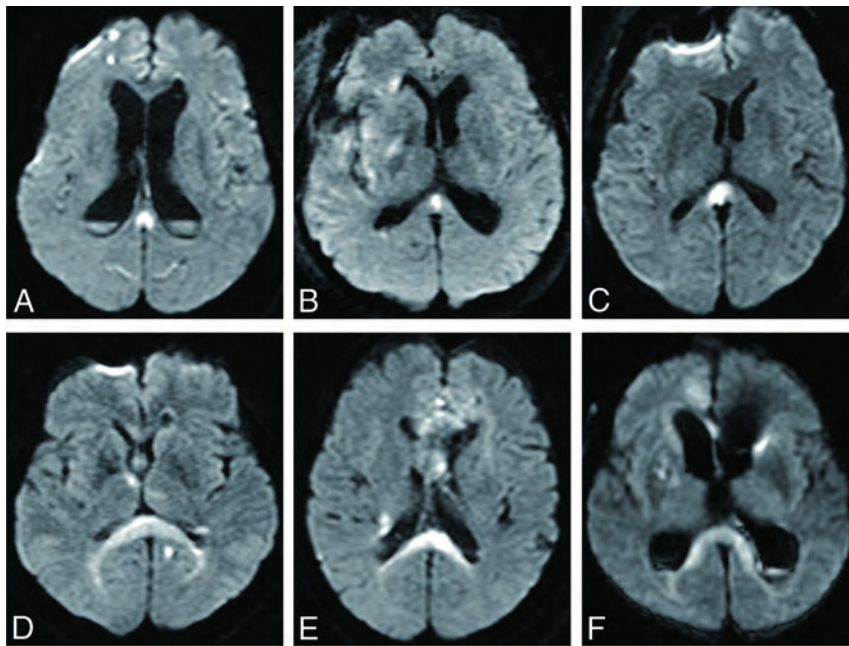


FIG 1. Two types of CLOCC: a small type localized to the splenium (A–C) and a large type spreading along the ventricle (D–F).

Table 1: Characteristics of patients with or without CLOCC

	No CLOCC (n = 226)	CLOCC (n = 33)	P Value
Age (mean) (yr)	68.6 [SD, 12.2]	63.7 [SD, 15.1]	.04
Male sex	69 (29.9%)	5 (15.2%)	.10
Hypertension	102 (45.1%)	20 (60.6%)	.07
Diabetes mellitus	20 (8.8%)	5 (15.2%)	.34
Location of aneurysm			.94
ACA	18	1	
AcomA	55	8	
ICA	15	2	
PcomA	56	9	
MCA	49	7	
VA-BA	33	6	
Hunt and Hess grade	3 (2–3)	4 (3–4)	.001
Fisher group			.009
1	8	0	
2	60	2	
3	100	15	
4	58	16	
Coil embolization	126 (55.8%)	25 (75.8%)	.04

Note:—ACA indicates anterior cerebral artery; AcomA, anterior communicating artery; PcomA, posterior communicating artery; VA-BA, vertebral artery and basilar artery.

CLOCC group was significantly younger, showed greater severity of SAH, and was more likely to undergo coil embolization than the group without CLOCC. No significant difference existed between groups regarding sex, history, or aneurysm location. Development of hydrocephalus and a poor mRS score at discharge were significantly more frequent in the group with CLOCC (Table 2), though no significant differences were seen between groups regarding DCI after SAH. In univariate analysis, advanced age, severity of the Hunt and Hess grade, large hematoma, coiling, and appearance of CLOCC correlated with poor outcome (Table 3). In multivariate analysis, only old age, severity of the Hunt and Hess grade, and large hematoma correlated with poor outcome (Table 3).

Multivariate analysis, thus, did not confirm CLOCC as a risk factor for poor outcome.

Illustrative Case

A 70-year-old woman presented with poor-grade SAH (Hunt and Hess grade 4). CT revealed Fisher group 3 SAH, and MRA demonstrated a 5-mm-diameter aneurysm on the anterior communicating artery. The patient underwent aneurysm coiling on day 2. This patient developed DCI and received regional arterial infusion of fasudil hydrochloride hydrate 3 times. She also developed hydrocephalus and underwent ventriculoperitoneal shunting. The patient had mild disorientation and was discharged home with an mRS score of 3. Although no abnormality was evident on DWI in this patient on admission (Fig 2A), a high-signal area appeared in the splenium of the corpus callosum on SAH day 7 (Fig 2B). The lesion gradually faded and had completely resolved by day 63 (Fig 2C–F). This change was thought to represent CLOCC and was also observable on FLAIR and T2WI (Fig 3).

DISCUSSION

Clinical Features of CLOCC Associated with SAH

The splenium is known as a region with characteristics differing from those of other parts of the corpus callosum. The splenium consists of fibers of the forceps major and communicates somatosensory information between the left and right parietal lobes and the visual cortex at the occipital lobes. Nerve fibers in the splenium show specific features, with the density of thin fibers reportedly decreasing and the density of large-diameter fibers increasing.¹⁹ Various congenital and acquired diseases can involve the splenium of the corpus callosum.

These include vascular diseases such as cerebral infarction and bleeding; demyelinating diseases such as multiple sclerosis and acute disseminated encephalomyelitis; brain tumors such as lipoma, glioma, and malignant lymphoma; traumatic lesions such as diffuse axonal injury; and encephalopathy caused by hypoxia, hypoglycemia, and carbon monoxide poisoning.

Starkey et al¹⁴ described CLOCC associated with SAH in 3 different cases that were nontraumatic and presumably aneurysmal, and in 1 case involving aneurysmal dissection. The Japanese literature includes a report by Yamazaki et al¹⁶ of 7 cases of CLOCC associated with SAH. Our study is by far the largest to

date. Uchida et al²⁰ also reported a case of ruptured arteriovenous malformation with CLOCC in the Japanese literature. Sorimachi et al²¹ reported hemorrhage in the splenium of the corpus callosum in association with SAH, but that change was deemed unrelated to CLOCC. Hadeishi et al²² reported that DWI findings at the onset of SAH were related to the initial brain injury, but they mainly discussed cortical lesions and did not mention splenial lesions.

The most important finding in the present study was that CLOCC, which have been described in relation to various diseases and conditions, were also observed in cases of aneurysmal

SAH and that the frequency of the lesions was found to be 12.7% among treated patients with SAH. The possibility remains that CLOCC are associated with elevated intracranial pressure because CLOCC appeared more frequently among patients with higher Hunt and Hess grades. Although no direct association between intracranial hypertension and CLOCC has been reported, intracranial hypertension is associated with strong activation of the inflammatory cascade, resulting in high cytokine levels in the brain.²³ Increased intracranial pressure is thus speculated to represent 1 cause of CLOCC. This possibility is not limited to CLOCC in cases of SAH rather than in CLOCC of other etiologies, but increased cytokine levels might be more prominent in severe cases of SAH because of the extremely high intracranial pressure. The high incidence of CLOCC among patients who underwent coil embolization may be related to the tendency to choose coiling in poor-grade cases. Hydrocephalus

usually becomes apparent around 7–10 days after SAH and is most prominent around 3–4 weeks, except for acute hydrocephalus appearing immediately after severe SAH.²⁴ Hydrocephalus usually shows normal pressure and is not associated with high intracranial pressure in the early stages of SAH.

Frequencies of poor mRS scores at discharge were higher in the CLOCC group, but multivariate analysis failed to identify CLOCC as a predictor of poor outcome. Unnecessary examinations and treatments thus appear avoidable even if this lesion is identified on MR imaging. Neurosurgeons do not need to perform repeat angiography or MR imaging and do not need to initiate treatment for encephalitis or encephalopathy.

Regarding lesion size, Takanashi et al⁹ classified CLOCC into 2 types: one isolated within the splenium and the other involving the entire corpus callosum. We therefore divided the CLOCC into a small type (isolated within the corpus callosum) and a large type (extended along the ventricle). Yamazaki et al¹⁶ reported 6 oval-type cases and 1 extended-type case among their 7 cases with CLOCC. Their oval-type cases were presumed to correspond to our small-type cases, while their extended-type cases corresponded to our large-type cases, though lesion size was not considered.¹⁶ No reports have clarified the reasons for asymmetric CLOCC. At

Table 2: Clinical outcomes of patients with or without CLOCC

	No CLOCC (n = 226)	CLOCC (n = 33)	P Value
DCI	41 (18.1%)	10 (30.3%)	.106
Hydrocephalus	36 (15.9%)	14 (42.4%)	.001
mRS	3 (1–4)	4 (3–5)	.002

Table 3: Uni- and multivariate analyses of variables associated with poor outcome^a

	Univariable Model			Multivariable Model ^b		
	OR	95% CI	P Value	OR	95% CI	P Value
Age (per 10-year increase)	1.79	1.47–2.19	<.001	2.04	1.58–2.65	<.001
Male sex	0.95	0.55–1.63	.84			
Hypertension	1.33	0.81–2.17	.26			
Diabetes mellitus	1.11	0.48–2.55	.81			
Location of aneurysm						
ACA	1.00					
AcomA	0.68	0.24–1.97	.48			
ICA	0.66	0.17–2.49	.54			
PcomA	0.50	0.18–1.43	.20			
MCA	0.72	0.25–2.11	.55			
VA-BA	0.84	0.27–2.60	.76			
Hunt and Hess grade (≥ 4)	10.2	4.80–21.79	<.001	5.53	2.21–13.82	<.001
Fisher group						
1	1.00			1.00		
2	2.23	0.25–19.65	.47	1.64	0.17–15.57	.67
3	8.48	1.01–71.17	.049	5.07	0.56–46.36	.15
4	30	3.41–263.95	.002	16.08	1.60–161.80	.018
Coil embolization	2.31	1.39–3.82	<.001	0.87	0.46–1.68	.92
CLOCC	3.71	1.55–8.90	.003	1.99	0.69–5.76	.46

Note:—ACA indicates anterior cerebral artery; AcomA, anterior communicating artery; PcomA, posterior communicating artery; VA-BA, vertebral artery and basilar artery.

^aWe defined poor outcome as mRS score of ≥ 3 at discharge.

^bMultivariate analysis included only those variables showing $P < .05$ in univariate analysis.

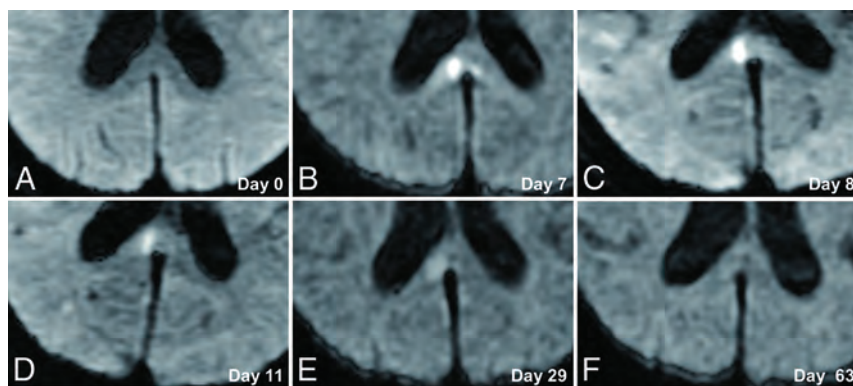


FIG 2. Serial DWI in an illustrative case. A 70-year-old woman presented with poor-grade SAH due to rupture of an aneurysm (diameter, 5 mm) at the anterior communicating artery. DWI on admission shows no lesion (A). CLOCC appear on days 7–8 (B and C) and gradually resolve (D–F).

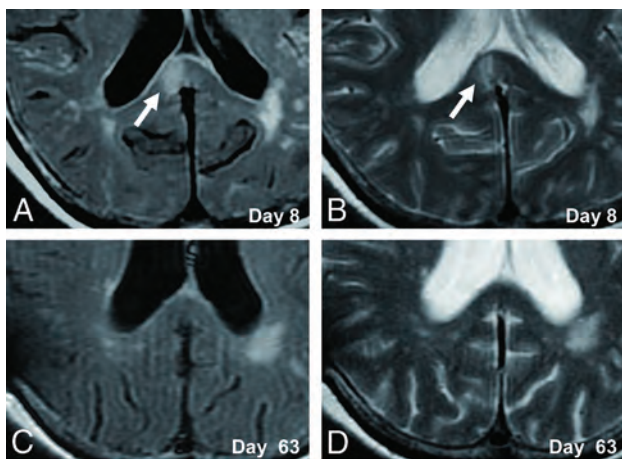


FIG 3. Serial FLAIR and T2WI in an illustrative case. CLOCC (white arrows) are observed in the splenium on FLAIR and T2WI on day 8 (A and B) and resolve by day 63 (C and D).

present, the implications of CLOCC size and shape remain obscure.^{9,16}

What Are CLOCC?

We speculated that CLOCC do not represent the initial brain injury due to SAH and should, instead, be considered a secondary change following SAH. First, CLOCC were detected within about a week after SAH onset and disappeared within around 1 month. Second, this MR imaging finding is observable in a wide variety of other diseases and conditions. CLOCC can be distinguished from ischemia because they also resolved on T2WI and FLAIR. CLOCC do not represent ordinary ischemia and seem related to some abnormality of the cerebral circulation and metabolism associated with SAH, considering that the lesion also resolved on T2WI and FLAIR. Liu and Lin²⁵ mentioned transient intramyelinic edema as a possible mechanism for CLOCC. The neuroradiologic finding of transient, isolated, high-intensity signal on DWI involving the lesion might indicate cytotoxic edema. Specifically, intramyelinic edema is a subtype of cytotoxic edema involving the myelin sheaths that was postulated by Liu and Lin²⁵ to be a possible mechanism underlying CLOCC.²⁶

Why CLOCC exclusively localize to the splenium remains unclear. We speculate on the mechanism of CLOCC associated with SAH as follows:¹⁴ SAH causes increases in levels of cytokine-like interleukin-6 and tumor necrosis factor- α in CSF;^{27,28} astrocytes might then be stimulated by cytokines to release glutamate and block glutamate reuptake, increasing extracellular glutamate levels. Ultimately, this cascade would lead to dysfunction of the neurons and microglia, with cytotoxic edema developing as water becomes trapped in these cells. The splenium of the corpus callosum is vulnerable to cytokinopathy because astrocytes and oligodendrocytes of the splenium have a higher density of receptors for cytokines and glutamate compared with those in other brain areas. This higher density would lead to a tendency for cytotoxic edema of the splenium, manifesting as CLOCC on DWI. Another hypothesis is based on the blood flow to the splenium. The splenium is supplied not only by the anterior circulation but also by the posterior circulation and so has more abundant blood flow than other areas of the corpus

callosum supplied solely by the anterior circulation.²⁹⁻³¹ The splenium may therefore be more susceptible to cytotoxic edema caused by cytokine release in the blood compared with other brain areas.

All patients received intravenous fasudil hydrochloride hydrate every 8 hours from day 4 to day 14. We administered fasudil to prevent cerebral vasospasm. Basic research has shown that intravenous administration of fasudil dose-dependently increased regional cerebral blood flow and blood velocity, without changing blood volume.³² On the basis of these results, fasudil can be inferred to not increase the cytokine exposure of the splenium. The present report is a study of patients with SAH who received standard treatment in Japan, although it cannot be completely ruled out that intravenous administration of fasudil may have affected the appearance of CLOCC.

The relevance of CLOCC to clinical symptoms is difficult to determine because clinical symptoms did not change when CLOCC appeared. Physicians should be aware that CLOCC occur frequently with SAH and are not a cause for panic, because this finding is not a predictor of poor outcome. However, the chronic effects of CLOCC are unknown, and careful follow-up is needed.

The present study has several limitations that warrant consideration. First, the sample size was not exceptionally large, and larger-scale research is warranted. However, this was the first report to investigate the incidence of CLOCC in patients with SAH and thus provides a contribution to future studies. Second, this was a retrospective study, and more systematic research is needed in the future. Third, we could not obtain any pathologic specimens for CLOCC. To solve the mystery of CLOCC, pathologic study and further accumulation of data are needed.

CONCLUSIONS

CLOCC occurred in SAH at a frequency of 12.7%. CLOCC associated with SAH developed in the acute phase, took several days to appear, and subsequently resolved within about a month. CLOCC were more likely to occur in high-grade cases of SAH but were not confirmed as a predictor of poor outcome. CLOCC represent a conspicuous imaging finding in treated patients with aneurysmal SAH, but their clinical importance should not be overemphasized.

ACKNOWLEDGMENTS

We appreciate the assistance of Yukari Ogawa, Keita Kinoshita, Satoshi Hirai, and Hiroki Takai (Department of Neurosurgery, Kawasaki Medical School, Kurashiki, Okayama, Japan) in the acquisition of data.

REFERENCES

1. Bulakbasi N, Kocaoglu M, Tayfun C, et al. **Transient splenial lesion of the corpus callosum in clinically mild influenza-associated encephalitis/encephalopathy.** *AJNR Am J Neuroradiol* 2006;27:1983-86 Medline
2. Gallucci M, Limbucci N, Paonessa A, et al. **Reversible focal splenial lesions.** *Neuroradiology* 2007;49:541-44 CrossRef Medline
3. Garcia-Monco JC, Cortina IE, Ferreira E, et al. **Cytotoxic lesions of the corpus callosum syndrome (RESLES): what's in a name?** *J Neuroimaging* 2011;21:e1-14 CrossRef Medline

4. Gürtler S, Ebner A, Tuxhorn I, et al. **Transient lesion in the splenium of the corpus callosum and antiepileptic drug withdrawal.** *Neurology* 2005;65:1032–36 CrossRef Medline
5. Güven H, Delibaş S, Comoğlu SS. **Transient lesion in the splenium of the corpus callosum due to carbamazepine.** *Turk Neurosurg* 2008;18:264–70 Medline
6. Kim SS, Chang KH, Kim ST, et al. **Focal lesion in the splenium of the corpus callosum in epileptic patients: antiepileptic drug toxicity?** *AJNR Am J Neuroradiol* 1999;20:125–29 Medline
7. Maeda M, Tsukahara H, Terada H, et al. **Cytotoxic lesions of the corpus callosum with restricted diffusion in a wide spectrum of diseases and conditions.** *J Neuroradiol* 2006;33:229–36 CrossRef Medline
8. Mori H, Maeda M, Takanashi J, et al. **Cytotoxic lesions of the corpus callosum in the corpus callosum following rapid withdrawal of carbamazepine after neurosurgical decompression for trigeminal neuralgia.** *J Clin Neurosci* 2012;19:1182–84 CrossRef Medline
9. Takanashi J, Barkovich AJ, Shiihara T, et al. **Widening spectrum of a reversible splenial lesion with transiently reduced diffusion.** *AJNR Am J Neuroradiol* 2006;27:836–38 Medline
10. Takanashi J, Tada H, Maeda M, et al. **Encephalopathy with a reversible splenial lesion is associated with hyponatremia.** *Brain Dev* 2009;31:217–20 CrossRef Medline
11. Abe E, Kajiwara H, Goda M, et al. **Clinically mild encephalitis/encephalopathy with a reversible splenial lesion, indistinguishable from multiple cerebral infarction: a case report** [in Japanese]. *Nosotchu* 2014;36:443–48 CrossRef
12. Tung CS, Wu SL, Tsou JC, et al. **Marchiafava-Bignami disease with widespread lesions and complete recovery.** *AJNR Am J Neuroradiol* 2010;31:1506–07 CrossRef Medline
13. Tada H, Takanashi J, Barkovich AJ, et al. **Clinically mild encephalitis/encephalopathy with a cytotoxic lesions of the corpus callosum.** *Neurology* 2004;63:1854–58 CrossRef Medline
14. Starkey J, Kobayashi N, Numaguchi Y, et al. **Cytotoxic lesions of the corpus callosum that show restricted diffusion: mechanisms, causes, and manifestations.** *Radiographics* 2017;37:562–76 CrossRef Medline
15. Gaur P, Dixon L, Jones B, et al. **COVID-19-associated cytotoxic lesions of the corpus callosum.** *AJNR Am J Neuroradiol* 2020;41:1905–07 CrossRef Medline
16. Yamazaki T, Sasaki T, Kubota T, et al. **Reversible focal splenial lesion of the corpus callosum in aneurysmal subarachnoid hemorrhage** [in Japanese]. *Progress in CI* 2012;34:93–98
17. Rinkel GJ, van Gijn J, Wijndicks EF. **Subarachnoid hemorrhage without detectable aneurysm: a review of the causes.** *Stroke* 1993;24:1403–09 CrossRef Medline
18. Vergouwen MD, Vermeulen M, van Gijn J, et al. **Definition of delayed cerebral ischemia after aneurysmal subarachnoid hemorrhage as an outcome event in clinical trials and observational studies: proposal of a multidisciplinary research group.** *Stroke* 2010;41:2391–95 CrossRef Medline
19. Aboitiz F, Scheibel AB, Fisher RS, et al. **Fiber composition of the human corpus callosum.** *Brain Res* 1992;598:143–53 CrossRef Medline
20. Uchida K, Shirakawa M, Sakamoto D, et al. **A case of reversible splenial lesion after surgical resection of arteriovenous malformation** [in Japanese]. *Brain Nerve* 2013;65:212–13 Medline
21. Sorimachi T, Yajima N, Sasaki O, et al. **Hematoma in the splenium of the corpus callosum in the subacute stage of subarachnoid hemorrhage: three case reports.** *Neurol Med Chir (Tokyo)* 2010;50:209–12 CrossRef Medline
22. Hadeishi H, Suzuki A, Yasui N, et al. **Diffusion-weighted magnetic resonance imaging in patients with subarachnoid hemorrhage.** *Neurosurgery* 2002;50:741–47 CrossRef Medline
23. Gaetz D, Nagel A, Schlenk F, et al. **High ICP as trigger of proinflammatory IL-6 cytokine activation in aneurysmal subarachnoid hemorrhage.** *Neurol Res* 2010;32:728–35 CrossRef Medline
24. Fujita K, Kusunoki T, Noda M, et al. **Normal pressure hydrocephalus (NPH) following subarachnoid hemorrhage (SAH)-clinical consideration of CT and development of hydrocephalus after SAH** [in Japanese]. *No To Shinkei* 1981;33:845–51 Medline
25. Liu WM, Lin CH. **A reversible stroke-like splenial lesion in viral encephalopathy.** *Acta Neurol Taiwan* 2013;22:117–21 Medline
26. Moritani T, Ekholm S, Westesson PL. *Diffusion-Weighted MR Imaging of the Brain. 2nd ed.* Springer-Verlag; 2009:37–38
27. Gaetani P, Tartara F, Pignatti P, et al. **Cisternal CSF levels of cytokines after subarachnoid hemorrhage.** *Neurol Res* 1998;20:337–42 CrossRef Medline
28. Mathiesen T, Edner G, Ulfarsson E, et al. **Cerebrospinal fluid interleukin-1 receptor antagonist and tumor necrosis factor-alpha following subarachnoid hemorrhage.** *J Neurosurg* 1997;87:215–20 CrossRef Medline
29. Kahilogullari G, Comert A, Ozdemir M, et al. **Arterial vascularization patterns of the splenium: an anatomical study.** *Clin Anat* 2013;26:675–81 CrossRef Medline
30. Kakou M, Velut S, Destrieux C. **Arterial and venous vascularization of the corpus callosum** [in French]. *Neurochirurgie* 1998;44(1 Suppl):31–37
31. Tetsuka S. **Reversible lesion in the splenium of the corpus callosum.** *Brain Behav* 2019;9:e0144 CrossRef Medline
32. Satoh S, Suzuki Y, Ikegaki I, et al. **The effects of HA1077 on the cerebral circulation after subarachnoid haemorrhage in dogs.** *Acta Neurochir (Wien)* 1991;110:185–88 CrossRef Medline

Diagnostic Accuracy of Arterial Spin-Labeling MR Imaging in Detecting the Epileptogenic Zone: Systematic Review and Meta-analysis

J.Y. Zeng, X.Q. Hu, J.F. Xu, W.J. Zhu, H.Y. Wu, and F.J. Dong



ABSTRACT

BACKGROUND: A noninvasive, safe, and economic imaging technique is required to identify epileptogenic lesions in the brain.

PURPOSE: Our aim was to perform a meta-analysis evaluating the accuracy of arterial spin-labeling in localizing the epileptic focus in the brain and the changes in the blood perfusion in these regions.

DATA SOURCES: Our sources were the PubMed and EMBASE data bases.

STUDY SELECTION: English language studies that assessed the diagnostic accuracy of arterial spin-labeling for detecting the epileptogenic zone up to July 2019 were included.

DATA ANALYSIS: The symptomatogenic foci of seizures in the brain were determined and used as the references. The relevant studies were evaluated using the Quality Assessment of Diagnostic Accuracy Studies-2 tool. The outcomes were evaluated using the pooled sensitivity, pooled specificity, pooled accuracy, diagnostic odds ratio, area under the summary receiver operating characteristic curve, and likelihood ratio.

DATA SYNTHESIS: Six studies that included 174 patients qualified for this meta-analysis. The pooled sensitivity, pooled specificity, and area under the summary receiver operating characteristic curve were 0.74 (95% CI, 0.65–0.82), 0.35 (95% CI, 0.03–0.90), and 0.73 (95% CI, 0.69–0.76), respectively. The accuracy of arterial spin-labeling for localizing the epileptic focus was 0.88 (accuracy in arterial spin-labeling/all perfusion changes in arterial spin-labeling) in cases of a positive arterial spin-labeling result. The epileptogenic zone exhibited hyperperfusion or hypoperfusion.

LIMITATIONS: Only a few studies were enrolled due to the strict inclusion criteria.

CONCLUSIONS: Arterial spin-labeling can be used for assessing, monitoring, and reviewing, postoperatively, patients with epilepsy. Blood perfusion changes in the brain may be closely related to the seizure time and pattern.

ABBREVIATIONS: ASL = arterial spin-labeling; QUADAS-2 = Quality Assessment of Diagnostic Accuracy Studies-2; SOZ = seizure onset zone

Epilepsy is the most common chronic neurologic disease, characterized by the occurrence of repeat seizures. Several diseases, including brain tumors, hypoxia-related brain diseases, and cerebral cortical dysplasia, can cause epilepsy. Electroencephalography, which identifies the epileptic discharges in the brain, was the earliest method applied for the diagnosis and localization of epileptic disorders.^{1,2} The development of imaging technology in recent years has

enabled the use of conventional (structural) MR imaging and CT, which can locate and visualize the structural brain lesions responsible for epilepsy. However, not all patients with epilepsy exhibit structural changes in their brain tissue. Several animal and clinical studies have found that seizures can alter the metabolism and vascular perfusion in the brain tissue.^{3–8} Therefore, PET and SPECT can be used to locate lesions with metabolic abnormalities and an abnormal blood supply.

Received July 18, 2020; accepted after revision December 15.

From the Department of Ultrasound (J.Z., X.H., J.X., H.W., F.D.), First Affiliated Hospital of Southern University of Science and Technology, Second Clinical College of Jinan University, Shenzhen Medical Ultrasound Engineering Center, Shenzhen People's Hospital, Shenzhen, China; Integrated Chinese and Western Medicine Postdoctoral Research Station (X.H.), Jinan University, Guangzhou, China; and QQ Music Business group of Tencent Music Entertainment Group (W.Z.), Shenzhen People's Hospital, Shenzhen, China.

J. Zeng and X. Hu shared the first authorship.

Please address correspondence to Fajin Dong, MD, Department of Ultrasound, First Affiliated Hospital of Southern University of Science and Technology, Second Clinical College of Jinan University, Shenzhen Medical Ultrasound Engineering Center, Shenzhen People's Hospital, Shenzhen, 518020, China; e-mail: dongfajin@szhospital.com

Indicates article with online supplemental data.

<http://dx.doi.org/10.3174/ajnr.A7061>

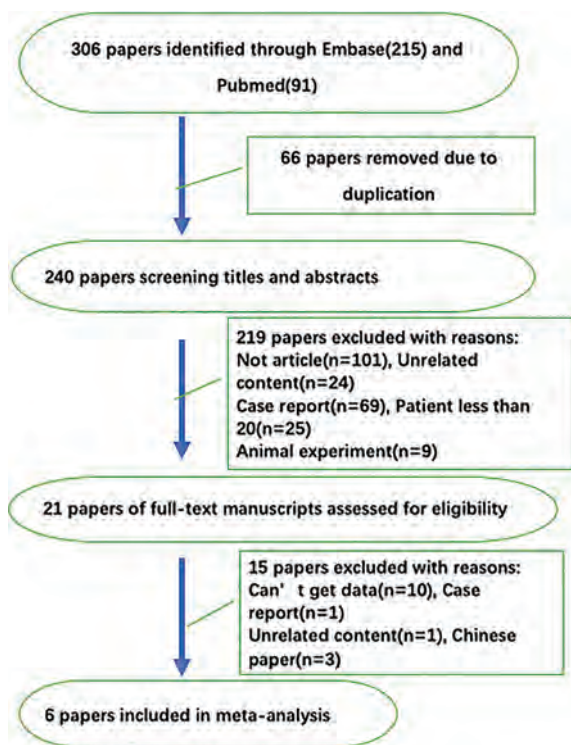


FIG 1. Data collection process.

Currently, the treatment of epilepsy is mainly based on pharmacotherapy, and 20%–40% of patients may have refractory seizures. Surgery is the treatment of choice in patients with refractory epilepsy.^{9,10} Patients who are not drug-resistant with surgical conditions can also benefit from surgery.¹¹ The accurate detection of the epileptic lesion is the key to the effectiveness of surgery. The surgical treatment plan mainly depends on the consistency of the clinical symptoms of the seizure and the findings of electroencephalography and structural MR imaging.¹² PET and SPECT are used if both electroencephalography and structural MR imaging fail to identify the lesion.^{13–15} However, the radiation exposure associated with PET and SPECT can have adverse effects on human health. Therefore, a noninvasive, safe, and economic imaging technique is required to identify the brain lesions responsible for epilepsy.

The development of functional MR imaging technology has made it possible to visualize the change in the CBF using arterial spin-labeling (ASL) (without the use of contrast agents) because ASL can magnetize protons in the circulating blood as an endogenous perfusion tracer.^{16,17} Several studies of neurologic diseases have shown a good correlation among ASL, DSC-perfusion MR imaging, and PET for evaluating the changes in CBF perfusion, and they support the credibility and feasibility of the clinical applications of ASL.^{18–21}

ASL can be used to identify the location of epileptic lesions, with the potential to replace interventional examinations. However,

most published research on this subject consists of experimental studies, with small samples and different results. There is controversy about the changes in the blood perfusion in the lesion area; some believe that perfusion is increased, and some believe that perfusion is reduced. The purpose of our study was to conduct a systematic review and meta-analysis of studies assessing the ability of ASL to locate epileptogenic foci. We aimed to obtain a clear idea of the accuracy of ASL for the localization of the epileptogenic focus and the changes of the blood perfusion of the lesion.

MATERIALS AND METHODS

Medical Subject Headings and terms such as “seizures” or “seizure” or “epilepsies” or “epilepsy” or “arterial spin-labeling” were used to search the PubMed and EMBASE data bases for studies published in English on ASL and epileptic foci up to July 13, 2019.

The search strategy was as follows: ((((((eclampsia) OR convulsion) OR epilepsy) OR epilepsies) OR seizure) OR seizures) AND arterial spin-labeling. We also manually sought related studies mentioned in

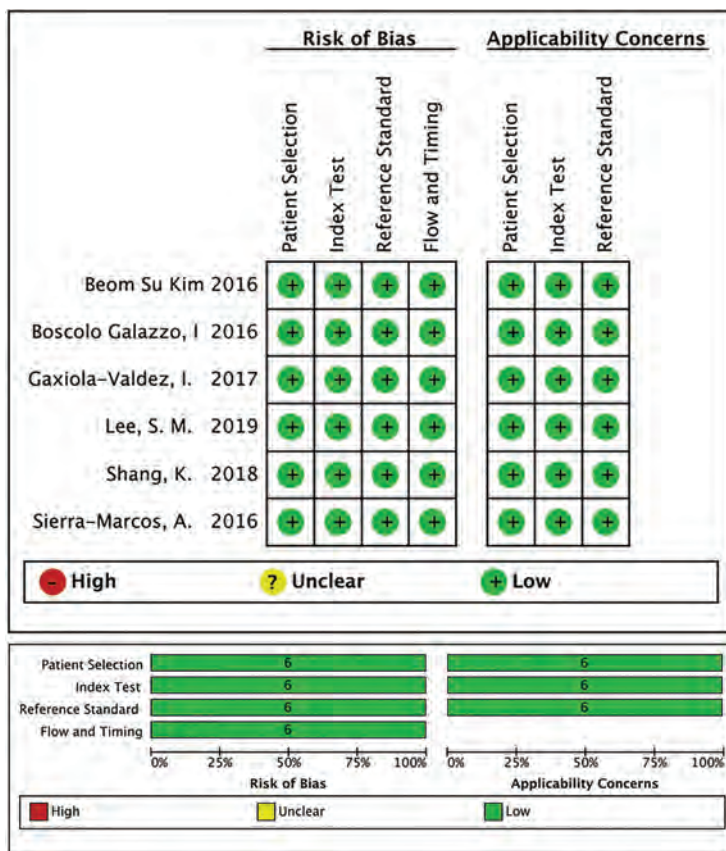


FIG 2. Results of the QUADAS-2 tool. Risk of bias and applicability concerns summary (upper table). Risk of bias and applicability concerns graph (lower table).

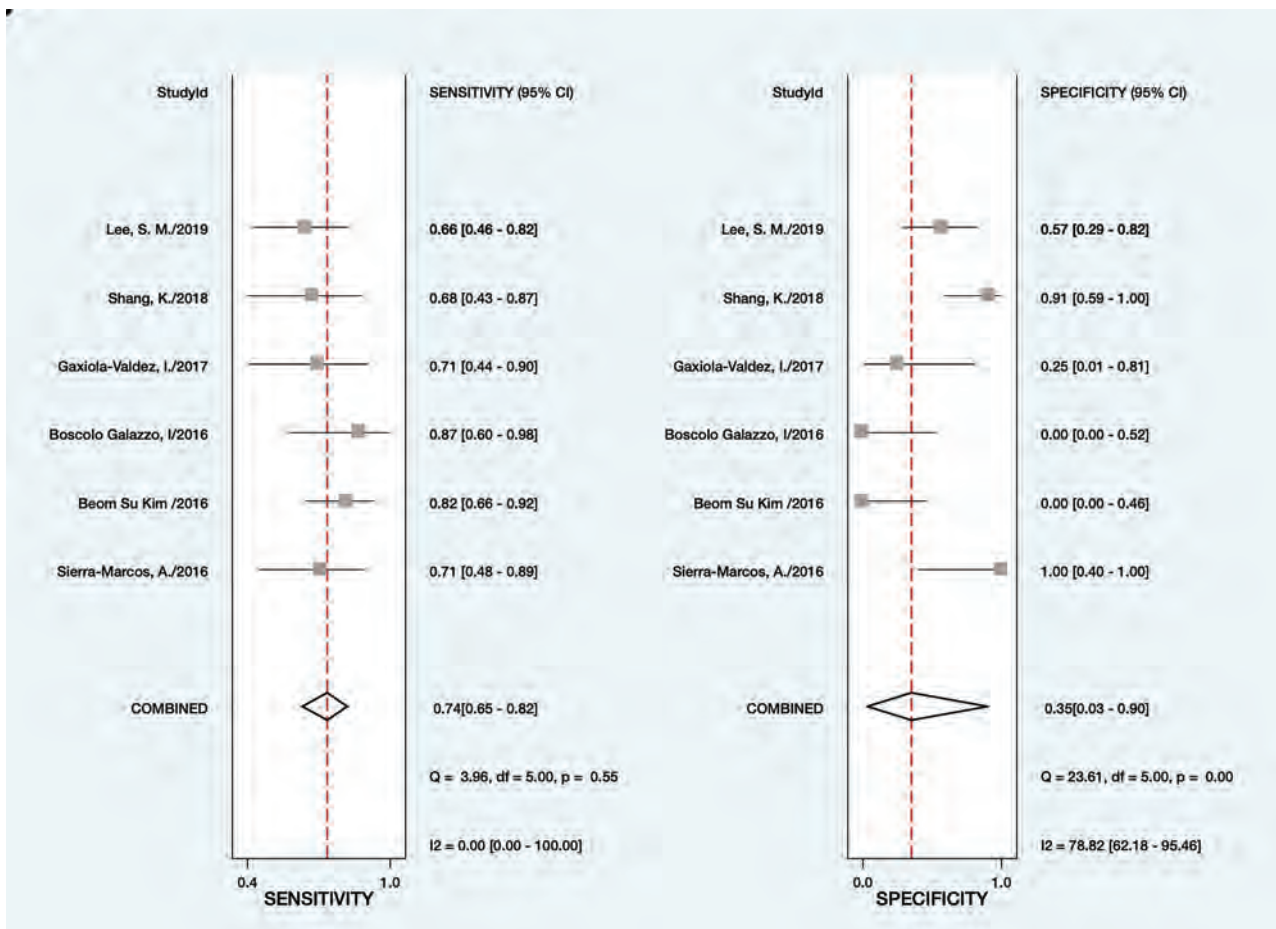


FIG 3. Forest plot showing the sensitivity for each specific study on the right y-axis and the specificity of the accuracy of ASL for detecting the epileptogenic zone.

the selected articles to ensure that all relevant research was included.

Studies that assessed the diagnostic accuracy of ASL in detecting the epileptogenic zone were included in the analysis. The symptomatogenic focus in the brain was determined from the studies that qualified for inclusion, and it was used as the reference. The outcomes were evaluated using the pooled sensitivity, pooled specificity, pooled accuracy, summary receiver operating characteristic, and likelihood ratio.

Study Selection

The inclusion criteria were as follows: 1) retrospective or prospective studies on epilepsy, 2) clinical studies that included at least 20 patients, 3) studies that located the brain lesions using ASL and used the clinical seizure focus (in the brain) as a reference, and 4) the availability of the true-positive, true-negative, false-positive, and false-negative nature of the findings in the given data. Reviews, abstracts, letters to the editor, editorials, and case reports were excluded. Two colleagues (F.J.D. and X.Q.H.) with extensive experience and expertise screened the qualified studies. Disagreements between the 2 analysts were resolved through discussion or by the third analyst (J.Y.Z.), who reassessed the search results, assessed the process, and read the included studies to ensure they met the inclusion criteria. We summarized the

characteristics of the qualified studies, such as the authors of the study, the country where it was conducted, publication year, and reported data, namely, true-positive, false-negative, false-positive, true-negative, sensitivity, and specificity information. Moreover, we summarized the characteristics of the results of ASL and analyzed the accuracy of ASL in detecting the cortical epileptogenic zone under different conditions, such as hyperperfusion or hypoperfusion, and structural MR imaging with positive or negative findings.

The qualifying studies were evaluated using the Quality Assessment of Diagnostic Accuracy Studies-2 (QUADAS-2) tool. Each domain of the QUADAS-2 is used to judge the risk of bias, and the first 3 domains were assessed to ascertain their applicability.^{22,23}

Statistical Analyses

MIDAS (Version 14.0; Stata module; <https://econpapers.repec.org/software/bococode/s456880.htm>) and RevMan (Version 5.3.5; <https://training.cochrane.org/online-learning/core-software-cochrane-reviews/revman/revman-5-download>) software were used to analyze the included studies. STATA (Version 14.0, with a bivariate mixed-effects regression model; StataCorp) was used to analyze the diagnostic test accuracy by collating the statistical indices (including the sensitivity, specificity, summary receiver operating characteristic, and so forth) and drawing a statistical chart.²³

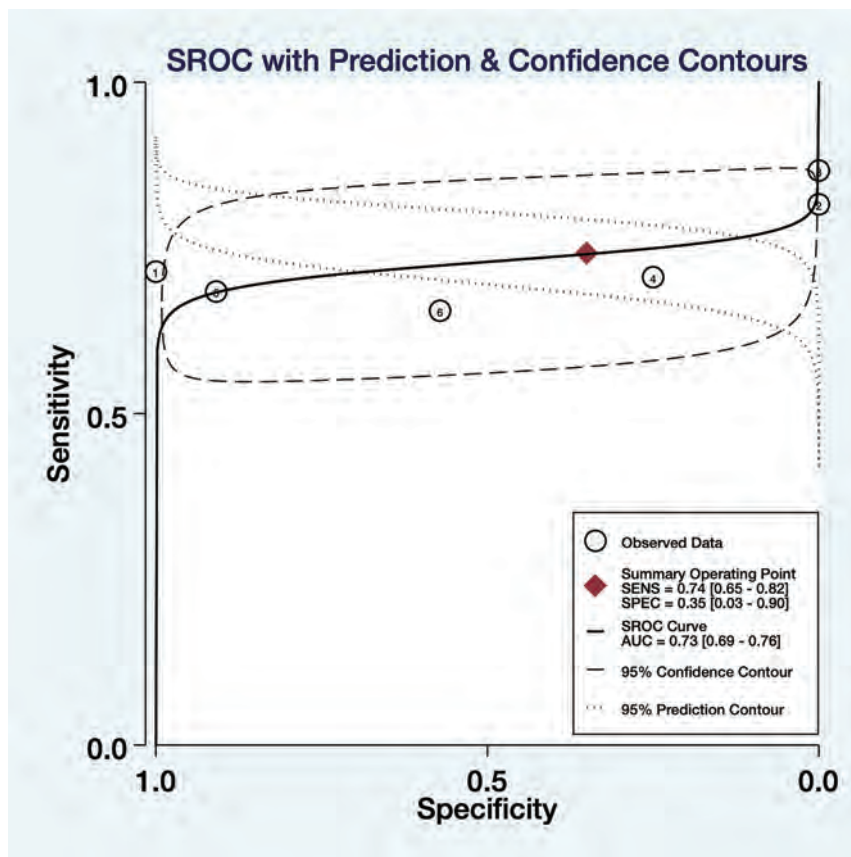


FIG 4. Summary receiver operating characteristic curves with prediction and confidence contour, 95% confidence contour, and 95% prediction contour for all included studies for analyzing the accuracy of ASL in detecting the epileptogenic zone ($n=6$). SENS indicates sensitivity; SPEC, specificity; AUC, area under the curve; SROC, summary receiver operating characteristic.

RevMan was used for the methodologic evaluation of the quality of the included studies. The heterogeneity of the qualifying studies was evaluated using the Cochrane Q Test statistic value (P) and the inconsistency index (I^2).²⁴

Publication Bias

The potential publication bias was evaluated using the Deek funnel plot asymmetry test. The slope coefficient: $P < .1$, indicated significant asymmetry.²⁵

RESULTS

Literature Search

A total of 306 studies were selected through the search strategy. Six of 306 studies met the inclusion criteria and were included in this meta-analysis (Fig 1).

Study Characteristics

The 6 retrospective diagnostic studies that qualified for inclusion in this meta-analysis^{21,26-30} included 174 patients. The symptomatogenic zone of 155 patients was used as the reference. The characteristics of the qualifying studies are summarized in the Online Supplemental Data. We classified the results of the 6

studies, which are summarized in the Online Supplemental Data. Three studies (studies 3-5)^{21,28,29} performed quantitative analyses, while the other 3 studies (studies 1, 2, and 6)^{26,27,30} performed qualitative analyses (Table).

Methodology Quality Assessment

The results of the QADAS-2 are presented in Fig 2. All the qualifying studies had a low risk of bias and were of high quality as per the QADAS-2 assessment.

Data Synthesis and Analysis

The pooled sensitivity, pooled specificity, and area under the summary receiver operating characteristic curve were 0.74 (95% CI, 0.65-0.82), 0.35 (95% CI, 0.03-0.90), and 0.73 (95% CI, 0.69-0.76), respectively (Figs 3 and 4). The positive and negative likelihood ratios were 1.1 (95% CI, 0.4-2.9) and 0.74 (95% CI, 0.13-4.09), respectively (Fig 5).

A total of 79 patients exhibited hypoperfusion in the epileptogenic zone; the epileptogenic zone was accurately located using ASL in 70 patients (accuracy rate, 88.6%) (Online Supplemental Data). However, 45 patients exhibited hyperperfusion in the epileptogenic zone; the epileptogenic zone was accurately located using ASL in 39 patients

(accuracy rate, 87.7%). The classification of the structural MR imaging findings revealed that 26 patients showed abnormalities in the brain tissue, which was accurately located in 21 patients using ASL (accuracy rate, 65.5%). The brain tissue was normal in 87 patients; ASL accurately detected the lesions in 57 of these patients (accuracy rate, 80.8%).

ASL accurately located the lesions in 98 of 151 patients whose lesions were localized using video electroencephalography, with an accuracy rate of 64.9%.

The actual epileptogenic focus corresponded exactly with the symptomatogenic focus in 72 of 109 patients whose lesions were accurately localized using ASL. The ASL-localized lesion was partially consistent with the symptomatogenic seizure focus (it was smaller or larger) in the remaining 37 patients (Online Supplemental Data).

The P values of the patients' ages, measurement method, and time of onset of epilepsy were all $> .01$ in univariate logistic regression analysis (Fig 6).

Publication Bias

The Deek funnel plot demonstrated a lack of evidence of publication bias, and the studies were dispersed symmetrically ($P = .73$, Fig 7).

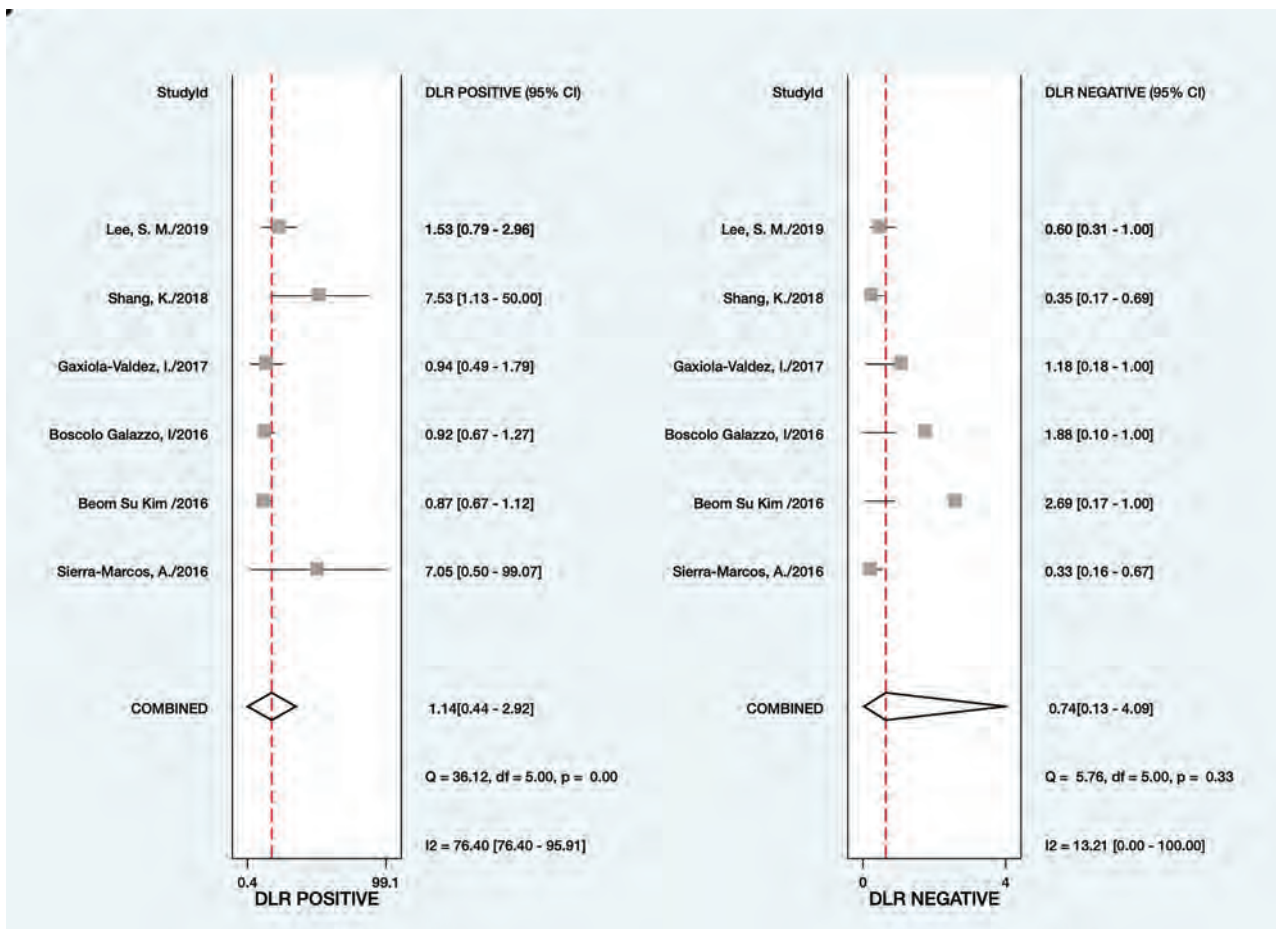


FIG 5. Forest plot showing the negative and positive likelihood ratios of the accuracy of ASL for each specific study on the right y-axis and in detecting the epileptogenic zone.

DISCUSSION

Our study found that ASL was highly sensitive (0.74) in detecting changes in the CBF in patients with epilepsy. This sensitivity was especially high in patients with negative results on structural MRI. Animal experiments have shown that the blood vessel changes in the brain lesions of rats mainly include hyperemia and neuronal degeneration and that hyperperfusion caused by vascular changes was inextricably linked to the incidence of epilepsy.³⁻⁶ Clinical studies have found that increased neuronal activity caused by seizures is associated with increased neuronal metabolism and local blood flow.⁷⁻⁹

In nonlesional epilepsy, when conventional MR imaging cannot detect a structural epileptogenic lesion, the goal is to identify the epileptogenic zone. During epileptic seizures, neuronal activity and metabolic demand in the focal area increase and the local blood flow produces corresponding changes to meet the needs of the neural activity.²⁸⁻³² Therefore, ASL can detect the seizure onset zone (SOZ) through the blood flow changes. The epileptogenic zone includes the SOZ, ie, the area of the cortex from which the epileptic discharge originates; the irritative zone, ie, the area of cortex where the epileptic discharge spreads; and the symptomatogenic zone, ie, the area of cortex that produces ictal symptoms and signs.

The irritative zone encompasses the SOZ and represents the seat of the hemodynamic response to neuronal activity and

metabolic demand that may be evaluated with ASL. Therefore, ASL can detect CBF changes larger than only the SOZ, thus overestimating the real extent of the lesion. However, this phenomenon also occurs in other methods that investigate brain perfusion in epilepsy.

The accuracy of ASL for locating lesions was approximately 0.9, irrespective of hyperperfusion or hypoperfusion on MR imaging, which was almost consistent with its accuracy for the clinical location. Recent studies have shown that the accuracy of ASL is in concordance with that of [¹⁸F] FDG-PET and DSC MR imaging.¹⁸⁻²¹ Therefore, ASL can be used to measure changes in the CBF in patients with epilepsy, and the positive results are reliable,^{18,21} consistent with the results of our included studies. However, our study found that the specificity and negative likelihood results of ASL are relatively poor and that its negative results had low credibility. The specificity ranged from 1 to 0 (it was lower than 0.5 in most studies), as seen in the Online Supplemental Data.

We analyzed the data from the studies, which included patients without symptomatogenic foci in whom ASL failed to locate the lesion. These patients were judged as having true-negative results. The first, fourth, and sixth studies included patients with true-negative results (no clinical seizure focus, and ASL failed to locate the brain lesions). The fifth study also included 10

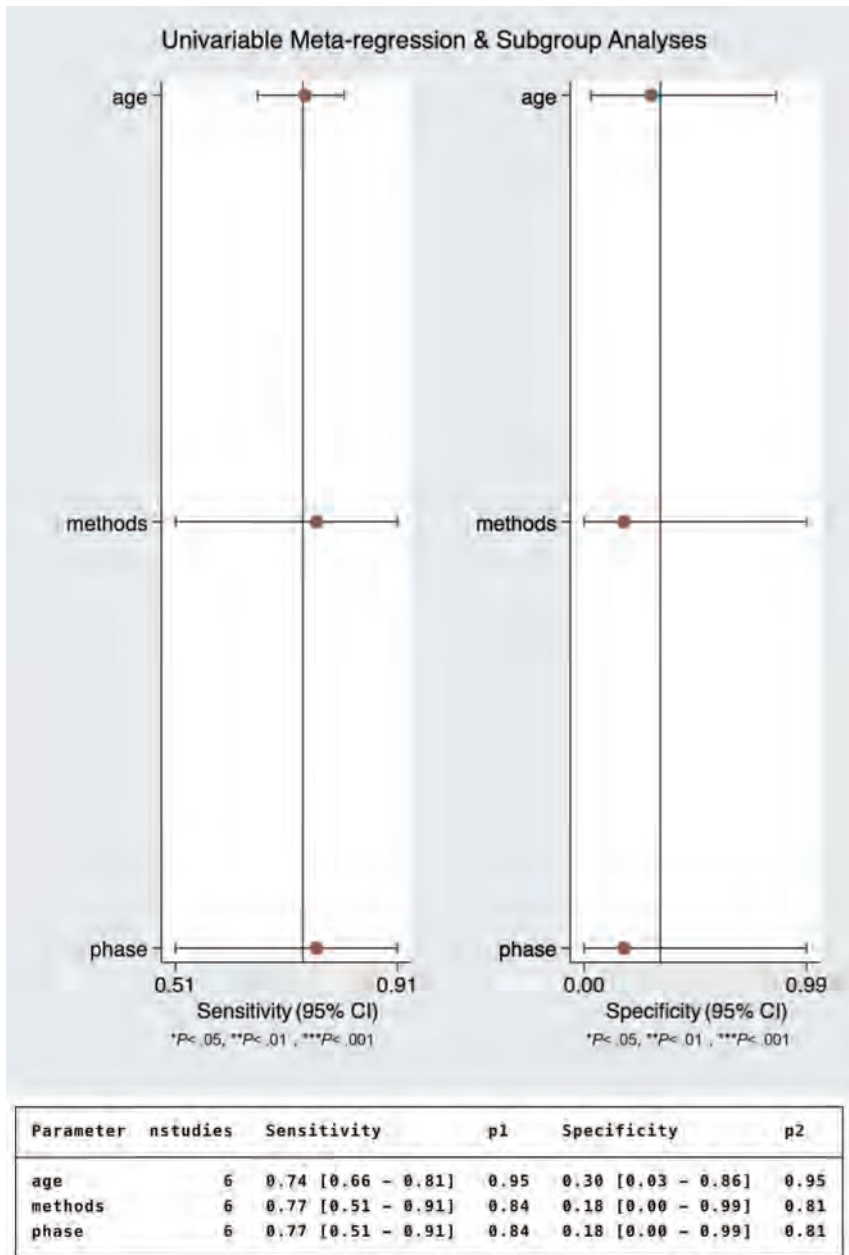


FIG 6. Subgroup analysis of the effect of age, measurement methods, and seizure phase on the detection of the epileptogenic zone using ASL.

healthy controls. Strictly speaking, these patients should have been excluded because our inclusion criteria entailed the presence of a symptomatogenic focus for comparison. Therefore, these 3 studies had no patients with true-negative results. The patients in the second and third studies had known epileptic lesions; thus, the number of those with true-negative results was zero. Therefore, the specificity of the included studies would be zero.

The study population in clinical research usually consists of patients, and there is no healthy group for comparison, resulting in few or no true-negative results, poor specificity of the experiment, and unreliable results. In general, ASL can be used to assist in the localization of epileptic lesions or in postoperative reviews, but other tests need to be performed in cases of negative results.

Second, the increase or decrease in the blood flow to epileptic lesions is a matter of controversy. The Online Supplemental Data show that the vascular flow in most lesions mainly decreased in the interictal and postictal periods, especially in patients with structural MR imaging negative for epilepsy. Our results are in agreement with those of previous studies in adults.³³⁻³⁵ An animal study indicated that hypoperfusion could be observed in epileptic lesions for up to 60 minutes after a seizure.³⁶ Clinical research in the same group found that ASL depicted hypoperfusion in >70% of patients within 60 minutes of the end of the seizure, and 80% of these were accurately localized.⁴

Only one of the included studies reported that hyperperfusion was the predominant alteration in the epileptic lesions (study 2). We carefully analyzed the data and speculated that the patients in this study might have had a high frequency of seizures. The time intervals (immediately to 65 days; average time interval, 101 hours; 39 patients, ≤ 3 days; 5 patients, >3 days) between the seizure episode and electroencephalography and between the seizure episode and ASL (1 hour to 60 days; average time interval, 97 hours; 38 patients ≤ 3 days; 6 patients, > 3 days) were both prolonged in study 2. Moreover, the 2 time intervals were not synchronized, and there was no significant difference between them.

The abnormal discharge time and abnormal perfusion time of the lesion areas were synchronized, unless the patients had frequent seizure attacks. Thus, the 2 examinations were performed at different times, but they

found the results during the same period (either during the ictal period or during abnormal brain firing). Hence, the results are consistent, and the time interval is meaningless. Moreover, some hyperperfusion changes were reported by 2 other studies (studies 1 and 6). Most interesting, most patients with hyperperfusion also had frequent seizures and/or abnormal discharges on electroencephalography. Recent animal and clinical studies have shown that the CBF increases during seizures and decreases in the postictal and interictal periods, thus disproving the previously recognized hypoxia-hyperperfusion theory.^{5,37}

Thus, we speculated that the blood flow to the lesion area usually increases in the interictal (abnormal neuronal firing but without clinical symptoms) and ictal periods in patients with frequent

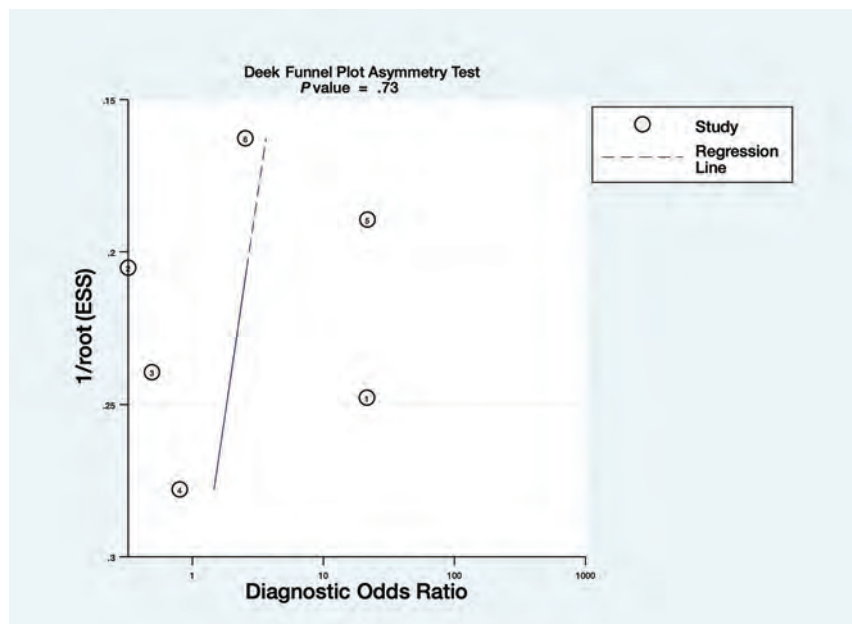


FIG 7. The Deek funnel plot for the diagnostic odds ratio of ASL for detecting the epileptogenic zone.

Characteristics of the included studies

Author	Country	Patients (Men)	Age (yr)	Study Design	Year	TP	FP	FN	TN	Sensitivity	Specificity
Sierra-Marcos et al ²⁶	Spain	26 (8)	32.4 (SD, 13.8)	Retrospective analysis	2016	15	0	6	4	0.74	1
Kim et al ²⁷	Korea	44 (21)	51 (average)	Retrospective analysis	2016	31	6	7	0	0.82	0
Galazzo et al ²¹	UK	20 (10)	34 (SD, 12)	Retrospective analysis	2016	13	5	2	0	0.87	0
Gaxiola-Valdez et al ²⁸	Canada	21 (10)	33.9 (average)	Retrospective analysis	2017	12	3	5	1	0.71	0.25
Shang et al ²⁹	USA	20 (13)	26.5 (SD, 9.48)	Retrospective analysis	2018	13	1	6	10	0.68	0.91
Lee et al ³⁰	South Korea	43 (17)	6.3 (SD, 3.3)	Retrospective analysis	2019	19	6	10	8	0.66	0.57

Note:—TP indicates True Positive; FP, False Positive; TN, True Negative; FN, False Negative.

seizures, while the blood flow decreases in the interictal and postictal periods if the patient's seizure frequency is low. There is a correlation between the perfusion pattern and frequency of seizures (or abnormal brain discharge). This hypothesis is consistent with the findings of other studies.^{19,38,39}

Limitations

First, the inclusion criteria were extremely strict, and only 6 studies were enrolled in the meta-analysis. Most of the included studies had small sample sizes, and their results were limited. Moreover, our results are dependent on the symptomatogenic focus as a standard reference, but the symptomatogenic zone is not easily ascertained in all types of epilepsy (such as insular epilepsy).⁴⁰ Therefore, our results are only meaningful for epilepsy with symptomatogenic focus localization. In addition, most of the included studies lacked symptomatic patients without epileptogenic lesions in the brain, which led to high heterogeneity in the results of our analysis. This reduced the reliability of the results of the specificity and negative likelihood of the ASL findings. However, the time,

place (where the study was conducted), and participants' ages differed among the studies included, and the results of PET and other tests were compared at the same time; hence, the positive results had high reliability. Future meta-analyses should include more studies with epilepsy diagnosed as negative to reduce the heterogeneity. In addition, our study found that the perfusion of the lesion area was closely related to the duration of the seizure episode and seizure pattern, though the exact period could not be judged in many of the included studies. Therefore, future studies should consider the duration and frequency of seizures to better understand the changes in cerebral perfusion using ASL.

Second, ASL is a new diagnostic technology. Thus, there are important differences in the diagnostic accuracy of ASL, which need improvement. For example, the participant's age influences the inflow time between the end of the marker pulse and the image-acquisition time; thus, ASL cannot be quantified among different age groups.¹⁶ Manufacturer-related differences in the MR imaging scanners and the lack of a quantitative threshold also affect the accuracy.

CONCLUSIONS

First, our meta-analysis showed that ASL has high sensitivity for the localization of lesions in patients with epilepsy, and the accuracy of the localization is very high for the positive results. Therefore, whether in patients with or without normal brain structure, ASL can be used for the assessment in diagnosis, in protocol, and post-operative review after surgery or other treatments, in association with the other methods currently used.

Second, the changes in the CBF may be closely related to the seizure time and seizure pattern.

REFERENCES

1. Krumholz A, Wiebe S, Gronseth G, et al. American Epilepsy Society. **Practice parameter: evaluating an apparent unprovoked first seizure in adults (an evidence-based review): report of the Quality Standards Subcommittee of the American Academy of Neurology and the American Epilepsy Society.** *Neurology* 2007;69:1996–2007 CrossRef Medline
2. van Donselaar CA, Schimsheimer RJ, Geerts AT, et al. **Value of the electroencephalogram in adult patients with untreated idiopathic first seizures.** *Arch Neurol* 1992;49:231–37 CrossRef Medline
3. Fabene PF, Marzola P, Sbarbati A, et al. **Magnetic resonance imaging of changes elicited by status epilepticus in the rat brain: diffusion-weighted and T2-weighted images, regional blood volume maps, and direct correlation with tissue and cell damage.** *Neuroimage* 2003;18:375–89 CrossRef Medline
4. Marchi N, Angelov L, Masaryk T, et al. **Seizure-promoting effect of blood-brain barrier disruption.** *Epilepsia* 2007;48:732–42 CrossRef Medline
5. Choy M, Wells JA, Thomas DL, et al. **Cerebral blood flow changes during pilocarpine-induced status epilepticus activity in the rat hippocampus.** *Exp Neurol* 2010;225:196–201 CrossRef Medline
6. Choy M, Cheung KK, Thomas DL, et al. **Quantitative MRI predicts status epilepticus-induced hippocampal injury in the lithium-pilocarpine rat model.** *Epilepsy Res* 2010;88:221–30 CrossRef Medline
7. Szabo K, Poepel A, Pohlmann-Eden B, et al. **Diffusion-weighted and perfusion MRI demonstrates parenchymal changes in complex partial status epilepticus.** *Brain* 2005;128:1369–76 CrossRef Medline
8. El-Koussy M, Mathis J, Lövbld K, et al. **Focal status epilepticus: follow-up by perfusion- and diffusion MRI.** *Eur Radiol* 2002;12:568–74 CrossRef Medline
9. Brodie MJ, Kwan P. **Staged approach to epilepsy management.** *Neurology* 2002;58:S2–S8 CrossRef Medline
10. Benbadis SR, Tatum WO, Vale FL. **When drugs don't work: an algorithmic approach to medically intractable epilepsy.** *Neurology* 2000;55:1780–84 CrossRef Medline
11. Wiebe S, Blume WT, Girvin JP, et al. **A randomized, controlled trial of surgery for temporal-lobe epilepsy.** *N Engl J Med* 2001;345:311–18 CrossRef Medline
12. Cukiert A, Cukiert CM, Argentoni M, et al. **Outcome after corticoamygdalohippocampectomy in patients with refractory temporal lobe epilepsy and mesial temporal sclerosis without preoperative ictal recording.** *Epilepsia* 2009;50:1371–76 CrossRef Medline
13. Jones AL, Cascino GD. **Evidence on use of neuroimaging for surgical treatment of temporal lobe epilepsy.** *JAMA Neurol* 2016;73:464–70 CrossRef Medline
14. LoPinto-Khoury C, Sperling MR, Skidmore C, et al. **Surgical outcome in PET-positive, MRI-negative patients with temporal lobe epilepsy.** *Epilepsia* 2012;53:342–48 CrossRef Medline
15. Sulc V, Stykel S, Hanson DP, et al. **Statistical SPECT processing in MRI-negative epilepsy surgery.** *Neurology* 2014;82:932–39 CrossRef Medline
16. Haller S, Zaharchuk G, Thomas DL, et al. **Arterial spin labeling perfusion of the brain: emerging clinical applications.** *Radiology* 2016;281:337–56 CrossRef Medline
17. Kong LM, Zeng JY, Zheng WB, et al. **Effects of acute alcohol consumption on the human brain: diffusional kurtosis imaging and arterial spin-labeling study.** *AJNR Am J Neuroradiol* 2019;40:641–47 CrossRef Medline
18. Jiang J, Zhao L, Zhang Y, et al. **Comparative analysis of arterial spin labeling and dynamic susceptibility contrast perfusion imaging for quantitative perfusion measurements of brain tumors.** *Int J Clin Exp Pathol* 2014;7:2790–99 Medline
19. Pizzini FB, Farace P, Manganotti P, et al. **Cerebral perfusion alterations in epileptic patients during peri-ictal and post-ictal phase: PASL vs DSC-MRI.** *Magn Reson Imaging* 2013;31:1001–05 CrossRef Medline
20. Ye FQ, Berman KF, Ellmore T, et al. **H215O PET validation of steady-state arterial spin tagging cerebral blood flow measurements in humans.** *Magn Reson Med* 2000;44:450–56 CrossRef Medline
21. Galazzo IB, Mattoli MV, Pizzini FB, et al. **Cerebral metabolism and perfusion in MR-negative individuals with refractory focal epilepsy assessed by simultaneous acquisition of (18)F-FDG PET and arterial spin labeling.** *Neuroimage Clin* 2016;11:648–57 CrossRef Medline
22. Whiting PF, Rutjes AW, Westwood ME, et al. **QUADAS-2: a revised tool for the quality assessment of diagnostic accuracy studies.** *Ann Intern Med* 2011;155:529–36 CrossRef Medline
23. van Houwelingen HC, Arends LR, Stijnen T. **Advanced methods in meta-analysis: multivariate approach and meta-regression.** *Stat Med* 2002;21:589–624 CrossRef Medline
24. Huedo-Medina TB, Sánchez-Meca J, Marín-Martínez F, et al. **Assessing heterogeneity in meta-analysis: Q statistic or I² index?** *Psychol Methods* 2006;11:193–206 CrossRef Medline
25. van Aert RC, Wicherts JM, van Assen MA. **Publication bias examined in meta-analyses from psychology and medicine: a meta-meta-analysis.** *PLoS One* 2019;14:e0215052 CrossRef Medline
26. Sierra-Marcos A, Carreño M, Setoain X, et al. **Accuracy of arterial spin labeling magnetic resonance imaging (MRI) perfusion in detecting the epileptogenic zone in patients with drug-resistant neocortical epilepsy: comparison with electrophysiological data, structural MRI, SISCO and FDG-PET.** *Eur J Neurol* 2016;23:160–67 CrossRef Medline
27. Kim BS, Lee ST, Yun TJ, et al. **Capability of arterial spin labeling MR imaging in localizing seizure focus in clinical seizure activity.** *Eur J Radiol* 2016;85:1295–303 CrossRef Medline
28. Gaxiola-Valdez I, Singh S, Perera T, et al. **Seizure onset zone localization using postictal hypoperfusion detected by arterial spin labelling MRI.** *Brain* 2017;140:2895–911 CrossRef Medline
29. Shang K, Wang J, Fan X, et al. **Clinical value of hybrid TOF-PET/MR imaging-based multiparametric imaging in localizing seizure focus in patients with MRI-negative temporal lobe epilepsy.** *AJNR Am J Neuroradiol* 2018;39:1791–98 CrossRef Medline
30. Lee SM, Kwon S, Lee YJ. **Diagnostic usefulness of arterial spin labeling in MR negative children with new onset seizures.** *Seizure* 2019;65:151–58 CrossRef Medline
31. Lee DS, Lee SK, Kim SK, et al. **Late postictal residual perfusion abnormality in epileptogenic zone found on 6-hour postictal SPECT.** *Neurology* 2000;55:835–41 CrossRef Medline
32. Ali II, Pirzada NA, Vaughn BV. **Periodic lateralized epileptiform discharges after complex partial status epilepticus associated with increased focal cerebral blood flow.** *J Clin Neurophysiol* 2001;18:565–69 CrossRef Medline
33. Blauwblomme T, Boddaert N, Chémaly N, et al. **Arterial spin labeling MRI: a step forward in non-invasive delineation of focal cortical dysplasia in children.** *Epilepsy Res* 2014;108:1932–39 CrossRef Medline
34. Pendse N, Wissmeyer M, Altrichter S, et al. **Interictal arterial spin-labeling MRI perfusion in intractable epilepsy.** *J Neuroradiol* 2010;37:60–63 CrossRef Medline

35. Lim YM, Cho YW, Shamim S, et al. **Usefulness of pulsed arterial spin labeling MR imaging in mesial temporal lobe epilepsy.** *Epilepsy Res* 2008;82:183–89 CrossRef Medline
36. Farrell JS, Gaxiola-Valdez I, Wolff MD, et al. **Postictal behavioural impairments are due to a severe prolonged hypoperfusion/hypoxia event that is COX-2 dependent.** *ELife* 2016;5:e19352 CrossRef Medline
37. Desai A, Bekelis K, Thadani VM, et al. **Interictal PET and ictal subtraction SPECT: sensitivity in the detection of seizure foci in patients with medically intractable epilepsy.** *Epilepsia* 2013;54:341–50 CrossRef Medline
38. Pollock JM, Whitlow CT, Tan H, et al. **Pulsed arterial spin-labeled MR imaging evaluation of tuberous sclerosis.** *AJNR Am J Neuroradiol* 2009;30:815–20 CrossRef Medline
39. Carmichael DW, Hamandi K, Laufs H, et al. **An investigation of the relationship between BOLD and perfusion signal changes during epileptic generalised spike wave activity.** *Magn Reson Imaging* 2008;26:870–73 CrossRef Medline
40. Yin C, Zhang X, Chen Z, et al. **Detection and localization of interictal ripples with magnetoencephalography in the presurgical evaluation of drug-resistant insular epilepsy.** *Brain Res* 2019;1706:147–56 CrossRef Medline

Dedicated 3D-T2-STIR-ZOOMit Imaging Improves Demyelinating Lesion Detection in the Anterior Visual Pathways of Patients with Multiple Sclerosis

E. Pravata,¹ L. Roccatagliata,² M.P. Sormani,³ L. Carmisciano,⁴ C. Lienherth,⁵ R. Sacco,⁶ A. Kaelin-Lang,⁷ A. Cianfoni,⁸ C. Zecca, and C. Gobbi⁹



ABSTRACT

BACKGROUND AND PURPOSE: Demyelinating lesions in the anterior visual pathways represent an underestimated marker of disease dissemination in patients with MS. We prospectively investigated whether a dedicated high-resolution MR imaging technique, the 3D-T2-STIR-ZOOMit, improves demyelinating lesion detection compared with the current clinical standard sequence, the 2D-T2-STIR.

MATERIALS AND METHODS: 3T MR imaging of the anterior visual pathways (optic nerves, chiasm, and tracts) was performed using 3D-T2-STIR-ZOOMit and 2D-T2-STIR, in patients with MS and healthy controls. Two experienced neuroradiologists assessed, independently, demyelinating lesions using both sequences separately. 3D-T2-STIR-ZOOMit scan-rescan reproducibility was tested in 12 patients. The Cohen κ was used for interrater agreement, and the intraclass correlation coefficient for reproducibility. Between-sequence detection differences and the effects of location and previous acute optic neuritis were assessed using a binomial mixed-effects model.

RESULTS: Forty-eight patients with MS with ($n = 19$) or without ($n = 29$) past optic neuritis and 19 healthy controls were evaluated. Readers' agreement was strong (3D-T2-STIR-ZOOMit: 0.85; 2D-T2-STIR: 0.90). The 3D-T2-STIR-ZOOMit scan-rescan intraclass correlation coefficient was 0.97 (95% CI, 0.96–0.98; $P < .001$), indicating excellent reproducibility. Overall, 3D-T2-STIR-ZOOMit detected more than twice the demyelinating lesions ($n = 89$) than 2D-T2-STIR ($n = 43$) (OR = 2.7; 95% CI, 1.7–4.1; $P < .001$). In the intracranial anterior visual pathway segments, 33 of the 36 demyelinating lesions (91.7%) detected by 3D-T2-STIR-ZOOMit were not disclosed by 2D-T2-STIR. 3D-T2-STIR-ZOOMit increased detection of demyelinating lesion probability by 1.8-fold in patients with past optic neuritis (OR = 1.8; 95% CI, 1.2–3.1; $P = .01$) and 5.9-fold in patients without past optic neuritis (OR = 5.9; 95% CI, 2.5–13.8; $P < .001$). No false-positive demyelinating lesions were detected in healthy controls.

CONCLUSIONS: Dedicated 3D-T2-STIR-ZOOMit images improved substantially the detection of MS disease dissemination in the anterior visual pathways, particularly in the intracranial segments and in patients without past optic neuritis.

ABBREVIATIONS: AON = acute optic neuritis; aVP = anterior visual pathway; DL = demyelinating lesion; HC = healthy controls; iCanal = intracanalicular optic nerve; iCran = intracranial optic nerve; iOrb = intraorbital optic nerve; OC = optic chiasm; OT = optic tract; pON = past optic neuritis

MS is the most common immune-mediated demyelinating disease in young adults,¹ with frequent involvement of the visual pathways.² Pathologic investigations demonstrated a high prevalence of demyelinating lesions (DLs) in the anterior visual pathways (aVPs), including the optic nerve, chiasm (OC), and tract (OT), in patients either with or without previous episodes of

acute optic neuritis (AON).³ Accordingly, ophthalmologic studies showed frequent occurrence of subclinical visual impairment in MS, even in patients without previous AON.⁴ Nevertheless and despite a previous proposal,⁵ the aVPs are currently not included among the sites investigated by MR imaging to demonstrate disease dissemination in space, due to the lack of supportive data

Received July 15, 2020; accepted after revision December 20.

From the Departments of Neuroradiology (E.P., A.C.) and Neurology (R.S., A.K.-L., C.Z., C.G.), Neurocenter of Southern Switzerland, Lugano, Switzerland; Department of Health Sciences (L.R., M.P.S., L.C.), University of Genova, Genova, Italy; Dipartimento di Scienze della Salute – DISSAL (L.R., M.P.S.), Istituto di Ricovero e Cura a Carattere Scientifico Ospedale Policlinico San Martino, Genoa, Italy; Bayer Vital GmbH (C.L.), Leverkusen, Germany; and Faculty of Biomedical Sciences (A.K.-L., A.C., C.Z., C.G.), Università della Svizzera Italiana, Lugano, Switzerland.

C. Zecca and C. Gobbi contributed equally to this work.

E.P. and R.S. received funding from the Advisory Board for Research of the Hospital Cooperation (Ente Ospedaliero Cantonale) and from the Swiss Society of Multiple Sclerosis for conducting this study (grant No. EOC.NEURORAD.1701).

Please address correspondence to Emanuele Pravata, MD, Neurocenter of Southern Switzerland, Department of Neuroradiology, Via Tesserete 46, 6903, Lugano, Switzerland; e-mail: emanuele.pravata@eoc.ch

Indicates article with online supplemental data.

<http://dx.doi.org/10.3174/ajnr.A7082>

about DL prevalence and MR imaging characteristics.⁶ Including highly sensitive examinations in the diagnostic workflow may potentially lead to earlier diagnosis and start of treatment⁵ and provide structural correlates for patients' asymptomatic visual loss.⁴ Furthermore, in the monitoring phase, an improved detection of new-onset lesions may help tailor treatment in individual patients.⁷

In a group of patients with MS with and without a history of AON and in a group of healthy controls (HC), we tested whether a dedicated inversion-recovery (STIR)-prepared T2-weighted technique, combining high spatial resolution and tissue contrast characteristics, the "3D-T2-STIR-ZOOMit" (Siemens), may improve DL diagnostic performance in the aVPs with respect to 2D-T2-STIR, the current standard technique.⁸

MATERIALS AND METHODS

The study was authorized by the Ethics Committee of Canton Ticino, Switzerland (2017-00814-CE3224, May 24, 2017). All participants provided written informed consent.

Study Participants

This was a prospective, cross-sectional, single-center study including 49 adult patients with relapsing-remitting MS according to the 2010 McDonald criteria⁹ and with or without previous AON history (pON+ and pON-, respectively), and 24 HC. Participants were enrolled between November 2017 and March 2019 at the MS Center of the Ospedale Regionale di Lugano (Neurocenter of Southern Switzerland), Switzerland, the regional center for neuro-ophthalmologic disorders. AON diagnosis was based on a history of visual acuity and color detection loss, typical field deficits, ocular pain, and fundus examination. MR imaging and visual evoked

potentials (prolonged P100 latency) were used as supportive tools when needed. All participants with MS were relapse- and steroid therapy-free for at least 3 months before enrollment. Specific exclusion criteria were other neurologic and ophthalmologic disorders (glaucoma, ocular hypertension, retinopathy, maculopathy).

MR Imaging Acquisition

Acquisition parameters of 3D-T2-STIR-ZOOMit and 2D-T2-STIR are reported in Table 1.

3D-T2-STIR-ZOOMit. We adapted the vendor-provided default T2-weighted sequence for small-FOV imaging with selective region excitation on a 3T Magnetom Skyra (Siemens) scanner^{10,11} with a 64-channel head/neck coil. We applied a nonselective inversion recovery preparation pulse,^{12,13} using an acquisition voxel size of 0.6 mm³. Scan duration was 8 minutes 54 seconds.

2D-T2-STIR. A standard 2D-T2-STIR sequence, with 2.5-mm section thickness, was acquired on the coronal plane, covering the orbits and the intracranial aVPs. The scan duration was 2 minutes 57 seconds

Additional information about sequences, image acquisition, and preparation, is provided in the Online Supplemental Data.

Image Quality

Figure 1 shows the normal anatomy of the aVPs as depicted by 3D-T2-STIR-ZOOMit and the segment boundaries defined for the analyses: intraorbital (iOrb), intracanalicular (iCanal), and intracranial (iCran) optic nerves, OC, and OT. The corresponding anatomic landmarks were also used for 2D-T2-STIR. One neuroradiologist (A.C.) and 1 neurologist (C.G.) with >15 years of experience in MS imaging rated, in each of the 5 aVP segments, field inhomogeneity and motion-related artifacts, according to a previously used scale: 0 = no relevant artifacts; 1 = mild artifacts not preventing image analysis; 2 = artifacts preventing accurate image analysis.¹⁴

Image Reading Sessions

Two neuroradiologists (E.P. and L.R.) with >15 years of experience in MS imaging performed 3 reading sessions each, >3 months apart to avoid recall bias.

Session 1. The blinded readers reviewed separately the 3D-T2-STIR-ZOOMit and 2D-T2-STIR image sets in a

Table 1: Acquisition parameters for 3D-T2-STIR-ZOOMit and 2D T2-STIR

Parameter	3D-T2-STIR-ZOOMit	2D-T2-STIR
Mode	3D	2D
Acquisition plane	Transversal	Coronal
TR/TE (ms)	240/119	4880/101
Magnetization preparation	Non-selective STIR	Non-selective STIR
T1 (ms)	220	220
FOV read/FOV phase	80 mm × 100%	180 mm × 100%
Base resolution/phase/section	128/100%/100%	320/100%/–
Acquired voxel size (X, Y, Z) (mm)	0.6, 0.6, 0.6	0.6, 0.6, 2.5
Interpolated voxel size (X, Y, Z) (mm)	0.3, 0.3, 0.6	
Flip angle	Variable	140°
Turbo factor	46	35
Averages	1.4	1
Acceleration factor (GRAPPA)	2	None
Scan duration (min/sec)	8/54	2/57

Note:—GRAPPA, generalized autocalibrating partially parallel acquisition; STIR, short tau inversion recovery.

Table 2: Confusion matrix illustrating DL detection rates of 3D-T2-STIR-ZOOMit and 2D-T2-STIR per each aVP segment in all patients with MS^a

		3D-T2-STIR-ZOOMit									
		iOrb–	iOrb+	iCanal–	iCanal+	iCran–	iCran+	OC–	OC+	OT–	OT+
2D-T2-STIR	–	67 (69.8)	9 (9.4)	68 (70.8)	8 (8.3)	87 (90.6)	7 (7.3)	79 (82.3)	16 (16.7)	86 (89.6)	10 (10.4)
	+	0 (0)	20 (20.8)	4 (4.2)	16 (16.7)	0 (0)	2 (2.1)	0 (0)	1 (1.0)	0 (0)	0 (0)

^a Data are number of DLs (n = 96, for each aVP segment) with percentages in parentheses and refer to 96 observations (left and right sides together in 48 patients) in each aVP segment. Absence of a lesion is indicated with –; presence, with +.

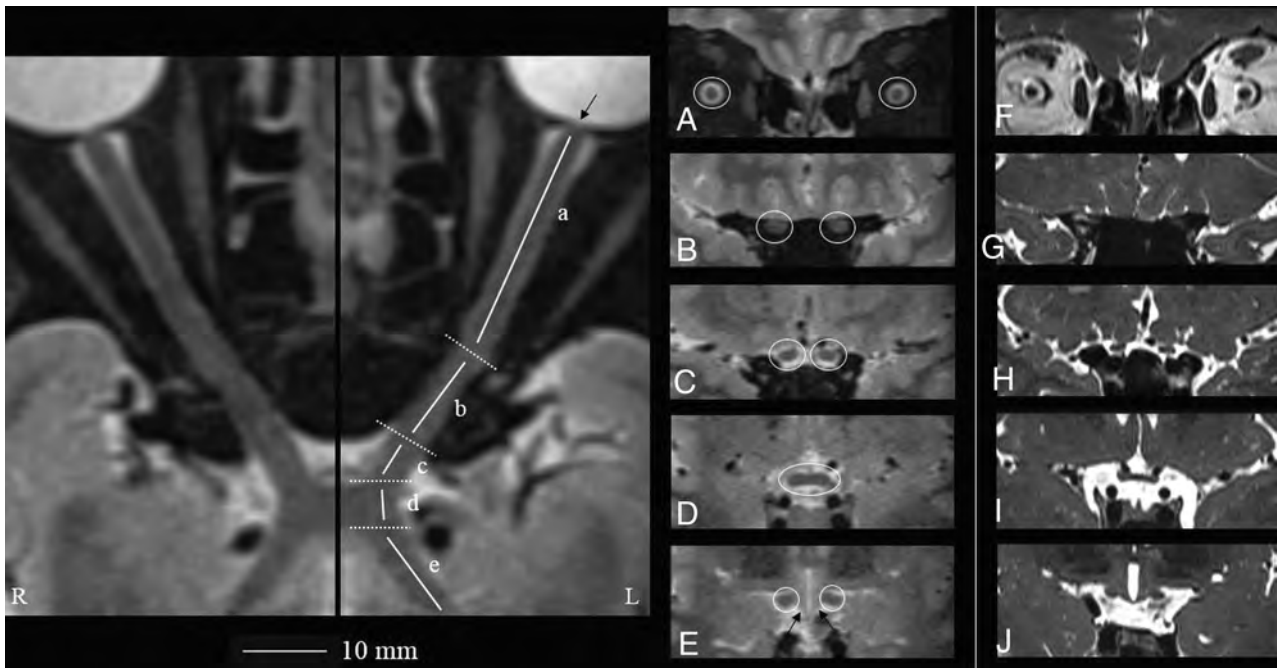


FIG 1. Geometrically unbiased, high-resolution representation of the aVP segment anatomy by 3D-T2-STIR-ZOOMit (healthy control No. 9001). The left panel shows curved reconstructions along the true long axis of the right and left aVPs. The *thin arrow* points to the porus opticus. Coronal-oblique reconstruction images corresponding to the iOrb (A, from the eye bulb to the optic canal), iCanal (B, in the optic canal), and iCran (C, from the optic canal to the chiasm) segments and OC (D) and OT (E) segments highlighted in *white circles* are presented. By comparison, the right panel (F–J, different healthy volunteer) shows corresponding coronal-oblique images obtained with a 3D-ZOOMit standard sequence without the STIR preparation pulse. Note substantial contrast resolution gain with 3D-T2-STIR-ZOOMit, particularly at interfaces between different signal tissues and between the OT and adjacent hypothalamus (*thin arrows* in E).

random order. 3D-T2-STIR-ZOOMit images were presented in orthogonally reconstructed planes, whereas 2D-T2-STIR images were presented in the acquisition (coronal) plane. To assess the presence of a lesion, we used a previously employed binary scale:¹⁴ 0 = no lesion; 1 = lesion. Lesions were defined as areas of signal hyperintensity, referenced to the normal-appearing white matter of the frontal lobes, either partially or completely involving the whole aVP short-axis section. A consensus was reached after resolving discrepancies during a subsequent separate session.

Session 2. To test the hypothesis that 3D-T2-STIR-ZOOMit may detect false-positive lesions in HC assuming that these had no DLs, the readers performed an additional joint session on scans of the 19 HC and 19 randomly chosen participants with MS.

Session 3. To assess scan-rescan reproducibility, a final joint session compared the 3D-T2-STIR-ZOOMit images re-acquired from 12 participants with MS with those from session 1.

Statistical Analysis

Categorical variables were reported with count and percentages; continuous variables, with mean (SD) or median and interquartile range. Interrater reliability was reported with accuracy, Cohen κ , and their 95% CIs. A Cohen κ of >0.8 suggests a strong level of agreement between the raters. To assess scan-rescan reproducibility of 3D-T2-STIR-ZOOMit images, we calculated the interclass correlation coefficient. Between-sequence detection differences and the effects of DL side and location in the aVPs, accounting for within-patient correlation, were assessed using a binomial mixed-

effects logistic model. OR, 95% confidence intervals, and *P* values were reported.

P values $< .05$ were considered significant. R statistical and computing software, Version 3.6.0 (<http://www.r-project.org/>) was used for all analyses.

RESULTS

Participant Characteristics

Of 73 initially included participants (49 with MS, 24 HC), 48 participants with MS (39.1 [SD, 13.1] years of age, 30 women) with ($n = 19$) or without ($n = 29$) past optic neuritis (pON+/pON-) and 19 HC (35.1 [SD, 8.1] years of age, 10 women) were finally evaluated (Fig 2). On image inspection, scans of 1 participant with MS and 3 HC were discarded due to poor image quality in all aVP segments (movement) and also scans of 2 HC for coil-related artifacts (shading artifacts). The main demographic and clinical characteristics of participants with MS are presented in the Online Supplemental Data. Patients' neurologic impairment severity, assessed with the Expanded Disability Status Scale,¹⁵ was mild (median = 2; range, 1–3.5). Twenty-nine participants (60.4%) were pON-. Among those with pON+ ($n = 19$, 39.6%), 4 had bilateral AON. When we counted individual eyes, 73 (76%) had no AON and 23 (24%) had previous AON.

Image Quality

The Online Supplemental Data illustrate samples of the encountered artifacts. As for 3D-T2-STIR-ZOOMit, grade I movement artifacts were noted in all aVP segments in 3 patients with MS

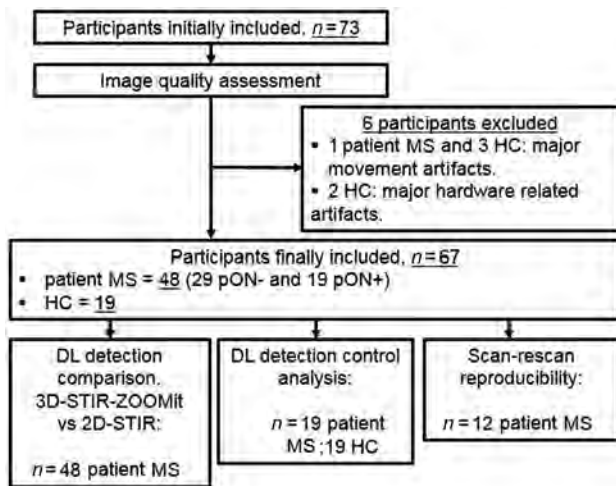


FIG 2. Flow chart showing the numbers of participants and healthy participants with MS included in the study who were assessed and evaluated.

and only in the iOrb segment in 7 patients. Field inhomogeneity artifacts occurred in the iCanal segment in 11 patients with grade 1 and 6 with grade 2, and in 3 (grade 1) and 3 (grade 2) HC. No relevant artifacts were recorded on 2D-T2-STIR images.

3D-T2-STIR-ZOOMit Reliability

Interrater Reliability. Accuracy for 3D-T2-STIR-ZOOMit was 0.96 (95% CI, 0.93–0.97), and the Cohen κ was 0.85 (95% CI, 0.78–0.91), whereas accuracy for 2D-T2-STIR was 0.98 (95% CI, 0.97–0.99) and the Cohen κ was 0.90 (95% CI, 0.83–0.97). The strong level of interrater reliability for 3D-T2-STIR-ZOOMit and the overlapping κ confidence intervals suggest similar agreement between the techniques.

HC Analysis. We assessed 19 HC and 19 randomly chosen participants with MS, for a total of 380 sites (10 aVP segments in 38 participants). At consensus, 28 lesions were found in participants with MS, whereas no lesions were found in HC. Agreement was 0.995 (95% CI, 0.981–0.999). κ was 0.96 (95% CI, 0.91–0.99).

For scan-rescan reproducibility, the ICC was 0.97 (95% CI, 0.96–0.98), $F(120) = 38$, $P < .001$, indicating excellent reproducibility (Online Supplemental Data).¹⁴

DL Detection Comparison: All Participants with MS

Figure 3 illustrates the DL appearance on 3D-T2-STIR-ZOOMit sequences. Lesions involved either completely or, partially, the aVP cross-section. Subtle and diffuse signal abnormalities without definite segmental boundaries were also encountered, but this pattern was not systematically assessed in the present investigation.

Ten aVP segments (5 for each side) were reviewed in 48 participants with MS and 96 eyes, for both techniques. Table 2 presents the DL detection rates of 3D-T2-STIR-ZOOMit and 2D-T2-STIR. With 3D-T2-STIR-ZOOMit, more than twice the DLs ($n = 89$) were detected compared with 2D-T2-STIR ($n = 43$) (OR = 2.7; 95% CI, 1.7–4.1; $P < .001$). Detection capability differences were similar across sides (right versus left, OR = 1.1; 95%

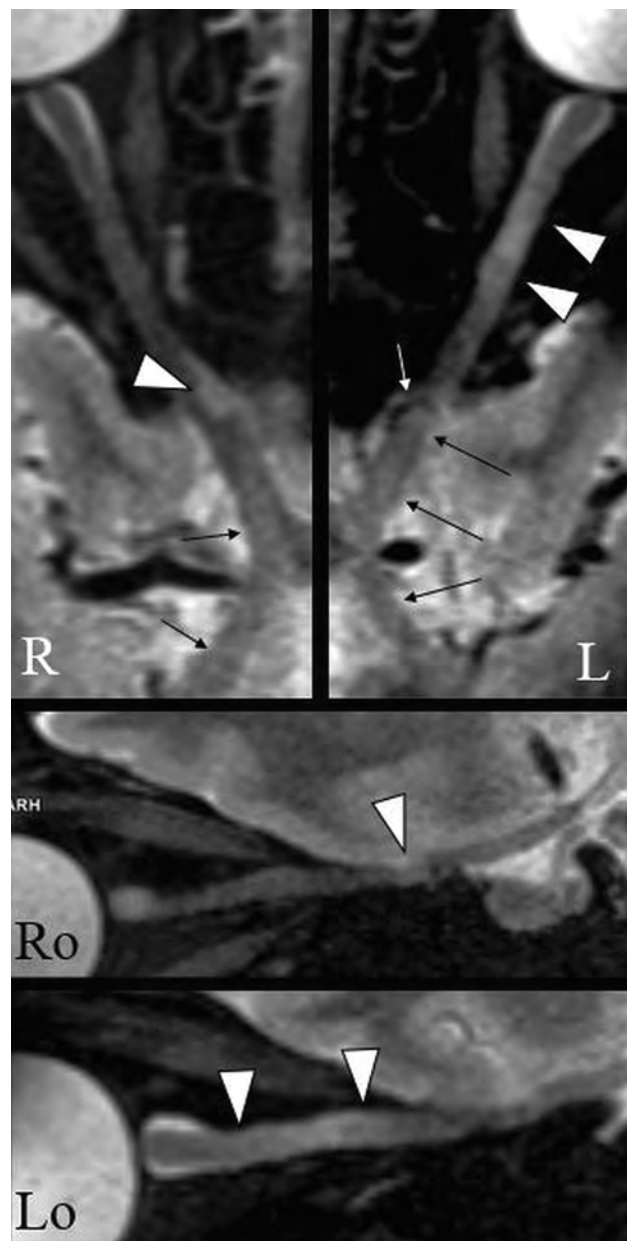


FIG 3. An example of the DL appearance on 3D-T2-STIR-ZOOMit images in a patient with MS (No. 0034). The upper panel shows curved reconstructions along the true long axis of the right and left aVPs. Focal signal hyperintensities indicate DLs with partial (right) and complete (left) involvement of the optic nerve cross-section (arrowheads). There are areas of diffuse signal hyperintensity with no definite boundaries along the aVP (thin arrows), possibly related to diffuse demyelination and/or degeneration. The white arrow indicates the ophthalmic artery causing nerve impression. Ro and Lo images present sagittal-oblique reconstructions of R and L.

CI, 0.7–1.7; $P = .47$), but not across segments ($\chi^2 [df=4] = 20.4$; $P < .001$).

In particular, in the iOrb segment (Fig 4), 9 of 29 DLs (31%, corresponding to 10.1% of all aVP lesions) detected by 3D-T2-STIR-ZOOMit were missed by 2D-T2-STIR.

In the iCanal segment only, 4 DLs were detected with 2D-T2-STIR, but not with 3D-T2-STIR-ZOOMit. Of these, one occurred in a participant with MS with grade 2 movement artifacts, and

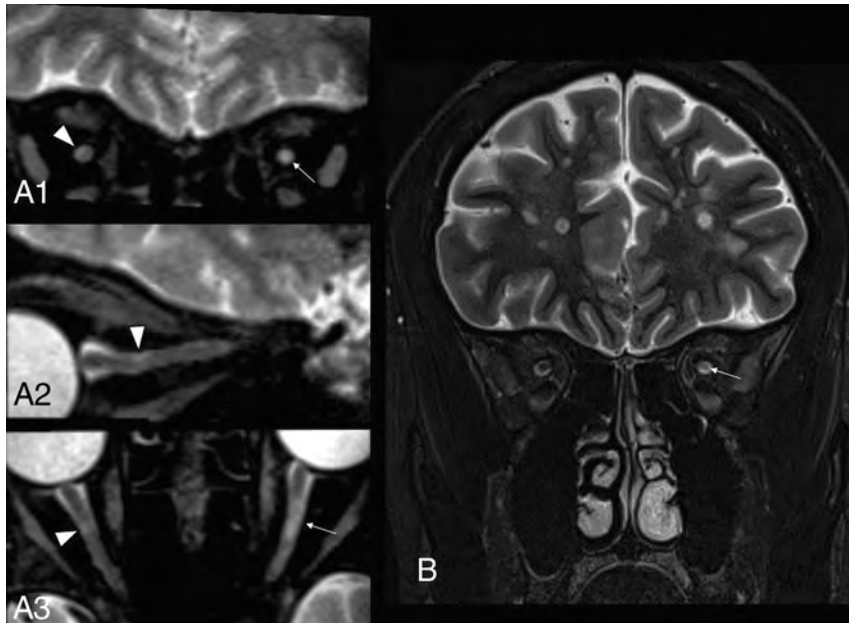


FIG 4. Comparison of extra cranial aVP detection in a participant with MS with previous unilateral AON on the left side (patient with MS No. 0038). A₁₋₃, A very small, asymptomatic DL partially involving the superolateral aspect of the right iOrb segment (arrowheads on coronal, sagittal-oblique, and axial-oblique images) was missed on the 2D-T2-STIR image (B). A larger L iOrb lesion was instead detected by both sequences (thin arrows in A₁, A₃ and B), possibly representing chronic changes related to the previous AON.

one was on a scan with grade 2 magnetic field inhomogeneity artifacts. Two DLs were missed by 3D-T2-STIR-ZOOMit but could be retrospectively noticed after being detected by 2D-T2-STIR.

If one takes all intracranial segments together (iCran, OC, and OT), 33 of 36 DLs (corresponding to 40.5% of all aVP lesions) detected by 3D-T2-STIR-ZOOMit were missed by 2D-T2-STIR. These DLs appeared generally smaller than the extracranial lesions (Fig 5). OT lesions, representing 10.4% of all aVP lesions, were characterized by signal contrast loss between the OT and the adjacent hypothalamus gray matter (Fig 5). Due to a resemblance to lobster antennas, we propose this appearance as the “lobster antenna” sign.

DL Detection Comparison: pON+ and pON-

3D-T2-STIR-ZOOMit revealed ≥ 1 lesion in 18 of the 19 (94.7%) pON+, and in 13 of the 29 (44.8%) pON- patients whereas 2D-T2-STIR revealed lesions only in 17 patients with pON+ (89.5%) and 5 (17.2%) patients with pON- (Online Supplemental Data and Fig 6). DLs were about 6.5 times more frequently found in pON+ than in pON- (OR=6.5; 95% CI, 2.8–15.1; $P < .001$). Lesion-detection probability using 3D-T2-STIR-ZOOMit was 1.8 times higher in pON+ (OR = 1.8; 95% CI, 1.2–3.1; $P = .01$) and 5.9 times higher in pON- (OR = 5.9; 95% CI, 2.5–13.8; $P < .001$) than when using 2D-T2-STIR. The larger detection increment in pON- compared with pON+ was statistically significant (P for interaction = .049). Among the 73 individual eyes with no AON, 3D-T2-STIR-ZOOMit revealed 32 DLs, whereas 2D-T2-STIR revealed only 4.

DISCUSSION

We showed that 3D-T2-STIR-ZOOMit may detect a substantially larger numbers of aVP DLs, particularly in the intracranial segments and in patients without pON-, compared with the standard 2D-T2-STIR.^{5,8} Because optic nerve lesions represent a hallmark of MS disease dissemination,¹⁶ including highly sensitive MR imaging examinations in the diagnostic workflow may lead to earlier diagnosis and start of treatment⁵ and provide structural correlates for patients’ asymptomatic vision loss.⁴ The technique specificity was supported by the absence of false-positive lesions in HC.

The classic 2D-T2-STIR uses a STIR pulse to both suppress orbital fat and increase image contrast by exploiting the T1 relaxation time difference among tissues,^{12,13} ultimately leading to an increased lesion conspicuity with respect to non-inversion recovery-prepared T2-TSE sequences using spectral fat saturation. However, 2D imaging offers suboptimal demarcation of anatomic details^{17–20} because of through-plane partial volume effects.²¹ The ZOOMit is a recently developed MR imaging technology that focuses on data sampling by applying an excitation pulse that is spatially selective in both section and phase-encoding directions.^{10,11} The dedicated 3D-T2-STIR-ZOOMit technology allowed disclosing aVP disease dissemination with a 5.9-fold probability increase compared with 2D-T2-STIR, thus revealing a substantially larger number of clinically asymptomatic DLs.

3D-T2-STIR-ZOOMit detected at least 1 DL in 44.8% of patients with pON-. Using a 3D double inversion recovery sequence, Sartoretti et al²² identified lesions in 72% of a group of patients with MS without visual symptoms within the past 3 years. Patient selection criteria might, at least in part, account for such a relatively higher percentage because patients who had visual symptoms before the previous 3 years might have been included. Indeed, with the same technique, Hadhoum et al²³ found lesions in 38.5% of optic nerves without AON history, while Riederer et al²⁴ observed subclinical lesions in 18% of their patients. However, these studies did not assess the OT, whose lesion burden constituted 10.4% of all DLs in our participants with MS.

Most interesting, DLs frequently targeted the intracranial aVP segments, which, altogether, had 40.5% of aVP lesions, a figure that was largely missed with 2D-T2-STIR. Although brain 3D techniques used in clinical practice, such as double inversion recovery or FLAIR, might detect a relatively higher number of intracranial aVP lesions than 2D-STIR, their spatial resolution is substantially lower than that of 3D-T2-STIR-ZOOMit.^{14,25} Here, we were able to disclose a frequent occurrence of the OT involvement in MS,

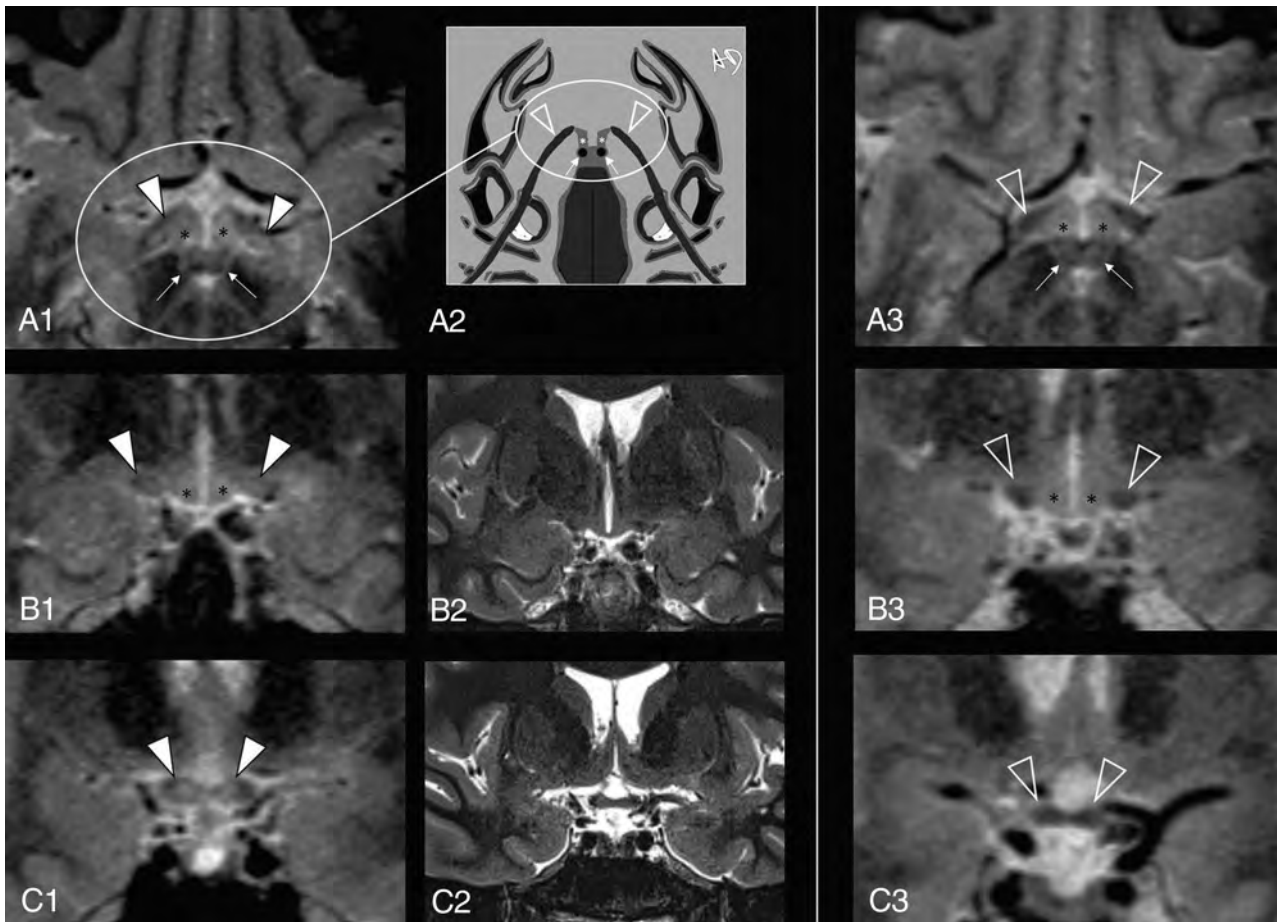


FIG 5. Intracranial aVP detection of asymptomatic DL in a participant with MS without a previous AON history (patient with MS No. 0020) on 3D-T2-STIR-ZOOMit images. A₁ and B₁, Bilateral DLs partially affecting the OTs and impairing tissue contrast (arrowheads) with the adjacent hypothalamus ventrolateral aspects (asterisks). C₁, Further depiction of DLs with partial involvement of the OC (arrowheads). All these lesions were not detectable on 2D-T2-STIR (middle panel, B₂, C₂). The right panel (A₃, B₃, C₃) provides the reference normal anatomy (empty arrowheads) from a healthy control (No. 9005). Because of the axial plane appearance of the OTs and hypothalamus ventrolateral aspects resembling lobster antennas, we propose the “lobster antenna” sign to indicate loss of normal tissue contrast between the OT and hypothalamus. Thin arrows in A₁ and A₃ indicate the mammillary bodies, corresponding to the lobster’s eyes in the artwork (A₂). Courtesy of Dr. Andrea Diociasi.

leading to the proposed lobster antenna sign appearance. Future investigations in larger cohorts and longitudinal studies are warranted to compare with other autoimmune disorders typically involving this region, such as the neuromyelitis optica spectrum and the antimyelin oligodendrocyte glycoprotein antibodies disorders.² Indeed, a detailed knowledge of DL appearance and spatial distribution patterns in the entire aVP may support prompt differential diagnosis and appropriate treatment initiation.

Our technique has several limitations. First, we did not use post-mortem specimens as a criterion standard to definitely assess 3D-T2-STIR-ZOOMit accuracy. As far as we are aware, no previous radiologic-pathologic correlation data are available in the literature for the aVP. However, our control analysis showed that 3D-T2-STIR-ZOOMit was unlikely to provide false-positive results in healthy participants. Moreover, between-reader agreement and scan-rescan consistency were high, suggesting adequate technique reproducibility. Second, scan duration was relatively long, and images from 3 participants had to be discarded for severe movement artifacts. Implementation in the clinical setting requires appropriate hardware as well as patient coaching before the examination (see

the MATERIALS AND METHODS section). This study was performed in patients with relatively mild disability. Future sequence developments, using, for example, compressed sensing,²⁶ 3D parallel imaging acceleration techniques,²⁷ and/or motion-correction techniques²⁸ may facilitate image acquisition by reducing the scan time and movement artifacts, therefore optimizing the examination workflow. Third, field inhomogeneity artifacts preventing visualization of the iCanal segment were relatively frequent, leading to a reduced DL-detection capability at this level. Finally, we did not assess here whether the increased sensitivity allowed by 3D-T2-STIR-ZOOMit may help to explain patients’ subclinical vision loss and to predict disability accrual and clinical relapses. Future studies are planned to investigate the relationships among DL load, precise ophthalmologic measurements of visual acuity loss, and neurologic disability.

CONCLUSIONS

We showed that the assessment of MS disease dissemination in the aVP may be substantially improved using dedicated high-spatial-resolution and contrast-optimized 3D-T2-STIR-ZOOMit

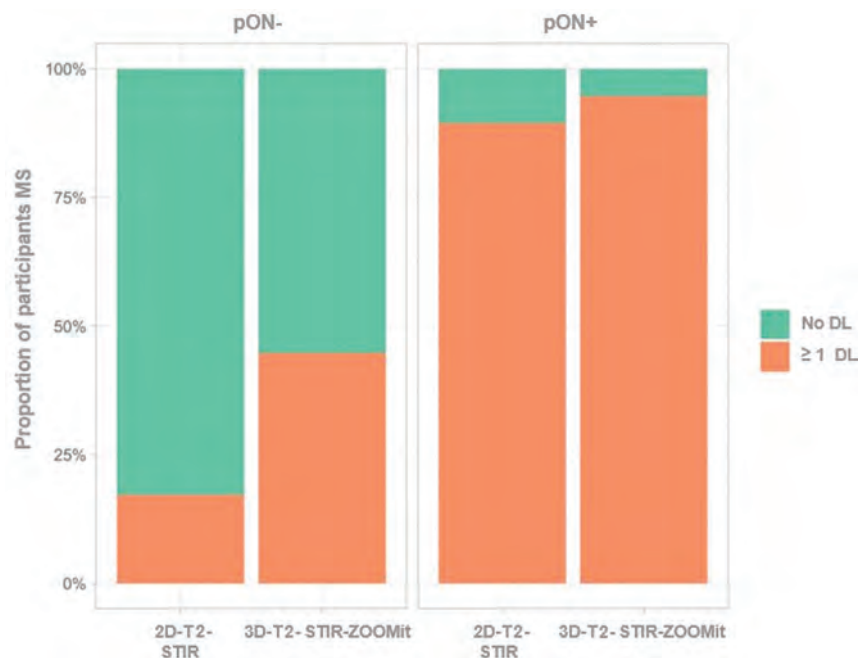


FIG 6. Proportion of participants with MS with at least 1 identified DL (at any site and any side) by previous AON history (pON-/pON+) and MR imaging technique (2D-T2-STIR/3D-T2-STIR-ZOOMit).

images. Advantages are particularly beneficial at the level of the intracranial segments and in patients without a history of acute optic neuritis.

ACKNOWLEDGMENTS

The authors thank Liliane Petrini, Neurocenter of Southern Switzerland (Lugano, Switzerland), for help with the bibliography and for finalizing the manuscript; Dr Andrea Diociai, University of Genoa (Italy), for Fig 5 artwork; and Mr. Navarajah Nadarajah, Ospedale Regionale di Lugano (Lugano, Switzerland), for MR imaging data acquisition.

Disclosures: Emanuele Pravatà—RELATED: Grant: Scientific Research Advisory Board of the Ente Ospedaliero Cantonale, Swiss Multiple Sclerosis Society*; UNRELATED: Grants/Grants Pending: Velux Stiftung; Maria Pia Sormani—UNRELATED: Board Membership: Biogen, Merck, Sanofi, Roche, Novartis, Immunic; Consultancy: Biogen, Merck, Sanofi, Roche, Novartis, Immunic, Celgene; Grants/Grants Pending: Roche, Merck; Payment for Lectures Including Service on Speakers Bureaus: Biogen, Merck, Sanofi, Roche, Novartis, Immunic, Celgene. Rosaria Sacco—UNRELATED: Board Membership: Employer, Department of Neurology, Regional Hospital Lugano, Lugano, Switzerland receives financial support from AbbVie, Almirall, Biogen Idec, Celgene, Sanofi, Merck, Novartis, Teva Pharmaceuticals, Roche*; Payment for Lectures Including Service on Speakers Bureaus: Novartis, Celgene; Payment for Development of Educational Presentations: Sanofi; Travel/Accommodations/Meeting Expenses Unrelated to Activities Listed: Merk. Alain Kaelin-Lang—UNRELATED: Consultancy: Advisory board about the therapeutic use of Abobotulinum toxinA to treat spasticity, Ipsen*; Employment: Ente Ospedaliero Cantonale, Bellinzona, Switzerland; Grants/Grants Pending: unrestricted research grant, Merz Pharma*; Travel/Accommodations/Meeting Expenses Unrelated to Activities Listed: Movement Disorders Meeting, Nizza, 2019; Honk-Kong, 2018; companies: Allergan, Merz Pharma.* Chiara Zecca—UNRELATED: Consultancy: Biogen, Celgene, Lilly, Merck, Sanofi, Teva Pharmaceuticals, Roche*; Grants/Grants Pending: Biogen, Merck*; Payment for Lectures Including Service on Speakers Bureaus: Novartis, Celgene, Lilly, Novartis, Teva Pharmaceuticals.* Claudio Gobbi—RELATED: Grants: Scientific Research Advisory Board of the Ente Ospedaliero Cantonale, Swiss Multiple Sclerosis Society, Comments: Scientific Research Advisory Board of the Ente

Ospedaliero Cantonale*; UNRELATED: Board Membership: Biogen Idec, Celgene, Sanofi, Merck Serono, Novartis, Roche, and Teva Pharmaceuticals*; Consultancy: Biogen Idec, Celgene, Sanofi, Merck Serono, Novartis, Roche, and Teva Pharmaceuticals*; Grants/Grants Pending: Biogen Idec, Celgene, Sanofi, Merck Serono, Novartis, Roche, and Teva Pharmaceuticals, * *Money paid to the institution.

REFERENCES

1. Reich DS, Lucchinetti CF, Calabresi PA. Multiple sclerosis. *N Engl J Med* 2018;378:169–80 CrossRef Medline
2. Dutra BG, Da Rocha AJ, Nunes RH, et al. Neuromyelitis optica spectrum disorders: spectrum of MR imaging findings and their differential diagnosis. *Radiographics* 2018;38:169–93 CrossRef Medline
3. Ulrich J, Groebke-Lorenz W. The optic nerve in multiple sclerosis: a morphological study with retrospective clinico-pathological correlations. *Neuro-Ophthalmology* 1983;3:149–59 CrossRef
4. Balcer LJ, Frohman EM. Evaluating loss of visual function in multiple sclerosis as measured by low-contrast letter acuity. *Neurology* 2010;74:S16–23 CrossRef Medline
5. Filippi M, Rocca MA, Ciccarelli O, et al. MRI criteria for the diagnosis of multiple sclerosis: MAGNIMS consensus guidelines. *Lancet Neurol* 2016;15:292–303 CrossRef Medline
6. Thompson AJ, Banwell BL, Barkhof F, et al. Diagnosis of multiple sclerosis: 2017 revisions of the McDonald criteria. *Lancet Neurol* 2018;17:162–73 CrossRef Medline
7. Sormani MP, De Stefano N. Defining and scoring response to IFN- β in multiple sclerosis. *Nat Rev Neurol* 2013;9:504–12 CrossRef Medline
8. Petzold A, Wattjes MP, Costello F, et al. The investigation of acute optic neuritis: a review and proposed protocol. *Nat Rev Neurol* 2014;10:447–58 CrossRef Medline
9. Polman CH, Reingold SC, Banwell B, et al. Diagnostic criteria for multiple sclerosis: 2010 Revisions to the McDonald Criteria. *Ann Neurol* 2011;69:292–302 CrossRef Medline
10. Blasche M, Riffel P, Lichy M. TimTX TrueShape and syngo ZOOMit: technical and practical aspects. *MAGNETOM Flash* 2012 https://cdn0.scrvt.com/39b415fb07de4d9656c7b516d8e2d907/1800000000118051/a06d5db36c83/TimTX_TrueShape_and_syngo_Zoomit_Aspects_1800000000118051.pdf. Accessed January 01, 2020
11. Fang S, Bai HX, Fan X, et al. A novel sequence: ZOOMit-blood oxygen level-dependent for motor-cortex localization. *Clin Neurosurg* 2020;86:E124–32 CrossRef Medline
12. Bot JC, Barkhof F, Lycklama À, et al. Comparison of a conventional cardiac-triggered dual spin-echo and a fast STIR sequence in detection of spinal cord lesion in multiples sclerosis. *Eur Radiol* 2000;10:753–58 CrossRef Medline
13. Thorpe JW, MacManus DG, Kendall BE, et al. Short tau inversion recovery fast spin-echo (fast STIR) imaging of the spinal cord in multiple sclerosis. *Magn Reson Imaging* 1994;12:983–89 CrossRef Medline
14. Hodel J, Outteryck O, Bocher AL, et al. Comparison of 3D double inversion recovery and 2D STIR FLAIR MR sequences for the imaging of optic neuritis: pilot study. *Eur Radiol* 2014;24:3069–75 CrossRef

15. Kurtzke JF. **Rating neurologic impairment in multiple sclerosis: An Expanded Disability Status Scale (EDSS).** *Neurology* 1983;33:1444–52 CrossRef Medline
16. Gerales R, Ciccarelli O, Barkhof F, et al. MAGNIMS study group. **The current role of MRI in differentiating multiple sclerosis from its imaging mimics.** *Nat Rev Neurol* 2018;14:199–213 CrossRef Medline
17. Bink A, Schmitt M, Gaa J, et al. **Detection of lesions in multiple sclerosis by 2D FLAIR and single-slab 3D FLAIR sequences at 3.0 T: initial results.** *Eur Radiol* 2006;16:1104–10 CrossRef Medline
18. Molyneux PD, Tubridy N, Parker GJ, et al. **The effect of section thickness on MR lesion detection and quantification in multiple sclerosis.** *AJNR Am J Neuroradiol* 1998;19:1715–20 Medline
19. Moraal B, Roosendaal SD, Pouwels PJ, et al. **Multi-contrast, isotropic, single-slab 3D MR imaging in multiple sclerosis.** *Eur Radiol* 2008;18:2311–20 CrossRef Medline
20. Kallmes DF, Hui FK, Mugler JP. **Suppression of cerebrospinal fluid and blood flow artifacts in FLAIR MR imaging with a single-slab three-dimensional pulse sequence: Initial experience.** *Radiology* 2001;221:251–55 CrossRef Medline
21. Kneeland JB, Shimakawa A, Wehrli FW. **Effect of intersection spacing on MR image contrast and study time.** *Radiology* 1986;158:819–22 CrossRef Medline
22. Sartoretti T, Sartoretti E, Rauch S, et al. **How common is signal-intensity increase in optic nerve segments on 3D double inversion recovery sequences in visually asymptomatic patients with multiple sclerosis?** *AJNR Am J Neuroradiol* 2017;38:1748–53 CrossRef Medline
23. Hadhoum N, Hodel J, Defoort-Dhellemmes S, et al. **Length of optic nerve double inversion recovery hypersignal is associated with retinal axonal loss.** *Mult Scler* 2016;22:649–58 CrossRef Medline
24. Riederer I, Mührlau M, Hoshi MM, et al. **Detecting optic nerve lesions in clinically isolated syndrome and multiple sclerosis: double-inversion recovery magnetic resonance imaging in comparison with visually evoked potentials.** *J Neurol* 2019;266:148–56 CrossRef Medline
25. Traboulsee A, Simon JH, Stone L, et al. **Revised recommendations of the consortium of MS centers task force for a standardized MRI protocol and clinical guidelines for the diagnosis and follow-up of multiple sclerosis.** *AJNR Am J Neuroradiol* 2016;37:394–401 CrossRef Medline
26. Yuhasz M, Hoch MJ, Hagiwara M, et al. **Accelerated internal auditory canal screening magnetic resonance imaging protocol with compressed sensing 3-dimensional T2-weighted sequence.** *Invest Radiol* 2018;53:742–47 CrossRef Medline
27. Fritz J, Fritz B, Thawait GG, et al. **Three-dimensional CAIPIRINHA SPACE TSE for 5-minute high-resolution MRI of the knee.** *Invest Radiol* 2016;51:609–17 CrossRef Medline
28. White N, Roddey C, Shankaranarayanan A, et al. **PROMO: real-time prospective motion correction in MRI using image-based tracking.** *Magn Reson Med* 2010;63:91–105 CrossRef Medline

A Novel Method to Measure Venular Perivascular Spaces in Patients with MS on 7T MRI

I.C. George, A. Arrighi-Allisan, B.N. Delman, P. Balchandani, S. Horng, and R. Feldman



ABSTRACT

SUMMARY: In MS, inflammatory cells accumulate within the perivascular spaces of acute and chronic lesions. Reliance on perivascular spaces as biomarkers for MS remains uncertain because various studies have reported inconsistencies in perivascular space anatomy. Distinguishing between venular and arteriolar perivascular spaces is pathophysiologically relevant in MS. In this pilot study, we leverage susceptibility-weighted imaging at 7T to better identify perivascular spaces of venular distribution on corresponding high-resolution T2 images.

ABBREVIATIONS: HC = healthy controls; PVS = perivascular space

In MS, immune cells, immunoglobulins, and proinflammatory factors cross 2 barriers to enter the CNS: the vascular endothelium, or blood-brain barrier, and the glia limitans.¹ Between these is the perivascular space (PVS), where immune cells may accumulate in both active and chronic MS lesions.²

The localization of immune cells and inflammatory markers in relation to perivascular spaces, along with formation of MS lesions around central veins, suggests that changes in PVS anatomy may reflect disease severity.³ Previous work reported differences in the PVS anatomy between patients with MS and healthy controls (HC), though results have conflicted.⁴⁻⁶ In addition to the heterogeneities of the study design, including differences in field strengths and MS phenotypes, discrepancies may relate to inadequate differentiation between venular and arteriolar PVSs, which are differentially affected in MS.⁷ We hypothesized that

selective analysis of venular PVSs may more accurately reflect pathophysiologic changes in MS.

We developed a novel technique coregistering T2-TSE images with SWI to identify venular PVSs (with central susceptibility suggesting deoxygenated blood) or nonvenular PVSs (lacking susceptibility). We present the pilot results at 7T on 3 persons with relapsing-remitting MS and 3 HC.

MATERIALS AND METHODS

Three persons with MS (1 woman/2 men; Expanded Disability Status Scale scores, 2.0, 3.0, and 0; 32, 33, and 35 years of age) and 3 age-matched HC (32, 33, and 35 years of age) were recruited through Mount Sinai Hospital. All persons with MS met the 2017 McDonald criteria⁸ and received disease-modifying therapy. Informed consent was obtained from all participants.

Subjects were scanned on a 7T scanner (Magnetom 7T; Siemens) using an SC72CD gradient coil (maximum slew rate = 200 T/m/s, Gmax = 70 mT/m) with single-channel transmit and 32-channel receive head coils (Nova Medical). Sequences included T2-TSE, SWI, and MP2RAGE with a uniform denoised reconstruction. Details are listed in the protocol.⁹

To detect vessels, we developed a vessel-segmentation tool in Matlab (MathWorks).¹⁰ Minimum-intensity-projection images were obtained from SWI. Vessel edge enhancement was performed by finding the eigenvalues of the Hessian matrix.^{11,12}

Uniform denoised images were used to create GM and WM volumetric segmentations of the brain using FreeSurfer, Version 6.0 (<http://surfer.nmr.mgh.harvard.edu>). Segmentations were used to calculate total WM volume and create GM and WM masks. Lesions were segmented by the lesion growth algorithm (<https://>

Received September 8, 2020; accepted after revision January 25, 2021.

From the Department of Neurology (I.C.G.), Massachusetts General Hospital, Boston, Massachusetts; Departments of Medical Education (A.A.-A.), Diagnostic, Molecular and Interventional Radiology (B.N.D., P.B.), Neuroscience and Psychiatry and the BioMedical Engineering and Imaging Institute (P.B.), and Department of Neurology (S.H.), Icahn School of Medicine at Mount Sinai, New York, New York; and Departments of Computer Science, Mathematics, Physics, and Statistics (R.F.), University of British Columbia, Kelowna, British Columbia, Canada.

S. Horng and R. Feldman contributed equally to this work.

This project was funded by National Institutes of Health R01MH109544.

An earlier version of this work previously presented at: European Committee for Treatment and Research in Multiple Sclerosis Conference in Berlin, Germany; October 10–12, 2018.

Please address correspondence to Ilena George, MD, 15 Parkman St—WAC 835, Boston, MA 02114; e-mail: igeorge@mgh.harvard.edu

Indicates open access to non-subscribers at www.ajnr.org

<http://dx.doi.org/10.3174/ajnr.A7144>

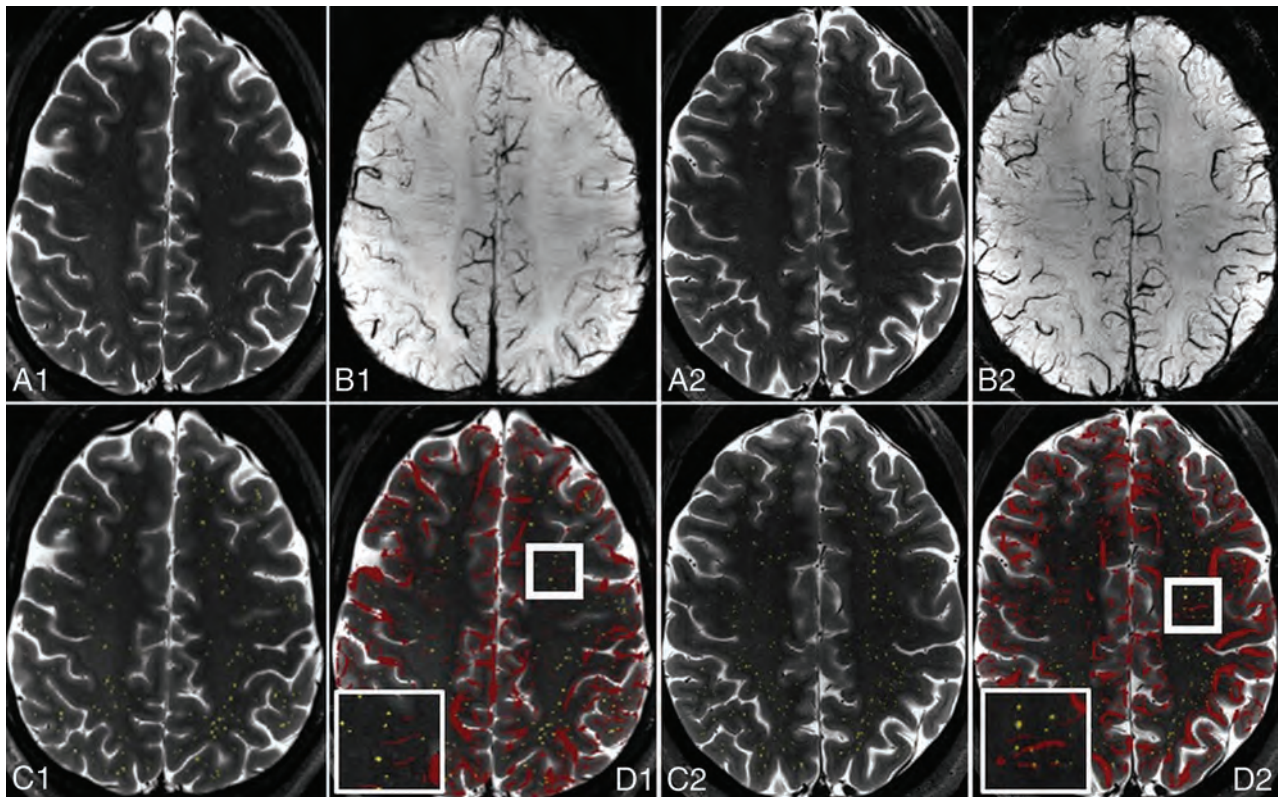


FIG 1. Overlay of pre- and postprocessed images of T2-TSE with manual PVS markings and SWI at 7T in a healthy control (A–D 1) and a person with MS (A–D 2) allows identification of venular and nonvenular PVSs. T2-TSE (A), SWI (B), T2-TSE with PVSs highlighted in yellow (C), and T2-TSE with SWI overlay in red (D) are depicted, with magnification of 1 sample area in the *thick white square* demonstrated in the *thinner white square inset*.

www.applied-statistics.de/lst.html).¹³ The uniform denoised, T2-TSE, and susceptibility-weighted images were coregistered using SPM12 (<http://www.fil.ion.ucl.ac.uk/spm/software/spm12>), and the FreeSurfer-derived masks were used to isolate WM of the cerebral hemispheres.

The resulting 3D datasets were connected along an 18-connected network through the nearest neighbors. Individual objects were characterized using the “bwlabel” function in Matlab, and principal axes were extracted. Networks were filtered to exclude objects with a major-/minor-axis length ratio of <4, to eliminate nonvessel punctate foci of susceptibility.

For all subjects, WM PVSs were manually marked on coregistered T2-TSE images by 2 raters (I.C.G. and A.A.-A.) on OsiriX Imaging Software, Version 9.0.2 (<http://www.osirix-viewer.com>). An individual ROI was identified for each marked PVS. PVSs were marked on the diameter through the short axis of the ROI (excluding diameters of <0.5 mm). Gray matter and posterior fossa PVSs were excluded because these areas are prone to artifacts at 7T. Interrater reliability was assessed comparing total PVSs marked per section by each reviewer.

Vessel and PVS masks were overlaid to quantify the coincidence of PVSs and segmented veins relative to the total number of detected PVSs. Total numbers of PVSs and venular PVSs were averaged across raters for persons with MS and HC.

A percentage perivenular space quotient was calculated for each subject by dividing the number of venular spaces detected by the total number of perivascular spaces. A nonparametric

Moods median test was performed to compare this percentage in HC versus persons with MS. A χ^2 test of independence was performed to assess the relationship between the number of venular PVSs and total PVSs in HC and persons with MS.

RESULTS

Alignment of PVSs manually marked on T2-TSE sequences with corresponding SWI demonstrated the feasibility of this approach (Fig 1).

Interrater reliability was high between reviewers, demonstrating correlation coefficients of $r = 0.95$ and $r = 0.85$ on 2 scans.

The total PVS number and percentage of venular PVSs were quantified for 3 persons with MS and 3 HC. The mean total PVSs were 4976 (SD, 282.6) in persons with MS versus 8487 (SD, 2645.1) in HC ($P = .15$). Of these, 15.19% were venular in the persons with MS group versus 10.26% venular in HC ($P = .014$) (Fig 2). In this sample, even though persons with MS had fewer detectable perivascular spaces than HC, a larger proportion of spaces in persons with MS were venular. Total brain volumes and WM volumes were similar between the persons with MS and HC, with a mean total volume of 1162 mL (range, 968–1319 mL) in persons with MS and 1042 mL (range, 996–1101 mL) in HC (t test, $P = .46$). Mean WM volume was 470 mL (range, 374–557 mL) in patients with MS and 444 mL (range, 441–449 mL) in HC (t test, $P = .68$). Mean lesion volume was 1.3 mL (range, 0.45–1.45 mL).

In HC, the number of venular PVSs was highly related to the number of PVSs ($\chi^2 = 0.26$, 2 *df*), while in the persons with MS

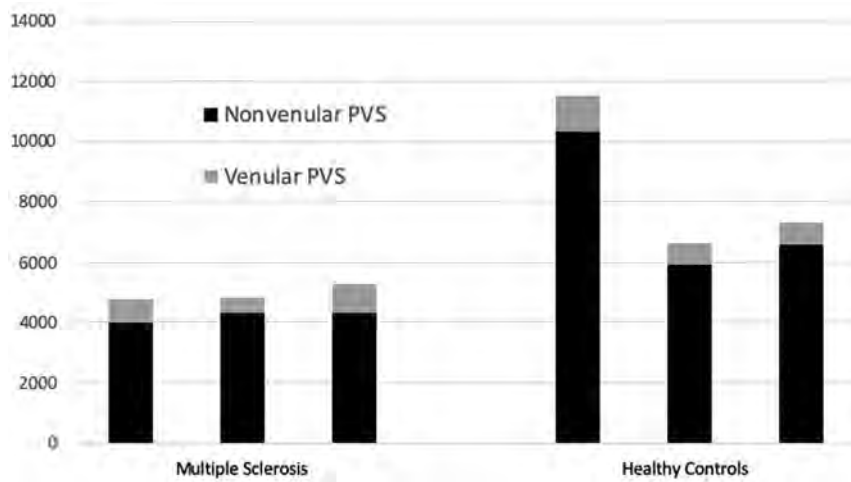


FIG 2. Nonvenular and venular PVS counts in 3 age-matched persons with MS and HC demonstrate more PVSs in HC but a higher proportion of venular PVSs in persons with MS. The number of nonvenular (black) and venular (dark gray) PVSs detected is depicted for each MS and healthy control subject.

group, the number of venular and total PVSs was independent of it ($\chi^2 = 99, 2 \text{ df}$).

DISCUSSION

We developed a method to identify venular PVSs using coregistered SWI-mapping deoxygenated blood signal and demonstrate the feasibility and reproducibility of this approach in the hemispheric white matter at 7T.

While our cohort is too small to draw definitive conclusions comparing persons with MS with HC, preliminary results suggest an increased proportion of venular PVSs in persons with MS. Furthermore, in HC, the venular PVS number was highly dependent on the total number of PVSs, while in persons with MS, these were independent ($P < .001$), implying that these differences are specific to this compartment and would not have been detected by analyzing total numbers or total volume of PVSs. We found lower numbers of total PVSs in persons with MS compared with HC; however, the difference was not statistically significant. The larger total PVS number found in our study suggests that previous findings at 1.5T may not extend to higher field strengths, which improve PVS detection. We plan to further explore these results in a larger cohort.

A recent meta-analysis demonstrated that enlarged PVSs are more prevalent in persons with MS versus HC, though study designs varied widely. No study differentiated venular and arteriolar PVSs.^{4-6,14,15} The total number of PVSs detected in our study is greater than those previously reported at 7T,¹² likely due to differences in measurement algorithms. A larger study using our approach would clarify how the venular PVS number and size differ in MS and whether treatment modulates these changes.

Limitations of the current study include the small number of subjects and raters. We are refining a semi-automated method to measure PVSs at 7T to improve feasibility and interrater reliability. Additionally, PVSs within gray matter, the posterior fossa, and T2-hyperintense lesions were not included in the analysis due to difficulty of detection on TSE images.

Controlling for nonlesional brain volume normalizes the dataset to normal-appearing white matter and may mitigate the exclusion of PVSs from within lesions, though our method may be limited in subjects with large, confluent white matter lesions.

Future steps include the validation of preliminary findings from this study in a larger cohort and developing an automated tool to identify PVSs in a shorter timeframe than manual detection. Critical questions remain as to whether PVS anatomy corresponds to disease activity, active relapse, response to treatment, brain atrophy, neurodegeneration, and disability progression.

CONCLUSIONS

We present a semi-automated method of differentiating venular and nonvenular PVSs. The algorithm is reproducible and feasible in a group of persons with MS and HC and has the potential to identify an important biomarker in MS.

Disclosures: Ilena George—UNRELATED: Grant: Biogen, Comments: I receive fellowship support from Biogen through the Anne B. Young Translational Neurology Fellowship of Massachusetts General Hospital.* Priti Balchandani—RELATED: Grant: National Institutes of Health, Comments: R01MH109544*; UNRELATED: Other: Dr Priti Balchandani is a named inventor on patents relating to MR imaging and radiofrequency pulse design. This intellectual property has been licensed to GE Healthcare, Siemens, and Philips International. Dr Balchandani received one-time royalty payments for this intellectual property. Sam Horn—RELATED: Grant: National Institutes of Health/National Institute of Neurological Diseases and Stroke K08NS102507-01A1, National Institutes of Health R25NS079102, a Career Transition Award jointly supported by the National Multiple Sclerosis Society and the Conrad N. Hilton Foundation, philanthropic support by the Jayne and Harvey Beker Foundation, and a postdoctoral Neuroscience fellowship from the Leon Levy Foundation. Rebecca Feldman—RELATED: Grant: Department of Defense, Comments: W81XWH1910616*; Support for Travel to Meetings for the Study or Other Purposes: National Sciences and Engineering Research Council of Canada, Discovery Grant RGPIN-2020-06005, Comments: money to support travel to Mount Sinai to meet with collaborators; OTHER RELATIONSHIPS: Adjunct Assistant Professor (voluntary faculty), Icahn School of Medicine at Mount Sinai. *Money paid to the institution.

REFERENCES

- Abbott NJ. Astrocyte-endothelial interactions and blood-brain barrier permeability. *J Anat* 2002;200:629–38 CrossRef Medline
- Lassmann H. Pathogenic mechanisms associated with different clinical courses of multiple sclerosis. *Front Immunol* 2018;9:3116 CrossRef Medline
- Kutzelnigg A, Lassmann H. Pathology of multiple sclerosis and related inflammatory demyelinating diseases. *Handb Clin Neurol* 2014;122:15–58 CrossRef Medline
- Cavallari M, Egorova S, Healy BC, et al. Evaluating the association between enlarged perivascular spaces and disease worsening in multiple sclerosis. *J Neuroimaging* 2018;28:273–77 CrossRef Medline
- Conforti R, Cirillo M, Saturnino PP, et al. Dilated Virchow-Robin spaces and multiple sclerosis: 3 T magnetic resonance study. *Radiol Med* 2014;119:408–14 CrossRef Medline
- Wuerfel J, Haertle M, Waiczies H, et al. Perivascular spaces—MRI marker of inflammatory activity in the brain? *Brain* 2008;131:2332–40 CrossRef Medline

7. Sati P, Oh J, Constable RT, et al. NAIMS Cooperative. **The central vein sign and its clinical evaluation for the diagnosis of multiple sclerosis: a consensus statement from the North American Imaging in Multiple Sclerosis Cooperative.** *Nat Rev Neurol* 2016;12:714–22 CrossRef Medline
8. Thompson AJ, Banwell BL, Barkhof F, et al. **Diagnosis of multiple sclerosis: 2017 revisions of the McDonald criteria.** *Lancet Neurol* 2018;17:162–73 CrossRef Medline
9. Arrighi-Allisan A, George I, Rutland J, et al. **Comparison of Perivenular Spaces at 7 Tesla in Relapsing-Remitting Multiple Sclerosis Patients and Healthy Controls.** In: *Proceedings of the ISMRM 27th Scientific Meeting*, Montréal, Canada. May 11-16, 2019. Poster: 2817.
10. Feldman RE, Rutland JW, Fields MC, et al. **Quantification of perivascular spaces at 7T: a potential MRI biomarker for epilepsy.** *Seizure* 2018;54:11–18 CrossRef Medline
11. Steger C. **An unbiased detector of curvilinear structures.** *IEEE Trans Pattern Anal Machine Intell* 1998;20:113–25 CrossRef
12. Frangi AF, Niessen WJ, Vincken KL, et al. **Multiscale vessel enhancement filtering.** In: Wells WM, Colchester A, Delp S, eds. *Medical Image Computing and Computer-Assisted Intervention: MICCAI'98*. Springer; 1998:130–37
13. Schmidt P, Gaser C, Arsic M, et al. **An automated tool for detection of FLAIR-hyperintense white-matter lesions in multiple sclerosis.** *Neuroimage* 2012;59:3774–83 CrossRef Medline
14. Granberg T, Moridi T, Brand JS, et al. **Enlarged perivascular spaces in multiple sclerosis on magnetic resonance imaging: a systematic review and meta-analysis.** *J Neurol* 2020;267:3199–3212 CrossRef Medline
15. Kilsdonk I, Steenwijk M, Pouwels P, et al. **Perivascular spaces in MS patients at 7 Tesla MRI: a marker of neurodegeneration?** *Mult Scler* 2015;21:155–62 CrossRef Medline

MRI Shrimp Sign in Cerebellar Progressive Multifocal Leukoencephalopathy: Description and Validation of a Novel Observation

N. Adra, A.E. Goodheart, O. Rapalino, P. Caruso, S.S. Mukerji, R.G. González, N. Venna, and J.D. Schmahmann

ABSTRACT

BACKGROUND AND PURPOSE: There are no validated imaging criteria for the diagnosis of progressive multifocal leukoencephalopathy in the cerebellum. Here we introduce the MR imaging shrimp sign, a cerebellar white matter lesion identifiable in patients with cerebellar progressive multifocal leukoencephalopathy, and we evaluate its sensitivity and specificity.

MATERIALS AND METHODS: We first identified patients with progressive multifocal leukoencephalopathy seen at Massachusetts General Hospital between 1998 and 2019 whose radiology reports included the term “cerebellum.” Drawing on a priori knowledge, 2 investigators developed preliminary diagnostic criteria for the shrimp sign. These criteria were revised and validated in 2 successive stages by 4 additional blinded investigators. After defining the MR imaging shrimp sign, we assessed its sensitivity, specificity, positive predictive value, and negative predictive value.

RESULTS: We identified 20 patients with cerebellar progressive multifocal leukoencephalopathy: 16 with definite progressive multifocal leukoencephalopathy (mean, 46.4 [SD, 9.2] years of age; 5 women), and 4 with possible progressive multifocal leukoencephalopathy (mean, 45.8 [SD, 8.5] years of age; 1 woman). We studied 40 disease controls (mean, 43.6 [SD, 21.0] years of age; 16 women) with conditions known to affect the cerebellar white matter. We defined the MR imaging shrimp sign as a T2- and FLAIR-hyperintense, T1-hypointense, discrete cerebellar white matter lesion abutting-but-sparing the dentate nucleus. MR imaging shrimp sign sensitivity was 0.85; specificity, 1; positive predictive value, 1; and negative predictive value, 0.93. The shrimp sign was also seen in fragile X-associated tremor ataxia syndrome, but radiographic and clinical features distinguished it from progressive multifocal leukoencephalopathy.

CONCLUSIONS: In the right clinical context, the MR imaging shrimp sign has excellent sensitivity and specificity for cerebellar progressive multifocal leukoencephalopathy, providing a new radiologic marker of the disease.

ABBREVIATIONS: JCV = JC polyomavirus; MS = multiple sclerosis; NPV = negative predictive value; PML = progressive multifocal leukoencephalopathy; PPV = positive predictive value; PRES = posterior reversible encephalopathy syndrome

Progressive multifocal leukoencephalopathy (PML) is an opportunistic demyelinating disease in which the human JC polyomavirus (JCV) causes lytic infection of oligodendrocytes, astrocytes, and, rarely, neurons.¹ It affects immunosuppressed patients with an

impaired T-lymphocyte response, including patients with chronic lymphocytic leukemia, Hodgkin lymphoma, and HIV/AIDS.²⁻⁵ The increase in the PML incidence associated with immune therapies such as natalizumab for multiple sclerosis⁶⁻⁸ underscores the importance of developing early, validated diagnostic criteria for PML.⁶⁻⁸

Cerebellar and brainstem involvement in PML was identified 4 decades ago. There are few studies of the diagnostic specificity of pontocerebellar findings on MR imaging in PML.^{9,10} A punctate pattern of T2 and FLAIR hyperintensity is described in natalizumab-associated PML and in PML-immune reconstitution inflammatory syndrome.^{11,12} The hot cross bun sign, a cruciform T2 hyperintense signal in the midpons, has been noted late in the course of PML, affecting posterior fossa structures, when both the brainstem and the cerebellum have lost considerable volume (olivopontocerebellar atrophy). The hot cross bun sign was described

Received June 24, 2019; accepted after revision January 7, 2021.

From the Department of Neurology (N.A., A.E.G., S.S.M., N.V., J.D.S.), Ataxia Center, Cognitive Behavioral Neurology Unit, Laboratory for Neuroanatomy and Cerebellar Neurobiology (N.A., A.E.G., J.D.S.); Neuroradiology Division (O.R., P.C., R.G.G.); and Department of Neurology, (S.S.M., N.V.), Neuroinfectious Diseases Unit, Massachusetts General Hospital and Harvard Medical School, Boston, Massachusetts; and Wellesley College (N.A.), Wellesley, Massachusetts.

Noor Adra and Anna E. Goodheart are joint first authors.

This work was supported, in part, by the National Ataxia Foundation, the MINDlink Foundation, and Mrs Mary Jo Reston.

Please address correspondence to Jeremy D. Schmahmann, MD, FAAN, FANA, FANPA, Department of Neurology, Massachusetts General Hospital, 100 Cambridge St, Suite 2000, Boston, MA 02114; e-mail: jschmahmann@mgh.harvard.edu; @SchmahmannLab <http://dx.doi.org/10.3174/ajnr.A7145>

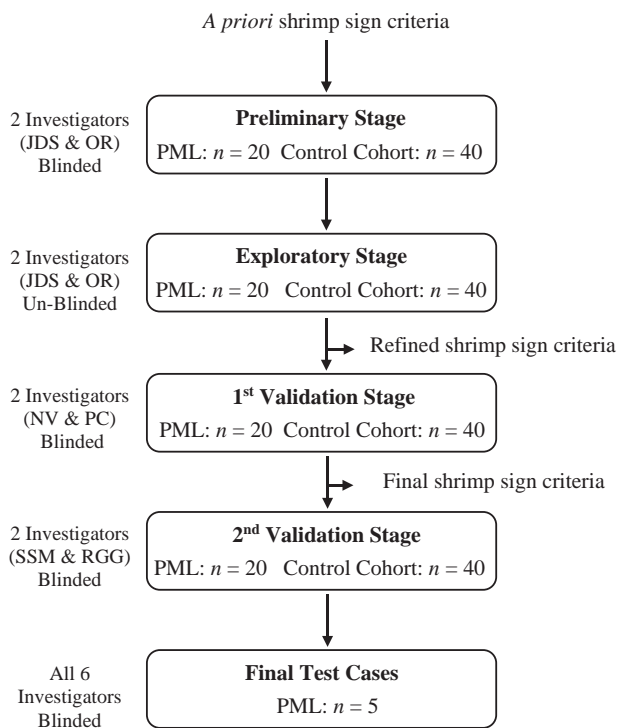


FIG 1. Flow diagram outlining the methodology for defining and validating the shrimp sign. In the preliminary stage, axial planes of T1-weighted imaging, T2-weighted imaging, FLAIR, and, when available, postgadolinium T1-weighted images were studied. In subsequent stages, these images were also examined in the sagittal and coronal planes.

initially in the cerebellar subtype of multiple system atrophy^{13,14} and is also seen in spinocerebellar ataxia, particularly spinocerebellar ataxia 1 and 2,¹⁵ and in variant Creutzfeldt-Jakob disease¹⁶ and cerebral vasculitis.¹⁷ Conditions other than PML affect the middle cerebellar peduncles, and disorders of immunocompromised patients such as toxoplasmosis, lymphoma, posterior reversible encephalopathy syndrome (PRES), neuro-Behçet disease, or HIV encephalitis may pose a diagnostic challenge. Cerebellar neuroimaging markers specific to PML may, therefore, aid diagnosis and preempt invasive procedures like brain biopsy.¹⁰

The shrimp sign was first proposed as a marker of cerebellar PML 25 years ago by N.V., who characterized it as a well-defined T2- or FLAIR-hyperintense and T1-hypointense lesion in the cerebellar white matter that abuts-but-sparcs the dentate nucleus and has the shape of a shrimp. It may also involve the hilum of the dentate nucleus. On axial MR imaging, the well-defined white matter lesion outlines the serrated, curvilinear-shaped dentate nucleus.

We designed this study to determine whether the shrimp sign is, indeed, a reliable indicator of cerebellar PML and to assess its sensitivity and specificity.

MATERIALS AND METHODS

Standard Protocol Approvals, Registrations, and Patient Consents

The study was approved by the Partners Human Research institutional review board.

Study Population

Cohorts were drawn from medical record review of patients with T2-hyperintense cerebellar lesions at Massachusetts General Hospital between 1998 and 2019. Radiologic images acquired during clinical care were identified in Render, a searchable repository of radiology reports and images. Medical record review confirmed the diagnosis and captured demographic data.

Imaging Sequences

All MR imaging was performed as part of standard clinical care. Initially, axial planes of T1WI, T2WI, FLAIR, and, when available, postgadolinium T1WI were studied. After the preliminary stage of the study, we also examined T1WI in the sagittal and coronal planes.

PML Cohort. Radiologic records were obtained using the search terms “progressive multifocal leukoencephalopathy” or “PML” and “cerebellar or cerebellum.” Using the American Academy of Neurology PML diagnostic criteria, we defined definite PML as patients with polymerase chain reaction positive for JCV from the CSF and pertinent clinical presentations and MR imaging findings.¹⁸ Possible PML was defined as patients who had not undergone lumbar puncture but were diagnosed using clinical presentations and MR imaging findings.

Control Cohort. Patients with diseases known to affect cerebellar white matter were chosen as controls.¹⁹ Terms from broad categories (demyelinating lesion, leukodystrophy, cerebellar white matter + hyperintensity, middle cerebellar + white matter + hyperintensity) and specific categories (fragile X-associated tremor ataxia syndrome, PRES, cerebrotendinous xanthomatosis, Alexander disease, Langerhans cell histiocytosis) were searched twice, in combination with the terms “cerebellar” or “cerebellum.” Patients whose cerebellar pathology included hemorrhage, ischemic stroke, or space-occupying tumors (medulloblastoma, astrocytoma, ependymoma, glioblastoma) were excluded because these lesions are unlikely to be confused with PML. Patients with small, nonspecific cerebellar white matter lesions were also excluded. Because cases of MS and PRES were disproportionately higher than diagnoses in the rest of the group, we randomly chose 5 cases of MS and 4 of PRES and kept all other controls in the cohort.

Defining and Validating the Shrimp Sign

The shrimp sign was assessed through 4 stages (Fig 1). In the preliminary stage, O.R. (neuroradiology) and J.D.S. (neurology), blinded to the diagnosis, developed the shrimp sign criteria based on a priori knowledge and assessed its presence in all cases. The a priori inclusion criteria were the following: 1) presence of a well-defined lesion in the cerebellar white matter that is hyperintense on T2-weighted and FLAIR imaging and hypointense on T1-weighted imaging, and 2) the lesion abutting and sharply demarcating the dentate nucleus and outlining the dentate nucleus on axial MR imaging (Fig 2). The a priori exclusion criteria were the following: 1) invasion of the dentate nucleus by the white matter lesion, 2) a small and nonspecific lesion of the middle cerebellar peduncle, and 3) presence of hemorrhage, ischemic stroke, or space-occupying tumor in the cerebellar pathology. Permissible features included involvement of the white matter hilum of the

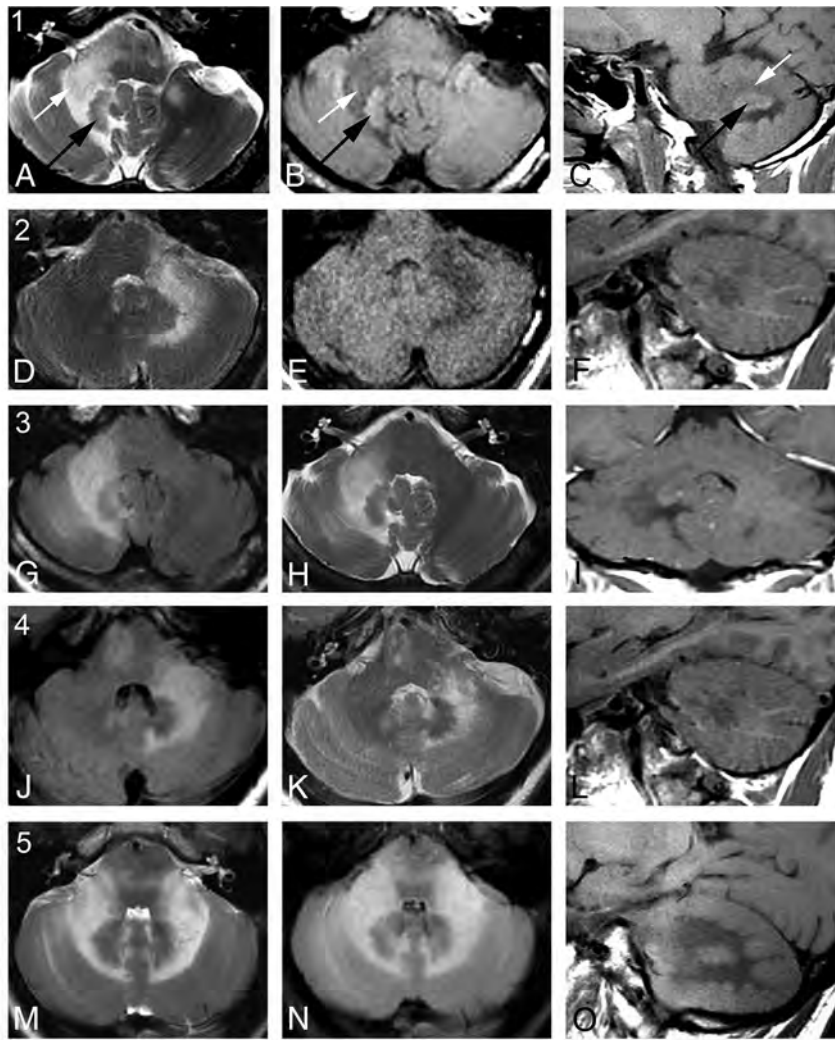


FIG 2. Representative MRIs from 5 patients with PML demonstrating the essential features of the MR imaging shrimp sign. Each row represents images taken from 1 patient, numbered cases 1–5: T2 axial (A), T1 axial (B), and T1 sagittal images (C). *White arrows* identify the white matter lesion; *black arrows*, the dentate nucleus. FLAIR axial (D), T1 axial (E), T1 sagittal (F), FLAIR axial (G), T2 axial (H), T1 coronal (I), FLAIR axial (J), T2 axial (K), T1 sagittal (L), T2 axial (M), FLAIR axial (N), and T1 sagittal (O) views. In case 5, the bilaterally symmetric shrimp sign is somewhat atypical in this patient with PML in the setting of confirmed HIV positive for CSF-JCV.

dentate nucleus, lesions in the cerebral hemisphere and brainstem, and pontocerebellar atrophy. In PML present for a long duration (years), there may be prominent atrophy of the cerebellar hemispheres, dentate nuclei, middle cerebellar peduncle, and brainstem, sometimes with a hot cross bun sign in the pons.^{13,14} This olivopontocerebellar atrophy pattern may develop as a primary neurodegenerative disorder (neuronal PML) or as the late/burned-out stage of PML.

In the exploratory stage, diagnoses were revealed and the investigators reviewed the cases to refine the shrimp sign criteria. These revised criteria were used for the first validation stage, in which P.C. (neuroradiology) and N.V. (neurology) evaluated the MR images blinded to diagnoses. The investigators were aided by canonical images of positive and negative shrimp signs. Core

inclusion and exclusion criteria were designated. The final criteria (Table 1) were subjected to a second validation stage by R.G.G. (neuroradiology) and S.S.M. (neurology), also blinded to the diagnoses. If reviewers disagreed, we erred on the side of specificity rather than sensitivity (ie, a determination of no for the presence of the shrimp sign prevailed over a yes determination). Sensitivity, specificity, positive predictive value (PPV), and negative predictive value (NPV) of the shrimp sign criteria were assessed following the preliminary and validation stages. In these stages, 20 patients with PML and 40 controls were evaluated for the presence of the shrimp sign by each investigator.

After the study had begun, 5 additional cases of PML were referred to Massachusetts General Hospital: 1 possible and 4 definite. These 5 were used as a test of the finalized shrimp sign criteria. All 6 senior investigators assessed the presence of the shrimp sign in these 5 cases, blinded to the diagnoses.

RESULTS

Patients with PML

The search for cases of PML generated 138 medical records. Of these, cerebellar white matter lesions were identified in 20 patients: 16 with definite PML (mean, 46.4 [SD, 9.2] years of age), 4 with possible PML (mean, 45.8 [SD, 8.5] years of age). See Table 2 for patient demographics. Of 16 cases of definite PML, 13 (81.25%) had HIV infection.

Control Patients

Medical records of 716 controls were generated. We excluded 645 (90%) due to hemorrhage, ischemic stroke, tumors, duplicate records, and/or no sizeable cerebellar lesions. Of the remaining 71 controls, 25 had MS and 15 had PRES. The disproportionately greater frequency of these 2 diagnoses was addressed by randomly choosing 5 cases of MS and 4 of PRES. The final cohort included 40 control patients (mean, 43.64 [SD, 21.0] years of age). See Table 2 for demographics and Table 3 for diagnoses.

Development of Preliminary Diagnostic Criteria

Assessment of a priori criteria of the first evaluators (J.D.S., O.R.) resulted in 4 false-negative and 8 false-positive cases, a sensitivity of 0.8, specificity of 0.8, NPV of 0.89, and PPV of 0.67 (Table 4). After unblinded re-examination of the false-negatives, we noted the

Table 1: Diagnostic criteria for the MR imaging shrimp sign of cerebellar PML

Core Inclusion Criteria of the Shrimp Sign	Core Exclusion Criteria of the Shrimp Sign
<p>White matter lesion</p> <p>Well-defined lesion in the cerebellar white matter</p> <p>The lesion is hyperintense on T2-weighted and FLAIR imaging</p> <p>The lesion is hypointense on T1-weighted imaging</p> <p>The lesion abuts and sharply demarcates the dentate nucleus and outlines the dentate nucleus in horizontal, parasagittal, and/or coronal views</p> <p>The lesion must encompass at least 50% of the dentate nucleus (partial shrimp); if there are multiple lesions adjacent to the dentate, they do not need to be contiguous</p> <p>Other features compatible with PML</p> <p>There may be a mottled appearance of the white matter lesion on T2-weighted imaging</p> <p>The white matter hilum of the dentate nucleus may be involved</p> <p>The lesion may occur together with, or independent of, cerebral hemisphere and brainstem PML lesions</p>	<p>White matter lesion</p> <p>Is not hypointense on T1-weighted imaging</p> <p>Is hazy and ill-defined on T2-weighted or FLAIR imaging</p> <p>Has cavitation within the substance of the lesion</p> <p>Demonstrates prominent focal, diffuse, or ring enhancement</p> <p>Dentate nucleus</p> <p>Is invaded by the white matter lesion</p> <p>Is displaced by the white matter lesion</p> <p>Shows enhancement of the nucleus itself (specifically excluding the hilum)</p> <p>Is severely atrophic early in the course of the disease</p> <p>Permissible atypical features^a</p> <p>Minimal enlargement of the MC P (up to 2–3 mm)</p> <p>Minimal mass effect on the fourth ventricle</p> <p>Faint enhancement of the white matter lesion or the hilum of the dentate nucleus</p> <p>Olivopontocerebellar atrophy in late-stage PML</p> <p>Bilateral, usually asymmetric white matter lesions</p>

Note:—MCP indicates middle cerebellar peduncle.

^a In the right clinical and imaging context and when all core inclusion and exclusion criteria are met.

Table 2: Patient demographics^a

	Definite PML (n = 16)	Possible PML (n = 4)	Control Cohort (n = 40)
Sex (F/M)	5:11	1:3	16:24
Age (mean) (SD) (yr)	46.4 (9.21)	45.8 (8.46)	43.6 (21.04)
Cause of PML			
HIV	13 (81.25%)	3 (75%)	—
Cancer	2 (12.5%)	0 (0%)	—
Immunosuppressant therapy	1 ^b (6.25%)	1 ^c (25%)	—
Ethnicity			
Hispanic	1 (6.25%)	0 (0%)	2 (5%)
Non-Hispanic	8 (50%)	1 (25%)	25 (62.5%)
Unknown	7 (43.75%)	3 (75%)	13 (32.5%)
Race			
White	10 (62.5%)	0 (0%)	30 (75%)
African American	2 (12.5%)	2 (50%)	3 (7.5%)
Asian	0 (0%)	0 (0%)	1 (2.5%)
Unknown	4 (25%)	2 (50%)	6 (15%)

^a Patients with PML with positive JCV-CSF findings were defined as having definite PML. Patients with PML without CSF samples but with clinical and MR findings indicative of PML were defined as having possible PML.

^b Rituxan and fludarabine.

^c Mycophenolate mofetil (Cellcept), tacrolimus (FK-506), and prednisone.

importance of evaluating all 3 cardinal planes. We determined that the white matter lesion outlining the dentate nucleus must encompass $\geq 50\%$ of the nucleus for a positive diagnosis. If there are multiple white matter lesions, they must abut the nucleus, but they do not have to be contiguous. Review of false-positive cases prompted us to add cavitation within the white matter lesion as an exclusion criterion, along with T1 isointensity of lesions and overt atrophy of the dentate nucleus. Bilateral lesions were found to be a permissible atypical feature in PML. An important consideration in the differential diagnosis is HIV encephalopathy without PML. In these cases, the cerebellar white matter lesions are hazy and ill-defined; whereas they may be hyperintense on T2WI or FLAIR imaging, they are T1 isointense (not hypointense). Furthermore, the lesions are diffusely distributed or bilaterally symmetric in the cerebellar and cerebral white matter, further distinguishing them from PML.

Table 3: Diagnoses in the 40 patients in the control cohort

Diagnosis	No.
Acute disseminated encephalomyelitis	5 (12.5%)
Multiple sclerosis	5 (12.5%)
Neurofibromatosis	4 (10%)
PRES	4 (10%)
Fragile X-associated tremor ataxia syndrome	3 (7.5%)
Lymphoma	3 (7.5%)
Neuro-Behçet disease	3 (7.5%)
Cerebrotendinous xanthomatosis	2 (5%)
HIV encephalopathy	2 (5%)
Susac disease	2 (5%)
Alexander disease	1 (2.5%)
Krabbe disease	1 (2.5%)
Langerhans cell histiocytosis	1 (2.5%)
Metachromatic leukodystrophy	1 (2.5%)
Neurosarcoidosis	1 (2.5%)
Toxoplasmosis	1 (2.5%)
Wilson disease	1 (2.5%)

Validation Stage 1

Assessment of the revised shrimp sign criteria resulted in 4 false-negatives and 1 false-positive, a sensitivity of 0.8, specificity of 0.98, PPV of 0.94, and NPV of 0.91 (Table 4). Imaging features of fragile X-associated tremor ataxia syndrome may resemble cases of PML with bilateral shrimp signs. We modified our criteria to highlight the permissible atypical feature of bilateral, usually asymmetric white matter lesions but draw attention to fragile X-associated tremor ataxia syndrome as a possible PML imaging mimic. Following review, we also amended the criteria, recognizing that when all core inclusion and exclusion criteria are met, minimal mass effect and enhancement following contrast administration remain compatible with the PML shrimp sign.

Validation Stage 2

By means of the amended criteria, the shrimp sign was evident in 17 of 20 patients with PML (85%). Of the 3 false-negatives, 1 had possible PML and 2 had definite PML. There were no false-positives; the shrimp sign was absent in all 40 controls. Assessment of

Table 4: Sensitivity and specificity of the MR imaging shrimp sign of cerebellar PML^a

	Sensitivity (PML, True-Positive/False-Negative)	Specificity (Controls, True-Negative/False-Positive)	PPV	NPV
Preliminary stage	0.8 (16/4)	0.8 (32/8)	0.67	0.89
Validation stage 1	0.8 (16/4)	0.98 (39/1)	0.94	0.91
Validation Stage 2	0.85 (17/3)	1 (40/0)	1	0.93

^aSensitivity and specificity of the shrimp sign of cerebellar PML in the exploratory stage and following the first and second validation stages.

the validity of the final shrimp sign criteria (Table 1) thus resulted in a sensitivity of 0.85, specificity of 1, NPV of 0.93, and PPV of 1 (Table 4). In the 17 patients with PML with the shrimp sign, it was noted at the first clinical presentation in 15 (88.2%), in all 3 patients with possible PML, and in 12/14 with definite PML. In the remaining 2 patients, the shrimp sign developed within a year of the PML diagnosis.

Final Test Cases

In the 5 additional PML patients evaluated using the final criteria there was unanimous agreement. Of the 4 definite PML cases the shrimp sign was present in 1 and absent in 3 (2 without cerebellar involvement, and 1 with end-stage olivopontocerebellar atrophy, white matter attenuation, and marked nuclear atrophy). There was no shrimp sign in the 5th patient with possible PML, who had leukoencephalopathy and patchy cerebellar white matter hyperintensities but was negative for JCV in the CSF.

DISCUSSION

The diagnosis of PML relies on clinical and MR imaging findings and detection of the JCV in the CSF by polymerase chain reaction. Because PML lesions may involve multiple brain areas, the clinical and imaging manifestations may vary.¹⁸ Characteristic features include multifocal distribution of patchy or confluent areas of white matter signal abnormality in the cerebral hemispheres, brainstem, and cerebellum. These lesions are T1 hypointense and T2 hyperintense^{4,20-22} and typically do not enhance or cause mass effect proportionate to the volume of the lesion, though faint contrast enhancement and minimal mass effect are noted.^{21,22} Diffusion restriction may detect active lesions.²²⁻²⁴

The absence of an MR imaging biomarker for cerebellar PML prompted us to assess whether the MR imaging shrimp sign may fill this gap. Results showed high sensitivity and NPV and excellent specificity and PPV, indicating that it is, indeed, a reliable imaging biomarker of cerebellar PML. The MR imaging shrimp sign is a distinct T2- or FLAIR-hyperintense and T1-hypointense lesion in the shape of a shrimp, located in the cerebellar white matter abutting-but-sparing the dentate nucleus. It outlines the serrated, curvilinear shape of the dentate nucleus, which stands out against this abnormal background.

Postmortem studies of cerebellar PML provide the neuropathologic basis for our imaging observations.^{9,25} One case revealed a very widespread demyelinating process involving mainly the right cerebellar hemisphere but also most of the pons and left cerebellum, with the typical morphologic characters of PML.⁹ Another demonstrated severe, confluent demyelination in the cerebellar white matter but, remarkably, sparing the dentate nucleus. Imaging in that case showed bilateral asymmetric lesions that were T2-hyperin-

tense and T1-hypointense, consistent with what we now identify as the MR imaging shrimp sign.²⁵ Histopathologic examination confirmed preservation of the dentate nuclei. The cerebellar white matter lesions were notable for complete loss of myelin sheaths, severe damage in the axons, infiltration of macrophages with increased microglial

cells, and scarcity in oligodendrocytes and perivascular lymphocytes. These observations demonstrate the magnitude of cerebellar injury in a patient with PML and may explain the T1-hypointensity characteristic of the shrimp sign.

In a study of PML and relapsing-remitting MS, MR imaging findings and clinical features were analyzed to distinguish these disorders.²⁶ Crescent-shaped white matter lesions were reported in 23% of the cerebellar PML cohort. Because that study examined only these 2 conditions, the specificity of this sign could not be assessed.

The finding of JCV in the CSF has been considered more sensitive and specific for PML than clinical and MR imaging findings. However, false-negative CSF JCV values are encountered when the immune system is relatively intact, as in MS and systemic lupus erythematosus.^{27,28} Patients with AIDS with PML on suppressive antiretroviral therapy may also have reduced or undetectable CSF JCV levels.²⁹⁻³¹ The good sensitivity and high specificity of the shrimp sign make it promising for the diagnosis and longitudinal study of cerebellar PML, complementing and supporting the clinical features. We note that disease survival in PML has increased with improved diagnostic techniques, earlier recognition, and the introduction of antiretroviral drugs.^{2,32} The shrimp sign was present at the onset of clinical disease in 75% (15/20) of our cohort of patients with PML, who were known retrospectively to have developed a cerebellar lesion at any point in their disease course, suggesting that the shrimp sign may be helpful for early diagnosis.

Limitations

By means of the final criteria, 3 cases in the original cohort of 20 patients who had known cerebellar PML were not diagnosed with the shrimp sign. One case did not have T1 hypointensity. This was a bona fide false-negative. Absence of the shrimp sign does not exclude a diagnosis of PML because the cerebellum may be spared or the radiologic findings may be only minimal. The remaining cases did not pass the criteria due to symmetric lesions across the cerebellar hemispheres. The reviewers were divided on these 2 cases: The neurologist used the shrimp sign because the symmetry was incomplete, but the radiologist was concerned about the symmetry. Because patients with widespread leukoencephalopathies, such as neuro-Behçet disease, Krabbe disease, or cerebrotendinous xanthomatosis may have more aggressive cerebellar involvement that extends to the middle cerebellar peduncles, brainstem, and white matter of the cerebellar folia, adhering to the diagnostic criteria will minimize false-positives, though it may result in occasional false-negatives. Consideration of the clinical details should help lead to the correct diagnosis.

A case in point is fragile X-associated tremor ataxia syndrome, which showed a striking resemblance to the shrimp sign. Unlike

most of our cases of PML, fragile X–associated tremor ataxia syndrome cerebellar and middle cerebellar peduncle lesions were bilateral and symmetric. This X-linked disorder of older men with a premutation expansion (55–200) of the CGG repeat is characterized by slow evolution over a period of years of tremor, ataxia, peripheral neuropathy, erectile dysfunction, and cognitive decline, and the patient may have a grandson/grandnephew with the full mutation fragile X syndrome and daughters who are fragile X carriers.³³ Imaging features notwithstanding, when the clinical context is considered, there should be little room for confusion between this genetic disorder and PML.

In most of our patients, PML occurred against a background of HIV. Of the 4 cases negative for HIV, the 1 case of possible PML and 2 of 3 cases of definite PML had the shrimp sign. PML is increasingly recognized in patients treated with immune therapies such as natalizumab and rituximab, but our study included only 1 patient with rituximab-associated PML, and this case was positive for the shrimp sign. Future studies will need to address the relative prevalence of the shrimp sign in patients with HIV-associated PML versus those with PML in the setting of other causes of immune compromise.

Severe dentate nucleus atrophy is an exclusion criterion for the shrimp sign, though it often accompanies olivopontocerebellar atrophy that may be observed in late-stage cerebellar PML. Dentate nucleus atrophy is generally not present in early cerebellar PML when the shrimp sign is evident. Measurement of the dentate nucleus diameter on clinical scans is technically challenging, and this issue precluded us from defining clear limits and quantitative comparisons of the nucleus diameters among cases. The subjective term “severe atrophy” in the exclusion criteria recognizes this reality and indicates that nucleus dimensions should be largely preserved relative to the remainder of the cerebellum.

Finally, we note that patients with PML may present with ataxia and cerebellar atrophy but no white matter lesions, reflecting JCV infection of the cerebellar granular cells, a constellation termed JCV granule cell neuronopathy.³⁴ We caution that the absence of the shrimp sign in a newly ataxic patient with HIV does not preclude the possibility of JCV infection, even though the imaging is not indicative of PML.

Implications. Our study is the first to identify a neuroimaging marker that is both sensitive and specific for cerebellar PML early in the disease. The clinical significance of our findings is highlighted by a recent case report of a patient with PML initially misdiagnosed with cerebellar ischemic stroke.³⁵ Imaging at presentation revealed a focal lesion in the middle cerebellar peduncle sparing the dentate nucleus. During the next few months as the patient worsened, increasing lesion size prompted consideration of PML. By means of our shrimp sign criteria, earlier detection of PML may have been facilitated. Future studies can assess the reliability of our shrimp sign criteria in other cohorts and the potential for this sign to facilitate earlier detection and treatment of PML.

CONCLUSIONS

In this retrospective review of brain MR imaging studies in 2 cohorts, patients with known PML and those with other disorders associated with T2-hyperintense cerebellar lesions, the shrimp

sign showed high sensitivity and NPV and excellent specificity and PPV for cerebellar PML. The shrimp sign is a valid and reliable radiologic biomarker for cerebellar PML and may aid in the diagnosis of cerebellar PML.

ACKNOWLEDGMENT

The assistance of Jason MacMore is gratefully acknowledged.

Disclosures: Anna E. Goodheart—UNRELATED: Consultancy: Harvard T.H. Chan School of Public Health, Comments: Medical consultant for an epidemiological study; Grants/Grants Pending: American Academy of Neurology training grant, Other: Massachusetts Alzheimer’s Disease Research Center, Comments: Grant to support coursework and educational activities. Shibani S. Mukerji—UNRELATED: Grants/Grants Pending: National Institute of Mental Health, Harvard University Center for AIDS Research, Comments: K23MH115812, P30AI060354*; Jeremy D. Schmahmann—UNRELATED: Consultancy: Biogen, IQVIA; Patents (Planned, Pending, or Issued): author of the Brief Ataxia Rating Scale, Cerebellar Cognitive Affective Syndrome Scale, Patient-Reported Outcome Measures for Ataxia, all copyrighted to the General Hospital Corporation; Royalties: Oxford Academic, Springer, Mac Keith Press; Payment for Development of Educational Presentations: Continuing Medical Education lectures at Harvard Medical School; Other: site Principal Investigator on Biohaven Pharmaceutical clinical trials NCT03701399 and NCT03952806. *Money paid to the institution.

REFERENCES

1. Major EO, Yousry TA, Clifford DB. **Pathogenesis of progressive multifocal leukoencephalopathy and risks associated with treatments for multiple sclerosis: a decade of lessons learned.** *Lancet Neurol* 2018;17:467–80 CrossRef Medline
2. Ferenczy MW, Marshall LJ, Nelson CD, et al. **Molecular biology, epidemiology, and pathogenesis of progressive multifocal leukoencephalopathy, the JC virus-induced demyelinating disease of the human brain.** *Clin Microbiol Rev* 2012;25:471–506 CrossRef Medline
3. Saribas AS, Ozdemir A, Lam C, et al. **JC virus-induced progressive multifocal leukoencephalopathy.** *Future Virol* 2010;5:313–23 CrossRef Medline
4. Major EO, Amemiya K, Tornatore CS, et al. **Pathogenesis and molecular biology of progressive multifocal leukoencephalopathy, the JC virus-induced demyelinating disease of the human brain.** *Clin Microbiol Rev* 1992;5:49–73 CrossRef Medline
5. Brooks BR, Walker DL. **Progressive multifocal leukoencephalopathy.** *Neurol Clin* 1984;2:299–313 CrossRef Ref
6. Berger JR, Houff S. **Progressive multifocal leukoencephalopathy: lessons from AIDS and natalizumab.** *Neurol Res* 2006;28:299–305 CrossRef Medline
7. Ho PR, Koendgen H, Campbell N, et al. **Risk of natalizumab-associated progressive multifocal leukoencephalopathy in patients with multiple sclerosis: a retrospective analysis of data from four clinical studies.** *Lancet Neurol* 2017;16:925–33 CrossRef Medline
8. Zaheer F, Berger JR. **Treatment-related progressive multifocal leukoencephalopathy: current understanding and future steps.** *Ther Adv Drug Saf* 2012;3:227–39 CrossRef Medline
9. Gagne F, Bouchard JP, Bernier JP. **Progressive multifocal leukoencephalopathy: observation with predominant pontocerebellar lesions and association with congenital immune deficiency.** *Acta Neuropathol* 1977;38:167–69 CrossRef Medline
10. Jones HR Jr, Hedley-Whyte ET, Freidberg SR, et al. **Primary cerebello-pontine progressive multifocal leukoencephalopathy diagnosed pre-mortem by cerebellar biopsy.** *Ann Neurol* 1982;11:199–202 CrossRef Medline
11. Hodel J, Darchis C, Outteryck O, et al. **Punctate pattern: a promising imaging marker for the diagnosis of natalizumab-associated PML.** *Neurology* 2016;86:1516–23 CrossRef Medline
12. Wattjes MP, Verhoeff L, Zentjens W, et al. **Punctate lesion pattern suggestive of perivascular inflammation in acute natalizumab-associated progressive multifocal leukoencephalopathy: productive**

- JC virus infection or preclinical PML-IRIS manifestation?** *J Neurol Neurosurg Psychiatry* 2013;84:1176–77 CrossRef Medline
13. Yadav R, Ramdas M, Karthik N, et al. **“Hot cross bun” sign in HIV-related progressive multifocal leukoencephalopathy.** *Neurol India* 2011;59:293–94 CrossRef Medline
 14. Padmanabhan S, Cherian A, Iype T, et al. **Hot cross bun sign in HIV-related progressive multifocal leukoencephalopathy.** *Ann Indian Acad Neurol* 2013;16:672–73 CrossRef Medline
 15. Lee YC, Liu CS, Wu HM, et al. **The “hot cross bun” sign in the patients with spinocerebellar ataxia.** *Eur J Neurol* 2009;16:513–16 CrossRef Medline
 16. Soares-Fernandes JP, Ribeiro M, Machado A. **“Hot cross bun” sign in variant Creutzfeldt-Jakob disease.** *AJNR Am J Neuroradiol* 2009;30:E37 CrossRef Medline
 17. Muqit MM, Mort D, Miskiel KA, et al. **“Hot cross bun” sign in a patient with parkinsonism secondary to presumed vasculitis.** *J Neurol Neurosurg Psychiatry* 2001;71:565–66 CrossRef Medline
 18. Berger JR, Aksamit AJ, Clifford DB, et al. **PML diagnostic criteria: consensus statement from the AAN Neuroinfectious Disease Section.** *Neurology* 2013;80:1430–38 CrossRef Medline
 19. Manto M, Gruol DL, Schmahmann J, et al. *Handbook of the Cerebellum and Cerebellar Disorders*. Vol 1. Springer-Verlag; 2013
 20. Whiteman ML, Post MJ, Berger JR, et al. **Progressive multifocal leukoencephalopathy in 47 HIV-seropositive patients: neuroimaging with clinical and pathologic correlation.** *Radiology* 1993;187:233–40 CrossRef Medline
 21. Shah R, Bag AK, Chapman PR, et al. **Imaging manifestations of progressive multifocal leukoencephalopathy.** *Clin Radiol* 2010;65:431–39 CrossRef Medline
 22. Sahraian MA, Radue EW, Eshaghi A, et al. **Progressive multifocal leukoencephalopathy: a review of the neuroimaging features and differential diagnosis.** *Eur J Neurol* 2012;19:1060–69 CrossRef Medline
 23. Kuker W, Mader I, Nagele T, et al. **Progressive multifocal leukoencephalopathy: value of diffusion-weighted and contrast-enhanced magnetic resonance imaging for diagnosis and treatment control.** *Eur J Neurol* 2006;13:819–26 CrossRef Medline
 24. Bergui M, Bradac GB, Oguz KK, et al. **Progressive multifocal leukoencephalopathy: diffusion-weighted imaging and pathological correlations.** *Neuroradiology* 2004;46:22–25 CrossRef Medline
 25. Arai Y, Tsutsui Y, Nagashima K, et al. **Autopsy case of the cerebellar form of progressive multifocal leukoencephalopathy without immunodeficiency.** *Neuropathology* 2002;22:48–56 CrossRef Medline
 26. Boster A, Hreha S, Berger JR, et al. **Progressive multifocal leukoencephalopathy and relapsing-remitting multiple sclerosis: a comparative study.** *Arch Neurol* 2009;66:593–99 CrossRef Medline
 27. Ryschkeiwitsch CF, Jensen PN, Monaco MC, et al. **JC virus persistence following progressive multifocal leukoencephalopathy in multiple sclerosis patients treated with natalizumab.** *Ann Neurol* 2010;68:384–91 CrossRef Medline
 28. Ikeda J, Matsushima A, Ishii W, et al. **Brain biopsy is more reliable than the DNA test for JC virus in cerebrospinal fluid for the diagnosis of progressive multifocal leukoencephalopathy.** *Intern Med* 2017;56:1231–34 CrossRef Medline
 29. Marzocchetti A, Di Giambenedetto S, Cingolani A, et al. **Reduced rate of diagnostic positive detection of JC virus DNA in cerebrospinal fluid in cases of suspected progressive multifocal leukoencephalopathy in the era of potent antiretroviral therapy.** *J Clin Microbiol* 2005;43:4175–77 CrossRef Medline
 30. De Luca A, Giancola ML, Ammassari A, et al. **The effect of potent antiretroviral therapy and JC virus load in cerebrospinal fluid on clinical outcome of patients with AIDS-associated progressive multifocal leukoencephalopathy.** *J Infect Dis* 2000;182:1077–83 CrossRef Medline
 31. Giudici B, Vaz B, Bossolasco S, et al. **Highly active antiretroviral therapy and progressive multifocal leukoencephalopathy: effects on cerebrospinal fluid markers of JC virus replication and immune response.** *Clin Infect Dis* 2000;30:95–99 CrossRef Medline
 32. Marshall LJ, Major EO. **Molecular regulation of JC virus tropism: insights into potential therapeutic targets for progressive multifocal leukoencephalopathy.** *J Neuroimmune Pharmacol* 2010;5:404–17 CrossRef Medline
 33. Hagerman PJ, Hagerman RJ. **Fragile X-associated tremor/ataxia syndrome.** *Ann N Y Acad Sci* 2015;1338:58–70 CrossRef Medline
 34. Koralnik IJ, Wuthrich C, Dang X, et al. **JC virus granule cell neuronopathy: a novel clinical syndrome distinct from progressive multifocal leukoencephalopathy.** *Ann Neurol* 2005;57:576–80 CrossRef Medline
 35. Willott RH, Sunman W, Munshi SK. **Progressive multifocal leukoencephalopathy masquerading as cerebellar infarction.** *Age Ageing* 2016;45:564–65 CrossRef Medline

Repeatability of Automated Image Segmentation with BraTumIA in Patients with Recurrent Glioblastoma

 N. Abu Khalaf,  A. Desjardins,  J.J. Vredenburg, and  D.P. Barboriak



ABSTRACT

BACKGROUND AND PURPOSE: Despite high interest in machine-learning algorithms for automated segmentation of MRIs of patients with brain tumors, there are few reports on the variability of segmentation results. The purpose of this study was to obtain benchmark measures of repeatability for a widely accessible software program, BraTumIA (Versions 1.2 and 2.0), which uses a machine-learning algorithm to segment tumor features on contrast-enhanced brain MR imaging.

MATERIALS AND METHODS: Automatic segmentation of enhancing tumor, tumor edema, nonenhancing tumor, and necrosis was performed on repeat MR imaging scans obtained approximately 2 days apart in 20 patients with recurrent glioblastoma. Measures of repeatability and spatial overlap, including repeatability and Dice coefficients, are reported.

RESULTS: Larger volumes of enhancing tumor were obtained on later compared with earlier scans (mean, 26.3 versus 24.2 mL for BraTumIA 1.2; $P < .05$; and 24.9 versus 22.9 mL for BraTumIA 2.0, $P < .01$). In terms of percentage change, repeatability coefficients ranged from 31% to 46% for enhancing tumor and edema components and from 87% to 116% for nonenhancing tumor and necrosis. Dice coefficients were highest (>0.7) for enhancing tumor and edema components, intermediate for necrosis, and lowest for nonenhancing tumor and did not differ between software versions. Enhancing tumor and tumor edema were smaller, and necrotic tumor larger using BraTumIA 2.0 rather than 1.2.

CONCLUSIONS: Repeatability and overlap metrics varied by segmentation type, with better performance for segmentations of enhancing tumor and tumor edema compared with other components. Incomplete washout of gadolinium contrast agents could account for increasing enhancing tumor volumes on later scans.

ABBREVIATIONS: BRATS = Multimodal Brain Tumor Image Segmentation Benchmark; CCC = concordance correlation coefficient; ICC = intraclass correlation coefficient; GCI = generalized conformity index; RC = absolute Bland-Altman repeatability coefficient; RC% = Bland-Altman repeatability coefficient in terms of percentage change

Automated tumor-segmentation software is usually evaluated by comparing automated segmentations with those obtained by or approved by human expert observers. For example, in the Multimodal Brain Tumor Image Segmentation Benchmark (BRATS) challenges, consensus segmentations were obtained by fusing the input of human expert observers, and segmentation software performance was measured using the Dice score, sensitivity, specificity, and 95th percentile of the Hausdorff distance.¹

Although this analysis is helpful for evaluating segmentation accuracy, it does not measure the variability of automated segmentation. Measurements of segmentation variability are important for quantifying the uncertainty for any given segmentation volume measurement and estimating the smallest change in these parameters that can be measured reliably. These estimates are useful to evaluate the suitability of automated segmentation software for clinical applications in which interval change in tumor size is the primary parameter of interest.

The primary goal of this study was to study the variability of segmentation volumes and spatial overlap obtained using the widely available software package, Brain Tumor Image Analysis (BraTumIA)² (Version 1.2 and Version 2.0; <https://www.nitrc.org/projects/bratumia>).² This software uses machine-learning techniques to produce fully automated segmentations of high-grade gliomas, which are highly correlated with the results of manual human rater segmentations.^{2,3}

Received March 18, 2020; accepted after revision January 10, 2021.

From the Department of Radiology (N.A.K., D.P.B.) and The Preston Robert Tisch Brain Tumor Center (A.D.), Duke University Medical Center, Durham, North Carolina; and Hematology Oncology Service (J.J.V.), St. Francis Hospital and Medical Center, Hartford, Connecticut.

Please address correspondence to Daniel P. Barboriak, MD, Duke University Medical Center, Department of Radiology, Box 3808, Durham, NC 27710; e-mail: daniel.barboriak@duke.edu

 Indicates article with online supplemental data.
<http://dx.doi.org/10.3174/ajnr.A7071>

MATERIALS AND METHODS

Patient Population

Segmentations were performed on MR image sets obtained from 20 patients (13 men, 7 women; age range, 39–64 years; mean, 52.9 [SD, 7.7] years of age) with pathologically confirmed glioblastoma diagnosed with recurrence who underwent repeat pretreatment imaging as part of a study of bevacizumab and irinotecan therapy.⁴ These patients were older than 18 years of age and had Karnofsky scores of at least 60%. Included patients had a minimum of 6 weeks between previous surgical resection and the beginning of the study and 4 weeks between previous radiation therapy or chemotherapy and the beginning of the study.

Written informed consent was obtained for the underlying clinical study, which was approved by the Duke Health Institutional Review Board, and also for this retrospective study on collected imaging data. Of note, 19 of the 20 patients reported here have publicly available imaging from the Cancer Imaging Archive (<https://wiki.cancerimagingarchive.net/display/Public/RIDER+NEURO+MRI>).

MR Imaging

MR images were obtained on a single 1.5T scanner (Avanto; Siemens). The imaging protocol included the following: axial pre-contrast 2D spin-echo T1WI (TE = 7.7 ms, TR = 500 ms, flip angle = 90°, FOV = 178.75 × 220 mm², voxel size = 0.430 × 0.430 × 7.5 mm³); axial 2D spin-echo T2WI (TE = 93 ms, TR = 4100 ms, flip angle = 150°, FOV = 192.50 × 220 mm², voxel size = 0.573 × 0.573 × 7.5 mm³); and axial 3D-FLAIR images (TE = 119 ms, TR = 9000 ms, TI = 2300 ms, flip angle = 180°, FOV = 175.31 × 220 mm², voxel size = .859 × 0.859 × 7.5 mm³). Gd-DTPA (Magnevist; Bayer HealthCare Pharmaceuticals) was injected intravenously at a dose of 0.1 mmol/kg for dynamic contrast-enhanced MR imaging. This was immediately followed by axial postcontrast 2D spin-echo T1WI (TE = 7.7 ms, TR = 500 ms, flip angle = 90°, FOV = 165 × 220 mm², voxel size = 0.430 × 0.430 × 7.5 mm³). Next, a T1-weighted 3D echo-spoiled gradient-echo sequence was performed. Repeat scans were generally performed 2 days after the initial scans (mean, 45.1 [SD, 7.6] hours; range, 23.2–54.6 hours).

Automatic Segmentation

The BraTumIA² software was used to automatically segment each MR imaging scan into 4 components: enhancing tumor, tumor edema, nonenhancing tumor, and tumor necrosis. Segmentation of white matter and gray matter components of normal brain are also provided. 2D-T1WI, contrast-enhanced T1WI, T2WI, and FLAIR MR imaging sequences described above were used as input. The machine learning–based methods used by the BraTumIA to produce segmentations are described separately.² Of note, the segmentations produced by BraTumIA 1.2 were deterministic, and those of BraTumIA 2.0 were not. For BraTumIA 2.0, a single summary segmentation was produced for each scan by repeating the segmentation 25 times and resolving disagreements using the same procedure used for resolving reader disagreements in the BRATS study.¹ Across the 25 repetitions, the variability of segmentation volumes was assessed using percentage coefficients of variation and variability of overlap, using the generalized conformity index (GCI),⁵ in which a GCI of

zero indicates no segmentation overlap across repetitions, a GCI of 1 indicates complete spatial overlap across repetitions, and a GCI of 0.7–1.0 is considered excellent performance.⁶

Statistical and Image Analysis

Standard repeatability metrics,⁷ including Bland-Altman repeatability coefficients (RC), intraclass correlation coefficients (ICC), and concordance correlation coefficients (CCC), were obtained for the volumes for each segmentation component as well as selected segmentation combinations. Segmentation combinations included total tumor-related abnormality (enhancing + edema + nonenhancing + necrosis), total nonenhancing tumor-related abnormality (edema + nonenhancing + necrosis), and nonenhancing non-necrotic tumor-related abnormality (edema + nonenhancing). Segmentation volumes obtained at the earlier and later scans using Version 1.2 and Version 2.0 of the software were compared using *t* tests. ICCs were interpreted using standard guidelines.⁸

The rigid body algorithm in 3D Slicer, Version 4.8.1⁹ (www.slicer.org) and the Mattes Mutual Information algorithm were used to spatially register the segmentations of 3D echo-spoiled gradient-echo sequences from the 2 time points. The registration matrix obtained from combining this registration with registration of the input images to the 3D echo-spoiled gradient-echo sequence from the same time point was then applied to align the output segmentations. Spatial overlap of segmentations was measured using EvaluateSegmentation¹⁰ (<https://github.com/Visceral-Project/EvaluateSegmentation>). To minimize possible bias due to head positioning, we calculated overlap metrics both after registration of the later-to-earlier scan and registration of the earlier-to-later scan and averaged them.

RESULTS

Summary Statistics

Measurements of the reproducibility of segmentation volumes and overlap for repeat BraTumIA 2.0 segmentations on identical datasets are summarized in the Online Supplemental Data. The mean coefficient of variation was <4%, and the GCI showed excellent segmentation overlap for all segmentation components and all combined segmentations except for the segmentations of nonenhancing and necrotic tumor, the 2 components with the smallest mean volume.

Mean segmentation volumes obtained by BraTumIA 1.2 and BraTumIA 2.0 software (using the summary segmentation for the latter) at baseline and repeat MR imaging scans are summarized in Table 1. For both BraTumIA 1.2 and 2.0, volumes of enhancing tumor were larger on the later dataset (mean, 26.3 versus 24.2 mL, *P* < .05; and 24.9 versus 22.9 mL, *P* < .01, respectively); an example of a case with a larger volume of enhancement on repeat imaging is shown in Fig 1. No significant differences in volumes for any of the remaining segmentation components and/or combinations were seen.

Repeatability coefficient in terms of both absolute volume (RC) and percent change (RC%) are summarized in Table 2. Other previously recommended repeatability measurements,⁷ including the mean total SD, mean within-subject SD, ICC, and CCC are also reported for each segmentation type and combined segmentations in the Online Supplemental Data.

Table 1: Differences between segmentation volumes obtained at baseline and repeat imaging (in mL)

Segmented Region	Mean Segmentation Volumes, BraTumIA 1.2 [SD]		Mean Segmentation Volumes, BraTumIA 2.0 [SD]		Mean Difference in Volume between Baseline and Repeat Scans [SD]	
	Baseline	Repeat	Baseline	Repeat	BraTumIA 1.2	BraTumIA2.0
	Enhancing	24.2 [17.1]	26.3 [18.5]	22.9 [16.6]	24.9 [18.1]	2.1 ^a
Edema	96.5 [34.3]	94.8 [39.2]	93.3 [33.2]	91.0 [37.7]	-1.8	-2.2
Nonenhancing	3.0 [3.2]	3.0 [3.0]	2.8 [2.5]	2.6 [2.4]	0.03	-0.2
Necrotic	5.9 [13.0]	5.6 [12.4]	6.6 [12.6]	7.0 [12.9]	-0.3	0.4
Total tumor-related abnormality	130 [51.3]	130 [56.7]	126 [48.4]	126 [52.8]	0.05	-0.1
Total nonenhancing tumor-related abnormality	105 [38.1]	103 [43.7]	103 [35.7]	101 [40.5]	-2.0	-2.1
Nonenhancing non-necrotic tumor-related abnormality	99.5 [36.2]	97.8 [41.2]	96.1 [34.3]	93.6 [38.4]	-1.7	-2.5
WM	545 [51.8]	543 [50.4]	549 [55.3]	546 [53.0]	-2.7	-2.6
GM	594 [56.8]	597 [54.2]	608 [59.0]	611 [54.6]	2.7	2.8

^a $P < .05$.

^b $P < .01$ by paired t tests; all others not significant.

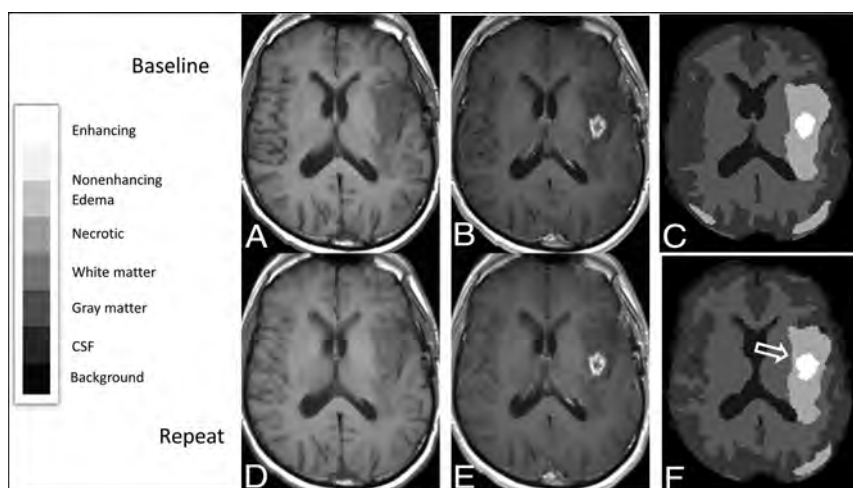


FIG 1. Registered baseline and repeat MR images from a 53-year-old man with multifocal left-hemispheric recurrent glioblastoma, with corresponding segmentations showing enlargement of enhancement segmentation on the repeat study compared with the baseline study. Registered T1-weighted axial slices obtained at baseline before (A) and after (B) administration of Gd-DTPA are shown along with segmentations obtained using BraTumIA 2.0 (C), as well as corresponding registered slices (D and E) and segmentation (F) from the repeat image set, aligned to match the baseline image set. The segmentation from the repeat image set appears larger along its anterior margin (open arrow). The overall enhancement volume increased by 2.2 mL on the repeat image set across all slices in the imaging volume. The legend for categorization of segmentation components within the segmentation is provided on the left.

CCCs were >0.8 for all tumor-related segmentations. By standard interpretation of ICCs, the reliability of segmentation volumes was excellent for segmentation of enhancement and necrosis for both software versions and for total tumor-related abnormality using BraTumIA 1.2, and it was good-to-excellent for all other segmentations (including all other combined segmentations) using both BraTumIA 1.2 and 2.0, except for segmentation of gray matter with BraTumIA 1.2 and of edema and white matter with BraTumIA 2.0, for which reliability was fair-to-excellent.

Repeatability varied across segmentation types. In terms of absolute volume, the mean RC was ≥ 24 mL for edema, total tumor-related abnormality, total nonenhancing tumor-related abnormality, and nonenhancing non-necrotic tumor-related abnormality for both software packages, and 95% CIs overlapped. For enhancing tumor volume, mean RCs were 6.9 and 5.2 mL for BraTumIA 1.2

and 2.0, respectively. For nonenhancing and necrotic tumor, the mean RCs were between 2 and 3 mL.

In terms of RC% for change in volume, CIs included or exceeded 100% change for nonenhancing tumor and necrosis segmentations. Mean RC% ranged from 26% to 46% for enhancing tumor; tumor edema; total tumor-related abnormality; total nonenhancing tumor-related abnormality; and total nonenhancing non-necrotic segmentations for both software packages.

Overlap Metrics

Analysis of Dice coefficients and 95th percentile and average Hausdorff distance (Table 3) showed that for the component segmentations, the Dice coefficients were highest (>0.7) for enhancing tumor and edema components; nonenhancing tumor had the lowest Dice coefficient; and necrosis was intermediate. An example of registered imaging slices and segmentations for a case with a relatively high Dice coefficient is illustrated in Fig 2. For all

combined tumor segmentations, Dice coefficients were, on average, ≥ 0.75 .

Average 95th percentile Hausdorff distances were <25 mm for enhancing, nonenhancing, and necrotic tumor and higher for tumor edema. Average Hausdorff distances were lowest (<1.2 mm) for enhancing tumor, tumor edema, and all combined tumor segmentations, and highest for nonenhancing and necrotic tumor.

Comparison of BraTumIA 1.2 and 2.0

The mean volumes for segmentations produced by the 2 versions of BraTumIA are reported in Table 4. BraTumIA 2.0 produced significantly smaller volumes for enhancing tumor and edema segmentations and significantly larger necrosis segmentations compared with BraTumIA 1.2 ($P < .01$ for all). The corresponding effect was also seen on the combined tumor segmentations,

Table 2: Measures of repeatability for automatically segmented volumes

BraTumIA Version	RC (95% CI), mL		%RC (95% CI)	
	1.2	2.0	1.2	2.0
Enhancing	6.9 (4.9–10)	5.2 (3.7–7.5)	46% (33%–67%)	39% (28%–57%)
Edema	24 (17–35)	30 (21–43)	31% (22%–45%)	36% (26%–52%)
Non-enhancing	2.1 (1.5–3.1)	2.0 (1.4–2.8)	95% ^a (68%–140%)	116% ^a (84%–174%)
Necrotic	3.1 (2.2–4.5)	2.0 (1.4–2.9)	87% (62%–130%)	81% (58%–117%)
Total tumor-related abnormality	25 (18–36)	31 (22–44)	26% (18%–37%)	32% (22%–47%)
Total non-enhancing tumor-related abnormality	24 (17–34)	30 (21–43)	30% (21%–44%)	35% (25%–51%)
Non-enhancing non-necrotic tumor-related abnormality	24 (17–35)	29 (21–42)	31% (22%–44%)	36% (25%–51%)
White matter	40 (28–58)	47 (33–67)	7.1% (5.1%–10%)	8.3% (5.9%–12%)
Gray matter	46 (33–67)	45 (32–65)	7.6% (5.3%–11%)	7.3% (5.1%–10%)

^a N = 19 because of average non-enhancing volume of 0 for 1 patient.

Table 3: Spatial measures of similarity across repeat image segmentations

BraTumIA Version	Dice Coefficient (95% CI)		95 th ile HD, mm (95% CI) ^b		Average HD, mm (95% CI) ^b	
	1.2	2.0	1.2	2.0	1.2	2.0
Enhancing	0.81 (0.75–0.86)	0.75 (0.70–0.81)	19 (17–21)	14 (12–16)	0.88 (0.72–1.1)	0.72 (0.60–0.84)
Edema	0.79 (0.75–0.84)	0.77 (0.73–0.81)	39 (34–45)	28 (24–31)	0.89 (0.72–1.1)	0.79 (0.66–0.94)
Nonenhancing	0.27 (0.19–0.36)	0.24 (0.16–0.31) ^a	22 (20–25)	17 (16–19) ^a	3.9 (3.2–4.8)	3.1 (2.7–3.6) ^a
Necrotic	0.51 (0.41–0.61)	0.45 (0.34–0.56)	18 (16–21)	16 (15–19)	2.3 (1.8–3.0)	2.3 (1.8–2.9)
Total tumor-related abnormality	0.85 (0.81–0.88)	0.83 (0.80–0.87)	39 (33–46)	27 (24–31)	0.59 (0.47–0.73)	0.59 (0.48–0.73)
Total nonenhancing tumor-related abnormality	0.80 (0.75–0.84)	0.77 (0.74–0.81)	40 (34–47)	27 (24–31)	0.70 (0.58–0.85)	0.76 (0.63–0.90)
Nonenhancing non-necrotic tumor-related abnormality	0.80 (0.75–0.84)	0.77 (0.73–0.81)	39 (33–48)	28 (24–31)	0.71 (0.59–0.86)	0.78 (0.65–0.93)
White matter	0.84 (0.83–0.85)	0.80 (0.79–0.82)	19 (18–20)	17 (17–18)	0.28 (0.26–0.30)	0.36 (0.34–0.38)
Gray matter	0.76 (0.75–0.78)	0.72 (0.70–0.74)	13 (12–13)	14 (13–14)	0.37 (0.36–0.39)	0.48 (0.46–0.50)

Note:—HD indicates Hausdorff distance.

^a N = 19 because no nonenhancing tumor identified by BraTumIA 2.0 for 1 case.

^b CIs were calculated by using logarithmic scale.

with BraTumIA 2.0 producing significantly smaller volumes on average ($P < .05$ for all). In contrast, the gray and white matter volumes reported by BraTumIA 2.0 were significantly larger than those reported by BraTumIA 1.2 ($P < .005$ and $P < .05$, respectively). A comparison of BraTumIA 1.2 and 2.0 segmentations performed on identical imaging data is shown in Fig 3. For all tumor segmentation components except for necrosis and for all combined tumor segmentations, the average 95th percentile Hausdorff distances were lower for BraTumIA 2.0 than for BraTumIA 1.2. Otherwise, no differences in the repeatability or overlap metrics were seen when comparing BraTumIA versions, and 95% CIs overlapped when measuring CCC, ICC, RC, RC%, Dice coefficients, and average Hausdorff distances for all segmentation components and combinations.

DISCUSSION

The purpose of this study was to establish benchmarks for segmentation software performance in terms of variability using widely accessible software developed using a machine-learning approach.² These results may be useful for comparison with results obtained from other automated software using machine-learning or other approaches.

Although methods for measuring segmentation variability in the absence of ground truth segmentations have been described, none have been widely accepted. One approach to evaluating variability is to measure the repeatability of results when applied to images obtained in close temporal succession, the so-called coffee break experiment²⁰ paradigm. For measurement of enhancing brain tumors using MR imaging, the choice of the interval between repeat scans represents a compromise between minimizing time during which the underlying tumor may change and maximizing time for washout of contrast agent from the circulation and tumor.

In this study, in which contrast-enhanced MR imaging scans were obtained between 23.2 to 54.6 hours apart, significantly larger volumes of enhancing tumor were obtained on the later scan than on the earlier scan using both BraTumIA 1.2 and 2.0, despite the relatively short time interval between scans. This result points out an important limitation in using repeat scans at short time intervals to measure the repeatability for segmentation of enhancing tumor. Although one cannot exclude this result possibly being, in part, due to tumor growth in the interval, this seems unlikely to entirely account for the magnitude of these changes. The median increase in enhancement volume in this short time period was approximately 3.0 mL (10.0% median volume increase) for BraTumIA 1.2, and 2.0 mL (10.3% median volume increase) for

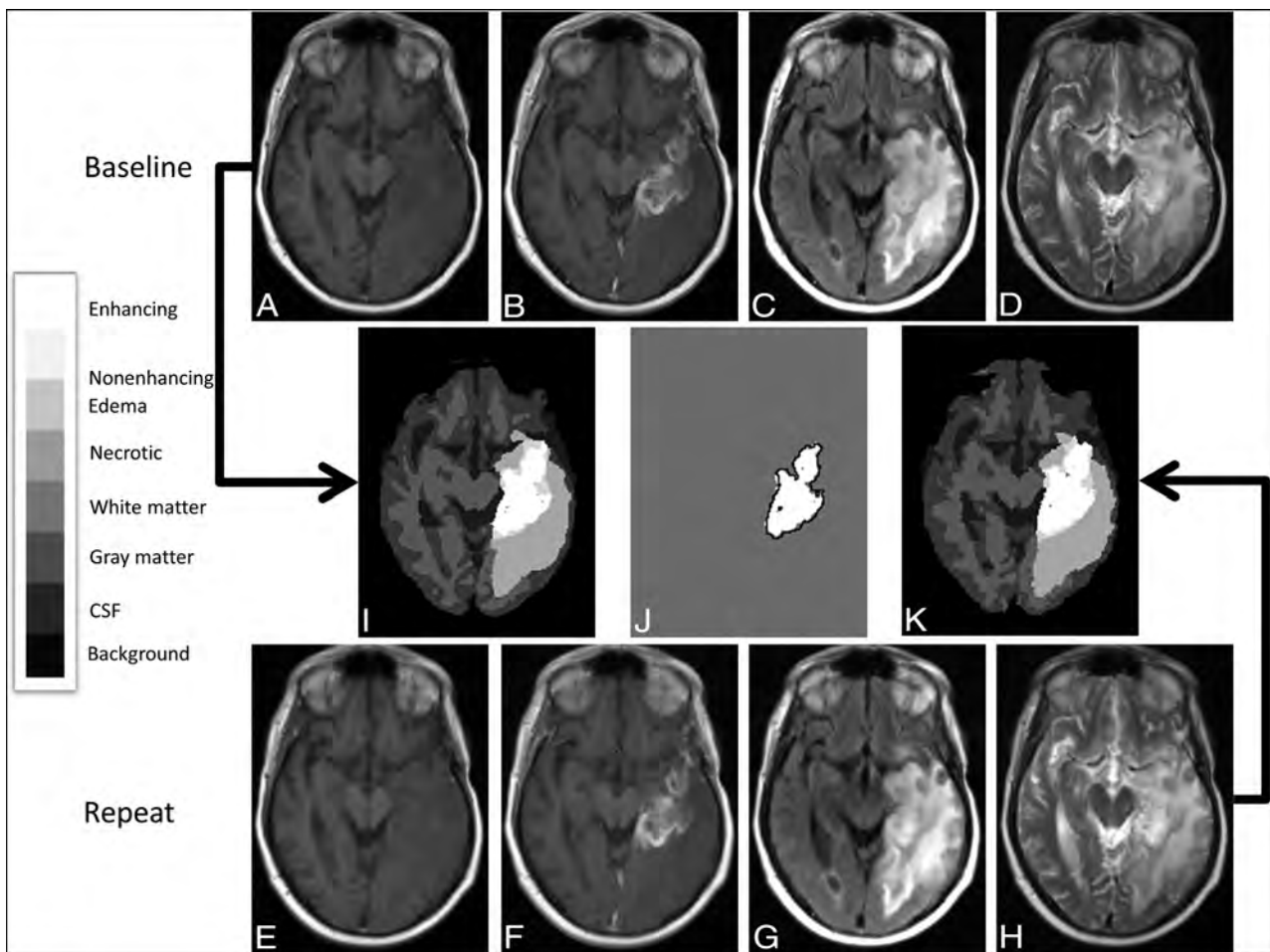


FIG 2. Registered baseline and repeat MR images from a 62-year-old man with recurrent glioblastoma in the left temporal lobe, with corresponding segmentations showing a relatively high Dice coefficient for segmentation of enhancing tumor. Registered axial slices from the baseline image set, including T1-weighted images before (A) and after (B) administration of contrast agent, as well as FLAIR (C) and T2-weighted images (D) produced segmentation (E) using BraTumIA 1.2. Corresponding registered slices from the repeat imaging set (F–I) produced segmentation (K) using BraTumIA 1.2. The legend for categorization of segmentation components within the segmentation is provided on the left. The overlap of enhancing tumor segmentations from baseline (white) and repeat (black outline) time points at this slice is shown (I). For this case, the overall Dice coefficient is 0.94 and the 95% Hausdorff distance was 4.3 mm for the enhancing tumor segmentations. The legend for categorization of segmentation components within the segmentation is provided on the left.

Table 4: Paired t test results for volumes reported by BraTumIA 1.2 and BraTumIA 2.0 (in mL)

Segmented Region	Average Volume BraTumIA 1.2		Average Volume BraTumIA 2.0		Average Difference in Volumes (BraTumIA 2.0–BraTumIA 1.2)
	Mean	SD	Mean	SD	Mean
Enhancing	25.2	17.6	23.9	17.1	–1.3 ^a
Edema	95.6	36.4	92.2	35.1	–3.4 ^b
Nonenhancing	3.02	3.04	2.69	2.43	–0.33
Necrotic	5.79	12.5	6.82	12.6	1.0 ^b
Total tumor-related abnormality	130	53.4	126	50.0	–4 ^b
Total nonenhancing tumor-related components	104	40.5	102	37.7	–2 ^c
Nonenhancing non-necrotic tumor-related components	98.7	38.3	94.8	36.0	–3.9 ^b
WM	544	50.5	547	53.5	3 ^c
GM	596	54.8	610	56.1	14 ^a

^a $P < .005$ level.

^b $P < .01$ level.

^c $P < .05$ level.

BraTumIA 2.0. These findings would suggest median specific growth rates of 2.1% and 2.3%/day, respectively, higher than the 1.2%/day rate reported for untreated glioblastoma.¹¹ There were

no significant differences in segmentation volumes for nonenhancing tumor and tumor edema between these time points; it seems unlikely that true tumor change of this magnitude would be

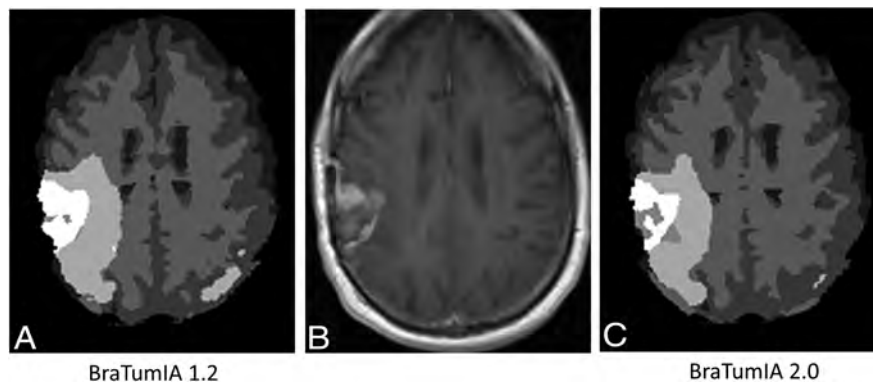


FIG 3. Contrast-enhanced T1-weighted image from an MR imaging study of a 47-year-old man with recurrent glioblastoma in the right parietal lobe with corresponding segmentations obtained using BraTumIA 1.2 and BraTumIA 2.0. Registered axial contrast-enhanced T1-weighted image from the baseline image set (B) is compared to segmentations obtained by BraTumIA 1.2 (A) and BraTumIA 2.0 (C). For this case, the overall volume of the enhancing tumor segmentations was 23.4 mL for BraTumIA 1.2 and 20.0 mL for BraTumIA 2.0. The legend for categorization of segmentation components within the segmentation is the same as for Figs. 1 and 2.

unaccompanied by change in the volumes of these segmentation components. Finally, segmentations of enhancement in patients with glioblastoma using human raters have not shown volume change during similarly short time intervals.¹²

Incomplete washout of gadolinium contrast agents for days to weeks as previously documented by mass spectroscopy of brain tumor specimens¹³ could contribute to this result. Retained gadolinium contrast agent from the initial injection may result in more voxels becoming detectable above the image noise after contrast agent administration at the later scan, or it may indicate that the software was unable to completely correct for retained contrast agent on the noncontrast T1-weighted imaging on the later scan.

As a result, measurements of repeatability for the enhancing tumor reported in this study should be interpreted with caution. Although some of our figures of merit such as RCs are primarily related to measurement variability, the relationship of this variability to measurement magnitude is not known. In addition, inclusion of larger areas of enhancement on the later images would be expected to affect overlap metrics, leading to decreased Dice coefficients and increased Hausdorff distances. Replicating this study with longer intervals between scans may not yield more valid repeatability measurements because of the length of time gadolinium contrast agents may be retained in tumors,¹³ as well as the possible confounding effect of tumor growth.

Our results show that RCs are variable and dependent on the segmentation type; in terms of percentage change, the RCs for both BraTumIA versions are high enough (>85%) that applications designed to reliably measure small changes in nonenhancing and necrotic tumor components in single patients across time are unlikely to be successful. In contrast, our results suggest that large changes in underlying tumor (for example, ≥ 24 mL in tumor edema, total tumor-related abnormality, total nonenhancing tumor, or nonenhancing non-necrotic tumor) could be reliably assessed, even in single patients.

Similarly, the performance of BraTumIA software segmentation in terms of overlap metrics varied across segmentation types. Dice coefficients were low, and average Hausdorff distance metrics were

high for the nonenhancing and necrotic tumor components. These segmentations were the smallest tumor-related components, raising the possibility that the known confounding relationship between poorer overlap metrics and smaller objects compared with larger ones, given a fixed resolution,¹⁴ could account for these findings. In addition, the task of delineating these regions from adjacent areas may be particularly challenging; this challenge could be due to a poor definition of boundaries, particularly between nonenhancing tumor and adjacent edema, and for tumor necrosis and normal CSF-containing structures such as the sulci. It is interesting that (except for necrotic tumor) the 95th percentile Hausdorff distances were smaller for segmentations produced by BraTumIA 2.0 compared with Version 1.2. This could be explained by more spatial smoothing of segmentation surfaces in the newer version, which would presumably lead to fewer outliers when comparing contours.

To place our results in context, we found that the mean Dice score between raters as noted in the BRATS challenge was 0.85 for whole tumor and 0.74 for active tumor;¹ this finding corresponds to 0.85 and 0.83 for whole tumor and 0.81 and 0.75 for enhancing tumor for BraTumIA 1.2 and 2.0, respectively, in our study. Thus, the performance of software in terms of the degree of overlap of segmentations on repeat image sets is roughly similar to the performance of different human raters on identical image sets. Similarly, the performance of BraTumIA software as measured by 95th percentile Hausdorff distances on repeat image sets was 40 and 27 mm for whole tumor and 19 and 14 mm for BraTumIA 1.2 and 2.0, respectively. This level of performance is well within the spectrum of performance of 20 software packages evaluated with similar measurements comparing software segmentations with consensus rater segmentations in the BRATS challenge.¹

In comparing the 2 software versions, we noted significant differences in the performance of the segmentations: BraTumIA 2.0 produces significantly smaller volumes of enhancing tumor and edema tumor segmentations (on average 5% smaller for tumor and 4% smaller for edema) compared with BraTumIA 1.2. If segmentation performance compared with expert raters is improved in the newer version, our finding that white and particularly gray matter volumes were higher in BraTumIA 2.0 raises

the possibility that the tumor segmentations may be more specific in the newer version. This possibility may help address concerns about overestimation of enhancing tumor volume when using BraTumIA 1.2, previously noted in preoperative patients,¹⁵ which was confirmed in a more recent study.¹⁶ Reliability measured by ICC, concordance measured by CCC, and overlap measured by Dice coefficients were similar between the 2 software versions.

This study has several limitations. Measurements of repeatability and overlap metrics reported in our study may only apply to a similar group of patients imaged under similar conditions. In this case, all patients were postoperative and had recurrent enhancing tumor, and volumes of enhancement were relatively large (mean volume of enhancement using BraTumIA 1.2 was 25.2 mL). Repeatability may be different if patients with smaller tumors are included; for comparison, in a study of the use of BraTumIA for estimating the extent of resection, preoperative and immediate postoperative scans had a mean volume of enhancement of 23.0 and 0.8 mL, respectively, using BraTumIA 1.2.¹³ Of note, when we studied the performance of the software version that produced nondeterministic results (BraTumIA 2.0) across identical datasets, the poorest performance in terms of variability in segmentation volume and segmentation overlap was seen with the segmentation components with the smallest volumes. Finally, factors related to the imaging, including MR imaging equipment (all imaging was performed on the same 1.5T scanner in our study) and the imaging protocol used, could further limit generalizability.

CONCLUSIONS

Segmentation software performance metrics for segmentation variability using BraTumIA, a widely accessible automated software package developed using machine learning, were calculated in patients with recurrent glioblastoma who underwent repeat MR imaging. These metrics can be used to inform evaluations of the practicality of using this software for applications for automated software volumetry, particularly for measuring interval changes in segmentation volumes. The finding that when MR images are obtained approximately 2 days apart, the volumes of enhancing tumors measure larger on later scans suggests that measuring reproducibility of this segmentation may be challenging. These results may be useful as a benchmark for comparison with results obtained from other automatic segmentation programs.

ACKNOWLEDGMENTS

We thank Gino Lerebours, MA, and Sheng Luo, PhD, for statistical advice, and David Radoff, MS, for analysis support.

Disclosures: Annick Desjardins—RELATED: Grant: Genentech/Roche, Comments: grant to the institution to support clinical trial work*; Consulting Fee or Honorarium: Advisory Board, Comments: Advisory Board more than 2 years ago; UNRELATED: Consultancy: Istari Oncology; Employment: Duke University Medical Center; Grants/Grants Pending: Celgene, Symphogen A/S, Orbus Therapeutics*;

Patents (Planned, Pending or Issued): patent for genetically modified poliovirus for the treatment of solid tumors*; Stock/Stock Options: less than 1% stock in Istari Oncology. Daniel P. Barboriak—UNRELATED: Board Membership: Blue Earth Diagnostics, Comments: Medical Advisory Board for evaluation of a radiopharmaceutical; compensated for time and travel, none in last year; Grants/Grants Pending: NVIDIA, Comments: received TITAN Xp as part of NVIDIA GPU Grant program for an unrelated project.* *Money paid to the institution.

REFERENCES

1. Menze BH, Jakab A, Bauer S, et al. **The Multimodal Brain Tumor Image Segmentation Benchmark (BRATS).** *IEEE Trans Med Imaging* 2015;34:1993–2024 CrossRef Medline
2. Meier R, Knecht U, Loosli T, et al. **Clinical evaluation of a fully-automatic segmentation method for longitudinal brain tumor volumetry.** *Sci Rep* 2016;6:23376 CrossRef Medline
3. Porz N, Habegger S, Meier R, et al. **Fully automated enhanced tumor compartmentalization: man vs. machine reloaded.** *PLoS One* 2016;11:e0165302 CrossRef Medline
4. Desjardins A, Barboriak DP, Herndon JE, et al. **Effect of bevacizumab (BEV) and irinotecan (CPT-11) on dynamic contrast-enhanced magnetic resonance imaging (DCE-MRI) in glioblastoma (GBM) patients.** *J Clin Oncol* 2008;26(15_Suppl):2026 CrossRef
5. Kouwenhoven E, Giezen M, Struikmans H. **Measuring the similarity of target volume delineations independent of the number of observers.** *Phys Med Biol* 2009;54:2863–73 CrossRef Medline
6. Visser M, Müller DJ, van Duijn RJ, et al. **Inter-rater agreement in glioma segmentations on longitudinal MRI.** *Neuroimage Clin* 2019;22:101727 CrossRef Medline
7. Barnhart HX, Barboriak DP. **Applications of the repeatability of quantitative imaging biomarkers: a review of statistical analysis of repeat data sets.** *Transl Oncol* 2009;2:231–35 CrossRef Medline
8. Cicchetti DV. **Guidelines, criteria, and rules of thumb for evaluating normed and standardized assessment instruments in psychology.** *Psychol Assess* 1994;6:284–90 CrossRef
9. Fedorov A, Beichel R, Kalpathy-Cramer J, et al. **3D Slicer as an image computing platform for the Quantitative Imaging Network.** *Magn Reson Imaging* 2012;30:1323–41 CrossRef Medline
10. Taha AA, Hanbury A. **Metrics for evaluating 3D medical image segmentation: analysis, selection, and tool.** *BMC Med Imaging* 2015; 15:29 CrossRef Medline
11. Stensjøen AL, Solheim O, Kvistad KA, et al. **Growth dynamics of untreated glioblastomas in vivo.** *Neuro Oncol* 2015;17:1402–11 CrossRef Medline
12. Jafari-Khouzani K, Emblem KE, Kalpathy-Cramer J, et al. **Repeatability of cerebral perfusion using dynamic susceptibility contrast MRI in glioblastoma patients.** *Transl Oncol* 2015;8:137–46 CrossRef Medline
13. Kiviniemi A, Gardberg M, Ek P, et al. **Gadolinium retention in gliomas and adjacent normal brain tissue: association with tumor contrast enhancement and linear/macrocyclic agents.** *Neuroradiology* 2019;61:535–44 CrossRef Medline
14. Rohlfing T. **Image similarity and tissue overlaps as surrogates for image registration accuracy: widely used but unreliable.** *IEEE Trans Med Imaging* 2012;31:153–63 CrossRef Medline
15. Meier R, Porz N, Knecht U, et al. **Automatic estimation of extent of resection and residual tumor volume of patients with glioblastoma.** *J Neurosurg* 2017;127:798–806 CrossRef
16. Zeppa P, Neitzert L, Mammi M, et al. **How reliable are volumetric techniques for high-grade gliomas? A comparison study of different available tools.** *Neurosurgery* 2020 Jul 6. [Epub ahead of print] CrossRef Medline

Flow-Diversion Treatment for Unruptured ICA Bifurcation Aneurysms with Unfavorable Morphology for Coiling

F. Cagnazzo, I. Derraz, C. Dargazanli, P.-H. Lefevre, I. Coelho Ferreira, G. Gascou, C. Riquelme, A. Fanti, R. Ahmed, J. Frandon, A. Bonafe, and V. Costalat



ABSTRACT

BACKGROUND AND PURPOSE: Few reports described flow diversion for ICA bifurcation aneurysms. Our aim was to provide further insight into flow diversion for ICA bifurcation aneurysms difficult to treat with other strategies.

MATERIALS AND METHODS: Consecutive patients receiving flow diverters for unruptured ICA bifurcation aneurysms were collected. Aneurysm occlusion (O'Kelly-Marotta grading scale) and clinical outcomes were evaluated.

RESULTS: Twenty saccular ICA bifurcation aneurysms were treated with the Pipeline Embolization Device deployed from the M1 to the ICA, covering the aneurysm and the A1 segment. All patients presented with an angiographic visualized contralateral flow from the anterior communicating artery. Mean aneurysm size was 6.5 (SD, 3.2) mm (range, 4.5–20 mm). All lesions had an unfavorable dome-to-neck ratio (mean/median, 1.6/1.6; range, 0.8–2.8; interquartile range = 0.5) or aspect ratio for coiling (mean/median = 1.5/1.55; range, 0.8–2.5; interquartile range = 0.6). One was a very large aneurysm (20 mm). Nineteen medium-sized lesions were completely occluded during the angiographic follow-up (13 months). No cases of aneurysm rupture or retreatment were reported. No adverse events were described. Aneurysm occlusion was associated with the asymptomatic flow modification of the covered A1 that was occluded and contralaterally filled among 10 patients (50%), narrowed among 9 patients (45%), and unchanged in 1 subject (5%). There was no difference in the mean initial diameter of the occluded (2.1 [SD 0.4] mm; range, 1.6–3 mm) and narrowed (2 [SD, 0.2] mm; range, 1.7–2.6 mm) A1 segments.

CONCLUSIONS: Medium-sized unruptured ICA bifurcation aneurysms with unfavorable morphology for coiling can be treated with M1 ICA flow diversion. Aneurysm occlusion is associated with flow modifications of the covered A1 that seems safe in the presence of a favorable collateral anatomy through the anterior communicating artery complex.

ABBREVIATIONS: AcomA = anterior communicating artery; ICAbifA = ICA bifurcation aneurysm; OKM = O'Kelly-Marotta grading scale; PED = Pipeline Embolization Device; WEB = Woven EndoBridge

The rapid expansion of the use of flow diversion for the treatment of intracranial aneurysms is quickly outpacing the availability of clinical evidence, and most current use of the flow-diversion strategy is off-label. Given their capability to redirect the flow, these devices can be used to treat bifurcation aneurysms such as ICA bifurcation aneurysms (ICAbifAs). These lesions are relatively uncommon, representing 2%–9% of all intracranial aneurysms¹ and are generally under-represented in the endovascular

series.² In addition, treatment of ICAbifAs remains challenging: Clipping carries potential morbidity due to the dissection of regional perforators,³ and coiling has a higher recurrence rate.⁴ Advanced endovascular techniques, such as stent-assisted coiling or Y-stent placement, are suitable options for lesions with an unfavorable dome-to-neck ratio or aspect ratio, but they can be technically demanding.^{5–7} Intracranial flow disruptors such as the Woven Endobridge (WEB; MicroVention)^{8,9} or other new devices such as the pCONus aneurysm implant (phenox)¹⁰ and the PulseRider aneurysm neck reconstruction device (Pulsar Vascular)¹¹ are also promising strategies to treat lesions too complex for simple coiling. Flow diversion on the ICA terminus region has rarely been reported, and very few series focused on the treatment of ICAbifAs with a flow-redirection technique.^{12–14} This technique can be an alternative option to treat these lesions. The concept of the flow modification for ICAbifAs was first reported by Nossek et al,^{13,14} describing the angiographic results among 4 patients treated with a flow diverter deployed into the ICA M1 segment. We described the

Received April 10, 2020; accepted after revision December 4.

From the Neuroradiology Department (F.C., I.D., C.D., P.-H.L., G.G., C.R., A.F., R.A., A.B., V.C.), University Hospital Gui de Chauliac, Centre Hospitalier Universitaire de Montpellier, Montpellier, France; Neurosurgical Department (I.C.F.), Hospital Santa Lucia, Distrito Federal, Brazil; and Medical Imaging Group (J.F.), Centre Hospitalier Universitaire Nimes, University of Montpellier, Montpellier, France.

Please address correspondence to Federico Cagnazzo, MD, Neuroradiology Department, CHU Gui de Chauliac, 80 Ave Augustin Fliche, 34000 Montpellier, France; e-mail: f.cagnazzo86@gmail.com

Indicates article with online supplemental data.

<http://dx.doi.org/10.3174/ajnr.A7125>

largest experience of flow diversion for unruptured ICabifAs, analyzing 20 cases treated with a single PED deployed from the proximal M1 to the distal supraclinoid ICA, covering the A1, for aneurysm treatment.

MATERIALS AND METHODS

Patient Selection

The Montpellier hospital institutional review board approved this retrospective study. Our institutional prospectively maintained data base of Endovascular Treatment of Intracranial Aneurysms was reviewed by 2 and, in case of inconsistency, 3 investigators. All cases of ICabifAs treated with flow-diverter stents between January 2014 and August 2020 were analyzed. Aneurysm and patient characteristics, as well as treatment-related and clinical outcomes, were collected. A multidisciplinary consensus was performed to select the most appropriate treatment strategy.

Reasons for Flow-Diversion Strategy and Technical Aspects

Technical aspects of flow diversion in the ICA bifurcation region were described in our previously published experience.¹⁵ ICabifAs were treated with flow diversion mainly for the following reasons: 1) large-neck lesions difficult to treat with coiling; 2) the presence of an unfavorable projection of the aneurysm dome for the microcatheterization and coiling; and 3) unfavorable dome-to-neck ratio and/or aspect ratio (Online Supplemental Data). A dome-to-neck ratio of <2 and an aspect ratio of <1.6 have been considered unfavorable for simple coiling,¹⁶ and flow diversion was evaluated.

Flow diverters were deployed from the proximal M1 to the supraclinoid ICA, covering the aneurysm and the A1 segment of the anterior cerebral artery. Sizing of the device was accurately performed, while choosing the shortest possible PED to avoid, as much as possible, the coverage of the M1 perforators and the ophthalmic artery, with the aim of reducing potential ischemic complications.¹⁷⁻¹⁹ Because of the more distal origin at the level of the supraclinoid ICA, the anterior choroidal artery, was, in general, covered by the device.

During the diagnostic angiography performed before treatment, the presence of a patent anterior communicating artery (AcomA) was tested in all patients through a contralateral ICA angiogram, while the ipsilateral common carotid artery was temporarily occluded by manual compression. Accordingly, we visualized 2 angiographic patterns: 1) patency of the AcomA: the A1 and the MCA ipsilateral to the target aneurysm fully visualized during the contralateral injection; and 2) absence (or stenosis) of the AcomA: the A1 segment ipsilateral to the target lesion not visualized. Flow diversion with the coverage of the A1 was performed only in case of a patent AcomA.¹⁵

Antiplatelet Therapy

All cases of flow diversion were unruptured. Antiplatelet therapy consisted of daily dual-antiplatelet drugs with aspirin, 75 mg, and clopidogrel, 75 mg, starting 5 days before treatment and maintained for 6 months (until the first follow-up). After 6 months, clopidogrel was normally stopped, and aspirin, 75 mg, was continued for an additional 6 months. Aspirin was continued for a longer period in case of the following: 1) the presence of a

patient's vascular risk factors; 2) in-stent stenosis of $>50\%$; or 3) ischemic events related to the stent.

The VerifyNow P2Y12 assay (Accumetrics) was used to test the platelet inhibition (platelet reactivity unit). In case of platelet inhibition of $<30\%$, patients were treated with an additional dose of clopidogrel, 150 mg, or were switched to prasugrel, 10–20 mg. Aspirin VerifyNow platelet reactivity was not tested. Intravenous heparinization was performed for all patients (activated clotting time maintained above 250 seconds).

Description of the Procedure

All patients were treated under general anesthesia via a transfemoral approach. A triaxial access was adopted in all patients. A 6F-long femoral sheath introducer was used. The size of the implanted flow diverter was chosen via biplane 3D rotational angiography of the parent artery and target aneurysm. Preimplantation virtual device simulation was routinely performed with Sim&Size software (Sim&Cure), and the size of the flow diverter was chosen on the basis of the simulation.^{15,20}

The stent was unsheathed under roadmap guidance through a Phenom (Medtronic) 0.027-inch microcatheter navigated beyond the aneurysm neck. The correct deployment and vessel wall apposition were visualized with VasoCT (Philips Healthcare), with a diluted iodinated contrast medium.

Clinical and Radiologic Assessment

Clinical evaluation was performed in the periprocedural period (24–48 hours) and during long-term follow-up (6, 12, and 24 months after treatment). The safety of the treatment was evaluated on the basis of the presence of new symptoms or new neurologic deficits related to the procedure. Treatment-related complications were further classified as transient (no impact on the neurologic status) or permanent (associated with an irreversible worsening of the neurologic condition).

Aneurysm occlusion was evaluated with MRA at 6 months and with DSA at 12 and 24 months. Angiographic occlusion was assessed according to the O'Kelly-Marotta grading scale (OKM)²¹ (occlusion grade: A = total, B = subtotal, C = entry remnant, D = no filling; degree of aneurysmal stasis: during the 1 = arterial, 2 = capillary, 3 = venous phase).^{15,22} Imaging analysis was performed by 2 readers (not directly involved in treatments) with 3 and 5 years' experience in interventional neuroradiology.

Because flow diverters were deployed from the M1 segment to the supraclinoid ICA, we studied the angiographic outcome of the covered A1 artery. Findings about A1 flow modification were reported in our previously published experience.¹⁵ When a collateral circulation from the AcomA complex is present, the antero-grade flow from the ipsilateral ICA decreases, allowing the hemodynamic compensation from the contralateral ICA through the AcomA. Accordingly, the status of the covered A1 was evaluated immediately after stent deployment and during angiographic follow-up as the following: 1) patent (unchanged), 2) narrowed (because of partial contralateral flow from the AcomA), and 3) occluded (absence of antero-grade flow due to complete flow reversal from the AcomA). In addition, the radiologic and clinical events related to the coverage of the branch were classified as 1) absence of either radiologic or clinical events related to the coverage of the A1

segment; and 2) symptomatic lesions on the territory of the covered A1.

Statistical Analysis

The overall frequency (percentage) and 95% confidence interval were calculated for all results. The Wald method was used to calculate the CI for event rates. Statistical analysis was performed with QuickCalcs software (GraphPad Software). A 2-tailed *t* test was used for continuous data, and the χ^2 test, for categorical variables. Statistical significance was set at $P < .05$.

RESULTS

Baseline Population Characteristics

Twenty consecutive patients (16 women, 4 men; mean age, 53 [SD, 12.6] years; range, 34–79 years) with 20 saccular unruptured ICAbifAs were treated with flow-diverter stents deployed from the ICA to the M1 (Online Supplemental Data). All patients presented with an mRS of 0 before treatment, except 2 subjects with mRS 2 and mRS 3 in relation to a previous SAH. Six patients (30%) were smokers, 4 patients (20%) had hypertension, and 1 (5%) was a smoker with hypertension, whereas 9 (45%) did not present with vascular risk factors (details in the Online Supplemental Data).

Aneurysm and Treatment Characteristics

All 20 ICAbifAs were saccular and unruptured lesions with a mean size of 6.5 (SD, 3.2) mm (range, 4.5–20 mm). All lesions had an unfavorable dome-to-neck ratio (mean/median = 1.6/1.6; range, 0.8–2.8; interquartile range = 0.5) or aspect ratio for coiling (mean/median = 1.5/1.55; range, 0.8–2.5; interquartile range = 0.6). Sixteen aneurysms had an aspect ratio of <1.6 , while 15 lesions had a dome-to-neck ratio of <2 (Online Supplemental Data). Nineteen aneurysms were medium-sized (5–9 mm), and 1 was very large (20 mm).

Based on the relationship between the parent artery and the origin of the aneurysm neck, there were 2 types of configurations: 1) Fifteen aneurysms presented with the neck at the midpoint of the ICA terminus; and 2) five aneurysms had the neck deviated to the origin of the A1 segment (ICA terminus to A1). Three patients had an ipsilateral ICA aneurysm (2 posterior communicating artery aneurysms and 1 ophthalmic artery aneurysm) that was covered with the same flow diverter. Four aneurysms (20%) were previously coiled and treated with flow diversion because of recanalization. Among these, 3 (15%) were previously ruptured and 1 had a 20-mm ICAbifA that was treated with flow-diversion-assisted coiling (patient 13).

A single PED was used for all patients.

Angiographic Outcome

The PED was successfully deployed from the M1 to the ICA in all patients.

The mean angiographic follow-up was 13 months (range, 9–24 months). Complete occlusion (OKM D) was achieved among 19 medium-sized (95%) aneurysms (Figs 1 and 2). Incomplete occlusion (OKM B) was found in 1 very large aneurysm (5%). This incompletely occluded aneurysm was stable at the last angiographic follow-up. No cases of aneurysm rupture were reported. There were no cases of in-stent stenosis.

Clinical Outcome and Procedure-Related Complications

There were no transient or permanent events related to the treatment. At the last angiographic follow-up (mean follow-up, 13 months), covered A1 vessels were occluded (complete flow reversal from the contralateral side) among 10 patients (50%) (Fig 1), narrowed among 9 patients (45%) (Fig 2), and patent (unchanged in diameter) in 1 subject (5%). A1 occlusion or narrowing was not associated with clinical adverse events or radiologic asymptomatic lesions at MR imaging. The mean diameter of the covered A1 presenting with occlusion at follow-up was 2.1 (SD, 0.4) mm (range, 1.6–3 mm), while those showing narrowing presented with a mean diameter of 2 (SD, 0.2) mm (range, 1.7–2.6 mm; $P > .05$). Only 1 patient (patient 13) with a 20-mm aneurysm showed patency of the covered A1 segment associated with incomplete occlusion of the aneurysm.

DISCUSSION

Our study showed that flow-diversion treatment for medium-sized ICAbifAs was a feasible and safe alternative endovascular strategy associated with quite a high rate of aneurysm occlusion. Currently, only a few reports with a small number of patients explored flow diversion in the ICA bifurcation region, and the present series could add further data about this strategy.

The concept of this strategy is based on flow redirection and flow remodeling in the ICA terminus region. This mechanism was reported >10 years ago by Kallmes et al,²⁰ who reported in an animal study that the coverage of elastase-induced aneurysms and adjacent arteries allowed occlusion of the aneurysms without compromising the branch arteries. This report was mainly related to the absence of collateral circulation causing a continued flow in these vessels, permitting ongoing patency. On the other hand, in the literature authors reported, in case of a well represented collateral circulation, the pressure gradient across the stent being normally not enough to maintain the patency of the covered artery, leading to progressive and usually asymptomatic branch occlusion.^{21–24}

The ICA terminus region provides unique challenges for endovascular treatment. First, aneurysms of the bifurcation, being the highest point of the circle of Willis, are often wide-neck lesions subjected to constant high hemodynamic stress leading to aneurysm growth, risk of rupture, and recanalization.²⁵ In addition, aneurysms of this region are close to the medial perforators (penetrating the medial portion of the anterior perforating substance).²⁶ The flow-remodeling strategy, using a flow diverter deployed from the M1 to the ICA, allowed a hemodynamic redirection, decreasing the anterograde flow into the A1 and the ICA terminus aneurysm. In our series, ICA M1 flow diverters were associated with delayed reversal of the flow in the covered A1 segment that was retrogradely filled through the AcomA. This phenomenon caused a slow flow in the adjacent aneurysm, leading to aneurysm thrombosis, with a contralateral filling of the A1 and the medial lenticulostriate arteries. Accordingly, this mechanism, while resulting in $>90\%$ of the complete occlusion of the aneurysm, was associated with no clinical and radiologic events related to impairment of the perforators.

On the basis of our results and treatment strategy, 2 main learning points should be stressed. First, the contralateral supply of the A1 with manual compression of the carotid artery is crucial

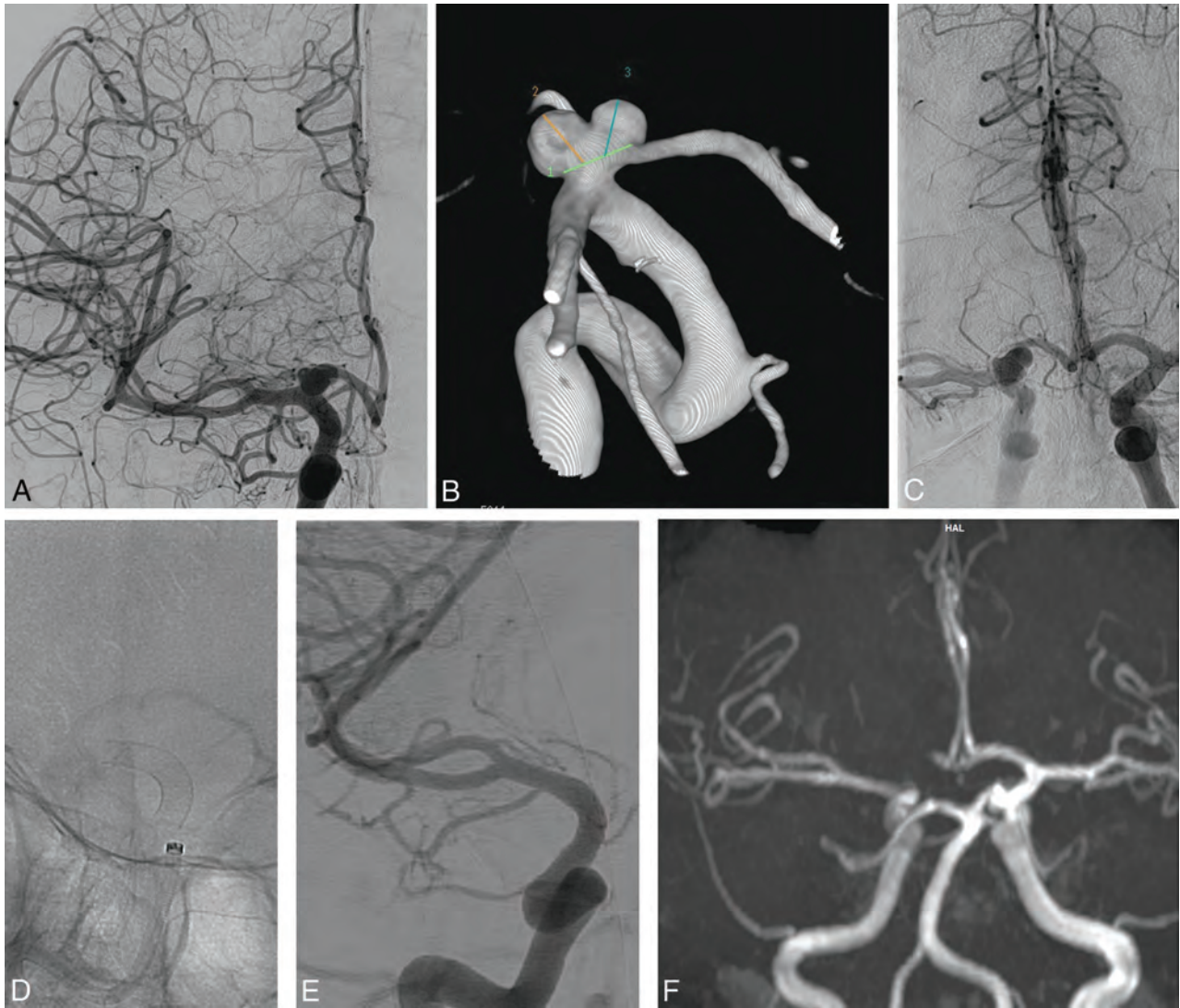


FIG 1. Patient 4. *A*, A right ICA angiogram (anterior-posterior view) shows a wide-neck medium-sized ICA terminus aneurysm. *B*, 3D reconstruction depicts a bilobate irregular shape of the aneurysm with the right A1 segment originating from the neck. *C*, Contralateral ICA angiogram demonstrates the patency of the AcomA with retrograde flow into the left ICA terminus segment. *D*, A 4.5 × 14 mm PED is deployed from the M1 (before the temporal branch) to the supraclinoid ICA, avoiding, as much as possible, the ostium of the ophthalmic artery. *E*, After 12 months, the aneurysm is completely occluded, and the right A1 shows absence of anterograde flow. The lateral lenticulostriate arteries and the temporal branch of the MCA are patent. *F*, The time-of-flight 3D reconstruction sequence shows absence of flow into the aneurysm (OKM D occlusion) and retrograde filling of the right anterior cerebral artery from the contralateral side through the AcomA.

to determine the safety of the coverage and flow remodeling of the ipsilateral A1. Second, accurate sizing of the device is essential and was performed with the use of virtual simulation, choosing the shortest flow diverter to avoid the coverage of the ophthalmic artery (when possible) and to reduce potential ischemic complications related to the coverage of the M1 perforators. Nossek et al¹⁴ reported complete occlusion without neurologic adverse events among 4 ICAbifAs treated with flow redirection from the supraclinoid ICA to the M1. On the other hand, a recent series of flow diversion for 10 ICA terminus aneurysms showed fewer promising results with this technique, reporting 50% adequate occlusion and 2 transient complications.¹² However, 50% of the reported aneurysms were fusiform lesions, and 60% were large or very large lesions. Conversely, our series explored medium-sized saccular aneurysms difficult to treat with coiling due to their

morphologic characteristics. Indeed, all lesions had an unfavorable dome-to-neck ratio (mean/median = 1.6/1.6) or aspect ratio for coiling (mean/median = 1.5/1.55), and flow reversal was effective among 19 of 20 lesions. Only 1 patient with a 20-mm aneurysm showed incomplete occlusion.

When we investigated the literature, the rate of long-term complete/near-complete occlusion after coiling of ICAbifAs was approximately 80%, with 6% procedure-related morbidity, a 3% rate of intraprocedural perforation, and a 14% retreatment rate.⁴ One of the most important findings of our study was the considerably high rate of stable occlusion. A series of coiling or balloon-assisted coiling of ICA terminus aneurysms reported rates of recanalization between 7% and 40%.²⁷ This outcome is likely in relation to the direct arterial pulsation and hemodynamic stress due to the T-bifurcation configuration of these lesions.

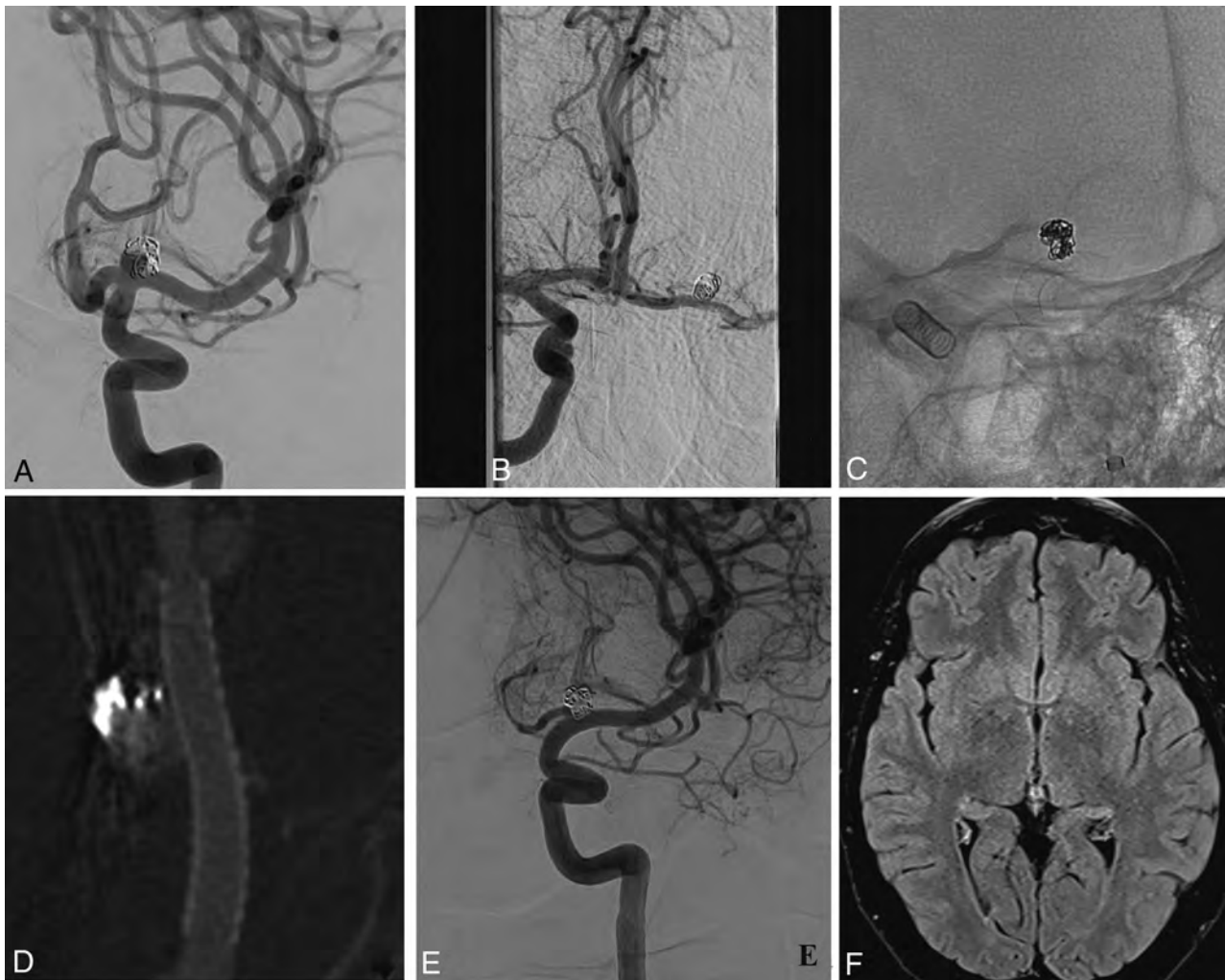


FIG 2. Patient 8. *A*, The left ICA (frontal view) depicts a previously ruptured and recanalized medium-sized ICAbifA treated with coiling during the acute phase. *B*, The presence of contralateral filling from the AcomA. *C*, A PED, 3.5 × 12 mm, is successfully deployed covering the aneurysm and the left A1 segment. The PED was delivered before the origin of the M1 lenticulostriate arteries. *D*, Flat panel angiography confirms good vessel wall apposition of the stent. *E*, A 14-month angiographic follow-up shows complete aneurysm occlusion as well as flow remodeling of the covered A1 with narrowing but without any lesions on the FLAIR sequences (*F*).

It has been shown that large-neck aneurysms (≥ 4 mm), with a dome-to-neck ratio of < 2 and an aspect ratio of < 1.6 , can predict the need for adjunctive techniques in the endovascular treatment of intracranial aneurysms.¹⁵ In our series, flow diversion was adopted as an alternative strategy for lesions having unfavorable aspect and dome-to-neck ratios. However, other techniques can be used for the treatment of these lesions. Y-stent placement²⁸ or T-stent placement⁷ has been reported to be associated with a high occlusion rate among large-neck bifurcation aneurysms. Recently, Pierot et al,²⁹ in a series of aneurysms treated with the WEB, described 14 ICAbifAs showing 36% and 29% complete and near-complete occlusion, respectively; the rate of occlusion after WEB treatment for ICA terminus aneurysms was lower compared with other locations, such as the AcomA and MCA.

Finally, all 19 occluded aneurysms were associated with occlusion or narrowing of the covered A1 due to flow reversal through the AcomA. Inversely, the only patient having incomplete aneurysm occlusion showed an unchanged diameter of the A1. A recent series reported outcomes of 42 A1 arteries covered with flow

diverters in the presence of a collateral supply³⁰ and described 31% and 52% asymptomatic occlusion and narrowing of the artery, respectively. This finding emphasizes the concept that flow remodeling for ICAbifA treatment can be effective in case of good collateral circulation from the AcomA, allowing flow reversal in the covered A1 and causing aneurysm thrombosis without neurologic sequelae.

Limitations of the Study

Our study has several limitations. This is a single-center, retrospective series with a relatively small number of patients. The influence of the platelet inhibition rate on the aneurysm occlusion or flow modifications on the covered A1 was not studied. Results cannot be generalized because most of the included aneurysms were medium-sized lesions.

CONCLUSIONS

In our experience, flow remodeling in the ICA terminus region with M1 ICA flow diversion is associated with high rates of

occlusion of medium-sized unruptured ICabifAs. In the presence of a favorable collateral anatomy through the AcomA complex, flow diversion can be a safe and effective alternative strategy for the treatment of these lesions.

Disclosures: Vincent Costalat—UNRELATED: Consultancy: Stryker, Medtronic, Balt, Cerenovus, MicroVention; Grants/Grants Pending: Stryker, Medtronic, Balt, Cerenovus, MicroVention*; Payment for Development of Educational Presentations: Stryker, Medtronic, Balt, Cerenovus, MicroVention. Pierre-Henri Lefevre—UNRELATED: Payment for Development of Educational Presentations: Medtronic. Alain Bonafe—UNRELATED: Consultancy: Medtronic, Stryker, MicroVention.* *Money paid to the institution.

REFERENCES

- Lehecka M, Dashti R, Romani R, et al. **Microneurosurgical management of internal carotid artery bifurcation aneurysms.** *Surg Neurol* 2009;71:649–67 CrossRef Medline
- Wiebers DO, Whisnant JP, Huston J 3rd, et al. **Unruptured intracranial aneurysms: natural history, clinical outcome, and risks of surgical and endovascular treatment.** *Lancet* 2003;362:103–10 CrossRef Medline
- Gonzalez-Darder JM, Gonzalez-Lopez P, Botella-Macia L. **Microsurgical treatment of internal carotid bifurcation aneurysms [in Spanish].** *Neurocirugia (Astur)* 2010;21:205–10 CrossRef Medline
- Morales-Valero SF, Brinjikji W, Murad MH, et al. **Endovascular treatment of internal carotid artery bifurcation aneurysms: a single-center experience and a systematic review and meta-analysis.** *AJNR Am J Neuroradiol* 2014;35:1948–53 CrossRef Medline
- Oishi H, Yamamoto M, Nonaka S, et al. **Endovascular therapy of internal carotid artery bifurcation aneurysms.** *J Neurointerv Surg* 2013;5:400–04 CrossRef Medline
- Fargen KM, Mocco J, Neal D, et al. **A multicenter study of stent-assisted coiling of cerebral aneurysms with a Y configuration.** *Neurosurgery* 2013;73:466–72 CrossRef Medline
- Aydin K, Stracke CP, Barburuglu M, et al. **Long-term outcomes of wide-necked intracranial bifurcation aneurysms treated with T-stent-assisted coiling.** *J Neurosurg* 2019 Dec 6. [Epub ahead of print] CrossRef Medline
- Arthur AS, Molyneux A, Coon AL, et al. **WEB-IT Study Investigators. The safety and effectiveness of the Woven EndoBridge (WEB) system for the treatment of wide-necked bifurcation aneurysms: final 12-month results of the pivotal WEB Intrasaccular Therapy (WEB-IT) study.** *J Neurointerv Surg* 2019;11:924–30 CrossRef Medline
- Pierot L, Gubucz I, Buhk JH, et al. **Safety and efficacy of aneurysm treatment with the WEB: results of the WEBCAST 2 study.** *AJNR Am J Neuroradiol* 2017;38:1151–55 CrossRef Medline
- Sorenson TJ, Iacobucci M, Murad MH, et al. **The pCONUS bifurcation aneurysm implants for endovascular treatment of adults with intracranial aneurysms: a systematic review and meta-analysis.** *Surg Neurol Int* 2019;10:24 CrossRef Medline
- Spiotta AM, Chaudry MI, Turner RD, et al. **An update on the Adjunctive Neurovascular Support of Wide-Neck Aneurysm Embolization and Reconstruction Trial: 1-year safety and angiographic results.** *AJNR Am J Neuroradiol* 2018;39:848–51 CrossRef Medline
- Pujari A, Howard BM, Madaelil TP, et al. **Pipeline Embolization Device treatment of internal carotid artery terminus aneurysms.** *J NeuroIntervent Surg* 2019;11:485–88 CrossRef Medline
- Nossek E, Chalif DJ, Chakraborty S, et al. **Modifying flow in the ICA bifurcation: Pipeline deployment from the supraclinoid ICA extending into the M1 segment—clinical and anatomic results.** *AJNR Am J Neuroradiol* 2014;35:2125–29 CrossRef Medline
- Nossek E, Chalif DJ, Levine M, et al. **Modifying flow in the ACA-ACoA complex: endovascular treatment option for wide-neck internal carotid artery bifurcation aneurysms.** *J Neurointerv Surg* 2015;7:351–56 CrossRef Medline
- Brinjikji W, Cloft HJ, Kallmes DF. **Difficult aneurysms for endovascular treatment: overdue or undertall?** *AJNR Am J Neuroradiol* 2009;30:1513–17 CrossRef Medline
- Rangel-Castilla L, Munich SA, Jaleel N, et al. **Patency of anterior circulation branch vessels after Pipeline embolization: longer-term results from 82 aneurysm cases.** *J Neurosurg* 2017;126:1064–69 CrossRef Medline
- Rouchaud A, Leclerc O, Benayoun Y, et al. **Visual outcomes with flow-diverter stents covering the ophthalmic artery for treatment of internal carotid artery aneurysms.** *AJNR Am J Neuroradiol* 2015;36:330–36 CrossRef Medline
- Touze R, Touitou V, Shotar E, et al. **Long-term visual outcome in patients treated by flow diversion for carotid-ophthalmic aneurysms.** *J Neurointerv Surg* 2018;10:1067–73 CrossRef Medline
- O’Kelly CJ, Krings T, Fiorella D, et al. **A novel grading scale for the angiographic assessment of intracranial aneurysms treated using flow diverting stents.** *Interv Neuroradiol* 2010;16:133–37 CrossRef Medline
- Kallmes DF, Ding YH, Dai D, et al. **A new endoluminal, flow-disrupting device for treatment of saccular aneurysms.** *Stroke* 2007;38:2346–52 CrossRef Medline
- Puffer RC, Kallmes DF, Cloft HJ, et al. **Patency of the ophthalmic artery after flow diversion treatment of paraclinoid aneurysms.** *J Neurosurg* 2012;116:892–96 CrossRef Medline
- Gascou G, Lobotesis K, Brunel H, et al. **Extra-aneurysmal flow modification following Pipeline embolization device implantation: focus on regional branches, perforators, and the parent vessel.** *AJNR Am J Neuroradiol* 2015;36:725–31 CrossRef Medline
- Cagnazzo F, Cappucci M, Dargazanli C, et al. **Flow-diversion effect of LEO stents: aneurysm occlusion and flow remodeling of covered side branches and perforators.** *AJNR Am J Neuroradiol* 2018;39:2057–63 CrossRef Medline
- Cagnazzo F, Lefevre PH, Mantilla D, et al. **Patency of the supraclinoid internal carotid artery branches after flow diversion treatment: a meta-analysis.** *J Neuroradiol* 2019;46:9–14 CrossRef Medline
- La Pira B, Brinjikji W, Burrows AM, et al. **Unruptured internal carotid artery bifurcation aneurysms: general features and overall results after modern treatment.** *Acta Neurochir (Wien)* 2016;158:2053–59 CrossRef Medline
- Grand W. **Microsurgical anatomy of the proximal middle cerebral artery and the internal carotid artery bifurcation.** *Neurosurgery* 1980;7:215–18 CrossRef Medline
- Ban SP, Hwang G, Kim CH, et al. **Risk factor analysis of recanalization and retreatment for patients with endovascular treatment of internal carotid artery bifurcation aneurysms.** *Neuroradiology* 2018;60:535–44 CrossRef Medline
- Cagnazzo F, Limbucci N, Nappini S, et al. **Y-stent-assisted coiling of wide-neck bifurcation intracranial aneurysms: a meta-analysis.** *AJNR Am J Neuroradiol* 2019;40:122–28 CrossRef Medline
- Pierot L, Moret J, Barreau X, et al. **Aneurysm treatment with Woven EndoBridge in the cumulative population of three prospective, multicenter series: 2-year follow-up.** *Neurosurgery* 2020;87:E78–79 CrossRef Medline
- Cagnazzo F, Ahmed R, Lefevre PH, et al. **Flow modification on the internal carotid artery bifurcation region and A1 segment after M1-internal carotid artery flow diverter deployment.** *J Neurointerv Surg* 2020;12:1226–30 CrossRef Medline

Propensity Score Analysis of Flow Diverters Placed in Scaffolding Stents

A. Pöker, O. Öcal, E. Öztürk, and A. Arat



ABSTRACT

BACKGROUND AND PURPOSE: Flow-diverter deployment within a stent remains controversial, but flow-diverter deployment within a scaffolding stent has been performed occasionally. To date, an analysis of this scaffolding technique has not been reported. We aimed to evaluate whether the scaffolding technique adversely affects the outcomes of flow diversion.

MATERIALS AND METHODS: Patients who had undergone intracranial aneurysm treatment using a Silk flow diverter with (scaffolding group) or without (bare flow-diverter group) a scaffolding stent were identified retrospectively and compared. Propensity score matching was used to match the aneurysms in both groups for variables with a significant difference between groups. Aneurysm occlusion rates and clinical outcomes were compared.

RESULTS: There were 84 patients (105 aneurysms) in the bare flow-diverter group and 21 patients (22 aneurysms) in the scaffolding group (using 20 LEO stents and 1 Enterprise stent). The aneurysms in the scaffolding group were larger (mean, 13.1 [SD, 10.7] versus 7 [SD, 4.5] mm, $P = .001$) and more likely to be fusiform (40.9% versus 5.7%, $P < .001$) than in the bare flow-diverter group. After 2:1 propensity score matching, 24 aneurysms in the bare flow-diverter group and 15 in the scaffolding group were matched. Aneurysm occlusion rates did not significantly differ between groups at 1–3 months (41.2 versus 33.3%, $P > .99$), 3–6 months (55.5 versus 75.0%, $P = .44$), 7–12 months (65.0 versus 90.0%, $P = .21$), or beyond 1 year (73.6 versus 91.6%, $P = .36$). There was no difference in complication rates between the groups ($P > .99$).

CONCLUSIONS: Placement of a scaffolding stent before flow diversion does not adversely affect aneurysm occlusion or complication rates.

ABBREVIATIONS: BG = bare flow-diverter group; FD = flow diverter; SG = scaffolding group

The Silk Plus stent (Balt Extrusion) has been used in the treatment of intracranial aneurysms with a favorable safety and efficacy profile.^{1–3} However, the deployment of flow diverters (FDs), including the Silk device, may be associated with technical difficulties. Placement of a flow diverter for the treatment of very large-neck or fusiform aneurysms can result in technical adverse events such as migration or prolapse of the device.⁴ Due to these difficulties, a “scaffolding technique,” in which a scaffold with a stent is created during the same procedure and just before the placement of a Silk device, has been

reported.^{1,3,5} However, as a rule of thumb, placement of a flow diverter within an indwelling stent has been contraindicated.⁶ Most interesting, this suggestion has neither been validated nor challenged to date because no study has compared the results of placement of bare (classic) flow diverters with those of scaffolded flow diverters. We conducted this study to compare the clinical and angiographic results of aneurysms treated by primary stent placement with the Silk device with those treated by Silk device placement in a freshly deployed scaffolding stent.

MATERIALS AND METHODS

Study Population

This retrospective study was approved by the Ethics Committee of our hospital. All intracranial aneurysms treated by a single operator using a Silk Plus flow diverter between April 2010 and March 2019 were identified. Patients were excluded if an appositing stent was deployed inside the Silk device and if a stent or flow diverter had been deployed in a previous session for the same

Received October 9, 2020; accepted after revision December 9.

From the Departments of Radiology (A.P., O.Ö., A.A.) and Biostatistics (E.Ö.), Faculty of Medicine, Hacettepe University, Sıhhiye 06100, Ankara, Turkey; and Department of Radiology (O.Ö.), University Hospital, Ludwig Maximilian University of Munich, Munich, Germany.

Please address correspondence to A. Arat, MD, Department of Radiology, School of Medicine, Hacettepe University, Ankara, Turkey; e-mail: anilarat@hotmail.com

Indicates article with online supplemental data.

<http://dx.doi.org/10.3174/ajnr.A7040>

aneurysm. Only those patients who were treated with the Silk device, directly or together with a scaffolding stent placed during the same procedure were included. Patients with concurrent endosaccular treatment were not excluded. In the case of tandem aneurysms treated with a single Silk device, both aneurysms were included in the analysis.

The age and sex of the patients and aneurysm location, maximum size, morphology, and history of rupture were recorded. Procedural details and clinically relevant adverse events, that is, any event resulting in a change in mRS, were recorded. Follow-up imaging results were evaluated on the basis of the Raymond-Roy scale. Aneurysms beyond the dural ring in the anterior circulation and above the superior cerebellar arteries in the posterior circulation were defined as distal circulation aneurysms, and the remaining aneurysms were denoted as proximal. The patients treated with a single flow diverter (bare FD group [BG]) and those treated with placement of a scaffolding stent and then a flow diverter in the same session (scaffolding group [SG]) were matched and compared.

General Description of the Interventional Procedure

The specifications, technical properties, and procedural details related to the Silk device have been described previously by different authors in the literature.^{2,6,7} Patients were administered 75 mg of clopidogrel and 300 mg of acetylsalicylic acid at least 5 days before the procedure and tested with a point-of-care test (VerifyNow P2Y12 assay; Accumetrics). We proceeded with treatment if the inhibition level, in percentages, was >40%. When it was available, patients were also tested simultaneously with the Multiplate test (Multiplate Analyzer; Roche; platelet inhibition calculated as 1-ADP/TRAP (thrombin receptor-activating peptide) ratio \times 100), and in these cases, concordance of the results was sought. If there was high on-treatment platelet reactivity in either test or both tests, these patients were switched from clopidogrel to 10 mg/day prasugrel. Patients treated in the acute-subacute period of subarachnoid hemorrhage were given a loading dose of 600 mg of clopidogrel.

All procedures were performed with the patient under general anesthesia via a transfemoral route in biplane angiography suites. After we catheterized the parent artery with a 6F guiding sheath and a distal-access catheter, the aneurysm was bypassed with a microcatheter (Vasco+21 or 25 [Balt] for the Silk Plus flow diverter and Excelsior SL 10 [Stryker] for the Silk Vista baby device) over a microguidewire, and the flow diverter was navigated through this catheter and deployed. The patients treated by this standard method were grouped as the BG.

If we encountered problems associated with device shortening, device prolapse into the aneurysm, excessive device expansion, or size discrepancy between the diameters of the distal-versus-proximal landing zones during the deployment of the Silk device, we navigated the deployment catheter over the partially deployed FD, resheathed the device, and proceeded with catheter navigation until the normal segment of the parent artery was reached distally. We then withdrew the device totally and deployed a stent through the indwelling microcatheter (mainly the LEO stent family [Balt] or an Enterprise self-expanding stent [Codman & Shurtleff]). The use of the Enterprise stent was preferred only when the parent artery was straight and the distal

parent artery was not tortuous. Its use was advantageous while deploying the FD because it did not impede the visualization of the FD. On the other hand, the use of this stent required an additional microcatheter exchange maneuver.

Less commonly, in the case of a fusiform aneurysm with a long segment of a diseased parent artery or in wide-neck aneurysms over arterial curves in which we anticipated a risk of device prolapse into the aneurysm, we directly proceeded with stent deployment without a preceding trial of flow-diverter deployment. The scaffolding stent was deployed across the aneurysm neck with at least a 5-mm landing zone on both ends. When this stent was used, the flow diverter was undersized so that the fully expanded diameter matched the maximum diameter of the deployed stent in situ. We undersized the flow diverter so that at its unconstrained, maximum expansion (beyond the nominal diameter), it would match the nominal size of the stent. In general, the nominal diameter of the flow diverter would be 0.5 mm lower than that of the stent. When possible, we preferred to deploy the flow diverter so that it would cover the whole length of the scaffolding stent. This deployment was frequently not possible due to the foreshortening of the Silk device. In these cases, we preferred to cover as much of the stent as possible proximally. The group treated with these procedures was noted as the SG.

After the procedure, the patients were imaged at 1–3 months by CT or MR angiography, at 3–6 months by DSA, and then at 9–12 months by noninvasive angiography. Further follow-up was scheduled on a patient-by-patient basis by noninvasive imaging. Patients were kept on dual-antiplatelet therapy for 6 months, and clopidogrel (or prasugrel) was discontinued after the 6-month DSA.

Statistical Analysis

Continuous variables are reported as mean [SD]. Categorical variables were compared using the χ^2 test or Fisher exact test, as appropriate. The Student *t* test and the Mann-Whitney *U* test were used for comparisons of continuous variables as appropriate. Significance was set as $P < .05$. Propensity score matching was performed to compare the bare group and the scaffolding group. SPSS Statistics, Version 22.0 (IBM) was used for calculations. Matching was performed using the MatchIt package in R statistical and computing software, Version 3.5.0 (<http://www.r-project.org/>). Variables with significant difference between groups were used as matching covariates. Groups were matched in a 1:2 ratio, with the nearest calculated propensity logit, with a caliper width of ≤ 0.20 of the SD of the propensity score logit. Subsequently, aneurysm occlusion rates were compared using the χ^2 test or Fisher exact test as appropriate.

RESULTS

A total of 105 patients with 127 aneurysms treated using the Silk device were included. Thirty-four patients were male, and 71 were female; the mean age of the cohort was 51.2 [SD, 11.2] years (range, 14–78 years). Eighty-four patients with 105 aneurysms were treated with a Silk device only (BG group), and 21 patients with 22 aneurysms were in the SG. The mean age was similar between BG (50.8 [SD, 10.9] years) and SG (54.5 [SD, 12.4] years) ($P = .8$). There was also no difference between the 2 groups with

Table 1: Characteristics of the patients and aneurysms before and after propensity score matching

	Before Propensity Score Matching			After Propensity Score Matching		
	Bare FD Group (n = 105)	Scaffolding Group (n = 22)	P Value	Bare FD Group (n = 24)	Scaffolding Group (n = 15)	P Value
Sex ^a (female)	77 (73.3)	12 (54.5)	.08	18 (75.0)	7 (46.6)	.072
Age (yr) ^b	51 (14–78)	54.5 (31–74)	.54	50 (32–76)	53 (35.0–74.0)	.777
Location ^a (anterior)	96 (91.4)	20 (90.9)	>.99	19 (79.1)	13 (86.6)	.685
Location ^a (proximal)	16 (15.2)	6 (27.3)	.21	6 (25)	4 (26.7)	>.99
Morphology ^a (saccular)	99 (94.3)	13 (59.1)	<.001 ^c	20 (83.3)	11 (73.3)	.685
Size ^b	7 (4.5)	13.1 (10.7)	<.001 ^c	9.8 (5.9)	9.9 (5.1)	.939
Recurrence ^a (yes)	9 (8.4)	3 (13.6)	.43	1 (4.1)	2 (13.3)	.547

Note:—Values are mean (range) for quantitative variables or numbers and percentages for qualitative variables.

^a Count (percentage).

^b Mean (SD).

^c Statistically significance.

Table 2: Follow-up imaging results before and after propensity score matching^a

	All Cohorts			After PSM		
	Silk Alone (n = 105)	SG (n = 22)	P Value	Silk Alone (n = 24)	SG (n = 15)	P Value
0- to 3-month follow-up						
Occlusion ^b	36 (60.0)	5 (33.3)	.063	7 (41.2)	3 (33.3)	>.99
Residual filling ^b	24 (40.0)	10 (66.6)		10 (58.8)	6 (66.6)	
3- to 6-month follow-up						
Occlusion ^b	50 (67.5)	13 (72.2)	.703	10 (55.5)	9 (75.0)	.440
Residual filling ^b	24 (32.4)	5 (27.7)		8 (44.5)	3 (25.0)	
7- to 12-month follow-up						
Occlusion ^b	61 (75.3)	14 (93.3)	.178	13 (65.0)	9 (90.0)	.210
Residual filling ^b	20 (24.6)	1 (6.6)		7 (35.0)	1 (10.0)	
>12-month follow-up						
Occlusion ^b	75 (88.2)	15 (93.7)	>.99	14 (73.6)	11 (91.6)	.363
Residual filling ^b	10 (11.7)	1 (6.2)		5 (26.4)	1 (8.4)	

Note:—PSM indicates propensity score matching.

^a Data are presented as numbers and percentages.

^b Count (percentage).

respect to the proportion of female patients ($P = .95$), aneurysm location (anterior-versus-posterior circulation, $P > .99$, or proximal versus distal to the circle of Willis, $P = .21$), and the proportion of treatments performed for recurrent aneurysms ($P = .43$). However, the aneurysms in the scaffolding group were significantly larger than those in the bare FD group (13.1 [SD, 10.7] mm versus 7 [SD, 4.5] mm, $P < .001$), and the proportion of fusiform/dissecting aneurysms was higher in the scaffolding group (40.9% versus 5.7%, $P < .001$). The level of platelet inhibition as per the VerifyNow test was similar between groups (mean, 83.0% [SD, 16.8%] in the BG versus 86.1% [SD, 17.3%] in the SG, $P = .66$). Eleven aneurysms in the bare FD group and 2 aneurysms in the scaffolding group had intrasaccular embolization in addition to flow diversion, and both groups were similar with regard to the rate of adjunctive coiling ($P = .84$).

Baseline characteristics of the patients are summarized in Table 1. In the scaffolding group, a LEO stent and a Silk device were combined in 19 patients; in 1 patient with a straight parent artery, an Enterprise stent and a Silk device were used; and in 1 patient, a LEO baby stent and a Silk Vista baby device were used. There was no significant difference in aneurysm occlusion rates at any follow-up period between treatment arms (Table 2). No imaging follow-up was available for 12 (9.4%) aneurysms. Considering patients with at least 1 follow-up, 99 (86.0%) aneurysms were occluded at

last available imaging (80 of 94 [85.1%] in the BG and 19 of 21 [90.4%] in the SG, $P = .732$).

Due to differences in aneurysm characteristics between the 2 groups, we performed propensity score matching to eliminate an inherent selection bias. After performing a 2:1 match based on aneurysm size, and morphology, 24 and 15 patients remained in the bare FD and scaffolding groups, respectively (Table 1). As expected, there was no difference between groups with respect to age; proportion of female patients; or aneurysm size, location, morphology, or history of recurrence (Table 1). Also, there were no significant differences between groups in terms of platelet inhibition levels (77.6% [SD, 19.6%] in the BG versus 86.4% [SD, 18.5%] in the SG, $P = .207$). There was no significant difference in the aneurysm occlusion rates between the groups in any of the 4 follow-up periods. More specifically, aneurysm occlusion rates were 41.2% versus 33.3% ($P > .99$) at 1–3 months, 55.5% versus 75.0% ($P = .44$) at 3–6 months, 65.0% versus 90.0% ($P = .210$) at 7–12 months, and 73.6% versus 91.6% ($P = .363$) beyond 1 year for the bare FD and scaffolding groups, respectively (Table 2).

There was no difference in the rate of adverse events between groups (2/24 [8.3%] versus 1/15 [6.6%], $P > .99$). There were no technical events that resulted in an alteration of the treatment plan in any of the matched patients. In the bare FD group, 1 patient had a delayed stent occlusion leading to a major stroke; on follow-up, the patient had died due to the consequences of the

stroke. Another patient was noted to have asymptomatic stent occlusion on the 6-month angiogram. In 1 patient in the scaffolding group, a small intraparenchymal hematoma was observed during the follow-up period, and the patient recovered without any permanent sequelae. No adverse events with neurologic implications developed in the remaining patients. Examples of aneurysms in both the bare FD and scaffolding groups are provided as Online Supplemental Data.

In the subgroup of patients with scaffolding stents who were not matched with propensity score matching, there were 7 patients. The average size of the aneurysms in this group was 20 mm, and 2 were saccular. They were located at the supraclinoid internal carotid artery (2 patients), cavernous internal carotid artery (2 patients), middle cerebral artery (2 patients), and anterior communicating artery (1 patient). All were treated by a combination of LEO stents and Silk Plus flow diverters. There was no perioperative permanent morbidity or mortality in this group. One patient in this group died secondary to a contralateral cerebral parenchymal hematoma. The total occlusion rate was 33.3% at 1–3 months. This had increased to 60% as of 6 months. At 12 months and beyond, it was 100%.

DISCUSSION

Flow diversion has become a standard endovascular treatment method, especially for large or wide-neck aneurysms, which are difficult to treat with conventional treatment methods. Among the numerous flow-diverting devices, the Silk Plus flow diverter stands out with its navigability and smaller delivery catheter size. It has been used in the treatment of intracranial aneurysms with a high technical success rate,^{2,3,5} that is, complete aneurysm occlusion rates of approximately 70%–87% at 6 months to 1 year.^{2,5,7} However, the Silk Plus flow diverter is also associated with some technical difficulties regarding the treatment of complex aneurysms.⁸ To overcome these issues, the LEO stent has been used as a scaffolding device, compensating for the low radial force of the Silk Plus flow diverter,³ to prevent the prolapse of the device into the aneurysm⁸ or to prevent delayed-configurational device changes due to device oversizing.⁹ However, to date, a comparison of the safety and efficacy of this scaffolding technique over bare flow diversion has not been performed. In fact, placement of a flow diverter within a stent has been regarded as controversial or even contraindicated by many authors.^{6,10}

On the other hand, our results indicate that scaffolding is not necessarily associated with a higher procedural risk nor is it related to a worse clinical or angiographic result during follow-up. We did not use the technique routinely, only when actual or possible problems related to device deployment or sizing existed. Consequently, it was used to treat large/giant aneurysms more often. However, once we performed propensity matching to eliminate confounding variables including aneurysm size, we observed again that neither the angiographic nor the clinical results were adversely affected by scaffolding. Because this technique was used as a bailout for bare FD placement, we can conclude that scaffolding increases technical success without significantly altering clinical or angiographic results. An analogy of our approach can be made with bailout stent placement used for balloon-assisted coiling in this regard.

Some possible explanations can account for the safety and efficacy of scaffolding stents in cases in which this technique needs to be used. They prevent foreshortening and prolapse of the flow-diverter stent into the aneurysm, which can be seen in up to 9.3% of large and giant aneurysms.¹¹ In addition to the procedural hassles these 2 phenomena may create, they may also lead to fish mouting or delayed endothelialization in the longer term.^{9,12,13} Deployment of a device with a length of at least 3 times the length of the aneurysm neck is advised to reduce prolapse risk,⁷ which may be practically impossible in cases of long-segment fusiform aneurysms or may be associated with a higher rate of parent artery occlusion after flow diversion with the Silk device.¹⁴ In our cohort, we did not observe any of these adverse events.

Another advantage brought about by scaffolding is to avoid telescoping flow-diverter placement. In large/giant aneurysms, placement of up to 19 devices in a single aneurysm in up to 5 treatment sessions has been described.¹⁵ Scaffolding obviates the need for telescoping FDs and hence lowers the risk of perforator compromise associated with telescoping flow diverters.¹⁶ It also decreases the cost compared with telescoping FDs.

There is a strong preconception in the literature about pre-existing stents being associated with failure of the flow diversion. This blanket statement was initially suggested by Nelson et al¹⁷ in the Pipeline Embolization Device for Uncoilable or Failed Aneurysms (PUFS) trial¹² but has not been proved. It was cited and suggested by other authors as well.^{10,18–20} One critical point about this concept is that it relates exclusively to FDs deployed inside laser-cut stents.^{17–20} Incomplete opening or ovalization with laser-cut stents is well-known.⁸ Placement of a flow diverter inside a stent with pre-existing malapposition may be the reason for an endoleak at the landing zone and subsequent flow-diverter failure.¹⁰ Scaffolding performed by a properly deployed braided stent is unlikely to have malapposition. Indeed, the Flow-Redirection Endoluminal Device (FRED flow diverter; MicroVention) is a type of scaffolding stent/flow-diverter combination. With the exception of a single Enterprise stent deployed in a straight arterial segment, all of the stents in our scaffolding group were LEO stents, which have been shown, *in vitro*, to have good conformability to the vessel wall due to a reduced tendency to buckle or kink as opposed to laser-cut stents.²¹ We suggest that stents that are well-apposed to the arterial wall do not inevitably lead to failure of further endovascular treatment with FDs. Braided stents may be better suited for this application.

There are alternatives to the scaffolding method as well. Some authors advocate partial coiling of an aneurysm in cases prone to intra-aneurysmal device prolapse to “hold” the flow diverter in the parent artery,²² but this bailout technique may also be associated with complications.²³ Dense coiling may lead to occlusion of the flow diverter due to increased thrombogenicity.²⁴ In addition, the presence of coils within the sac makes noninvasive follow-up with CTA (and to some extent, with MRA) less reliable.

We chose the Silk device for the comparative analysis of scaffolding. This device is a nitinol-based device that, as its name implies, is very soft, navigable, and pliable. However, these benefits come at the expense of a propensity to foreshorten and, at times, a delay in configurational change.^{9,12} Hence, scaffolding stent placement has been used in a certain proportion of

patients treated by authors who prefer to use this device.^{1,3,5,25} The availability of matching sizes of the braided LEO stents for each Silk device size that can be deployed through the same delivery microcatheter also renders this technique attractive and relatively easy to perform. In our practice, most scaffolding stent placements accompanied the placement of the Silk device for these reasons. To eliminate the flow-diverter architecture and mechanics as confounding variables, we included in our study only aneurysms treated with the Silk device.

When placement of a scaffolding stent was planned, we followed several technical principles. To achieve a good wall apposition of the stent, we used only braided stents at the carotid siphon because closed-cell stents do not appose well in the siphon. We made sure that the stent was long enough to cover about 10 mm of the parent artery on both sides of the aneurysm to minimize the risk of stent migration into the aneurysm as we navigated the microcatheter through the deployed stent. We kept the tip of the delivery wire distal to the aneurysm to avoid re-crossing of a freshly deployed stent with a guidewire, which may result in an inadvertent exit of the guidewire/delivery catheter from the stent lumen through the stent struts and then re-entry into the stent lumen at a distal point. Then, flow-diverter expansion will not be possible at the re-entry point, and if the scaffolding stent is an open-cell stent, the partially opened flow diverter may get entangled with it. Thus, we avoided open-cell stents and also stents without a distal delivery wire.

For stent delivery, we preferred microcatheters with angled tips (such as a multipurpose curve or 90° angle) because the tip of the delivery microcatheter frequently got caught by a stent strut during the crossing of the deployed stent. If this situation occurred, we refrained from pushing the microcatheter further but, instead, pulled the microcatheter back slightly, torqued it gently, pulled or pushed the wire slightly, and then advanced the microcatheter, trying to avoid hitting the spot on the stent at which the microcatheter got caught. Finally, as long as optimal expansion and wall apposition of the scaffolding stent was clearly documented and the flow diverter was deployed only at the aneurysmal segment, we did not intentionally try to cover the entire length of the stent by the flow diverter.

The main limitations of this study include its retrospective nature and the relatively small sample size that remained after matching of the heterogeneous groups by propensity score analysis. Due to the retrospective nature, the imaging follow-up at 1–3 months, 3–6 months, 7–12 months, and beyond 1 year was not consistent for every case. In addition, success rates may be lower with other stent types because matching stent/flow-diverter pairs that are deliverable through the same microcatheter are not available for all devices on the market. This issue may mandate the use of an exchange maneuver once the stent is deployed,²⁶ increasing the risk and complexity of flow diversion with some devices. However, as the first study on the comparative efficacy and safety of scaffolding stents, our study highlights the critical points in scaffolding stent placement. It also justifies the need for larger-scale prospective studies or verification of these results in larger cohorts.

CONCLUSIONS

Scaffolding stent placement to help flow diversion of intracranial aneurysms has been criticised by many authors. This may be the result of earlier publications that disparaged previously placed stents as a cause of flow-diversion failure. We propose that when flow diversion with a single FD is risky or impossible, scaffolding can be used with a good rate of success and without a significant increase in complications.

REFERENCES

1. Briganti F, Napoli M, Leone G, et al. **Treatment of intracranial aneurysms by flow diverter devices: long-term results from a single center.** *Eur J Radiol* 2014;83:1683–90 CrossRef Medline
2. Pumar JM, Banguero A, Cuellar H, et al. **Treatment of intracranial aneurysms with the Silk embolization device in a multicenter study: a retrospective data analysis.** *Neurosurgery* 2017;81:595–601 CrossRef Medline
3. Strauss I, Maimon S. **Silk flow diverter in the treatment of complex intracranial aneurysms: a single-center experience with 60 patients.** *Acta Neurochir (Wien)* 2016;158:247–54 CrossRef Medline
4. Lubicz B, Collignon L, Raphaëli G, et al. **Flow-diverter stent for the endovascular treatment of intracranial aneurysms: a prospective study in 29 patients with 34 aneurysms.** *Stroke* 2010;41:2247–53 CrossRef Medline
5. Piano M, Valvassori L, Quilici L, et al. **Midterm and long-term follow-up of cerebral aneurysms treated with flow diverter devices: a single-center experience.** *J Neurosurg* 2013;118:408–16 CrossRef Medline
6. Park MS, Taussky P, Albuquerque FC, et al. Off-label use. In: Rivet DJ II, Reavey-Cantwell J, Moran CJ, eds. *Flow Diversion of Cerebral Aneurysms*. Thieme 2017; 40–63
7. Maimon S, Gonen L, Nossek E, et al. **Treatment of intra-cranial aneurysms with the Silk flow diverter: 2 years' experience with 28 patients at a single center.** *Acta Neurochir (Wien)* 2012;154:979–87 CrossRef Medline
8. Gurkas E, Kaya T, Daglioglu E, et al. **Silk device for the treatment of intracranial aneurysms, Part 1: peri-procedural results, technical aspects and learning curve.** *Turk Neurosurg* 2016;26:525–32 CrossRef Medline
9. Peker A, Akgul E, Daglioglu E, et al. **Tapered flow diverters in the treatment of intracranial aneurysms.** *Turk Neurosurg* 2017;27:863–66 CrossRef Medline
10. Shapiro M, Becske T, Nelson PK. **Learning from failure: persistence of aneurysms following Pipeline embolization.** *J Neurosurg* 2017;126:578–85 CrossRef Medline
11. Srinivasan VM, Carlson AP, Mokin M, et al. **Prolapse of the Pipeline Embolization Device in aneurysms: incidence, management, and outcomes.** *Neurosurg Focus* 2017;42:E16 CrossRef Medline
12. Cohen JE, Gomori JM, Moscovici S, et al. **Delayed complications after flow-diverter stenting: reactive in-stent stenosis and creeping stents.** *J Clin Neurosci* 2014;21:1116–22 CrossRef Medline
13. Shapiro M, Raz E, Becske T, et al. **Variable porosity of the Pipeline embolization device in straight and curved vessels: a guide for optimal deployment strategy.** *AJNR Am J Neuroradiol* 2014;35:727–33 CrossRef Medline
14. Macdonald IR, Shankar JJS. **Delayed parent artery occlusions following use of Silk flow diverters for treatment of intracranial aneurysms.** *J Neurointerv Surg* 2019;11:690–93 CrossRef Medline
15. Bhogal P, Pérez MA, Ganslandt O, et al. **Treatment of posterior circulation non-saccular aneurysms with flow diverters: a single-center experience and review of 56 patients.** *J Neurointerv Surg* 2017;9:471–81 CrossRef Medline
16. Chalouhi N, Tjoumakaris S, Phillips JL, et al. **A single Pipeline Embolization Device is sufficient for treatment of intracranial aneurysms.** *AJNR Am J Neuroradiol* 2014;35:1562–66 CrossRef Medline

17. Nelson PK, Lylyk P, Szikora I, et al. **The Pipeline Embolization Device for the Intracranial Treatment of Aneurysms Trial.** *AJNR Am J Neuroradiol* 2011;32:34–40 CrossRef Medline
18. Daou B, Starke RM, Chalouhi N, et al. **Pipeline Embolization Device in the treatment of recurrent previously stented cerebral aneurysms.** *AJNR Am J Neuroradiol* 2016;37:849–55 CrossRef Medline
19. Heiferman DM, Billingsley JT, Kasliwal MK, et al. **Use of flow-diverting stents as salvage treatment following failed stent-assisted embolization of intracranial aneurysms.** *J Neurointerv Surg* 2016;8:692–95 CrossRef Medline
20. Bender MT, Vo CD, Jiang B, et al. **Pipeline embolization for salvage treatment of previously stented residual and recurrent cerebral aneurysms.** *Interv Neurol* 2018;7:359–69 CrossRef Medline
21. Ebrahimi N, Claus B, Lee CY, et al. **Stent conformity in curved vascular models with simulated aneurysm necks using flat-panel CT: an in vitro study.** *AJNR Am J Neuroradiol* 2007;28:823–29 Medline
22. Ferrigno AS, Caro-Osorio E, Martinez HR, et al. **Coiling as a rescue strategy for flow diverter prolapse into a giant intracranial aneurysm.** *World Neurosurg* 2020;133:392–97 CrossRef Medline
23. Trivelato FP, Wajnberg E, Rezende MT, et al. **Safety and effectiveness of the Pipeline Flex embolization device with shield technology for the treatment of intracranial aneurysms: midterm results from a multicenter study.** *Neurosurgery* 2020;87:104–11 CrossRef Medline
24. Siddiqui AH, Kan P, Abila AA, et al. **Complications after treatment with Pipeline embolization for giant distal intracranial aneurysms with or without coil embolization.** *Neurosurgery* 2012;71:E509–13; discussion 13 CrossRef Medline
25. de Andrade GC, Alves HP, Clímaco V, et al. **Two-stage reconstructive overlapping stent LEO+ and Silk for treatment of intracranial circumferential fusiform aneurysms in the posterior circulation.** *Interv Neuroradiol* 2016;22:516–23 CrossRef Medline
26. Ocal O, Arat A. **The exchange-free technique: a novel technique for enhancing Surpass flow diverter placement.** *Asian J Neurosurg* 2020;15:620–26 CrossRef Medline

Predictors of the Effects of Flow Diversion in Very Large and Giant Aneurysms

H.J. Bae, Y.K. Park, D.Y. Cho, J.H. Choi, B.S. Kim, and Y.S. Shin



ABSTRACT

BACKGROUND AND PURPOSE: The treatment paradigm for very large and giant aneurysms has recently changed to flow diversion, in light of the results of the Pipeline for Uncoilable or Failed Aneurysms trial. However, the effects of flow diversion were definitely unknown. We explored this topic and identified the predictors of such effects.

MATERIALS AND METHODS: We retrospectively reviewed 51 patients with unruptured aneurysms admitted to our institution for flow diversion between February 2014 and August 2019. Patients were categorized into an effect group (no filling or remnant entry) and a no-effect group (subtotal or total filling). We evaluated the aneurysm size and shape, incorporation vessel, parent artery stenosis and curvature, stagnation of contrast medium within the aneurysm, use of balloon angioplasty, and intra-aneurysm thrombus as potential predictors of the effects of flow diversion.

RESULTS: The effect group comprised 34 patients (66.7%, 34/51; no filling, 35.3%, 18/51; and remnant entry, 31.4%, 16/51). The no-effect group comprised 17 patients (33.3%, 17/51; subtotal filling, 29.4%, 15/51; and total filling, 3.9%, 2/51). An incorporation vessel and balloon angioplasty were independent risk factors for the no-effect group in multivariate logistic regression analyses (OR = 0.13 and 0.05; 95% confidence intervals, 0.02–0.62 and 0.00–0.32; *P* values, .021 and .004, respectively).

CONCLUSIONS: Flow diversion is effective for very large and giant aneurysms, but the outcomes require further improvement. The results of this study show that an incorporated vessel and excessive balloon angioplasty might compromise flow diversion. This finding can help improve the outcomes of flow diversion.

ABBREVIATIONS: FD = flow diversion; FDs = flow-diverter stent

Very large (15–25 mm) and giant (>25 mm) cerebral aneurysms are at high risk for fatal rupture.^{1,2} Conventional surgical treatment is associated with a low rate of complete ligation and a high incidence of surgical complications.^{3,4} Given the development of new endovascular techniques and devices and the results of the International Subarachnoid Aneurysm Trial (ISAT),⁵ coil embolization is now the preferred treatment for many kinds of cerebral aneurysms. However, many studies reported that coil

embolization for very large and giant aneurysms has a high recurrence rate.^{6–8} Thus, considering the results of the Pipeline for Uncoilable or Failed Aneurysms (PUFS) trial,⁹ the preferred treatment has recently been changed to flow diversion (FD). However, the effects of FD remain definitely unknown. We explored this topic and identified the predictors of the effects of FD.

MATERIALS AND METHODS

Patient Selection

We retrospectively reviewed the records of patients with unruptured aneurysms consecutively admitted to our institution for FD by a single surgeon (Y.S. Shin) from February 2014 to August 2019. According to the approval criteria of the Korean government (Health Insurance Review and Assessment Service) for flow-diverter stents, these were placed in patients with unruptured intracranial aneurysms of ≥ 15 mm in maximum diameter without coil embolization. A total of 64 patients underwent FD; catheter-based angiographic follow-up data were available for 51 patients. We retrospectively analyzed their outcomes and sought their predictors.

Received August 18, 2020; accepted after revision December 24.

From the Department of Neurosurgery (H.J.B.), Yeouido St. Mary's Hospital, The Catholic University of Korea College of Medicine, Seoul, Korea; Department of Neurosurgery (Y.K.P.), Inje University Ilsan Paik Hospital, Goyang, Korea; Department of Neurosurgery (D.Y.C.), Ewha Womans University, Seoul, Korea; Departments of Neurosurgery (J.H.C., Y.S.S.) and Radiology (B.S.K.), Seoul St. Mary's Hospital, The Catholic University of Korea College of Medicine, Seoul, Korea.

Please address correspondence to Yong Sam Shin, MD, PhD, Department of Neurosurgery, Seoul St. Mary's Hospital, The Catholic University of Korea College of Medicine, Banpo-daero 222, Seocho-gu, Seoul 137-701, Korea; e-mail: nsshin@catholic.ac.kr

Indicates article with online supplemental data.

<http://dx.doi.org/10.3174/ajnr.A7085>

The study was approved by the institutional review board of Seoul St. Mary's Hospital.

Baseline and Follow-up Assessments

The records included patient sex and age; the presence of diabetes mellitus, hypertension, and hyperlipidemia; current smoking status; aneurysm size, location, neck diameter, and shape (saccular or fusiform); intra-aneurysm thrombus and incorporated vessel status; stenosis status and curvature of the parent artery in the aneurysm neck region; contrast medium stagnation during angiography; balloon angioplasty in the procedure; and angiographic and clinical outcomes. All angiographic outcomes were blindly evaluated by 1 neurointerventionalist and 1 neuroradiologist using the O'Kelly-Marotta scale based on the degree of filling in catheter-based angiographic follow-up (no filling, remnant entry, subtotal filling, and total filling).¹⁰ MR angiography and catheter-based angiography were performed 6 months after treatment. If incomplete occlusion was evident in the first catheter-based angiography, follow-up was performed at 12 and 24 months. Patients were categorized into an effect group (no filling or remnant entry) and a no-effect group (subtotal or total filling) based on the catheter-based angiographic data. The 5-year results of the PUPS trial¹¹ indicated that aneurysms evidencing remnant entry were likely to completely occlude across time without further treatment.

Predictors of the Effects of FD

The parameters evaluated were aneurysm shape (saccular or fusiform), size, and neck diameter; intra-aneurysmal thrombus and incorporated vessel status; stenosis and curvature of the parent artery in the region of the aneurysm neck; balloon angioplasty status; and contrast medium stagnation during angiography as potential predictors of the effects of FD.^{9,12} The curvature of the parent artery involving the aneurysm neck region was classified as outer or non-outer, depending on the location of the aneurysm neck (Fig 1). Because the pore density of flow-diverter stents is greatly affected by curvature, metal coverage is relatively higher over the inner curve than over the outer curve.¹³ If the aneurysm neck lies on the outer curve, any effects of flow-diverter stents are likely to be reduced. The stagnation grade of contrast medium was categorized as arterial, capillary, or venous on pre- and post-FD cerebral angiography. Immediately after

flow-diverter stent (FDs) deployment, it was determined whether the stagnation grade increased. In addition, prolonged stagnation (for >1 minute) was recorded after FDs deployment. We assume that balloon angioplasty changes the stent pore density because the flow-diverter stents are braided and the aneurysm neck lies in the unconstrained zone.

Procedure

All procedures were performed with the patient under general anesthesia following systemic intravenous heparinization and premedication with antiplatelet drugs (aspirin, 100 mg, and clopidogrel, 75 mg, daily for at least 7 days). After the dual-antiplatelet therapy for 6 months, only aspirin, 100 mg, was maintained continuously. The platelet function test was routinely performed on the day of the procedure. The antiplatelet medication was not modified in patients with resistance because our other study showed that antiplatelet drug resistance did not increase the thromboembolic events after stent-assisted coiling.¹⁴ Because we encountered delayed rupture of aneurysms treated via FD, dexamethasone was prescribed for 3 weeks after FDs deployment as prophylaxis for intradural aneurysms. The Pipeline Embolization Device (PED; Medtronic) and the Flow-Redirection Endoluminal Device (FRED; MicroVention) were used for flow-diverter stents. When parent artery stenosis or poor stent apposition to the vessel wall was evident in conebeam CT performed immediately after FDs deployment, balloon angioplasty was performed using the Scepter device (MicroVention) along with the FDs.

Statistical Analyses

Categorical and continuous variables are reported as means (SD) and ranges and as frequencies with percentages, respectively. Demographic, clinical, and radiologic variables were compared between the 2 groups using the Student *t* test, the Mann-Whitney *U* test, the Fisher exact test, or the χ^2 test, as appropriate. Predictors with $P < .20$ in univariate analyses were included in the multivariate logistic regression model in a backward stepwise method to identify the effects of FD.¹² All data were analyzed using R statistical and computing software, Version 3.3.2 (<https://www.r-project.org/>).



FIG 1. This image shows the curvature type of the parent artery involving the neck region of the aneurysm. A, Non-outer type. B, Outer type.

RESULTS

The clinical characteristics of the 51 patients who underwent follow-up angiography after FD are summarized in the Online Supplemental Data. There were 34 patients in the effect group (66.7%, 34/51; no filling, 35.3%, 18/51; remnant entry, 31.4%, 16/5). The no-effect group comprised 17 patients (33.3%, 17/51; subtotal filling, 29.4%, 15/51; total filling, 3.9% 2/51). The mean age of the effect group was lower than that of the no-effect group (51.2 [SD, 14.9] years versus 57.8 [SD, 12.8] years; $P = .126$). The mean aneurysm size and neck diameter were 21.9 (SD,

Table 1: Results of univariate analysis for predictors of effect group

Variables	OR (95% CI)	P Value
Aneurysm shape (saccular)	2.23 (0.5–11.14)	.27
Intra-aneurysmal thrombus	1.44 (0.35–7.35)	.63
Vessel incorporation	0.38 (0.11–1.24)	.11
Aneurysm size (mm)	0.93 (0.82–1.01)	.19
Aneurysm neck diameter (mm)	0.96 (0.87–1.03)	.30
Stenosis of parent artery	0.51 (0.13–2.09)	.34
Outer curve type	2.62 (0.80–9.22)	.12
Balloon angioplasty	0.18 (0.03–0.79)	.029
Stagnation before FD	0.86 (0.39–1.85)	.70
Stagnation after FD	0.26 (0.01–1.38)	.20
Increased stagnation after FD	0.82 (0.26–2.47)	.71
Prolonged stagnation (>1 min)	0.39 (0.08–1.51)	.20

Table 2: Results of multivariate logistic regression analysis for predictors of effect group

Variables	OR (95% CI)	P Value
Vessel incorporation	0.13 (0.02–0.62)	.0205
Aneurysm size (mm)	0.90 (0.75–1.01)	.1874
Balloon angioplasty	0.05 (0.00–0.32)	.0040

4.3) mm and 10.1 (SD, 4.8) mm, respectively (effect group: 21.4 [SD, 4.1] mm, 9.8 [SD, 4.4] mm; no-effect group: 25.4 [SD, 12.7] mm, 13.2 [SD, 15.4] mm; $P = .231$, $P = .385$, respectively). The mean aneurysm size and neck diameters were larger in the no-effect group, but these differences did not reach statistical significance. The effect group was observed in 11/19 (57.8%) aneurysms involving the infraclinoid internal carotid artery, 14/20 (70.0%) aneurysms involving the supraclinoid internal carotid artery, 3/4 (75.0%) aneurysms involving the anterior and middle cerebral arteries, and 6/8 (75.0%) aneurysms involving the vertebrobasilar artery. The factors such as aneurysm size, vessel incorporation into the aneurysm, aneurysm neck located on an outer curve of the parent artery, and intraprocedural balloon angioplasty yielded P values $< .200$ in univariate analyses; thus, these were included as predictors of the effect in multivariate analyses (Table 1). Vessel incorporation into the aneurysm and intraprocedural balloon angioplasty (OR = 0.13 and 0.05; 95% CI, 0.02–0.62 and 0.00–0.32; P value, .021 and .004, respectively) were significant risk factors for the no-effect group in multivariate logistic regression analyses (Table 2). Among all 51 patients, complications occurred in 7, including 4 deaths (3 delayed ruptures and 1 thromboembolic event) and 3 major complications (1 each of rupture, thromboembolic event, and aneurysm mass effect). The overall morbidity and mortality rates were 3.9% (2/51) and 7.8% (4/51), respectively.

DISCUSSION

Despite recent improvement in endovascular devices, the treatment outcomes of very large and giant aneurysms remain unsatisfactory.^{6,7,15,16} Sluzewski et al¹⁶ reported a 41% (12/29) incomplete occlusion rate after initial and repeat coiling for very large and giant aneurysms. In addition, recurrence after coil embolization for very large and giant aneurysms was more common than after coil embolization for simple aneurysms. Chalouhi et al¹⁵ reported recurrence and retreatment rates of 46.8% (29/62) and 37.1% (23/62) for very large aneurysms and 52% (11/21) and

47.6% (10/21) for giant aneurysms, respectively, after coil embolization. After the PUFs trial, the introduction of FD induced a paradigm shift in endovascular treatment of such aneurysms.^{11,17–19} For large and giant aneurysms after FD, Peschillo et al¹⁷ and Oishi et al¹⁹ reported 61.5% (16/26) and 63% (63/100) no-filling rates, respectively. In our study, the no-filling and remnant entry rates were 35.3% (18/51) and 31.4% (16/51), respectively. When we considered remnant entry to be equivalent to no filling, our occlusion rate was similar to those reported in other studies.^{17,19}

However, the actual no-filling rate in this study was lower than those reported in other studies^{9,12} for several reasons: First, the size of the aneurysms in our study was at least 15 mm, and the mean aneurysm size was 21.9 (SD, 4.3) mm, which is larger than the 18.2 mm reported in the PUFs trial. To the best of our knowledge, this is the largest average aneurysm size reported in any study to date. The aneurysm size is known to affect FD.^{12,18,20–22} Second, only a single FDs was placed in all but 5 patients (in whom a single FDs could not cover the aneurysm neck or it was foreshortened) because the Korean National Insurance scheme does not usually permit using multiple flow-diverter stents or combined with coil embolization.²³ Other studies that used multiple flow-diverter stents or coiling combined with FD have reported that these approaches are better than the placement of a single FDs.^{17,24–26} In addition, other studies with the same treatment inclusion criteria as ours showed similar results. The authors reported an approximately 77% complete or near-complete occlusion rate in a multicenter study.²⁷ Third, the patient inclusion criteria in the PUFs trial were aneurysms involving the internal carotid artery from the petrous segment to the supraclinoid segment. In our study, there were 14/51 (27.4%) aneurysm cases (posterior circulation, 8 cases; internal carotid artery bifurcation, 2; middle cerebral artery, 3; anterior communicating artery, 1) that did not correspond to the PUFs trial. These 14 cases may have more incorporated vessels that were or were not angiographically visible. However, there is a lack of studies analyzing FD outcomes based on the location of aneurysm. Fourth, our study reported short-term results (follow-up duration, 83.0 [SD, 60.5] weeks). The results of the 5-year PUFs trial suggest that the aneurysm healing process following FD occurs progressively. The trial reported that 7 of the 9 remnants identified were occluded on subsequent angiographic studies without retreatment.¹¹ Therefore, we considered remnant entry as the effect group.

In this study, it was confirmed that the presence of incorporated vessels (OR = 0.13, $P = .021$) was a significant factor in predicting the effects of FD. Among cases with no incorporated vessel, 22/29 (75.8%) showed the effect of FD, whereas in cases with incorporation, only 12/22 (54.6%) cases showed the effect of FD. In patients exhibiting remnant entry or subtotal filling on follow-up angiography, a significant proportion of aneurysms developed thromboses and occlusion, but sometimes remnant aneurysms were apparent close to the incorporated vessels (Fig 2). Bender et al¹² studied a single-institution series of 445 cases and reported that vessel incorporation was a risk factor for incomplete occlusion after FD (OR = 2.206, $P = .035$).

In-stent balloon angioplasty is performed when the stent-to-wall apposition is poor or stenosis is evident in the parent artery because either condition greatly increases the risk of thromboembolic events

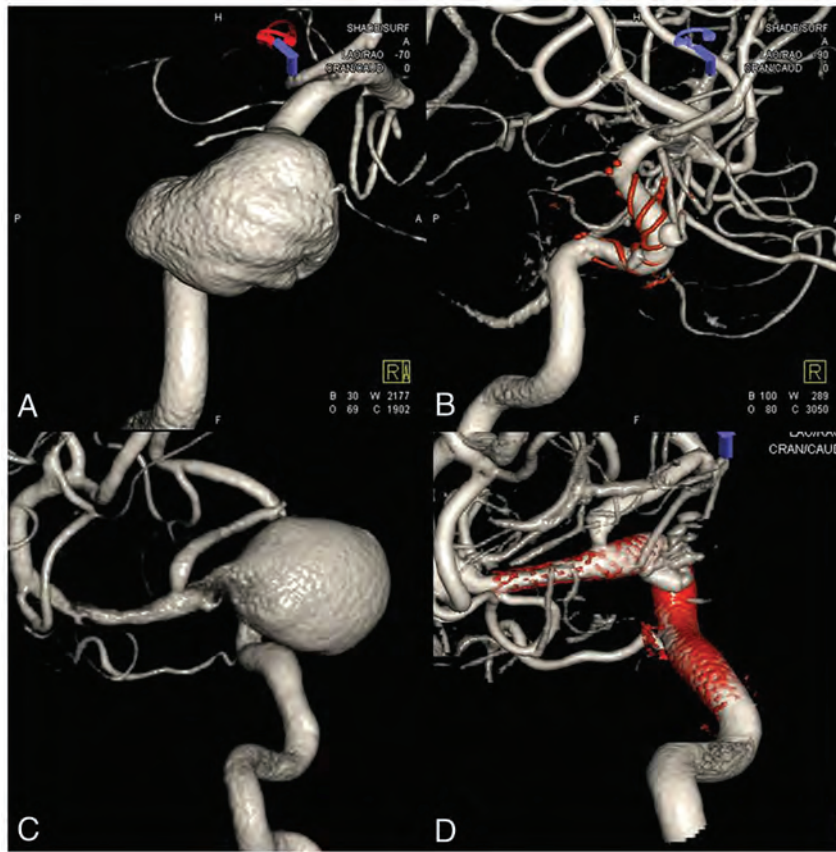


FIG 2. Remnant aneurysms are apparent close to the incorporated ophthalmic artery on 6-month follow-up angiography.



FIG 3. High-velocity blood flow into the aneurysm was caused by proximal parent artery stenosis after flow diversion. Early artery phase (A) and late artery phase (B). The high-velocity blood flow disappears immediately (D) after balloon angioplasty in the stent (C).

and subsequent parent artery occlusion.^{18,28,29} In addition, high-velocity blood flow into the aneurysm caused by stenosis of the proximal parent artery compromises the effect of FD and might induce delayed aneurysm rupture (Fig 3).^{20,30,31} However, we found that patients who underwent in-stent balloon angioplasty are more likely to be in the no-effect group (OR = 0.05, $P = .004$). Of the no-effect group, 6/17 (35.3%) patients underwent in-stent balloon angioplasty, while 3/34 (8.8%) in the effect group underwent angioplasty. To the best of our knowledge, no other study has shown that balloon angioplasty compromises the effect of FD. Because FD efficacy is greatly affected by pore density, interventionists sought to maximize this density using the push-and-pull technique at the unconstrained area of the parent artery during FDs deployment. This balloon angioplasty might increase the pore density in the non-neck area and decrease it in the neck area. However, stenosis of the parent artery confounds the effects of balloon angioplasty on the FDs. As mentioned above, angioplasty was performed when stenosis was apparent. Such stenosis of the parent artery is more likely to occur owing to the mass effect than the size of the aneurysm. However, there was no significant trend toward increased aneurysm size in parent artery stenosis in our study (effect group, 21.9 mm [SD, 8.6 mm] and no-effect group, 25.9 mm [5.4 mm], $P = .151$). In addition, this information should be interpreted with caution, given the low incidence of balloon angioplasty. Many studies have found that balloon angioplasty is required during FD. Our findings imply that excessive balloon angioplasty, which is performed along the whole stent or when there is a slight suspicion of poor stent-to-wall apposition, should be avoided.

Limitations

The present study has several limitations. First, this is a retrospective study of a relatively small number of cases in a single center. Follow-up angiography was not completed in all cases, and the follow-up duration was not long enough. Therefore, the inability to

obtain statistically significant results for all data analyzed is a limitation of this study. Second, the self-adjudication of aneurysm occlusion is known to be considerably overestimated according to another study.³² However, we treated only large and giant aneurysms, so there was relatively little difference in distinguishing the effect group from the no-effect group according to the O'Kelly-Marotta grading scale criteria.

CONCLUSIONS

FD is effective for treating very large and giant aneurysms, but the outcomes require further improvement. The results of this study show that an incorporated vessel and excessive balloon angioplasty might compromise the effect of FD. Considering this finding can help improve the outcomes of FD.

REFERENCES

- Nakase H, Shin Y, Kanemoto Y, et al. **Long-term outcome of unruptured giant cerebral aneurysms.** *Neurol Med Chir (Tokyo)* 2006;46:379–86 CrossRef Medline
- Pia HW, Zierski J. **Giant cerebral aneurysms.** *Neurosurg Rev* 1982;5:117–48 CrossRef Medline
- Lemole GM, Henn J, Spetzler RF, et al. **Surgical management of giant aneurysms.** *Operative Techniques in Neurosurgery* 2000;3:239–54 CrossRef
- Sano H. Treatment of complex intracranial aneurysms of anterior circulation using multiple clips. In: Laasko A, Hernesniemi C, Yonekawa Y, et al, eds. *Surgical Management of Cerebrovascular Disease: Acta Neurochirurgica Supplementum*. SpringerWien; 2010; 27–31
- Molyneux A, Kerr R, Stratton I, et al. International Subarachnoid Aneurysm Trial (ISAT) Collaborative Group. **International Subarachnoid Aneurysm Trial (ISAT) of neurosurgical clipping versus endovascular coiling in 2143 patients with ruptured intracranial aneurysms: a randomized trial.** *J Stroke Cerebrovasc Dis* 2002;11:304–14 CrossRef Medline
- Henkes H, Fischer S, Weber W, et al. **Endovascular coil occlusion of 1811 intracranial aneurysms: early angiographic and clinical results.** *Neurosurgery* 2004;54:268–80; discussion 280–85 CrossRef Medline
- Jahromi BS, Mocco J, Bang JA, et al. **Clinical and angiographic outcome after endovascular management of giant intracranial aneurysms.** *Neurosurgery* 2008;63:662–74; discussion 674–75 CrossRef Medline
- Murayama Y, Viñuela F, Ishii A, et al. **Initial clinical experience with Matrix detachable coils for the treatment of intracranial aneurysms.** *J Neurosurg* 2006;105:192–99 CrossRef Medline
- Becske T, Kallmes DF, Saatci I, et al. **Pipeline for Uncoilable or Failed aneurysms: results from a multicenter clinical trial.** *Radiology* 2013;267:858–68 CrossRef Medline
- O'Kelly CJ, Krings T, Fiorella D, et al. **A novel grading scale for the angiographic assessment of intracranial aneurysms treated using flow diverting stents.** *Interv Neuroradiol* 2010;16:133–37 CrossRef Medline
- Becske T, Brinjikji W, Potts MB, et al. **Long-term clinical and angiographic outcomes following Pipeline Embolization Device treatment of complex internal carotid artery aneurysms: five-year results of the Pipeline for Uncoilable or Failed Aneurysms Trial.** *Neurosurgery* 2017;80:40–48 CrossRef Medline
- Bender MT, Colby GP, Lin LM, et al. **Predictors of cerebral aneurysm persistence and occlusion after flow diversion: a single-institution series of 445 cases with angiographic follow-up.** *J Neurosurg* 2018;130:259–67 CrossRef Medline
- Makoyeva A, Bing F, Darsaut TE, et al. **The varying porosity of braided self-expanding stents and flow diverters: an experimental study.** *AJNR Am J Neuroradiol* 2013;34:596–602 CrossRef Medline
- Song J, Shin YS. **Antiplatelet drug resistance did not increase the thromboembolic events after stent-assisted coiling of unruptured intracranial aneurysm: a single center experience of 99 cases.** *Neurol Sci* 2017;38:879–85 CrossRef Medline
- Chalouhi N, Tjoumakaris S, Gonzalez LF, et al. **Coiling of large and giant aneurysms: complications and long-term results of 334 cases.** *AJNR Am J Neuroradiol* 2014;35:546–52 CrossRef Medline
- Sluzewski M, Menovsky T, van Rooij WJ, et al. **Coiling of very large or giant cerebral aneurysms: long-term clinical and serial angiographic results.** *AJNR Am J Neuroradiol* 2003;24:257–62 Medline
- Peschillo S, Caporlingua A, Resta MC, et al. **Endovascular treatment of large and giant carotid aneurysms with flow-diverter stents alone or in combination with coils: a multicenter experience and long-term follow-up.** *Oper Neurosurg (Hagerstown)* 2017;13:492–502 CrossRef Medline
- Brinjikji W, Murad MH, Lanzino G, et al. **Endovascular treatment of intracranial aneurysms with flow diverters: a meta-analysis.** *Stroke* 2013;44:442–47 CrossRef Medline
- Oishi H, Teranishi K, Yatomi K, et al. **Flow diverter therapy using a Pipeline Embolization Device for 100 unruptured large and giant internal carotid artery aneurysms in a single center in a Japanese population.** *Neurol Med Chir (Tokyo)* 2018;58:461–67 CrossRef Medline
- Larrabide I, Aguilar ML, Morales HG, et al. **Intra-aneurysmal pressure and flow changes induced by flow diverters: relation to aneurysm size and shape.** *AJNR Am J Neuroradiol* 2013;34:816–22 CrossRef Medline
- Saatci I, Yavuz K, Ozer C, et al. **Treatment of intracranial aneurysms using the Pipeline flow-diverter embolization device: a single-center experience with long-term follow-up results.** *AJNR Am J Neuroradiol* 2012;33:1436–46 CrossRef Medline
- Cebral JR, Castro MA, Appanaboyina S, et al. **Efficient pipeline for image-based patient-specific analysis of cerebral aneurysm hemodynamics: technique and sensitivity.** *IEEE Trans Med Imaging* 2005;24:457–67 CrossRef Medline
- Choi JH, Lee KS, Kim B, et al. **Treatment outcomes of large and giant intracranial aneurysms according to various treatment modalities.** *Acta Neurochir (Wien)* 2020;162:2745–52 CrossRef Medline
- Dai D, Ding YH, Kadirvel R, et al. **Patency of branches after coverage with multiple telescoping flow-diverter devices: an in vivo study in rabbits.** *AJNR Am J Neuroradiol* 2012;33:171–74 CrossRef Medline
- Kojima M, Irie K, Fukuda T, et al. **The study of flow diversion effects on aneurysm using multiple Enterprise stents and two flow diverters.** *Asian J Neurosurg* 2012;7:159–65 CrossRef Medline
- Siddiqui AH, Kan P, Abla AA, et al. **Complications after treatment with Pipeline embolization for giant distal intracranial aneurysms with or without coil embolization.** *Neurosurgery* 2012;71:E509–13; discussion E513 CrossRef Medline
- Kim BM, Shin YS, Baik MW, et al. **Pipeline Embolization Device for large/giant or fusiform aneurysms: an initial multi-center experience in Korea.** *Neurointervention* 2016;11:10–17 CrossRef Medline
- Cohen JE, Gomori JM, Moscovici S, et al. **Delayed complications after flow-diverter stenting: reactive in-stent stenosis and creeping stents.** *J Clin Neurosci* 2014;21:1116–22 CrossRef Medline
- Guédon A, Clarençon F, Maria FD, et al. **Very late ischemic complications in flow-diverter stents: a retrospective analysis of a single-center series.** *J Neurosurg* 2016;125:929–35 CrossRef Medline
- Mut F, Raschi M, Scivano E, et al. **Association between hemodynamic conditions and occlusion times after flow diversion in cerebral aneurysms.** *J Neurointerv Surg* 2015;7:286–90 CrossRef Medline
- Kulcsár Z, Augsburger L, Reymond P, et al. **Flow diversion treatment: intra-aneurysmal blood flow velocity and WSS reduction are parameters to predict aneurysm thrombosis.** *Acta Neurochir (Wien)* 2012;154:1827–34 CrossRef Medline
- Taschner CA, Chapot R, Costalat V, et al. **GREAT: a randomized controlled trial comparing HydroSoft/HydroFrame and bare platinum coils for endovascular aneurysm treatment: procedural safety and core-lab-assessed angiographic results.** *Neuroradiology* 2016;58:777–86 CrossRef Medline

Differential Contribution of ASPECTS Regions to Clinical Outcome after Thrombectomy for Acute Ischemic Stroke

 S.M. Seyedsaadat,  A.A. Neuhaus,  P.J. Nicholson,  E.C. Polley,  C.A. Hilditch,  D.C. Mihal,  T. Krings,  J. Benson,  I. Mark,  D.F. Kallmes,  W. Brinjikji, and  J.D. Schaafsma



ABSTRACT

BACKGROUND AND PURPOSE: Ischemic stroke is the leading cause of long-term disability in adults, but our ability to prognosticate from baseline imaging data is limited. The ASPECTS measures ischemic change in the middle cerebral artery territory on non-contrast CT based on 10 anatomic regions. Here, we investigated whether infarction in particular regions was associated with worse long-term outcome.

MATERIALS AND METHODS: We identified consecutive patients receiving mechanical thrombectomy for ICA/MCA occlusion at 2 comprehensive stroke centers. Pretreatment ASPECTS was assessed by 2 blinded reviewers. Clinical data including demographics, baseline NIHSS score, and 90-day mRS were collected. The relationship between individual ASPECTS regions and the mRS score (0–2 versus 3–6) was assessed using multivariable logistic regression.

RESULTS: Three hundred fifty-three patients were included (mean age, 70 years; 46% men), of whom 214 had poor outcome (mRS = 3–6). Caudate (OR = 3.26; 95% CI, 1.33–8.82), M4 region (OR = 2.94; 95% CI, 1.09–9.46), and insula (OR = 1.75; 95% CI, 1.08–2.85) infarcts were associated with significantly greater odds of poor outcome, whereas M1 region infarction reduced the odds of poor outcome (OR = 0.38; 95% CI, 0.14–0.99). This finding remained unchanged when restricted to only patients with good recanalization. No significant associations were found by laterality. Similarly, no region was predictive of neurologic improvement during the first 24 hours or of symptomatic intracerebral hemorrhage.

CONCLUSIONS: Our results indicate that ASPECTS regions are not equal in their contribution to functional outcome. This finding suggests that patient selection based on total ASPECTS alone might be insufficient, and infarct topography should be considered when deciding eligibility for thrombectomy.

ABBREVIATION: sICH = symptomatic intracranial hemorrhage

Recent advances in the field of endovascular thrombectomy have led to a sea change in the management of large-vessel-occlusion acute ischemic stroke, with several initial trials showing benefit with new-generation endovascular approaches.^{1–6} The time window for thrombectomy has subsequently expanded to up to 24 hours from onset.^{7,8} In all these trials, imaging was crucial to identify patients likely to benefit. Most trials in 2015 used lesion size on CT as part of their selection criteria, quantified as

the ASPECTS. ASPECTS was first described in 2000 and separates the middle cerebral artery territory into 10 regions (6 superficial, 4 deep; Figure). These are then assigned a value of 0 if there are early ischemic changes—parenchymal hypoattenuation, loss of gray-white differentiation, and focal swelling—and a value of 2 if the region is normal in appearance.⁹ Correspondingly, lower scores imply more extensive ischemia and intuitively suggest that the outcome is more likely to be poor; indeed, the ASPECTS is known to have value in long-term prognostication after stroke,¹⁰ and has previously been shown to correlate with functional

Received November 14, 2019; accepted after revision December 17, 2020.

From the Departments of Radiology (S.M.S., E.C.P., J.B., I.M., D.F.K., W.B.) and Neurosurgery (W.B.), Mayo Clinic, Rochester, Minnesota; Department of Radiology (S.M.S.), Mayo Clinic, Jacksonville, Florida; Radcliffe Department of Medicine (A.A.N.), University of Oxford, Oxford, UK; Department of Medicine (P.J.N., C.A.H., T.K., J.D.S.), Division of Neurology, University Health Network/University of Toronto, Toronto, Ontario, Canada; Department of Neuroradiology (C.A.H.), Manchester Centre for Clinical Neurosciences, Salford Royal National Health Service Foundation Trust, Salford, UK; and Department of Radiology (D.C.M.), Division of Neuroradiology, Cleveland Clinic, Cleveland, Ohio

W. Brinjikji and J.D. Schaafsma contributed equally as senior and supervising authors.

This work was supported by an Award from the American Heart Association (19POST34381067) to S.M. Seyedsaadat. A.A. Neuhaus was supported by an award from the Oxford University Clinical Academic Graduate School.

Please address correspondence to Waleed Brinjikji, MD, Department of Radiology, Mayo Clinic, 200 1st St SW, Rochester, MN 55902; e-mail: Brinjikji.Waleed@mayo.edu; @wbrinjikji

 Indicates article with online supplemental data.
<http://dx.doi.org/10.3174/ajnr.A7096>

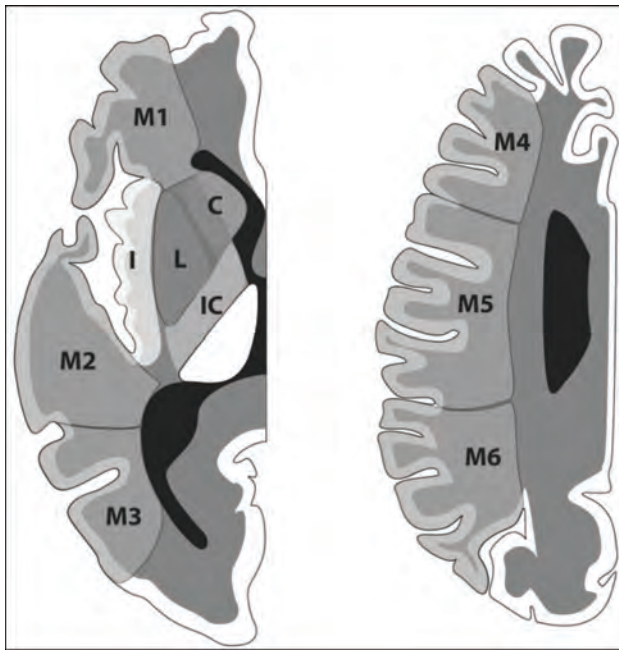


FIGURE. Illustration of ASPECTS, showing 10 regions in 1 hemisphere. C indicates caudate; IC, internal capsule; L, lentiform; I, insula. Reproduced from Neuhaus et al²⁵ with permission from BMJ Publishing Group Ltd.

independence in intra-arterial thrombolysis.¹¹ Thus, low ASPECTS values continue to be used as an exclusion criterion for thrombectomy because these patients are assumed to have a low likelihood of meaningful improvement.

However, there are a number of disadvantages in using ASPECTS. First, although it significantly correlates with long-term function on a group level, individual outcomes are discriminated less accurately, particularly when the ASPECTS is moderate to high (eg, 6–10, implying limited ischemic change).¹² Second, it is known that involvement of specific regions leads to particular functional deficits, eg, the angular gyrus in language¹³ and multiple cortical and subcortical areas in motor function.¹⁴ The ASPECTS treats all 10 areas equally; therefore, a composite ASPECTS of 7 may reflect very different lesion patterns, and there is no a priori reason to think these would be equivalent in terms of functional consequences. Third, the volumes of ASPECTS regions are not equal, and the loss of a single point can reflect a wide range of ischemic volumes, depending on which areas are affected. Indeed, it has been previously reported that some regions confer a greater risk of poor long-term outcome.¹⁵ Variation in outcome based on the affected area has also been described with ASPECTS regions from baseline CT,^{15–18} though with inconsistent findings.

The implication of this finding is that a significant number of patients with a poor composite ASPECTS might, in fact, have a greater likelihood of good outcome than the total score would suggest, which may influence treatment decisions. In this study, we sought to estimate regional contributions to long-term function using pretreatment ASPECTS data in a thrombectomy cohort.

MATERIALS AND METHODS

Study Subjects

We conducted a retrospective analysis of 353 consecutively treated patients with a diagnosis of acute ischemic stroke related to an emergent large-vessel occlusion from January 2015 to December 2018. One hundred seventy-eight patients were treated at the first participating center, and 175 patients, at the second (Mayo Clinic and Toronto Western Hospital). ASPECTS ≥ 6 was a prerequisite for proceeding with thrombectomy at our institutions.

The inclusion criteria were as follows:

1. Clinical diagnosis of acute stroke in the anterior circulation
2. Eighteen years of age or older
3. Availability of NCCT images acquired within 24 hours of onset of symptoms
4. Patients with intracranial ICA, M1, or M2 occlusion identified on CTA who were treated by endovascular thrombectomy.

Among the exclusion criteria were nonischemic pathology found on baseline imaging (eg, intracerebral hemorrhage), poor quality of baseline scans (eg, excessive artifacts preventing regional ASPECTS estimation), and denial of consent following checking for research authorization.

Baseline clinical characteristics collected from subjects included age, sex, NIHSS score, and time of last known well; post-treatment characteristics included the mRS score at 90 days and recanalization status after thrombectomy. The study was approved by the institutional review boards at both institutions; because this was a retrospective study, informed consent was waived. However, per Minnesota state law, after checking the status of all patients residing in the state of Minnesota, 21 patients who denied access to their medical records for research use were not included in this study.

CT Acquisition and Analysis

Noncontrast CT scans with 5-mm section thickness were obtained at admission, with a maximal delay of <24 hours from stroke onset. ASPECTS was independently determined by 2 neuroradiologists at each site, for a total of 4 raters who were blinded to clinical outcome. In case of any disagreement, a third neuroradiologist in each center reviewed and adjudicated the score.^{9,19} In contrast to the original methodology of using 1 supraganglionic and 1 ganglionic section for ASPECTS, assessors had access to the entire NCCT scan. Evidence of early ischemic change was defined as the presence of hypoattenuation and/or loss of gray matter–white matter differentiation, with or without cortical swelling. Assessors were aware of the presumed laterality of the stroke but blinded to other clinical details.

Statistical Analysis

A summary of clinical and imaging characteristics is presented in the Online Supplemental Data as mean (SD) (age, NIHSS) or median with interquartile range (ASPECTS). The relationship between individual ASPECTS regions and the ordinal functional outcome score (mRS) was assessed using multivariable logistic regression. mRS was dichotomized as good (0–2) or poor (3–6). Ten-fold cross-validation was then used to estimate the predictive value of each region, and a multivariable logistic regression with

Table 1: Predictive value of ASPECTS regions for mRS at 90 days

Region	OR of Poor Outcome	95% CI	P Value
Overall			
M1	0.38	0.14–0.99	.047
M2	1.55	0.77–3.26	.234
M3	0.69	0.24–2.00	.487
M4	2.94	1.09–9.46	.046
M5	1.87	0.84–4.51	.141
M6	1.66	0.52–6.01	.407
Lentiform	0.93	0.52–1.66	.803
Insula	1.75	1.08–2.85	.023
Caudate	3.26	1.33–8.82	.013
Internal capsule	0.76	0.29–2.03	.575
Right hemisphere			
M1	0.24	0.05–0.94	.048
M2	1.98	0.73–5.71	.189
M3	0.48	0.11–1.99	.309
M4	3.70	0.87–21.8	.100
M5	1.36	0.42–4.68	.615
M6	3.71	0.72–29.4	.148
Lentiform	0.87	0.39–1.93	.734
Insula	1.67	0.82–3.46	.162
Caudate	2.74	0.81–10.5	.117
Internal capsule	1.39	0.33–6.63	.659
Left hemisphere			
M1	0.57	0.14–2.51	.438
M2	1.70	0.56–5.94	.372
M3	1.19	0.21–8.27	.843
M4	2.88	0.69–19.6	.193
M5	2.80	0.81–13.2	.135
M6	0.70	0.10–5.04	.717
Lentiform	1.25	0.53–3.10	.613
Insula	1.74	0.88–3.49	.112
Caudate	3.20	0.83–16.6	.118
Internal capsule	0.50	0.13–1.98	.312

Table 2: Comparison of total ASPECTS between patients with caudate or insular infarct with the rest of cohort

	Total ASPECTS (Mean) (SD)	P Value
In the presence of insular infarction (n = 96)	7.29 (1.34)	<.0001
In the absence of insular infarction (n = 257)	8.97 (1.2)	
In the presence of caudate infarction (n = 172)	7.65 (1.34)	<.0001
In the absence of caudate infarction (n = 181)	9.34 (0.99)	

the 10 regions in a single model was fitted. This was also used for subgroup analyses based on laterality (left and right hemispheres separately) and recanalization status based on angiographic findings (dichotomized as TICI 2b/3 for successful recanalization and also examining TICI 3 separately). We also explored the predictive value of regional ASPECTS for symptomatic intracranial hemorrhage following thrombectomy and for NIHSS change within the first day following stroke onset (calculated simply as NIHSS_{24 hours} – NIHSS_{baseline}) as an indicator of acute neurologic deterioration or improvement. Data were collected in Excel (Microsoft) and analyzed using R statistical and computing software (<http://www.r-project.org/>).

RESULTS

Baseline Characteristics

The baseline characteristics of the patient population are presented in the Online Supplemental Data. The mean age of patients was 70 years, and 46% were men. Baseline imaging showed a median total ASPECTS of 9; early ischemic changes were most commonly seen in the insula (172 patients, 48.7%) and lentiform nucleus (96 patients, 27.2%) and least frequently in M6 (16 patients, 4.5%).

Primary Outcome

Logistic regression for regional ASPECTS irrespective of laterality (Table 1) showed that the regions significantly associated with poor outcome were the caudate nucleus (OR_{caudate} = 3.26; 95% CI, 1.33–8.82), M4 (OR_{M4} = 2.94; 95% CI, 1.09–9.46), and insula (OR_{insula} = 1.75; 95% CI, 1.08–2.85). Conversely, M1 was associated with reduced odds of poor outcome (OR_{M1} = 0.38; 95% CI, 0.14–0.99). The remaining 6 areas (M2, M3, M5, M6, lentiform nucleus, and internal capsule) did not reach statistical significance. When we separated them by the side of the stroke, no regions reached statistical significance, though similar trends were observed; on the right, there was an additional trend for M6 in particular (OR_{M6} = 3.71; 95% CI, 0.72–29.4) and on the left for M5 (OR_{M5} = 2.80; 95% CI, 0.81–13.2).

Subgroup Analyses

The average total ASPECTS for patients without insular or caudate infarcts was higher than for those with insula or caudate involvement (P value < .0001) (Table 2).

Of the studied population, 302 (85.6%) had successful recanalization, defined as TICI 2b/3. When this cohort was analyzed as a subgroup, the results were effectively unchanged from the total population (Table 3), with the caudate nucleus (OR_{caudate} = 4.02; 95% CI, 1.51–12.2), M4 (OR_{M4} = 3.54; 95% CI, 1.26–11.9), and insula (OR_{insula} = 1.69; 95% CI, 1.01–2.85) being associated with poor outcome; again, M1 infarction was associated with lower odds of poor outcome (OR_{M1} = 0.28; 95% CI, 0.09–0.83). When this cohort was restricted to only TICI 3 (n = 154), suggesting complete reperfusion, only the caudate nucleus (OR_{caudate} = 14.86; 95% CI, 3.22–114.94) reached statistical significance. The group of patients with unsuccessful recanalization (TICI 0/1/2a, n = 51) was too small to reliably estimate ORs.

ASPECTS Regions and Short-Term Outcomes

We then repeated the analyses using symptomatic intracranial hemorrhage (sICH) as an outcome. In our sample, 27 patients (7.6%) developed sICH within the first 24 hours following thrombectomy. Due to the small sample size, there was no significant association with any ASPECTS region; because the lowest P value was .299, it was not possible to characterize any trends in the data (Table 4). We also used changes in the NIHSS score during the first 24 hours as the outcome metric to explore the impact of individual regions on short-term neurologic improvement. No individual ASPECTS region showed significant correlation with NIHSS change (Online Supplemental Data), with a slight trend toward the lentiform nucleus (OR_{lentiform} = 6.89; 95% CI, 0.57–83.10).

Table 3: Predictive value of ASPECTS regions for mRS at 90 days, stratified by recanalization status

Region	OR of Poor Outcome	95% CI	P Value
TICI 2b/3			
M1	0.28	0.09–0.83	.025
M2	1.87	0.84–4.41	.137
M3	0.56	0.17–1.75	.318
M4	3.54	1.26–11.9	.024
M5	1.89	0.79–4.92	.167
M6	1.59	0.47–5.87	.463
Lentiform	0.98	0.53–1.81	.935
Insula	1.69	1.01–2.85	.048
Caudate	4.02	1.51–12.2	.008
Internal capsule	1.00	0.35–3.05	.994
TICI 3			
M1	0.093	0.00–1.23	.064
M2	2.18	0.56–10.00	.279
M3	0.50	0.06–4.07	.511
M4	3.08	0.88–12.74	.091
M5	3.66	0.88–19.49	.089
M6	8.55	0.95–209.20	.092
Lentiform	0.83	0.33–2.02	.679
Insula	1.87	0.86–4.12	.116
Caudate	14.86	3.22–114.94	.002
Internal capsule	0.52	0.10–2.38	.404

Table 4: Predictive value of ASPECTS regions for sICH

Region	OR of sICH	95% CI	P Value
M1	0.82	0.20–5.57	.805
M2	1.49	0.47–5.93	.531
M3	1.00	0.19–8.26	.999
M4	1.07	0.27–7.25	.935
M5	1.04	0.31–4.88	.950
M6	0.56	0.11–4.46	.524
Lentiform	1.37	0.49–4.44	.572
Insula	0.80	0.34–1.89	.612
Caudate	0.51	0.15–1.97	.299
Internal capsule	0.50	0.14–2.08	.301

DISCUSSION

In this study, we have characterized the long-term functional impact of ischemia in specific regions of the ASPECTS system in patients who underwent thrombectomy after baseline imaging. Our main finding is that infarction in the caudate, M4, and insula areas is significantly associated with poor outcome (mRS = 3–6) following thrombectomy, whereas patients with M1 infarctions have reduced odds of poor outcome. The same observation was made when analyses were restricted to only those patients in whom good recanalization was achieved. Analyses by laterality or looking at neurologic improvement and sICH as outcomes did not reach statistical significance. The implication of these results may be that the use of a composite ASPECTS should be re-evaluated because the total score may be less informative than individual territories, as discussed below.

Previous studies have examined the contribution of individual ASPECTS regions to outcome. However, the results reported in the literature show significant disagreement. For example, Khan et al¹⁸ reported that M3 and M6 infarction on either side, M2 on the right, and M5 on the left were associated with poor outcome. Beare et al¹⁷ also reported M2 and M5 infarction as a poor prognostic factor, without specifying side. In the largest study looking

at admission NCCT, Payabvash et al²⁰ found M5, caudate, lentiform, and insula infarction to be associated with poor outcome in patients treated with intravenous thrombolysis. Phan et al¹⁶ only found significant results from interaction terms between age and lentiform, and age and M6. There have also been studies using the ASPECTS template with modalities other than NCCT. Haranhalli et al²¹ found that insula, M2, and M5 infarcts on CT perfusion were associated with poor outcome. Payabvash et al¹⁵ also reported that insula infarction predicted poor outcome, using DWI at admission.

One important difference with the results reported here is the clinical care provided to the patient population. Most patients in the aforementioned studies were either managed conservatively or treated with intravenous thrombolysis. Payabvash et al^{15,20} and Haranhalli et al²¹ did include patients with subsequent intra-arterial therapy, but given that data collection occurred before 2015, these likely represented intra-arterial thrombolysis and thrombectomy with first-generation devices, which were notably less effective. In contrast, our study included only patients who underwent stent retriever or aspiration thrombectomy and is, therefore, more reflective of the current criterion standard approach to management of large-vessel-occlusion stroke.

We can only speculate on why the regions identified by our study were associated with worse outcomes. M4 represents the frontal cortex on the supraganglionic section, whereas M1 is more the caudal frontal cortex. In terms of function, infarcts involving M1 might lead to deficits in behavioral planning due to involvement of the operculum and may also lead to nonfluent aphasia if the dominant hemisphere (ie, left in most individuals) is affected. Hemiplegia, in particular, might be expected to have a substantial effect on mRS because the scale is largely based on mobility. M4 might similarly be associated with aphasia and apraxia on the dominant side, though limb weakness is less likely. Similarly, the caudate nucleus is part of the basal ganglia and crucial for motor control, as well as being associated with cognitive changes. The insula is primarily associated with autonomic function, but also with motor control, cognition, and emotion.^{22,23}

Limitations

There are limitations to this study. First, although our total cohort was relatively large, subgroup analyses for sICH, stroke laterality, and outcome in poorly recanalized patients were limited by small sample sizes. In addition, we had relatively few cases with stroke in some of the cortical areas (most notably M6) and the internal capsule. This spectrum bias is probably the consequence of selection bias for endovascular thrombectomy. Second, the median ASPECTS in this study was 9, suggesting only limited ischemic changes. Although this was also the median ASPECTS value in the meta-analysis of the 2015 trials¹ and is therefore representative of patients receiving endovascular thrombectomy, it, nonetheless, complicates applying these findings to patients with more extensive ischemic changes and lower total ASPECTS. Third, our analyses currently assume that regional ischemic changes were independent of each other, and we have not adjusted for collinearity; however, preliminary analyses did not show significant collinearity in our dataset. Although in our cohort, patients with infarcts in the insula or caudate nucleus had poorer total ASPECTS, this still warrants

further follow-up studies. Fourth, there is potential interobserver variability, as was reported by Nicholson et al²⁴ in their study of 375 patients with acute ischemic stroke, which showed substantial interobserver variability among readers in scoring different ASPECTS regions. They found that readers had the highest agreement in scoring the insula ($\kappa = 0.56$; range, 0.48–0.64) and the lowest agreement in scoring M3 ($\kappa = 0.34$; range, 0.12–0.56).

CONCLUSIONS

We have characterized outcome based on regional infarction as determined by the ASPECTS template on baseline NCCT. This work is hypothesis-generating and may be of potential use in the development of scoring systems that take infarct topography into account and allow improved patient-selection algorithms for thrombectomy. Therefore, larger datasets are required to validate our findings and provide more definitive quantification of the impact of ischemia in different ASPECTS areas on outcome.

Disclosures: Seyed Mohammad Seyedasadat—RELATED: Grant: American Heart Association, Comments: 2 years postdoctoral fellowship American Heart Association research grant. Timo Krings—UNRELATED: Consultancy: Stryker, Medtronic, Penumbra; Royalties: Thieme; Stock/Stock Options: Marblehead Medical LLC. Ain A. Neuhaus—RELATED: Grant: Oxford University Clinical Academic Graduate School, Comments: internal grant from the Oxford University Clinical Academic Graduate School to support travel and living expenses for medical elective at the Mayo Clinic. David F. Kallmes—UNRELATED: Stock/Stock Options: Superior Medical Experts LLC, Marblehead Medical LLC.

REFERENCES

- Goyal M, Menon BK, van Zwam WH, et al. HERMES Collaborators. **Endovascular thrombectomy after large-vessel ischaemic stroke: a meta-analysis of individual patient data from five randomised trials.** *Lancet* 2016;387:1723–31 CrossRef Medline
- Campbell BC, Mitchell PJ, Kleinig TJ, et al. EXTEND-IA Investigators. **Endovascular therapy for ischemic stroke with perfusion-imaging selection.** *N Engl J Med* 2015;372:1009–18 CrossRef Medline
- Jovin TG, Chamorro A, Cobo E, et al. REVASCAT Trial Investigators. **Thrombectomy within 8 hours after symptom onset in ischemic stroke.** *N Engl J Med* 2015;372:2296–2306 CrossRef Medline
- Saver JL, Goyal M, Bonafe A, et al. SWIFT PRIME Investigators. **Stent-retriever thrombectomy after intravenous t-PA vs. t-PA alone in stroke.** *N Engl J Med* 2015;372:2285–95 CrossRef Medline
- Goyal M, Demchuk AM, Menon BK, et al. ESCAPE Trial Investigators. **Randomized assessment of rapid endovascular treatment of ischemic stroke.** *N Engl J Med* 2015;372:1019–30 CrossRef
- Berkhemer OA, Fransen PS, Beumer D, et al. MR CLEAN Investigators. **A randomized trial of intraarterial treatment for acute ischemic stroke.** *N Engl J Med* 2015;372:11–20 CrossRef Medline
- Albers GW, Marks MP, Kemp S, et al. DEFUSE 3 Investigators. **Thrombectomy for stroke at 6 to 16 hours with selection by perfusion imaging.** *N Engl J Med* 2018;378:708–18 CrossRef Medline
- Nogueira RG, Jadhav AP, Haussen DC, et al. DAWN Trial Investigators. **Thrombectomy 6 to 24 hours after stroke with a mismatch between deficit and infarct.** *N Engl J Med* 2018;378:11–21 CrossRef Medline
- Barber PA, Demchuk AM, Zhang J, et al. **Validity and reliability of a quantitative computed tomography score in predicting outcome of hyperacute stroke before thrombolytic therapy: ASPECTS Study Group—Alberta Stroke Programme Early CT Score.** *Lancet* 2000;355:1670–74 CrossRef Medline
- Hill MD, Buchan AM; Canadian Alteplase for Stroke Effectiveness Study (CASES) Investigators. **Canadian Alteplase for Stroke Effectiveness Study I: thrombolysis for acute ischemic stroke—results of the Canadian Alteplase for Stroke Effectiveness Study.** *CMAJ* 2005;172:1307–12 CrossRef Medline
- Hill MD, Rowley HA, Adler F, et al. PROACT-II Investigators. **Selection of acute ischemic stroke patients for intra-arterial thrombolysis with pro-urokinase by using ASPECTS.** *Stroke* 2003;34:1925–31 CrossRef Medline
- Deir NU, Pexman JH, Hill MD, et al. CASES Investigators. **How well does ASPECTS predict the outcome of acute stroke treated with IV tPA?** *Neurology* 2006;67:516–18 CrossRef Medline
- Payabvash S, Kamalian S, Fung S, et al. **Predicting language improvement in acute stroke patients presenting with aphasia: a multivariate logistic model using location-weighted atlas-based analysis of admission CT perfusion scans.** *AJNR Am J Neuroradiol* 2010;31:1661–68 CrossRef Medline
- Payabvash S, Souza LC, Kamalian S, et al. **Location-weighted CTP analysis predicts early motor improvement in stroke: a preliminary study.** *Neurology* 2012;78:1853–59 CrossRef Medline
- Payabvash S, Benson JC, Tyan AE, et al. **Multivariate prognostic model of acute stroke combining admission infarct location and symptom severity: a proof-of-concept study.** *J Stroke Cerebrovasc Dis* 2018;27:936–44 CrossRef Medline
- Phan TG, Demchuk A, Srikanth V, et al. **Proof of concept study: relating infarct location to stroke disability in the NINDS rt-PA trial.** *Cerebrovasc Dis* 2013;35:560–65 CrossRef Medline
- Beare R, Chen J, Phan TG; VISTA-Acute Collaboration. **Googling stroke ASPECTS to determine disability: exploratory analysis from VISTA-Acute Collaboration.** *PLoS One* 2015;10:e0125687 CrossRef Medline
- Khan M, Baird GL, Goddeau RP Jr, et al. **Alberta Stroke Program Early CT Score infarct location predicts outcome following M2 occlusion.** *Front Neurol* 2017;8:98 CrossRef Medline
- Pexman JH, Barber PA, Hill MD, et al. **Use of the Alberta Stroke Program Early CT Score (ASPECTS) for assessing CT scans in patients with acute stroke.** *AJNR Am J Neuroradiol* 2001;22:1534–42 Medline
- Payabvash S, Noorbalooshi S, Qureshi AI. **Topographic assessment of acute ischemic changes for prognostication of anterior circulation stroke.** *J Neuroimaging* 2017;27:227–31 CrossRef Medline
- Haranhalli N, Mbabuie N, Grewal SS, et al. **Topographic correlation of infarct area on CT perfusion with functional outcome in acute ischemic stroke.** *J Neurosurg* 2019;132:33–41 CrossRef Medline
- Berman SA, Hayman LA, Hinck VC. **Correlation of CT cerebral vascular territories with function, 3: middle cerebral artery.** *AJR Am J Roentgenol* 1984;142:1035–40 CrossRef Medline
- Fink JN, Selim MH, Kumar S, et al. **Insular cortex infarction in acute middle cerebral artery territory stroke: predictor of stroke severity and vascular lesion.** *Arch Neurol* 2005;62:1081–85 CrossRef Medline
- Nicholson P, Hilditch CA, Neuhaus A, et al. **Per-region interobserver agreement of Alberta Stroke Program Early CT Scores (ASPECTS).** *J Neurointerv Surg* 2020;12:1069–71 CrossRef Medline
- Neuhaus A, Seyedasadat SM, Mihal D, et al. **Region-specific agreement in ASPECTS estimation between neuroradiologists and e-ASPECTS software.** *J Neurointerv Surg* 2020;12:720–23 CrossRef Medline

Teleproctoring for Neurovascular Procedures: Demonstration of Concept Using Optical See-Through Head-Mounted Display, Interactive Mixed Reality, and Virtual Space Sharing—A Critical Need Highlighted by the COVID-19 Pandemic

A.T. Rai, G. Deib, D. Smith, and S. Boo



ABSTRACT

BACKGROUND AND PURPOSE: Physician training and onsite proctoring are critical for safely introducing new biomedical devices, a process that has been disrupted by the pandemic. A teleproctoring concept using optical see-through head-mounted displays with a proctor's ability to see and, more important, virtually interact in the operator's visual field is presented.

MATERIALS AND METHODS: Test conditions were created for simulated proctoring using a bifurcation aneurysm flow model for WEB device deployment. The operator in the angiography suite wore a Magic Leap-1 optical see-through head-mounted display to livestream his or her FOV to a proctor's computer in an adjacent building. A Web-based application (Spatial) was used for the proctor to virtually interact in the operator's visual space. Tested elements included the quality of the livestream, communication, and the proctor's ability to interact in the operator's environment using mixed reality. A hotspot and a Wi-Fi-based network were tested.

RESULTS: The operator successfully livestreamed the angiography room environment and his FOV of the monitor to the remotely located proctor. The proctor communicated and guided the operator through the procedure over the optical see-through head-mounted displays, a process that was repeated several times. The proctor used mixed reality and virtual space sharing to successfully project images, annotations, and data in the operator's FOV for highlighting any device or procedural aspects. The livestream latency was 0.71 (SD, 0.03) seconds for Wi-Fi and 0.86 (SD, 0.3) seconds for the hotspot ($P = .02$). The livestream quality was subjectively better over the Wi-Fi.

CONCLUSIONS: New technologies using head-mounted displays and virtual space sharing could offer solutions applicable to remote proctoring in the neurointerventional space.

ABBREVIATIONS: COVID-19 = coronavirus disease 2019; OST-HMD = optical see-through head-mounted display

Proctoring is a key component for safe introduction of new devices in not only the neuroendovascular space but all procedural/surgical fields dependent on comprehensive physician training for device familiarity and use. For neuroendovascular devices, typical training programs have included didactic elements, hands-on training on flow models, and onsite proctoring of the initial cases. Interest in developing

remote capabilities for physician training and procedural oversight is not new, and the concept of teleproctoring for surgical procedures has been explored for almost 2 decades.¹⁻³ As technology evolves, specifically in the field of near-eye optics, miniaturization, wearable tech with virtual spaces, and high-speed networking, the ability to remotely project expertise may become more mainstream.

The travel restrictions and social isolation imposed by the coronavirus disease 2019 (COVID-19) pandemic have hampered onsite training, bringing the need for reliable remote proctoring solutions to the forefront. There has been a renewed interest and surge in telehealth solutions and online collaboration. Many platforms, services, and companies have emerged focusing on virtual alternatives for in-person interactions, leading to a digital transformation of practice-related clinical medicine, education, and research. A

Received September 15, 2020; accepted after revision January 11, 2021.

From the Department of Interventional Neuroradiology (A.T.R., G.D., S.B.), Rockefeller Neuroscience Institute, WV University School of Medicine, Morgantown, West Virginia; and West Virginia University Reed College of Media (D.S.), Morgantown, West Virginia.

Please address correspondence to Ansaar T. Rai, MD, MBA, Interventional Neuroradiology, Rockefeller Neuroscience Institute, WV University School of Medicine, 1 Medical Center Dr, Morgantown, WV 26506-8258; e-mail: ansaar.ra@gmail.com; @Ansaar_Rai

<http://dx.doi.org/10.3174/ajnr.A7066>

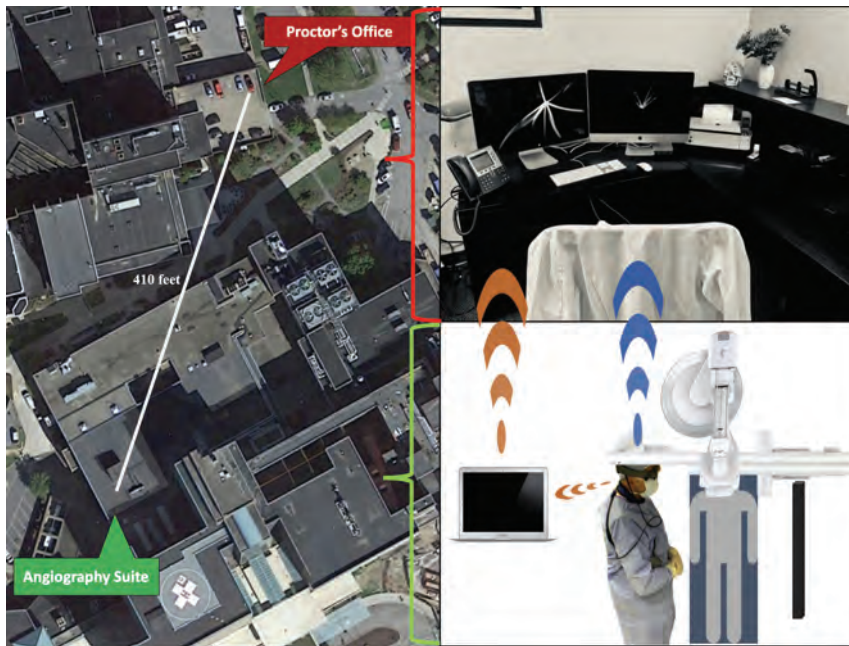


FIG 1. The setup. The *left panel* is an aerial view of the location of the experiment. The angiography suite (labeled) is in the hospital, which is separate from the proctor's location in the adjacent building (labeled). The *right panel* shows the operator's environment in the angiography suite (*lower panel*) with the operator wearing the OST-HMD and the spatial computer. The hotspot connection is demonstrated by the *orange link* between the OST-HMD and the laptop in the angiography suite and between the laptop and the computer in the proctor's office via the Zoom link. The direct Wi-Fi connection is demonstrated by the *blue link* between the OST-HMD worn by the operator with direct streaming to the computer in the proctor's office.

remotely proctored cardiovascular procedure was recently demonstrated using video conferencing and an intraoperative telemonitoring robot.⁴ Other proprietary outfits offering similar capabilities have emerged on the market as well, but none are portable. These generally require hardware capital investment and a continued subscription model.

Previous studies have tested the potential of wearable technology for remote mentoring to project expertise and training across the world.⁵ A recent review covered the role of augmented reality in surgical education⁶ to supplement traditional training before proceeding to real cases. The natural evolution could be to disseminate this training remotely. Studies have evaluated optical see-through head-mounted displays (OST-HMDs) such as GLASS by Google (<https://www.google.com/glass/start/>) and HoloLens 2 by Microsoft (<https://www.microsoft.com/en-us/hololens>) for medical and surgical applications, including intraoperative use.⁷⁻¹¹ Augmented and mixed-reality integration within Smartglasses (<https://uploadvr.com/waveguides-smartglasses/>) connected through networks and cloud-based servers has opened the possibility of using these wearable devices to project training across geographic boundaries.¹²⁻¹⁷ The portability of these devices makes them an attractive tool for teleproctoring applications; however, there are important challenges such as image stabilization that need to be addressed before these can be used for mainstream remote proctoring. The pandemic has highlighted the need for easy-to-

use tools and is spawning research and development to make these user-friendly. The goal of this investigation was to demonstrate a proof of concept that uses an optical headset for remote proctoring.

The objectives were to use a currently available device and network to test the concept of teleproctoring. The key requirement was the ability of the proctor to see the operator's FOV and virtually interact in that visual field by either pointing out key elements or displaying images, without disrupting it and with seamless bidirectional communication.

MATERIALS AND METHODS

There was no institutional review board approval required for the project, and it does not involve any human subjects.

Test Environment

A test environment was created using a flow model (Vascular Simulations) to mimic proctoring of a neurovascular bifurcation aneurysm case using a Woven EndoBridge intrasaccular device (WEB; MicroVention). The same biplane angiography suite used for actual cases was the setting of virtual proctoring. The "operator" is defined as the person doing the procedure, and the "proctor" as the one guiding the procedure. The proctor had extensive experience in WEB proctoring, and the operator had never used the device before. The operator was in sterile garb in the angiography suite, and the proctor was remotely located in an adjacent building just over 400 feet away in direct line (Fig 1). The ceiling- and wall-mounted cameras of the angiography suite captured the room environment (Fig 2). The fluoroscopy video feed from the C-arm captured the procedure.

Hardware

The primary hardware used for this experiment was Magic Leap-1 (Magic Leap; <https://www.magicleap.com/en-us>). The device has a small wearable computer and an optical headset worn by the operator (Figs 1 and 2). For mixed-reality applications, the eyewear provides a 50-degree-wide FOV from 14.6 inches in front of the face to infinity, with 1.3 megapixels per eye at a refresh rate of 120 hertz and supporting almost 17 million colors. The eyewear is a fixed multifocal headset with 2 focal planes, and the near clipping plane for the device is 37.084 cm. Due to this dual focal plane design, the 2 optimal distances for viewing objects in the wearer's FOV are 50 cm and 1.5 m (<https://developer.magicleap.com/en-us/learn/guides/design-comfort>). Magic Leap-1 is produced in 2 different sizes based on the user's interpupillary distance. Size 1, which was used for this procedure, is designed for wearers with an interpupillary distance of <65. Size 2 is

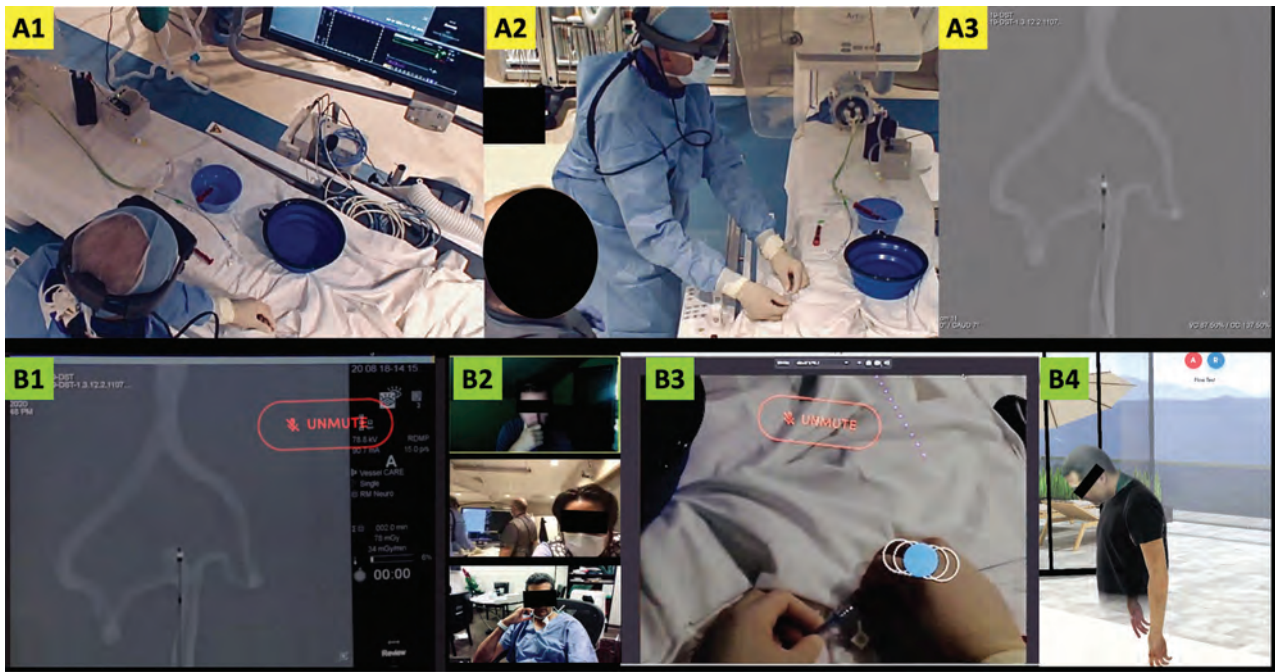


FIG 2. Operator's environment: The *upper panel* shows the operator in the angiography suite as viewed from the ceiling- (A1) and the wall-mounted (A2) cameras. The flow model can be observed on the angiography table. The operator is wearing the Magic Leap-1 and performing the procedure while listening to any instructions from the proctor. The angiography monitor (A3) shows a roadmap image of the basilar apex aneurysm with the WEB device ready for deployment. Proctor's environment: The *lower panel* shows the proctor's perspective. The same image as on the angiography monitor (A3) is livestreamed through the Magic Leap-1 and displayed on the proctor's computer (B1). The proctor's desktop also shows the participants on the Zoom bridge; from top to bottom, these include the media engineer, the backup neurointerventionalist in the angiography suite, and the proctor (B2). The proctor can also see the operator's hands (B3) when he looks down and can advise on hand positioning for device deployment. The operator's avatar in the virtual room on the Spatial app is also displayed on the proctor's screen (B4) and follows the head movements of the operator, as in this case, when the operator is looking down at his hands.

designed for wearers with an interpupillary distance of >65 . (<https://www.magicleap.care/hc/en-us/articles/360008834511-Sizing>). The device is also equipped with surround audio for communication. The headset allows the wearer to clearly see through the lenses and projects any augmented reality images directly on to the user's eyes using waveguide¹⁸ technology, a tool used in near-eye optics (Smartglasses). The third component of the system is a hand controller with haptic feedback, which could be used to move or zoom into mixed-reality images.

The operator livestreamed his FOV to a standard laptop (MacBook Pro; Apple) using the Magic Leap "device stream" function, which is a beta application available to developers only. A Zoom bridge (<https://zoom.us>) was established so that the live-stream could be viewed from anywhere. For the purpose of this experiment, this was viewed by 2 other people, the proctor and a moderator. The moderator had expertise in media and information technology and acted as an observer and recorder of the experiment. The proctor used a standard desktop (Apple iMac) to view the live-stream of the operator's FOV and communicate with the operator.

Networks

The experiment was tested with 2 networks. For the first (Fig 1), a hotspot was created in the angiography suite for the operator's OST-HMD livestreaming to the laptop in the angiography control room. The hotspot used Wi-Fi-protected access (WPA2) to establish a connection between the OST-HMD and the laptop.

The remote Zoom connection was established over a standard Wi-Fi network at the 2 locations, ie, the operator's angiography environment and the proctor's office in a separate-but-adjacent building. The Zoom connection supports Health Insurance Portability and Accountability Act compliance with end-to-end encryption (<https://zoom.us/docs/doc/Zoom-hipaa.pdf>).

For the second (Fig 1), a secure Wi-Fi network operating in both locations (operator and proctor) was used. A requirement for operating over a Wi-Fi is that both the OST-HMD streaming the operator's FOV and the proctor's computer to which it is streaming are on the same network. The Wi-Fi network assigned static Internet Protocol addresses to the OST-HMD and the proctor's computer. The difference from the hotspot was that the operator could directly livestream to the proctor's computer without using a Zoom bridge.

Virtual Space Sharing and Mixed Reality

Both the operator and the proctor securely logged into a virtual space-sharing platform app, Spatial (<https://spatial.io>). This third-party, free application enables multiple users to join a room from any device, including a mixed-reality head-mounted display such as HoloLens or Magic Leap, a virtual reality head-mounted display such as Quest (Oculus), or through a Web browser on a desktop. The operator logged into Spatial through the app installed on the OST-HMD (Fig 3), and the proctor did this through the office desktop. The Spatial software is not

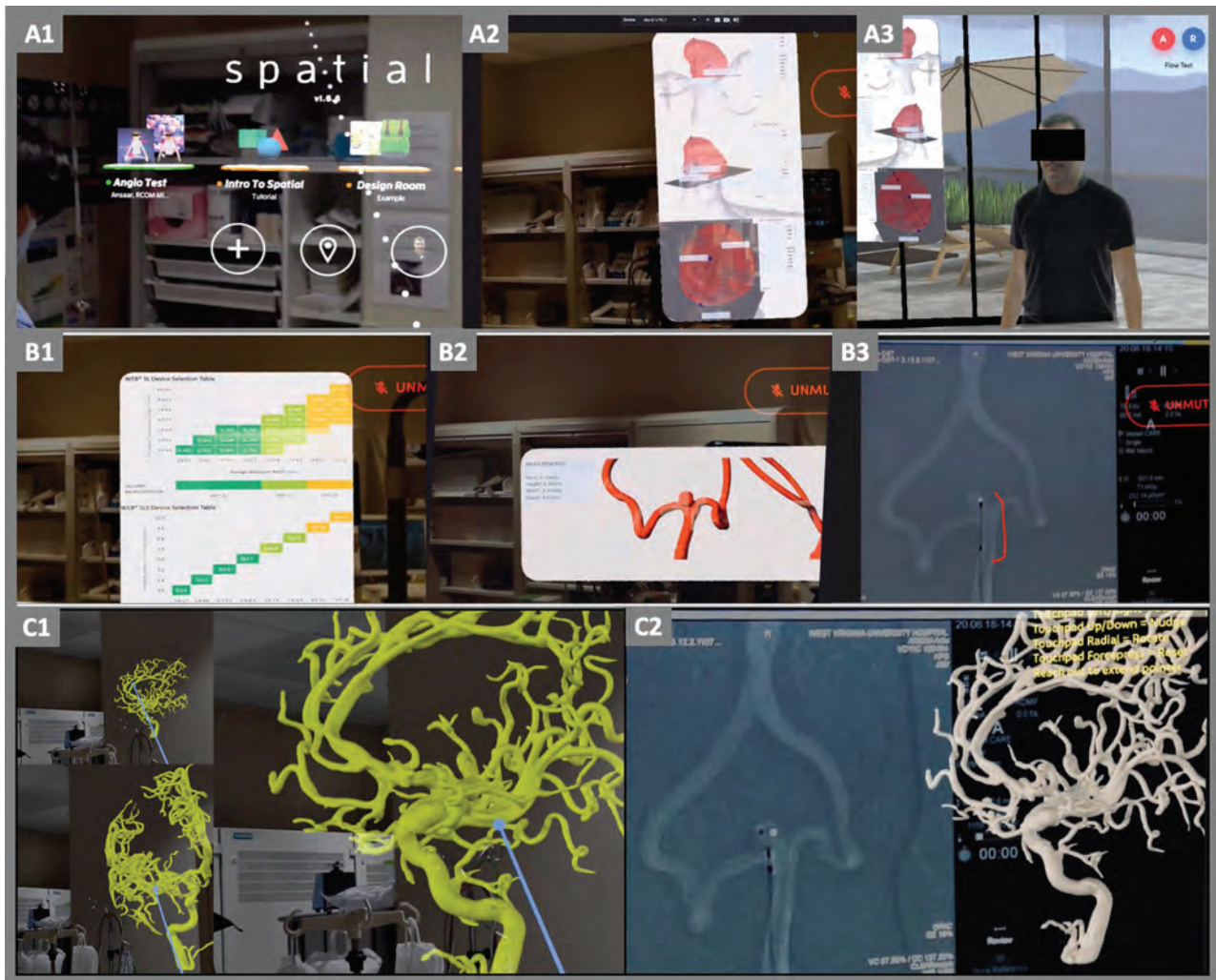


FIG 3. Virtual space sharing and mixed reality. The images in this figure are screenshots from the proctor's computer livestreamed from the operator in the angiography suite. The *upper panel* shows a view through the operator's headset as displayed on the proctor's computer. It shows the operator logging into the Spatial app (A1). The proctor has displayed an image regarding aneurysm size and morphology in the operator's visual field at about 10 o'clock (A2) using the Spatial app and the same image with the operator's avatar looking at it in the virtual room created on the app. The *middle panel* shows a WEB-sizing chart (B1), 3D image of the aneurysm flow model (B2), and an angiography image annotated by the proctor defining the WEB device (B3). The *lower panel* shows a 3D model of another aneurysm showing that the operator can manipulate and anchor in his FOV as a reference to be used when necessary.

Health Insurance Portability and Accountability Act-compliant. A virtual "room" was created that both the operator and the proctor could access. The purpose of space sharing was for the proctor to "drop" images in the operator's FOV. For example, These images could be screenshots of the angiography monitor annotating procedural aspects, a 3D model of the aneurysm highlighting a specific aspect or data regarding the neurovascular device such as measurements (Fig 3). The images could be placed anywhere in the operator's FOV so as not to hinder the primary view of the angiography monitor. Typically, if the angiography monitor is in the operator's 12 o'clock view (directly ahead when the operator is performing and facing the monitor), the virtual images were placed at 10 o'clock or 2 o'clock (Fig 3) and the operator could review with slight head turning. The app created an avatar of the operator and displayed it in the virtual room. The avatar followed the head position of the operator

and displayed it in the virtual room on the proctor's computer. The avatar was used to evaluate the full scope of possibilities for virtual space sharing; however, the avatar was not critical for conducting the remote proctoring. The proctor could thus follow the operator's head movements via the avatar displayed in the virtual room (Fig 3).

Communication

The OST-HMD contains a speaker and a microphone through which the operator could communicate with the proctor. The proctor used his desktop microphone. The communication was conducted via the virtual room using the space-sharing app (Spatial).

Latency

The latency between the operator visualizing an object through the OST-HMD and its livestream to the proctor's computer was tested

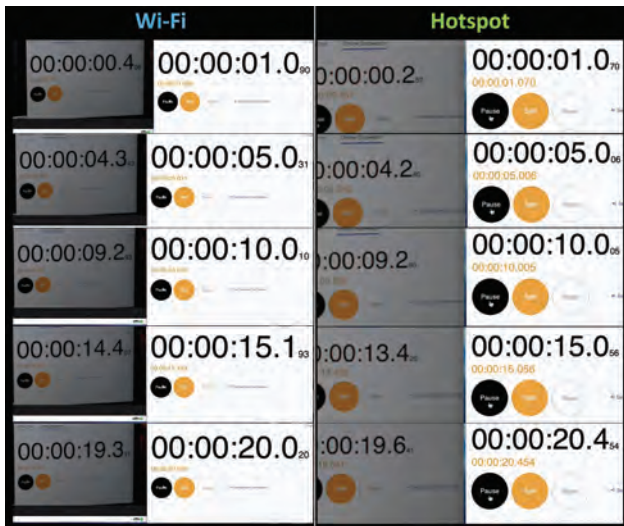
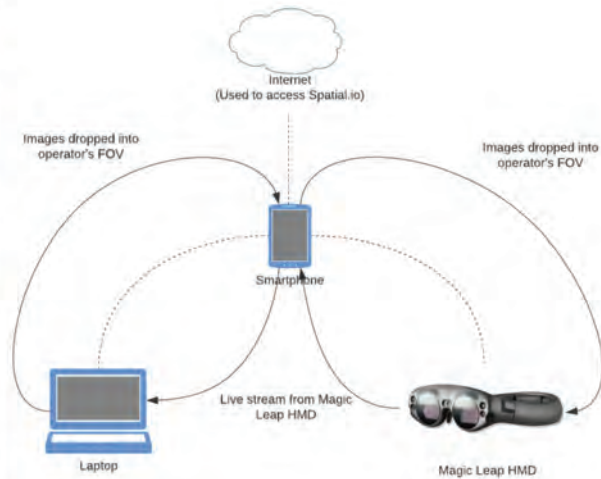


FIG 4. Latency test. Screenshots from the latency test recordings for the Wi-Fi and hotspot networks at 1, 5, 10, 15, and 20 seconds are displayed. Three recordings were made for each network, yielding 15 measurements each. The *left panel* demonstrates livestreaming directly over the Wi-Fi network. These show a side-by-side display of the stopwatch running on the computer and a livestreamed image of the stopwatch through the OST-HMD (Magic Leap-1) next to it. The *right panel* shows the same display when using the hotspot. The difference in time between the computer stopwatch and its livestreamed image constitutes the latency in milliseconds. The graphic scheme next to the screenshots shows the different components in the stream that can impact the latency.



using a digital stopwatch displayed on the computer. The operator observed the stopwatch using the OST-HMD, which streamed it back to the computer that was displaying the running stopwatch. The live and streamed stopwatches were displayed side by side, and the computer screen was recorded for 20 seconds. The recording could then be viewed and paused to observe the duration displayed on the live and streamed stopwatches, allowing calculation of the time difference. Five measurements were made at 1, 5, 10, 15, and 20 seconds, and this was repeated 3 times each for both the hotspot and Wi-Fi networks, yielding 15 latency calculations each (Fig 4).

RESULTS

A flow model of a basilar apex aneurysm was used for the experiment. On the basis of the aneurysm measurements, an appropriately sized WEB device was selected. A Via-21 microcatheter (MicroVention) was placed in the aneurysm. The operator who had never used the WEB device before wore the OST-HMD. Although the eyewear device-calibration process includes a user-specific procedure to improve comfort and eye-tracking performance, this procedure was not deemed necessary because the applications used do not enable eye-tracking. The “spatial computer” was strapped over the shoulder (Fig 1). Apart from the operator, a vendor representative to manage the flow model and another neurointerventional physician were present in the angiography suite to monitor the progress and act as a backup. A secure connection was established between the OST-HMD and the laptop in the angiography suite for device-streaming. Calibration of the OST-HMD using the angiography screen was performed to center the image in its FOV while the operator was wearing it and stream it to the laptop. Once the image was centered, the operator secured the OST-HMD in place using the adjustments on the headset. The Zoom link was successfully activated using the hotspot to stream the operator’s FOV to the proctor’s computer in

the adjacent building and also to a media engineer in another city. The operator logged into the virtual space-sharing application (Spatial) through the OST-HMD, and the proctor and the media engineer did the same on their respective computers. The proctor could view the operator’s avatar in the virtual room (Fig 3). The proctor communicated with the operator via the headset and proceeded to instruct the WEB deployment. The proctor could view the operator’s FOV whether looking at the angiography monitor or the table (Fig 3). The proctor could ask the operator to look at his hands and advise on appropriate hand positioning and technique for device insertion and advancement. During the procedure, the proctor also displayed a WEB-sizing chart, aneurysm morphology, and annotated angiography images in the operator’s FOV in predesignated spaces (Fig 3). If required, the operator could manipulate the dropped images, ie, move or magnify using the hand controller. The operator deployed the WEB device successfully without detaching. The device was resheathed and redeployed several times with the proctor observing and advising.

This experiment was then repeated using the Wi-Fi network with the operator livestreaming directly from the headset to the proctor’s computer. For this experiment, the virtual space-sharing application was not used, and the proctor instructed the operator on the basis of livestream communication through the OST-HMD.

The latency between visualizing an image through the headset and its display on the computer was 0.71 (SD, .03) seconds over the Wi-Fi and 0.86 (SD, 0.3) seconds over the hotspot ($P = .02$). Subjectively, the quality of the livestream was also smoother over the Wi-Fi compared with the hotspot, which had infrequent-but-noticeable pixilation of the images.

DISCUSSION

The overarching goal of the experiment was to create a teleproctoring environment that mimicked reality. A proctor typically

stands behind or next to the operator in the angiography suite. Guidance is in the form of verbal cues and occasionally pointing out elements on the monitor or the operating table. The operator's hands are occupied manipulating the catheters and devices while the eyes are focused on the screen and the ears tuned to the proctor. We wanted to maintain these relationships and define these concepts before choosing the setup. An OST-HMD seemed to satisfy these requirements by allowing the proctor to see what the operator was seeing, by allowing clear communications, and, most important, using mixed reality to display images or annotations in the operator's FOV without obstructing it, while the operator maintained his posture, ie, hands on the device and eyes on the screen. The system as tested using currently available off-the-shelf components met these objectives. The only tool not commercially available was the livestreaming functionality of Magic Leap, which is currently only accessible as a developer beta application. Livestreaming an environment or even a first-person view by itself is not novel, but the ability to interact in that visual space is the differentiating feature for this study. Even though we used Magic Leap for this experiment, the capability of virtually interacting in the wearer's visual field is not limited to Magic Leap, and other optical platforms allow similar interactions.

We identified several aspects that are suboptimal in the current configuration and constitute substantial areas for improvement. The first is image stabilization of the livestream. If the operator moves his or her head suddenly, it will cause a jerky imaging stream. This is because the cameras and sensors on the head-mounted display track not just the wearer's eyes but are also affected by head movement. Some of this issue can be offset by practice and awareness of head movements, but the more reliable way is through technology. A discourse on the technical methodologies to improve stability of the livestream is beyond the scope of the current study, and the reader is directed to the US patent office Web site where considerable interest in this direction is evident (<https://www.usa.gov/federal-agencies/u-s-patent-and-trademark-office>).

The headset has to be light and comfortable to avoid strain and operator fatigue. The Magic Leap-1 solves this requirement by separating the computing platform from the OST-HMD to make the headset lighter. Because it is snug on the face, it cannot be worn by an operator wearing glasses and requires prescription inserts that click into the headset. There is extensive ongoing research and development into making these devices more portable and realistic. All of the leading tech companies have programs focused on mixed-reality, wearable, visual devices with iterations geared toward ease of use, seamless blending of augmented reality, smooth eye-tracking, and superfast image-processing.

The second key requirement for this concept to work is a smooth, continuous, jitter-free livestream from the operator to the proctor and an equally swift and seamless display of the proctor's mixed-reality interactions in the operator's visual field. We used a commercial hotspot and a standard internal Wi-Fi network for the experiment because our goal was to test the most easily available and least complex methods. This use also sets the lowest bar for a network, and anything over it would be an improvement. The latency was lower over the Wi-Fi, which could be expected, but it needs to be much lower for mainstream

applications. Different hospital systems have different networks, and generally, it is cumbersome to interface with these. A medium that resides outside these networks may have better acceptability and standardization than one that has to interface with an institution's informatics outfit. Our latency over the Wi-Fi from OST-HMD to the computer was 700 ms; interactive games have latencies that vary between 100 and 1000 ms.¹⁹ While we evaluated total latency times, ie, from object visualization via OST-HMD to its display on the remote computer, there are several elements within the latency pipeline (Fig 4), including the capacity of the hardware to process and transmit images that affect this performance that were not tested, thus a limitation of the experiment. Another limitation is that we did not use network packet measurements to test latency, which would be important to incorporate in future testing. Lowering latency has been an area of active research and development. Latencies up to 500 ms were considered adequate in 1 article evaluating the impact of latency on completing surgical tasks using remote robotic-assisted surgery.²⁰ Our latency was around 700 ms over the Wi-Fi network, which can certainly be improved, but we were testing only the latency for streaming and not remote robotic operations. For teleproctoring applications, ultra-reliable and low-latency communications-specific²¹ content delivery networks²² and many other technical innovations can improve performance and reliability.

We did not test security and used devices with end-to-end encryption, but with all the advances in telehealth,^{23,24} we do not consider this is a major limiting step. Widespread adoption, however, will require assessing and addressing data and privacy concerns for the regulatory authorities. The current interest in robotic neurovascular interventions^{25,26} offers the tantalizing possibility of merging remote proctoring with robotics to project expertise across distances. Other advances in hologram technologies^{27,28} can even put the proctor virtually in the operating room with an operator. Similarly, wearable skin-stretch hand or finger devices incorporating haptic feedback,²⁹⁻³¹ with the ability to stream that feel to a proctor, add another dimension to what is possible by bringing technology together to build the concept of remote proctoring.

CONCLUSIONS

The investigation in this article explores and demonstrates the concept of remote proctoring using commercially available tools. The proctor could visualize the operator's visual field and, more critically, could virtually interact in that field by annotating images and dropping content without disrupting the workflow. Portability of equipment was a key requirement of the experiment, highlighted using an optical see-through display. We identified certain areas that require improvement and reviewed the literature showing that there is active work in key technologic areas that can enhance this concept. In the future, further incorporation of technologies aimed at distance-immersive interactions will make these experiences very realistic. Necessity is the mother of invention, and the current pandemic has exposed the need to conduct all aspects of our lives remotely, spawning industries and ventures geared toward solving that need.

Disclosures: Ansaar T. Rai—RELATED: Consulting Fee or Honorarium: Stryker Neurovascular, MicroVention, Cerenovus; UNRELATED: Consultancy: Stryker

Neurovascular, MicroVention, Cerenovus; *Payment for Lectures Including Service on Speakers Bureaus*: MicroVention, Stryker Neurovascular; *Payment for Development of Educational Presentations*: Stryker Neurovascular, MicroVention. Gerard Deib—UNRELATED: *Employment*: West Virginia University. SoHyun Boo—UNRELATED: *Consultancy*: MicroVention, *Comments*: proctor for WEB embolization device providing consultation for new device users as mandated by the FDA; invited to educational speaking engagements.

REFERENCES

- Ballantyne GH. **Robotic surgery, telerobotic surgery, telepresence, and telementoring: review of early clinical results.** *Surg Endosc* 2002;16:1389–402 CrossRef Medline
- Rassweiler J, Frede T. **Robotics, telesurgery and telementoring—their position in modern urological laparoscopy.** *Arch Esp Urol* 2002;55:610–28. *Arch Esp Urol* Medline
- Smith CD, Skandalakis JE. **Remote presence proctoring by using a wireless remote-control videoconferencing system.** *Surg Innov* 2005;12:139–43 CrossRef Medline
- Goel SS, Greenbaum AB, Patel A, et al. **Role of teleproctoring in challenging and innovative structural interventions amid the COVID-19 pandemic and beyond.** *JACC Cardiovasc Interv* 2020;13:1945–48 CrossRef Medline
- Datta N, MacQueen IT, Schroeder AD, et al. **Wearable technology for global surgical teleproctoring.** *J Surg Educ* 2015;72:1290–95 CrossRef Medline
- Williams MA, McVeigh J, Handa AI, et al. **Augmented reality in surgical training: a systematic review.** *Postgrad Med J* 2020;96:537–42 CrossRef Medline
- Hiranaka T, Nakanishi Y, Fujishiro T, et al. **The use of Smart Glasses for surgical video streaming.** *Surg Innov* 2017;24:151–54 CrossRef Medline
- García-Cruz E, Bretonnet A, Alcaraz A. **Testing Smart Glasses in urology: clinical and surgical potential applications.** *Actas Urol Esp* 2018;42:207–11 CrossRef Medline
- Carrera JF, Wang CC, Clark W, et al. **A systematic review of the use of Google Glass in Graduate Medical Education.** *J Grad Med Educ* 2019;11:637–48 CrossRef Medline
- Kulak O, Drobysheva A, Wick N, et al. **Smart Glasses as a surgical pathology grossing tool.** *Arch Pathol Lab Med* 2020 Jul 27. [Epub ahead of print] CrossRef Medline
- Mitrasinovic S, Camacho E, Trivedi N, et al. **Clinical and surgical applications of Smart Glasses.** *Technol Health Care* 2015;23:381–401 CrossRef Medline
- Deib G, Johnson A, Unberath M, et al. **Image guided percutaneous spine procedures using an optical see-through head mounted display: proof of concept and rationale.** *J Neurointerv Surg* 2018;10:1187–91 CrossRef Medline
- García-Vázquez V, von Haxthausen F, Jäckle S, et al. **Navigation and visualisation with HoloLens in endovascular aortic repair.** *Innov Surg Sci* 2018;3:167–77 CrossRef Medline
- Hanna MG, Ahmed I, Nine J, et al. **Augmented reality technology using microsoft HoloLens in anatomic pathology.** *Arch Pathol Lab Med* 2018;142:638–44 CrossRef Medline
- Amini S, Kersten-Oertel M. **Augmented reality mastectomy surgical planning prototype using the HoloLens template for healthcare technology letters.** *Healthc Technol Lett* 2019;6:261–65 CrossRef Medline
- Mitsuno D, Ueda K, Hirota Y, et al. **Effective application of mixed reality device HoloLens: simple manual alignment of surgical field and holograms.** *Plast Reconstr Surg* 2019;143:647–51 CrossRef Medline
- Al Janabi HF, Aydin A, Palaneer S, et al. **Effectiveness of the HoloLens mixed-reality headset in minimally invasive surgery: a simulation-based feasibility study.** *Surg Endosc* 2020;34:1143–49 CrossRef Medline
- Xia H, Chen T, Hu C, et al. **Recent advances of the polymer micro/nanofiber fluorescence waveguide.** *Polymers* 2018;10: 1086 CrossRef Medline
- Kay R. **Pragmatic Network Latency Engineering Fundamental Facts and Analysis.** cPacket Networks, White Paper. 2009;1–31. <https://docplayer.net/3464921-Pragmatic-network-latency-engineering-fundamental-facts-and-analysis.html>. Accessed December 23, 2020
- Anvari M, Broderick T, Stein H, et al. **The impact of latency on surgical precision and task completion during robotic-assisted remote telepresence surgery.** *Comput Aided Surg* 2005;10:93–99 CrossRef Medline
- She C, Chen Z, Yang C, et al. **Improving network availability of ultra-reliable and low-latency communications with multi-connectivity.** *IEEE Trans Commun* 2018;66:5482–96 CrossRef
- Farber DA, Greer RE, Swart AD, et al. **Internet content delivery network: Google Patents;** 2003. <https://patents.google.com/patent/US6654807B2/en>. Accessed December 23, 2020
- Parisien LR, Shin M, Constant M, et al. **Telehealth utilization in response to the novel coronavirus (COVID-19) pandemic in orthopaedic surgery.** *J Am Acad Orthop Surg* 2020;28:e487–92 CrossRef Medline
- Ben-Zeev D. **The digital mental health genie is out of the bottle.** *Psychiatr Serv* 2020;71:1212–13 CrossRef Medline
- Nogueira RG, Sachdeva R, Al-Bayati AR, et al. **Robotic assisted carotid artery stenting for the treatment of symptomatic carotid disease: technical feasibility and preliminary results.** *J Neurointerv Surg* 2020;12:341–44 CrossRef Medline
- Mendes Pereira V, Cancelliere NM, Nicholson P, et al. **First-in-human, robotic-assisted neuroendovascular intervention.** *J Neurointerv Surg* 2020;12:338–40 CrossRef Medline
- Neves CA, Vaisbuch Y, Leuze C, et al. **Application of holographic augmented reality for external approaches to the frontal sinus.** *Int Forum Allergy Rhinol* 2020;10:920–25 CrossRef Medline
- Moro C, Phelps C, Jones D, et al. **Using holograms to enhance learning in health sciences and medicine.** *Med Sci Educ* 2020;30:1351–52 CrossRef Medline
- Chossat JB, Chen DKY, Park YL, et al. **Soft wearable skin-stretch device for haptic feedback using twisted and coiled polymer actuators.** *IEEE Trans Haptics* 2019;12:521–32 CrossRef Medline
- Maisto M, Pacchierotti C, Chinello F, et al. **Evaluation of wearable haptic systems for the fingers in augmented reality applications.** *IEEE Trans Haptics* 2017;10:511–22 CrossRef Medline
- Cosco F, Garre C, Bruno F, et al. **Visuo-haptic mixed reality with unobstructed tool-hand integration.** *IEEE Trans Vis Comput Graph* 2013;19:159–72 CrossRef Medline

Delayed Contrast-Enhanced MR Angiography for the Assessment of Internal Carotid Bulb Patency in the Context of Acute Ischemic Stroke: An Accuracy, Interrater, and Intrarater Agreement Study

W. Boisseau, A. Benaissa, R. Fahed, J.-L. Amegnizin, S. Smajda, S. Benadjaoud, A.M. Benadjaoud, L. Saint-Val, Q. Alias, P. Iorio, S. Yang, K. Zuber, E. Kalsoum, and J. Hodel



ABSTRACT

BACKGROUND AND PURPOSE: CTA has shown limited accuracy and reliability in distinguishing tandem occlusions and pseudo-occlusions on initial acute stroke imaging. The utility of early and delayed contrast-enhanced MRA in this setting is unknown. We aimed to assess the accuracy and reliability of early and delayed contrast-enhanced MRA for carotid bulb patency in patients with acute ischemic stroke.

MATERIALS AND METHODS: We retrospectively reviewed patients who had ICA occlusion and underwent thrombectomy with pre-procedural early and delayed contrast-enhanced MRA in a single comprehensive stroke center. During 2 sessions, 10 raters independently assessed 32 cases with early contrast-enhanced MRA (with an additional delayed contrast-enhanced MRA sequence during the second reading session). Their judgments were compared with DSA as a reference standard. Accuracy and interrater agreement were measured. Five raters undertook a third reading session to assess intrarater agreement.

RESULTS: Accuracy for the assessment of carotid bulb patency with early contrast-enhanced MRA was limited (69%; 95% CI, 59%–79%), with moderate interrater agreement ($\kappa = 0.42$; 95% CI, 0.27–0.55). The second reading with an additional delayed contrast-enhanced MRA sequence improved both accuracy (82%; 95% CI, 73%–91%; $P < .001$) (raters corrected 43%–77% of incorrect diagnoses with early contrast-enhanced MRA alone; mean = 59%) and interrater agreement ($\kappa = 0.56$; 95% CI, 0.41–0.73; $P = .07$). Intrarater agreement was almost perfect, substantial, and moderate for 3, 1, and 1 raters.

CONCLUSIONS: Early contrast-enhanced MRA has limited accuracy and repeatability for the evaluation of carotid bulb patency in acute ischemic stroke. The additional delayed contrast-enhanced MRA sequence may improve accuracy and reliability.

ABBREVIATIONS: AIS = acute ischemic stroke; CE = contrast-enhanced; PO = pseudo-occlusion

Several trials have demonstrated the benefit of mechanical thrombectomy in acute ischemic stroke (AIS) with anterior circulation large-vessel occlusion¹ depicted by noninvasive intracranial vascular imaging (CTA or MRA). However, in case of tandem occlusion (ie, an ICA occlusion with an intracranial large-vessel

occlusion), there remains uncertainty regarding the optimal management of the carotid bulb lesion,² and the benefits of acute angioplasty/stent placement are controversial.^{3,4} Randomized controlled trials are needed to determine the best strategy and will thus require an accurate and repeatable noninvasive imaging method to select patients with an intracranial large-vessel occlusion and an additional carotid bulb occlusion,⁵ which will typically appear as an absence of visualization of the whole symptomatic carotid artery from the bulb.

However, in AIS, a single, large clot located above the ICA bulb can impede contrast ascension from the common carotid artery, leading to a false image of bulbar occlusion, an entity called ICA pseudo-occlusion (PO).^{6–9} It can, thus, be challenging to distinguish tandem occlusions and POs on initial acute stroke imaging. A previous study has shown limited accuracy and reliability of CTA for this task.¹⁰ CTA might thus be limited for the detection of tandem occlusions, whether in clinical routine (for

Received May 21, 2020; accepted after revision December 21.

From the Department of Neuroradiology (W.B., A.B., J.-L.A., S.B., L.S.-V., Q.A., P.I., S.Y., E.K.), Centre-Hospitalier-Universitaire Henri Mondor, Créteil, France; Department of Interventional Neuroradiology (R.F., S.S.) and Clinical Research Unit (K.Z.), Fondation Ophthalmologique Adolphe de Rothschild, Paris, France; Department of Radiology, (J.H.), Groupe-Hospitalier-Paris-Saint-Joseph, Paris, France; and Department of Radiobiology and Epidemiology (A.M.B.), Institute for Radiological Protection and Nuclear Safety, Fontenay-Aux-Roses, France.

Please address correspondence to William Boisseau, MD, Henri Mondor Hospital, Department of Neuroradiology, 51, Ave du Maréchal de Lattre de Tassigny, 94010 Créteil, France; e-mail: boisseau.william@gmail.com

Indicates article with online supplemental data.

<http://dx.doi.org/10.3174/ajnr.A7054>

endovascular management planning) or in research settings (for patient selection in a randomized controlled trial).

MR imaging offers several interesting features for acute stroke imaging and decision-making, including a high sensitivity for the detection of early ischemic lesions¹¹ and the ability to detect stroke mimics¹² and identify patients who will benefit from reperfusion therapy in case of unknown onset stroke.¹³ Noninvasive vascular imaging can then be performed with MRA: The TOF sequence is usually performed for the depiction of intracranial large-vessel occlusion, and early contrast-enhanced MRA (CE-MRA), for the assessment of the complete supra-aortic vasculature. As with CTA, cases with an intraluminal filling defect of the bulb on ICA on the stroke side might correspond to either a tandem occlusion or a PO. Delayed acquisition after gadolinium injection (delayed CE-MRA) might overcome this issue, but CE-MRA performance has not been thoroughly studied in this setting.

In this study, we aimed to assess the accuracy and reliability of early and delayed CE-MRA for the assessment of carotid bulb patency in patients with AIS.

MATERIALS AND METHODS

The local ethics committee (Centre Hospitalo-Universitaire Henri Mondor, Créteil) approved the study protocol and waived written informed consent. This study was prepared in accordance with the Standards for Reporting of Diagnostic Accuracy studies¹⁴ and the Guidelines for Reporting Reliability and Agreement Studies.¹⁵

Patients

We reviewed a prospectively collected endovascular data base in a single comprehensive stroke center between September 2016 and April 2018. We identified patients who underwent endovascular thrombectomy for AIS of the anterior circulation and in whom DSA showed occlusion of the ICA (at any level) on the symptomatic side. We excluded patients with other occlusion sites (such as isolated middle cerebral artery or posterior circulation occlusions) and patients who did not undergo MR imaging with early and additional delayed CE-MRA. The number of cases in the present study ($n = 32$) was superior to the recommendations of Donner and Rotondi¹⁶ for agreement studies.

Reference Standard

DSA was the reference standard for this study, similar to that in a previous study.¹⁰ Two interventional neuroradiologists (with 7 and 10 years of experience in neuroradiology, respectively) reviewed, in consensus, the DSA images obtained during thrombectomy, along with the patient's follow-up imaging and the report from the interventional neuroradiologist who performed the procedure, to determine the location of the occlusion.

DSA was performed with a biplane angiographic system (Axiom Artis dBA; Siemens). Carotid bulb occlusion on DSA was defined as an angiographically viewed obstacle that hindered the passage of contrast agent and/or the guidewire or catheter and the lack of backfilling of the carotid bulb during microcatheter angiography.⁹

In case of suprabulbar occlusion, 2 interventional neuroradiologists indicated the exact occlusion site based on the classification of Gibo et al,¹⁷ dividing the ICA into 4 parts: the cervical, petrous, cavernous, and intracranial portions.

Pseudo-Occlusion

ICA PO was defined as a unilateral intraluminal filling defect from the carotid bulb on the symptomatic side shown on early CE-MRA and in which DSA showed a suprabulbar occlusion.

MR Imaging

For all patients, MR imaging was performed at the same care center as thrombectomy. MRA examinations were performed at 3T (Magnetom Skyra; Siemens), including DWI, T2 FLAIR, SWI, and TOF-MRA.

When required, intravenous thrombolysis was directly initiated in the MR imaging scanner after these 4 sequences and before the acquisition of CE-MRA. Early CE-MRA was acquired after an intravenous injection of gadolinium-based contrast agent. A delayed CE-MRA acquisition was initiated immediately after the early CE-MRA sequence (without further contrast agent administration). This acquisition protocol resulted in fixed amount of time between gadolinium injection and CE-MRA acquisitions. Acquisition parameters of early and delayed CE-MRA are detailed in the Online Supplemental Data.

Raters

All raters were radiologists experienced in neurovascular imaging. Ten raters from 2 institutions, including 5 neuroradiologists and 5 interventional neuroradiologists with various levels of experience (detailed in the Online Supplemental Data) participated in the present study.

Readings

The MR imaging studies were first anonymized and uploaded in the PACS. Raters had no access to other imaging studies or clinical information other than sex, age, symptoms (ie, left or right motor deficit, aphasia), the initial NIHSS score, the time of symptom onset (when available), and the time of the brain MR imaging examination. Each rater performed 2 independent readings as follows: During the first reading, DWI, FLAIR, SWI, TOF-MRA and early CE-MRA were provided; during the second reading (performed 1 month later in a different order), an additional delayed CE-MRA sequence was provided for each patient.

For each case, raters indicated whether there was an occlusion of the ICA at the bulb level. The raters were blinded to the final diagnosis on DSA. Five raters (including 2 neuroradiologists and 3 interventional neuroradiologists) performed a third reading session (similar to the second one), at least 1 month later, to evaluate intrarater agreement.

Statistical Analysis

Mean [SD] was calculated for continuous variables, and frequency was reported for categorical variables. Sensitivity, specificity, and accuracy rates were calculated for each rater using 2×2 contingency tables. Group and subgroup validation parameters were calculated using mean sensitivity, specificity, and accuracy.

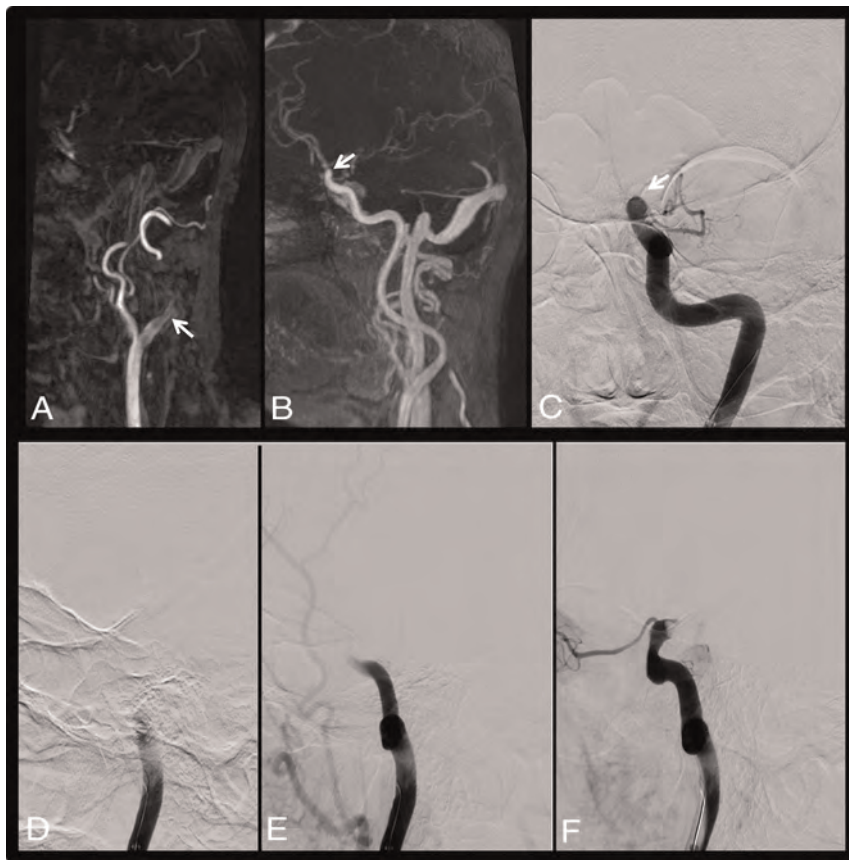


FIG 1. Case 10. The patient presented 2 hours after acute onset of right-sided hemiparesis and aphasia (NIHSS score of 24). Early CE-MRA (A) shows an intraluminal filling defect of the left proximal bulb ICA. Delayed CE-MRA (B) shows opacification of the left carotid artery up to the terminal ICA. DSA with selective catheterization of the left ICA confirms distal occlusion of the ICA (C, frontal DSA) with slow progression of iodine contrast (PO) (D–F, lateral DSA). White arrows indicates the occlusion site.

Interrater and intrarater agreement for the diagnosis of an ICA bulb occlusion was measured using Fleiss κ statistics with 95% bias-corrected and accelerated confidence intervals obtained by 10,000 bootstrap resampling.¹⁸ The κ comparison inference was conducted according to the method described by Vanbelle and Albert.¹⁹

All analyses were performed with R statistical and computing software, Version 3.3.2 (<http://www.r-project.org/>) and a significance level of 5%. Slight, fair, moderate, and substantial agreement categories were reported according to Landis and Koch.²⁰

RESULTS

Patients

A total of 176 consecutive patients with AIS were treated by mechanical thrombectomy at our institution between September 2016 and April 2018. Among them, 102 patients with an isolated middle cerebral artery occlusion, 21 with vertebrobasilar artery occlusion, and 2 patients who did not receive endovascular treatment (because of catheterization failure) were excluded. Among the 51 remaining patients, 9 patients underwent CTA and 10 patients a early without delayed-phase CE-MRA were also excluded. The remaining 32 patients were thus included in the present study.

Patients' clinical, radiologic, and treatment characteristics are presented in the Online Supplemental Data. On the basis of DSA (reference standard), among the 32 patients, 6 patients had an isolated carotid bulb occlusion and 26 had a suprabulbar occlusion (5 with cervical, 2 with petrous, 3 with cavernous, and 16 with terminus occlusions). Among these same 26 patients, 8 patients had a radiologic pattern of PO (defined as a unilateral intraluminal filling defect from the carotid bulb on the symptomatic side shown with early CE-MRA, while DSA showed a patent bulb with a suprabulbar occlusion).

Illustrative cases of PO on CE-MRA and DSA are shown in Figs 1 and 2. Additional cases are shown in the Online Supplemental Data.

Accuracy Study Results for the Assessment of Internal Carotid Bulb Patency

The assessment of internal carotid bulb patency using early CE-MRA alone (first reading) or with additional delayed CE-MRA (second reading) for all 10 raters is graphically displayed in the Online Supplemental Data. Accuracy parameters (sensitivity, specificity, and accuracy) are detailed in the Table. Graphic representations of the accuracy of each

rater for the first, second, and third reading sessions are shown in Fig 3.

During the first reading session, raters' accuracy for the diagnosis of carotid bulb occlusion ranged between 59% and 79% (mean accuracy, 69%; 95% CI, 59%–79%). Sensitivity rates ranged between 33% and 83% (mean sensitivity, 70%; 95% CI, 33%–83%), whereas specificity rates ranged between 50% and 92% (mean specificity, 68%; 95% CI, 50%–92%). No rater achieved 100% sensitivity, ie, no rater correctly identified all patients with a carotid bulb occlusion. The number of erroneous diagnoses (compared with DSA as the reference standard) ranged between 12.5% and 47% among raters (mean, 31%).

The second reading session (with access to an additional delayed CE-MRA sequence) improved accuracy for 9/10 raters (90%), now ranging between 73% and 91% (mean accuracy, 82%; 95% CI, 73%–91%; $P < .001$). For the last rater (rater 5), accuracy was identical during the first and second readings. Sensitivity was improved for 6/10 raters (including 5 raters with 100% sensitivity) and ranged between 67% and 100% (mean sensitivity, 87%; 95% CI, 67%–100%). Specificity was improved for 7/10 raters and ranged between 65% and 88% (mean specificity, 80%; 95% CI, 65%–88%). During this second reading session with access to

delayed CE-MRA, raters corrected 43%–77% of incorrect diagnoses from the previous reading session (mean, 59%), while they erroneously modified 0%–20% of previously correct diagnoses (mean, 8%). Despite the use of additional delayed CE-MRA, most raters (>5/10) continued to provide incorrect diagnoses in 6/32 cases (18.7%) exclusively, by misdiagnosing ICA PO as a bulb occlusion: In 3/6 cases, DSA revealed a preocclusive stenosis of the carotid bulb associated with an intracranial ICA occlusion.



FIG 2. Case 19. This patient with unknown stroke onset presented with left-side hemiplegia and aphasia (NIHSS score of 20). Early CE-MRA (A) shows an intraluminal filling defect of the right proximal bulb ICA. Delayed CE-MRA (B) shows opacification of the right carotid artery up to the terminal ICA. DSA confirms distal occlusion of the right ICA (C, lateral DSA) and the absence of critical stenosis at the proximal ICA (D, lateral DSA). White arrows indicates the occlusion site.

In the 3 remaining cases, the quality of delayed CE-MRA was poor due to movement artifacts.

Interrater Agreement

Interrater agreement regarding the diagnosis of carotid bulb patency on early CE-MRA is shown in the Table and Fig 4A. Interrater agreement was moderate for all raters ($\kappa = 0.41$; 95% CI, 0.27–0.55), without significant differences between junior and senior raters. In 7/32 cases (22%), all raters agreed on the presence/absence of a carotid bulb occlusion. Interrater agreement during the second reading session (with access to delayed CE-MRA) was improved ($\kappa = 0.56$; 95% CI, 0.41–0.73) (Fig 4A) ($P = .07$): In 17/32 cases (47%), all raters agreed on the presence/absence of a carotid bulb occlusion.

Intrarater Agreement

Intrarater agreement study results are shown in the Online Supplemental Data and Fig 4B. Intrarater agreement was at least substantial for 4/5 raters, including 2 raters with a perfect intrarater agreement ($\kappa = 1.0$). Compared with the second reading session, accuracy performance during the third reading session was unchanged for 3/5 raters, improved for 1 rater, and decreased for 1 rater (but still improved compared with the first reading session).

DISCUSSION

This is, to our knowledge, the first study addressing the diagnostic accuracy and reliability of CE-MRA for the assessment of carotid bulb patency in patients with acute ischemic stroke. Our study demonstrates a limited accuracy and agreement for the diagnosis of internal carotid bulb occlusion with early CE-MRA compared with the reference DSA. The addition of delayed CE-MRA to our comprehensive MR imaging protocol improved both accuracy and interrater agreement.

ICA PO is a relatively common entity in case of acute terminal ICA occlusion, occurring in about 11%–46% of cases.^{6–9} The prevalence of ICA PO in our cohort (according to the reference standard DSA) was 8/32 cases (25%), which is in line with results from previous studies.^{6–9} The lack of differentiation between a “true” bulb carotid occlusion and ICA PO could lead to several issues. First, it may alter the inclusion of patients in future trials focusing on the management of tandem occlusions (for example, the ongoing French multicenter prospective randomized Thrombectomy In TANdem Occlusion [TITAN] trial²¹), by falsely enrolling patients with an aspect of tandem occlusion on

Diagnostic accuracy parameters and interrater agreement for the presence of carotid bulb occlusion^a

	Accuracy (%)	Sensitivity (%)	Specificity (%)	Interrater Agreement
All raters (n = 10)				
1st Session, CE-MRA alone	69% (59%–79%)	70% (33%–83%)	68% (50%–92%)	0.41 (0.27–0.55)
2nd Session, additional delayed CE-MRA	82% (73%–91%)	87% (67%–100%)	80% (65%–88%)	0.56 (0.41–0.73)
Senior raters (n = 5)				
1st Session, CE-MRA alone	74% (69%–78%)	67% (33%–83%)	76% (65%–85%)	0.47 (0.27–0.68)
2nd Session, additional delayed CE-MRA	84% (78%–87%)	83% (67%–100%)	84% (81%–88%)	0.57 (0.40–0.76)
Junior raters (n = 5)				
1st Session, CE-MRA alone	63% (53%–87%)	77% (67%–83%)	60% (50%–92%)	0.42 (0.27–0.60)
2nd Session, additional delayed CE-MRA	79% (72%–87%)	90% (67%–100%)	77% (65%–92%)	0.51 (0.33–0.70)

^a Values are presented as percentage or κ value (95% confidence interval).

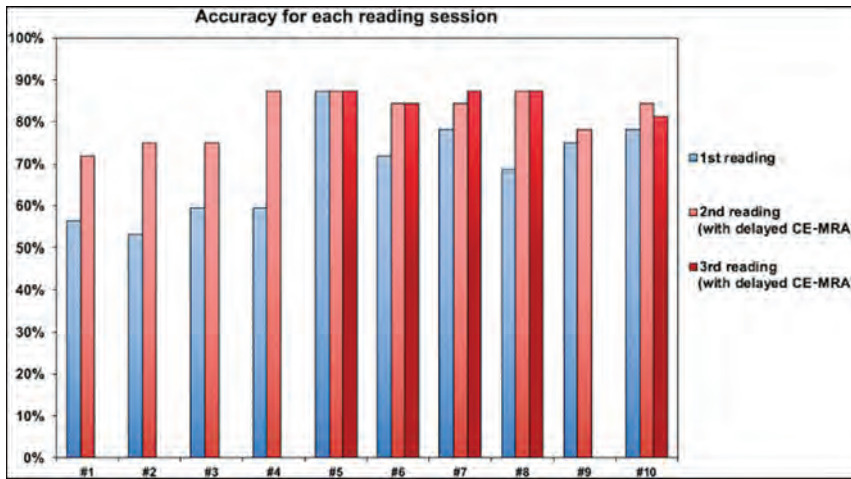


FIG 3. Graphic representation of the accuracy parameters of each rater for the assessment of internal carotid bulb patency for the first, second, and third reading sessions.

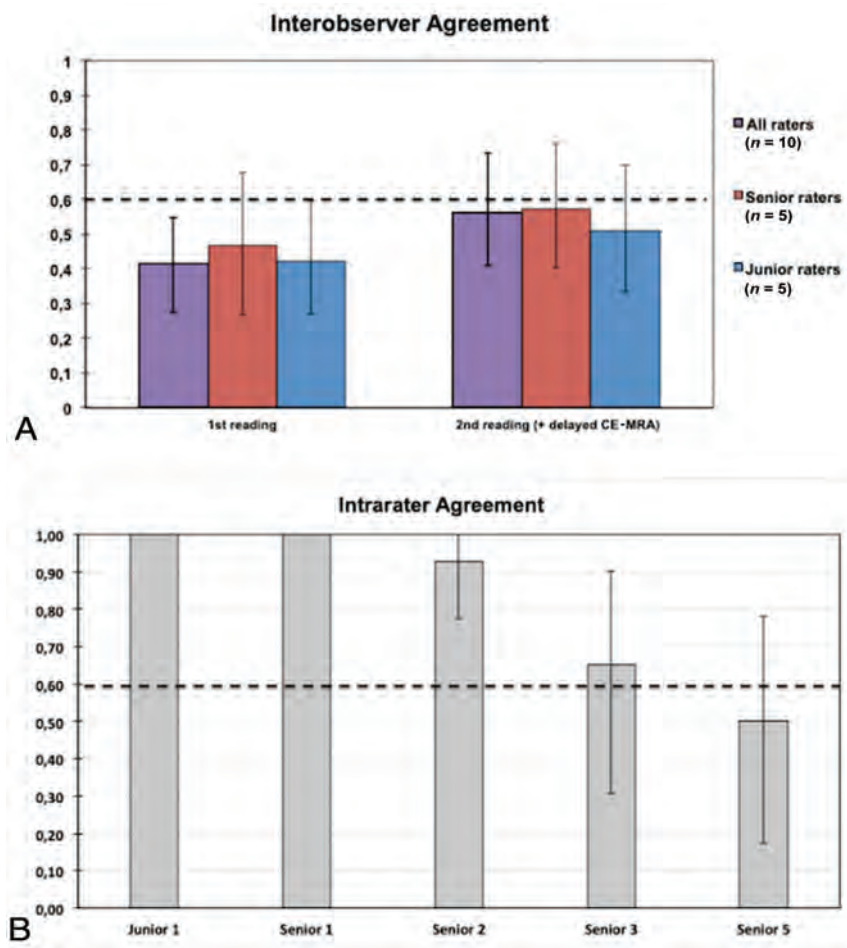


FIG 4. A, Graphic representation of interrater agreement among all raters for the assessment of internal carotid bulb patency with early CE-MRA (first reading session) and with additional delayed CE-MRA (second reading session) (Fleiss κ). B, Graphic representation of intrarater agreement for 5 raters between the second and third reading session (both with access to delayed CE-MRA) (Cohen κ). κ values >0.6 (dotted line) define a "substantial" agreement.

initial noninvasive imaging while showing only an ICA PO on DSA.

Conversely, trials excluding patients with a tandem occlusion might erroneously exclude patients with an isolated intracranial occlusion. This exclusion might have happened in previous mechanical thrombectomy trials: In the Solitaire with the Intention for Thrombectomy as PRiMary Endovascular Treatment (SWIFT PRIME) study,²² for example, patients with a suspicion of extracranial ICA occlusion on initial imaging were excluded. Some of these patients possibly having an ICA PO could explain why the proportion of intracranial ICA occlusions was low in this study (15%)²² compared with other mechanical thrombectomy trials with no such exclusion criterion (for example, 31% in the Endovascular Treatment for Small Core and Proximal Occlusion Ischemic Stroke [ESCAPE] trial²³).

Second, the misdiagnosis of a carotid bulb occlusion instead of an isolated intracranial ICA terminus occlusion might alter the preprocedural management of the patient. According to recent studies, carotid stent placement with antiplatelet therapy seems to be the most effective therapeutic approach for tandem occlusion.^{3,24,25} Moreover, the efficacy of tPA in case of tandem occlusion has been reported to be weak,²⁶ and the association of antiplatelet and tPA in the early phase of AIS is known to increase the risk of hemorrhagic transformation with no additional benefit.²⁷

Given these results, physicians could be tempted to give antithrombotic agents and withhold intravenous thrombolysis because of a suspicion of tandem occlusion while the patients might have a PO. Finally, it may also misguide the operator for procedural planning: Carotid bulb occlusion necessitates specific tools that are not necessary in case of intracranial ICA occlusion such as noncompliant balloons and stents. The optimal management of tandem occlusions for both drugs and devices is still currently unknown, but an accurate and repeatable diagnosis on noninvasive imaging will be necessary in the future to tailor the treatment strategy.

A previous study has shown limited reliability of CTA for the distinction between a tandem occlusion and a PO.¹⁰ To overcome this issue, several studies have tested the utility of delayed-phase CTA.^{7,28-30} Similar to delayed CE-MRA, delayed-phase CTA (with multiphase CTA^{28,29} or 4D-CTA³⁰) improved the accuracy over arterial phase-only acquisitions. However, regarding 4D-CTA, given the limited coverage length acquisition (about 20 mm in thin-thickness reconstruction modes³⁰), only ICA PO with distal intracranial occlusion might be detected. Moreover, the time necessary for image reconstruction may also restrict its use.³⁰ Finally, these techniques also increase overall patient x-ray exposure.³¹

Early CE-MRA could be an alternative imaging technique. However, in our study, it showed a limited accuracy and repeatability for the assessment of carotid bulb patency in patients with acute ischemic stroke. Additional delayed CE-MRA improved both the accuracy and interrater agreement and showed strong intrarater agreement. Moreover, delayed CE-MRA does not need further contrast agent administration and requires little extra time: In our protocol, imaging-acquisition delay for delayed CE-MRA was 43 seconds. Otherwise, a range of techniques, such as compressed sensing and/or denoising techniques, could further reduce this delay.³² Other advanced MR imaging sequences such as high-resolution vessel wall imaging have been reported to accurately differentiate true tandem occlusion and ICA PO.³³ However, given the acquisition time (7 minutes 43 seconds in the study mentioned above³³), this type of sequence does not seem appropriate in the context of acute ischemic stroke. The time spent to perform a brain MR imaging, including postcontrast MRA, is a critical factor for the implementation of this technique in the setting of acute ischemic stroke, which is an absolute emergency. As an example, 8 minutes were necessary for DWI, FLAIR, SWI, and 3D-TOF acquisitions in our protocol. Additional early and delayed CE-MRA requires only 2–3 minutes (including localize sequence acquisitions, bolus-tracking, and the acquisition of the 2 aforementioned sequences). Although this scan duration is slightly longer than CT, a previous study has shown that MR imaging does not significantly change decision-making or impact functional outcome.³⁴

We recognize certain limitations to our study. Our study population included patients scanned with MR imaging, which is not the main imaging technique for the diagnosis of acute ischemic stroke in most centers. Therefore, our findings cannot be extrapolated to centers using CT as first-line imaging. The large number of raters with varying degrees of experience could impact the accuracy of results. However, all raters except one (with identical accuracy during the first and second readings) improved their accuracy with the access to delayed CE-MRA. Greater agreement might have been reached if the readers received standardized training before the reading sessions.

We also cannot exclude the probability that the improved accuracy and interrater agreement during the second reading could be due to a “training effect” from the first reading session; however, the results of each reading session were not disclosed to the readers, so they did not have any feedback to adjust their judgments. Moreover, the second reading session was performed in a different order and at least 1 month later. We also cannot exclude the possibility of cervical clot migration between MRA and DSA

in patients treated with intravenous tPA infusion. However, given the low efficacy of tPA in case of tandem occlusion²⁶ and the short time between MRA and DSA (all patients were managed in a mothership paradigm), we can speculate that this phenomenon is very unlikely to occur. We did not assess the accuracy and reliability of the identification of the underlying cause of each tandem occlusion (dissection, atheroma, other). The etiology might modify the endovascular management,³⁵ and the ability of noninvasive imaging to differentiate each cause necessitates further studies.

CONCLUSIONS

Our study demonstrated a limited accuracy and repeatability for the assessment of carotid bulb patency with early CE-MRA compared with the reference DSA in the context of AIS. The addition of delayed CE-MRA to our comprehensive MR imaging protocol improved both accuracy and reliability in this setting.

REFERENCES

1. Goyal M, Menon BK, van Zwam WH, et al. HERMES Collaborators. **Endovascular thrombectomy after large-vessel ischaemic stroke: a meta-analysis of individual patient data from five randomised trials.** *Lancet* 2016;387:1723–31 CrossRef Medline
2. Jacquin G, Poppe AY, Labrie M, et al. **Lack of consensus among stroke experts on the optimal management of patients with acute tandem occlusion.** *Stroke* 2019;50:1254–56 CrossRef Medline
3. Papanagiotou P, Haussen DC, Turjman F, et al. TITAN Investigators. **Carotid stenting with antithrombotic agents and intracranial thrombectomy leads to the highest recanalization rate in patients with acute stroke with tandem lesions.** *JACC Cardiovasc Interv* 2018;11:1290–99 CrossRef Medline
4. Blassiau A, Gawlitza M, Manceau PF, et al. **Mechanical thrombectomy for tandem occlusions of the internal carotid artery—results of a conservative approach for the extracranial lesion.** *Front Neurol* 2018;9:928 CrossRef Medline
5. Powers WJ, Rabinstein AA, Ackerson T, et al. American Heart Association Stroke Council. **Guidelines for the early management of patients with acute ischemic stroke: a guideline for healthcare professionals from the American Heart Association/American Stroke Association.** *Stroke* 2018;49:e46–110 CrossRef Medline
6. Chen Z, Zhang M, Shi F, et al. **Pseudo-occlusion of the internal carotid artery predicts poor outcome after reperfusion therapy.** *Stroke* 2018;49:1204–09 CrossRef Medline
7. Wareham J, Crossley R, Barr S, et al. **Cervical ICA pseudo-occlusion on single phase CTA in patients with acute terminal ICA occlusion: what is the mechanism and can delayed CTA aid diagnosis?** *J Neurointerv Surg* 2018;10:983–87 CrossRef Medline
8. Grossberg JA, Haussen DC, Cardoso FB, et al. **Cervical carotid pseudo-occlusions and false dissections: intracranial occlusions masquerading as extracranial occlusions.** *Stroke* 2017;48:774–77 CrossRef Medline
9. Rocha M, Delfyett WT, Agarwal V, et al. **Diagnostic accuracy of emergency CT angiography for presumed tandem internal carotid artery occlusion before acute endovascular therapy.** *J Neurointerv Surg* 2018;10:653–56 CrossRef Medline
10. Diouf A, Fahed R, Gaha M, et al. **Cervical internal carotid occlusion versus pseudo-occlusion at CT angiography in the context of acute stroke: an accuracy, interobserver, and intraobserver agreement study.** *Radiology* 2018;286:1008–15 CrossRef Medline
11. Fiebach JB, Schellinger PD, Jansen O, et al. **CT and diffusion weighted MR imaging in randomized order: diffusion-weighted imaging results in higher accuracy and lower interrater variability**

- in the diagnosis of hyperacute ischemic stroke. *Stroke* 2002;33:2206–10 CrossRef Medline
12. Paolini S, Burdine J, Verenes M, et al. **Rapid short MRI sequence useful in eliminating stroke mimics among acute stroke patients considered for intravenous thrombolysis.** *J Neurol Disord* 2013;1:137 CrossRef Medline
 13. Thomalla G, Simonsen CZ, Boutitie F, et al. WAKE-UP Investigators. **MRI-guided thrombolysis for stroke with unknown time of onset.** *N Engl J Med* 2018;379:611–22 CrossRef Medline
 14. Bossuyt PM, Reitsma JB, Bruns DE, et al. STARD Group. **Stard 2015: an updated list of essential items for reporting diagnostic accuracy studies.** *Radiology* 2015;277:826–32 CrossRef Medline
 15. Kottner J, Audigé L, Brorson S, et al. **Guidelines for Reporting Reliability and Agreement Studies (GRRAS) were proposed.** *J Clin Epidemiol* 2011;64:96–106 CrossRef Medline
 16. Donner A, Rotondi MA. **Sample size requirements for interval estimation of the kappa statistic for interobserver agreement studies with a binary outcome and multiple raters.** *Int J Biostat* 2010;6: Article 31 CrossRef Medline
 17. Gibo H, Lenkey C, Rhoton AL. **Microsurgical anatomy of the supraclavicular portion of the internal carotid artery.** *J Neurosurg* 1981;55:560–74 CrossRef Medline
 18. DiCiccio TJ, Efron B, Hall P, et al. **Bootstrap confidence intervals.** *Statistical Science* 1996;11:189–212 CrossRef
 19. Vanbelle S, Albert A. **A bootstrap method for comparing correlated kappa coefficients.** *Journal of Statistical Computation and Simulation* 2008;78:1009–15 CrossRef
 20. Landis JR, Koch GG. **The measurement of observer agreement for categorical data.** *Biometrics* 1977;33:159–74 CrossRef Medline
 21. **Thrombectomy In TANdem Occlusion (TITAN).** Published June 7, 2019. Updated August 12, 2020. <https://clinicaltrials.gov/ct2/show/record/NCT03978988>. Accessed February 18, 2021
 22. Saver JL, Goyal M, Bonafe A, et al. SWIFT PRIME Investigators. **Stent-retriever thrombectomy after intravenous t-PA vs. t-PA alone in stroke.** *N Engl J Med* 2015;372:2285–95 CrossRef Medline
 23. Goyal M, Demchuk AM, Menon BK, et al. ESCAPE Trial Investigators. **Randomized assessment of rapid endovascular treatment of ischemic stroke.** *N Engl J Med* 2015;372:1019–30 CrossRef Medline
 24. Zhu F, Bracard S, Anxionnat R, et al. **Impact of emergent cervical carotid stenting in tandem occlusion strokes treated by thrombectomy: a review of the TITAN Collaboration.** *Front Neurol* 2019;10:206 CrossRef Medline
 25. Sadeh-Gonik U, Tau N, Friehmann T, et al. **Thrombectomy outcomes for acute stroke patients with anterior circulation tandem lesions: a clinical registry and an update of a systematic review with meta-analysis.** *Eur J Neurol* 2018;25:693–700 CrossRef Medline
 26. Tsvigoulis G, Katsanos AH, Schellinger PD, et al. **Successful reperfusion with intravenous thrombolysis preceding mechanical thrombectomy in large-vessel occlusions.** *Stroke* 2018;49:232–35 CrossRef Medline
 27. Zinkstok SM, Roos YB; ARTIS Investigators. **Early administration of aspirin in patients treated with alteplase for acute ischaemic stroke: a randomized controlled trial.** *Lancet* 2012;380:731–37 CrossRef Medline
 28. Chung HJ, Lee BH, Hwang YJ, et al. **Delayed-phase CT angiography is superior to arterial-phase CT angiography at localizing occlusion sites in acute stroke patients eligible for intra-arterial reperfusion therapy.** *J Clin Neurosci* 2014;21:596–600 CrossRef Medline
 29. Choi JH, Jang J, Koo J, et al. **Multiphase computed tomography angiography findings for identifying pseudo-occlusion of the internal carotid artery.** *Stroke* 2020;51:2558–62 CrossRef Medline
 30. Ng FC, Choi PM, Datta M, et al. **Perfusion-derived dynamic 4D CT angiography identifies carotid pseudo-occlusion in hyperacute stroke.** *J Neuroimaging* 2016;26:588–91 CrossRef Medline
 31. Yang CY, Chen YF, Lee CW, et al. **Multiphase CT angiography versus single-phase CT angiography: comparison of image quality and radiation dose.** *AJNR Am J Neuroradiol* 2008;29:1288–95 CrossRef Medline
 32. Lustig M, Donoho D, Pauly JM. **Sparse MRI: the application of compressed sensing for rapid MR imaging.** *Magn Reson Med* 2007;58:1182–95 CrossRef Medline
 33. Chai S, Sheng Z, Xie W, et al. **Assessment of apparent internal carotid tandem occlusion on high-resolution vessel wall imaging: comparison with digital subtraction angiography.** *AJNR Am J Neuroradiol* 2020;41:693–99 CrossRef Medline
 34. Provost C, Soudant M, Legrand L, et al. **Magnetic resonance imaging or computed tomography before treatment in acute ischemic stroke.** *Stroke* 2019;50:659–64 CrossRef Medline
 35. Eker OF, Bühlmann M, Dargazanli C, et al. **Endovascular treatment of atherosclerotic tandem occlusions in anterior circulation stroke: technical aspects and complications compared to isolated intracranial occlusions.** *Front Neurol* 2018;9:1046 CrossRef Medline

MRI Posttreatment Surveillance for Head and Neck Squamous Cell Carcinoma: Proposed MR NI-RADS Criteria

M.M. Ashour, E.A.F. Darwish, R.M. Fahiem, and T.T. Abdelaziz

ABSTRACT

BACKGROUND AND PURPOSE: The current Neck Imaging Reporting and Data System (NI-RADS) criteria were designed for contrast-enhanced CT with or without PET. Prior studies have revealed the capability of DWI and T2 signal intensity in distinguishing locoregional tumor residual and recurrence from posttreatment benign findings in head and neck cancers. We aimed to propose MR imaging NI-RADS criteria by adding diffusion criteria and T2 signal intensity to the American College of Radiology NI-RADS template.

MATERIALS AND METHODS: This retrospective study included 69 patients with head and neck squamous cell carcinoma (HNSCC) who underwent posttreatment contrast-enhanced MRI imaging surveillance using a 1.5T scanner. The scans were interpreted by 2 neuroradiologists. Image analysis assessed the primary tumor site using the current American College of Radiology NI-RADS morphologic lexicon (mainly designed for contrast-enhanced CT with or without PET). NI-RADS rescoring was then performed based on our proposed criteria using T2 signal and diffusion features. The reference standard was a defined set of criteria, including clinical and imaging follow-up and pathologic assessment.

RESULTS: Imaging assessment of treated HNSCC at the primary tumor site using T2 signal intensity and diffusion features as modifying rules to NI-RADS showed higher sensitivity, specificity, positive predictive value, negative predictive value, and accuracy (92.3%, 90.7%, 85.7%, 95.1%, and 91.3%, respectively) compared with the current NI-RADS lexicon alone (84.6%, 81.4%, 73.3%, 89.8%, and 82.6%, respectively).

CONCLUSIONS: The addition of diffusion features and T2 signal to the American College of Radiology NI-RADS criteria for the primary tumor site enhances the specificity, sensitivity, positive predictive value, negative predictive value, and NI-RADS accuracy.

ABBREVIATIONS: ACR = American College of Radiology; LTR = locoregional tumor residual or recurrence; NI-RADS = Neck Imaging Reporting and Data System; NPV = negative predictive value; PPV = positive predictive value; SI = signal intensity; CECT = contrast-enhanced CT; CEMRI = contrast-enhanced MRI; HNSCC = head and neck squamous cell carcinoma; RTH = radiation therapy; CRTH = chemoradiation therapy; FP = false-positive; FN = false-negative

The Neck Imaging Reporting and Data System (NI-RADS) was recently introduced by the American College of Radiology (ACR) to precisely convey the level of radiologic suspicion regarding the existence of a recurrent or residual disease.^{1,2} Initial studies showed high performance of the NI-RADS system.^{3,4} NI-RADS criteria and risk categories were developed for contrast-enhanced CT (CECT) imaging with or without PET for posttreatment neck imaging. Later, these risk categories were applied to contrast-enhanced MRI (CEMRI).^{1,2,5} However, there is still no published ACR NI-RADS lexicon for MR imaging surveillance.

Although not included in the NI-RADS scoring system, several studies have revealed the usefulness of DWI and signal intensity on T2WI in identifying residual and recurrent tumors in patients with treated head and neck cancer.⁶⁻⁹ Based on previous studies, tissues with diffusion facilitation and either low T2 signal intensity (SI) (less than or equal to muscles) that usually represents fibrotic tissue or high T2 SI (approaching the CSF signal), which usually represents edema and granulation, have no to low-level suspicion for malignancy.^{6,8} Studies examining the effectiveness of DWI in detecting locoregional tumor residual or recurrence (LTR) in the posttreatment neck consider that the histopathologic features of malignant tissues, such as increased cellularity and nuclear hyperchromatism, result in a diminution of intra- and extracellular spaces available for the diffusion of water protons with a consequent decrease in ADC values. This contrasts with the low cellularity with an increase in interstitial water associated with edema and inflammation, causing subsequent elevation of ADC values.^{7,10,11}

Received June 28, 2020; accepted after revision December 20.

From the Department of Diagnostic Radiology, Faculty of Medicine, Ain Shams University, Cairo, Egypt.

Please address correspondence to Manar M. Ashour, MD, Department of Diagnostic Radiology, Faculty of Medicine, Ain Shams University, 38 Ramsis street, Abbassia Square, PO Box 11381, Cairo, Egypt; e-mail: manar.ashour@gmail.com; @manarmaamoun

<http://dx.doi.org/10.3174/ajnr.A7058>

We hypothesized that tailoring NI-RADS criteria for MR imaging with DWI features and T2 SI may improve the diagnostic performance of the existing NI-RADS system for MR imaging surveillance.

This study aimed to recommend new NI-RADS criteria for MR imaging surveillance based on the current system using DWI and T2 signals and to evaluate the diagnostic performance of integrating these criteria into the existing NI-RADS algorithm.

MATERIALS AND METHODS

Study Design and Patient Selection

Our institution's ethics committee approved this single-center, retrospective study and waived the requirement for informed consent. Data were retrieved from the medical records and PACS. This study included 69 patients with head and neck squamous cell carcinoma (HNSCC) who were referred for posttreatment MR imaging surveillance between June 2018 and September 2020. Patients with histopathologically diagnosed primary HNSCC who underwent CEMRI surveillance within the first year after treatment, starting from 8–10 weeks after completing their treatment course, were included in this study. We considered the first posttreatment MR imaging scan, irrespective of whether it was the baseline scan or preceded by CECT with or without PET. We excluded patients with inadequate clinical or imaging follow-up or who had missing data, NI-RADS 4 with confirmed recurrence before scanning, non-contrast-enhanced scans, and scans with low-quality images that showed remarkable artifacts.

An initial search in the PACS revealed that 335 CEMRI neck scans were performed for 221 patients between June 2018 and September 2020, of whom 87 patients had HNSCC. We excluded 15 patients because of inadequate histopathologic data or follow-up, 2 patients because of lack of postcontrast sequences, and 1 patient because of profound artifacts from an inserted maxillary prosthesis.

Image Acquisition

Images were acquired with a 1.5T scanner (Ingenia, Philips Healthcare) using a 16-channel neurovascular coil. Imaging started from the skull base to the thoracic inlet, with FOV anterior to posterior 230 mm, and 4-mm section thickness with no gap. Axial single-shot SE EPI DWI was acquired ($b=0$ and 800 seconds/mm², TR/TE 2920/67 ms, section thickness 4 mm, and voxel size 3.2 × 2.6 × 4.0 mm). ADC was automatically generated by the implemented software, including precontrast axial SE T1WI (TE/TR: 21/633 ms), coronal SE T1 (TE/TR: 14/555 ms), axial SE T2WI (TE/TR: 10/7039 ms), sagittal SE T2WI (TE/TR: 100/3196.7 ms), and coronal T2 STIR (TR/TI=3500/150, TE=80 ms). A gadolinium-based contrast agent (dimeglumine gadopentetate) (0.1 mmol/kg) was administered using an injector with a flow rate of 2–3 mL/s followed by postcontrast T1WI with fat saturation, in the axial (TR/TE: 611/21 ms), sagittal (TR/TE:570/14 ms), and coronal (TR/TE:570/14 ms) planes.

Image Analysis and Applied Diagnostic Criteria

Data were transferred to an IntelliSpace Portal 9.0 workstation (Philips Healthcare). Scans were interpreted by 2 neuroradiologists with different levels of experience (5 and 15 years) in head and neck imaging, both of whom have been trained on NI-RADS

reporting at our institution. NI-RADS has been the reporting template in use for posttreatment of HNSCC cases since early 2018 according to the ACR NI-RADS lexicon and the directions published in the Aiken and Hudgins⁵ guide article and the white paper of the ACR NI-RADS committee.¹ Readers had access to patients' demographic data (names and identification numbers had been anonymized), the therapeutic history, the pretreatment scans, and any other preceding posttreatment CECT with or without PET scan and were blinded to the clinical or pathologic outcome. Discrepant interpretations were resolved by consensus.

Three polygonal ROIs were inserted manually by the neuroradiologist with 5 years' experience on $b=800$ images either on the same or consecutive axial sections, according to the size and extent of the primary targets and copied automatically on the corresponding ADC maps. ROIs were placed on the most enhancing parts in the presence of enhancement, excluding necrotic areas guided by contrast-enhanced-T1WI and T2WI in the same axial sections. The average ADC_{mean} value for the 3 measurements was estimated for all targets.

Two reporting template forms were used to evaluate primary targets, including the primary tumor site and any regional non-nodal target as associated perineural tumor spread; 1 was template confined to the existing NI-RADS lexicon and scoring system,^{1,5} and the final score was provided according to the higher numeric scoring lesion in case of more than 1 primary target. The other template included the diffusion criteria in qualitative and quantitative forms and T2 SI of primary targets, and scoring was performed according to our modified rules to the current NI-RADS lexicon.

Based on the available literature^{6,8} and the authors' experience, a defined scale for T2 SI evaluation was set: 1) isointense SI to the normal-appearing surrounding tissues, 2) very dark T2 SI (much lower than original tumor and muscle) (Figs 1A and 2A), 3) intermediate T2 SI (similar to the initial tumor signal), (Fig 1A), and 4) high T2 SI for tissues displaying SI between muscle SI and fluid, or much higher than the original tumor. Correlation with the pretreatment tumor signal was performed for 56 cases with available pretreatment CEMRI.

For diffusion criteria, the scale used for visual interpretation of the signal to determine whether it was high or low was compared with the brain stem signal in ADC maps as follows: 1) diffusion restriction for low signal in the ADC map compared with the brain stem signal with high signal in DWI corresponding to abnormal enhancement (Fig 1C) and/or similar to the original tumor signal; and 2) facilitated diffusion for high signal in the ADC map compared with the brain stem with high or low signal on DWI (Figs 1D and 2C) or higher than the original tumor signal.

Image Analysis Using T2 SI and DWI as Modified Rules for NI-RADS Categories

We incorporated diffusion features and T2 SI into NI-RADS as modified rules. The presence of both diffusion restriction and intermediate T2 SI would upgrade the NI-RADS categories by 1 grade (from categories 1 to 2 and 2 to 3). Conversely, the absence of both would downgrade NI-RADS categories by 1 grade (Fig 2) (from categories 3 to 2 and 2 to 1). The presence of only 1 feature without the other feature would not alter the original NI-RADS risk category.

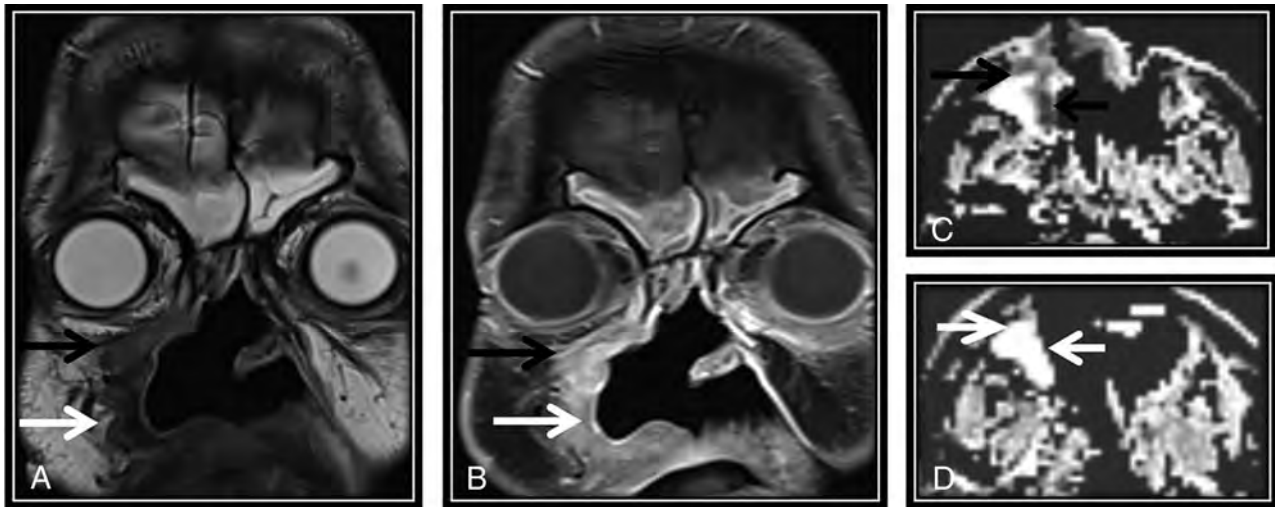


FIG 1. Concordance between NI-RADS category, T2 SI, and DWIs is demonstrated in this posttreatment MR imaging surveillance scan done after surgery and RTH for sinonasal squamous cell carcinoma. Coronal T2WI (A) and coronal contrast-enhanced T1WI (B) show a surgical bed discrete nodule (black arrow) that displays intermediate T2 SI (A) and postcontrast enhancement (B), fulfilling NI-RADS 3 and confirmed to be squamous cell carcinoma by histopathology. C. Axial ADC map of the surgical bed shows a corresponding low-ADC signal (black arrow). White arrows point to circumferential soft tissue thickening with sheetlike enhancement (B), which shows low T2 SI (A), absent diffusion restriction (D), and was confirmed to be posttreatment fibrous tissue.



FIG 2. The first post-CRTH MR imaging follow-up for a known case of nasopharyngeal carcinoma with perineural tumor spread (PNTS) showing discordant findings between NI-RADS category, T2 SI, and DWI. There is a clear primary tumor site at the nasopharynx (not demonstrated here), yet a regional non-nodal target was noted. A. Axial T2WI shows orbital apex dark T2 SI tissue keeping with fibrotic scarring (arrow). B. This lesion shows discrete postcontrast enhancement (arrow) (secondary to PNTS along the ophthalmic nerve) categorized as NI-RADS 3. C. Axial ADC map of the surgical bed shows a corresponding facilitated diffusion (arrow). According to our proposed modifying rules, downgrading to category 2 was done. Follow-up by PET/CT showed no FDG uptake (not demonstrated here) that was confirmed to be post-RTH fibrotic scarring by further follow-up. Note the right temporal lobe after RTH injury.

Standard of Reference

Criteria for negative disease included negative clinical and MR imaging follow-up performed after 12 months or negative biopsy results. Criteria for LTR included positive biopsy results, evident tumor on clinical examination, or evidence of disease progression on subsequent follow-up scans as determined by the Response Evaluation Criteria in Solid Tumors.¹²

Ethics Approval

All procedures performed in the study were in accordance with the ethical standards of the institutional research committee and with the 1964 Helsinki Declaration and its later amendments. For this type of study informed consent was not required and waived by the ethical committee.

Statistical Analysis

The collected data were revised, coded, and tabulated using SPSS 20 (IBM). For descriptive statistics, the mean, SD, and range were used for numerical data; frequency and percentage were used for non-numeric data. For analytical statistics, the Student *t* test was used to assess the statistical significance of the difference in ADC_{mean} values between LTR and benign lesions. ROC curve analysis of ADC_{mean} values was performed according to the standard of reference. The diagnostic performance of ACR NI-RADS, DWI in its qualitative and quantitative forms, T2 SI, and NI-RADS combined with T2 SI and DWI were assessed in terms of sensitivity, specificity, positive predictive value (PPV), negative predictive value (NPV), and accuracy. Kappa statistics were used to compute the measure of agreement

between 2 investigational methods, with values of 0.2–0.4 indicating fair agreement; 0.41–0.6, moderate agreement; 0.61–0.8, substantial agreement; and 0.8–1.0, almost perfect agreement. $P < .05$ was considered significant.

RESULTS

Patients and Tumor Characteristics

The study population consisted of 69 patients: 41 males (59.4%) and 28 females (40.6%), with the mean age of 50.55 ± 16.82 (range, 18–85 years). Twenty-two (31.9%) patients underwent surgical excision and received radiation therapy (RTH), 19 (27.5%) received chemoradiation therapy (CRTH), 12 (17.4%) underwent surgery only, 9 (13.0%) underwent surgery combined with CRTH, and 7 (10.1%) received RTH. Table 1 demonstrates the tumor demographics and scan order.

Descriptive Statistics for LTR and Benign Posttreatment Lesions

Pathology or follow-up confirmed diagnosis in 26/69 (37.7%) patients, and imaging follow-up confirmed diagnosis in 43/69 (62.3%) patients. LTR occurred in 26/69 (37.7%) patients.

Results of Image Interpretation and Applied Diagnostic Criteria Relative to the Standard of Reference

The results of the imaging analysis of the primary targets and the results of the diagnostic performance of T2 SI, DWI (qualitative and quantitative), NI-RADS, and NI-RADS rescoring, for the detection of LTR for the primary targets, are listed in Table 2 and 3.

For diffusion criteria, there was no statistically significant difference between the qualitative and quantitative assessment of DWI, with 28/69 lesions (40.6%) showing diffusion restriction with a low ADC signal; 24/28 were LTR, and 4/28 were post-treatment changes. A total of 41/69 lesions (59.4%) demonstrated no diffusion restriction, 39/41 showed no recurrence, and 2/41 had LTR.

The mean ADC value for LTR was 0.94 ± 0.38 , and the mean ADC value

Table 1: Tumor characteristics and scan order of the included population

		Patients (n)	Patients (%)
Subsite	Larynx	12	17.4
	Oral cavity and oropharynx	25	36.2
	Hypopharynx	2	2.9
	Sinonasal	10	14.5
	Skull base	1	1.4
	Nasopharynx	13	18.8
	Salivary	6	8.7
Pathologic grade	Low	14	20.3
	Moderate	37	53.6
	High	18	26.1
Tumor stage ^a	Tis	1	1.4
	T1	7	10.14
	T2	24	34.8
	T3	22	31.9
	T4	15	21.7
Scan order	First follow-up	54	78.3
	Second follow-up	8	10.1
	Third follow-up	8	11.6

Note:—Tis indicates carcinoma in situ.

^a American Joint Committee on Cancer.²⁰

Table 2: Results of image analysis by T2 SI, DWI (qualitative and quantitative), NI-RADS, and NI-RADS rescoring for the primary targets

		Standard of Reference	
		Negative n (%)	Positive n (%)
NI-RADS	NI-RADS 1	20 (46.51)	1 (3.85)
	NI-RADS 2	15 (34.88)	3 (11.54)
	NI-RADS 3	8 (18.6)	22 (84.62)
T2 SI	Isointense to surrounding tissue	4 (9.3)	1 (3.85)
	Dark	15 (34.88)	1 (3.85)
	Intermediate	5 (11.63)	24 (92.31)
	High	19 (44.19)	0 (0)
DWI	Facilitated	39 (90.7)	2 (7.69)
	Restricted	4 (9.3)	24 (92.31)
NI-RADS combined with T2 and DWI	NI-RADS 1	30 (69.77)	1 (3.85)
	NI-RADS 2	10 (23.26)	2 (7.69)
	NI-RADS 3	3 (6.98)	23 (88.46)

Table 3: Diagnostic performance of T2 SI, DWI (qualitative and quantitative), NI-RADS, and NI-RADS rescoring for the detection of LTR for the primary targets

	T2 SI	DWI with ADC ≤ 1.3	NI-RADS	NI-RADS-DWI-T2 SI
TP (n)	24	24	22	23
TN (n)	38	39	35	40
FP (n)	5	4	8	3
FN (n)	2	2	4	3
Sensitivity (%) (95% CI)	92.31 (74.87–99.05)	92.3 (74.87–99.05)	84.62 (65.13–95.64)	88.46 (69.85–97.55)
Specificity (%) (95% CI)	88.37 (74.92–96.11)	90.7 (77.86–97.41)	81.4 (66.60–91.61)	93.02 (80.94–98.54)
PPV (%) (95% CI)	82.76 (67.64–91.68)	85.71 (70.10–93.89)	73.33 (59.03–84.00)	88.46 (71.84–95.84)
NPV (%) (95% CI)	95.00 (83.32–98.64)	95.12 (83.69–98.67)	89.74 (77.84–95.61)	93.02 (82.10–97.49)
Accuracy (%) (95% CI)	89.86 (80.21–95.82)	91.30 (82.03–96.74)	82.61 (71.59–90.68)	91.30 (82.03–96.74)

Note:—TP indicates true-positive; TN, true-negative.

Table 4: Agreement between DWI (qualitative and quantitative), T2 SI, NI-RADS, and NI-RADS combined with DWI and T2 SI for the primary targets and the standard of reference

		Standard of Reference		Agreement		
		Negative n (%)	Positive n (%)	Kappa	95% CI	P Value
DWI	Restricted	4 (9.3)	24 (92.31)	0.818	0.68–0.96	<.001
	Facilitated	39 (90.7)	2 (7.69)			
T2 SI	Intermediate	5 (11.63)	24 (92.3)	0.789	0.64–0.94	<.001
	No abnormality; low or high SI	38 (88.37)	2 (7.69)			
NI-RADS combined with T2 and DWI	Category 3	3 (6.98)	23 (88.46)	0.815	0.67–0.96	<.001
	Categories 1 and 2	40 (93.02)	3 (11.54)			
NI-RADS	Category 3	8 (18.6)	22 (84.62)	0.641	9.46–0.82	<.001
	Categories 1 and 2	35 (81.4)	4 (15.38)			

for benign posttreatment changes was 1.98 ± 0.55 ($P < .001$).

ROC curve analysis showed an AUC of 0.945 (0.875–0.990 CI), with cutoff $ADC_{mean} \leq 1.3 \times 10^{-3} \text{ mm}^2/\text{s}$, which showed the highest sensitivity, specificity, PPV, and NPV (92.31%, 90.7%, 85.7%, and 95.1%, respectively).

For T2 SI, 29/69 lesions showed intermediate T2 SI, 24/29 were LTR, and 5/29 lesions were posttreatment benign changes. A total of 40 lesions demonstrated no abnormality, low or high SI in T2WI, 38/40 showed no recurrence, and 2/40 showed LTR.

Regarding NI-RADS, 39/69 targets were categorized as NI-RADS 1 ($n = 21$) or 2 ($n = 18$), 35/39 were found to be negative, and 4 lesions were LTR; 30 lesions were categorized as NI-RADS 3, 22/30 lesions proved to be LTR, and 8 lesions were negative according to the criterion standard.

After inclusion of T2 SI and DWI as modifying rules to NI-RADS categories, 7 NI-RADS category 3 targets were downgraded to category 2, 3 NI-RADS 2 targets were upgraded to category 3, and 10 NI-RADS 2 targets were downgraded to NI-RADS 1.

Agreement between DWI, T2 SI, NI-RADS, and NI-RADS combined with DWI and T2 SI of the primary targets, and the standard of reference is shown in Table 4.

DISCUSSION

In the current study, incorporation of T2 SI and diffusion features into NI-RADS as modifying rules showed high diagnostic performance, with higher sensitivity, specificity, PPV, and NPV of 88.46%, 93.02%, 88.46%, and 93.02%, respectively, compared with the current ACR NI-RADS template, which showed a sensitivity, specificity, PPV, and NPV of 84.62%, 81.40%, 73.33%, and 89.74%, respectively, with the difference being more notable in specificity than in sensitivity.

Several previous studies evaluated the utility of DWI in differentiating posttreatment changes from recurrence and concluded that DWI showed high diagnostic performance.^{7,11,13–16} Morphologic imaging features for LTR described in previous literature included infiltrative mass appearance, with intermediate to high SI in T2 WIs and postcontrast enhancement. However, these features could overlap with those of benign posttreatment findings such as posttherapy inflammation and fibrosis.^{13,16} Therefore, dependence on only morphologic features could result in increased false-positive (FP) cases. The current ACR NI-RADS lexicon was developed for CECT with or without PET; thus, it does not include MR imaging-specific sequences. We suggest the addition of T2 SI and diffusion

features to the current lexicon to adapt it to posttreatment surveillance with CEMRI, taking advantage of its routine use in daily practice.

In the available literature, the performance of NI-RADS was assessed for CECT with or without PET at different time points in terms of discrimination between categories.⁴ Two other studies investigated the predictive value of the first posttreatment PET/CT using NI-RADS.^{3,17} Wangaryattawanich et al¹⁸ investigated the PPV of NI-RADS categories 3 and 4 for PET/CT and concluded that NI-RADS 3 and 4 have a PPV of 56% and 100%, respectively. Our results showed a higher PPV and lower NPV for NI-RADS compared with the previous studies. This could be attributable to the inherent difference between the performance of CEMRI and contrast-enhanced PET/CT in posttreatment imaging surveillance, as also supported by the results of Kreiger et al,⁴ which showed a much higher rate of true-positive disease with the use of CECT (91.7%) compared with PET/CT (40%).

In this study, we assessed the T2 SI and diffusion features of the primary targets; both showed high diagnostic performance relative to patient outcome. Comparing the diagnostic performance of T2 SI and DWI and combining both with NI-RADS showed that DWI had a higher specificity and accuracy of 90.70% and 91.30%, respectively, compared with 88.37% and 89.86%, respectively, for T2 SI; both showed similar sensitivities of 92.31%. Incorporating T2 SI and DWI within the NI-RADS yielded higher specificity (93.02%) and higher PPV compared with either T2 SI or DWI alone, and accuracy (91.30%) similar to the diffusion criteria. The kappa coefficient for the concordance between NI-RADS scoring of the primary tumor site and the outcome was 0.641, and higher agreement (0.815) was obtained by combining DWI and T2 SI with NI-RADS scoring.

Ailianou et al⁶ concluded that morphologic MR imaging with defined criteria had a similar diagnostic performance to DWI, with the combination of both yielding higher results. Precise analysis of signal intensities on morphologic MR imaging increased the specificity of DWI, whereas the overall effect on sensitivity was less pronounced. The results of the current study are concordant with those of Ailianou et al⁶ regarding the higher sensitivity and specificity obtained after incorporation of DWI into NI-RADS morphologic features, with a more pronounced effect on specificity than sensitivity.

The current study showed an optimal ADC_{mean} threshold of $1.3 \times 10^{-3} \text{ mm}^2/\text{s}$ to discriminate between benign changes and

LTR with a sensitivity, specificity, and accuracy of 92.31%, 90.70%, and 91.30%, respectively. This agrees with Jajodia et al,¹⁰ who showed the same ADC threshold with a sensitivity, specificity, and accuracy of 94%, 83.3%, and 93.6%, respectively. Minor differences in diagnostic parameters could be due to the different characteristics of the included population; for example, they included patients with lesions >5 mm, presenting between 3 months and 2 years, whereas we included scans performed within the first year after treatment with no specific size criteria for lesions for inclusion.

In our study, analysis of T2 SI performance individually revealed 2 false-negative (FN) and 5 FP cases; 1 of the FN cases was a pathologically proved residual tongue squamous cell carcinoma. The residual tumor was not detected during the first post-treatment MR imaging scan, including DWI, T2, and the NI-RADS system. This could be explained by the presence of microscopic residual tumor cells in the initial study beyond MR imaging resolution because the discrete enhancing lesion became apparent on the follow-up scans. The second FN case was a case with a primary target lesion with low T2 SI that resembled fibrotic tissue; it was proved pathologically to contain a small 6-mm residual tumor, suggesting that tiny residual tumors may exist within a sizable fibrotic tissue, for which follow-up would be useful.

Five FP cases by T2 SI corresponded to posttreatment fibrotic scarring, suggesting that fibrotic tissue may present with intermediate SI in the early posttreatment phase.

Two FN and 4 FP cases were identified by DWI; the FN results in DWI are explained by either microscopic tumor tissue or the presence of posttreatment edema or inflammation in the early posttreatment scans. The FP results with DWI were attributed to lymphoid hyperplasia and early stages of fibrosis that may show diffusion restriction, which requires further follow-up.

Adding DWI and T2 signal features helped in reducing the number of FP findings caused by NI-RADS 3 criteria because of the enhancement associated with posttreatment benign findings that can present as masslike lesions.¹⁶ Although our results showed a very comparable diagnostic performance between DWI (quantitative and qualitative forms) alone and the combined criteria, further studies on a larger scale are required to confirm these results. Taking into consideration the limitations of dependence on diffusion and ADC values with related motion and susceptibility artifacts, variations in ADC values using different MR imaging scanners and different b-values, and the lack of a definite cutoff value for ADC,^{7,13,19} we recommend incorporating diffusion criteria and T2 SI into the NI-RADS system to benefit from combined functional, morphologic, and enhancement features and to overcome the intrinsic limitations of each of them when used individually.

Limitations of the Study

One limitation of our study is that it is a retrospective, single-center study. Hence, minor variations in scan timing occurred. Further multicenter studies with larger sample volumes are required to support these results.

CONCLUSIONS

Incorporation of diffusion criteria and T2 SI into the current NI-RADS criteria for primary tumor site assessment as modifying

rules enhanced the diagnostic validity and accuracy of the ACR NI-RADS template.

REFERENCES

1. Aiken AH, Rath TJ, Anzai Y, et al. **ACR Neck Imaging Reporting and Data Systems (NI-RADS): a white paper of the ACR NI-RADS Committee.** *J Am Coll Radiol* 2018;15:1097–08 CrossRef Medline
2. Aiken AA, Farley A, Bagnon KL, et al. **Implementation of a novel surveillance template for head and neck cancer: Neck Imaging Reporting and Data System (NI-RADS).** *J Am Coll Radiol* 2016;13:743–46 CrossRef Medline
3. Wangyattawanich P, Branstetter BF, Hughes M, et al. **Negative predictive value of NI-RADS category 2 in the first posttreatment FDG-PET/CT in head and neck squamous cell carcinoma.** *AJNR Am J Neuroradiol* 2018;39:1884–88 CrossRef Medline
4. Krieger DA, Hudgins PA, Nayak GK, et al. **Initial performance of NI-RADS to predict residual or recurrent head and neck squamous cell carcinoma.** *AJNR Am J Neuroradiol* 2017;38:1193–99 CrossRef Medline
5. Aiken AH, Hudgins PA. **Neck Imaging Reporting and Data System.** *Magn Reson Imaging Clin N Am* 2018;26:51–62 CrossRef Medline
6. Ailianou A, Mundada P, De Perrot T, et al. **MRI with DWI for the detection of posttreatment head and neck squamous cell carcinoma: why morphologic MRI criteria matter.** *AJNR Am J Neuroradiol* 2018;39:748–55 CrossRef Medline
7. Vaid S, Chandorkar A, Atre A, et al. **Differentiating recurrent tumours from post-treatment changes in head and neck cancers: does diffusion-weighted MRI solve the eternal dilemma?** *Clin Radiol* 2017;72:74–83 CrossRef Medline
8. King AD, Keung CK, Yu KH, et al. **T2-weighted MR imaging early after chemoradiotherapy to evaluate treatment response in head and neck squamous cell carcinoma.** *AJNR Am J Neuroradiol* 2013;34:1237–41 CrossRef Medline
9. Becker M, Varoquaux D, Combescure C, et al. **Local recurrence of squamous cell carcinoma of the head and neck after radio(chemo)therapy: diagnostic performance of FDG-PET/MRI with diffusion-weighted sequences.** *Eur Radiol* 2018;28:651–63 CrossRef Medline
10. Jajodia A, Aggarwal D, Chaturvedi AK, et al. **Value of diffusion MR imaging in differentiation of recurrent head and neck malignancies from post treatment changes.** *Oral Oncol* 2019;96:89–96 CrossRef Medline
11. Connolly M, Srinivasan A. **Diffusion-weighted imaging in head and neck cancer: technique, limitations, and applications.** *Magn Reson Imaging Clin N Am* 2018;26:121–33 CrossRef Medline
12. Eisenhauer EA, Therasse P, Bogaerts J, et al. **New response evaluation criteria in solid tumours: revised RECIST guideline (version 1.1).** *Eur J Cancer* 2009;45:228–47 CrossRef Medline
13. Tshering Vogel DW, Zbaeren P, Geretschlaeger A, et al. **Diffusion-weighted MR imaging including bi-exponential fitting for the detection of recurrent or residual tumour after (chemo)radiotherapy for laryngeal and hypopharyngeal cancers.** *Eur Radiol* 2013;23:562–69 CrossRef Medline
14. Zhou Q, Zeng F, Ding Y, et al. **Meta-analysis of diffusion-weighted imaging for predicting locoregional failure of chemoradiotherapy in patients with head and neck squamous cell carcinoma.** *Mol Clin Oncol* 2018;8:197–203 CrossRef Medline
15. Fujima N, Yoshida D, Sakashita T, et al. **Residual tumour detection in post-treatment granulation tissue by using advanced diffusion models in head and neck squamous cell carcinoma patients.** *Eur J Radiol* 2017;90:14–19 CrossRef Medline
16. Abdel Razek AAK, Kandeel AY, Soliman N, et al. **Role of diffusion-weighted echo-planar MR imaging in differentiation of residual or recurrent head and neck tumors and posttreatment changes.** *AJNR Am J Neuroradiol* 2007;28:1146–52 CrossRef Medline

17. Hsu D, Chokshi FH, Hudgins PA, et al. **Predictive value of first post-treatment imaging using standardized reporting in head and neck cancer.** *Otolaryngol Head Neck Surg* 2019;161:978–85 CrossRef Medline
18. Wangaryattawanich P, Branstetter BF, Ly JD, et al. **Positive predictive value of neck imaging reporting and data system categories 3 and 4 post treatment FDG-PET/CT in head and neck squamous cell carcinoma.** *AJNR Am J Neuroradiol* 2020;41:1070–75 CrossRef Medline
19. Chung SR, Choi YJ, Suh CH, et al. **Diffusion-weighted magnetic resonance imaging for predicting response to chemoradiation therapy for head and neck squamous cell carcinoma: a systematic review.** *Korean J Radiol* 2019;20:649–61 CrossRef Medline
20. Amin MB, Edge SB, Greene FL, et al. *AJCC Cancer Staging Manual.* Springer; 2017.

Detection of Optic Neuritis on Routine Brain MRI without and with the Assistance of an Image Postprocessing Algorithm

A. Schroeder, G. Van Stavern, H.L.P. Orłowski, L. Stunkel, M.S. Parsons, L. Rhea, and A. Sharma

ABSTRACT

BACKGROUND AND PURPOSE: At times, there is a clinical need for using routine brain MR imaging performed close to the time of onset of patients' visual symptoms to firmly establish the diagnosis of optic neuritis. Our aim was to assess the diagnostic performance of radiologists in detecting optic neuritis on routine brain MR images and whether this performance could be enhanced using a postprocessing algorithm.

MATERIALS AND METHODS: In this retrospective case-control study of 60 patients (37 women, 23 men; mean age, 47.2 [SD, 17.9] years), 2 blinded neuroradiologists evaluated T2-weighted FLAIR and contrast-enhanced T1WI from brain MR imaging for the presence of imaging evidence of optic neuritis. Images were processed using an image-processing algorithm that aimed to selectively accentuate the signal intensity of diseased optic nerves. We assessed the effect of image processing on the contrast-to-noise ratio between the optic nerves and normal-appearing white matter and on the diagnostic performance of the neuroradiologists, including the interobserver reliability.

RESULTS: The average sensitivity of readers was 55%, 56.5%, and 30.0% on FLAIR, coronal contrast-enhanced T1WI, and axial contrast-enhanced T1WI, respectively. Sensitivities were lower in the absence of fat saturation on FLAIR ($P = .001$) and coronal contrast-enhanced T1WI ($P = .04$). Processing increased the contrast-to-noise ratio of diseased (P value range = .03 to $<.001$) but not of control optic nerves. Processing did not improve the sensitivity but improved the specificity and positive predictive value. Interobserver agreement improved from slight to good.

CONCLUSIONS: Detection of optic neuritis on routine brain MR imaging is challenging. Specificity, positive predictive value, and interobserver agreement can be improved by postprocessing of MR images.

ABBREVIATIONS: CE = contrast-enhanced; CNR = contrast-to-noise ratio; ON = optic nerve; PPV = positive predictive value

Optic neuritis typically presents as a unilateral optic neuropathy characterized by decreased visual acuity, orbital pain exacerbated by extra-ocular movement, a relative afferent pupillary defect, and, occasionally, optic disc swelling.¹⁻⁸ Symptoms generally improve, and about 60% of patients regain full visual acuity within 2 months.⁹ MR imaging, often used to confirm the diagnosis, is especially useful in atypical cases.⁵ Dedicated MR imaging of the orbits obtained with and without intravenous

contrast has a reported sensitivity of 76.1%–100% when performed within 30 days of symptom onset.¹⁰⁻¹³ This sensitivity decreases with time since the onset of vision loss, and the mean duration of optic nerve (ON) enhancement, even with triple-dose gadolinium administration, is only 63 days.¹³

While the clinical diagnosis of typical optic neuritis may be straightforward for neuro-ophthalmologists, misdiagnosis by other providers who often encounter the patients at the time of initial presentation reportedly occurs in up to 60% of referrals.¹⁴ The combination of the self-limiting nature of the disease, frequent misdiagnosis at the initial encounter, long referral wait times, and decreased sensitivity of imaging in a delayed setting presents a diagnostic challenge: Neuro-ophthalmologists often have to rely on the imaging ordered by other providers to confirm the diagnosis. Often, this initial imaging is a routine brain MR imaging rather than a dedicated orbital MR imaging.

Most studies documenting the role of imaging in the detection of optic neuritis have focused on dedicated orbital MR imaging.

Received April 30, 2020; accepted after revision December 20.

From the Washington University in Saint Louis School of Medicine, (A. Schroeder), Departments of Ophthalmology and Visual Sciences (G.V.S., L.S.), Neurology (G.V.S., L.S.), Mallinckrodt Institute of Radiology (H.L.P.O., M.S.P., A. Sharma), and Department of Biostatistics (L.R.), Washington University in Saint Louis School of Medicine, St. Louis, Missouri.

Paper previously presented at: Annual Meeting of the North American Neuro-Ophthalmology Society, March 7–12, 2020; Amelia Island, Florida.

Please address correspondence to Aseem Sharma, MD, Mallinckrodt Institute of Radiology, Washington University in Saint Louis, Campus Box 8131, 510 S. Kingshighway Blvd, St. Louis, MO 63110; e-mail: aseemsharma@wustl.edu
<http://dx.doi.org/10.3174/ajnr.A7068>

Table 1: Scan parameters for axial 2D FLAIR,^a coronal CE-T1WI, and axial CE-T1WI used in the study

	FLAIR ^{a,b}	Coronal CE-T1WI ^b	Axial CE-T1WI ^b
Section thickness (mm)	5	5	5
TR (ms)	8000–11,000	300–742	276–780
TE (ms)	82–142	9–17	8.4–20
T1 (ms)	2000–2500	–	–
FOV (mm)	172–230 × 210–230	172–230 × 172–230	172–230 × 210–230
Matrix	224–512 × 256–512	224–512 × 256–512	224–384 × 256–512
Subset of scans obtained with fat saturation	19 (63.3%)	17 (73.9%)	6 (20%)

Note:— indicates N/A.

^a In 3 patients, FLAIR images had been acquired using a 3D sequence with a 1-mm section thickness of images reconstructed in the coronal plane (TR = 5000 ms, TE = 395 ms, T1 = 1800 ms, FOV = 256 × 256 mm, matrix = 256 × 256).

^b For patients with optic neuritis, 19/30 (63.3%), 17/23 (73.9%), and 6/30 (20%) FLAIR, coronal CE-T1WI, and axial CE-T1WIs were performed using fat saturation.

The objective of this study was 2-fold. First, we aimed to assess the diagnostic performance of radiologists in detecting optic neuritis on routine brain MR imaging. Second, we sought to evaluate whether the diagnosis of optic neuritis on routine brain MR imaging could be facilitated using an image-postprocessing algorithm that has previously been shown to be helpful in the detection of optic neuritis on dedicated orbital MR imaging.¹⁵ We hypothesized that the diagnostic accuracies of radiologists in detecting optic neuritis on routine brain MR imaging would be lower than the previously reported rates and that these could be improved by increasing the contrast-to-noise ratio (CNR) of the diseased ON by image postprocessing.

MATERIALS AND METHODS

The institutional review board at Washington University in Saint Louis approved this retrospective study and waived the need for consent for the use of pre-existing data.

Cases and Controls

This was a retrospective case-control study of 60 patients (37 women, 23 men; mean age 47.2 [SD, 17.9] years) who had undergone brain MR imaging, including T2-weighted FLAIR and CE-T1WI sequences. Patients were selected from the clinical database of 1 neuro-ophthalmologist and were seen during a 4-year period dating from June 2015 to June 2019. All patients with clinically proven unilateral optic neuritis were included if brain MR imaging performed within 4 weeks of symptom onset was available. The clinical diagnosis was established in all cases by an expert neuro-ophthalmologist based on clinical presentation, ophthalmologic examination, and evaluation of all relevant investigations. This search generated 30 patients with 30 eyes diagnosed with clinically proven optic neuritis. An equal number ($n = 30$) of brain MRIs of patients with third, fourth, or sixth cranial neuropathies but with clinically proven normal ON function were included as controls.

Images and Image Processing

For each patient, we included available FLAIR images to assess ON signal alteration and available CE-T1WI to assess ON enhancement. Imaging had been performed with variable scan parameters (Table 1). FLAIR, coronal CE, and axial CE images were available for 30 cases and 58 control eyes, for 23 cases and 44 control eyes, and for 30 cases and 58 control eyes, respectively.

FLAIR images were in the axial plane except in 3 patients in whom coronal reformations from the 3D-FLAIR sequence were used. Enhancement of the ONs was assessed individually on axial CE-T1WI, and, when available, on coronal CE-T1WI. Images were acquired using 1.5T (Magnetom Espree, Magnetom Aera, Magnetom Avanto, or Magnetom Sonata; Siemens) or 3T (Magnetom Trio or Magnetom Skyra; Siemens) scanners.

A blinded investigator processed these images using a proprietary algorithm (CIE; Correlative Enhancement) on a Horos workstation (<https://horosproject.org/>) using a custom-built plug-in. The processing involved the manual placement of an ROI to define the normal white matter signal. If the images were originally obtained with fat saturation, the algorithm accentuated the signal intensity of the ONs if the ON signal was determined to be significantly higher than this reference (Fig 1). For images that did not have inherent fat saturation, the algorithm was chosen to accentuate the signal intensity of the ON only if it fell in a range that was higher than the normal white matter intensity but lower than the intensity of fat (Fig 1F, -J, -L), while decreasing the intensity of fat (Fig 1F, -L). The processed images were saved as separate DICOM series for further analysis.

Blinded Imaging Review

Two blinded board-certified neuroradiologists rated each ON Horos FLAIR and CE images on a 5-point Likert scale, ranging from 1 (definitely normal) to 5 (definitely abnormal). For subsequent analyses, ratings of 4 (probably abnormal) or 5 were taken as abnormal test results, while ratings ≤ 3 (possibly normal) were taken as a normal test result. Reviewers first rated the ONs on baseline images; then, after a gap of several days, they again rated the ONs with the availability of both baseline and processed images.

Quantitative Analysis

We manually measured the signal intensities of each ON (SI^{on}) and the ipsilateral normal-appearing white matter (SI^{wm}) for both baseline and processed images on each sequence. For ONs with obvious signal abnormality, the ROI was placed in the region of abnormal signal. Otherwise, the ON was sampled in its retrolubar portion on an image that allowed its best visualization, free from partial volume averaging effects. Using the SD of the signal intensity of air in the image as a measure of noise, we calculated the CNR for each sequence using the following formula: $CNR = (SI^{on} - SI^{wm}) / \text{Noise}$.

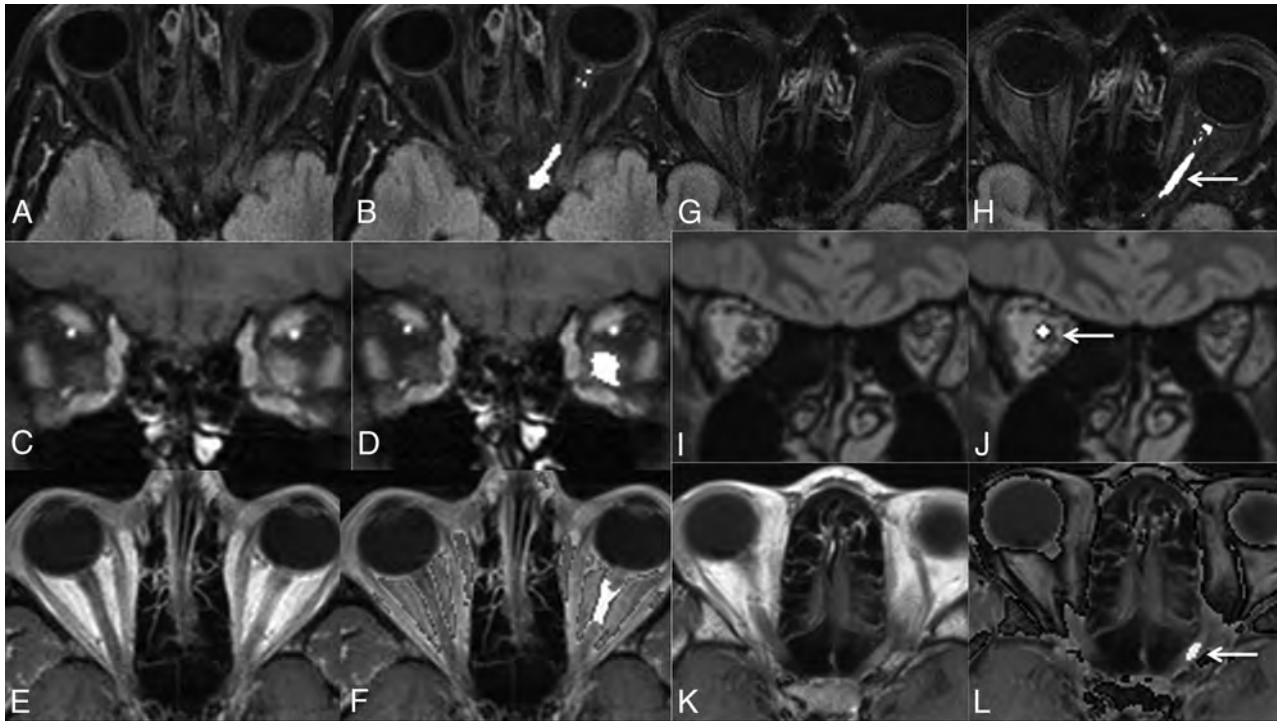


FIG 1. Axial FLAIR (A and B), coronal CE-T1WI (C and D), and axial CE-T1WI (E and F) images from routine brain MR imaging of a patient with clinically proven left optic neuritis before (A, C, and E) and after (B, D, and F) processing with a proprietary postprocessing algorithm showing accentuation of the signal intensity of the diseased optic nerve and the unaffected contralateral optic nerve. Axial FLAIR (G and H), coronal 3D-FLAIR (I and J), and axial CE-T1WI of different patients with clinically proven unilateral optic neuritis again demonstrating accentuation of intensity in diseased optic nerves (arrows) after processing (H, J, and L). Note that the detection of alteration in the optic nerve signal is especially challenging in images obtained without fat saturation (E, I, and K).

Statistical Analysis

Diagnostic performance for each reader and the average for both readers were assessed for baseline images in terms of sensitivity, specificity, positive predictive value (PPV), and negative predictive value for each sequence. Subset analysis was performed for images obtained with and without fat saturation. We quantitated the interrater reliability of confidence ratings for each sequence using κ (kappa).

Descriptive statistics were used to summarize the data. Continuous variables were summarized using means [SD] and medians (25th–75th percentiles), and categorical data were summarized using counts and percentages. The difference between cases and controls was tested using the nonparametric Kruskal-Wallis test for continuous variables and the Pearson χ^2 or Fisher exact test for categorical variables, as appropriate.

The effect of image processing on the confidence of categorization was assessed nonparametrically. The median of the scores across all readers and by individual readers, for cases and controls, was identified for both images, and the difference in the median (processed baseline image) was computed and compared using a signed rank test. Comparisons for each parameter pre- and postprocessing by an individual reader were performed using nonparametric signed rank tests.

Parameters for diagnostic performance and the interrater reliability of confidence ratings for reads with the availability of processed images were calculated and compared with corresponding parameters for baseline images to assess the effect of

processing on readers' diagnostic performance. We used the McNemar test for paired and Fisher exact test for unpaired binary diagnostic accuracy statistics, including sensitivity, specificity, and diagnostic accuracy.

RESULTS

Diagnostic Performance of Radiologists in the Detection of Optic Neuritis on Brain MR Imaging without Postprocessing

On FLAIR, sensitivities for readers 1 and 2 were 57% and 53% (Table 2), lower for images without fat saturation ($P = .001$, Table 3). Corresponding specificities were 62% and 90%, respectively (Table 2).

On coronal CE-T1WI, readers 1 and 2 identified abnormal enhancement in 48% and 57% of cases with specificities of 82% and 95%, respectively (Table 2). Detection of contrast-enhancement was negatively impacted by the absence of fat saturation ($P = .04$). Sensitivities were much lower on axial CE images but not significantly decreased in the absence of fat saturation ($P = .4$, Tables 2 and 3).

Quantitative Analysis of Images before and after Processing

For images before processing, there was a significant difference between the CNR of the diseased and control ONs for FLAIR ($P < .001$) and coronal CE-T1WI ($P < .001$), but not for axial CE-T1WI ($P = .17$, Table 4).

Table 2: Results of diagnostic performance of 2 neuroradiologists in the detection of changes of optic neuritis on T2-weighted FLAIR, coronal CE-T1WI, and axial CE-T1WI of brain without and with the availability of postprocessed images that aimed to selectively accentuate the signal intensity of diseased optic nerves

Parameter	Reader 1			Reader 2			Average	
	Before Processing	After Processing	P ^a Value	Before Processing	After Processing	P ^a Value	Before Processing	After Processing
Sensitivity (FL)	56.7%	56.7%	.34	53.3%	53.3%	.31	55.0%	55.0%
Specificity (FL)	62.1%	89.7%	.01	89.7%	93.1%	.5	75.9%	91.4%
Accuracy (FL)	59.3%	72.9%	.03	71.2%	72.9%	.5	65.3%	72.9%
PPV (FL)	60.7%	85%	NA	84.2%	88.9%	NA	72.5%	86.9%
NPV (FL)	58.1%	66.7%	NA	65%	65.9%	NA	61.5%	66.3%
Sensitivity (CCE)	47.8%	56.5%	.31	56.5%	56.5%	.24	52.2%	56.5%
Specificity (CCE)	81.8%	100%	.07	95.5%	100%	.5	88.7%	100%
Accuracy (CCE)	64.4%	77.8%	.04	75.5%	77.8%	.5	69.9%	77.8%
PPV (CCE)	73.3%	100%	NA	92.9%	100%	NA	83.1%	100%
NPV (CCE)	60%	68.8%	NA	67.7%	68.8%	NA	63.9%	68.8%
Sensitivity (ACE)	20.0%	30.0%	.22	13.3%	30.0%	.07	16.7%	30.0%
Specificity (ACE)	86.2%	100%	.07	100%	100%	0	93.1%	100.0%
Accuracy (ACE)	52.5%	64.4%	.04	55.9%	64.4%	.07	54.2%	64.4%
PPV (ACE)	60%	100%	NA	100%	100%	NA	80.0%	100%
NPV (ACE)	51%	58%	NA	52.7%	58%	NA	51.9%	58%

Note:—FL indicates FLAIR; CCE, coronal CE-T1WI; ACE, axial CE-T1WI; NPV, negative predictive value; NA, not applicable.

^aOne-tailed McNemar test.

Table 3: Effect of fat saturation on the sensitivity of readers in detecting changes of optic neuritis on FLAIR and CE images before and after postprocessing

Sequence Type	Reader 1		Reader 2	
	Fat Saturation+	Fat Saturation–	Fat Saturation+	Fat Saturation–
FL before processing	13/19 (68.4%)	4/11 (36.6%)	12/19 (63.1%)	4/11 (36.4%)
FL after processing	12/19 (63.2%)	5/11 (45.5%)	11/19 (57.9%)	5/11 (45.5%)
CCE before processing	10/17 (58.8%)	1/6 (16.7%)	11/17 (64.7%)	2/6 (33.3%)
CCE after processing	12/17 (70.6%)	1/6 (16.7%)	12/17 (70.6%)	1/6 (16.7%)
ACE before processing	1/6 (16.7%)	5/24 (20.8%)	2/6 (33.3%)	2/24 (8.3%)
ACE after processing	2/6 (33.3%)	7/24 (29.2%)	2/6 (33.3%)	7/24 (29.2%)

Note:—FL indicates FLAIR; CCE, coronal CE-T1WI; ACE, axial CE-T1WI.

Table 4: Effect of processing on the CNR of optic nerves relative to ipsilateral normal-appearing white matter in cases with optic neuritis and controls with normal optic nerve function

Sequence Type	Median CNR (25th–75th Percentiles) for Optic Nerves with Optic Neuritis		Median CNR (25th–75th Percentiles) for Normal Optic Nerves	
	Median CNR	P Value	Median CNR	P Value
FL before processing	–1.05 (–46.7–81.3)	<.001	–12.7 (–86.9–106.9)	.25
FL after processing	54.4 (–46.7–795.6)		–12.7 (–86.9–137.9)	
CCE before processing	9.8 (–181.8–129.2)	<.001	2.6 (–83.2–179.1)	.50
CCE after processing	6.2 (–181.8–238.1)		–0.37 (–83.2–66.8)	
ACE before processing	11.8 (–29.6–267.8)	.03	–14.3 (–63.1–2.5)	.27
ACE after processing	93.9 (–29.6–543.3)		–14.3 (–63.1–2.5)	

Note:—FL indicates FLAIR; CCE, coronal CE-T1WI; ACE, axial CE-T1WI.

The median (25th–75th percentiles) CNR of diseased ONs increased from –1.1 (–47–81) to 54 (–47–796) on FLAIR ($P < .001$), from 12 (–30–268) to 94 (–30–543) on axial CE-T1WI ($P = .03$), and from 10 (–182–129) to 6 (–182–238) on coronal CE-T1WI ($P < .001$) after processing. These group differences resulted from an increase in the CNR of 17/30 (57%), 8/30 (24%), and 14/23 (61%) cases on FLAIR, axial CE-T1WI, and coronal CE-T1WI, respectively.

The CNRs of control eyes as a group were not significantly affected by processing (Table 4). There were 2/58 false-positives on FLAIR image and none on CE images.

Effect of Processing on Confidence Ratings

For a subset of nerves with optic neuritis that showed accentuation of the CNR after processing, processing improved the confidence of both readers in categorizing nerves as abnormal. On average, an increase in rating was seen in 10.5/17 (62%), 3.5/13 (27%), and 7.5/9 (83%) cases on FLAIR, coronal CE, and axial CE images. The confidence rating never decreased in the presence of processing-related accentuation of the CNR. This favorable effect was associated with correct categorization of 3/17 (18%), 2/13 (15%), and 5.5/9 (61%) cases as abnormal, which were initially categorized as false-negatives. In cases in which imaging

remained unaffected after processing, there was a consistent decrease in the confidence rating of both readers with false-negative categorizations of 2.5/13 (19%), 1/10 (10%), and 1/16 (6.3%) FLAIR, coronal CE, and axial CE sequences, respectively, which were correctly categorized before processing. For all cases combined, the confidence ratings of readers were largely unaffected.

For control nerves, no change in the CNR was observed after processing in 55/58 (95%) FLAIR, 44/44 (100%) coronal CE, and 58/58 (100%) axial CE images. This lack of accentuation of the ON signal increased the confidence for both readers in categorizing ONs as normal. On average, an appropriate decrease in ratings was seen in 25/55 (45%), 20/44 (45%), and 32/58 (55%) controls on FLAIR, coronal CE, and axial CE images, respectively. There were no instances of an increase in rating in the absence of processing-related accentuation of the CNR. This favorable effect was associated with correct categorization of 5.5/58 (9.5%), 6/44 (14%), and 7.5/58 (13%) eyes as normal that were initially categorized as false-positives. In 3/58 (5%) controls with false-positive accentuation of the CNR, there was no increase in the false-positive rate because these eyes were categorized as false-positive even before processing. Overall, with image processing, there was a significant favorable shift in the median confidence ratings of controls for each reader on FLAIR ($P < .001$, $.007$), axial CE-T1WI ($P < .001$, $.002$), and coronal CE-T1WI ($P < .001$, $.004$) and a corresponding improvement in specificity (Table 2).

Effect of Processing on Diagnostic Performance

The sensitivities of readers were relatively unaffected (Table 2). There was an increase in the specificity of readers in detecting optic neuritis-related changes on all sequences, with the average specificity for the 2 readers increasing from 76% to 91% on FLAIR ($P = .01$ and $.5$ for the 2 readers), from 88.7% to 100% on coronal CE-T1WI ($P = .07$ and $.5$ for the 2 readers), and from 93% to 100% on axial CE-T1WI ($P = .07$ for reader 1, no change observed for reader 2) (Table 2). The overall diagnostic accuracy improved for one reader on FLAIR ($P = .03$ with either improvement or a trend towards improvement on other sequences (Table 2). Average PPVs for FLAIR, axial CE-T1WI, and coronal CE-T1WI improved from 73% to 87%, from 80% to 100%, and from 83% to 100%, respectively. Negative predictive values were relatively unchanged for other sequences. The overall trend was similar for subgroups with and without fat saturation (Table 3).

Interobserver agreement increased for all sequences after processing, with κ increasing from 0.08 to 0.67 on FLAIR, from 0.12 to 0.68 on axial CE-T1WI, and from 0.29 to 1 on coronal CE-T1WI.

DISCUSSION

In patients who happen to be evaluated by routine brain MR imaging at the time of symptom onset, there may still be a clinical need to evaluate this scan for imaging signs of optic neuritis. Our results indicate that in such scans that are not optimized for ON assessment, sensitivities for the detection of either signal alteration on FLAIR (55% in our study, Table 3) or abnormal contrast-enhancement (53% on coronal images, Table 3) are much lower

than the corresponding values of 76%–100% reported in the literature for dedicated orbital MR images.^{10–13,15}

To the best of our knowledge, there is only 1 previous study investigating the diagnostic performance of brain MR imaging regarding the detection of optic neuritis on FLAIR images.¹⁶ In this study, specifically on fat-suppressed FLAIR images, the authors reported a sensitivity of 76%–77%,¹⁶ significantly higher than that in our study. This difference is likely because our study included images acquired from a multitude of scanners with inconsistent fat suppression. The detection of optic neuritis on MR imaging is assisted by fat-saturated sequences,¹⁷ and our results support this finding (Table 3). Indeed, the sensitivity in our study was significantly affected by the presence or absence of fat suppression (Table 3), with an average sensitivity of 66% for a subgroup with fat-saturated FLAIR images being much closer to that reported previously by McKinney et al.¹⁶

No prior studies have explored the detection of ON enhancement in the setting of optic neuritis on routine brain CE sequences. With an average sensitivity of 53%, it is notable that in 74% of patients in our study (Table 1), coronal CE-T1WI had been performed with fat saturation. This is not always the case for routine brain MR imaging. For patients scanned without such a sequence, the sensitivity for the detection of ON enhancement can be substantially lower, with an average of 25% in our study (Table 3).

Because a coronal CE-T1WI may not always be included in a routine brain MR imaging protocol, we also assessed the ability of radiologists to detect the presence of enhancement on axial CE-T1WI. The average sensitivity for detecting ON enhancement in the axial plane (17%) was substantially lower, likely resulting from a combination of partial volume averaging effects, which is more likely to impact a horizontally extending ON in the axial plane, and an infrequent use of fat saturation in axial CE images (Table 1).

These challenges in detecting optic neuritis on routine brain MR imaging are also highlighted by only slight interobserver agreement for FLAIR and coronal CE-T1WI and fair interobserver agreement on axial CE-T1WI.

It has been previously shown that the detection of optic neuritis on FLAIR and CE-T1WI can be improved using an image-postprocessing algorithm that can selectively accentuate the CNR between diseased ONs and the normal white matter.¹⁵ We observed a similar beneficial effect of the algorithm on the CNR of diseased ONs on FLAIR as well as CE-T1WI (Table 4 and Fig 1). While this resulted in an improvement of diagnostic accuracy, unlike in the previous study, this improvement in the CNR did not translate into improvement in the sensitivity for the detection of signal alterations on FLAIR images (Table 2). The analysis of change in confidence ratings indicates that this issue was at least partly a result of decreased confidence in assigning disease status in the cases in which the processed images failed to accentuate the CNR. We did, however, observe some improvement in sensitivity for the detection of ON enhancement (Table 2).

As reported previously,¹⁵ rates of false-positive accentuation of signal in control ONs (3.4% for FLAIR and 0% for CE images) were low in our study. This finding translated into an improvement in the specificity and PPVs for FLAIR and CE images

(Table 2). Also, as seen previously, the availability of processed images resulted in substantial improvement in the interobserver agreement to substantial or almost perfect levels.¹⁵

In addition to use in patients presenting with optic neuritis, this processing could find use in patients with MS. While the ON is not currently a cardinal location, it has been recommended as a potential addition to diagnose MS at its early stages.¹⁸ Sartoretti et al¹⁹ have previously shown that patients with MS may have subclinical episodes of optic neuritis. Given that routine surveillance brain MR imaging is currently recommended to monitor disease progression,²⁰ this algorithm may be useful to detect clinical and/or subclinical optic neuritis in such scans.

A few limitations should be noted. First, our study used only 2 expert neuroradiologists as blinded readers who read each sequence only once. Intraobserver reliability, therefore, could not be evaluated. It is possible that in instances in which image processing did not produce any change in the original images of cases or controls, differences in ratings of original and processed images by a given reader could at least partly be due to intraobserver variability. Consistency of change in reader responses in the absence of processing-induced image alteration, however, indicates that the improved specificity seen in our study is indeed a beneficial effect of the algorithm. Additionally, the use of this algorithm by radiologists who are not subspecialized in neuroradiology could not be evaluated, restricting the evaluation of the use of this algorithm in communities without subspecialized care. While our study did include scans from different scanners and with different parameters, we think that this feature makes it more representative of the reality of clinical practice, in which the patients may present to expert neuro-ophthalmology services already having been scanned at varying facilities.

CONCLUSIONS

Assessment of routine brain MR imaging without optimized sequences for the assessment of the ON has relatively poor sensitivity (approximately 55%), modest specificity, and only slight-to-fair interobserver agreement for the detection of optic neuritis-related changes on FLAIR and CE-T1WI. The sensitivity can be expected to be even lower if FLAIR and/or coronal CE-T1WI images are acquired without fat saturation. By selectively accentuating the CNR of diseased-but-not-normal ONs, our image-postprocessing algorithm can improve the diagnostic performance of readers with improved specificity and PPVs, accompanied by a substantial improvement in interobserver agreement. The image processing, however, was unable to bring the sensitivity to a level comparable with the reported values for dedicated orbital MR imaging, which should still be the criterion standard examination if ordered within the appropriate timeframe.

Disclosures: Gregory Van Stavern—UNRELATED: Royalties: UpToDate online data base, Comments: yearly royalties for review article. Lee Rhea—UNRELATED: Employment: Washington University Medical School, Comments: I was a salaried employee of the Washington University Medical School at the time I contributed to the preparation of the article (statistical analyses). Aseem Sharma—RELATED: Other: Correlative Enhancement LLC, Comments: I am coinventor of the postprocessing algorithms used in this study. I am cofounder of Correlative Enhancement LLC, a company that aims to commercialize the postprocessing algorithms used in this study; UNRELATED: Stock/Stock Options: GE Healthcare, Comments: I own

publicly traded stocks in GE Healthcare, a company that makes imaging equipment among other things.

REFERENCES

1. The clinical profile of optic neuritis: experience of the Optic Neuritis Treatment Trial—Optic Neuritis Study Group. *Arch Ophthalmol* 1991;109:1673–78 Medline
2. Rizzo JF 3rd, Lessell S. Optic neuritis and ischemic optic neuropathy: overlapping clinical profiles. *Arch Ophthalmol* 1991;109:1668–72 CrossRef Medline
3. Bee YS, Lin MC, Wang CC, et al. Optic neuritis: clinical analysis of 27 cases. *Kaohsiung J Med Sci* 2003;19:105–12 CrossRef Medline
4. Balcer LJ. Clinical practice: optic neuritis. *N Engl J Med* 2006;354:1273–80 CrossRef Medline
5. Toosy AT, Mason DF, Miller DH. Optic neuritis. *Lancet Neurol* 2014;13:83–99 CrossRef Medline
6. Hoorbakht H, Bagherkashi F. Optic neuritis, its differential diagnosis and management. *Open Ophthalmol J* 2012;6:65–72 CrossRef Medline
7. Keltner JL, Johnson CA, Spurr JO, et al. Baseline visual field profile of optic neuritis: the experience of the optic neuritis treatment trial—Optic Neuritis Study Group. *Arch Ophthalmol* 1993;111:231–34 CrossRef Medline
8. Fang JP, Donahue SP, Lin RH. Global visual field involvement in acute unilateral optic neuritis. *Am J Ophthalmol* 1999;128:554–65 CrossRef Medline
9. Wilhelm H, Schabet M. The diagnosis and treatment of optic neuritis. *Dtsch Arztebl Int* 2015;112:616–25; quiz 626 CrossRef Medline
10. Rizzo JF 3rd, Andreoli CM, Rabinov JD. Use of magnetic resonance imaging to differentiate optic neuritis and nonarteritic anterior ischemic optic neuropathy. *Ophthalmology* 2002;109:1679–84 CrossRef Medline
11. Bursztyn L, De Lott LB, Petrou M, et al. Sensitivity of orbital magnetic resonance imaging in acute demyelinating optic neuritis. *Can J Ophthalmol* 2019;54:242–46 CrossRef Medline
12. Kupersmith MJ, Alban T, Zeiffer B, et al. Contrast-enhanced MRI in acute optic neuritis: relationship to visual performance. *Brain* 2002;125:812–22 CrossRef Medline
13. Hickman SJ, Toosy AT, Miszkil KA, et al. Visual recovery following acute optic neuritis: a clinical, electrophysiological and magnetic resonance imaging study. *J Neurol* 2004;251:996–1005 CrossRef Medline
14. Stunkel L, Kung NH, Wilson B, et al. Incidence and causes of overdiagnosis of optic neuritis. *JAMA Ophthalmol* 2018;136:76–81 CrossRef Medline
15. Stunkel L, Sharma A, Parsons MS, et al. Evaluating the utility of a postprocessing algorithm for MRI evaluation of optic neuritis. *AJNR Am J Neuroradiol* 2019;40:1043–48 CrossRef Medline
16. McKinney AM, Lohman BD, Sarikaya B, et al. Accuracy of routine fat-suppressed FLAIR and diffusion-weighted images in detecting clinically evident acute optic neuritis. *Acta Radiol* 2013;54:455–61 CrossRef Medline
17. Guy J, Mao J, Bidgood WD Jr, et al. Enhancement and demyelination of the intraorbital optic nerve: fat suppression magnetic resonance imaging. *Ophthalmology* 1992;99:713–19 CrossRef Medline
18. Thompson AJ, Banwell BL, Barkhof F, et al. Diagnosis of multiple sclerosis: 2017 revisions of the McDonald criteria. *Lancet Neurol* 2018;17:162–73 CrossRef Medline
19. Sartoretti T, Sartoretti E, Rauch S, et al. How common is signal-intensity increase in optic nerve segments on 3D double inversion recovery sequences in visually asymptomatic patients with multiple sclerosis? *AJNR Am J Neuroradiol* 2017;38:1748–53 CrossRef Medline
20. Giorgio A, De Stefano N. Effective utilization of MRI in the diagnosis and management of multiple sclerosis. *Neurol Clin* 2018;36:27–34 CrossRef Medline

Susceptibility-Weighted Imaging of the Pediatric Brain after Repeat Doses of Gadolinium-Based Contrast Agent

K. Ozturk and D. Nascene

ABSTRACT

BACKGROUND AND PURPOSE: Gadolinium complexes have paramagnetic properties; thus, we aimed to determine the susceptibility changes in the globus pallidus and dentate nucleus following administration of linear or macrocyclic gadolinium-based contrast agents in children.

MATERIALS AND METHODS: Thirty-three patients with linear gadolinium-based contrast agent gadopentetate dimeglumine administration, 33 age- and sex-matched patients with macrocyclic gadolinium-based contrast agent gadobutrol administration, and 33 age- and sex-matched control subjects without gadolinium exposure were enrolled in this retrospective study. The signal intensity on SWI and T1WI was determined in the dentate nucleus, middle cerebellar peduncle, globus pallidus, and pulvinar of the thalamus in an ROI-based analysis to calculate dentate nucleus-to-middle cerebellar peduncle and globus pallidus-to-thalamus ratios. A repeated measures ANOVA was performed to compare SWI_{minimum}, SWI_{mean}, and T1WI signal intensity ratios between gadolinium-based contrast agent groups and control subjects. Pearson correlation analysis was performed to determine any correlation between signal intensity ratios and variables.

RESULTS: Dentate nucleus-to-middle cerebellar peduncle and globus pallidus-to-thalamus ratios for both SWI_{mean} and SWI_{minimum} were lower for the linear gadolinium-based contrast agent group compared with macrocyclic gadolinium-based contrast agent and control groups ($P < .05$). No significant difference of the SWI_{mean} and SWI_{minimum} ratios were noted between the macrocyclic gadolinium-based contrast agent group and the control group ($P > .05$). Both dentate nucleus-to-middle cerebellar peduncle and globus pallidus-to-thalamus ratios on T1WI in the linear gadolinium-based contrast agent group were higher than in the control group and the macrocyclic gadolinium-based contrast agent group ($P < .05$). A negative correlation was identified between SWI_{mean} and SWI_{minimum} ratios and the number of linear gadolinium-based contrast agent administrations (dentate nucleus-to-middle cerebellar peduncle ratio: SWI_{mean}, $r = -0.43$, $P = .005$; SWI_{minimum}, $r = -0.38$, $P = .011$; globus pallidus-to-thalamus ratio: SWI_{mean}, $r = -0.39$, $P = .009$; SWI_{minimum}, $r = -0.33$, $P = .017$).

CONCLUSIONS: SWI analysis of the pediatric brain demonstrated a statistically significant decrease in SWI_{minimum} and SWI_{mean} values for the dentate nucleus and globus pallidus after administration of linear gadolinium-based contrast agents but not macrocyclic gadolinium-based contrast agents.

ABBREVIATIONS: DN = dentate nucleus; GBCA = gadolinium-based contrast agent; GP = globus pallidus; MCP = middle cerebellar peduncle; min = minimum; SI = signal intensity; Th = pulvinar of the thalamus

Gadolinium-based contrast agents (GBCAs) are essential components of clinical diagnosis and treatment decision-making for millions of patients worldwide.¹ Recent studies have shown gadolinium deposition in multiple organs,² including the brain, after repeat administration of GBCAs.³ Intracranial

gadolinium deposition in the brain has been associated with increased signal intensity (SI) on T1WI,⁴ most notably in the globus pallidus (GP) and cerebellar dentate nucleus (DN).⁵ Substantial evidence has been provided by histopathologic analysis indicating that the reported T1WI SI increase in the DN and GP corresponds to gadolinium deposition.⁶

SI changes in the brain parenchyma on unenhanced T1-weighted MR imaging have been identified in association with various histopathologic processes.⁷ Particularly, hyperintensity within the DN on T1WI due to shortening of the T1 relaxation time is believed to occur secondary to several factors, including ferric iron accumulation, ferritin accumulation associated with lipid

Received August 6, 2020; accepted after revision December 17.

From the Department of Radiology, University of Minnesota, Minneapolis, Minnesota.

Please address correspondence to Kerem Ozturk, MD, Division of Neuroradiology, Department of Radiology, University of Minnesota, B-226 Mayo Memorial Building, MMC 292, 420 Delaware St SE, Minneapolis, MN 55455; e-mail: ozturk027@umn.edu; @keremozturk_rad
<http://dx.doi.org/10.3174/ajnr.A7143>

Table 1: Exclusion criteria

Exclusion Parameters	Control Group	Macrocytic GBCA Group	Linear GBCA Group
Initially selected	57	64	61
Age younger than 2 years	3	5	6
Renal dysfunction	2	0	0
Hepatic dysfunction	3	2	2
Lesion in the cerebellum, midbrain, corpus striatum, or pulvinar of the thalamus	3	2	1
Missing documentation of the prior contrast agent	8	11	7
Missing or unsatisfactory T1WI	2	2	3
Missing or unsatisfactory SWI	3	4	3
Different sequences and parameters between comparison T1WIs	0	5	6
Final No. of groups	33	33	33

peroxidation, and the presence of paramagnetic free radicals as well as paramagnetic compounds like metal ions such as iron and manganese.^{8,9} Any of these histopathologic mechanisms could play a role in the T1WI SI observed in the DN and GP of patients with gadolinium retention. Recently, numerous studies have focused on the association between increased SI on unenhanced T1WI and exposure to intravenously administered GBCAs.¹⁰

SWI is a high-resolution 3D gradient-echo sequence that incorporates phase and magnitude data to identify variations in magnetic susceptibility between adjacent tissues with a sensitivity greater than conventional gradient-echo sequences.¹¹ Its higher sensitivity in the detection of paramagnetic and diamagnetic compounds such as iron particles, blood-breakdown products, and calcifications provides clinically relevant information in the assessment of various conditions, including neurodegeneration, cerebral neoplasm, vascular malformation, and intracranial hemorrhage.¹² Because gadolinium has a paramagnetic effect, SWI can be used for noninvasive visualization of gadolinium retention within the DN and GP that may not be apparent by T1WI.¹³

In this study, we hypothesized that sequential use of GBCAs would increase the magnetic susceptibility within the DN and GP as seen on SWI. Thus, we analyzed the susceptibility values in the DN and GP of children who had consecutive applications of the linear GBCA gadopentetate dimeglumine or the macrocytic GBCA gadobutrol compared with control subjects who had no history of GBCA administration.

MATERIALS AND METHODS

All procedures were performed in accordance with the ethical standards of the institutional research committee and with the 2013 revised Helsinki declaration and its later amendments or comparable ethical standards. This study was approved by the local institutional review board and the requirement to obtain informed consent was waived.

Patients

This was a retrospective single-center study of children and adolescents (age at final contrast-enhanced MR imaging

examination younger than 18 years) who underwent brain MR imaging with administration of the macrocytic GBCA gadobutrol or the linear GBCA gadopentetate dimeglumine between 2010 and 2020. Before January 1, 2014, a linear GBCA, gadopentetate dimeglumine (Magnevist; Bayer HealthCare Pharmaceuticals), was used at our institution for nearly all brain MR imaging examinations. Since January 1, 2014, our institution changed to the macrocytic GBCA gadobutrol (Gadavist; Bayer Schering Pharma). This allowed us to have a population of children who had acquired only the macrocytic GBCA gadobutrol to compare with a similar

earlier population who had received only the linear GBCA gadopentetate dimeglumine. We retrospectively screened our database to identify children who met the following inclusion criteria: 1) the patients' ages ranged from 2 to 18 years, 2) MR imaging follow-up was performed exclusively in our department, and 3) contrast-enhanced MR imaging with the exclusive use of the macrocytic GBCA gadobutrol or the linear GBCA gadopentetate dimeglumine was followed by another 3T MR imaging including unenhanced T1WI and SWI. The lower limit of 2 years of age was selected to exclude younger children with possible incomplete myelination.¹³ Exclusion criteria were the following: 1) renal insufficiency; 2) liver dysfunction; 3) missing data or unsatisfactory image quality of unenhanced T1WI and/or SWI; 4) structural brain abnormality in the cerebellum, midbrain, corpus striatum, or pulvinar of the thalamus (Th), determined by the study investigators at the time of retrospective image review; and 5) broadly varying MR imaging parameters among the MR imaging scans (>5% for TR or >10% for TE). The exclusion criteria of the study design are shown in Table 1. In total, 33 patients with exclusive use of linear GBCAs and 33 age- and sex-matched patients receiving macrocytic GBCAs were finally enrolled in this study.

A total of 33 control subjects matched for age and sex were selected for each case patient and consisted of pediatric patients who underwent nonenhanced brain MR imaging between 2010 and 2020 without any record of GBCA administration.

Clinical Data

Data on demographics were acquired from a standardized review of the health records of all children through a radiology search. For all included patients, age, sex, intrinsic disease, and number and type of GBCA administrations, along with the accumulated GBCA dose and history of chemotherapy or radiation therapy, were assessed by chart review (Table 2).

The number of macrocytic GBCA and linear GBCA administrations was abstracted from the medical charts. The macrocytic GBCA gadobutrol and the linear GBCA gadopentetate dimeglumine were dosed at 0.1 mmol per kilogram of the patient's body weight.

Table 2: Clinical and radiologic characteristics of the study population^a

Characteristic	Linear GBCA– Exposed Children	Macrocytic GBCA– Exposed Children	GBCA-Naive Control Subjects
Age (yr)			
Mean (SD)	8.2 (SD, 5.4)	8.2 (SD, 5.1)	8.2 (SD, 3.6)
Range	2–18	2–18	2–18
Sex			
Male	23	23	23
Female	10	10	10
Mean (SD) No. of contrast-enhanced MR imaging	2.4 (SD, 2.4)	4.03 (SD, 2.9)	0
Mean (SD) time interval between MR imaging (mo)	7.16 (SD, 7.5)	7.4 (SD, 7.3)	0
Mean (SD) accumulated gadolinium dose (mmol)	17.5 (SD, 24.1)	13.3 (SD, 11.9)	0
Diagnosis			
Intracranial neoplasm	7	7	10
Extracranial neoplasm	2	0	1
Pituitary abnormality	3	6	2
Orbit/optic nerve pathology	6	7	2
Adrenoleukodystrophy	5	5	10
Benign conditions	10	8	8
History of radiation treatment	3	2	3
History of chemotherapy	6	5	4
History of neurosurgery	2	2	3

^a Data are number of patients unless indicated otherwise and mean (SD).

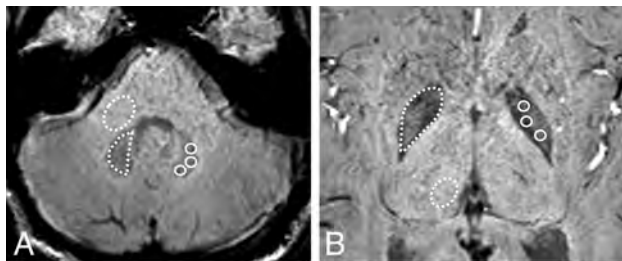


FIG 1. SWI at the level of the DN (A) and GP (B) used for drawing the ROIs in the DN and GP with the corresponding MCP and Th for normalization, respectively. *Dotted lines* illustrate the freehand ROI used to obtain SWI_{mean} from the DN, GP, MCP, and Th; *solid lines* illustrate the circular ROIs used to obtain SWI_{min} from the DN and GP.

Image Acquisition

All examinations were performed on 3T MR imaging scanners (Tim Trio and Magnetom Skyra; Siemens) with 16- or 20-channel head coils. The scanning sequences included the conventional MR images and SWI. The parameters for conventional MR images were as follows: FLASH T1WI before and after GBCA injection (TR, 250 ms; TE, 2.48 ms; section thickness, 2.0 mm; FOV, 250 mm), fast spin-echo T2WI (TR, 6000 ms; TE, 99 ms; section thickness, 2.0 mm; section interval, 1.0 mm; FOV, 250 mm), FLAIR T2WI (TR, 9000 ms; TE, 81 ms; TI, 2400 ms; section thickness, 2.0 mm; section interval, 1.0 mm; FOV, 250 mm).

All patients underwent precontrast SWI scanning (TR, 27 ms; TE, 20 ms; flip angle, 15; bandwidth, 250 kHz; matrix size, 256 × 134; parallel factor, 2; FOV, 250 mm; and acquisition time, approximately 2 minutes and 30 seconds). Presaturation slabs were used to saturate air-containing structures such as the petrous pyramids and

paranasal sinuses. SWI was performed as a 1-mm isotropic 3D acquisition with minimum intensity projections of the SWI, and images were reconstructed on an axial plane with a 2-mm section thickness.

ROI Analysis

Image analysis of unenhanced T1WI was performed as described in detail previously by Kanda et al¹⁴ and replicated in other reports on studies of brain gadolinium deposition. Placement of ROIs was performed by a neuroradiology fellow (K.O.), who was blinded to the clinical data. The images were also reviewed independently by a second radiologist (D.N.) with 10 years of experience in neuroradiology for the correct placement of the ROIs into the DN, middle cerebellar peduncle (MCP), GP, and Th. The DN and GP were selected because they are commonly analyzed regions of T1WI SI hyperintensity in the brain after GBCA administration.^{14–16} Also, McDonald et al¹⁷

reported that the DN contains the highest concentration of gadolinium deposition in the brain tissue of deceased patients.

ROI placement and subsequent image-based analysis was performed using a dedicated software, Vitrea (Vital Images). Freehand ROIs were drawn within both the DN and GP; then, an elliptic ROI was placed in MCP and Th, respectively, on SWI to determine SWI_{mean} SI ratios with an average of 3 measurements. $SWI_{minimum (min)}$ was extracted from the manual placement of at least 5 circular ROIs into the DN and GP that encompassed 5 voxels (approximately 5 mm²), and the lowest value was determined (Fig 1). Compatible with the previous study,¹⁸ SI ratios were calculated as follows: T1WI ratio = (T1WI SI of DN)/(T1WI SI of MCP) or (T1WI SI of GP) / (T1WI SI of Th); SWI_{mean} ratio = (SWI_{mean} of DN) / (SWI_{mean} of MCP) or (SWI_{mean} of GP) / (SWI_{mean} of Th); and SWI_{min} ratio = (SWI_{min} of DN) / (SWI_{min} of MCP) or (SWI_{min} of GP) / (SWI_{min} of Th). Eventually, all ROIs were visually inspected for correctness to modify possible structural displacement from baseline due to suboptimal coregistration.

Statistics

Data were tested for normality using the Shapiro-Wilk test, and the choice of parametric-versus-nonparametric tests was made on the basis of the outcome of this test. We conducted a repeated measures ANOVA with post hoc Bonferroni tests for pair-wise multiple comparisons for the DN-to-MCP and GP-to-Th ratios on unenhanced T1WI and SWI among the following: 1) only macrocyclic GBCA administration in the GBCA group versus the non-GBCA group; 2) only linear GBCA administration in the GBCA group versus the non-GBCA group; and 3) only macrocyclic GBCA administration in the GBCA group versus only linear GBCA administrations in the GBCA group. Pearson correlation

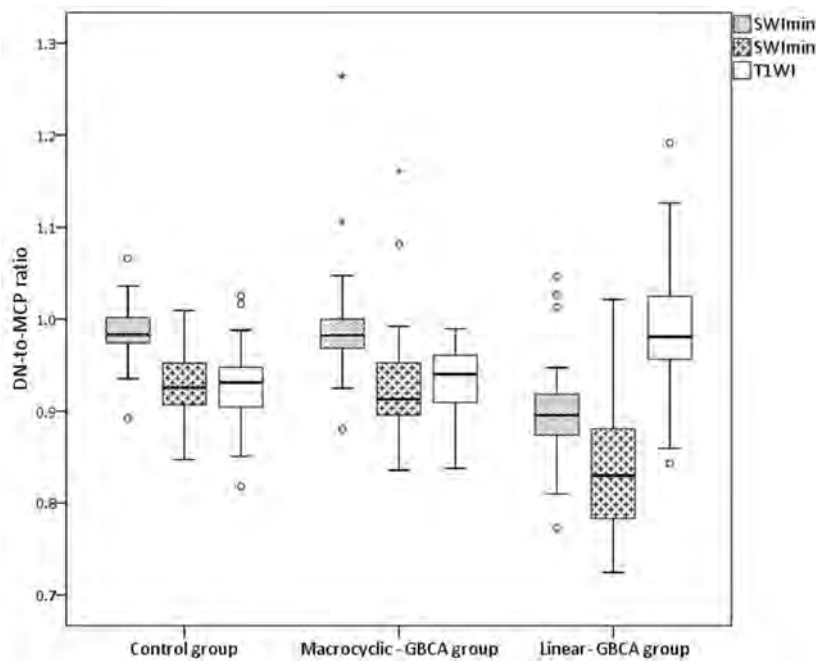


FIG 2. Boxplots of the mean DN-to-MCP ratios on SWI and T1WI among the linear GBCA, macrocytic GBCA, and control groups. The error bars for boxplots represent the minimum and maximum data points within each group, and the Middle box represents the 25th, 50th, and 75th percentiles of the data within each group.

analyses were performed to evaluate associations between DN-to-MCP and GP-to-Th ratios from the most recent brain MR imaging examinations in patients exposed to GBCA and confounding parameters, including the number of MR images, total cumulative linear or macrocytic GBCA dose, the mean duration between MR imaging, and age. The independent samples *t* test or 1-way ANOVA was used to assess the DN-to-MCP and GP-to-Th ratio difference in the GBCA-exposed groups according to sex, intrinsic disease, history of brain radiation therapy, and chemotherapy. Consequently, the variables that were found to be statistically different on univariate analyses were further subjected to multivariate linear regression analysis. Intraobserver agreement of reader 1 (K.O.) for the quantitative measurements of the SI ratio was determined with Lin concordance correlation coefficients. The a priori significance level was set to .05, and all reported *P* values are 2-tailed. A Bonferroni correction with an adjusted *P* value < .05 was considered statistically significant for 3-subgroup comparison. Analyses were performed using SPSS 23 for Windows (IBM).

RESULTS

Patient Characteristics

Our cohort included 33 children who had only the linear GBCA gadopentetate dimeglumine (mean age, 8.2 [SD, 5.4] years; range, 2–18 years), 33 sex- and age-matched children who had only the macrocytic GBCA gadobutrol (mean age, 8.2 [SD, 5.1] years; range, 2–18 years), and 33 sex- and age-matched controls (mean age, 8.2 [SD, 3.6] years; range, 2–18 years). Patient characteristics and radiologic data are presented in Table 2. The mean number of doses of linear GBCA gadopentetate dimeglumine and macrocytic

GBCA gadobutrol were 2.4 (SD, 2.4) and 4.03 (SD, 2.9), respectively.

Intraobserver Agreement

The intraobserver agreement was substantial for T1WI values for both the DN-to-MCP ratio (Concordance correlation coefficient = 0.96; 95% CI, 0.92–0.98; *P* < .001) and the GP-to-Th ratio (Concordance correlation coefficient = 0.95; 95% CI, 0.91–0.98; *P* < .001); it was less concordant for SWI_{mean} and SWI_{min} for both the DN-to-MCP ratio (SWI_{mean}, Concordance correlation coefficient = 0.85; 95% CI, 0.79–0.90; *P* = .003; SWI_{min}, Concordance correlation coefficient = 0.83; 95% CI, 0.77–0.88; *P* = .005) and the GP-to-Th ratio (SWI_{mean}, Concordance correlation coefficient = 0.83; 95% CI, 0.78–0.89; *P* = .004; SWI_{min}, Concordance correlation coefficient = 0.82; 95% CI, 0.76–0.87; *P* = .007).

DN-to-MCP Ratio on SWI and T1WI

The DN-to-MCP ratios for SWI_{mean} and SWI_{min} were lower in those with only linear GBCA administration (SWI_{mean}, 0.898 [SD, 0.056]; SWI_{min}, 0.835 [SD, 0.073]) than in both the macrocytic GBCA group (SWI_{mean}, 0.992 [SD, 0.061]; SWI_{min}, 0.928 [SD, 0.064]) and the control group (SWI_{mean}, 0.985 [SD, 0.032]; SWI_{min}, 0.925 [SD, 0.037]) (adjusted *P* value < .001). No significant differences in the DN-to-MCP ratio for SWI_{mean} and SWI_{min} were noted between the macrocytic GBCA group and the control group (*P* = .595 and .829, respectively). The mean DN-to-MCP ratios on T1WI in the linear GBCA group (0.986 [SD, 0.073]) were also higher than those in the non-GBCA group (0.926 [SD, 0.042]) and the macrocytic GBCA group (0.930 [SD, 0.043]) (adjusted *P* value < .001) (Fig 2). A moderate negative correlation was identified between the DN-to-MCP ratio for SWI_{mean} and SWI_{min} and the number of linear GBCA administrations (SWI_{mean}, *r* = −0.43 and *P* = .005; SWI_{min}, *r* = −0.38 and *P* = .011) (Fig 3).

The Pearson correlation coefficient revealed no significant correlation between SWI/T1WI-derived values and the mean time interval among MR imaging scans, total GBCA dose, and age (all *P* > .05). There was no significant difference in the SWI/T1WI-derived SI ratios regarding sex, intrinsic disease, and history of radiation or chemotherapy (all *P* > .05). Multivariate linear regression analyses derived from univariate analysis demonstrated that SWI_{mean} and SWI_{min} ratios were associated with the number of linear GBCA administrations (adjusted *R*² for the model = 0.227) (SWI_{mean}: regression coefficient β = −0.026, *P* = .012; SWI_{min}: β = −0.03, *P* = .02). Additionally, no significant correlation was noted between SWI-derived values and age in the control groups (SWI_{mean}: *r* = −0.11 and *P* = .13; SWI_{min}: *r* = −0.15 and *P* = .20).

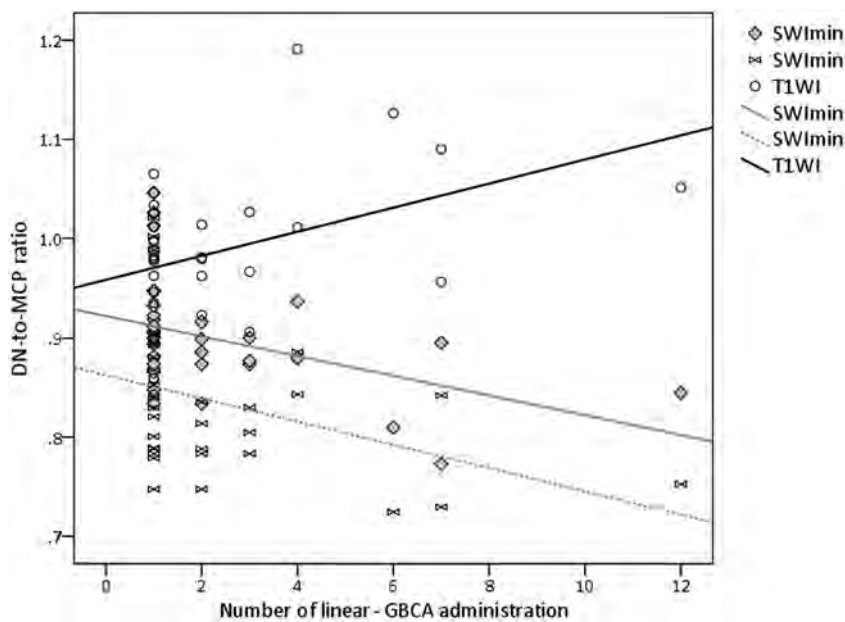


FIG 3. Scatterplot of the DN-to-MCP ratios for SWI_{mean} , SWI_{min} , and T1WI versus the number of intravenous linear GBCA administrations, with *linear regression lines* for each group.

Figure 4 demonstrates representative MR images. Figures 5 and 6 reveal scatterplots of the correlation between the DN-to-MCP ratios on unenhanced T1WI and SWI.

GP-to-Th Ratio on SWI and T1WI

The GP-to-Th ratios for SWI_{mean} and SWI_{min} were lower in those with only linear GBCA administration (SWI_{mean} , 0.765 [SD, 0.041]; SWI_{min} , 0.751 [SD, 0.038]) than in both the macrocyclic GBCA group (SWI_{mean} , 0.804 [SD, 0.047]; SWI_{min} , 0.793 [SD, 0.045]) and the control group (SWI_{mean} , 0.857 [SD, 0.052]; SWI_{min} , 0.841 [SD, 0.048]) (adjusted P value < .001). No significant differences of the GP-to-Th ratio for SWI_{mean} and SWI_{min} were noted between the macrocyclic GBCA group and the control group ($P = .503$ and 0.778 , respectively). Mean GP-to-Th ratios on T1WI in the linear GBCA group (1.001 [SD, 0.072]) were also higher than in the non-GBCA group (0.953 [SD, 0.047]) and the macrocyclic GBCA group (0.958 [SD, 0.049]) (adjusted P value < .001). A moderate negative correlation was identified between the GP-to-Th ratio for SWI_{mean} and SWI_{min} and the number of linear GBCA administrations (SWI_{mean} , $r = -0.39$, $P = .009$; SWI_{min} , $r = -0.33$, $P = .017$). The Pearson correlation coefficient revealed no significant correlation between SWI/T1WI-derived values and the mean time interval among MR imaging, total GBCA dose, and age (all $P > .05$). There was no significant difference in the SWI/T1WI-derived SI ratios regarding sex, intrinsic disease, and a history of radiation or chemotherapy (all $P > .05$). Multivariate linear regression analyses derived from univariate analysis demonstrated that SWI_{mean} and SWI_{min} ratios were associated with the number of linear GBCA administrations (adjusted R^2 for the model = 0.185) (SWI_{mean} ; $\beta = -0.022$, $P = .015$; SWI_{min} ; $\beta = -0.026$, $P = .028$). Additionally, no significant correlation was noted between SWI-derived values and age in the control groups (SWI_{mean} ; $r = -0.14$, $P = .15$; SWI_{min} ; $r = -0.11$, $P = .24$).

DISCUSSION

In this study, we aimed to determine whether administration of the macrocyclic GBCA gadobutrol or the linear GBCA gadopentetate dimeglumine in children is correlated with the development of a susceptibility signal within the DN or GP as an imaging surrogate for gadolinium deposition. The DN-to-MCP and GP-to-Th ratios for SWI_{mean} and SWI_{min} in children who received only linear GBCAs were lower than those in the non-GBCA group (control group) and macrocyclic GBCA group. On T1WI, previous reports have shown a strong relationship between the hyperintensity in the DN/GP and linear GBCA administration,¹⁶ our results also reinforce the previous results.

The clinical relevance of intracranial gadolinium retention, if any, remains unknown. Nevertheless, the pediatric brain may be more prone to the deleterious effects of gadolinium deposition because the pediatric brain is typically more susceptible to a number of toxins.^{19,20} Additionally, the cumulative dose and duration of exposure to GBCAs may be greater in children than in adults.²⁰ Thus, it is essential to determine the safest GBCAs for the pediatric population.²¹ Recent studies investigating pediatric intracranial gadolinium deposition have concentrated on the linear GBCA gadopentetate dimeglumine,²² though a few studies in the pediatric population have analyzed the effect of repeat administration of macrocyclic GBCAs.²³ Radbruch et al²⁴ and Ryu et al¹⁵ examined the sequential administration of the macrocyclic GBCA gadoterate meglumine in pediatric patients and found that this agent was not correlated with T1WI hyperintensity in the DN. In addition, Tibussek et al²³ analyzed a group of pediatric patients receiving repeat administration of the macrocyclic GBCAs gadoteridol and gadoterate meglumine and did not observe any T1WI hyperintensity within the DN.

The DN and GP are known to have a rich iron content, and a high susceptibility signal within DN and GP has been reported previously due to its paramagnetic potency.²⁵ The magnitude SI on SWI depends on $T2^*$, geometry, orientation to the B_0 , and differences in magnetic susceptibility, as well as serving as a function of T1.¹¹ If additional gadolinium is deposited in the DN, SI values on SWI should theoretically decrease after serial GBCA administration because gadolinium is a strong paramagnetic substance with a molar susceptibility of 325 ppm L/mol.²⁶ In this study, the susceptibility values in the DN and GP were better correlated with the number of linear GBCA administrations than T1WI SI ratios were. One explanation for a stronger association between susceptibility values and the number of linear GBCA administrations is that the endogenous substances cause susceptibility changes in the DN and GP but induce less T1 shortening.⁷ This explanation conflicts with the results of Hinoda et al,²⁶ which demonstrated that the susceptibility values on quantitative susceptibility mapping in the DN correlated

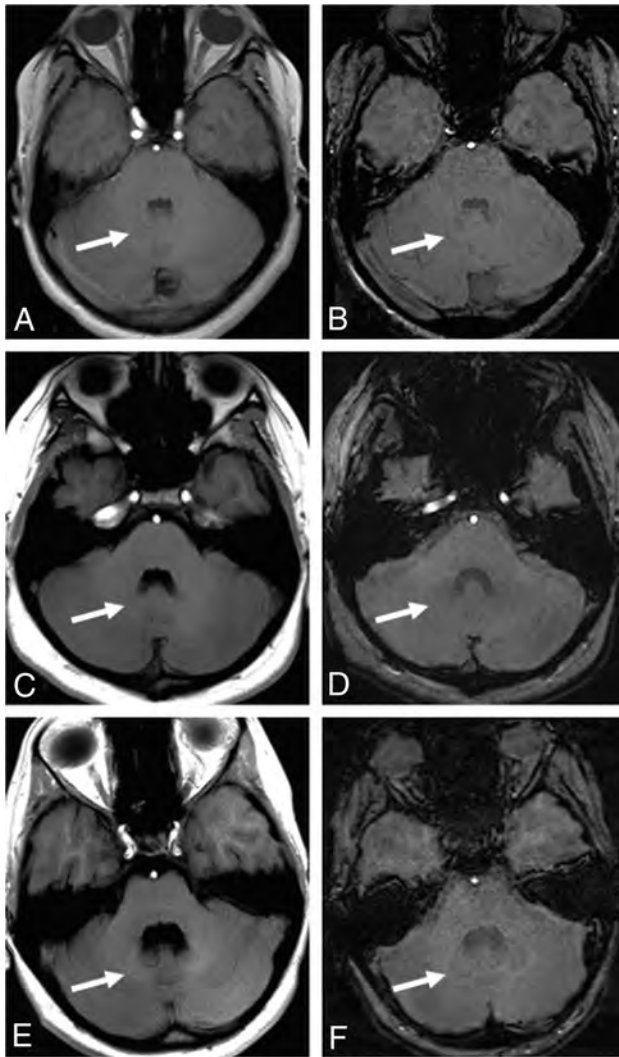


FIG 4. A 13-year-old male patient without gadolinium exposure (A and B), an age- and sex-matched patient after 5 doses of macrocyclic GBCA (C and D), and another 13-year-old adolescent boy after 7 doses of linear GBCA administration (E and F). Note the brighter signal in the DN on T1WI (E) and lower signal in the DN on SWI (F), which is not present in the other 2 children. (White arrows represent DN)

worse with the number of linear GBCA administrations than T1 ratios did. The reason for the difference in results between the study by Hinoda et al²⁶ and our present study could be partially explained by the potential washout effect or precipitation of gadolinium²⁷ after consecutive administration of linear and macrocyclic GBCAs because the GBCA group in their study had both linear and macrocyclic GBCA administration. Additionally, we used a matched case-control design in a pediatric population, given that age-dependent maturational effects in different areas of the developing brain may cause SI changes on SWI with time. A better correlation of the number of linear GBCA administrations and susceptibility values in the DN and GP than T1WI SI ratios supports the initial hypothesis that SWI could be a biomarker of gadolinium retention in vivo and could better depict gadolinium deposition compared with T1WI.

SWI is an imaging approach that maximizes sensitivity to susceptibility effects by integrating a long-TE, fully flow-compensated,

3D gradient-echo series with filtered phase data in each voxel to improve the contrast in magnitude images. This limitation is being addressed with the recent development of quantitative susceptibility mapping.²⁸ While SWI generates contrast on the basis of phase images, quantitative susceptibility mapping further computes the underlying susceptibility of each voxel as a scalar quantity and may be better for evaluating subtle susceptibility signal changes related to the possible gadolinium deposition in the brain parenchyma.²⁹

The SI changes on SWI occur from both T2 and susceptibility signal variations among tissues and are very sensitive to the in vivo detection of iron deposition.³⁰ In a previous postmortem study,³¹ the DN demonstrated varying signal intensity on SWI; in particular, the susceptibility values of the DN significantly changed due to iron deposition with aging.³² In this study, the result of the Pearson correlation coefficient between the susceptibility values in DN or GP and subject age revealed no significant correlation in this pediatric population. Furthermore, no significant correlation was noted between SWI-derived values and age in the control groups, which might need a larger patient cohort and larger age range with possible involvement of the adult population. However, in a time (eg, 2–3 years) in which age-related changes are minimal, SWI appears to provide a means to monitor gadolinium deposition in the DN due to its quantitative nature and high gadolinium sensitivity.

There were some limitations to this retrospective study investigating the relationship between SWI and gadolinium deposition in the DN and GP. First, the number of GBCA administrations has been obtained from medical charts at a single institution, and some patients with long-term follow-up in the GBCA group might have had additional GBCA exposure at outside facilities of which we were not aware in this analysis. Second, a larger number of control subjects could have been included to minimize the error in the control data; however, in this regard, an increased number of control subjects would technically decrease the variance between the patients receiving GBCA and the control subjects, which could potentially disclose other significant variations between the 2 groups. Third, a possible limitation in all DN SI-change studies is the choice of the proper comparator. We considered the DN-to-MCP ratio because it has been used in other studies and the anatomic position of the DN is closer to the MCP compared with the pons, allowing collection of all ROIs on the same section, which might be beneficial in case of regional variances in the images. We conducted a case-control design because as fiber maturation and associated SWI/T1WI signal changes develop in a nonlinear way and demonstrate considerable variability, modeling of these effects would be very complicated. Also, histologic analyses of brain tissue samples are likely even more sensitive for detecting lower-level gadolinium deposition that may not be detectable on SWI.³³

CONCLUSIONS

This study demonstrated a statistically significant decrease in SWI_{\min} and SWI_{mean} values for the DN and GP after consecutive administrations of linear GBCA but not macrocyclic GBCA in pediatric patients.

Disclosures: David Nascene—UNRELATED: Consultancy: WorldCare Clinical; Payment for Lectures Including Service on Speakers Bureaus: Biogen; Royalties: Springer. *Money paid to individual author.

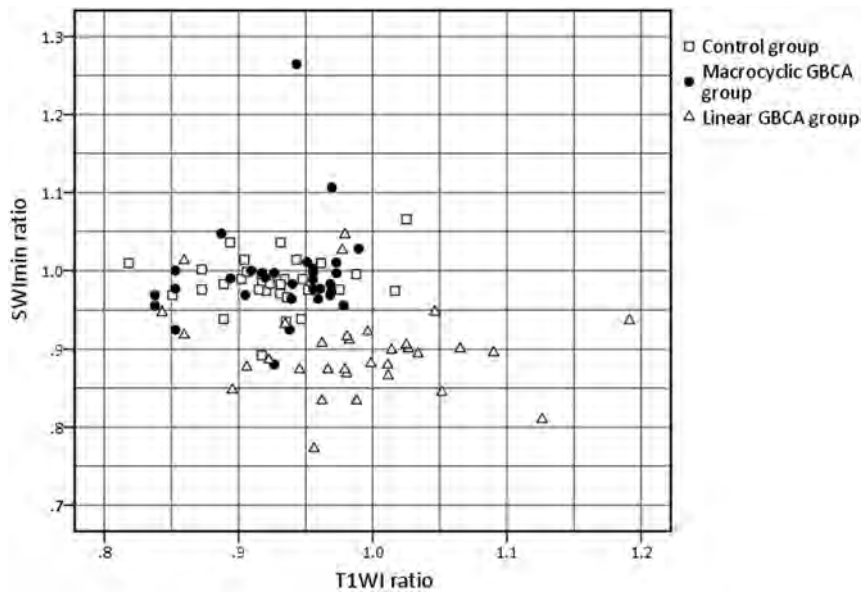


FIG 5. Scatterplot of the DN-to-MCP ratios on unenhanced T1WI and SWI. Increased T1WI and decreased SWI_{mean} ratios in the linear GBCA group compared with macrocytic GBCA and control groups are seen.

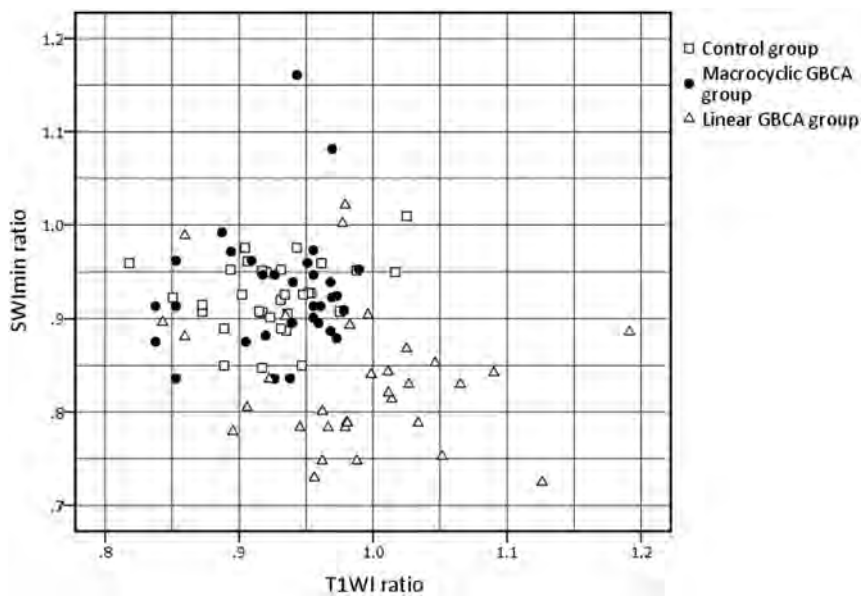


FIG 6. Scatterplot of the DN-to-MCP ratios on unenhanced T1WI and SWI. Note increased T1WI and decreased SWI_{min} ratios in the linear GBCA group compared with macrocytic GBCA and control groups.

REFERENCES

- Boehm I, Hungerbuhler M, Heverhagen JT. **Insight into the dynamic of gadolinium based contrast agent (GBCA) hypersensitivity: acquisition, persistence and disappearance.** *Magn Reson Imaging* 2018;49:1-3 CrossRef Medline
- Khawaja AZ, Cassidy DB, Al Shakarchi J, et al. **Revisiting the risks of MRI with gadolinium-based contrast agents: review of literature and guidelines.** *Insights Imaging* 2015;6:553-58 CrossRef Medline
- Choi JW, Moon WJ. **Gadolinium deposition in the brain: current updates.** *Korean J Radiol* 2019;20:134-47 CrossRef Medline

- Rossi Espagnet MC, Bernardi B, Pasquini L, et al. **Signal intensity at unenhanced T1-weighted magnetic resonance in the globus pallidus and dentate nucleus after serial administrations of a macrocyclic gadolinium-based contrast agent in children.** *Pediatr Radiol* 2017;47:1345-52 CrossRef Medline
- Tedeschi E, Palma G, Canna A, et al. **In vivo dentate nucleus MRI relaxometry correlates with previous administration of gadolinium-based contrast agents.** *Eur Radiol* 2016;26:4577-84 CrossRef Medline
- McDonald RJ, McDonald JS, Kallmes DF, et al. **Intracranial gadolinium deposition after contrast-enhanced MR imaging.** *Radiology* 2015;275:772-82 CrossRef Medline
- Tamrazi B, Nguyen B, Liu CJ, et al. **Changes in signal intensity of the dentate nucleus and globus pallidus in pediatric patients: impact of brain irradiation and presence of primary brain tumors independent of linear gadolinium-based contrast agent administration.** *Radiology* 2018;287:452-60 CrossRef Medline
- Valdés Hernández M, Maconick LC, Tan EMJ, et al. **Identification of mineral deposits in the brain on radiological images: a systematic review.** *Eur Radiol* 2012;22:2371-81 CrossRef Medline
- Ginat DT, Meyers SP. **Intracranial lesions with high signal intensity on T1-weighted MR images: differential diagnosis.** *Radiographics* 2012;32:499-516 CrossRef Medline
- Young JR, Orosz I, Franke MA, et al. **Gadolinium deposition in the paediatric brain: T1-weighted hyperintensity within the dentate nucleus following repeated gadolinium-based contrast agent administration.** *Clin Radiol* 2018;73:290-95 CrossRef Medline
- Haacke EM, Mittal S, Wu Z, et al. **Susceptibility-weighted imaging: technical aspects and clinical applications, Part 1.** *AJNR Am J Neuroradiol* 2009;30:338-43 CrossRef Medline
- Nandigam RN, Viswanathan A, Delgado P, et al. **MR imaging detection of cerebral microbleeds: effect of susceptibility-weighted imaging, section thickness, and field strength.** *AJNR Am J Neuroradiol* 2009;30:338-43 CrossRef Medline
- El-Koussy M, Schenk P, Kiefer C, et al. **Susceptibility-weighted imaging of the brain: does gadolinium administration matter?** *Eur J Radiol* 2012;81:272-27 CrossRef Medline
- Kanda T, Ishii K, Kawaguchi H, et al. **High signal intensity in the dentate nucleus and globus pallidus on unenhanced T1-weighted MR images: relationship with increasing cumulative dose of a gadolinium-based contrast material.** *Radiology* 2014;270:834-41 CrossRef Medline
- Ryu YJ, Choi YH, Cheon JE, et al. **Pediatric brain: gadolinium deposition in dentate nucleus and globus pallidus on unenhanced T1-**

- weighted images is dependent on the type of contrast agent. *Invest Radiol* 2018;53:246–55 CrossRef Medline
16. Moser FG, Watterson CT, Weiss S, et al. **High signal intensity in the dentate nucleus and globus pallidus on unenhanced T1-weighted MR images: comparison between gadobutrol and linear gadolinium-based contrast agents.** *AJNR Am J Neuroradiol* 2018;39:421–26 CrossRef Medline
 17. McDonald RJ, McDonald JS, Kallmes DF, et al. **Gadolinium deposition in human brain tissues after contrast-enhanced MR imaging in adult patients without intracranial abnormalities.** *Radiology* 2017;285:546–54 CrossRef Medline
 18. Ozturk K, Nas OF, Soylyu E, et al. **Signal changes in the dentate nucleus and globus pallidus on unenhanced T1-weighted magnetic resonance images after intrathecal administration of macrocyclic gadolinium contrast agent.** *Invest Radiol* 2018;53:535–40 CrossRef Medline
 19. Lanphear BP. **The impact of toxins on the developing brain.** *Annu Rev Public Health* 2015;36:211–30 CrossRef Medline
 20. Roberts DR, Chatterjee AR. **The critical need for pediatric and juvenile animal research addressing gadolinium retention in the developing body.** *Invest Radiol* 2019;54:72–75 CrossRef Medline
 21. Runge VM. **Dechelation (transmetalation): consequences and safety concerns with the linear gadolinium-based contrast agents, in view of recent health care rulings by the EMA (Europe), FDA (United States), and PMDA (Japan).** *Invest Radiol* 2018;53:571–78 CrossRef Medline
 22. Ichikawa S, Omiya Y, Onishi H, et al. **Linear gadolinium-based contrast agent (gadodiamide and gadopentetate dimeglumine)-induced high signal intensity on unenhanced T1-weighted images in pediatric patients.** *J Magn Reson Imaging* 2019;49:1046–49 CrossRef Medline
 23. Tibussek D, Rademacher C, Caspers J, et al. **Gadolinium brain deposition after macrocyclic gadolinium administration: a pediatric case-control study.** *Radiology* 2017;285:223–30 CrossRef Medline
 24. Radbruch A, Haase R, Kickingereder P, et al. **Pediatric brain: no increased signal intensity in the dentate nucleus on unenhanced T1-weighted MR images after consecutive exposure to a macrocyclic gadolinium-based contrast agent.** *Radiology* 2017;283:828–36 CrossRef Medline
 25. Chai C, Yan S, Chu Z, et al. **Quantitative measurement of brain iron deposition in patients with haemodialysis using susceptibility mapping.** *Metab Brain Dis* 2015;30:563–71 CrossRef Medline
 26. Hinoda T, Fushimi Y, Okada T, et al. **Quantitative assessment of gadolinium deposition in dentate nucleus using quantitative susceptibility mapping.** *J Magn Reson Imaging* 2017;45:1352–58 CrossRef Medline
 27. Radbruch A, Weberling LD, Kieslich PJ, et al. **Intraindividual analysis of signal intensity changes in the dentate nucleus after consecutive serial applications of linear and macrocyclic gadolinium-based contrast agents.** *Invest Radiol* 2016;51:683–90 CrossRef Medline
 28. Schweser F, Sommer K, Deistung A, et al. **Quantitative susceptibility mapping for investigating subtle susceptibility variations in the human brain.** *Neuroimage* 2012;62:2083–2100 CrossRef Medline
 29. Wang Y, Spincemaille P, Liu Z, et al. **Clinical quantitative susceptibility mapping (QSM): biometal imaging and its emerging roles in patient care.** *J Magn Reson Imaging* 2017;46:951–71 CrossRef Medline
 30. Haacke EM, Makki M, Ge Y, et al. **Characterizing iron deposition in multiple sclerosis lesions using susceptibility weighted imaging.** *J Magn Reson Imaging* 2009;29:537–44 CrossRef Medline
 31. Bilgic B, Pfefferbaum A, Rohlfing T, et al. **MRI estimates of brain iron concentration in normal aging using quantitative susceptibility mapping.** *Neuroimage* 2012;59:2625–35 CrossRef Medline
 32. Harder SL, Hopp KM, Ward H, et al. **Mineralization of the deep gray matter with age: a retrospective review with susceptibility-weighted MR imaging.** *AJNR Am J Neuroradiol* 2008;29:176–83 CrossRef Medline
 33. Kanda T, Fukusato T, Matsuda M, et al. **Gadolinium-based contrast agent accumulates in the brain even in subjects without severe renal dysfunction: evaluation of autopsy brain specimens with inductively coupled plasma mass spectroscopy.** *Radiology* 2015;276:228–32 CrossRef Medline

Accumulation of Brain Hypointense Foci on Susceptibility-Weighted Imaging in Childhood Ataxia Telangiectasia

R.A. Dineen, C.V. Blanchard, S. Pszczolkowski, S. Paine, M. Prasad, G. Chow, W.P. Whitehouse, and D.P. Auer



ABSTRACT

BACKGROUND AND PURPOSE: SWI hypointense cerebral lesions have been reported in adults with the inherited cerebellar neurodegenerative disorder ataxia telangiectasia. This study aims to establish the prevalence, age-dependency, and spatial distribution of these lesions in children and young people with ataxia telangiectasia.

MATERIALS AND METHODS: Participants with classic ataxia telangiectasia and matched controls underwent SWI acquisition at 3T at 1 or 2 time points. SWI hypointense lesions were manually labeled according to the Microbleed Anatomical Rating Scale. Differences in prevalence of lesion number between groups with ataxia telangiectasia and without ataxia telangiectasia were tested with the Fisher exact test, and differences in age between participants with ataxia telangiectasia with and without lesions were tested using independent samples Mann-Whitney U test. The relationship between age and lesion number was modeled as an exponential function.

RESULTS: Analyzable SWI datasets from 17 participants with ataxia telangiectasia (with median age at first scan of 12.4 years; range, 4.6–20.2 years; 8 [47%] were female) and 22 matched healthy controls showed prevalence of SWI hypointense lesions in 41% of participants with ataxia telangiectasia and 0% in controls ($P = .001$, Fisher exact test). Lesions were exclusively supratentorial and predominantly lobar. Participants with ataxia telangiectasia with SWI hypointense lesions were older than those without (median age 5.2 years versus 9.3 years, $U = 10.5$, $P = .014$). An exponential curve described the relationship between age and lesion number ($R^2 = 0.67$).

CONCLUSIONS: SWI hypointense lesions are common in children and young people with ataxia telangiectasia, accumulating from 12 years of age onward. In contrast to cerebellar-dominant neurodegeneration in ataxia telangiectasia, SWI hypointense lesions were exclusively supratentorial. Further investigation is needed to establish the clinical relevance of these imaging-detected lesions.

ABBREVIATIONS: A-T = ataxia telangiectasia; ATM = ataxia-telangiectasia mutated; CATNAP = Childhood A-T Neuroimaging Assessment Project; SWI = susceptibility weighted imaging

Ataxia telangiectasia (A-T, Online Mendelian Inheritance in Man, No. 208900) is an autosomal recessive multisystem disorder associated with cerebellar neurodegeneration, telangiectasia (particularly conjunctival), immunodeficiency, pulmonary disease, radiation sensitivity, and cancer predisposition.¹ People with “classical” A-T have either no production of the ataxia-telangiectasia mutated (ATM) protein or produce completely nonfunctioning ATM protein. People who produce a significantly reduced amount of functioning ATM have a milder variant of A-T.²

Cerebellar atrophy is the dominant neuroimaging finding in A-T (reviewed in detail by Sahama et al³), but several case series and individual case reports describe hypointense foci in the brain parenchyma using SWI or T2WI. In a series of 10 adults with A-T, 19–34 years of age, Lin et al⁴ observed hypointense foci using SWI in 7 (70%) of the participants. These ranged from a single hypointense focus in a 21-year-old through to “innumerable” foci in individuals with 28 and 34 years of age. Wallis et al⁵ presented a series of 12 adults with A-T, 23–47 years of age, 4 of whom had hypointense foci (solitary in 2, multiple in 2) in the

Received November 16, 2020; accepted after revision December 24.

From the Radiological Sciences, Division of Clinical Neuroscience (R.A.D., C.V.B., S. Pszczolkowski, D.P.A.), Sir Peter Mansfield Imaging Centre (R.A.D., D.P.A.), and Division of Child Health (W.P.W.), University of Nottingham, Nottingham, England; National Institute for Health Research Nottingham Biomedical Research Centre (D.P.A.), Nottingham, England; and Department of Pathology (S. Paine) and Nottingham Children’s Hospital (M.P., G.C., W.P.W.), Nottingham University Hospitals National Health Service Trust, Nottingham, England.

The funding for the research was from research grants awarded jointly by A-T Children’s Project and Action for A-T (grant reference: “The CATNAP Study”), and jointly by Action for A-T and BraShA-T (grant reference: 17NOT03).

The funders had no role in the study design; the collection, analysis, and interpretation of data; the writing of the report; and the decision to submit the article for publication.

Please address correspondence to Robert A. Dineen, PhD, Room A39i, Medical School, Queen’s Medical Center, Derby Road, Nottingham, NG7 2UH, United Kingdom; e-mail: rob.dineen@nottingham.ac.uk

Indicates open access to non-subscribers at www.ajnr.org

Indicates article with online supplemental data.

<http://dx.doi.org/10.3174/ajnr.A7107>

brain parenchyma on T2WI. Further examples are provided by Liu et al⁶ (27-year-old man with multiple hypointense foci on SWI) and Ciemins and Horowitz⁷ (31-year-old woman with multiple hypointense foci on both T1- and T2WI).

To date, the prevalence, age distribution, and spatial distribution of SWI hypointense foci in the brains of children with A-T has not been investigated. To address this, we used data from the Childhood A-T Neuroimaging Assessment Project (CATNAP)⁸ to test the hypothesis that SWI hypointensities accumulate during childhood in children and young people with classical A-T.

MATERIALS AND METHODS

The data for this analysis are from the first and second phases of CATNAP. In brief, the first phase of CATNAP involved the acquisition of multiparametric MR imaging and neurologic data from children and young people 6–18 years of age with A-T and matched healthy controls. As described previously,⁸ participants with A-T were recruited from the UK National Pediatric A-T Clinic and were excluded if they had contraindication to MR imaging, concurrent or previous cancer or cancer treatment, or other non-A-T neurologic or neurosurgical conditions. Healthy volunteers were recruited from local community groups and excluded if they had contraindications to MR imaging or any neurologic, neurosurgical, or other medical conditions. Recruitment ran from January 2015 to September 2016. The results of volumetric analysis and spectroscopy have been reported.⁸ The second phase of CATNAP involved invitation of previous participants for repeat multiparametric MR imaging on the same scanner using an identical protocol after an interval of 2–4 years, and recruitment of new participants 3–6 years of age to test the feasibility of the data acquisition in very young children. Informed consent was obtained from participants who were 16–18 years of age and from parents/guardians of participants under the age of 16 years of age. The first and second phases of CATNAP were approved by UK National Research Ethics Service (references 14/EM/1175 and 18/SW/0078, respectively).

Image Acquisition and Analysis

All participants underwent MR imaging scanning on a 3D Discovery MR750 (GE Healthcare) with a 32-channel head coil, without sedation. In addition to standard pediatric MR imaging preparation, younger participants were shown an animation to prepare them for MR imaging⁹ and were able to watch video content during the scan on a monitor compatible with MR imaging. The full MR imaging protocol is detailed in the Online Supplemental Data. The results presented here relate to the axial SWI acquisition performed using the T2* weighted angiography susceptibility-based 3D multiecho gradient sequence (216 slices, section thickness = 1 mm with 0.5 mm between slices, FOV = 256 × 256, TR = 39.3 ms, effective TE = 24.68 ms, flip angle = 15°, scan duration = 4:19 minutes).

Two experienced neuroradiologists (R.A.D., D.P.A.), who were unaware of disease status, independently labeled all hypointensities manually on SWI according to the anatomic classification specified in the Microbleed Anatomical Rating Scale¹⁰ using the paintbrush drawing tool in ITK-SNAP software ([http://www.](http://www.itksnap.org)

itksnap.org).¹¹ After the independent review, any discrepancies in lesion labeling were resolved through discussion leading to consensus.

Statistical Analysis

Comparison of age distribution between the groups with A-T and without A-T was performed using the independent samples Mann-Whitney U test. Prevalence of SWI hypointense lesions (using the second scan for those with 2 scans) was expressed as a percentage with 95% CI for each group, and differences in prevalence of SWI hypointense lesions between groups with A-T and without A-T were tested using the Fisher exact test. Within the group with A-T, differences in age distribution between those with and without SWI hypointense lesions was determined using the independent samples Mann-Whitney U test, using age at second scan for those with 2 scans. Exact significance (2-tailed) was calculated, and the significance level was set at $\alpha < .05$. We modeled the relationship between age and observed number of SWI hypointense lesions as an exponential function $y = a \cdot e^{b \cdot x}$, where x is age, y is the observed number of lesions, and a and b are unknown parameters. To find the values of a and b that best fitted the data, we ran a trust-region reflective optimization^{12,13} with a starting point of $a = 0.01$, $b = 0.5$.

RESULTS

Twenty-two children and young people with A-T and 22 without A-T underwent at least 1 SWI acquisition. Of these, 8 with A-T and 13 without A-T had a second SWI scan. In total, 13 of the SWI datasets (10 from the group with A-T and 3 from the group without A-T group) were excluded from the analysis because of significant participant motion artifacts. One scan where the image quality was felt to be borderline showed a clear parenchymal SWI hypointense lesion, and this scan was retained in the analysis. The analyzed images were from 17 children and young people with A-T (with median age at first scan of 12.4 years; range, 4.6–20.2 years; 8 [47%] were female) and 22 without A-T (median age at first scan was 13.0 years; range, 5.5–17.8 years; 11 [50%] were female). There was no group difference in age distribution ($U = 188$, exact $P = .977$). Analyzable second SWI scans were available from 2 people in the group with A-T (interscan intervals of 3.3 and 3.5 years) and from 10 in the group without A-T (median interscan interval of 2.4 years, range, 2.3–3.5 years). Of the 17 participants with A-T included in this report, 8 had no ATM expression, 8 had ATM expression but no kinase activity, and 1 had ATM expression with some residual kinase. No participant with A-T reported (or had parental/guardian report of) an alternative cause for cerebral microbleeds, such as history of head trauma, hypertension, or coagulopathy. Sixteen of the participants with A-T and 21 of the participants without A-T were included in our previous publication relating to cerebellar volumetry, diffusion, and spectroscopy.⁸ Recruitment to CATNAP and CATNAP-2 and the availability of acceptable-quality SWI data are summarized in the flowchart (Online Supplemental Data).

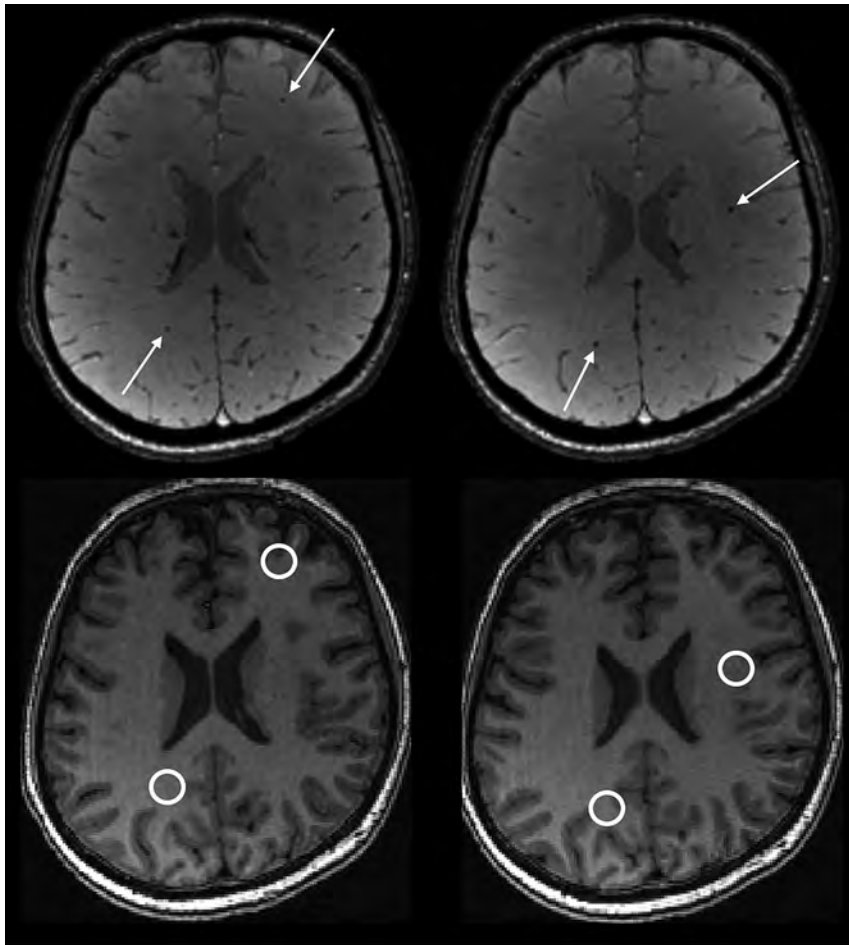


FIG 1. Upper row: Example of parenchymal SWI hypointense lesions in a participant with A-T aged 17.8 years. Axial images showing 4 separate lesions (white arrows). A total of 23 similar lesions (not all shown) were present on the imaged volume. Lower row: Corresponding axial fast-spoiled gradient-recalled images showing that the lesions are not clearly visible on the T1-weighted volumetric acquisition.

SWI hypointense lesions were present in 7 of 17 participants with A-T on at least 1 scan, giving a prevalence of 41% (95% CI, 22%–64%) (Fig 1). For the 7 participants with A-T who had SWI hypointense lesions, the number of lesions ranged from 1 to 41 (median = 3) (Fig 2). Lesions ranged in size from 2 mm (the lower limit for inclusion) up to 4 mm.¹⁰ No lesions were identified in any participants in the group without A-T, 0/22 (95% CI, 0%–18%). The prevalence of lesions differed significantly between the groups with A-T and without A-T ($P = .001$, the Fisher exact test). Anatomic distribution of SWI hypointense lesions in the group with A-T is shown in the Table and Fig 3. No SWI hypointense lesions were found in the cerebellum and brain stem, and supratentorial lesions were overwhelmingly lobar rather than deep. The SWI hypointense lesions were not clearly visible on the T1-weighted fast-spoiled gradient-recalled images (Fig 1, bottom row).

A significant age difference was identified between participants with A-T who did and did not have SWI hypointense lesions (median age was 15.2 years [range, 12.4–20.2 years] versus

9.3 years [range, 4.6–17.6 years], respectively, $U = 10.5$, $P = .014$; Fig 4). No lesions were identified in children with A-T younger than 12 years of age. The 2 participants with A-T who had analyzable scans at 2 time points both showed an increase in the number of lesions between the first and second scans (Figs 2 and 5). The curve fitted for the number of SWI hypointense lesions against age for the A-T group (Fig 2) had $R^2 = 0.67$ and was described by the equation:

$$\begin{aligned} \text{number of lesions} \\ = 0.00168 \cdot e^{0.4841 \cdot \text{age}} \end{aligned}$$

The 95% confidence limits for coefficient a are -0.00917 and 0.01252 , and for coefficient b are 0.1575 and 0.8106 .

DISCUSSION

In our cohort of children and young people with A-T, we identified a prevalence of SWI hypointense lesions of 41%. In comparison, no such lesions were identified in any participants of the well-matched control group. Furthermore, despite the limited number of data points in the group with A-T, we demonstrate a clear relationship between the number of SWI hypointense lesions and age across the group, as well as direct evidence on new lesion accumulation in the 2 participants with A-T who had analyzable SWI at 2 time points.

Previous case reports and series have reported SWI hypointense lesions in adults with A-T, but the prevalence and natural history of these lesions in children with A-T were not known. Indeed, Lin et al⁴ state that in their clinical experience, SWI hypointense lesions are absent in children with A-T; and that lesions are acquired and only cross a threshold of detectability in early adulthood. Our findings support the notion that lesions are acquired in an age-related manner but counter the statement relating to absence in childhood. It is possible that improvements in acquisition of SWI since the time of that publication in 2014 allow us to visualize lesions more clearly.

The nature and significance of these imaging-detected lesions remain uncertain. Histopathologic studies have demonstrated the presence of a distinctive vascular abnormality in people with A-T, referred to as “gliovascular nodules.”¹⁴ These consist of dilated capillary loops, often containing fibrin thrombi, around which is perivascular hemorrhage and hemosiderin deposition, with associated demyelination and astrocytic gliosis, including atypical forms (some of

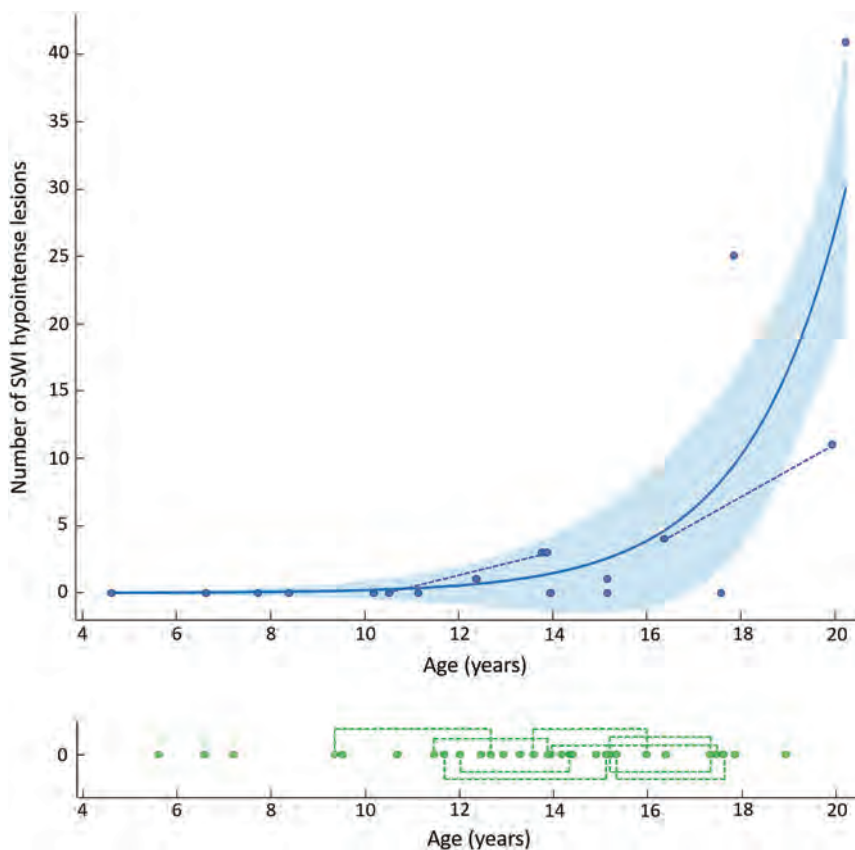


FIG 2. Scatterplots showing relationship between age and number of lesions in people with A-T (upper chart, blue) and people without A-T (lower chart, green). Dotted lines indicate pairs of scans performed in the same individual. The curved blue line indicates the exponential model fitted to the data, with the blue shaded area indicating the 95% confidence intervals.

Anatomic distribution of SWI hypointense lesions in the group with A-T

	Participants with A-T (n = 17)	
	Number of Subjects with Lesions	Total Number of Lesions
Lobar	6 (35%)	82
Deep Gray Matter	4 (24%)	7
Cerebellum	0 (0%)	0
Brain Stem	0 (0%)	0
All Sites	7 (41%)	89

which contain eosinophilic cytoplasmic inclusions) in the adjacent parenchyma.^{15,16} It is likely that the focal hypointensities detected in our work and by previous studies are the in vivo imaging correlation of these gliovascular nodules, though direct correlation between imaging and histopathology has not been performed to our knowledge. Notably, pathologic studies show that the distribution of gliovascular nodules is predominantly in the cerebral white matter, occasionally in the basal ganglia and cerebral cortex, but not in the cerebellum. This description of location matches closely the distribution of lesions found in our data. The reason for the observed distribution of lesions is not known, nor why the posterior fossa appears to be spared. There may be underlying factors related to vascular structure and/or

vascular expression of different molecules or receptors, or there may be a relationship to hemodynamic parameters. Combined imaging, histopathologic studies, and molecular studies may help to clarify the underlying causes of the formation and distribution of the lesions.

However, it is also possible that pathologic changes other than gliovascular nodules could account for the imaging appearances. A histopathologic case report described hyalinization of cerebral blood vessels associated with intimal and adventitial hypertrophy in a patient with advanced disease,¹⁷ indicating the presence of cerebrovascular degenerative pathology that is separate from the gliovascular nodules. However, the limited available reports do not suggest that this cerebrovascular hyalinization occurring with A-T is directly associated with localized microhemorrhage or hemosiderin deposition detected by SWI. Lin et al⁴ comment that CNS irradiation can cause similar appearances on SWI because of the development of radiation-induced cavernous hemangiomas, which may be a late sequela of cancer treatment.¹⁸ This may be relevant because A-T is associated with an increased cellular sensitivity to ionizing radiation¹⁹ and abnormal DNA damage

response. However, the histopathologic description of vascular changes seen in A-T do not closely overlap with those described for radiation-induced cavernous hemangiomas, which appear to show 2 distinct histologic patterns: those resembling typical cerebral cavernous hemangiomas, and those caused by radiation-induced fibrinoid vascular necrosis and vascular leakage.²⁰

It is currently unclear whether the presence of the hypointense lesions on SWI in people with A-T confers an increased risk of intracerebral hemorrhage. In other conditions with similar-appearing lesions on SWI, such as cerebral amyloid angiopathy and cerebral cavernous hemangiomas, the presence of lesions indicates an increased macrohemorrhage risk.^{21,22} There are only 2 reports of macrohemorrhage in people with A-T,^{23,24} but the relationship to any underlying SWI hypointensities has not been explored.

In other regards, the relationship between presence or number of SWI hypointense lesions and other clinical or imaging manifestations of A-T is also not known. Of particular interest is the question of whether SWI hypointense lesions could have an impact on cognitive function. Previous studies have identified cognitive deficits in people with A-T, including in the domains of language, processing speed, visuospatial processing, working memory, attention, and abstract reasoning,^{25,26} which have been

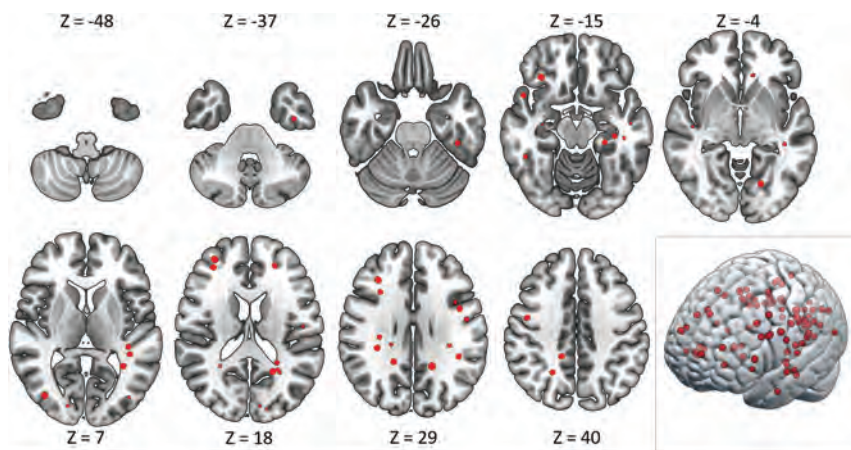


FIG 3. Distribution of SWI hypointense lesions. Representative axial images from the summed SWI hypointense lesion maps from all participants with A-T, displayed on a Montreal Neurological Institute 152 template. Axial section locations indicated by the z-axis coordinate. Note the absence of cerebellar or brain stem lesions. *Lower right image:* The same summed lesion map data displayed as a 3D rendered image.

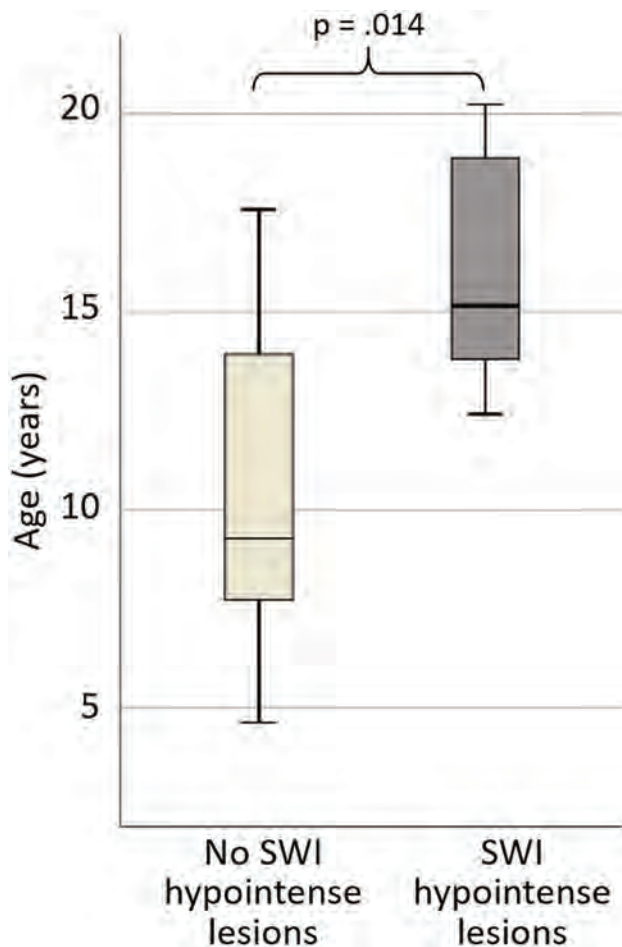


FIG 4. Boxplot showing age distribution for A-T participants without (light gray) and with (dark gray) SWI hypointense lesions.

attributed to the cerebellar cognitive affective syndrome.²⁷ Given that other diseases associated with multifocal cerebral white matter lesions, such as multiple sclerosis²⁸ and small-vessel disease,²⁹ are associated with cognitive dysfunction, an impact of cerebral

SWI hypointense lesions on cognition in people with A-T is possible. The small number of participants with A-T showing SWI hypointense lesions in our dataset limits further exploration of the relationship between the presence or number of these lesions and other neurologic, cognitive, or imaging metrics. Ideally future, larger imaging studies in A-T will include SWI acquisitions, allowing the clinical relevance of these lesions to be formally investigated.

This study is the largest reported series of SWI in childhood A-T, and has a well-matched control group, but is still limited by small sample size. There was a high rate of data rejection in the group with A-T (one-third of the SWI datasets), because of excessive participant motion rendering the image unreliable for analysis, which reduced the number

of longitudinal SWI datasets in the group with A-T from 8 to 2. We used careful participant preparation and carefully immobilized the participant's head in the head coil using inflatable pads. However, A-T is a movement disorder and those affected are prone to involuntary movements. In addition, the SWI acquisition was toward the end of a multisequence research MR imaging protocol, which is likely to have affected tolerance and led to restlessness. We have taken steps to reduce observer bias during the identification of SWI hypointense lesions, which was performed independently by 2 experienced neuroradiologists who were not aware of the disease status. However, people with A-T typically have overt cerebellar atrophy that would have been visible on the SWI datasets during the labeling of SWI hypointense lesions and it is possible that the reviewing neuroradiologists may have unintentionally recognized that a scan was from a participant with A-T.

CONCLUSIONS

This work demonstrates that SWI hypointense lesions are present in children and young people with A-T with a prevalence of 41% and accumulation is shown across the childhood age range. No lesions were seen in children younger than 12 years of age. Furthermore, in our cohort, lesions were exclusively supratentorial in an overwhelmingly lobar distribution, which is notable because the burden of neurodegeneration in people with A-T occurs in the cerebellum.³ Further investigation is needed to elucidate the nature and relevance of these imaging-detected lesions.

ACKNOWLEDGMENTS

The authors would like to thank the children, young people, and families who participated in the CATNAP studies. We also gratefully acknowledge the support Kay Atkins, Anne Murray, and William Davis and at the A-T Society for support with publicizing

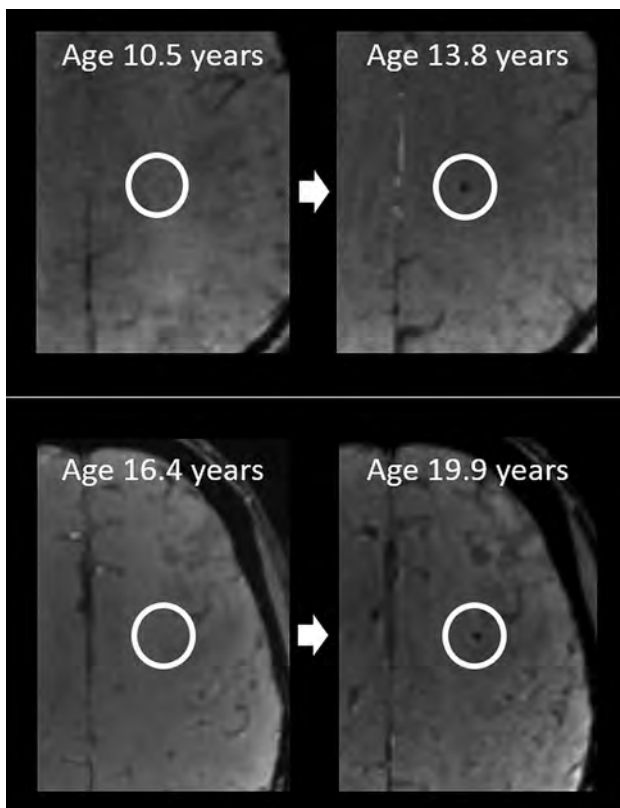


FIG 5. Examples of new lesions in participants with A-T who had scans at 2 time points. *Upper and lower rows indicate different participants; ages indicated on each image.*

the study and arranging schedules and transport for participant visits; Dr Min Ong and Dr Ouliana Panagiotti for additional support with neurologic assessments; Mr Andrew Cooper for performing the MR imaging scans; Mrs Catherine Gibney for undertaking play preparation with younger participants; and Dr Felix Raschke, Ms Hannah McGlashan, and Dr Jeyanthi Rangaraj for recruitment and additional participant assessments.

Disclosures: Robert A. Dineen—*RELATED: Grant:* charity funding. Caroline V. Blanchard—*RELATED: Grant:* charity funding. Stefan Psczolkowski—*RELATED: Grant:* charity funding. Gabriel Chow—*RELATED: Grant:* charity funding. William Whitehouse—*RELATED: Grant:* charity funding. *UNRELATED: Consultancy:* pharma company advice. *Comments:* Eli Lilly, expert meeting to discuss a new migraine drug trial. No relevance to the submitted study; GW Pharmaceuticals, expert meeting to discuss the marketing authorization of a new antiepileptic drug. No relevance to the submitted study. Dorothee P. Auer—*RELATED: Grant:* charity funding; *UNRELATED: Grants/Grants Pending:* National Institute for Health Research, Versus Arthritis, Parkinson's UK, Michael J. Fox Foundation, Biogen*; *Travel/Accommodations/Meeting Expenses Unrelated to Activities Listed:* German and Irish National Research Foundations. *Comments:* Reimbursement of travel/accommodation for grant review panel meeting*.

REFERENCES

- Rothblum-Oviatt C, Wright J, Lefton-Greif MA, et al. **Ataxia telangiectasia: a review.** *Orphanet J Rare Dis* 2016;11:159 CrossRef Medline
- Schon K, van Os NJ, Oscroft N, et al. **Genotype, extrapyramidal features, and severity of variant ataxia-telangiectasia.** *Ann Neurol* 2019;85:170–80 CrossRef Medline
- Sahama I, Sinclair K, Pannek K, et al. **Radiological imaging in ataxia telangiectasia: a review.** *Cerebellum* 2014;13:521–30 CrossRef Medline
- Lin DD, Barker PB, Lederman HM, et al. **Cerebral abnormalities in adults with ataxia-telangiectasia.** *AJNR Am J Neuroradiol* 2014;35:119–23 CrossRef Medline
- Wallis LI, Griffiths PD, Ritchie SJ, et al. **Proton spectroscopy and imaging at 3T in ataxia-telangiectasia.** *AJNR Am J Neuroradiol* 2007;28:79–83 Medline
- Liu HS, Chen YC, Chen CY. **Cerebral microbleeds and iron depletion of dentate nuclei in ataxia-telangiectasia.** *Neurology* 2016;87:1062–63 CrossRef Medline
- Ciemins JJ, Horowitz AL. **Abnormal white matter signal in ataxia telangiectasia.** *AJNR Am J Neuroradiol* 2000;21:1483–85 Medline
- Dineen RA, Raschke F, McGlashan HL, et al. **Multiparametric cerebellar imaging and clinical phenotype in childhood ataxia telangiectasia.** *Neuroimage Clin* 2020;25:102110 CrossRef Medline
- McGlashan HL, Dineen RA, Szeszak S, et al. **Evaluation of an internet-based animated preparatory video for children undergoing non-sedated MRI.** *Br J Radiol* 2018;91:20170719 CrossRef Medline
- Gregoire SM, Chaudhary UJ, Brown MM, et al. **The Microbleed Anatomical Rating Scale (MARS): reliability of a tool to map brain microbleeds.** *Neurology* 2009;73:1759–66 CrossRef Medline
- Yushkevich PA, Piven J, Hazlett HC, et al. **User-guided 3D active contour segmentation of anatomical structures: significantly improved efficiency and reliability.** *Neuroimage* 2006;31:1116–28 CrossRef Medline
- Branch MA, Coleman TF, Li Y. **A subspace, interior, and conjugate gradient method for large-scale bound-constrained minimization problems.** *SIAM J Sci Comput* 1999;21:1–23 CrossRef
- Coleman TF, Li Y. **On the convergence of interior-reflective Newton methods for nonlinear minimization subject to bounds.** *Mathematical Programming* 1994;67:189–224 CrossRef
- Boder EA. *Telangiectasia.* In: Gomez MR, ed. *Neurocutaneous Disorders.* Butterworth Publishers; 1987: 95–117
- Amromin GD, Boder E, Teplitz R. **Ataxia-telangiectasia with a 32 year survival. a clinicopathological report.** *J Neuropathol Exp Neurol* 1979;38:621–43 CrossRef Medline
- Agamanolis DP, Greenstein JJ. **Ataxia-telangiectasia. Report of a case with Lewy bodies and vascular abnormalities within cerebral tissue.** *J Neuropathol Exp Neurol* 1979;38:475–89 CrossRef Medline
- Kamiya M, Yamanouchi H, Yoshida T, et al. **Ataxia telangiectasia with vascular abnormalities in the brain parenchyma: report of an autopsy case and literature review.** *Pathol Int* 2001;51:271–76 CrossRef Medline
- Jain R, Robertson PL, Gandhi D, et al. **Radiation-induced cavernomas of the brain.** *AJNR Am J Neuroradiol* 2005;26:1158–62 Medline
- Huo YK, Wang Z, Hong JH, et al. **Radiosensitivity of ataxia-telangiectasia, X-linked agammaglobulinemia, and related syndromes using a modified colony survival assay.** *Cancer Res* 1994;54:2544–47 Medline
- Kleinschmidt-DeMasters BK, Lillehei KO. **Radiation-induced cerebral vascular “malformations” at biopsy.** *J Neuropathol Exp Neurol* 2016;75:1081–92 CrossRef Medline
- Charidimou A, Imaizumi T, Moulin S, et al. **Brain hemorrhage recurrence, small vessel disease type, and cerebral microbleeds: a meta-analysis.** *Neurology* 2017;89:820–29 CrossRef Medline
- Kearns KN, Chen CJ, Yagmurlu K, et al. **Hemorrhage risk of untreated isolated cerebral cavernous malformations.** *World Neurosurg* 2019;131:e557–61 CrossRef Medline
- Casari M, Gabrielli GB, Capra F, et al. **Ataxia telangiectasia. Description of a case with multiple cerebral hemorrhages and liver cirrhosis.** *Minerva Med* 1982;73:2183–88 Medline
- Nardelli E, Fincati E, Casari M, et al. **Multiple cerebral hemorrhages in ataxia-telangiectasia. A case report.** *Acta Neurol (Napoli)* 1985;7:494–99 Medline
- Hoche F, Frankenberg E, Rambow J, et al. **Cognitive phenotype in ataxia-telangiectasia.** *Pediatr Neurol* 2014;51:297–310 CrossRef Medline

26. Vinck A, Verhagen MM, Gerven M, et al. **Cognitive and speech-language performance in children with ataxia telangiectasia.** *Dev Neurorehabil* 2011;14:315–22 CrossRef Medline
27. Hoche F, Daly MP, Chutake YK, et al. **The cerebellar cognitive affective syndrome in ataxia-telangiectasia.** *Cerebellum* 2019;18:225–44 CrossRef Medline
28. Dineen RA, Vilisaar J, Hlinka J, et al. **Disconnection as a mechanism for cognitive dysfunction in multiple sclerosis.** *Brain* 2009;132:239–49 CrossRef Medline
29. Meng D, Hosseini AA, Simpson RJ, et al. **Lesion topography and microscopic white matter tract damage contribute to cognitive impairment in symptomatic carotid artery disease.** *Radiology* 2017;282:502–15 CrossRef Medline

Ganglionic Eminence Anomalies and Coexisting Cerebral Developmental Anomalies on Fetal MR Imaging: Multicenter-Based Review of 60 Cases

M. Scarabello, A. Righini, M. Severino, L. Pinelli, C. Parazzini, E. Scola, G. Palumbo, M. Di Maurizio, I. D'Errico, A. Rossi, F. Triulzi, and P.D. Griffiths



ABSTRACT

BACKGROUND AND PURPOSE: The ganglionic eminences are transient fetal brain structures that produce a range of neuron types. Ganglionic eminence anomalies have been recognized on fetal MR imaging and anecdotally found in association with a number of neurodevelopmental anomalies. The aim of this exploratory study was to describe and analyze the associations between ganglionic eminence anomalies and coexisting neurodevelopmental anomalies.

MATERIALS AND METHODS: This retrospective study includes cases of ganglionic eminence anomalies diagnosed on fetal MR imaging during a 20-year period from 7 centers in Italy and England. Inclusion criteria were cavitation or increased volume of ganglionic eminences on fetal MR imaging. The studies were analyzed for associated cerebral developmental anomalies: abnormal head size and ventriculomegaly, reduced opercularization or gyration, and abnormal transient layering of the developing brain mantle. The results were analyzed using χ^2 and Fisher exact tests.

RESULTS: Sixty fetuses met the inclusion criteria (21 females, 24 males, 15 sex unknown). Thirty-four had ganglionic eminence cavitations (29 bilateral and 5 unilateral), and 26 had increased volume of the ganglionic eminences (19 bilateral, 7 unilateral). Bilateral ganglionic eminence cavitations were associated with microcephaly ($P = .01$), reduced opercularization, ($P < .001$), reduced gyration ($P < .001$), and cerebellar anomalies ($P = .01$). Unilateral ganglionic eminence cavitations were not significantly associated with any particular feature. Bilateral increased volume of the ganglionic eminences showed an association with macrocephaly ($P = .03$). Unilateral increased volume was associated with macrocephaly ($P = .002$), abnormal transient layering ($P = .001$), unilateral polymicrogyria ($P = .001$), and hemimegalencephaly ($P < .001$).

CONCLUSIONS: Ganglionic eminence anomalies are associated with specific neurodevelopmental anomalies with ganglionic eminence cavitations and increased ganglionic eminence volume apparently having different associated abnormalities.

ABBREVIATIONS: GA = gestational age; GE = ganglionic eminence

The ganglionic eminences (GEs) develop in the ventral telencephalon, adjacent to the lateral ventricles during embryonic and early fetal life¹ and are important proliferative zones that

produce a wide variety of projection neurons and interneurons. Most important, they produce the cortical GABAergic interneurons that migrate tangentially to the neocortex.^{2,3} Recent studies have shown the complexity of the proliferative and migratory pathways from the GE, and some of the possible consequences of derangement in those processes include epilepsy, autism, and schizophrenia.⁴⁻⁸ The human GE is visible on fetal MR imaging both *ex vivo*⁹ and *in vivo*, and recent case series by Righini et al^{10,11} have shown that GE anomalies can be shown during the late second and third trimesters.

Most GE anomalies fall into 2 broad categories: cavitations in the GE and increased volume of the GE; a range of associated structural brain anomalies have been described. The purpose of this exploratory study was to investigate the association between GE anomalies and coexisting cerebral developmental abnormalities in a large series.

Received October 26, 2020; accepted after revision December 17.

From the Pediatric Radiology and Neuroradiology Department (M. Scarabello, A.R., C.P.), Children's Hospital V. Buzzi, Milan, Italy; Neuroradiology Department (M. Severino, A. Rossi), Istituto Di Ricovero e Cura a Carattere Scientifico-Gaslini Children's Research Hospital, Genoa, Italy; Neuroradiology (L.P.) and Radiology Departments (G.P.), Azienda Ospedaliera Spedali Civili Di Brescia, Brescia, Italy; Neuroradiology Department (E.S., F.T.), Istituto Di Ricovero e Cura a Carattere Scientifico-Fondazione Policlinico di Milano, Milan, Italy; Radiology Department (M.D.M.), Children's Hospital Meyer, Florence, Italy; Neuroradiology Department (I.D.), University Hospital, Padua, Italy; and Academic Unit of Radiology (P.D.G.), University of Sheffield, Sheffield, UK.

Please address correspondence to Giovanni Palumbo, MD, Radiology Department, Università degli Studi di Brescia, Brescia, Piazza del Mercato, 15, 25121 Brescia BS, Brescia, Italy; e-mail: gio17.palumbo@gmail.com



Indicates article with online supplemental data.

<http://dx.doi.org/10.3174/ajnr.A7062>

MATERIALS AND METHODS

Case Selection

GE anomalies detected by fetal MR imaging are rare, so it was necessary to pool cases from a number of sources: 1) thirteen cases previously reported by Righini et al;^{10,11} 2) twenty-one cases reported in a publication describing cortical formation anomalies from our collaborating network;¹² and 3) twenty-six unpublished cases from our network identified after 2018. Appropriate ethics approval was obtained separately from the 6 centers in Italy and 1 in England. Specifically, if the fetal MR imaging study was performed for research purposes, informed consent from the woman was obtained before the MR imaging study, alternatively, if the fetal MR imaging was performed as a clinical examination, written consent was obtained from the woman retrospectively for use of the imaging data for the retrospective analysis. The MR imaging examinations were performed for either clinical or research purposes after expert sonographic evaluation with written informed consent from each woman in cases performed for research purposes. Cases with necrosis and/or hemorrhage in the GE (ie, increased T1-weighted signal/decreased T2*-weighted signal at echo-planar $b = 0$ images) or with evidence of associated acquired brain injury were not included because the aim of the study was to investigate associated developmental brain abnormalities, not generalized brain injury such as infection or hemorrhage.

MR Imaging Acquisition and Assessment

MR imaging protocols were not standardized across the centers due to the retrospective nature of the study and different MR imaging scanners at the sites, however, all studies were performed at 1.5T using abdominal or cardiac phased array coils. Each study included single-shot fast spin-echo T2-weighted sequences in 3 orthogonal planes (TE, between 80 and 180 ms; section thickness, between 3 and 4 mm; in-plane resolution, between 1.1 and 1.3 mm²) and axial T1-weighted sequences (FSE or gradient recalled-echo, 4- to 5-mm section thickness). All cases were consensus-reviewed by 3 senior pediatric neuroradiologists (A.R., C.P., P.D.G.), each with >15 years' experience in fetal MR imaging. The presence of GE unilateral or bilateral cavitations or enlargement was recorded, along with details of any associated developmental brain anomalies (Online Supplemental Data). A cavitation in the GE region was defined as a small, well-demarcated ovoid or crescentic structure with CSF signal, lying between the GE and the adjacent parenchyma. Enlargement of the GE region was defined subjectively after a qualitative analysis on 3-plane images, taking into account a pool of cases with normal findings as a reference. The 2 main centers (1 in Italy and 1 in England) provided >70% of the collected cases and had access to a pool of fetal MR studies with normal findings ranging from 17 to 37 weeks' gestational age (GA) (110 in Italy and 200 in England), which were used as reference cases. From those cases, we believe that the GE is visible between 17 and 30 weeks' GA, though its prominence reduces with increasing maturity and is barely visible after the 30th week.

Head size was categorized on the basis of GA-matched reference centiles:¹³ microcephaly less than the third centile, normal size between the third and 97th centiles, and macrocephaly >97th centile. Other anomalies such as ventriculomegaly (mild, 10–12 mm;

moderate-severe, >12 mm), agenesis or hypogenesis of corpus callosum, reduced opercularization, reduced gyration, cerebellar anomalies or hypoplasia, brain stem anomalies, abnormal transient layering of the developing brain mantle, unilateral or bilateral polymicrogyria, and hemimegalencephaly were recorded and included in the analysis.

Statistical Analysis

All variables are reported as median (interquartile range) unless stated otherwise. χ^2 and Fisher exact tests were performed to assess the differences between the expected and observed frequencies of the associated cerebral developmental anomalies in fetuses with different types of GE anomalies. The Fisher exact test was selected over the χ^2 test when the expected count in any cell of a 2×2 table was <5. A P value $\leq .05$ was statistically significant. Statistical analysis was performed with SPSS statistical and computing software, Version 20 (IBM).

RESULTS

Sixty fetuses met the inclusion criteria (21 females, 24 males, and 15 sex not known; Online Supplemental Data). The average GA at MR imaging was 23.08 [SD, 3.5] weeks (range, 17–33 weeks). Thirty-four of 60 (57%) fetuses had GE cavitations (29 bilateral, 5 unilateral), and 26/60 (43%) had increased GE volume (19 bilateral, 7 unilateral). Figure 1 shows the type and frequencies of the associated brain anomalies.

Bilateral cavitations of the GE were associated with microcephaly ($P = .01$), cerebellar anomalies ($P = .01$), reduced opercularization ($P = .001$), and reduced gyration ($P < .001$). Unilateral cavitations of the GE did not show any positive, specific association with head size, while the negative correlation of the absence of reduced opercularization was significant ($P = .01$). Bilateral increased volume of the GE showed an association with macrocephaly ($P = .03$). Unilateral increased volume of the GE was associated with macrocephaly ($P = .002$), abnormal transient layering ($P = .001$), unilateral polymicrogyria ($P = .001$), hemimegalencephaly ($P < .001$), and significant absence of the following: agenesis or severe hypogenesis of the corpus callosum ($P = .03$), and cerebellar anomalies ($P = .02$).

DISCUSSION

GE abnormalities are a very rare finding on fetal MR imaging studies as highlighted by our ability to locate only 60 cases from 7 centers performing high numbers of fetal MR imaging studies during a 20-year period. Despite the rarity of a GE, the collaboration among the recruiting centers allowed sufficient numbers of cases of GE anomalies to uncover statistically significant associations between types of GE abnormalities and coexisting developmental brain abnormalities. Our categorization of GE abnormalities used a straightforward anatomic approach, describing either cavitations or increased size of the GE. We acknowledge, however, that there are problems in making subjective assessments of the size of structures such as the GE, whose borders may be somewhat indistinct. We also recognize the possibility that the GE can have reduced size, which could be associated with brain abnormalities. This article has not covered that subject, but it may be relevant for conditions such as primary microcephaly/microencephaly.

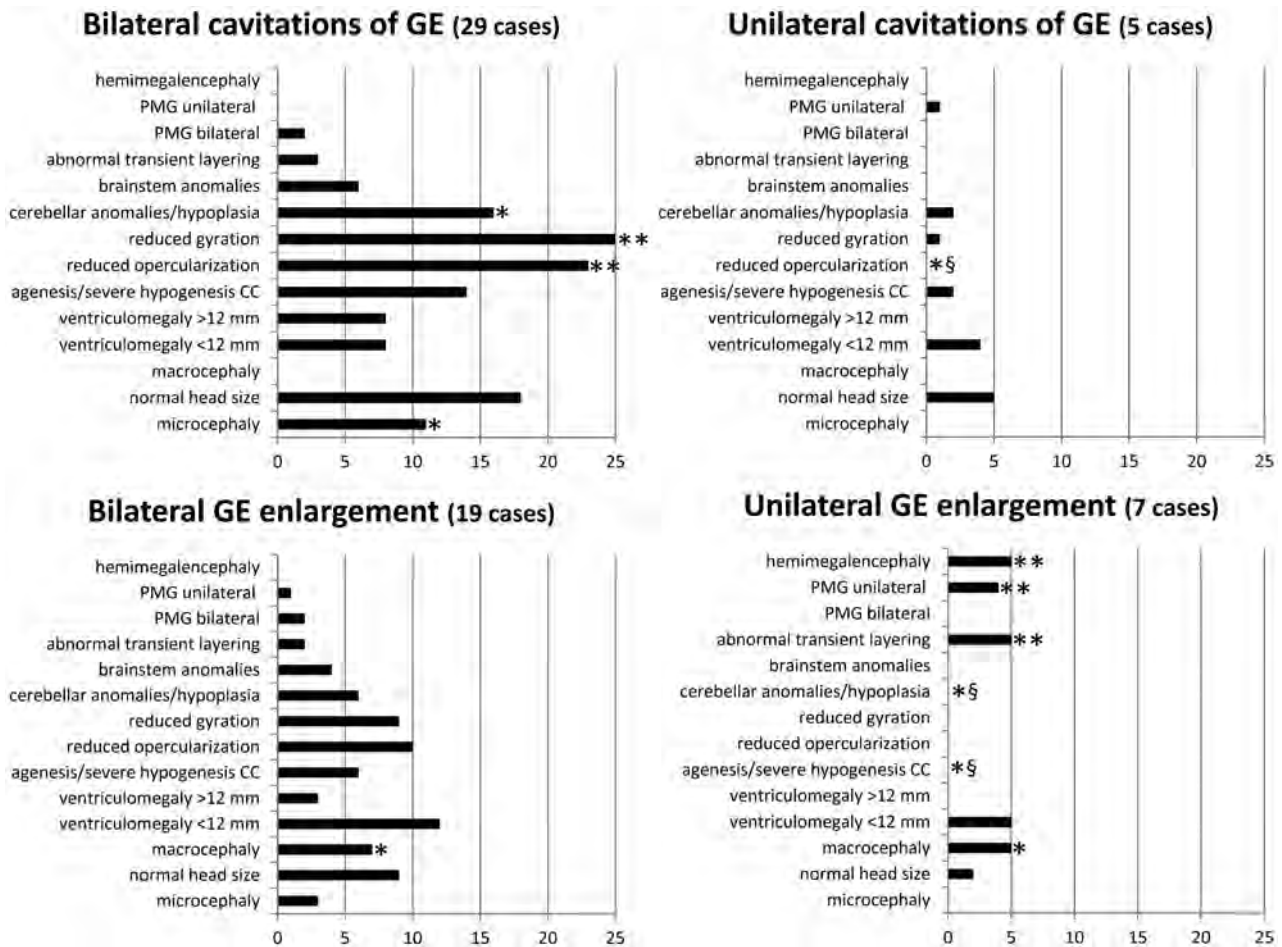


FIG 1. Plots of the frequency of the associated brain anomalies for each of the 4 categories of GE anomaly reported. Asterisk indicates $P < .05$; double asterisks, $P \leq .001$; section sign, a significant negative association. PMG indicates polymicrogyria; CC, corpus callosum.

Within those limitations, we found that GE cavitations occur slightly more frequently than the increased size of the GE (34/60 versus 26/60), and each category of GE anomalies appears to be preferentially associated with specific types of brain abnormalities. When GE cavitations are present, they are much more likely to be bilateral rather than unilateral (29/36 versus 5/36). Bilateral GE cavitations were the most prevalent abnormality in our cohort and were most frequently associated with abnormalities of brain development, in the spectrum of microlissencephalies and cerebellar anomalies (Fig 2). The association between GE cavitations and cerebellar anomalies, albeit significant, is not readily explainable, but it is well-known that posterior fossa structures may be aberrant in microlissencephaly.

As reported previously,^{10,11} the bilateral, symmetric inverted C-shaped morphology of GE cavitations with a clear margin from the adjacent basal ganglia and the absence of high signal on T1-weighted images are highly associated with brain malformation. Familial recurrence of these cases has been reported^{10,11,14} and further supports the argument. Reduction in head size and delayed opercularization and gyration were also found to be associated with bilateral GE cavitations in our cohort. This association may be explained by disruption of normal cell proliferation and migration in and from the GE, mediated by a genetic

mutation in one of the many genes involved in GE neurogenesis.⁷ At present, however, no pathophysiologic explanation has been demonstrated in human subjects, but it is likely that numerous genetic mutations will be discovered in the future. Five of 60 fetuses showed unilateral cavitation of the GE (Fig 3 and Online Supplemental Data): In this subgroup, there were no demonstrable positive associations with other developmental brain anomalies. Given the small number, this finding should be interpreted cautiously.

Nineteen of 60 fetuses had bilateral increased volume of GEs (Fig 4 and Online Supplemental Data), and we showed an association only with macrocephaly. This finding leads, however, to a hypothesis about an underlying mechanism involving excessive and abnormal neuroblast proliferation and migration. The overall lack of other associations suggests that the finding is not specific for a pathophysiologic process but can be found in a wide array of neurodevelopmental abnormalities, encompassing macrocephaly, opercularization and gyration anomalies, and cerebellar anomalies. It seems intuitive that in cases of a generalized brain size increase (ie, brain gigantism associated with a *mammalian target of rapamycin kinase [MTOR]* gene mutation), the GE volume may be concordantly enlarged as well (Fig 4 and Online Supplemental Data). The opposite condition is more difficult to

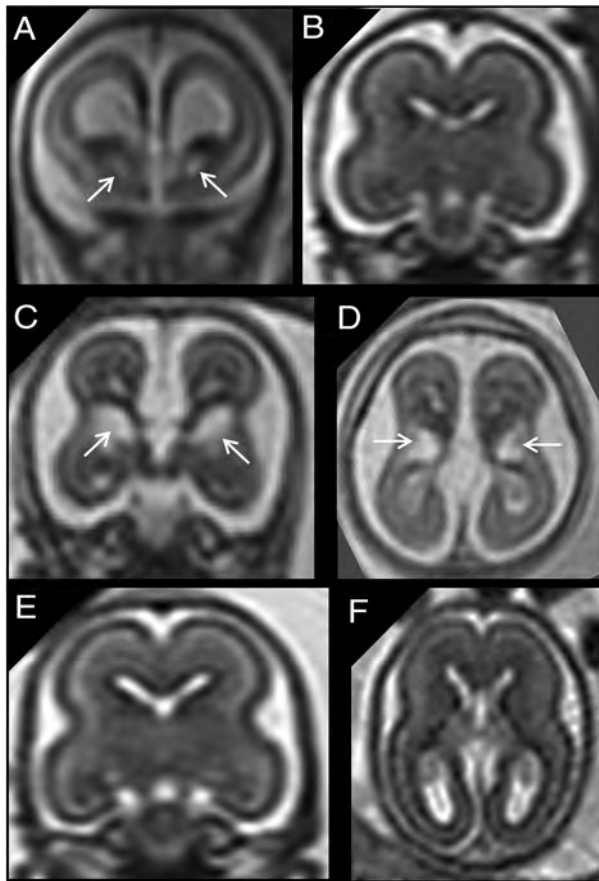


FIG 2. A, Coronal single-shot [SS]-FSE T2-weighted section of a 20 weeks' GA fetus shows bilateral cavitation of the GE (arrows). B, A GA-matched control. C and D, Coronal and axial SS-FSE T2-weighted sections of a 21 weeks' GA fetus showing bilateral cavitation of the GE regions (arrows). The fetus had microcephaly (less than the third centile), reduced opercularization and gyration (ie, parieto-occipital sulcus), brain stem and cerebellar anomalies (not shown), and agenesis of corpus callosum. E and F, A GA-matched control.

explain, ie, when enlarged GEs are found in fetuses with small heads (present in 3 of our cases with bilateral and 1 with unilateral GE enlargement). Previous reports have linked the enlargement of the GE to reduced opercularization¹⁵ and *Tubulin* gene mutation-related lissencephaly (*tubulin alpha 1a* [*TUBA1A*] gene defect).^{16,17} As previously suggested,¹⁰ one of the hypothetical causes of an enlarged GE could be an excessive accumulation of neuroblasts in the GE due to a delay/arrest of the migration to the cortical destination or delay in the physiologic involution of the GE itself during neurogenesis. The animal model of the *aristaless related homeobox* (*ARX*) gene mutation,¹⁸ which is characterized by microlissencephaly and an enlarged GE during the fetal period, could support, at least in part, this hypothesis. A recently reported human fetal case with the *ARX* gene mutation and showing clear GE enlargement supports this view.¹⁹ Given the different morphologic features of the developing brain with bilateral increased volume of the GE, multiple pathophysiologic mechanisms are likely at play and specific genetic mutations are required to classify specific associated malformations, as also reported by Amir et al.²⁰

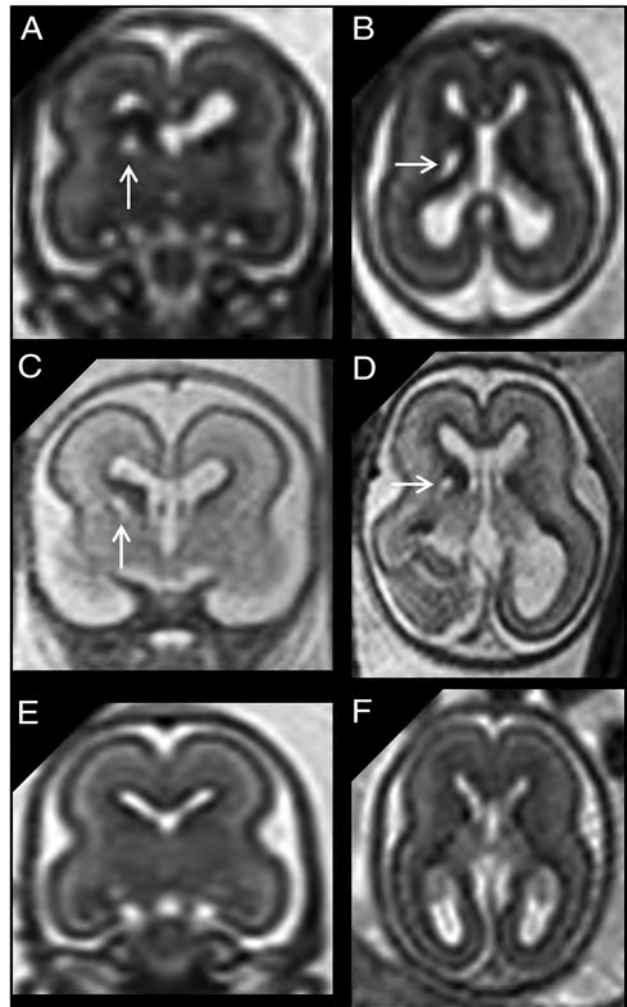


FIG 3. A and B, Coronal and axial single-shot [SS]-FSE T2-weighted sections of a 21 weeks' GA fetus show unilateral cavitation of the GE (arrows). Brain size was normal, and no associated anomalies were found. C and D, Coronal and axial SS-FSE T2-weighted sections of another 21 weeks' GA fetus show unilateral cavitation of the GE (arrows). Head size was normal, but an ipsilateral temporal-occipital large polymicrogyric area was found. E and F, A GA-matched control.

Seven of 60 patients were found to have a unilateral increased volume of the GE (Fig 5), and 5 of those fetuses had hemimegalencephaly. We found a statistically significant association between unilateral enlargement of the GE and macrocephaly, abnormal transient layering, and unilateral polymicrogyria, but these are explained by the large number of cases with hemimegalencephaly in this subgroup. The explanation for the association between GE enlargements concordant with ipsilateral cerebral hemisphere enlargement is intuitive. Unilateral GE enlargement was also associated with the significant negative correlation of the absence of agenesis or hypogenesis of corpus callosum, reduced opercularization, and reduced gyration. All of these associations can be explained by the high prevalence of hemimegalencephaly and the characteristic MR imaging findings of this entity.²¹ The 2 cases without hemimegalencephaly had normal brain size and showed no other neurodevelopmental abnormalities. It is likely

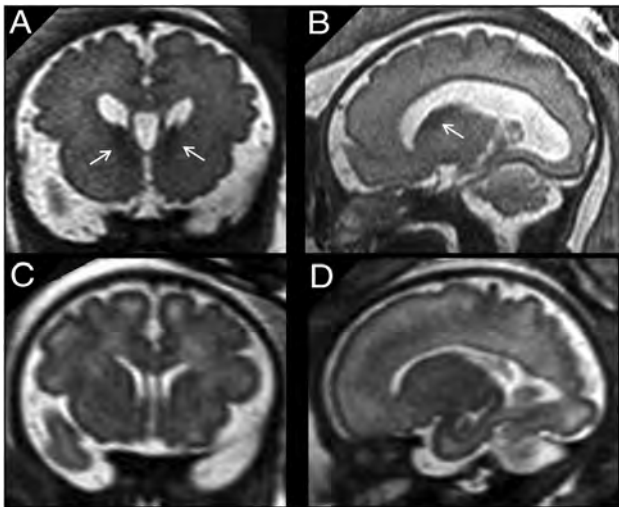


FIG 4. A and B, Coronal and sagittal single-shot-FSE T2-weighted sections of a 33 weeks' GA fetus show bilateral increased volume/abnormal persistence of the GE (arrows). Macrocephaly (>97th centile) and mild ventriculomegaly (<12mm) are also noted. An activating mutation of *MTOR* gene was identified. C and D, A GA-matched control.

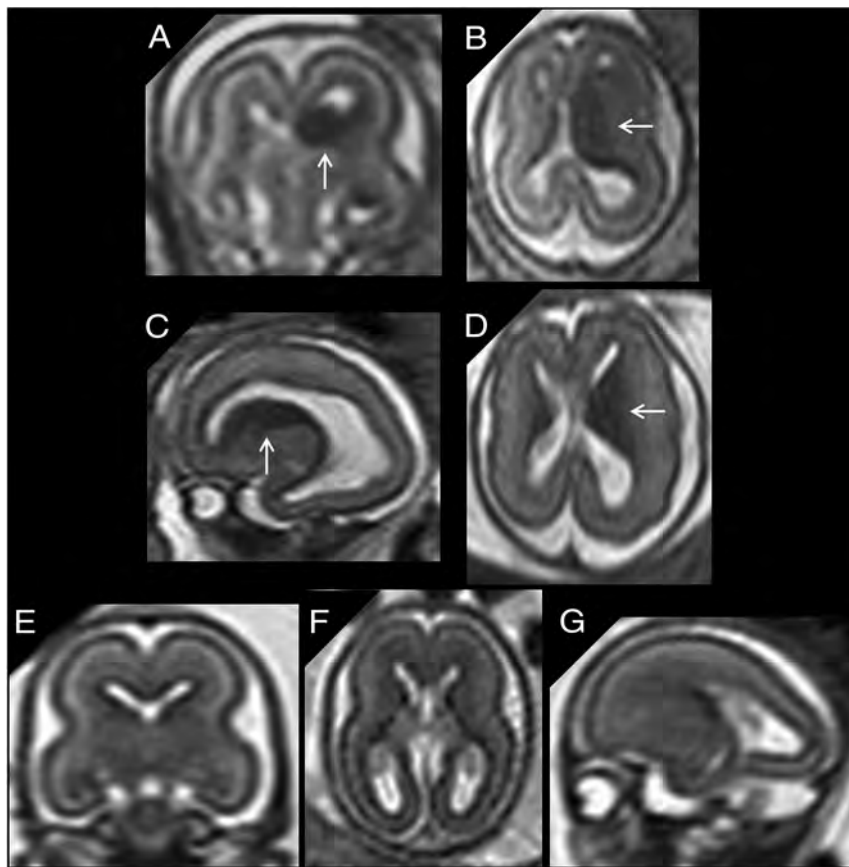


FIG 5. A and B, Coronal and axial single-shot [SS]-FSE T2-weighted sections of a 21 weeks' GA fetus show unilateral increased volume of the GE (arrows) with homolateral hemimegalencephaly. C and D, Sagittal and axial SS-FSE T2-weighted sections of another 21 weeks' GA fetus showing unilateral increased volume of the GE (arrows). Associated anomalies were early-stage unilateral polymicrogyria and hemimegalencephaly. In both cases, the normal brain mantle layering for age was deranged in the enlarged hemisphere. E–G, A GA-matched control.

that these cases belong to a different pathophysiologic entity with a less severe phenotype and probably a rarer occurrence or, conversely, are more difficult to detect at prenatal screening.

We elected not to correct for multiple tests (using, for example, the Bonferroni correction) because our study was not specifically hypothesis-directed, rather, it was an exploratory study with the view that future studies would use our current data to perform prospective, formally powered studies. Correction for multiple tests was not performed, to maximize the chance of finding possible associations in this exploratory study and hence minimizing the risk of false-negatives when correcting *P* values for multiple comparisons. We accept, however, that this approach will lead to an increased risk of type I errors.

Only 19/60 cases did not have any form of ventriculomegaly; this finding should be taken into account because prenatal sonographic detection of ventriculomegaly is one of the leading findings prompting MR imaging investigation. Thus, in our cohort, the real proportion of cases with GE anomalies but without ventriculomegaly might have been underestimated.

Our work suggests that GE abnormalities are central to a range of neurodevelopmental abnormalities that encompass abnormal neuroblast proliferation-differentiation and migration processes, which often lead to generalized or local abnormal neuronal organization.

We recognize, however, that we have reported several associations that are not readily explainable with known etiologic and pathophysiologic data. For example, unilateral cavitations of the GE region were not specifically associated with a prevalent anomaly, hinting at a “milder” phenotype whose pathophysiology and prognosis could be very different from those in the fetuses with bilateral GE cavitations. Of note, all 5 fetuses with unilateral cavitation had normal head size.

Clinical follow-up studies and the results of genetic analysis are required in this field of work and will make an invaluable contribution to the definition of possible subgroups, which will allow improved counseling of pregnant women whose fetuses have GE abnormalities.

CONCLUSIONS

This study expands on the understanding of GE anomalies in the fetus and provides statistically validated insights into the associated neurodevelopmental anomalies. We cannot currently provide a specific etiologic/genetic classification of the GE and associated anomalies, but we believe that our data strengthen the current understanding and build a valid framework for future studies.

Disclosures: Mariasavina Severino—UNRELATED: Employment: neuroradiology consultant, Istituto Di Ricovero e Cura a Carattere Scientifico—Istituto Giannina Gaslini.

REFERENCES

1. Stiles J, Jernigan TL. **The basics of brain development.** *Neuropsychol Rev* 2010;20:327–48 CrossRef Medline
2. Anderson SA, Eisenstat DD, Shi L, et al. **Interneuron migration from basal forebrain to neocortex: dependence on *Dlx* genes.** *Science* 1997;278:474–76 CrossRef Medline
3. Le TN, Zhou Q, Cobos I, et al. **GABAergic interneuron differentiation in the basal forebrain is mediated through direct regulation of glutamic acid decarboxylase isoforms by *Dlx* homeobox transcription factors.** *J Neurosci* 2017;37:8816–29 CrossRef Medline
4. Arber C, Li M. **Cortical interneurons from human pluripotent stem cells: prospects for neurological and psychiatric disease.** *Front Cell Neurosci* 2013;13:7–10 CrossRef Medline
5. Lavdas AA, Grigoriou M, Pachnis V, et al. **The medial ganglionic eminence gives rise to a population of early neurons in the developing cerebral cortex.** *J Neurosci* 1999;19:7881–88 CrossRef Medline
6. Miyoshi G, Hjerling-Leffler J, Karayannis T, et al. **Genetic fate mapping reveals that the caudal ganglionic eminence produces a large and diverse population of superficial cortical interneurons.** *J Neurosci* 2010;30:1582–94 CrossRef Medline
7. Shinozaki K, Miyagi T, Yoshida M, et al. **Absence of Cajal-Retzius cells and subplate neurons associated with defects of tangential cell migration from ganglionic eminence in *Emx1/2* double mutant cerebral cortex.** *Development* 2002;129:3479–92 Medline
8. Miyoshi G. **Elucidating the developmental trajectories of GABAergic cortical interneuron subtypes.** *Neurosci Res* 2019;138:26–32 CrossRef Medline
9. Vasung L, Charvet CJ, Shiohama T, et al. **Ex vivo fetal brain MRI: recent advances, challenges, and future directions.** *Neuroimage* 2019;195:23–37 CrossRef Medline
10. Righini A, Frassoni C, Inverardi F, et al. **Bilateral cavitations of ganglionic eminence: a fetal MR imaging sign of halted brain development.** *AJNR Am J Neuroradiol* 2013;34:1841–45 CrossRef Medline
11. Righini A, Cesaretti C, Conte G, et al. **Expanding the spectrum of human ganglionic eminence region anomalies on fetal magnetic resonance imaging.** *Neuroradiol* 2016;58:293–300 CrossRef Medline
12. Righini A, Genovese M, Parazzini C, et al. **Cortical formation abnormalities on foetal MR imaging: a proposed classification system trialled on 356 cases from Italian and UK centres.** *Eur Radiol* 2020;30:5250–60 CrossRef Medline
13. Tilea B, Alberti C, Adamsbaum C, et al. **Cerebral biometry in fetal magnetic resonance imaging: new reference data.** *Ultrasound Obstet Gynecol* 2009;33:173–81 CrossRef Medline
14. Prefumo F, Petrilli G, Palumbo G, et al. **Prenatal ultrasound diagnosis of cavitation of ganglionic eminence.** *Ultrasound Obstet Gynecol* 2019;54:558–60 CrossRef Medline
15. Guibaud L, Selleret L, Larroche JC, et al. **Abnormal Sylvian fissure on prenatal cerebral imaging: significance and correlation with neuropathological and postnatal data.** *Ultrasound Obstet Gynecol* 2008;32:50–60 CrossRef Medline
16. Fallet-Bianco C, Loeuillet L, Poirier K, et al. **Neuropathological phenotype of a distinct form of lissencephaly associated with mutations in *TUBA1A*.** *Brain* 2008;131:2304–20 CrossRef Medline
17. Fallet-Bianco C, Laquerrière A, Poirier K, et al. **Mutations in tubulin genes are frequent causes of various foetal malformations of cortical development including microlissencephaly.** *Acta Neuropathol Commun* 2014;2:69–91 CrossRef Medline
18. Colombo E, Collombat P, Colasante G, et al. **Inactivation of *Arx*, the murine ortholog of the X-linked lissencephaly with ambiguous genitalia gene, leads to severe disorganization of the ventral telencephalon with impaired neuronal migration and differentiation.** *J Neurosci* 2007;27:4786–98 CrossRef Medline
19. Ffrench-Constant S, Kachramanoglou C, Jones B, et al. **Fetal and neonatal MRI features of *ARX*-related lissencephaly presenting with neonatal refractory seizure disorder.** *Quant Imaging Med Surg* 2019;9:1767–72 CrossRef Medline
20. Amir T, Poretti A, Boltshauser E, et al. **Differential diagnosis of ventriculomegaly and brainstem kinking on fetal MRI.** *Brain Dev* 2016;38:103–08 CrossRef Medline
21. Williams F, Griffiths PD. **The diagnosis of hemimegalencephaly using in utero MRI.** *Clin Radiol* 2014;69:291–97 CrossRef Medline

Anatomic Variation of the Superficial Temporal Artery and Posterior Auricular Artery in a Pediatric Moyamoya Disease Population

S. Lee, S.-K. Kim, and J.H. Phi



ABSTRACT

BACKGROUND AND PURPOSE: In certain cases of pediatric patients with Moyamoya disease undergoing encephaloduroarteriosynangiosis (EDAS) treatment, the posterior auricular artery can be used as an alternative when the parietal branch of the superficial temporal artery is unavailable. In this study, anatomic variations of the superficial temporal and posterior auricular arteries in pediatric patients with Moyamoya disease and postoperative outcomes of posterior auricular artery-EDAS are explored.

MATERIALS AND METHODS: Medical records of 572 patients with Moyamoya disease who underwent surgical procedures from 2007 to 2017 at the Seoul National University Children's Hospital were reviewed. Anatomic classifications of the superficial temporal and posterior auricular arteries were based on previous classifications. Postoperative hemodynamic changes of posterior auricular artery-EDAS were analyzed using the Matsushima grade. Also, Karnofsky Performance Scale and mRS scores of posterior auricular artery-EDAS cases were reviewed to identify postoperative clinical outcomes.

RESULTS: Among 1144 hemispheres, 24 were considered posterior auricular artery-EDAS candidates (2.1%). Of those, 10 hemispheres underwent posterior auricular artery-EDAS (41.7%, in total hemispheres 0.9%). Comparing the Matsushima grades of the superficial temporal artery-EDAS and posterior auricular artery-EDAS groups showed similar postoperative revascularization. Postoperative Karnofsky Performance Scale and mRS scores of patients having undergone posterior auricular artery-EDAS did not show deterioration.

CONCLUSIONS: In approximately 2% of pediatric patients with Moyamoya disease for whom the superficial temporal artery is unavailable as the EDAS donor, the posterior auricular artery can be considered an alternative. On the basis of the results, the clinical outcome of posterior auricular artery-EDAS was not inferior to that of superficial temporal artery-EDAS. Hence, we suggest an in-depth consideration of the posterior auricular artery as the donor artery if the superficial temporal artery parietal branch is unavailable.

ABBREVIATIONS: EDAS = encephaloduroarteriosynangiosis; EGS = encephalogaleosynangiosis; MMD = Moyamoya disease; PAA = posterior auricular artery; STA = superficial temporal artery

Moyamoya disease (MMD) is one of the most common pediatric cerebrovascular diseases in East Asia, characterized by slowly progressive occlusion of the internal carotid arteries or their branches. Such progression causes the development of extensive collateral vessels known as Moyamoya vessels at the base of the brain.^{1,2}

Among various symptoms, repeated TIAs are most prevalent in pediatric patients.³ To increase the blood supply in MMD, direct or indirect bypass surgery is performed to enhance collateral revascularizations to the ischemic areas of the brain. Traditionally, due to technical difficulties involving the small size of donor and recipient vessels, indirect extracranial-intracranial bypass has been favored for pediatric patients with MMD.⁴⁻⁸ Among various indirect bypass techniques, encephaloduroarteriosynangiosis (EDAS) is commonly performed to increase the blood supply to the MCA territory. Here, the parietal branch of the superficial temporal artery (STA) is commonly used as the donor artery, given its proximity to the motor cortex. However, the parietal branch of the STA is sometimes unavailable, as with a previously used STA parietal branch and hypoplasia, absence, or anterior positioning of the STA parietal branch. Then, the posterior auricular artery (PAA) with the appropriate anatomic criteria met could be used as an alternative.

Received September 30, 2020; accepted after revision December 17.

From the Division of Pediatric Neurosurgery, Seoul National University Children's Hospital, Seoul National University College of Medicine, Seoul, Korea.

This study was supported by a grant from the Seoul National University Hospital (No. 0320200090).

Please address correspondence to Ji Hoon Phi, MD, PhD, Division of Pediatric Neurosurgery, Seoul National University Children's Hospital, Seoul National University College of Medicine, 03080, 101 Daehak-ro, Jongno-gu, Seoul, Korea; e-mail: phi.jihoon@gmail.com



Indicates article with online supplemental data.

<http://dx.doi.org/10.3174/ajnr.A7059>

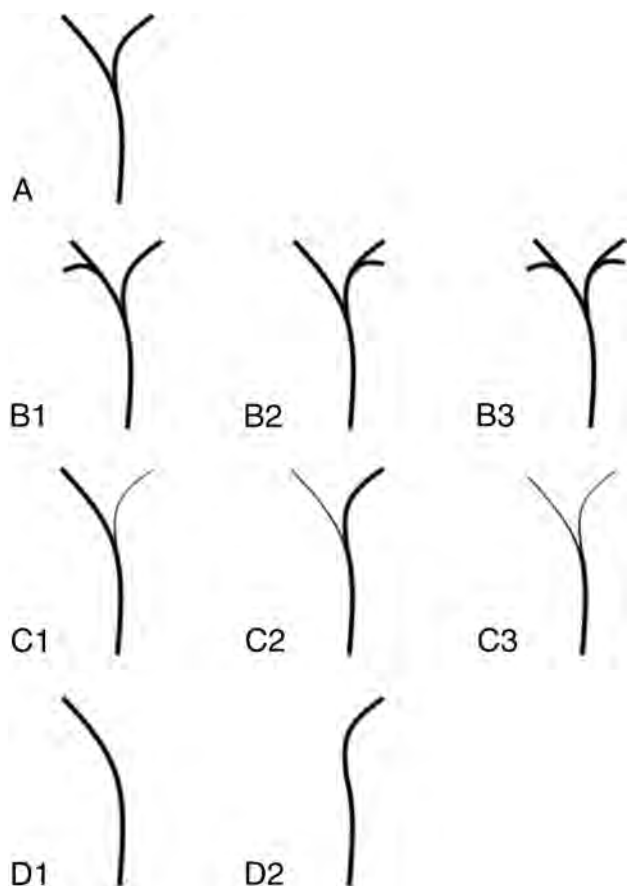


FIG 1. STA classification. Class A corresponds to classic STA anatomy with a single frontal and parietal branch. Classes B1, B2, and B3 illustrate additional frontal, parietal, or both branches, respectively. Class C1, C2, and C3 illustrate hypoplasia of the parietal, frontal, or both branches, respectively. Class D1 and D2 illustrate aplasia of the parietal and frontal branches, respectively.

There are several reports in the literature of successful use of the PAA as an alternative.⁹⁻¹² Yet, no research has been conducted on PAA use as an indirect bypass alternative, especially in pediatric patients. Also, there has been no thorough investigation of STA and PAA anatomic variations on a large number of pediatric patients with MMD.

In this article, we investigate the anatomic variations of both the STA and PAA in pediatric patients with MMD and examine the STA and PAA anatomic variation combinations that are considered adequate for performing PAA-EDAS. Additionally, postoperative clinical outcomes and the degree of postoperative revascularization of STA-EDAS and PAA-EDAS are compared.

MATERIALS AND METHODS

From January 1, 2007, to December 31, 2017, we surgically treated 600 patients with MMD. Of those, 572 patients with MMD were enrolled in this study after using the following exclusion criteria: 12 patients with Moyamoya syndrome and 16 with insufficient electronic medical record data or radiologic records. To classify the STA, we initially considered adopting the STA classification coined by Marano et al.¹³ However, due to excessive subgroups and complexity, as illustrated in Fig 1, we opted for the classification by

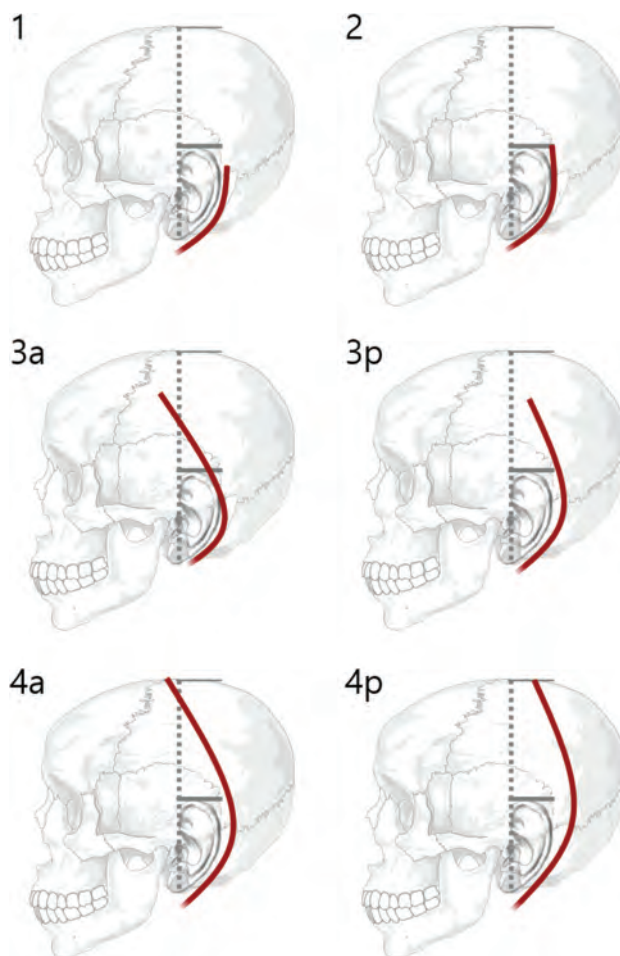


FIG 2. PAA classification. The *thin solid line* indicates the vertex; the *dashed vertical line* indicates the external auditory canal midline; and the *thick solid line* indicates the helix. Class 1 illustrates PAA terminating below the helix, class 2 illustrates the PAA terminating at the helix, class 3 illustrates the PAA terminating between the helix and the vertex, and class 4 illustrates the PAA terminating at the vertex. For classes 3 and 4, if the PAA advances anteriorly passing the vertical line, the class is annotated with “a” for anteriority and, if not, “p” for posteriority.

Medved et al¹⁴ without class E which illustrates an additional superior auricular artery, which is not crucial to surgical planning.

Likewise, we adopted the PAA classification coined by Tokugawa et al¹⁵ with some modifications. The alphabetic classification was changed to numeric for easier distinction between STA and PAA classes, as well as the anteriority and posteriority of classes 3 and 4 as illustrated in Fig 2.

To evaluate the postoperative technical outcomes of PAA-EDAS and STA-EDAS, we compared the degree of revascularization on follow-up transfemoral cerebral angiography between the PAA-EDAS and STA-EDAS groups based on the Matsushima grade: Grade A denotes revascularization of more than two-thirds of the MCA territory, grade B denotes revascularization of between one- and two-thirds of the MCA territory, and grade C denotes revascularization of a slight amount or none of the territory.¹⁶ Twice as many patients having undergone STA-EDAS ($n = 20$) as those in the PAA-EDAS group ($n = 10$) were selected for the same age-

Table 1: Demographics of 572 patients

Demographics	Value
Sex (n = 572)	
Male	255 (44.6%)
Female	317 (55.4%)
Age of diagnosis (yr)	
Younger than 3	55 (9.7%)
3~7	230 (40.2%)
8~11	188 (32.8%)
12~14	73 (12.7%)
15~18	26 (4.5%)
Unilateral (n = 112)	
Right	58 (51.8%)
Left	54 (48.2%)
Average follow-up period (yr)	6.1

Table 2: Distribution of STA and PAA

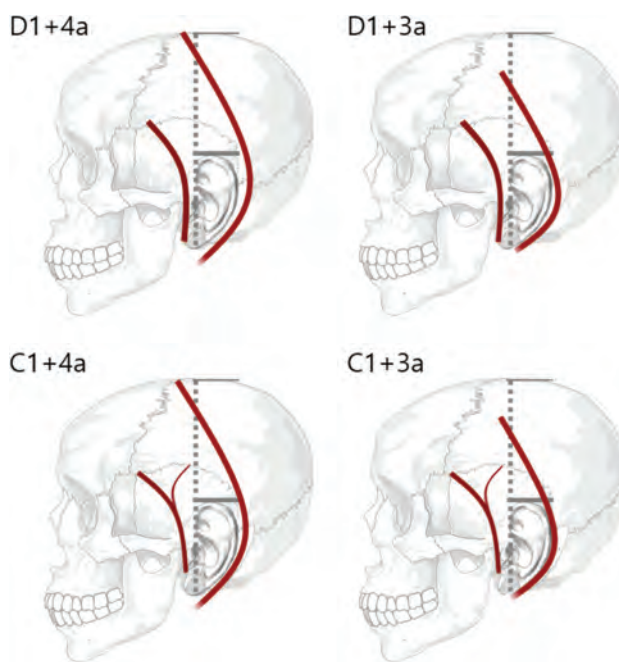
Distribution	No. (%)
STA	
A	380 (33.2%)
B1	254 (22.2%)
B2	139 (12.2%)
B3	250 (21.8%)
C1	33 (2.8%)
C2	26 (2.3%)
C3	26 (2.3%)
D1	19 (1.7%)
D2	17 (1.5%)
Total	1144 (100%)
PAA	
1	563 (49.2%)
2	127 (11.1%)
3a	162 (14.2%)
3p	267 (23.3%)
4a	18 (1.6%)
4p	8 (0.6%)
Total	1144 (100%)

sex-orientation follow-up period. Given the lack of follow-up trans-femoral cerebral angiography in 3 patients having undergone PAA-EDAS and the failed matching of 1 patient having undergone PAA-EDAS, angiography for a total of 6 patients having undergone PAA-EDAS and 12 having undergone STA-EDAS was reviewed. On the basis of 1-year postoperative medical records, the functional status of the patients was assessed using the following 3 assessments: the clinical outcome grading system and the Karnofsky Performance Scale and mRS scoring methods.^{1,17,18} This study protocol was approved by the institutional review board (No. H-1806-116-952).

RESULTS

Table 1 depicts the enrolled patients' demographics; 572 subjects comprised 255 male (44.6%) and 317 female (55.4%) patients. The median age of first diagnosis was 8 years (range, 9 months to 18 years). Of the 572 patients, 112 patients (19.6%) were initially found to have unilateral MMD, with 58 patients (51.8%) being right-sided and 54 patients (48.2%) being left-sided. The average follow-up period was 6.1 years.

As described in Table 2, the most abundant STA class was A (380 hemispheres, 33.2%), 33 hemispheres (2.8%) were class C1, and 19 hemispheres (1.7%) were class D1. For the PAA, the most

**FIG 3.** PAA-EDAS candidates.

abundant was class 1 with 563 hemispheres (49.2%), 18 hemispheres (1.6%) were class 4a, and 162 hemispheres (14.2%) were class 3a.

STA classes A, B, C2, and D2 were considered adequate for performing STA-EDAS. A total of 1066 of 1144 hemispheres (93.2%) had adequate STAs. On the other hand, C1, C3, and D1 were considered inadequate STAs due to the absence or hypoplasia of the parietal branch. A total of 78 hemispheres (6.8%) showed inadequate STAs. Among 78 hemispheres with inadequate STAs, a total of 24 hemispheres derived from 23 patients had STA-PAA combinations of D1 + 4a, D1 + 3a, C1 + 4a, and C1 + 3a, which were considered PAA-EDAS candidates (Fig 3) with 1 patient having bilateral PAA-EDAS candidacy. C3 + 3a and C3 + 4a were omitted as PAA-EDAS candidates because such combinations were not observed in our patients. Among these cases, PAA-EDAS was performed on 10 hemispheres (9 total patients). Three cases with 3a showed PAA terminating over the 50% mark between the helix and vertex (54%, 67%, and 73% for the 3 cases), which was considered adequate for performing PAA-EDAS. The operative cases are listed in the Online Supplemental Data.

For the remaining 14 hemispheres, 4 cases were unilateral MMD, in which the normal side contained STA and PAA configurations of a PAA-EDAS candidacy, and 4 cases were operated as encephalogalectosynangiosis (EGS) due to surgeon's preference. Three cases showed the combination of C1 + 4a in which 1 case had an additional frontal branch that advanced close to the hypoplastic parietal branch, allowing the surgeon to use the frontal branch. For the other 2 cases, a hypoplastic parietal branch was used for STA-EDAS due to surgeon's preference. For the remaining 3 cases that showed a C1 + 3a configuration, the proportion of the PAA termination points between the helix and vertex was below the 50% mark (28%, 17%, and 42% for the 3 cases); hence, the STA parietal branch was used despite being hypoplastic.

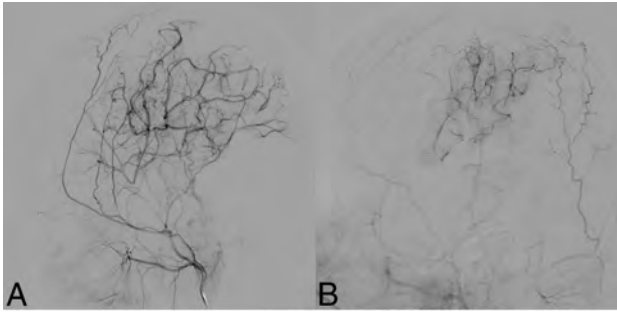


FIG 4. Representative illustrations of late arterial phase external carotid artery angiography with postoperative collateral formation after PAA-EDAS. A, Right PAA-EDAS case of 17-year-old boy representing Matsushima grade A. B, Right PAA-EDAS case of 8-year-old boy representing Matsushima grade B.

For postoperative clinical outcomes, 8 of 9 patients had Karnofsky Performance Scale scores of 100 and mRS = 0, while 1 had a Karnofsky Performance Scale score of 80 with mRS = 2, which was due to an initial preoperative infarction on the left MCA territory. In addition, 6 of 9 patients had excellent clinical outcome, 1 had good clinical outcome, and 2 had fair clinical outcomes.

When we compared the Matsushima grade on follow-up transfemoral cerebral angiography between the PAA-EDAS and STA-EDAS groups, 50% (3 of 6) of the PAA-EDAS and 33% (4 of 12) of the STA-EDAS groups had grade A, 33% (2 of 6) of the PAA-EDAS and 50% (6 of 12) of the STA-EDAS groups had grade B, and 17% (1 of 6) of PAA-EDAS and 17% (2 of 12) of STA-EDAS groups had grade C. Postoperative angiography of illustrative PAA-EDAS cases is presented in Fig 4.

DISCUSSION

Various studies regarding the anatomic variations of STA have been reported in previous literature. One of the earliest investigations was conducted by Marano et al,¹³ who classified 10 STA variations based on 50 consecutive human postmortem specimens. Thereafter, Medved et al¹⁴ reported 11 STA variations using a more advanced radiologic technology of digital subtraction angiography on 93 individuals. Regarding ethnic STA variations, Chen et al¹⁹ reported differences between East Asians and whites by comparing the location of STA bifurcation. Kim et al²⁰ explored STA variations in the Korean adult population using 3D CT angiography, concluding that the STA of Koreans is similar to that of the Chinese, while smaller in diameter compared with that of the Western population. However, a thorough investigation of STA variations in the pediatric population has not been illustrated in the literature. When we compared the results with that of Medved et al,¹⁴ our data also showed that class A (33.2%) was one of the abundant types. However, the proportions of classes B (56.2%), C (7.4%), and D (3.2%) were radically different because Medved et al reported a lower rate of class B (8.6%) and higher proportions of classes C (22.6%) and D (10.8%). These findings may be due to the patients with MMD developing vault Moyamoya collaterals, which could have caused additional formation of frontal and parietal branches.

PAA is well-recognized in plastic and reconstructive surgery for its frequent use in pedicled flaps.²¹ However, limited studies have been conducted on its neurosurgical use. Although in 2015, Tokugawa et al¹⁵ coined a novel classification of PAA variations based on the angiographic appearance of 424 subjects, the PAA variation is yet to be discussed for children. On the basis of our study on pediatric patients, classes 3 and 4, the 2 viable candidates for PAA-EDAS, were at 37.5% and 2.2%, respectively. These results were similar to the adult data from Tokugawa et al, which reported classes 3 and 4 to be 48.8% and 1.2%, respectively. However, Germans et al¹⁰ and Pinar et al,²² respectively, reported 5.7% and 33% of dominant PAAs reaching up to the parietotemporal area in the adult population. This wide discrepancy may be due to ethnic differences, but the dominant PAA described by Germans et al and Pinar et al included classes 3 and 4 combined, which could yield results similar to that of our data when adjusted for the classification suggested by Tokugawa et al. On the basis of the results, we believe that adults and children do not differ in the formation of PAA.

To treat MMD, establishment of sufficient revascularization to the ischemic brain tissue is essential, especially in developing brains. Classically, the STA parietal branch has been used for MCA territory revascularization. Recent studies, however, have reported the potential use of the PAA for MCA territory revascularization in certain cases in which the STA is unfit to be a donor. To use the PAA as a donor, Germans et al¹⁰ mentioned that the PAA must extend to the temporoparietal area with a diameter of at least 1 mm. Similarly, Tokugawa et al reported that an adequate PAA must have a diameter of >1 mm with a length >70 mm from the superior margin of the zygomatic arch. Although both studies briefly mentioned the association of STA and PAA anatomic variations, a close analysis of STA and PAA variants has not been conducted. Hence, by implementing anterior advancement of the PAA through modification of the classification suggested by Tokugawa et al and combining such variants of PAA with certain STAs, we devised 4 combinations of STA and PAA variants that could be considered potential PAA-EDAS candidates. The PAA diameter was not considered in this study because subjects underwent indirect revascularization via EDAS. In addition, C3 (both hypoplastic frontal and parietal STA branches) was omitted as a viable candidate of PAA-EDAS because none of the cases had STA-PAA combination of C3 + 3a or C3 + 4a. This could be because despite the frontal and parietal branches being considerably narrower than the STA trunk, most parietal branches of C3 were suitable to be used as the donor. Unlike the hypoplasia of C1, in which most blood flows toward the dominant frontal branch, making the parietal branch truly hypoplastic, the hypoplastic parietal branch of C3 seemed to deliver a sufficient amount of blood flow, which is supported by the fact that the dominant PAA was not formed in patients with STA class of C3.

A total of 24 hemispheres from 1144 (2.1%) were considered PAA-EDAS candidates. Only 1 patient of 23 subjects had bilateral STA and PAA variants adequate for consideration as a PAA-EDAS candidate. Given the scarcity of intrapersonal bilateral PAA-EDAS candidacy, the intrapersonal development of STA and PAA variants seems mutually independent of each hemisphere. Of the 24 hemispheres, 10 underwent PAA-EDAS (41.7%). We believe that the

proportion of PAA-EDAS could have been increased if adequate combinations of STA and PAA were located in the ipsilateral hemisphere of the patients with unilateral MMD because 4 cases of unilateral MMD had STA-PAA combination patterns on the normal hemisphere. Additionally, 4 of the 24 hemisphere candidates were treated with EGS instead of PAA-EDAS. According to our data base, the last PAA-EDAS candidate to receive EGS was in 2009, and considering the recent use of PAA for extracranial-intracranial bypass in the literature,⁹⁻¹² the numbers for PAA-EDAS could have been increased had EDAS been performed on the 4 cases that underwent EGS. Hence, although PAA-EDAS candidacy may be rare, the STA and PAA variant combinations we devised seemed to sufficiently reflect the opportunity for PAA use in performing EDAS, giving surgeons more options for appropriate treatment.

The efficacy of PAA-EDAS compared with STA-EDAS has not been studied in the previous literature. Hence, we compared the Matsushima grade of 6 patients having undergone PAA-EDAS with that of the 12 subjects having undergone STA-EDAS matched for the age-sex-orientation follow-up period. In both PAA-EDAS and STA-EDAS groups, 83% of subjects had grade A or B on follow-up transfemoral cerebral angiography. In the PAA-EDAS group, based on the 1-year postoperative records, 6 patients were asymptomatic, 1 patient had a fixed neurologic deficit but was asymptomatic in terms of ischemic symptoms, and 2 patients postoperatively showed subsided intensity and frequency of ischemic symptoms, such as TIA and headaches. Also, no patient having undergone PAA-EDAS showed deterioration on the Karnofsky Performance Scale and mRS. Thus, the postoperative clinical course of PAA-EDAS does not appear inferior to that of STA-EDAS.

There are a few limitations to this study. First, due to the wide spectrum of class 3 PAA variants, some PAAs failed to adequately reach the parietotemporal area to be used as an STA alternative, despite subjects having D1 + 3a and C1 + 3a STA-PAA variants. Hence, we analyzed the proportion of PAA termination points between the helix and vertex for cases that used the subclassification 3a and cases that did not. Review of the data for D1 + 3a and C1 + 3a groups showed that in all cases using subclassification 3a as the donor, the PAA terminated above the 50% mark between the helix and vertex. On the contrary, in cases that used the hypoplastic STA parietal branch as the donor, subclassification 3a terminated below the 50% mark. On the basis of this result, we believe that further subclassification of class 3a based on its adequacy may be helpful in surgical planning.

Second, due to the scarcity of adequate PAAs, the number of subjects having undergone PAA-EDAS and corresponding STA-EDAS subjects was limited. Consequently, the clinical outcome of patients having undergone PAA-EDAS may have been prone to selection bias.

Nevertheless, this study with the largest number of patients enrolled is the first to comprehensively investigate the anatomic variations of both STA and PAA in pediatric patients with MMD. Also, close observation of the relationship between STA and PAA variants has been made to discern the potential candidates for PAA-EDAS. Finally, in comparison of the PAA-EDAS and STA-EDAS clinical outcomes, the prognosis of PAA-EDAS is not inferior to that of STA-EDAS.

CONCLUSIONS

On the basis of the results, with the appropriate combination of STA and PAA variants, we strongly recommend that surgeons consider MCA territory revascularization with the use of the PAA when the STA parietal branch is unfit for use.

REFERENCES

1. Kim SK, Wang KC, Kim IO, et al. **Combined encephaloduroarterio-synangiosis and bifrontal encephalogaleo(periosteal)synangiosis in pediatric Moyamoya disease.** *Neurosurgery* 2002;50:88–96 CrossRef Medline
2. Suzuki J, Kodama N. **Moyamoya disease: a review.** *Stroke* 1983;14:104–09 CrossRef Medline
3. Ueki K, Meyer FB, Mellinger JF. **Moyamoya disease: the disorder and surgical treatment.** *Mayo Clin Proc* 1994;69:749–57 CrossRef Medline
4. Adelson PD, Scott RM. **Pial synangiosis for moyamoya syndrome in children.** *Pediatr Neurosurg* 1995;23:26–33 CrossRef Medline
5. Endo M, Kawano N, Miyaska Y, et al. **Cranial burr hole for revascularization in Moyamoya disease.** *J Neurosurg* 1989;71:180–85 CrossRef Medline
6. Golby AJ, Marks MP, Thompson RC, et al. **Direct and combined revascularization in pediatric moyamoya disease.** *Neurosurgery* 1999;45:50–58; discussion 58–60 CrossRef Medline
7. Ishikawa T, Houkin K, Kamiyama H, et al. **Effects of surgical revascularization on outcome of patients with pediatric Moyamoya disease.** *Stroke* 1997;28:1170–73 CrossRef Medline
8. Veeravagu A, Guzman R, Patil CG, et al. **Moyamoya disease in pediatric patients: outcomes of neurosurgical interventions.** *Neurosurg Focus* 2008;24:E16 CrossRef Medline
9. Horiuchi T, Kusano Y, Asanuma M, et al. **Posterior auricular artery-middle cerebral artery bypass for additional surgery of Moyamoya disease.** *Acta Neurochir (Wien)* 2012;154:455–56 CrossRef Medline
10. Germans MR, Regli L. **Posterior auricular artery as an alternative donor vessel for extracranial-intracranial bypass surgery.** *Acta Neurochir (Wien)* 2014;156:2095–2101; discussion 2101 CrossRef Medline
11. Torazawa S, Hasegawa H, Kin T, et al. **Long-term patency of posterior auricular artery-middle cerebral artery bypass for adult-onset Moyamoya disease: case report and review of literature.** *World Neurosurg* 2017;108:994.e1–e5 CrossRef Medline
12. Tokugawa J, Nakao Y, Kudo K, et al. **Posterior auricular artery-middle cerebral artery bypass: a rare superficial temporal artery variant with well-developed posterior auricular artery-case report.** *Neurol Med Chir (Tokyo)* 2014;54:841–44 CrossRef Medline
13. Marano SR, Fischer DW, Gaines C, et al. **Anatomical study of the superficial temporal artery.** *Neurosurgery* 1985;16:786–90 CrossRef Medline
14. Medved F, Manoli T, Medesan R, et al. **In vivo analysis of the vascular pattern of the superficial temporal artery based on digital subtraction angiography.** *Microsurgery* 2015;35:380–86 CrossRef Medline
15. Tokugawa J, Cho N, Suzuki H, et al. **Novel classification of the posterior auricular artery based on angiographical appearance.** *PLoS One* 2015;10:e0128723 CrossRef Medline
16. Matsushima T, Inoue T, Suzuki S, et al. **Surgical treatment of Moyamoya disease in pediatric patients: comparison between the results of indirect and direct revascularization procedures.** *Neurosurgery* 1992;31:401–05 CrossRef Medline
17. Kinugasa K, Mandai S, Kamata I, et al. **Surgical treatment of Moyamoya disease: operative technique for encephalo-duro-arterio-miosynangiosis, its follow-up, clinical results, and angiograms.** *Neurosurgery* 1993;32:527–31 CrossRef Medline
18. Ha EJ, Kim KH, Wang KC, et al. **Long-term outcomes of indirect bypass for 629 children with Moyamoya disease.** *Stroke* 2019;50:3177–83 CrossRef Medline

19. Chen TH, Chen CH, Shyu JF, et al. **Distribution of the superficial temporal artery in the Chinese adult.** *Plast Reconstr Surg* 1999;104:1276–79 CrossRef Medline
20. Kim BS, Jung YJ, Chang CH, et al. **The anatomy of the superficial temporal artery in adult Koreans using 3-dimensional computed tomographic angiogram: clinical research.** *J Cerebrovasc Endovasc Neurosurg* 2013;15:145–51 CrossRef Medline
21. Moschella F, Cordova A, Pirrello R, et al. **The supra-auricular arterial network: anatomical bases for the use of superior pedicle retro-auricular skin flaps.** *Surg Radiol Anat* 2003;24:343–47 CrossRef Medline
22. Pinar YA, Ikiz ZA, Bilge O. **Arterial anatomy of the auricle: its importance for reconstructive surgery.** *Surg Radiol Anat* 2003;25:175–79 CrossRef Medline

Congenital Nasal Pyriform Aperture Stenosis: Evidence of Premature Fusion of the Midline Palatal Suture

T.M. Wine, J.D. Prager, and D.M. Mirsky

ABSTRACT

BACKGROUND AND PURPOSE: Various etiologies have been theorized for the development of congenital nasal pyriform aperture stenosis (CNPAS). Imaging possibly implicates abnormal fusion of the midline palatal suture and deficient lateral growth of the midface in affected neonates.

MATERIALS AND METHODS: A single-center, retrospective study was performed at a tertiary care pediatric hospital involving neonates and infants between 0 and 90 days of life. Maxillofacial CT scans of patients were reviewed. Abnormality of the palatal suture and midface transverse dimensions were measured and analyzed in patients with and without CNPAS.

RESULTS: A total of 109 patients between 0 and 90 days of life had maxillofacial CT scans. Thirteen patients were classified as having CNPAS, 27 patients had normal scans (control group), and 69 patients were excluded because of the presence of other craniofacial anomalies. All patients with CNPAS had evidence of abnormal fusion of the midline palatal suture. Zero patients without CNPAS had a midline palatal suture abnormality. The mean widths of the pyriform aperture were 5.7 mm (SD, 1.7) in the CNPAS group and 13.1 mm (SD, 2.7) in the control group ($P < .0001$). The mean distance between the superior portions of the nasolacrimal ducts was 9.1 mm (SD, 2.1) in the CNPAS group, and the mean of the control group was 13.4 mm (SD, 2.2) ($P < .0001$).

CONCLUSIONS: Patients with CNPAS have abnormal fusion of the midline palatal suture and exhibit lateral growth restriction of the midface. This may implicate synostosis of the midline palatal suture and abnormal midface growth.

ABBREVIATIONS: CNPAS = congenital nasal pyriform aperture stenosis; NLD = nasolacrimal duct

Infants are obligate nasal breathers. As such, any degree of nasal airway obstruction may result in respiratory distress. Soft tissue edema caused by viral or idiopathic rhinitis is the most common cause of bilateral nasal obstruction in neonates. Less common, though clinically important, causes include choanal atresia and congenital nasal pyriform aperture stenosis (CNPAS).

CNPAS was first described in 1988 and 1989 in the radiology and otolaryngology literature, respectively.^{1,2} Since then, numerous case reports have highlighted 2 possible theories in the embryogenesis, as well as the presentation, diagnosis, and treatment.³⁻⁸ Historically, the 2 theories of embryogenesis are bony overgrowth of the nasal process of the maxilla and a primary

deficiency of the hard palate, with most studies citing the former as the cause. Classically, symptoms include respiratory distress relieved by crying, difficulty feeding, nasal congestion, apnea, and failure to thrive. Physical examination may raise the suspicion for CNPAS when a 5F suction catheter cannot be passed through either nasal cavity; note that choanal atresia could have a similar finding. The diagnosis requires a maxillofacial CT revealing the pyriform aperture width to measure less than 11 mm.^{3,4} Associated imaging abnormalities include a median central incisor, a triangular-shaped palate, and a median palatal ridge. The presence of a median central incisor warrants further evaluation with MR imaging of the brain because it can occur as part of the holoprosencephaly spectrum.⁹ Genetic consultation may be useful to help define the presence of a syndrome. Treatment starts with medical therapy and, if needed, surgical therapy. Classically, surgical therapy involves drilling bone from the lateral extent of the pyriform aperture, though other entities such as dilation and rapid maxillary expansion have also been described.³⁻¹³

As part of the primary author's previous work on CNPAS,¹¹ a unique, never described radiographic feature was noted. The midline palatal suture appeared abnormally ossified and potentially

Received July 1, 2020; accepted after revision December 22.

From the Departments of Otolaryngology (T.M.W., J.D.P.) and Radiology (D.M.M.), University of Colorado School of Medicine, Aurora, Colorado; and Children's Hospital Colorado (T.M.W., J.D.P., D.M.M.), Aurora, Colorado.

Data previously presented at: American Society of Pediatric Otolaryngology Spring Meeting, May 2015; Boston, Massachusetts.

Please address correspondence to Todd M. Wine, MD, 13123 E. 16th Avenue, B455, Children's Hospital Colorado, University of Colorado School of Medicine; e-mail: todd.wine@childrenscolorado.org

<http://dx.doi.org/10.3174/ajnr.A7056>

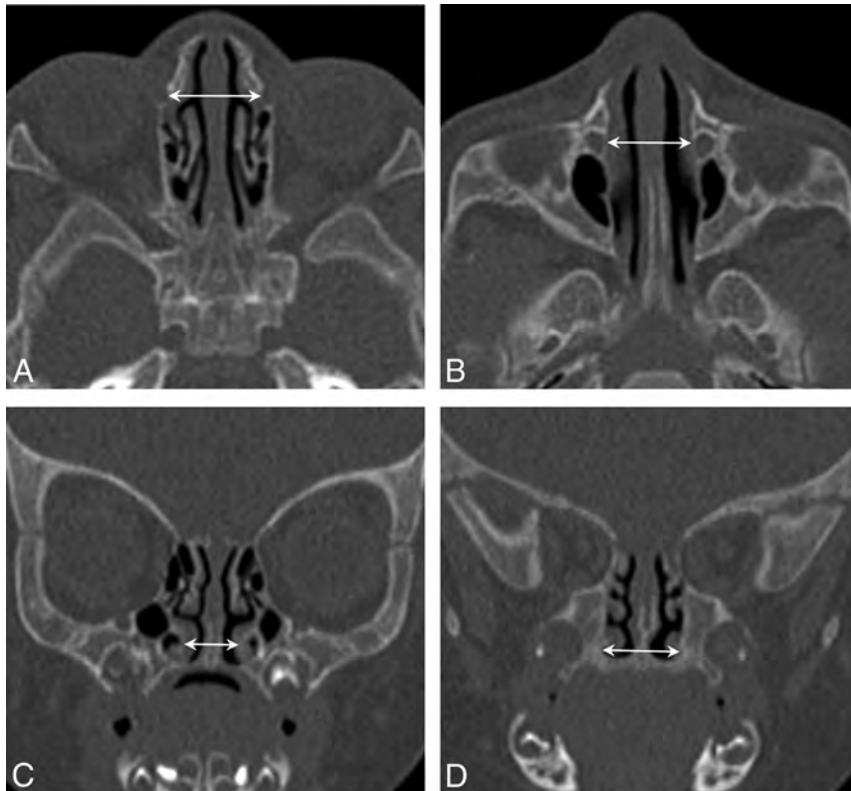


FIG 1. Normal midface measurements (*arrows*) of a control patient. A and B, Axial noncontrast CT images demonstrate normal widths between the superior and inferior aspects of the NLD, respectively. C, Coronal noncontrast CT image illustrates a normal width between the inferior nasal turbinates. D, Coronal noncontrast CT image shows a normal palatal width, which is measured at the level of the first molar.

fused, raising the possibility that CNPAS may be related to lateral growth restriction of the midface akin to craniosynostosis. Other studies have shown that narrowing of the nasal cavity extends posteriorly to include the middle and posterior portions of the nasal cavity, supporting this theory.^{3,14} With this in mind, we hypothesize that patients with CNPAS have abnormal midline palatal sutures and decreased midface dimensions compared with a control population.

MATERIALS AND METHODS

This single-center, retrospective study was approved by the local institutional review board of the University of Colorado and was compliant with the Health Insurance Portability and Accountability Act. Informed consent was waived. Pediatric patients aged 0 to 90 days who underwent maxillofacial CT between January 2003 and December 2013 were identified from our institution's electronic medical record data base. All scans were reviewed by a pediatric neuroradiologist (D.M.M.). Measurements of the width of the pyriform aperture were performed, with CNPAS defined as a pyriform aperture width less than 11 mm adhering to the original description of CT findings.^{3,4} Additionally, the width of the palate using the distance between the first molars, distance between the inferior turbinates, distance between the inferior aspects of the nasolacrimal ducts (NLDs), and distance between the superior aspects of the NLDs were acquired (Fig 1). Last, the midline palatal suture was

evaluated for the presence or absence of ossification of the suture (Fig 2). Patients with additional craniofacial anomalies (eg, cleft lip and palate, Pierre Robin sequence, NLD cyst, and tumors of the head and neck) not associated with CNPAS were excluded. Gestational birth age, age at the time of CT, and other medical comorbidities were recorded. Descriptive statistics in each cohort were reported as median values (interquartile range [IQR]). The Mann-Whitney test was used to compare the 2 cohorts using $P < .05$ as the threshold allowing the null hypothesis to be rejected. The 95% CI between the medians of each cohort was computed using the Hodges-Lehmann estimate. Descriptive and comparative statistics were calculated using GraphPad Prism version 8.0.0 for Windows (GraphPad Software).

RESULTS

A total of 109 patients aged 0–3 months underwent maxillofacial CT imaging at the Children's Hospital Colorado between January 2003 and December 2013. Thirteen patients had CNPAS, 27 had normal scans, and 69 had an additional craniofacial anomaly

and were thus excluded from the study. The median gestational ages at birth were 38.0 (IQR, 35.0–40.0) weeks in the CNPAS and 40.0 (IQR, 38–40) weeks in the control group ($P = .03$). The ages at time of CT scan were 8.0 (IQR, 2.0–35.0) days in the CNPAS group and 15 (IQR, 5.0–47.0) days in the control group ($P = .16$). Fifty-four percent of patients were male.

The CNPAS cohort had a median pyriform aperture width of 6.0 (IQR, 4.8–7.6) mm compared with the control group measurement of 13.3 (IQR, 12.4–14.0) mm ($P < .0001$). The median width of the palate was 8.9 (IQR, 7.8–11.4) mm in the CNPAS group and 17.5 (IQR, 17.1–18.9) mm in the control group ($P < .0001$). The median distance between the inferior turbinates was 3.6 (IQR, 3.2–3.6) mm in the CNPAS group and 8.8 (IQR, 7.9–9.6) mm in the control group ($P < .0001$). The median distance between the inferior NLDs was 8.9 (IQR, 7.5–10.6) mm in the CNPAS group and 15.3 (IQR, 13.1–15.8) mm in the control group ($P < .0001$). The median distance between the superior NLDs was 9.3 (IQR, 7.8–11.3) mm in the CNPAS group and 13.6 (IQR, 12.7–14.5) mm in the control group ($P < .0001$). The difference between the medians and the 95% CI of difference for each measurement is listed in the Table. Thirteen of 13 patients in the CNPAS group had evidence of fusion of the midline palatal suture, of whom 11 had an associated midpalatal ridge (Fig 3). The midpalatal ridge actually appears as bony spinelike protrusion from the palate. Zero of 27 in the control group had a suture abnormality. Four of 13 patients with CNPAS had a median

central incisor. Thirteen of 13 patients in the CNPAS cohort had nasal obstruction.

DISCUSSION

The first clinical account of congenital nasal pyriform aperture stenosis (termed bony inlet stenosis) was in 1988.¹ In this initial description, the authors proposed 2 theories of embryogenesis. The first was that excess ossification of the nasal process of the maxilla results in bony overgrowth and narrowing of the

pyriform aperture. This theory is echoed throughout the literature.¹⁻¹³ The second was that insufficient growth of the palate reduces the width of the pyriform aperture.

Many studies have demonstrated decreased width of the nasal cavity and palate in CNPAS. In our study, we also demonstrated that the midface was reduced in width by measuring the distance between the superior and inferior aspects of the NLDs. These findings provide evidence that CNPAS has deficient lateral growth of the midface to go along with the decreased width of the palate and the nasal cavity. With respect to the other developmental theory of CNPAS, excess ossification of the nasal process of the maxilla does not readily account for the reduced midface width between the inferior and superior aspects of the NLDs seen in our data.

Understanding the maturation process of the midline palatal suture has been clinically integral to understanding outcomes regarding rapid maxillary expansion.¹⁴ Although it is accepted that the midline palatal suture is open at birth, maturation and fusion start to happen in late adolescence.¹⁵ Knowing this, ossification of the midline palatal suture, seen in all 13 of our patients with CNPAS, is certainly intriguing. As a bony suture ossifies and closes, growth perpendicular to the long axis of the suture slows. If this occurs at the developmentally correct time, this occurs as the body is no longer growing. If this happens prematurely, as in the case of craniosynostosis, fusion of the cranial suture leads to growth restriction perpendicular to the suture. The features of CNPAS are similar. If the midline palatal suture matures prematurely, this could account for both the decreased horizontal palate growth and decreased midface growth, ultimately resulting in a restricted nasal cavity width consistent with CNPAS. Furthermore, this would explain the midline palatal ridge seen in most of our patients, similar to the type of ridging present in premature closure of the cranial sutures.

If growth restriction of the palate and midpalatal suture ossification occur in CNPAS, is overgrowth of the nasal maxillary process a cause of CNPAS as well? This study was not designed to discuss the presence of overgrowth of the nasal process of the maxilla in our CNPAS cohort. Thus, we are limited in our ability to compare the validity of 2 competing theories of CNPAS embryogenesis. It is possible that these 2 entities occur simultaneously as part of a developmental field defect as has been previously described,^{9,14} or it is possible that the relationship between them may be more akin to a sequence in which growth restriction causes an apparent overgrowth of the nasal maxillary process.

Another limitation of this study is that it is a single-center, retro-

spective review with a small cohort of patients. The study is further limited in that it was not intended to analyze clinical outcomes associated with these radiographic findings because the clinical outcomes of CNPAS are well described.

The importance of this study is that it highlights abnormal ossification of the midline palatal suture and decreased midfacial dimensions in CNPAS. This can clarify the etiology and can lead to

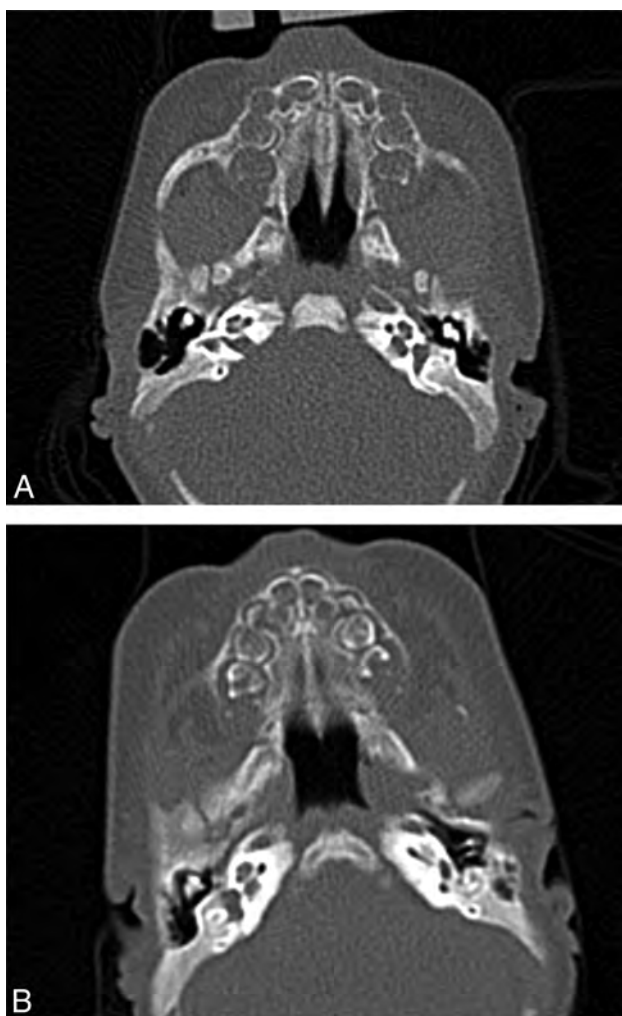


FIG 2. Midpalatal suture in control versus CNPAS. *A*, A normal midline palatal suture with no evidence of fusion. *B*, The midline palatal suture with midline ossification at the site of the suture.

The difference in the median values of measured widths in CNPAS and control participants

Location of Measurement	Difference in Median Width (mm)	Percentage Change from Normal	95% CI of Difference (mm)
Palate	8.6	-49.1	6.7-9.9
Pyriform aperture	7.4	-55.6	6.0-8.1
Between inferior turbinates	5.1	-58.0	4.3-5.8
Between NLD inferior	7	-45.8	4.3-7.4
Between NLD superior	4.4	-32.4	2.8-5.3

Note:—95% CI calculated using the Hodges-Lehmann estimate.



FIG 3. Normal and abnormal pyriform apertures and palates. A, Axial noncontrast CT image of a control patient where the *arrow* demonstrates normal pyriform aperture width. B, Coronal noncontrast CT image with *arrowhead* depicting absence of spinelike protrusion along the undersurface of the palate in the same control patient. C, Axial noncontrast CT image of a patient with CNPAS where the *arrow* depicts the abnormal narrowing of the pyriform aperture. D, Coronal noncontrast CT image with *arrowhead* depicting a spinelike protrusion along the undersurface of the reduced width palate in the same patient with CNPAS.

further study involving the origin and treatment of CNPAS. Although we are unable to prove causality, it is quite plausible that CNPAS is secondary to premature ossification of the midline palatal suture, which we term “palatal synostosis.” If CNPAS is the result of palatal synostosis, like craniosynostosis, early surgical intervention to the prematurely fused suture could provide consideration for new therapeutic options.

CONCLUSIONS

Congenital nasal pyriform aperture stenosis has reduction of midface growth. Premature ossification of the midline palatal suture, palatal synostosis, may be central to the development of CNPAS. Further experience following these patients may allow more understanding into the long-term growth characteristics of the midface in patients with CNPAS.

Disclosures: Jeremy Prager—UNRELATED: Board Membership: EvoEndo Inc, Comments: Board member, medical device company focused on endoscopy*; Patents (Planned, Pending or Issued): EvoEndo Inc, Comments: Several patents issued*; Stock/Stock Options: EvoEndo Inc.*, Comments: Founders stock. *Money paid to the individual author.

REFERENCES

1. Ey EH, Han BK, Towbin RB, et al. **Bony inlet stenosis as a cause of nasal airway obstruction.** *Radiology* 1988; 168:477–79 CrossRef Medline
2. Brown OE, Myer CM, III, Manning SC. **Congenital nasal pyriform aperture stenosis.** *Laryngoscope* 1989;99: 86–91 CrossRef Medline
3. Belden CJ, Mancuso AA, Schmalfuss IM. **CT features of congenital nasal pyriform aperture stenosis: initial experience.** *Radiology* 1999;213:495–501 CrossRef Medline
4. Lee J-C, Yang C-C, Lee K-S, et al. **The measurement of congenital nasal pyriform aperture stenosis in infant.** *Int J Pediatr Otorhinolaryngol* 2006;70: 1263–67 CrossRef Medline
5. De Mot P, Hermans R, Jorissen M, et al. **Congenital nasal pyriform aperture stenosis or bony inlet stenosis: a report of three cases.** *Am J Rhinol* 2004;18:179–82 CrossRef Medline
6. Lee KS, Yang CC, Huang JK, et al. **Congenital pyriform aperture stenosis: surgery and evaluation with three-dimensional computed tomography.** *Laryngoscope* 2002;112:918–21 CrossRef Medline
7. Devambe M, Delattre A, Fayoux P. **Congenital nasal pyriform aperture stenosis: diagnosis and management.** *Cleft Palate Craniofac J* 2009;46:262–67 CrossRef Medline
8. Visvanathan V, Wynne DM. **Congenital nasal pyriform aperture stenosis: a report of 10 cases and literature review.** *Int J Pediatr Otorhinolaryngol* 2012;76:28–30 CrossRef Medline
9. Arlis H, Ward RF. **Congenital nasal pyriform aperture stenosis: isolated abnormality vs developmental field defect.** *Arch Otolaryngol Head Neck Surg* 1992;118:989–91 CrossRef Medline
10. Losken A, Burstein FD, Williams JK. **Congenital nasal pyriform aperture stenosis: diagnosis and treatment.** *Plast Reconstr Surg* 2002;109:1506–11; discussion 1512 CrossRef Medline
11. Wine TM, Dedhia K, Chi DH. **Congenital nasal pyriform aperture stenosis: is there a role for nasal dilation?** *JAMA Otolaryngol Head Neck Surg* 2014;140:352–56 CrossRef Medline
12. Gonik NJ, Cheng J, Lesser M, et al. **Patient selection in congenital pyriform aperture stenosis repair—14 year experience and systematic review of literature.** *Int J Pediatr Otorhinolaryngol* 2015;79:235–39 CrossRef Medline
13. Collares MVM, Tovo AHS, Duarte DW, et al. **Novel treatment of neonates with congenital nasal pyriform aperture stenosis.** *Laryngoscope* 2015;125:2816–19 CrossRef Medline
14. Reeves TD, Discolo CM, White DR. **Nasal cavity dimensions in congenital pyriform aperture stenosis.** *Int J Pediatr Otorhinolaryngol* 2013;77:1830–32 CrossRef Medline
15. Angelieri F, Cevidanes LHS, Goncalves JR, et al. **Midpalatal suture maturation for individual assessment before repaid maxillary expansion.** *Am J Orthod Dentofacial Orthop* 2013;144:759–69 CrossRef Medline

Neuroimaging Features of Ectopic Cerebellar Tissue: A Case Series Study of a Rare Entity

G. Orman, S.F. Kralik, R. Battini, B. Buchignani, N.K. Desai, R. Goetti, A. Meoded, C. Mitter, B. Wallacher-Scholz, E. Boltshauser, and T.A.G.M. Huisman



ABSTRACT

SUMMARY: Ectopic cerebellar tissue is a rare entity likely secondary to multiple, interacting, developmental errors during embryogenesis. Multiple sites of ectopic cerebellar tissue have been reported, including extracranial locations; however, an intracranial location is most common. We report on the MR imaging findings of a multi-institutional series of 7 ectopic cerebellar tissue cases (2 males, 4 females, 1 fetal) ranging from 22 weeks 5 days' gestational age to 18 years of age. All cases of ectopic cerebellar tissue were diagnosed incidentally, while imaging was performed for other causes. Ectopic cerebellar tissue was infratentorial in 6/7 patients and supratentorial in 1/7 patients. All infratentorial ectopic cerebellar tissue was connected with the brain stem or cerebellum. MR imaging signal intensity was identical to the cerebellar gray and white matter signal intensity on all MR imaging sequences in all cases. Ectopic cerebellar tissue should be considered in the differential diagnoses of extra-axial masses with signal characteristics similar to those of the cerebellum. Surgical biopsy or resection is rarely necessary, and in most cases, MR imaging is diagnostic.

ABBREVIATION: ECT = ectopic cerebellar tissue

The term “ectopia” refers to an abnormal congenital or acquired position of an organ or tissue. Ectopic cerebellar tissue (ECT) is an extremely rare condition. Only individual case reports of ECT have been reported to date.¹⁻²⁰

ECT can be composed of mature or immature cerebellar tissue.¹² The exact mechanism of ECT development is unknown, but it is believed to be the result of an anomalous cell migration during embryogenesis.^{14,16} Five major mechanisms have been proposed to explain the development of ECT: 1) herniation of fetal brain tissue during embryogenesis, 2) embryonic neural rests, 3) preferential differentiation of 1 germ layer of a teratoma along neural lines, 4) true astrocytomas, and 5) similar to split spinal

cord malformation pathogenesis, differentiation of pluripotent cells leading to the formation of a structure resembling the cerebellum.^{9,10,12,21}

The goal of this article was to report a multi-institutional series of ECT cases, to discuss the common and unique imaging features of each case, and to review the existing cases in the literature. To the best of our knowledge, this is the first series of ECT cases.

Case Series

We collected cases with a diagnosis of ECT from 5 institutions for this retrospective, multicenter, international case series study. Informed consent was waived due to the retrospective nature of the study. Patient information including demographics, history, and MR imaging studies was collected. MR imaging studies were re-evaluated at Texas Children's Hospital by 2 pediatric neuroradiologists (S.F.K. and T.A.G.M.H., with 9 and 29 years of experience, respectively). Seven patients (2 males, 4 females, 1 fetal case) ranging from 22 weeks 5 days' gestational age to 18 years of age were included in this study.

Patient 1 is a 17-year-old adolescent girl with a history of gross total resection of a congenital nasopharyngeal mature teratoma after developing dyspnea after birth. In addition, a subtotal resection of a suprasellar mass lesion was performed, which was proved to be ECT without any attachment to the brain stem or cerebellum. Furthermore, an additional interhemispheric arachnoid cyst was

Received November 10, 2020; accepted after revision January 5, 2021.

From the Edward B. Singleton Department of Radiology (G.O., S.F.K., N.K.D., A.M., T.A.G.M.H.), Texas Children's Hospital, Houston, Texas; Department of Developmental Neuroscience (R.B.), Istituto di Ricovero e Cura a Carattere Scientifico Fondazione Stella Maris, Pisa, Italy; Department of Clinical and Experimental Medicine (R.B., B.B.), University of Pisa, Pisa, Italy; Department of Medical Imaging (R.G.), The Children's Hospital at Westmead, The University of Sydney, Sydney, Australia; Department of Biomedical Imaging and Image-Guided Therapy (C.M.), Medical University of Vienna, Vienna, Austria; Department of Pediatric Neurology and Developmental Medicine and LMU Center for Children with Medical Complexity (B.W.-S.), Dr. von Hauner Children's Hospital, LMU University Hospital, Ludwig-Maximilians-Universität, Munich, Germany; and Department of Pediatric Neurology (E.B.), University Children's Hospital Zürich, Zurich, Switzerland.

Please address correspondence to Gunes Orman, MD, Texas Children's Hospital, Edward B. Singleton Department of Radiology, 6701 Fannin St, Suite 470, Houston, TX 77030; e-mail: gorman@texaschildrens.org

Indicates article with online supplemental data.

<http://dx.doi.org/10.3174/ajnr.A7105>

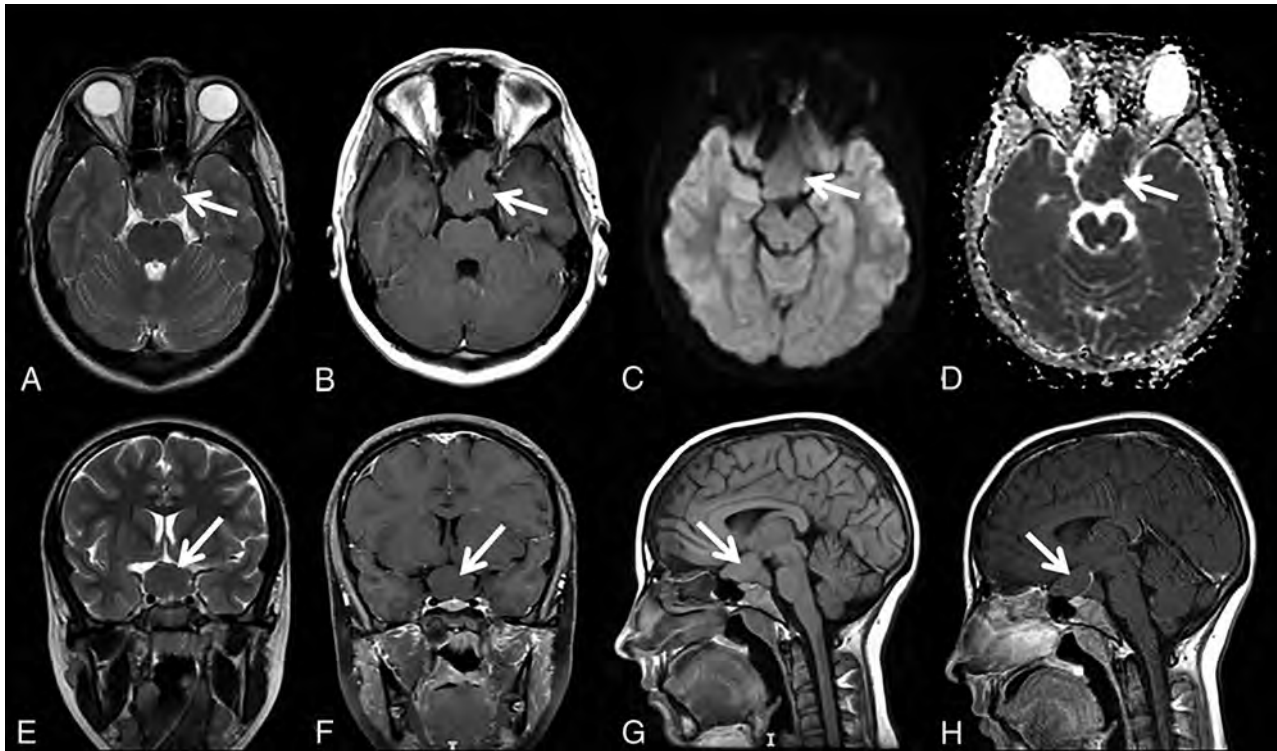


FIG 1. Axial T2- (A) and T1- (B) weighted, DWI (C), ADC (D), coronal T2-weighted (E), contrast-enhanced coronal T1-weighted (F), and sagittal pre- and postcontrast enhanced T1-weighted (G and H) MR images and map of patient 1 at 17 years of age show well-defined, ectopic, cerebellar tissue (A–H, arrows) in the suprasellar region. Note that the signal intensity is similar to that of the cerebellum in all sequences, and there is no contrast enhancement on postcontrast imaging.

resected when she was 4 months of age.^{11,12} The recovery after the operation was complicated by moderate atrophy of the right optic nerve, which was treated with temporary eye patch coverage of the healthy left eye. She underwent an additional operation for correction of her eyesight at 12 years of age. Her growth parameters were within normal limits during her follow-up visits; however, her language skills were a bit delayed, yet within the normal variation. MR imaging (Fig 1) performed at 17 years of age showed the stable, residual, suprasellar ECT.

Patient 2 is a 25-month-old boy who was born preterm at 33 weeks via cesarean delivery secondary to maternal preeclampsia. The mother also had gestational diabetes mellitus. There were no complications during pregnancy or delivery. The patient had a benign hospital course and spent 4 weeks in the neonatal intensive care unit before being discharged. Parents first noticed problems at discharge, when they noted a profound hearing loss of the left ear. A CT scan showed an incomplete partition type I anomaly of the left inner ear. At 6 months of age, he was seen by an ophthalmologist due to concern for possible crossed eyes and was diagnosed with pseudostrabismus. He was also diagnosed with bilateral optic nerve hypoplasia, with the left side being more affected than the right side. He was then referred to an endocrinologist to rule out pituitary dysfunction, given the concern for septo-optic dysplasia, but the results of hormone and stimulation testing were normal. A brain MR imaging did not show any evidence of septo-optic dysplasia (Fig 2); however, ECT was noted superior to the vermis to the left of the midline, which was connected to the adjacent brain stem via a thin stalk. The patient has

not experienced any major illnesses. Developmentally, his motor milestones are on track, and he has never required any therapy.

Patient 3 is an 18-year-old young woman with a history of global developmental delay with intellectual disability, right sensorineural hearing loss, and simple febrile seizures. The patient developed an increasing frequency of episodes with eyes rolling back and behavioral arrest at 13 years of age. There were no preceding symptoms of the patient and mother. The episodes occurred while walking, talking, or sitting. She had no associated shaking, loss of bowel or bladder control, or facial twitching. Further work-up with MR imaging, electroencephalography, and metabolic lab tests was performed to rule out the possibility of seizures and to further investigate the etiology for her intellectual disability/developmental delay. The findings of electroencephalography were abnormal, consistent with a diagnosis of a primary generalized epilepsy. Metabolic lab test results were within normal limits. MR imaging at 13 years of age showed ECT as a well-defined right cerebellopontine angle lesion, which was stable on annual follow-up MR imaging (Fig 3).

Patient 4 is a 32-month-old girl who was born at term in good condition and with all growth parameters between the 25th and 50th percentiles. She showed a delay in reaching her motor and language skills. At 32 months of age, she presented with microcephaly (45.5 cm, below the second percentile), minor facial dysmorphic features, and mild postural ataxia. MR imaging revealed a ECT along the superior/lateral contour of the right cerebellar hemisphere (Fig 4). During follow-up, the patient developed a complex neuromotor disease with dyskinetic movement disorder, ataxia,

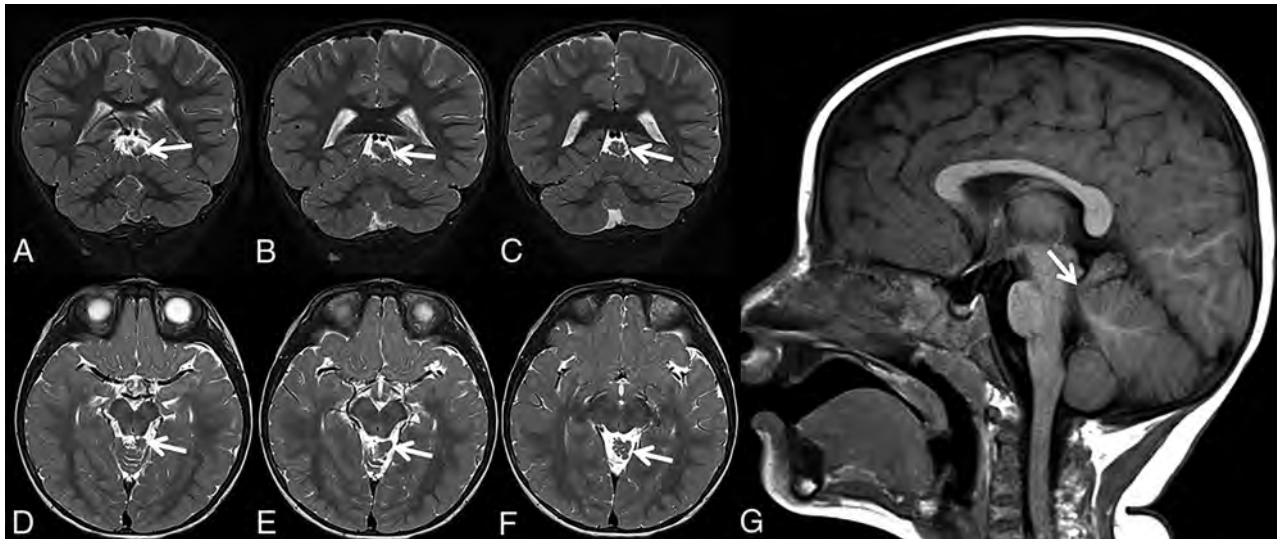


FIG 2. Coronal (A–C) and axial (D–F) T2-weighted and sagittal T1-weighted (G) MR images of patient 2 at 25 months of age show triangular-shaped ectopic cerebellar tissue on consecutive slices (A–F, arrows). Note the thin stalk connecting the ectopic cerebellar tissue with the brain stem (G, arrow).

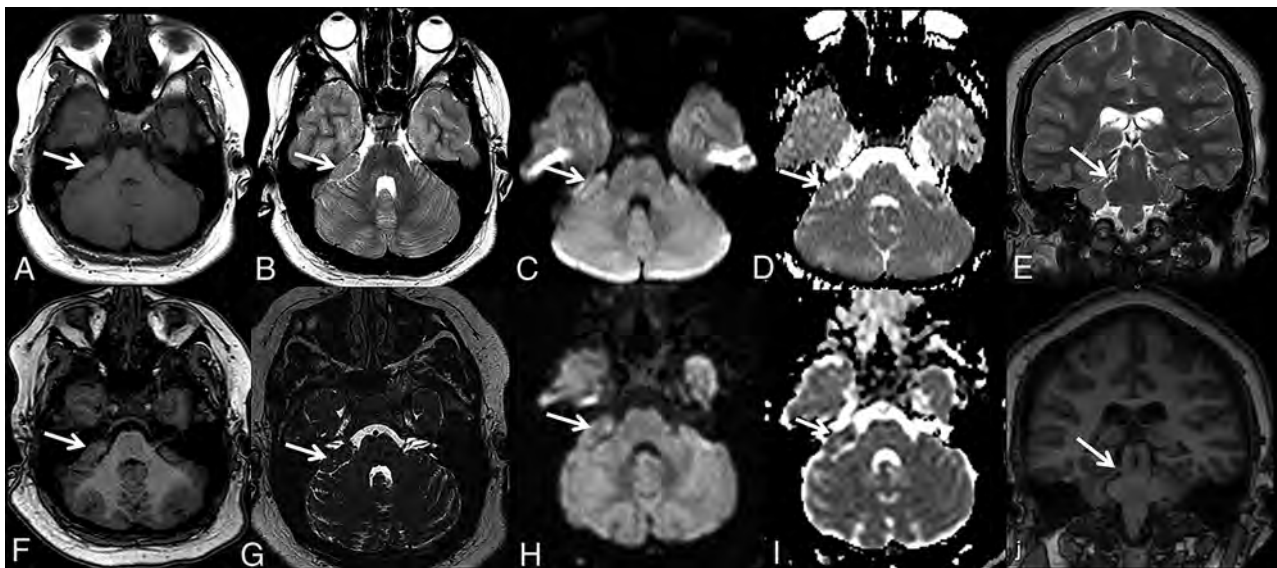


FIG 3. Axial T1- (A and F) and T2- (B and G) weighted, axial DWI (C and H), ADC (D and I), and coronal T2- (E) and T1- (J) weighted MR images and maps of patient 3 at 13 years of age (upper row, arrows) and 18 years of age (lower row, arrows). The patient had a history of global developmental delay with intellectual disability, right sensorineural hearing loss, and simple febrile seizures. MR imaging shows well-defined ectopic cerebellar tissue in the right cerebellopontine angle (A–D, arrows), which was stable on follow-up MR imaging (E–H, arrows). Note the thin stalk connecting the ectopic cerebellar tissue with the middle cerebellar peduncle (E and J, arrows).

pyramidal signs in the lower limbs, a language disorder, and mild cognitive impairment; mild asymmetry was observed with the left side being more involved than the right. Findings of the follow-up MR imaging scans were stable when the girl was 4 and 6 (Fig 5) years of age. Other specific examinations performed included an electroencephalogram, which revealed, at 6 years of age, spike temporal waves while falling asleep and spike waves in the fronto-centro-temporal areas and vertex during sleep.

Patient 5 is a 4-year-old girl who was referred for postnatal assessment of antenatally detected ventriculomegaly, which appeared stable on postnatal follow-up sonography. She was

developing normally, reaching all developmental milestones. Her head circumference was following a normal growth curve, and her extraocular movements were normal. MR imaging acquired at 3 years of age showed a thin stalk arising from the midbrain, which extended to a triangular-shaped ECT superior to the right anterior cerebellar hemisphere, with an arachnoid cyst posteriorly (Fig 6). The findings were unchanged on follow-up MR imaging 1 year later.

Patient 6 is a 5-year-old boy who was born preterm at 34 weeks with moderate respiratory problems necessitating ventilatory support during the first few days of life. Otherwise, he had

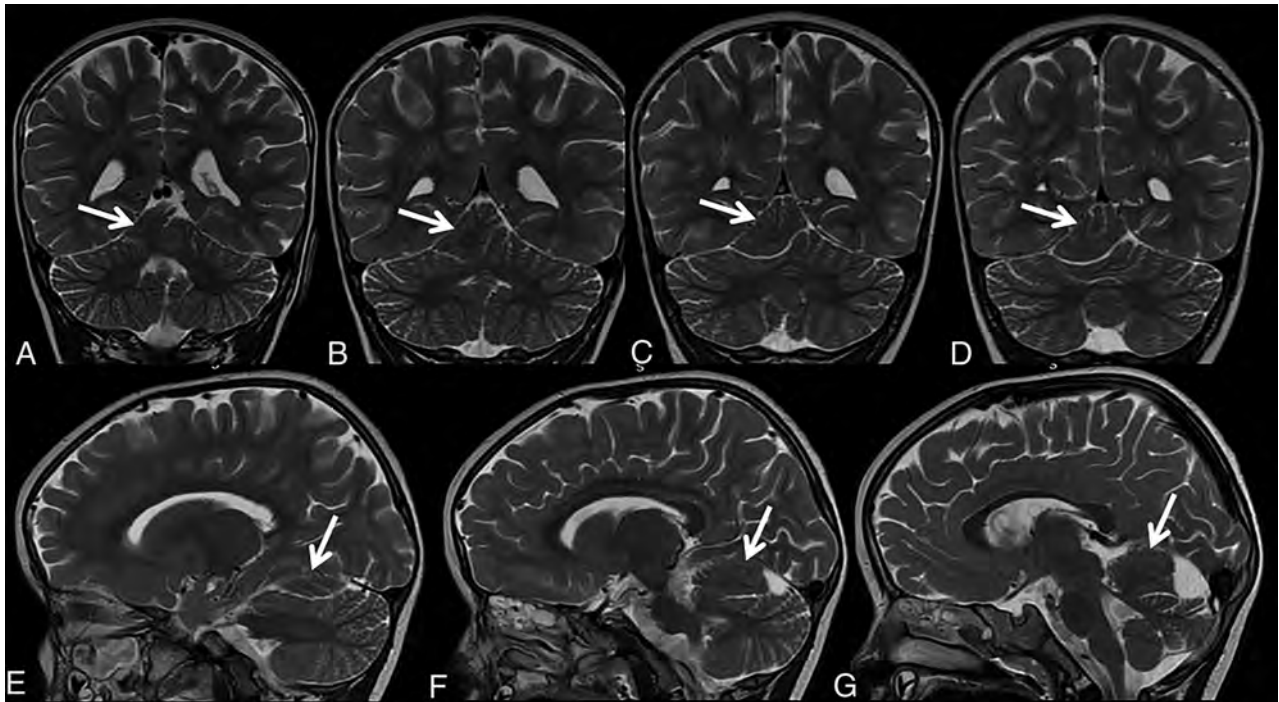


FIG 4. Coronal (A–D) and sagittal T2-weighted (E–G) MR imaging of patient 4 at 32 months of age shows a distorted/dysmorphic superior portion of the right cerebellar hemisphere, which also shows folial and sulcal anomalies. The dysmorphic superior portion also displaces the adjacent vermis. Ectopic cerebellar tissue (A–G, arrows) is connected to the cerebellum. Its MR signal is isointense with the cerebellum, and its morphology is elongated with irregular borders. Additional brain malformations included temporal lobe dysgyria and malrotated hippocampi (not shown).

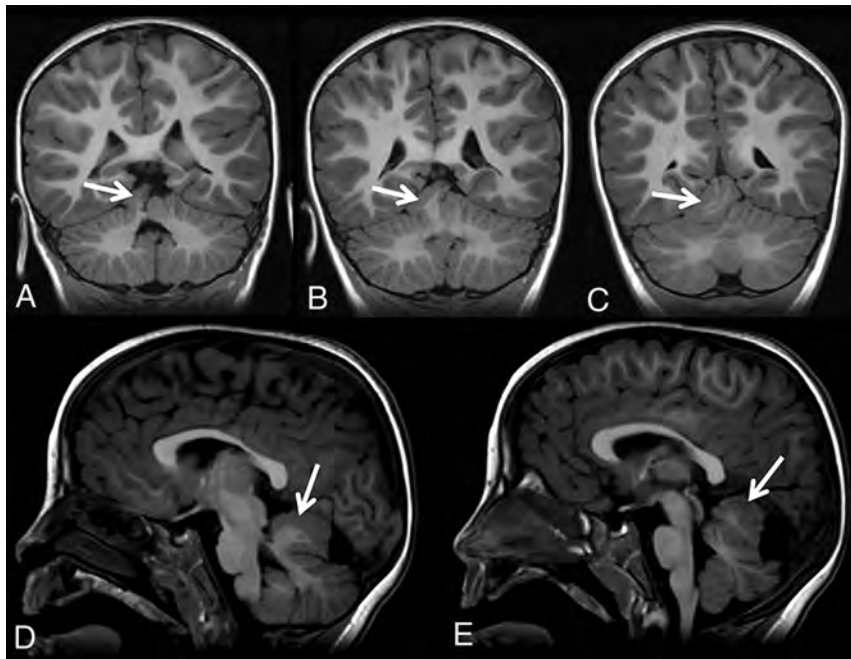


FIG 5. Follow-up coronal and sagittal T1-weighted MR imaging of patient 4 at 6 years of age shows a stable imaging pattern of the ECT (arrows) with respect to the already-described findings in Fig 4.

an uncomplicated early neonatal period and uncomplicated feeding; he was thriving with no signs of infection. Neurologic examination showed a slanting posture of his head (turning

left/slanting right), which was more prominent from 1.5 to approximately 3 years of age. Since then, neurologic examination findings were regressive in frequency and intensity; association with strabismus was suspected, presently hardly seen, as well as congenital alternate strabismus divergens and a slight ptosis of the left eye. The patient showed delayed motor, language, and cognitive development. MR imaging performed at 17 months of age revealed ECT connected to the brain stem by a thin stalk (Fig 7).

Patient 7 was a fetus of 22 weeks 5 days' gestational age after termination of pregnancy due to prenatal diagnosis of vertebral defects, anal atresia, cardiac defects, tracheo-esophageal fistula, renal anomalies, and limb abnormalities (VACTERL) association. Macroscopic examination of the brain and postmortem 3T fetal MR imaging showed an incidental finding of a small appendage with a ribbed surface located superior to the left cerebellar hemisphere and originating from the left dorsal pontomesencephalic junction (Fig 8). Histologic analysis revealed this structure to be of cerebellar origin with distinguishable

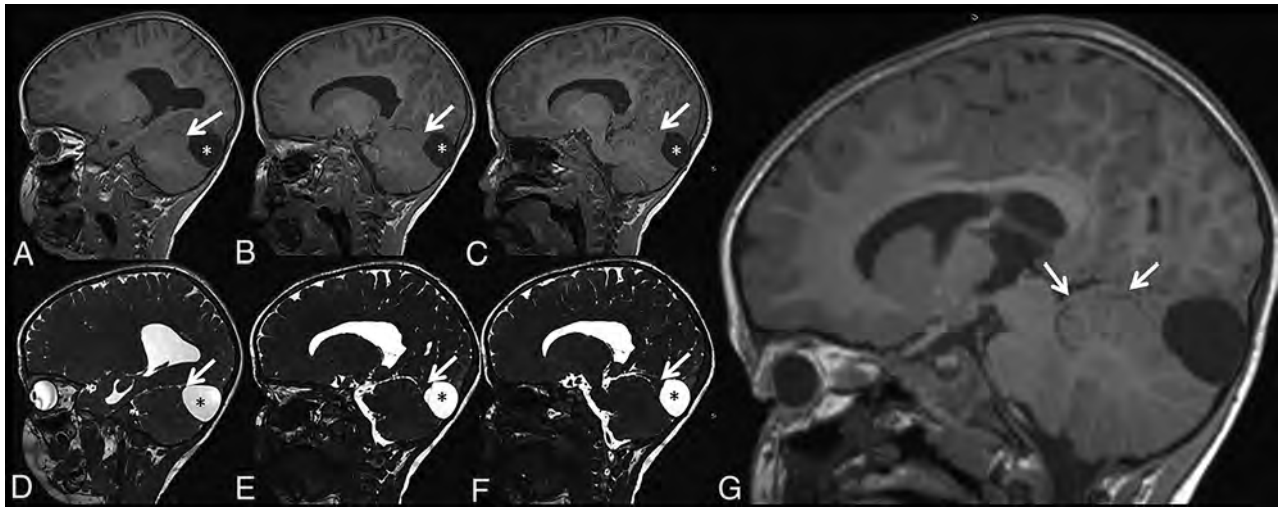


FIG 6. Sagittal T1- (upper row) and T2-weighted (lower row) MR images of patient 5 at 3 years of age show a thin stalk arising from the pontomesencephalic junction below the right inferior colliculus dorsolaterally, which extends to triangular-shaped ectopic cerebellar tissue (A–F, arrows) superior to the right anterior cerebellar lobe, with an arachnoid cyst (A–F, asterisks) posteriorly. The sagittal oblique reformat T1-weighted MR imaging shows the continuous stalk (G, arrows) between the triangular-shaped ECT and the brain stem. The findings were unchanged 1 year later (not shown).

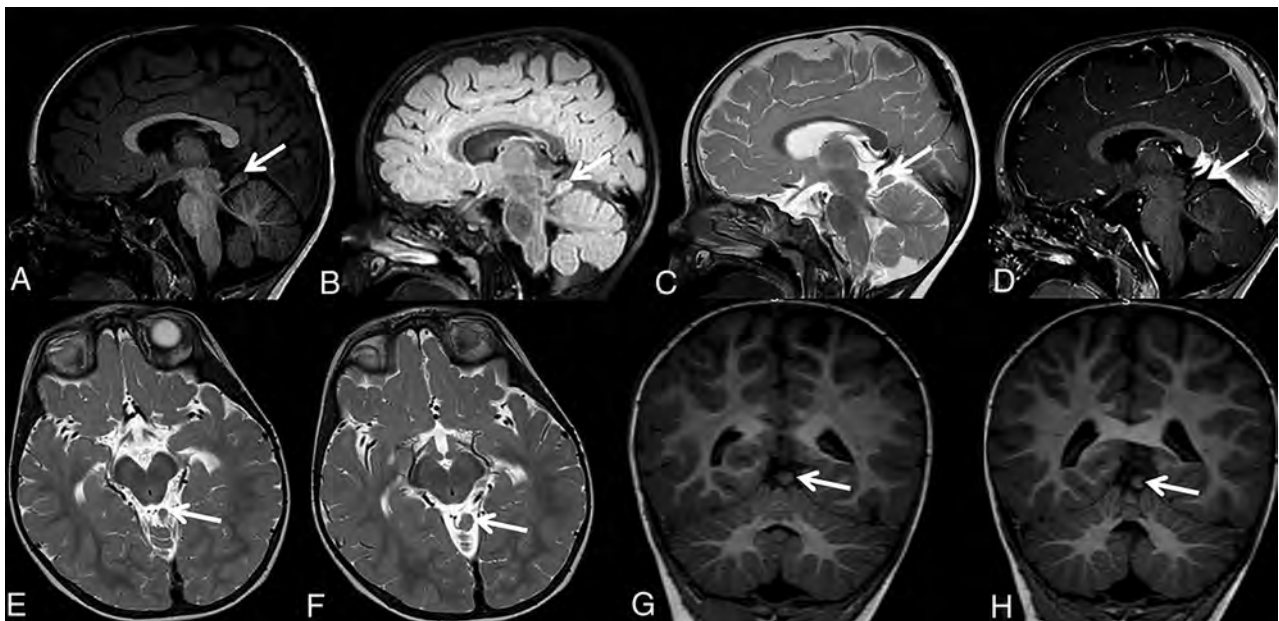


FIG 7. Sagittal T1-weighted (A), sagittal FLAIR (B), sagittal T2-weighted (C), sagittal contrast-enhanced T1-weighted (D), axial T2-weighted (E and F), and coronal T1-weighted (G and H) MR images of patient 6 at 17 months of age show ECT connected with the brain stem by a thin stalk (A–H, arrows). Most interesting, the MR imaging appearance of ectopic cerebellar tissue in this patient is almost identical to the MR imaging findings of patient 2.

external granular and molecular layers and developing Purkinje cells and an internal granular layer.

All cases of ECT were diagnosed incidentally when imaging was performed for other causes or by symptoms that were directly attributable to brain stem or cerebellar dysfunction. The Online Supplemental Data summarize the neuroimaging findings of the patients. ECT was infratentorial in 6/7 patients and supratentorial in 1/7 patients. All infratentorial ECTs were connected with the brain stem or cerebellum. ECT volume compared with the

cerebellar volume was 20%–30% in 1/7 patients, 10%–20% in 2/7 patients, and 1%–10% in 4/7 patients. MR imaging signal intensity was identical to that of the cerebellar gray and white matter on all MR images. In addition, none of the patients had a concomitant brain stem or spinal/craniocervical junction malformation.

DISCUSSION

We report 7 cases of ECT. All cases of ECT (7/7) were diagnosed incidentally, when imaging was performed for other causes. Most

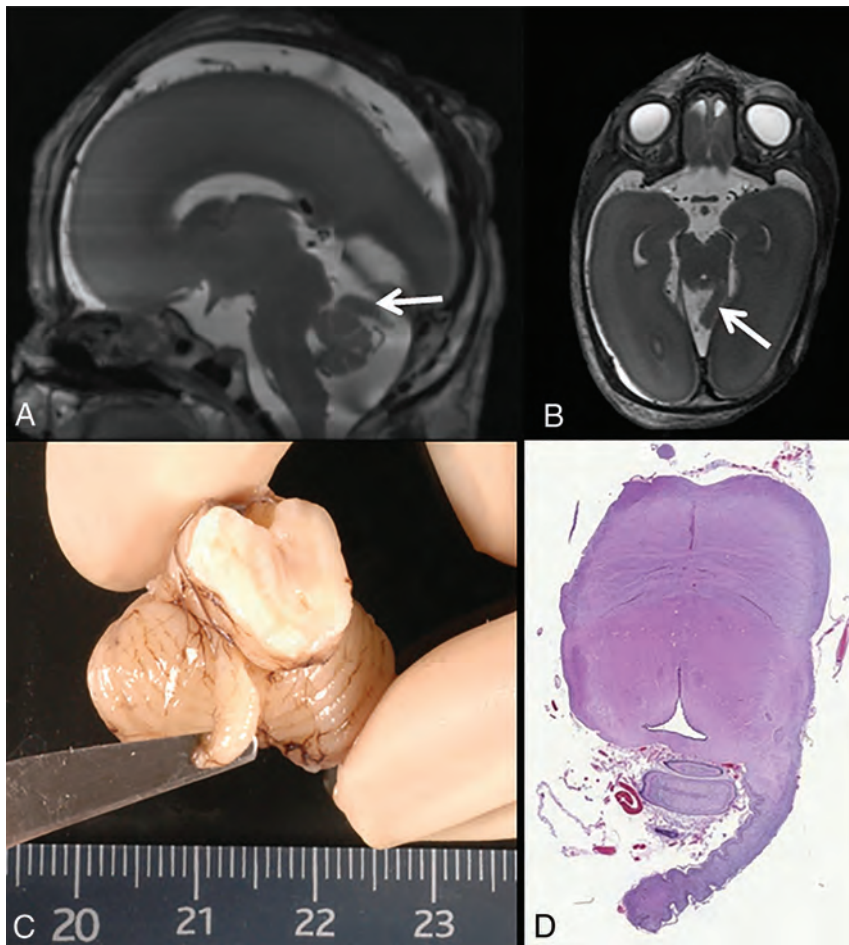


FIG 8. Postmortem sagittal (A) and axial (B) T2-weighted fetal MR images at the gestational age of 22 weeks 5 days and a matching macroscopic postmortem image (C) of the brain show an incidental finding (A and B, arrows) of a small appendage with a ribbed surface located superior to the left cerebellar hemisphere, originating from the left dorsal pontomesencephalic junction. Histologic analysis (D) reveals that this structure is of cerebellar origin with distinguishable external granular and molecular layers and developing Purkinje cells and an internal granular layer. Adapted with permission.²³

cases were located infratentorially (6/7) and had a normal cerebellar morphology (6/7). In 1 patient (patient 1), the ECT was located supratentorially, and 1 patient (patient 4) showed an abnormal cerebellar morphology (Online Supplemental Data). Similar to our results, all previous cases (20/20) were diagnosed incidentally when imaging was performed for other causes, and most reported cases (10/15) in the literature had a normal cerebellar morphology (Online Supplemental Data).

ECT was located intracranially in all our cases. However, we found previous case reports identifying ECT in the ovaries, orbits, spinal cord, or occipital bone (Online Supplemental Data).^{2,4,5,7-10,17,20} On the basis of the wide spectrum of clinical, imaging, and histopathologic findings in the previously reported ECT cases, multiple mechanisms are likely involved in the development of ECT.^{12,13}

The exact mechanism of ECT development remains currently unknown. However, 5 major mechanisms proposed in previous reports include the following: 1) herniation of fetal brain tissue

during embryogenesis, 2) embryonic neural rests, 3) preferential differentiation of 1 germ layer of a teratoma along neural lines, 4) true astrocytomas, and 5) similar to split spinal cord malformation pathogenesis, differentiation of pluripotent cells leading to the formation of a structure resembling the cerebellum.^{9,10,12,21} From a histopathologic point of view, true ECTs should be distinguished from the more frequent focal cerebellar cortical dysplasias.¹² Focal cerebellar cortical dysplasias are more prevalent and usually small and, in most cases, consist of a single cell type or poorly organized mixed-cell clusters.¹² True ECTs are usually larger lesions composed of organized mature or maturing cerebellar tissue.¹²

The isthmic organizer is located below the mesencephalon at the pontomesencephalic junction and provides structural polarity of adjacent regions and organizes mesencephalic and cerebellar development. The isthmic organizer signaling is essential for cerebellar development.²² We observed 3 different types of ECTs in our case series: 1) suprasellar ECT (patient 1), 2) ECT sitting on a small stalk connected with the adjacent brain stem (patients 2, 5, 6, and 7), and 3) ECT sitting on a cerebellar hemisphere (patients 3 and 4). In the second group (patients 2, 5, 6, and 7), the stalk and ECT were all located in the region of the isthmic organizer. An alteration of isthmic organizer signaling during embryogenesis may possibly explain the pathogenesis of these cases.

possibly explain the pathogenesis of these cases.

Two of our patients had associated arachnoid cysts (Online Supplemental Data). Patient 1 had an interhemispheric arachnoid cyst, which was removed surgically during the neonatal period, and patient 5 had an arachnoid cyst adjacent to the ECT. The association of arachnoid cysts and a CSF collection adjacent to ECT may indicate the importance of meningeal stimulus/interaction during cerebellar development.¹⁶ During formation of the normal cerebellum, the germinal tissue possibly migrates through the ependymal cell lines into the CSF. Therefore, obstruction of normal flow of the CSF may result in ECT, with inflammation of the arachnoid membrane and an arachnoid cyst.

Differentiating ECT from low-grade tumors by neuroimaging is necessary to avoid unnecessary surgery, especially in cases centered at the vulnerable cerebellopontine angle (patient 3). Distinguishing MR imaging features include a lack of contrast enhancement of the lesion, signal characteristics similar to those of the adjacent cerebellum on all MR imaging sequences, diffusion characteristics similar

to those of the normal cerebellum, a sulcation pattern mimicking the normal cerebellum, a thin parenchymal stalk that connects the ECT to the adjacent cerebellum or brain stem, and a stable appearance on follow-up imaging without any sign of abnormal, noncommensurate growth.¹⁸

In conclusion, ECT is a rare entity, which is attributed to possible multiple, interacting, developmental errors during embryogenesis. Multiple locations were reported; however, the intracranial and infratentorial locations appear most common. ECT should be considered in the differential diagnoses of extra-axial masses with signal characteristics similar to those of the cerebellum. Surgical biopsy or resection is rarely necessary; in most cases, MR imaging is diagnostic.

Disclosures: Roberta Battini—UNRELATED: Board Membership: Teva Pharmaceutical Industries for trial ongoing on dyskinetic cerebral palsy, Ionis Pharmaceuticals for new genetic treatment on Angelman syndrome.

REFERENCES

1. Billings KJ, Danziger FS. **Cerebellar heterotopia: case report.** *J Neurosurg* 1973;38:218–20 CrossRef Medline
2. Boor PJ, Schoene WC. **Fetal cerebellar tissue associated with a primitive neuro-epithelial tumor in an ovarian teratoma.** *Can J Neurol Sci* 1975;2:139–41 CrossRef Medline
3. Marubayashi T, Matsukado Y. **Intracranial extracerebral brain heterotopia: case report.** *J Neurosurg* 1978;48:470–74 CrossRef Medline
4. Suneson A, Kalimo H. **Myelocystocele with cerebellar heterotopia: case report.** *J Neurosurg* 1979;51:392–96 CrossRef Medline
5. Call NB, Baylis HI. **Cerebellar heterotopia in the orbit.** *Arch Ophthalmol* 1980;98:717–19 CrossRef Medline
6. Sarnat HB, deMello DE, Blair JD, et al. **Heterotopic growth of dysplastic cerebellum in frontal encephalocele in an infant of a diabetic mother.** *Can J Neurol Sci* 1982;9:31–35 CrossRef Medline
7. Ferrer I, Galofré E, Soler T. **Structure of an isolated cerebellum and related nuclei developed within the matrix of a mature ovarian teratoma.** *Childs Nerv Syst* 1986;2:266–69 CrossRef Medline
8. Kudryk BT, Coleman JM, Murtagh FR, et al. **MR imaging of an extreme case of cerebellar ectopia in a patient with Chiari I malformation.** *AJNR Am J Neuroradiol* 1991;12:705–06 Medline
9. Kagotani Y, Takao K, Nomura K, et al. **Intraorbital cerebellar heterotopia associated with Chiari I malformation.** *J Pediatr Ophthalmol Strabismus* 1996;33:262–65 Medline
10. Chung CJ, Castillo M, Fordham L, et al. **Spinal intradural cerebellar ectopia.** *AJNR Am J Neuroradiol* 1998;19:897–99 Medline
11. Takhtani D, Melhem ER, Carson BS. **A heterotopic cerebellum presenting as a suprasellar mass with associated nasopharyngeal teratoma.** *AJNR Am J Neuroradiol* 2000;21:1119–21 Medline
12. Chang AH, Kaufmann WE, Brat DJ. **Ectopic cerebellum presenting as a suprasellar mass in infancy: implications for cerebellar development.** *Pediatr Dev Pathol* 2001;4:89–93 CrossRef Medline
13. Matyja E, Grajkowska W, Marchel A, et al. **Ectopic cerebellum in anterior cranial fossa: report of a unique case associated with skull congenital malformations and epilepsy.** *Am J Surg Pathol* 2007;31:322–25 CrossRef Medline
14. Nagaraj U, Boue DR, Humphrey B, et al. **Ectopic cerebellum in the posterior cranial fossa.** *Pediatr Radiol* 2012;42:1391–94 CrossRef Medline
15. Algin O, Ozmen E. **Ectopic anterior cerebellum (ala lobule centralis).** *Neuroradiol J* 2015;28:278–80 CrossRef Medline
16. Gunbey HP, Bilgici MC, Aslan K, et al. **Ectopic cerebellar tissue of the posterior cranial fossa: diffusion tensor tractography and MR spectroscopy findings.** *Childs Nerv Syst* 2016;32:195–98 CrossRef Medline
17. Kawashima M, Kobayashi M, Ishizawa K, et al. **Ectopic cerebellar tissue in the occipital bone: a case report.** *J Med Case Rep* 2017;11:231 CrossRef Medline
18. Hobohm RE, Codd P, Malinzak MD. **Ectopic cerebellar brain parenchyma.** *Neurographics* 2019;9:285–87 CrossRef
19. De Benedictis A, Rossi-Espagnet MC, Diomedi-Camassei F, et al. **Intraventricular ectopic cerebellum.** *World Neurosurg* 2020;137:158–63 CrossRef Medline
20. Wild E, Sun H, Georgescu MM. **Multiple occipital bone lytic lesions containing ectopic cerebellar parenchyma mimicking neoplasia.** *World Neurosurg* 2020;138:115–19 CrossRef Medline
21. Newman NJ, Miller NR, Green WR. **Ectopic brain in the orbit.** *Ophthalmology* 1986;93:268–72 CrossRef Medline
22. Leto K, Arancillo M, Becker EB, et al. **Consensus paper: cerebellar development.** *Cerebellum* 2016;15:789–828 CrossRef Medline
23. Mitter C. **Teaching case.** *Clinl Neuropathol* 2014;33(2):167

Comparison of Radiologists and Other Specialists in the Performance of Lumbar Puncture Procedures Over Time

 D.R. Johnson,  M.D. Waid,  E.Y. Rula,  D.R. Hughes,  A.B. Rosenkrantz, and  R. Duszak



ABSTRACT

BACKGROUND AND PURPOSE: Lumbar punctures may be performed by many different types of health care providers. We evaluated the percentages of lumbar punctures performed by radiologists-versus-nonradiologist providers, including changes with time and discrepancies between specialties.

MATERIALS AND METHODS: Lumbar puncture procedure claims were identified in a 5% sample of Medicare beneficiaries from 2004 to 2017 and classified by provider specialty, site of service, day of week, and patient complexity. Compound annual growth rates for 2004 versus 2017 were calculated; t test and χ^2 statistical analyses were performed.

RESULTS: Lumbar puncture use increased from 163.3 to 203.4 procedures per 100,000 Medicare beneficiaries from 2004 to 2017 (overall rate, 190.3). Concurrently, the percentage of lumbar punctures performed by radiologists increased from 37.1% to 54.0%, while proportions performed by other major physician specialty groups either declined (eg, neurologists from 23.5% to 10.0%) or were largely unchanged. While radiologists saw the largest absolute increase in the percentage of procedures, the largest relative increase occurred for nonphysician providers (4.2% in 2004 to 7.5% in 2017; +78.6%). In 2017, radiologists performed most procedures on weekdays (56.2%) and a plurality on weekends (38.2%). Comorbidity was slightly higher in patients undergoing lumbar puncture by radiologists ($P < .001$).

CONCLUSIONS: Radiologists now perform most lumbar puncture procedures for Medicare beneficiaries in both the inpatient and outpatient settings. The continuing shift in lumbar puncture responsibility from other specialists to radiologists has implications for clinical workflows, cost, radiation exposure, and postgraduate training.

ABBREVIATIONS: CAGR = compound annual growth rate; CCI = Charlson Comorbidity Index; CPT = Common Procedural Terminology

Lumbar puncture is a vital procedure in the diagnostic evaluation of patients with a wide variety of neurologic conditions. Often performed electively in the diagnosis of inflammatory, neoplastic, and neurodegenerative conditions, lumbar puncture is also frequently performed emergently in patients with suspected central nervous system infection or subarachnoid hemorrhage.¹

Less commonly, the procedure is performed for therapeutic purposes (eg, to remove excess CSF or deliver intrathecal medications). With the introduction of lumbar puncture by Quincke in 1890, these procedures were typically performed without imaging guidance, using only palpation of anatomic landmarks.² Serious adverse complications are uncommon following lumbar puncture regardless of whether fluoroscopic guidance is used.^{3,4} As recently as 1991, only about 10% of lumbar punctures in the Medicare beneficiary population were performed by radiologists.⁵

While lumbar puncture can be successfully performed in many patients without the need for real-time imaging, there are a number of reasons why fluoroscopic guidance may be used. Palpation of anatomic landmarks can be difficult or impossible in patients with obesity, and the rate of obesity is increasing in the US population.⁶ Additionally, older patients are more likely to have spondylotic changes or previous spinal surgery, which can complicate needle access. Other factors that may influence referral of lumbar punctures to radiology include practice momentum, in which

Received July 25, 2020; accepted after revision November 26.

From the Departments of Radiology and Neurology (D.R.J.), Mayo Clinic, Rochester, Minnesota; Harvey L. Neiman Health Policy Institute (M.D.W., E.Y.R., D.R.H.), Reston, Virginia; School of Economics (D.R.H.), Georgia Institute of Technology, Atlanta, Georgia; Department of Radiology (A.B.R.), NYU Langone Health, New York, New York; and Department of Radiology and Imaging Sciences (R.D.), Emory University School of Medicine, Atlanta, Georgia.

Paper previously presented as a Featured Paper at: Scientific Assembly and Annual Meeting of the Radiological Society of North America, November 20 to December 5; Virtual.

Please address correspondence to Derek R. Johnson, MD, Mayo Clinic, 200 First St SW, Rochester, MN, 55905; e-mail: Johnson.derek1@mayo.edu

 Indicates article with online supplemental data.

<http://dx.doi.org/10.3174/ajnr.A7049>

some health care providers are less comfortable across time with an infrequently performed procedure and new providers complete their training without mastering the technique,^{7,8} as well as financial disincentives, given the relatively modest compensation for the procedure.

Although previous research has demonstrated a shift in lumbar puncture volume to radiologists,⁵ several important questions must be answered to better understand the implications of this shift for clinical work flow, costs, and specialist training. First, it is not clear whether this trend has plateaued, continued at the previous pace, or even, as the authors' anecdotal experience suggests, accelerated. If the trend is continuing, in what practice settings is it most pronounced? Furthermore, it is unknown whether factors such as patient complexity or day of the week (ie, weekday versus weekend) influence which specialty performs lumbar punctures, though these questions have been evaluated for other tasks performed both by radiologists and nonradiology providers.⁹⁻¹¹ We evaluated the percentages of lumbar punctures performed by radiologists versus nonradiologist providers, including changes with time and discrepancies among specialties.

MATERIALS AND METHODS

This retrospective study was performed using Medicare administrative claims data in a Health Insurance Portability and Accountability Act-compliant manner, with prior approval by the Institutional Review Board of the American College of Radiology.

The data collection and analysis methods used in this study were similar to those in previous reports.⁹⁻¹¹ The 5% Research Identifiable Files from the Centers for Medicare & Medicaid Services from 2004 through 2017 were acquired under a data use agreement. This dataset includes all final action (Parts A and B) claims associated with a 5% nationally representative random sample of Medicare enrollees, totaling approximately 2.5 million beneficiaries each year, providing details such as patient demographic information, Current Procedural Terminology (CPT) codes associated with all procedures, procedure dates, and the self-reported specialties of health care providers.¹² Patient selection criteria for this study beyond inclusion in the 5% Research Identifiable File dataset from the Centers for Medicare & Medicaid Services included being at least 65 years of age, residence in the United States, enrollment in both Medicare hospital insurance and supplementary medical insurance, and lack of separate health maintenance organization insurance coverage for all 12 months of the year in question.

Lumbar puncture procedures were identified by CPT code 62270 (diagnostic lumbar puncture) and CPT code 62272 (therapeutic lumbar puncture), which were considered collectively in all analyses. All professional and globally billed services corresponding to these lumbar puncture CPT codes during the period of interest were identified within the dataset. CPT modifier codes for imaging guidance were not evaluated due to changes in coding during the study period and on the assumption that use of imaging guidance would be strongly associated with provider specialty. Aborted or unsuccessful lumbar punctures were identified via CPT modifier codes when present and made up only a small fraction of procedures (<3% of total lumbar punctures) and thus were not evaluated

separately. With regard to identifying the specialty of the health care provider performing the lumbar puncture, radiologists were collectively identified using the Health Care Provider Taxonomy codes for diagnostic radiology (taxonomy code 30), interventional radiology (94), and nuclear medicine (36). The category of primary care was defined as internal medicine (11), family practice (8), and general practice (1). Other physician specialty groups were classified by their individual specialty taxonomy codes. Our category of non-physician providers included physician assistants (97), nurse practitioners (50), certified registered nurse anesthetists (43), anesthesia assistants (32), and certified clinical nurse specialists (89). Provider groups performing $\geq 3\%$ of all lumbar punctures between 2004 and 2017 were evaluated individually in each analysis; those specialties performing <3% of lumbar punctures were grouped collectively as "all others." For illustration purposes, only provider groups that performed $\geq 5\%$ of lumbar punctures in each specific subanalysis during the study period as a whole were included individually in figures.

Lumbar puncture use on a per-100,000 beneficiary basis for each year of the analysis period was calculated using a separately acquired Medicare Fee-for-Service beneficiary enrollment file.¹³ Weighted averages for the service volumes per 100,000 beneficiaries and proportions reported were calculated for the entire study sample, using each year's share of the overall patient population as weights, except when otherwise indicated. Due to the structure of the Medicare 5% Research Identifiable Files dataset, absolute procedural counts may be misleading (ie, multiplying the procedure count from the 5% sample by 20 does not accurately approximate the procedure count in the Medicare population as a whole for technical reasons), and the reporting of event rates better reflects use at the population level. Additional statistics evaluated for each specialty group included the percentage of lumbar punctures performed in each year and overall, the percentage of lumbar punctures performed on weekends versus weekdays, the percentage performed in various care settings, and the degree of medical comorbidity of patients undergoing the procedure. χ^2 tests were performed to assess differences in the change in proportion and distribution of lumbar punctures by specialty between 2004 and 2017. Compound annual growth rates (CAGR) were calculated using the 2004 and 2017 proportion of lumbar punctures performed by each specialty. Percentages of lumbar punctures performed by radiology were also calculated on a state-by-state level using the rates for radiology as a percentage of total lumbar puncture rates for a given state.

The Charlson Comorbidity Index (CCI), a weighted index of 19 diseases, is a validated surrogate for patient medical complexity and is widely used by health service researchers working with administrative databases.^{14,15} Each beneficiary's prospective CCI was calculated using Medicare claims during the year before their lumbar puncture procedure following a standard method.¹⁶ As a consequence, CCI information was available only for procedures performed between 2005 and 2017, because prior-year claims data were not available for the first year of the case-ascertainment period. Medicare beneficiaries without any claims filed during the year before the lumbar puncture were, by necessity, excluded from our CCI analysis. The mean CCI was compared for lumbar puncture procedures performed by different specialty groups.

The *t* test was used to evaluate differences in mean CCI by provider group. Analyses were performed using SAS, Version 9.4 software (SAS Institute) and Excel 2016 (Microsoft).

RESULTS

Lumbar Puncture Volume and Performing Specialty

For the entire 2004–2017 period, the total lumbar puncture procedure count in the 5% Research Identifiable Files sample was 37,026, and the overall lumbar puncture use rate was 190.3 per 100,000 Medicare beneficiaries, with annual lumbar puncture use rates varying from a low of 163.3 per 100,000 in 2004 to a high of 203.4 per 100,000 in 2017. When evaluating procedures regardless of year, provider groups performing $\geq 3\%$ of lumbar punctures were radiologists (46.9%), emergency physicians (18.5%), neurologists (14.6%), nonphysician providers (4.6%), neurosurgeons (4.4%), primary care physicians (3.8%), and anesthesiologists (3.6%). The remaining 3.5% of all lumbar

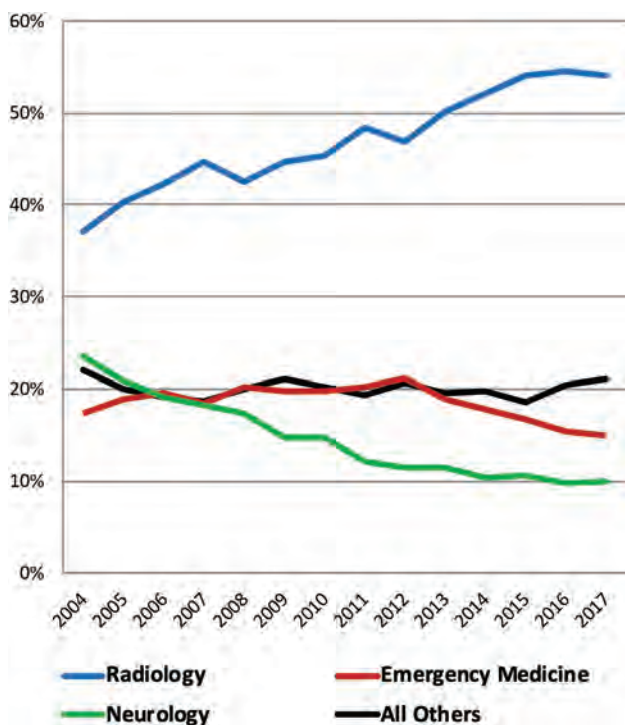


FIG 1. Percentage of lumbar puncture procedures performed by specialty across time.

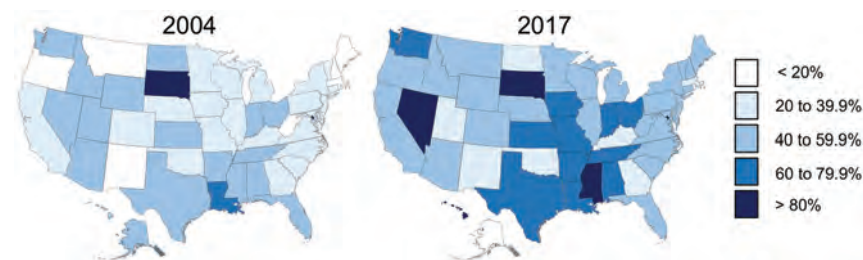


FIG 2. Heat maps by state showing the percentage of lumbar punctures performed by radiologists in 2004 and 2017.

puncture procedures were performed by all other specialties collectively. Annual lumbar puncture counts, rates, and percentages of procedures by provider specialty with time are shown in Online Supplemental Data. Between 0.4% and 1.8% of lumbar punctures performed by radiologists were reported as aborted or incomplete in each year, while among all other providers collectively, the annual rate of procedures reported as aborted or incomplete ranged from 1.0% and 2.7%. Among radiologists, the percentage of lumbar punctures performed by providers with self-reported specialty taxonomy codes for diagnostic radiology varied between 92.0% and 96.0%; for interventional radiology, between 4.0% and 7.6%; and for nuclear medicine, no more than 0.4% in any year. Given that self-identified specialty codes often do not match actual radiologist clinical practice patterns,^{17,18} these radiology provider groups were considered collectively in all subsequent analyses.

The Online Supplemental Data display the percentage of lumbar punctures performed by provider type in each year and associated 2004-versus-2017 CAGR. The percentage of lumbar punctures performed by radiologists rose from a low of 37.1% in 2004 to a high of 54.5% in 2016 before falling slightly to 54.0% in 2017, representing a relative increase of 45.6% between 2004 and 2017. The percentage of lumbar punctures performed by nonphysician providers was from 4.2% in 2004 to 7.5% in 2017, an increase of 78.6%. The provider group with the largest decrease in the percentage of lumbar punctures performed was neurologists, from a high of 23.5% in 2004 to a low of 9.8% in 2016, increasing slightly to 10.0% in 2017, representing a decrease of 57.5% between 2004 and 2017. The increase in radiologist-performed lumbar punctures, for years 2004 and 2017, relative to all other specialties combined was statistically significant ($P < .001$) as was the change in the distribution of lumbar punctures across all specialties ($P < .001$). Figure 1 illustrates trends in the percentages of lumbar punctures performed by the 3 specialties that individually performed $> 5\%$ of procedures during the entire period.

The percentage of lumbar punctures performed by radiologists and the degree of change with time varied by state. Figure 2 shows the percentage of lumbar punctures performed by radiology in each state in 2004 and 2017. Among the 5 most populous states, the percentages of lumbar punctures performed by radiologists in 2004 and 2017 were 33.5% versus 45.9% in California (37.0% increase), 55.2% versus 67.8% in Texas (22.8% increase), 50.4% versus 58.9% in Florida (16.9% increase), 24.7% versus 43.5% in New York (76.1% increase), and 29.3% versus 56.4% in Pennsylvania (92.5% increase).

Lumbar Puncture Volume by Performing Specialty and Site of Service

Across the entire analysis period, most lumbar punctures were performed in the inpatient hospital setting (45.9%), followed by the outpatient setting (30.3%), and then the emergency department (22.7%). Only a small percentage was performed in any other practice setting (1.0%). Figure 3 illustrates the percentages of lumbar punctures performed

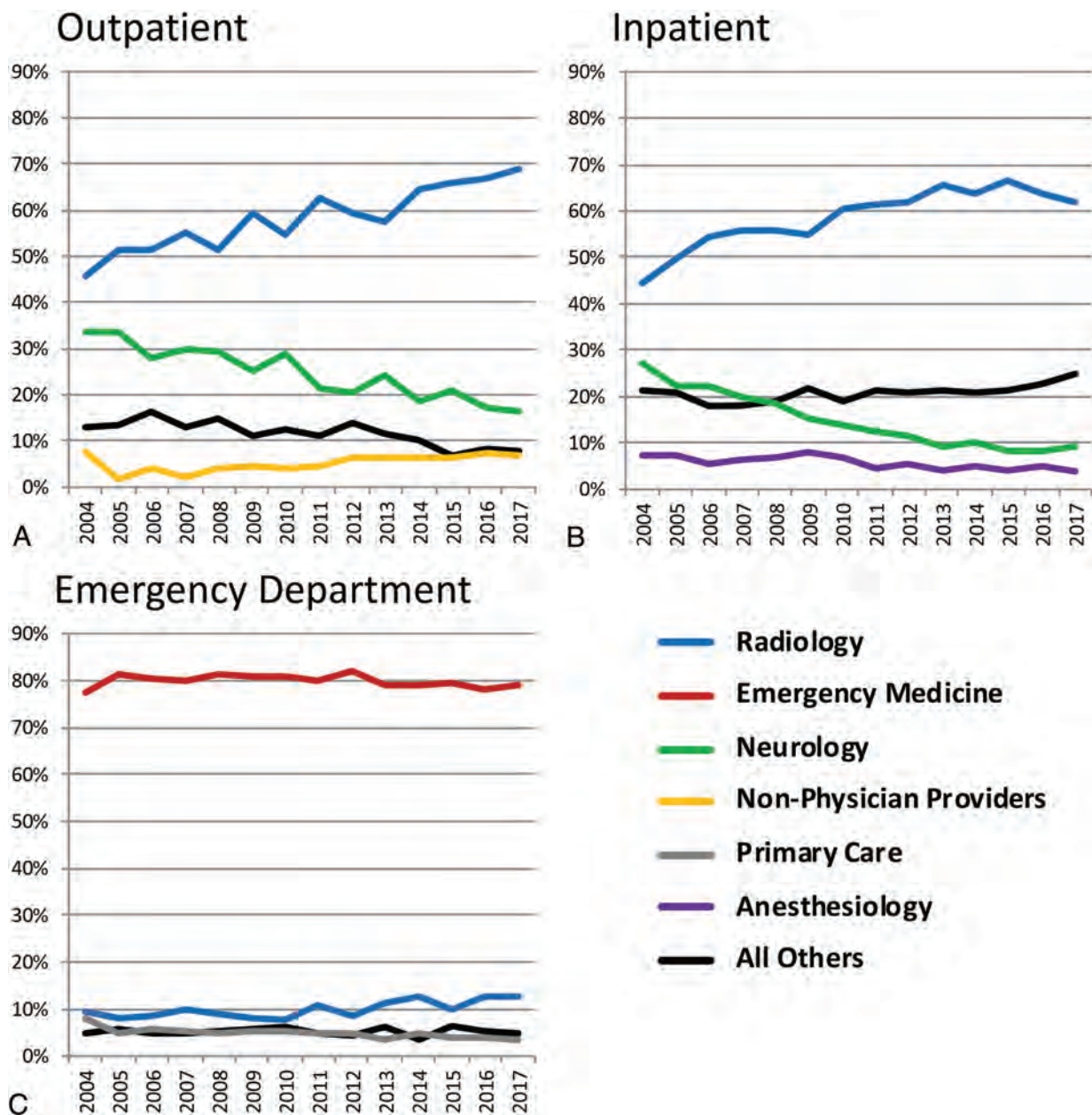


FIG 3. Percentage of lumbar puncture procedures performed by specialty across time in outpatient (A), inpatient (B), and emergency department (C) settings.

by the predominant providers in the inpatient, outpatient, and emergency department settings.

Of lumbar punctures performed in the inpatient hospital setting, radiologists were the most frequent providers in every year, with an increasing proportion from a low of 44.4% in 2004 to a maximum of 66.5% in 2015, before falling slightly to 62.0% in 2017 (2004 versus 2017, CAGR = 2.6%). The share of inpatient lumbar punctures performed by neurologists fell from 27.2% to 9.3% during this period (2004 versus 2017, CAGR = -7.9%). Nonphysician providers performed an increasing share of inpatient lumbar punctures across time, from only 3.1% in 2004 to 8.8% in 2017 (2004 versus 2017, CAGR = 8.4%). In the outpatient setting, radiologists and neurologists were the predominant providers of lumbar punctures, collectively performing between 79.3% and 86.9% in each year. However,

the percentage of outpatient lumbar punctures performed by radiologists increased from a low of 45.7% in 2004 to a high of 68.9% in 2017 (2004 versus 2017, CAGR = 3.2%), while the percentage performed by neurologists fell from a high of 33.7% to a low of 16.4% during this same interval (2004 versus 2017, CAGR = -5.4%). Lumbar punctures performed in the emergency department were predominantly performed by emergency medicine physicians, who performed between 77.4% and 82.0% of the emergency department lumbar punctures in each year.

Lumbar Puncture Volume by Performing Specialty and Day of Week

For the entire period, most lumbar punctures (86.8%) were performed on weekdays, with use rates of 165.1 per 100,000 Medicare

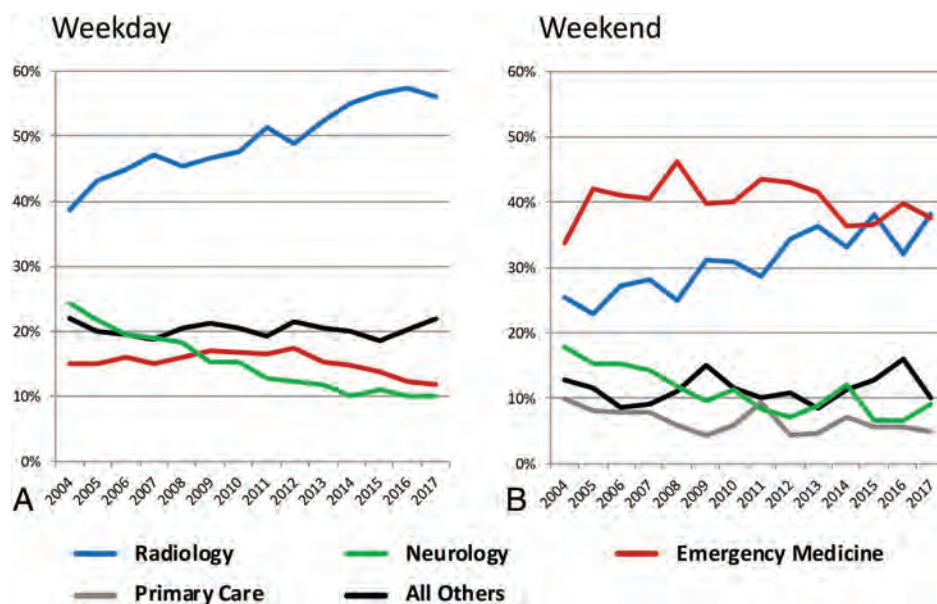


FIG 4. Percentage of lumbar puncture procedures performed by specialty across time on weekdays (A) and weekends (B).

beneficiaries on weekdays versus 25.2 per 100,000 on weekends. The overall rates of lumbar punctures performed by radiologists were 81.5 per 100,000 Medicare beneficiaries on weekdays and 7.8 per 100,000 on weekends, while the rates performed by all other specialties collectively were 83.6 and 17.5 per 100,000, respectively. Emergency medicine physicians had the smallest relative decline in lumbar puncture procedure rates on weekends, performing 25.1 per 100,000 on weekdays to 10.2 per 100,000 on weekends. Figure 4 shows the distribution of weekday and weekend lumbar punctures performed by different specialty groups across time. The percentage of weekday lumbar punctures performed by radiologists increased from 38.7% in 2004 to 56.2% in 2017 (2004 versus 2017, CAGR = 2.9%). Neurologists saw the greatest coinciding decrease in the percentage of weekday lumbar punctures, from 24.3% in 2004 to 10.1% in 2017 (2004 versus 2017, CAGR = -6.6%). Of the 13.2% of lumbar punctures performed on weekends, emergency physicians performed a plurality of procedures for the 2004 through 2017 period as a whole (40.3%). However, the percentage of weekend lumbar punctures performed by radiologists rose from 25.5% to 38.2% during this period (2004 versus 2017, CAGR = 3.1%), with radiologists performing the plurality in 2015 and 2017.

Lumbar Puncture Volume by Performing Specialty and Patient Complexity

A CCI could be determined for >99% of the patient group in each year, 2005 through 2017. The mean patient CCI during this entire period for lumbar punctures performed by radiologists was 2.6 [SD, 2.8], modestly but statistically significantly higher than the mean CCI of 2.4 [SD, 2.6] in patients who underwent lumbar punctures performed by all nonradiology providers collectively ($P < .001$). Mean CCI figures for individual nonradiologist provider groups were 2.3 [SD, 2.5] for neurologists, 2.2 [SD, 2.5] for neurosurgeons, 2.4 [SD, 2.6] for emergency medicine physicians, 2.6 [SD, 2.8] for nonphysician providers, 2.5 [SD, 2.6] for primary care physicians, 2.4 [SD, 2.6] for anesthesiologists, and 2.7 [SD, 2.8] for all other providers.

The Online Supplemental Data report the mean patient CCI for lumbar punctures performed by radiologists versus all other specialties across time and associated 2005-versus-2017 CAGR. The mean CCI of patients undergoing lumbar puncture by radiologists increased from 2.0 in 2005 to 3.1 in 2017. While the mean CCI of patients undergoing lumbar punctures by nonradiologists also increased from 1.8 to 2.9 during the period, the mean CCI score of patients undergoing lumbar puncture by radiologists was significantly higher ($P < .05$) overall and in 9 of these 13 years individually.

DISCUSSION

In recent years, radiologists have become majority providers of lumbar punctures for Medicare Fee-for-Service beneficiaries, and the percentage of lumbar punctures performed by radiologists has increased in almost every practice setting and patient group. A dramatic shift in lumbar puncture procedures in the Medicare population to radiologists had been previously demonstrated using aggregate claims data, which reported that in 1991, only 10% of lumbar punctures were performed by radiologists, increasing to >45% by 2011.⁵ The present study uses a different and more detailed patient encounter-level Medicare dataset with procedural information through 2017 and confirms that this trend has continued. It additionally provides insight into discrepancies between specialty in factors such as place of service, day of week, and patient comorbidity.

Potential causes for the shift in lumbar punctures to radiology in Medicare beneficiaries can be conceptually subdivided into patient-level and provider-level factors. Patient-level factors include issues that impact the feasibility of lumbar puncture or increase the need for imaging guidance, including but not limited to patient habitus, scoliosis or spondylotic changes, and other medical comorbidities. Provider-level factors are issues that impact the ability or desire of medical practitioners to perform lumbar punctures themselves rather than refer the procedure to other providers. Provider-

level factors include practice environment, which may or may not be conducive to bedside procedures, personal ability or confidence in performing lumbar punctures, and economic considerations.

In this study, the findings regarding lumbar punctures performed in the emergency department setting may provide insight into the relative importance of patient-specific and provider-specific factors in influencing what specialty group performs the procedure. In the emergency department, emergency medicine physicians performed most lumbar punctures, and this proportion remained steady during the study. However, there was minimal difference in the CCI between patients undergoing lumbar punctures by emergency medicine physicians and radiologists. While the CCI imperfectly captures patient-level factors that may make lumbar puncture technically challenging, the modest difference in comorbidity supports the hypothesis that lesser case complexity is not the primary factor behind the low proportion of lumbar punctures performed by radiology in the emergency department. Thus, the high percentage of emergency department lumbar punctures performed by emergency medicine physicians suggests that the procedure is technically feasible without fluoroscopic guidance in many patients, even within a typically older Medicare beneficiary population. The logical implication is thus that the shift of lumbar punctures to radiology from other specialties in the outpatient and hospital inpatient practice settings is likely due to provider-related factors rather than technical necessity.

If lumbar puncture practice is driven by provider-level factors, it is possible that the trend could reverse if those factors change. However, we believe that the chance of this happening decreases with time. For example, if extrinsic factors regularly interfere with nonradiology providers performing lumbar punctures, across time, those same providers may be less inclined to perform lumbar punctures due to limited recent experience. In surveys conducted by the American College of Physicians, 73% of internal medicine physician respondents in 1986 reported that performing lumbar punctures was part of their clinical practice, with a median of 5 lumbar punctures performed in the year preceding the survey; by 2004, only 26% of respondents performed lumbar punctures, and even this group reported a decrease in case numbers, to a median of 3 per year.¹⁹ In the present study, by 2017, just 2.6% of lumbar punctures in the Medicare population were performed by primary care specialties collectively, despite internists and family and general practitioners representing by far the largest physician specialty groups in the United States, illustrating the long-term consequences of these practice trends.²⁰

Ultimately, the determinant of whether specialties other than radiology and emergency medicine will continue to perform lumbar punctures in a meaningful capacity will be specialty training. If residents do not become facile with lumbar puncture during training, either because of expectations that the procedure should be performed by others or because their supervising faculty are themselves uncomfortable performing and teaching the procedure,^{8,21} they are not likely to develop the skill thereafter. Neither neurology residency nor internal medicine residency training have a specific Accreditation Council for Graduate Medical Education–mandated number of lumbar punctures necessary for graduation, so it is likely that expectations vary greatly among programs. Furthermore, in internal medicine certification, the American Board of Internal

Medicine no longer mandates demonstration of procedural skill for lumbar punctures, but simply, the cognitive competence of understanding procedural indications, technique, complication recognition and management, and other information needed to obtain informed consent.²² As might be expected, a recent publication found that 84% of lumbar punctures performed on internal medicine service inpatients at a single tertiary academic medical center were performed by radiology or a dedicated hospital procedural service rather than by the primary team.²³ To the authors' knowledge, no similar studies have been published evaluating the performance of lumbar punctures on inpatients by neurology services.

The potential for improvement in resident procedural training is well-recognized, and efforts are underway to improve trainee access to procedure opportunities.^{24,25} In fact, some movement in this direction may already be occurring. In the hospital inpatient setting, the trend toward performance of lumbar punctures by radiology appears to have reached a plateau or even reversed slightly, with the proportion of lumbar punctures performed by radiology decreasing in 2016 and 2017. While future research will be needed to establish whether this reversal is a durable trend, it could plausibly be explained by some of the measures noted above.

Aside from radiologists, the only provider group that performed an increasing percentage of lumbar punctures across time was nonphysician providers. Although they performed only 7.5% of lumbar punctures in 2017, the most recent year of analysis, that was sufficient to make them the fourth most common provider group overall. Medicare claims by nonphysician providers are insufficient to determine their practice affiliations, and it is unclear what proportion are working within radiology groups to perform imaging-guided lumbar punctures versus performing bedside lumbar punctures in other settings. Increased collaboration between radiologists and nonphysician providers may represent a potential strategy for dealing with the demand for lumbar puncture.

Several potentially disadvantageous consequences of the shift in lumbar puncture performance to radiology merit discussion. From a patient care standpoint, it is often desirable to obtain CSF as expeditiously as possible, such as before or soon after the initiation of antibiotics for suspected bacterial meningitis or when ruling out subarachnoid hemorrhage. When one accounts for logistical considerations such as procedure scheduling, patient transportation, and fluoroscopy room preparation, even the most efficient radiology service is unlikely to rival the speed with which CSF can be collected at the bedside by an experienced provider. From a health system use-of-resources perspective, a lumbar puncture under fluoroscopic guidance requires the presence of both a radiologist and a radiologic technologist as well as use of a fluoroscopy suite, all increasing the per-procedure cost relative to bedside lumbar puncture. This cost is undoubtedly justified when lumbar puncture cannot be successfully performed without imaging, but may not be appropriate in all circumstances. Furthermore, the diversion of radiologists from other tasks to lumbar punctures carries significant opportunity cost. As of 2020, performing a lumbar puncture with imaging guidance yields 1.73 work-relative value units, less than that for interpretation of an MR imaging of the brain with and without contrast, which yields 2.29 work-relative value units. Last, although the radiation dose to the patient and provider associated with a lumbar puncture is

generally quite low, we must ask if even this minimal dose is justified by the corresponding benefits.²⁶

The primary limitations of this study are that it is restricted to the Medicare beneficiary population and that the administrative Medicare dataset does not contain all clinical variables that would be of interest. It is possible that the observed trend toward increased lumbar puncture performance by radiologists is less pronounced in younger adults, and particularly in children. In the pediatric population, lumbar punctures are often performed by pediatricians, though even in this group, the reported success rate of lumbar punctures is variable.^{27,28} With regard to potentially relevant information not fully captured by the Medicare dataset, patient-level variables such as body mass index, the presence of scoliosis, and history of spine surgery would be indicators of lumbar puncture difficulty and would likely be superior to the CCI for this purpose. Additionally, aborted or incomplete lumbar punctures are likely under-reported, so the true rates of procedural success by specialty and the proportion of patients in whom lumbar puncture was attempted by other services before radiology referral cannot be determined. In light of these limitations, future studies in other patient populations will be necessary to fully understand practice patterns in lumbar puncture performance.

CONCLUSIONS

Radiologists now perform most lumbar punctures in the Medicare beneficiary population in the United States. Even if the long-term trend toward steadily increasing performance of lumbar puncture by radiologists were to plateau, the US Census Bureau projects that the number of adults 65 years of age and older, the demographic group included in this study, will increase from approximately 56 million in 2020 to almost 95 million by 2060.²⁹ Barring unforeseen changes in medical practice, radiologists will continue to be asked to fill this growing clinical void. In preparation, it will be necessary for radiology residency programs to produce graduates able to perform this vital service without the need for additional fellowship training. Furthermore, radiology practices will need to consider how to appropriately triage lumbar puncture requests from referring providers, and they may need to develop operational infrastructures to perform lumbar punctures in ever-increasing numbers.

ACKNOWLEDGMENTS

The authors thank Desiree J. Lanzino, PhD, for her assistance in figure creation.

Disclosures: Danny R. Hughes—RELATED: Grant: Neiman Health Policy Institute.* Andrew B. Rosenkrantz—RELATED: Grant: Harvey L. Neiman Health Policy Institute.* Richard Duszak—RELATED: Grant: Harvey L. Neiman Health Policy Institute*. UNRELATED: Stock/Stock Options: stock shareholder medical advisor for Ethos Medical. *Money paid to the institution.

REFERENCES

1. Fishman RA. *Cerebrospinal Fluid in Diseases of the Nervous System*. Saunders; 1992
2. Frederiks JA, Koehler PJ. **The first lumbar puncture**. *J Hist Neurosci* 1997;6:147–53 CrossRef Medline

3. Evans RW. **Complications of lumbar puncture**. *Neurol Clin* 1998;16:83–105 CrossRef Medline
4. Rodriguez D, Branstetter BF, Agarwal V, et al. **JOURNAL CLUB: incidence of complications following fluoroscopically guided lumbar punctures and myelograms**. *AJR Am J Roentgenol* 2016;206:20–25 CrossRef Medline
5. Kroll H, Duszak R Jr, Nsiah E, et al. **Trends in lumbar puncture over 2 decades: a dramatic shift to radiology**. *AJR Am J Roentgenol* 2015;204:15–19 CrossRef Medline
6. Wang Y, Beydoun MA. **The obesity epidemic in the United States: gender, age, socioeconomic, racial/ethnic, and geographic characteristics—a systematic review and meta-regression analysis**. *Epidemiol Rev* 2007;29:6–28 CrossRef Medline
7. Allard M, Jelovac I, Leger PT. **Treatment and referral decisions under different physician payment mechanisms**. *J Health Econ* 2011;30:880–93 CrossRef Medline
8. Vaisman A, Cram P. **Procedural competence among faculty in academic health centers: challenges and future directions**. *Acad Med* 2017;92:31–34 CrossRef Medline
9. Prabhakar AM, Gottumukkala RV, Wang W, et al. **Day of week, site of service, and patient complexity differences in venous ultrasound interpreted by radiologists versus nonradiologists**. *J Am Coll Radiol* 2018;15:1698–1703 CrossRef Medline
10. Sharp P, Harkey P, Wang W, et al. **Day of week, site of service, and patient complexity disparities in musculoskeletal MRI interpretations by radiologists versus nonradiologists**. *AJR Am J Roentgenol* 2018;211:827–30 CrossRef Medline
11. Gottumukkala RV, Prabhakar AM, Hemingway J, et al. **Disparities over time in volume, day of the week, and patient complexity between paracentesis and thoracentesis procedures performed by radiologists versus those performed by nonradiologists**. *J Vasc Interv Radiol* 2019;30:1769–78 CrossRef Medline
12. Rosenkrantz AB, Hughes DR, Duszak R, et al. **Medicare Claims Data Resources: a primer for policy-focused radiology health services researchers**. *J Am Coll Radiol* 2017;14:1538–44 CrossRef Medline
13. Harvey L. Neiman Health Policy Institute. **Medicare Beneficiary Enrollment Numbers: A Research Tool**. <https://neimanhpi.org/medicare-beneficiary-enrollment-tool>. Accessed November 20, 2020
14. Hwang J, Chow A, Lye DC, et al. **Administrative data is as good as medical chart review for comorbidity ascertainment in patients with infections in Singapore**. *Epidemiol Infect* 2016;144:1999–2005 CrossRef Medline
15. Stavem K, Hoel H, Skjaker SA, et al. **Charlson comorbidity index derived from chart review or administrative data: agreement and prediction of mortality in intensive care patients**. *Clin Epidemiol* 2017;9:311–20 CrossRef Medline
16. Quan H, Sundararajan V, Halfon P, et al. **Coding algorithms for defining comorbidities in ICD-9-CM and ICD-10 administrative data**. *Med Care* 2005;43:1130–39 CrossRef Medline
17. Balthazar P, Hawkins CM, Vijayasarithi A, et al. **Current clinical practice patterns of self-identified interventional radiologists**. *AJR Am J Roentgenol* 2018;210:663–68 CrossRef Medline
18. Balthazar P, Schuster DM, Grady EE, et al. **Current clinical practice patterns of self-identified nuclear medicine specialists**. *AJR Am J Roentgenol* 2018;211:978–85 CrossRef Medline
19. Wigton RS, Alguire P; American College of Physicians. **The declining number and variety of procedures done by general internists: a resurvey of members of the American College of Physicians**. *Ann Intern Med* 2007;146:355–60 CrossRef Medline
20. Colleges American Academy of Oral Medicine. **Physician Specialty Data Report**. <https://www.aamc.org/data-reports/workforce/interactive-data/active-physicians-us-doctor-medicine-us-md-degree-specialty-2015>. Accessed May 15, 2020
21. Mourad M, Kohlwes J, Maselli J, et al; MERN Group. **Supervising the supervisors: procedural training and supervision in internal medicine residency**. *J Gen Intern Med* 2010;25:351–56 CrossRef Medline
22. Duffy FD, Holmboe ES. **What procedures should internists do?** *Ann Intern Med* 2007;146:392–93 CrossRef Medline

23. Kay C, Wozniak EM, Szabo A, et al. **Examining invasive bedside procedure performance at an academic medical center.** *South Med J* 2016;109:402–07 CrossRef Medline
24. Lenhard A, Moallem M, Marrie RA, et al. **An intervention to improve procedure education for internal medicine residents.** *J Gen Intern Med* 2008;23:288–93 CrossRef Medline
25. Gorgone M, McNichols B, Lang VJ, et al. **The procedure coordinator: a resident-driven initiative to increase opportunity for inpatient procedures.** *J Grad Med Educ* 2018;10:583–86 CrossRef Medline
26. Brook AD, Burns J, Dauer E, et al. **Comparison of CT and fluoroscopic guidance for lumbar puncture in an obese population with prior failed unguided attempt.** *J Neurointerv Surg* 2014;6:324–28 CrossRef Medline
27. Auerbach MA, White ML, Bhargava S, et al. **Are graduating pediatric residents prepared to perform infant lumbar punctures? A multi-institutional descriptive study.** *Pediatr Emerg Care* 2018;34:116–20 CrossRef Medline
28. Baxter AL, Fisher RG, Burke BL, et al. **Local anesthetic and stylet styles: factors associated with resident lumbar puncture success.** *Pediatrics* 2006;117:876–81 CrossRef Medline
29. United States Census Bureau. **2017 National Population Projections Tables: Main Series.** <https://www.census.gov/data/tables/2017/demo/popproj/2017-summary-tables.html>. Accessed June 20, 2020

Acute Stroke Imaging in Transfer Patients Who Received Recent Intravenous Iodinated Contrast at an Outside Facility: An Unrecognized Problem That Deserves More Attention

We read with great interest the recent article by Copelan et al¹ titled, “Recent Administration of Iodinated Contrast Renders Core Infarct Estimation Inaccurate Using RAPID Software.” In a cohort of patients with acute stroke who received recent intravenous iodinated contrast as part of another imaging study, the authors demonstrated that the rapid processing of perfusion and diffusion (RAPID; iSchemaView) CTP platform may underestimate the core infarct size. This article importantly highlights inherent challenges present in interpreting scans for patients with acute stroke transferred from outside facilities who underwent recent CT imaging with iodinated contrast.

We experienced a different challenge while interpreting scans for transferred patients with stroke who also received recent iodinated contrast at the outside facility.² We observed parenchymal hyperdensities, likely related to contrast enhancement of acute infarcts. These parenchymal hyperdensities limited our ability to confidently exclude intracranial hemorrhage, and we described using dual-layer spectral imaging to address this problem. Nevertheless, these challenges collectively bring to light the phenomenon of recent intravenous contrast administration hindering interpretation of acute stroke examinations after a patient’s arrival to a tertiary care center for potential mechanical thrombectomy. Despite this, sparse literature exists to investigate these issues. As the authors have shown that recent contrast administration may underestimate the core infarct size with the RAPID software, we

postulate that a similar phenomenon may result in overestimation of the calculated ASPECTS.

Evaluation for intracranial hemorrhage, ASPECTS decay, and perfusion abnormalities is paramount for appropriate patient selection for mechanical thrombectomy after interfacility transfer. Administration of contrast material at the first facility may limit this ability at the recipient facility. We thank the authors for their important work, and we feel that additional studies are essential to address these issues.

REFERENCES

1. Copelan AZ, Smith ER, Drocton GT, et al. **Recent administration of iodinated contrast renders core infarct estimation inaccurate using RAPID software.** *AJNR Am J Neuroradiol* 2020;41:2235–42 CrossRef Medline
2. Gulko E, Ali S, Gomes W, et al. **Differentiation of hemorrhage from contrast enhancement using dual-layer spectral CT in patients transferred for acute stroke.** *Clin Imaging* 2021;69:75–78 CrossRef Medline

✉ E. Gulko

✉ S. Ali

✉ J. Schefflein

✉ H. Mehta

✉ W. Gomes

Division of Neuroradiology, Department of Radiology
Westchester Medical Center
Valhalla, New York

<http://dx.doi.org/10.3174/ajnr.A7041>

Notification of a Voluntary Product Recall for Software Used in a Prior Published Article

On December 14, 2020, a voluntary product recall was issued for the Neuroreader Medical Image Processing Software that we utilized in our article “Improved Detection of Subtle Mesial Temporal Sclerosis: Validation of a Commercially Available Software for Automated Segmentation of Hippocampal Volume,”¹ published in the March 2019 issue of *AJNR*. The recall was issued because the normative data base used for demographic correction of the postprocessed volumes was produced from MRIs performed on 218 healthy patients, instead of the 231 MRIs expected by the FDA. This normative data base was used to calculate the proprietary Neuroreader Index that we reported as a secondary outcome in our research. The normative data did not affect our main outcome variable of segmented hippocampal volume as a percentage of intracranial volume.

We believe that the results of our research are still valid, as only small changes in normative values would be expected when

adding 13 additional healthy brains to the 218 already in the data base. Furthermore, only the results of our secondary outcome could be affected. Nevertheless, we felt obligated to immediately inform the editorial staff of the *AJNR* and your readers of this unfortunate event. The latest version of the Neuroreader software has corrected this flaw.

REFERENCE

1. Mettenburg JM, Branstetter BF, Wiley C, et al. **Improved detection of subtle mesial temporal sclerosis: validation of a commercially available software for automated segmentation of hippocampal volume.** *AJNR Am J Neuroradiol* 2019;40:440–45 CrossRef Medline

 **J.M. Mettenburg**

Department of Radiology
University of Pittsburgh School of Medicine
Pittsburgh, Pennsylvania

<http://dx.doi.org/10.3174/ajnr.A7063>

Improving Access to Fast MRI for Emergent Shunt Evaluation

The use of rapid MRI techniques to avoid CT in patients with indwelling shunt catheters is a well-known means of reducing radiation exposure to a vulnerable population. Fast MRIs of the brain avoid the risks related to sedation, can be accomplished quickly, and provide a sensitive means to assess ventricular size. In 2012, Koral et al¹ estimated that the use of fast MRI of the brain instead of standard CT could prevent 1 excess fatal cancer per 97 pediatric patients.

Ordering providers and radiology departments may fail to promote the use of this technique for patients requiring emergent shunt evaluation despite this benefit, as CT is simply faster and more convenient. At the institution described by Koral et al,¹ 86% of the 679 fast brain MRIs ordered for ventricular size evaluation in 2016 were performed on an outpatient basis, while only 3% were ordered by the emergency department, and 22 patients received at least 5 head CTs for shunt evaluation during the year. During the same year, the emergency department requested 71% of the 502 head CTs performed for shunt evaluation, even though 90% of the CTs were ordered during a shift when an MRI technologist was available on site. This means that the cancer-reducing benefit of the fast brain MRI was rarely realized by patients presenting to the emergency department with a need for shunt evaluation.

While it is unlikely that fast MRIs for ventricle evaluation will replace CT entirely, radiologists should ensure that providers are

aware of the utility of rapid MRI techniques and encourage workflow strategies that allow for fast MRI to be performed emergently, especially because these patients are often subject to multiple imaging examinations to evaluate these devices. This may serve as an opportunity to create MRI volume overnight, which can justify staffing of MRI personnel during an era in which hospitals are increasingly demanding extended coverage for radiology services. If the fast MRI is the most appropriate test for a patient, and the patient needs the examination emergently, then it seems reasonable to ensure that the patient has access to that examination.

REFERENCE

1. Koral K, Blackburn T, Bailey AA, et al. **Strengthening the argument for rapid brain MR imaging: estimation of reduction in lifetime attributable risk of developing fatal cancer in children with shunted hydrocephalus by instituting a rapid brain MR imaging protocol in lieu of head CT.** *AJNR Am J Neuroradiol* 2012;33:1851–54 CrossRef Medline

© C.M. Pfeifer

© N. Karbhari

Department of Radiology
University of Texas Southwestern Medical Center
Dallas, Texas

<http://dx.doi.org/10.3174/ajnr.A7065>